AD-A059 834 ARMY MATERIALS AND MECHANICS RESEARCH CENTER WATERTO--ETC F/G 20/11
PROCEEDINGS OF THE ARMY SYMPOSIUM ON SOLID MECHANICS, 1978 - CA--ETC(U)
SEP 78

UNCLASSIFIED AMMRC-MS-78-3

NL

1 OF 4
AD
A059834



AD A059834

DDC FILE COPY

12 SC
AD29735
1976

AMMRC MS 78-3

AD

LEVEL II

PROCEEDINGS OF THE ARMY SYMPOSIUM ON SOLID MECHANICS, 1978 - CASE STUDIES ON STRUCTURAL INTEGRITY AND RELIABILITY

DDC
RECEIVED
OCT 11 1978
F

September 1978

Approved for public release; distribution unlimited.

ARMY MATERIALS AND MECHANICS RESEARCH CENTER
Watertown, Massachusetts 02172

78 10 10 026

The findings in this report are not to be construed as an official Department of the Army position, unless so designated by other authorized documents.

Mention of any trade names or manufacturers in this report shall not be construed as advertising nor as an official endorsement or approval of such products or companies by the United States Government.

DISPOSITION INSTRUCTIONS

Destroy this report when it is no longer needed.
Do not return it to the originator.

UNCLASSIFIED

SECURITY CLASSIFICATION OF THIS PAGE (When Data Entered)

REPORT DOCUMENTATION PAGE

READ INSTRUCTIONS BEFORE COMPLETING FORM

1. REPORT NUMBER: AMMRC-MS-78-3	2. GOVT ACCESSION NO.
3. RECIPIENT'S CATALOG NUMBER	
4. TITLE (and Subtitle): Proceedings of the Army Symposium on Solid Mechanics, 1978 - Case Studies on Structural Integrity and Reliability	5. TYPE OF REPORT & PERIOD COVERED: Final Report
6. PERFORMING ORG. REPORT NUMBER	
7. AUTHOR(s)	8. CONTRACT OR GRANT NUMBER(s)
9. PERFORMING ORGANIZATION NAME AND ADDRESS: Army Materials and Mechanics Research Center, Watertown, Massachusetts 02172, DRXMR-T	10. PROGRAM ELEMENT, PROJECT, TASK AREA & WORK UNIT NUMBERS
11. CONTROLLING OFFICE NAME AND ADDRESS: U. S. Army Materiel Development and Readiness Command, Alexandria, Virginia 22333	12. REPORT DATE: September 1978 13. NUMBER OF PAGES: 386
14. MONITORING AGENCY NAME & ADDRESS(if different from Controlling Office)	15. SECURITY CLASS. (of this report): Unclassified 15a. DECLASSIFICATION/DOWNGRADING SCHEDULE

16. DISTRIBUTION STATEMENT (of this Report)

Approved for public release; distribution unlimited.

17. DISTRIBUTION STATEMENT (of the abstract entered in Block 20, if different from Report)

12) 365 p.

18. SUPPLEMENTARY NOTES

19. KEY WORDS (Continue on reverse side if necessary and identify by block number)

(See Reverse Side)

20. ABSTRACT (Continue on reverse side if necessary and identify by block number)

Proceedings of the Army Symposium on Solid Mechanics, 1978 - Case Studies on Structural Integrity and Reliability, held at Bass River (Cape Cod), MA 3-5 October 1978

403 705

DD FORM 1 JAN 73 1473 EDITION OF 1 NOV 65 IS OBSOLETE

UNCLASSIFIED

SECURITY CLASSIFICATION OF THIS PAGE (When Data Entered)

Block No. 19

KEY WORDS

Adhesive Bonding
Aircraft
Assessment
Bearings
Blast
Catapults
Cold Working
Composite Materials
Cracks
Crack Propagation
Cycles
Damage
Defects (Materials)
Elastomers
Engines
Epoxy Resins
Explosives
Failure
Fasteners
Fatigue (Mechanics)
Fracture (Mechanics)
Fragmentation
Fuselages
Fuzes (Ordnance)
Gages
Graphite
Guided Missiles
Helicopters
Impact
Intensity
Joining
Joints
Loads (Forces)
Materials
Mechanics
Moiré Effects
Nondestructive Testing
Ordnance
Photoelasticity
Predictions
Probability
Projectiles
Quality Assurance
Reliability
Risk
Rotor Blades
Rotors
Sensitivity
Shelters
Sizes (Dimensions)
Spoilers
Statistics
Strain (Mechanics)
Strength (General)
Strength (Mechanics)
Stress Concentration
Stresses
Structural Properties
Structural Response
Structures
Survival (General)
Turbines
Vulnerability
Wings

PREFACE

The Army Symposium on Solid Mechanics, 1978 was the sixth in a series of biennial meetings sponsored by the U.S. Army Materials and Mechanics Research Center in Watertown, Massachusetts. The first conference was held in 1968 on the general theme of Solid Mechanics. Subsequent meetings were held on such themes as: Lightweight Structures (in 1970), Ballistic Problems (in 1972), Structural Joints (in 1974) and Failure of Composite Materials (in 1976). Starting in 1974, a Work-In-Progress Session was incorporated into these conferences (called Ongoing Case Studies Session in this 1978 meeting). These sessions are comprised of a series of brief presentations and discussions of current, but not necessarily complete, research relating to the theme of the meeting. Abstracts of these presentations are published in a companion document to the regular proceedings. The transactions of earlier symposia are listed on page iv of this document. Abstracts of ongoing case studies presented at this 1978 symposium are published in AMMRC MS 78-4, dated September 1978.

Participation in these symposia has broadened with time. Starting with the 1972 meeting, papers have been solicited from in-house and contract researchers and designers for the Navy, Air Force and other Government Agencies, in addition to those for the Army. Beginning with the 1974 meeting, the Symposium Committee was expanded to include representation from the Navy, Air Force, NASA and the U. S. Army Corps of Engineers. These expansions recognize that many mechanics research and/or design problems are not unique to a single service or government agency.

Essentially, these symposia are a vehicle for enhancing the responsiveness of the mechanics research efforts for the design of advanced military systems. They also facilitate communications and coordination between and among researchers and designers having common military theme interests whether they work for a government service or agency, industry, or at a university or research institute. No endeavor of the magnitude of this 1978 symposium could have been successfully conducted without the enthusiastic cooperation and support of many individuals and organizations. We gratefully acknowledge:

Headquarters, U. S. Army Materiel Development and Readiness Command for their support and cooperation in this undertaking.

The many authors, participants, Invited Speakers who made the presentations in Session I, Session Chairmen and members of the Panel Session who made this conference such a success.

The manuscript reviewers from universities, industry and government organizations, for their diligence in carrying out a thankless task.

Richard S. Hartenberg, Professor of Mechanical Engineering (Emeritus) of The Technology Institute, Northwestern University, who delivered a delightful and very interesting historic type Keynote Address on "Design: Right, Risk or Disaster."

And finally, the clerical staff of the Mechanics Research Laboratory and the Technical Reports Office of AMMRC for their unflagging efforts in the preparation and printing of numerous symposium materials.

PREVIOUS DOCUMENTS IN THIS SYMPOSIA SERIES*

Proceedings of the Army Symposium on Solid Mechanics, 1968,
AMMRC MS 68-09, September 1968, AD 675 463

Proceedings of the Army Symposium on Solid Mechanics, 1970 -
Lightweight Structures,
AMMRC MS 70-5, December 1970, AD 883 455L

Proceedings of the Army Symposium on Solid Mechanics, 1972 -
The Role of Mechanics in Design - Ballistic Problems,
AMMRC MS 73-2, September 1973, AD 772 827

Proceedings of the Army Symposium on Solid Mechanics, 1974:
The Role of Mechanics in Design - Structural Joints,
AMMRC MS 74-8, September 1974, AD 786 543

Work-In-Progress Presented at the Army Symposium on Solid Mechanics, 1974:
The Role of Mechanics in Design - Structural Joints,
AMMRC MS 74-9, September 1974, AD 786 524

Stress Analysis of Structural Joints and Interfaces -
A Selective Annotated Bibliography
by M. M. Murphy and E. M. Lenoe,
AMMRC MS 74-10, September 1974, AD 786 520

Proceedings of the Army Symposium on Solid Mechanics, 1976 -
Composite Materials: The Influence of Mechanics of Failure on Design,
AMMRC MS 76-2, September 1976, AD A029 735

Work-In-Progress Presented at the Army Symposium on Solid Mechanics, 1976 -
Composite Materials: The Influence of Mechanics of Failure on Design,
AMMRC MS 76-3, September 1976, AD A029 736

*These documents may be ordered from the National Technical Information Service, U.S. Department of Commerce, Springfield, VA 22161

SYMPOSIUM COMMITTEE

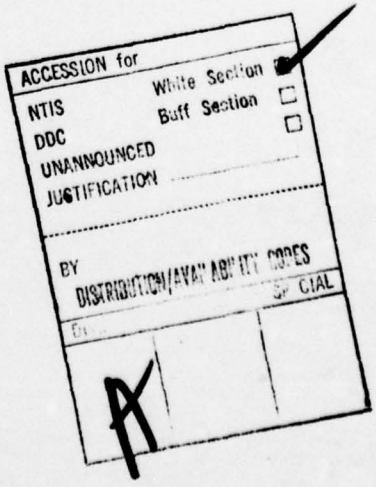
R. SHEA, Chairman, AMMRC
E. M. LENOE, Vice Chairman, AMMRC
R. J. MORRISSEY, Coordinator, AMMRC

TECHNICAL PAPERS AND PROGRAM

E. M. LENOE, Chairman, AMMRC
J. I. BLUHM, AMMRC
H. D. CURCHACK, Harry Diamond Laboratories
C. M. ELDRIDGE, Army Missile R&D Command
J. FEROLI, Army Test & Evaluation Command
G. L. FILBEY, Jr., Ballistic Research Laboratories
R. FOYE (Representative of NASA)
Army Research and Technology Laboratory
NASA-Ames Research Center
A. J. GUSTAFSON, Army Aviation R&D Command
G. E. MADDUX (Representative of U.S. Air Force)
Air Force Flight Dynamics Laboratory
D. R. MULVILLE (Representative of U.S. Navy)
Office of Naval Research
R. P. PAPIRNO, AMMRC
E. W. ROSS, Jr., Army Natick R&D Command
E. SAIBEL, Army Research Office
T. SIMKINS, Army Armaments R&D Command
G. WILLIAMSON (Representative of U.S. Army Corps of Engineers)
Army Construction Engineering Research Laboratory

ONGOING CASE STUDIES SESSION

G. E. MADDUX, Co-Chairman, Air Force Flight Dynamics Laboratory
R. P. PAPIRNO, Co-Chairman, AMMRC



CONTENTS

OPENING SESSION

WELCOME AND INTRODUCTORY REMARKS 3

R. Shea
Chief, Mechanics Research Laboratory
Army Materials and Mechanics Research Center

KEYNOTE ADDRESS - DESIGN: RIGHT, RISK OR DISASTER 5

R. S. Hartenberg
The Technology Institute, Northwestern University

SESSION I: THE SERVICE VIEWS ON STRUCTURAL INTEGRITY AND RELIABILITY

SOME PHILOSOPHICAL THOUGHTS ON THE ARMY'S VIEW OF STRUCTURAL INTEGRITY AND RELIABILITY 9

S. J. Lorber
Director, Directorate for Quality Assurance
Headquarters, Army Materiel Development and Readiness Command

NAVY DEVELOPMENT OF FRACTURE CONTROL TECHNOLOGY 10

H. H. Vanderveldt
Program Manager, Ship Materials and Structures R&D
Naval Sea Systems Command

CURRENT AIR FORCE AIRCRAFT STRUCTURAL INTEGRITY PRACTICES 11

R. M. Bader
Chief, Structural Integrity Branch
Air Force Flight Dynamics Laboratory

SESSION IIa: AIRCRAFT

ADVANCES IN FASTENER HOLE QUALITY THROUGH THE APPLICATION OF SOLID MECHANICS 15

J. M. Potter, Air Force Flight Dynamics Laboratory

PRECEDING PAGE BLANK-NOT FILMED

CONTENTS (continued)

STUDY OF STRAIN FIELDS CREATED BY A COLDWORKED FASTENER SYSTEM USING ADVANCED MOIRÉ TECHNIQUES 30

G. Cloud, Michigan State University, and
D. Corbly, Air Force Materials Laboratory

AN EVALUATION OF THE CRACK GAGE TECHNIQUE FOR INDIVIDUAL AIRCRAFT TRACKING 63

T. D. Gray, Air Force Flight Dynamics Laboratory, and
A. F. Grandt, Jr., Air Force Materials Laboratory

PREDICTION OF DEBOND SHAPE AND SIZE IN CRACKED, ADHESIVELY BONDED STRUCTURES 83

M. M. Ratwani, Northrop Corporation

SESSION IIb: AIRCRAFT

TENSILE LOADS IN HIGH CAPACITY LAMINATED ELASTOMERIC BEARINGS 103

D. P. Scala and R. H. Finney, Lord Kinematics

OPTICAL FRACTURE MECHANICS AND STRESS ANALYSIS OF A TURBINE ENGINE FAN DISK 113

V. J. Parks, The Catholic University of America,
R. J. Sanford, Naval Research Laboratory, and
J. W. Dally, University of Maryland

MODEL 540 MAIN ROTOR BLADE RISK ASSESSMENT 132

A. J. Gustafson, Army Aviation Research and Development Command

PREMATURE FAILURES OF AIRCRAFT CARRIER CATAPULT "TENSION BARS" CAUSED BY ILL-CONCEIVED REDESIGN 144

T. W. Butler, U.S. Naval Academy

SESSION IIc: AIRCRAFT

IMPACT DAMAGE TOLERANCE OF GRAPHITE/EPOXY LAMINATES 155

N. M. Bhatia, Northrop Corporation

CONTENTS (continued)

REPRODUCIBILITY OF STRUCTURAL STRENGTH AND STIFFNESS FOR GRAPHITE-EPOXY AIRCRAFT SPOILERS 167

W. E. Howell, NASA-Langley Research Center, and C. E. Reese, University of Kansas

DAMAGE TOLERANCE OF LIGHTWEIGHT AIRCRAFT STRUCTURE 188

D. F. Haskell, Army Armaments Research and Development Command

SESSION III: OTHER EQUIPMENT

STRESS-STRENGTH-STRUCTURAL RELIABILITY OF A ROAD WHEEL SPINDLE 203

J. E. Bilikam, B. Bordenkircher, and J. Hendriks, FMC Corporation

DESIGN OF EXPLOSIVE BLAST CONTAINMENT VESSELS FOR EXPLOSIVE ORDNANCE DISPOSAL UNITS 215

B. D. Trott, J. E. Backofen, Jr., and J. J. White, III, Battelle-Columbus Laboratories, and J. Petty, Army Armaments Research and Development Command

INTEGRITY ANALYSIS OF THE SEWARD STATION NUMBER 5 STEAM TURBINE ROTOR 229

C. W. Marschall, A. T. Hopper, and S. H. Smith, Battelle-Columbus Laboratories, and W. J. Moll, Pennsylvania Electric Company

FINITE ELEMENT ANALYSIS OF THE MAGIS IAC ADP/COMM SHELTER 248

C. M. Blackmon, Naval Surface Weapons Center

SESSION IV: ONGOING CASE STUDIES

This session was comprised of a series of brief presentations and discussions of current (but not necessarily complete) case studies relating to the theme of the symposium. Abstracts of these presentations are published in a companion document to these proceedings: Army Materials and Mechanics Research Center Monograph Series Report, AMMRC MS 78-4, dated September 1978.

CONTENTS (continued)

SESSION Va: ORDNANCE AND MISSILES

CRITICAL SIZE FLAW INVESTIGATION OF THE HIFRAG PROJECTILE 265

C. B. Palmer, Naval Surface Weapons Center

DESIGN OF THE XM-753 ROCKET MOTOR TO BULKHEAD JOINT UTILIZING PINS . . 285

J. Adachi, M. Benicek, and T. Tsui, Army Materials and Mechanics Research Center, and G. A. Benedetti, Sandia Livermore Laboratories

CRACK INSPECTION MAPS - AN APPLICATION TO COPPERHEAD 307

J. I. Bluhm and C. E. Freese, Army Materials and Mechanics Research Center

SESSION Vb: ORDNANCE AND MISSILES

PLANE STRAIN RESPONSE OF A CYLINDER TO BLAST LOADING 323

N. J. Huffington, Jr., Army Armament Research and Development Command

SENSITIVITY ANALYSIS OF FATIGUE LIFE ESTIMATES IN CANNON BORES 343

M. Shinozuka and R. Vaicaitis, Modern Analysis Incorporated, and E. M. Lenoe, Army Materials and Mechanics Research Center

FINITE ELEMENT STRESS ANALYSIS OF U.S. NAVY MARK 83 BASE DETONATING FUZE BUDY 365

O. H. Griffin, Jr., and C. M. Blackmon, Naval Surface Weapons Center

PANEL SESSION MEMBERS 375

AUTHOR INDEX 377

OPENING SESSION

Chairman: R. Shea
Symposium Chairman
Chief, Mechanics Research Laboratory
Army Materials and Mechanics Research Center

WELCOME AND INTRODUCTORY REMARKS 3

R. Shea
Chief, Mechanics Research Laboratory
Army Materials and Mechanics Research Center

KEYNOTE ADDRESS - DESIGN: RIGHT, RISK OR DISASTER (Abstract) 5

R. S. Hartenberg
Emeritus Professor of Mechanical Engineering
The Technology Institute
Northwestern University

WELCOME AND INTRODUCTORY REMARKS

RICHARD SHEA
Symposium Chairman
Chief, Mechanics Research Laboratory
Army Materials and Mechanics Research Center

It is indeed a pleasure to open the Army Symposium on Solid Mechanics, 1978, and to welcome all of you here today.

This is the sixth in a series of biennial symposia held under the aegis of the US Army Materiel Development and Readiness Command (DARCOM) through its Materials Advisory Group (MAG) or more specifically the Mechanics of Materials Technical Working Group (TWG).

The Mechanics of Materials TWG is directed by AMMRC with members from all of DARCOM's R&D commands. The Symposium Committee is comprised of the Mechanics of Materials TWG membership, augmented by representatives of the US Army Corps of Engineers, the US Air Force, the US Navy and the National Aeronautics and Space Administration. This broader participation, which began with the 1974 meeting, recognizes that solid mechanics is a key ingredient in the development of any advanced system, regardless of the service involved.

During the course of these symposia we have attempted to make the themes more and more relevant to the needs of systems developers. We have also introduced a work-in-progress session beginning with 1974, and this year are trying a case studies approach, as well as a panel session. We have also invited speakers from each of the services to present the service views of structural integrity and reliability. These innovations are a direct attempt to make the systems development community more cognizant of the need to have mechanics analysis built into their designs, early in the development cycle and continuing right on through the cycle.

This year, in particular, we are trying to meet this issue head on. We have established the Symposium theme as Structural Integrity and Reliability, and specifically have tried to get the systems development community involved.

The theme, in my opinion, is most appropriate. The solid mechanics community has been, is now, and always will be vitally concerned with structural integrity. The job of assuring structural integrity continues to become more difficult because of more severe demands on new systems. These demands are not solely due to enhanced performance, but also to cost, reliability and schedule considerations. These requirements are at crossed purposes, which really makes the achievement of structural integrity a demanding job for the systems developer.

PRECEDING PAGE BLANK-NOT FILMED

I mentioned that the solid mechanics community will continue to be vitally concerned with structural integrity, and that its attainment will continue to be more difficult. One of the ways to minimize these difficulties is to minimize whatever uncertainty we can afford to minimize. Uncertainty comes in many disguises. There is uncertainty in loads definition; there is uncertainty in the mechanics analyses; there is uncertainty in materials properties; there is uncertainty in critical dimensions. I feel that dialog between the developers and the mechanics practitioners can identify those uncertainties which can be reduced.

From the solid mechanics point of view, the underlying issue is the lack of ability to predict integrity with the high level of reliability we feel is necessary. However, if history is any barometer, we will never be satisfied with our ability to predict structural and material response. While the quest for predictability must certainly go on, current capabilities must simultaneously be applied as best they can. As I see it, that is what this meeting is all about.

Today and during the next two days we will be hearing about better ways of predicting response as well as how to apply both straightforward and sophisticated, but well established, predictive models to insure the structural integrity and reliability of equipment.

I have had an opportunity to read most of these papers, and I feel that they really accomplish what we had hoped. They demonstrate that the problems of insuring structural integrity of materiel, while varying in specifics, have one very strong common denominator. What is required is the common sense, application of good mechanics analysis before important design decisions are made. To accomplish this requires a better interaction between the system development and solid mechanics communities. Speaking for at least that segment of the solid mechanics community sited at AMMRC I would like to have the systems developers leave the symposium with this message: We stand ready to help. We will be happy to serve as your consultants to ensure that good mechanics analyses are being applied to your systems, or we will be happy to carry out the analyses for you.

Again welcome to the Army Symposium on Solid Mechanics, 1978. I hope that when it is over you will all have found it as worthwhile as I feel it will be.

KEYNOTE ADDRESS - DESIGN: RIGHT, RISK OR DISASTER

RICHARD S. HARTENBERG
Emeritus Professor of Mechanical Engineering
The Technological Institute
Northwestern University

ABSTRACT

What rules, guidelines, standards, or tests of materials the ancient designers and builders may have followed are not a matter of record. The earliest approach to a design manual of sorts is given the date of 25 B.C. in the time of Augustus. Forgotten during most of the following centuries, it surfaced as the handbook in the fifteenth century, and was soon supplemented by more comprehensive, lavishly illustrated "how-to-build-it" manuscripts.

Mythology, in terms of the story of Daedalus and his son Icarus, publicized the first in-flight structural failure prompted by going beyond the design limits. The "hero engineer" figure (was Daedalus the first?) is a rare specimen in modern literature. Two such characters are found in stories by Rudyard Kipling and Nevil Shute; both deal with fatigue failure, one at sea, the other in the air.

It is with the Renaissance that searching questions about loads on beams and columns are put on record, but the answers come much later. Leonardo made some guesses, but it was Galileo who founded strength of materials as a science with his book, Two New Sciences, (1636), the second science being dynamics. Robert Hooke in England observed springs of various configurations – "As the extension so the force" (1678). The French were very active at this time, making substantial contributions to the experimental side. Using Leibniz' newly invented calculus, Jacob Bernoulli investigated the deflection curve of an elastic bar (1694); Euler, also working on geometric forms of elastic curves, found the buckling-load equation for columns (1774).

Steam boilers and railway bridges fostered structural thought and tests of many kinds, safety legislation and building codes. The early work (1830's) of Philadelphia's Franklin Institute on boilers, their materials, and their accessories brought legislation and led to the ASME Boiler Code decades later. Disasters such as those which befell the Tay Bridge (1879, Dundee, Scotland) and the Tacoma Narrows Bridge (1940) not only bracketed the aerodynamic aspects but are also examples of designer callousness. The construction (1850) of the Britannia Tubular Bridge over Menai Strait posed uniqe problems of span, load, materials and methods that were solved by that great trio, Robert Stephenson, William Fairbairn and Eaton Hodgkinson.



Daedalus and Icarus: Earliest recorded structural failure of a composite during flight, about 1300 B.C. The wax securing Icarus' wing feathers melted because of his flying too close to the hot sun, plunging him to his death in (what is now) the Icarian Sea. The accident report noted that it was a clear case of exceeding the design limits, and that there was a lack of backup, such as stitching. Daedalus made it to Sicily as per flight plan. (From a woodcut of 1493.)

SESSION I: THE SERVICE VIEWS OF STRUCTURAL INTEGRITY AND RELIABILITY

Chairman: R. Shea
Chief, Mechanics Research Laboratory
Army Materials and Mechanics Research Center

SOME PHILOSOPHICAL THOUGHTS ON THE ARMY'S VIEW OF STRUCTURAL INTEGRITY AND RELIABILITY 9

S. J. Lorber
Director, Directorate of Quality Assurance
Headquarters, U.S. Army Materiel Development and Readiness Command

NAVY DEVELOPMENT OF FRACTURE CONTROL TECHNOLOGY. 10

H. H. Vanderveldt
Program Manager, Ship Materials and Structures Research and Development
Naval Sea Systems Command

CURRENT AIR FORCE AIRCRAFT STRUCTURAL INTEGRITY PRACTICE 11

R. M. Bader
Chief, Structural Integrity Branch
Air Force Flight Dynamics Laboratory
Wright-Patterson Air Force Base

SOME PHILOSOPHICAL THOUGHTS ON THE ARMY'S VIEW OF STRUCTURAL INTEGRITY AND RELIABILITY

SEYMOUR J. LORBER
Director, Directorate of Quality Assurance
Headquarters, U.S. Army Materiel Development and Readiness Command

SUMMARY

Structural integrity is a basic and an essential requirement for producing reliable systems. The responsibility for providing structural integrity lies with the designer. The responsibility for insuring that structural integrity has been provided throughout the life cycle of the equipment lies with the individual services. The Army has developed what we consider to be a unique and effective means of insuring that the design performance characteristics have been properly and thoroughly characterized in the technical data package (TDP). The vehicle for this procedure is what has been termed the Quality Readiness Review (QRR).

The QRR is conducted by a team of experts which include government production and quality engineers, government inspectors, material experts, nondestructive test experts, and contractor personnel. A major portion of the review is directed toward evaluations of tests and inspections, such as ultrasonic and eddy current inspections, to determine their applicability with respect to assessing the actual structural integrity of the system. Recommendations are ultimately made for updating the TDP, if required, and quality assurance problems during the transition from development to production are, therefore, minimized. In this paper, a discussion of the Army's Quality Readiness Review Procedure will be presented.

PRECEDING PAGE BLANK-NOT FILMED

NAVY DEVELOPMENT OF FRACTURE CONTROL TECHNOLOGY

HANS H. VANDERVELDT
Program Manager, Ship Materials and Structures Research and Development
Naval Sea Systems Command

SUMMARY

Fracture Control Technology as currently viewed within the framework of technology development is discussed. Particular emphasis is given to the notion that Fracture Control Technology is one aspect of the overall structural integrity assessment and consists of an integration of management concepts with existing fracture mechanics technology. Candidate application for the development of Fracture Control Technology Concept will be discussed.

CURRENT AIR FORCE AIRCRAFT STRUCTURAL INTEGRITY PRACTICE

ROBERT M. BADER
Chief, Structural Integrity Branch
Air Force Flight Dynamics Laboratory
Wright-Patterson Air Force Base, OH 45433

SUMMARY

Historical events in the evolution of the Air Force Aircraft Structural Integrity Program (ASIP) are summarized. Factors influencing the current Air Force recommended practice of structural life prediction based on fracture mechanics principles are reviewed. Air Force standards and specifications that guide current practice are discussed in relationship to metallic and composite aircraft structure. The impact of these requirements in new aircraft designs as well as the application of the intent of these requirements to existing aircraft designs is also covered.

Applications of current structural integrity practice to aircraft systems are presented to illustrate key points of the ASIP and to amplify the thrust of efforts to improve the damage tolerance and durability of aircraft structure. The major elements of a damage tolerance and durability assessment are discussed to illustrate the interrelationship of the technologies involved in an ASIP. Emphasis is placed on the force structural maintenance plan, the individual airplane tracking program and the loads/environmental spectra survey which are the elements of the ASIP force management task. The value of these assessments that are being accomplished on many Air Force aircraft is addressed.

A brief look into the future is made in an attempt to identify research and development activities necessary for the solution to potential aircraft structural problems and to provide improved methods for the application of current structural integrity practice.

SESSION IIa: AIRCRAFT

Chairman: J. R. Davidson
Head, Structural Integrity Branch
NASA-Langley Research Center

ADVANCES IN FASTENER HOLE QUALITY THROUGH THE APPLICATION OF SOLID MECHANICS 15

J. M. Potter
Air Force Flight Dynamics Laboratory

STUDY OF STRAIN FIELDS CREATED BY A COLDWORKED FASTENER SYSTEM USING ADVANCED MOIRE TECHNIQUES 30

G. Cloud
Michigan State University, and
D. Corbly
Air Force Materials Laboratory

AN EVALUATION OF THE CRACK GAGE TECHNIQUE FOR INDIVIDUAL AIRCRAFT TRACKING 63

T. D. Gray
Air Force Flight Dynamics Laboratory, and
A. F. Grandt, Jr.
Air Force Materials Laboratory

PREDICTION OF DEBOND SHAPE AND SIZE IN CRACKED, ADHESIVELY BONDED STRUCTURES 83

M. M. Ratwani
Northrop Corporation

PRECEDING PAGE BLANK-NOT FILMED

ADVANCES IN FASTENER HOLE QUALITY THROUGH THE APPLICATION OF SOLID MECHANICS

JOHN M. POTTER
Aerospace Engineer
Air Force Flight Dynamics Laboratory
Air Force Systems Command
Wright-Patterson Air Force Base, OH 45433

ABSTRACT

A case study is presented for the use of the solid mechanics concept of the Equivalent Initial Flaw Size to characterize the quality of fastener holes. As a result of this study, the source of flaws responsible for relatively quick initiation and flaw growth was identified. The cause of these flaws was determined as being inherent in the production tooling used to make the holes. The tooling was modified slightly to eliminate the offending flaws with the result that the mean equivalent initial flaw size was decreased from 0.0006 inch to 0.0003 inch. This translates into a one-quarter lifetime delay in structural problems associated with flaw growth which can have significant impact on the cost of ownership of the structure.

INTRODUCTION

The recent tightening of durability requirements for military aircraft structures (1,2) has created renewed interest in the subject of hole quality and its effect on crack growth. Preparation of fasteners and fastener holes are significant to the cost and performance of an aircraft structure. An aircraft the size of the General Dynamics F-16 has over 250,000 fastener holes while a Lockheed C-5A or Boeing 747 contains over 2,500,000 fastener holes. Each hole must receive individual attention and preparation in the manufacturing process. The fastener holes have been identified as being primary locations for flaw initiation that lead to structural problems (3).

While many problem holes in the past have been identified as being caused by "poor quality holes", there has been little effort to determine a relationship between flaw growth and hole quality. The term "hole quality" has been treated with ambivalence; it has been either associated with the overall surface characteristic (i.e. surface roughness, existence of "rifles", etc.) or with some measure of the life of the structure but with little quantitative connection. Little fracture mechanics based data exists to describe the flaw growth potential of fastener holes. The majority of the flaw growth data that exists is derived from artificially prepared flaws (4). Thus, there is a gap in information concerning flaw growth behavior from naturally prepared fastener holes. Rudd and Gray (5) describe the flaw growth potential of naturally occurring flaws in fighter-attack aircraft structure. Their fastener holes had variations in stress level, load transfer, and flaw geometry that could limit the generality of that data.

PRECEDING PAGE BLANK-NOT FILMED

Two possible ways to characterize the small flaw size crack growth behavior of natural flaws are: (1) to determine the flaw growth behavior of microscopic cracks (6), and (2) to determine an equivalent initial flaw by analytically extrapolating the large flaw behavior to its initial size. The first of these ways requires an experimental verification of stress intensity factors and crack growth rates for a great number of flaw geometries. The second only requires a crack growth analysis in order to obtain the apparent initial flaw size in solid mechanics terms. The second method was chosen for this study of fastener hole quality of production fastener holes.

The objective of this study was to quantify the initial quality of individual production fastener holes in terms of crack length and relate this to the existence of measurable hole surface defects. The concept of the equivalent initial flaw size was used to quantitatively characterize the durability of the fastener holes. The Equivalent Initial Flaw Size (EIFS) process develops an initial crack length value that can be used in a fracture mechanics analysis. In order to accomplish these objectives, two major tasks were required: (1) non-destructive inspection of all fastener holes to detect hole defects, and (2) equivalent initial flaw size determination to quantify the structural durability in solid mechanics terms.

After manufacturing of holes and non-destructive inspection, the specimens were subjected to a load history derived from fighter aircraft usage for two equivalent lifetimes. Following the determination of the equivalent initial flaw size, the location and size of the EIFS was correlated with the NDI data from each specimen. The purpose of this correlation was to determine the severity of those defects detected by NDI in terms of their propensity to initiate a fatigue crack.

OVERVIEW OF RESEARCH

Table 1 shows an overview of the approach and tasks utilized in this study. The program begins with the manufacture of specimens; for this program it was felt necessary to have fastener holes that were representative of those to be found on flying aircraft. Automatic hole drilling procedures were chosen to hold down the potential amount of variation in hole quality while giving a representative sample of production quality. No specimens were intentionally preflawed. All coupons were treated as if they were made for aircraft usage. Drilling supports were prepared to make sure that the drill had fixturing similar to production practice.

Following the hole production phase, each fastener hole was inspected with five NDI methods. The objective of this phase was to quantify, as much as possible, the hole surface condition. Attempts were made with each NDI method to obtain repeatable, quantitative data on each fastener hole. For instance, when employing eddy current the operator was instructed to make each set of measurements using the same instrumentation, frequencies and sensitivities to minimize measurement variations. Measurements were made and recorded at multiple locations on each fastener hole.

TABLE I - PROGRAM OUTLINE

1. Manufacture Test Specimens
2. Perform NDI on all Specimens
3. Install Fasteners
4. Subject Test Specimens to Two Design Lifetimes of Loading
5. Determine EIFS on all Specimens
6. Compare EIFS Data to NDI Measurements

Subsequent to the NDI task, fasteners were installed. Each specimen was individually tested to a fighter load history for the equivalent of two design lifetimes usage. Loads were applied in a flight-by-flight format. Thus, the fatigue experience was under conditions similar to that which a structure would be exposed.

At the end of two lifetimes each unfailed specimen was broken apart and the equivalent initial flaw size was determined by combining the fractographic crack growth data with an analytical prediction technique and extrapolating to the flaw size at the first loading application. Subsequently, the EIFS data were correlated with data obtained in the NDI phase.

SPECIMEN DESIGN AND MANUFACTURE

A sketch of the specimen employed in the testing program is shown in Figure 1. Thirty-five specimens of 7475-T7351 aluminum alloy were prepared for this study. Specimen blanks were prepared and sent to the structural manufacturing department for hole preparation and fastener installation. Fastener holes were drilled with the Winslow Spacematic automatic drill using a 0.248 inch (6.30 mm) diameter drill. Hole tolerance was held to 0.250 in. to 0.253 in. (6.35 to 6.42 mm) diameter. Straight shank fasteners (Designation NAS 6208) were installed using plant manufacturing torque specifications (60 in.-lbs minimum).

NON-DESTRUCTIVE INSPECTION PROCEDURES

Each of the fastener holes in each specimen was examined using five (5) NDI methods: Ultrasonic, Eddy Current, Linear & Rotary Profilometer and Dial Bore Gage. These methods were chosen as being most likely to give quantitative measurements of the characteristic flaws that were previously identified as being responsible for shortening structural life.

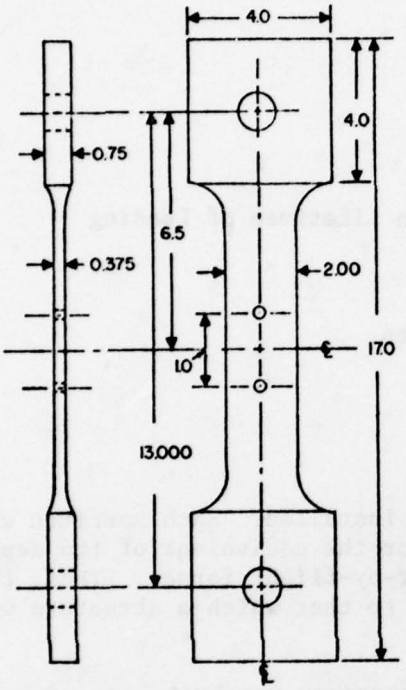


Figure 1 Test Specimen Geometry

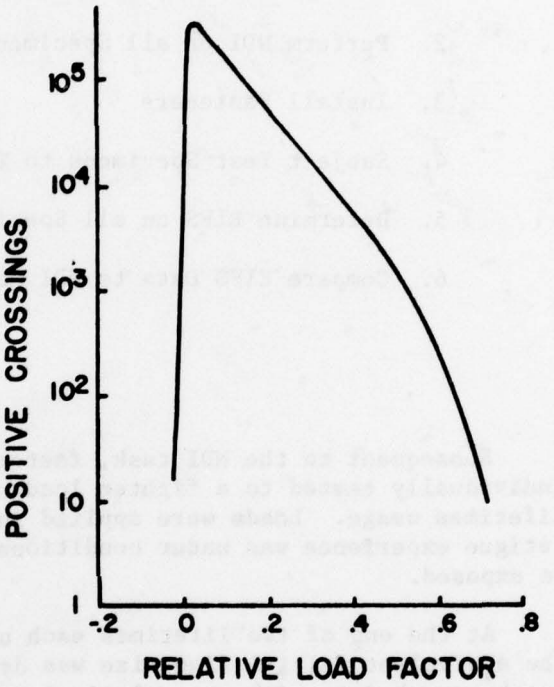


Figure 2 Load Exceedance Plot

TEST PROCEDURE

Each specimen was individually tested in one of a set of six hydraulic axial loading frames. A load history based on the F-16 was applied to each coupon for a duration of two design lifetimes or until failure, whichever came first. The load history was applied as a blocked flight-by-flight history. The history was repeated every 400 equivalent flight hours. The exceedance curve is shown in Figure 2. The maximum stress applied in this period was 34 ksi (234 MPa). This stress level and history is representative of the F-16 lower wing skin design loading environment. If a specimen survived two lifetimes at these conditions, it was removed from the test frame and taken to a static load frame where it was subject to an increasingly high load until it failed statically. The load history was created by a mini-computer and loads were applied at an average rate of 5Hz. Standard analog servo load controllers were used in the feedback circuit.

DETERMINATION OF EQUIVALENT INITIAL FLAW SIZE

The separated halves of the specimens were fractographically inspected to trace the progress of the crack front. The 400 hour repeated history left distinctive markings on the fracture surface that aided the fractographic traceback process.

An analytical crack growth curve was prepared for the 400 hour repeated history presuming a hemispherical initial flaw geometry (a/2c of 0.5) at the center of the thickness of the specimen. The Wheeler (7) crack growth retardation model was used with an M of 1.6 and a threshold of 0 ksi $\sqrt{in}$. These constants were fitted from the crack growth behavior of the first few specimens tested to the history.

In order to determine the EIFS from each specimen, an a vs. N template was prepared from the analytical crack growth data. The template was placed over the fractographic a vs. N data sheet and moved horizontally until the crack growth prediction matched the observed level over the range of 0.020 in. to 0.050 in. (0.51 to 1.27 mm). With this comparison, it was possible to determine the analytical flaw size that would have existed at "cycle one."

RESULTS

FLAW SIZE DISTRIBUTIONS

The majority of the specimens tested survived the two lifetime application of loading. All of the survivors were found to contain cracks of some finite size when they were broken apart. The equivalent initial flaw size distribution that resulted from these specimens is shown in Figure 3. This flaw size population has a mean flaw size of 0.0006 inch with 10% of the flaws having a size greater than 0.0012 inch. The fractographic backtracking process yielded flaw size data periodically during the cyclic load history. Figure 3 also shows the flaw depth distributions at intervals of one half design lifetime from the start of the test to two lifetimes. The data at flaw depths over 0.010 inch is primarily from the fractographic investigation and the smaller flaws were obtained from analytical extrapolation. This figure indicates that the EIFS distribution is of the same family as the intermediate and final flaw size distributions as shown by the fact that the curves do not have different slopes. Because of this the EIFS can be used directly to predict the flaw growth at later times. Figure 4 shows the mean flaw size and 90% flaw size data plotted as a function of lifetime. The data shows a log-linear relationship between flaw size and lifetime. The mean flaw size is seen to increase by a factor of 10 per lifetime

NDI CAPABILITY

The flaw size data from each of the coupons were then correlated to the measurements made with each of the NDI methods. The comparisons of each to the maximum signal determined by eddy current and ultrasonic equipment is shown in Figures 5 and 6, respectively. These figures indicate that there is no

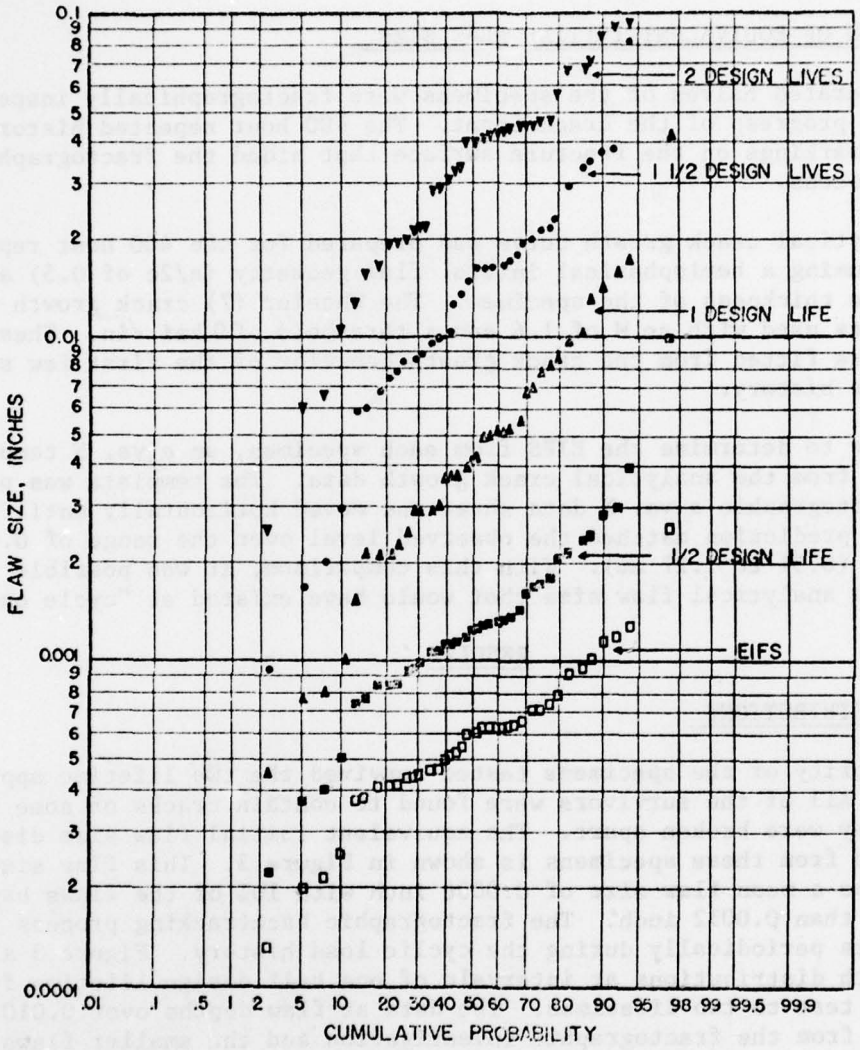


Figure 3 Flaw Size Distributions

direct relationship apparent between measurements done using eddy current or ultrasonic NDI.

Figure 7 shows a comparison between the measurements of hole roundness as measured by the dial bore gauge and the EIFS. Again, there appeared to be no correlation between measurable quantities and the EIFS. The surface roughness data measured by the linear and rotary profilometer also indicated no correlation with the EIFS but no comprehensive figure could be compiled.

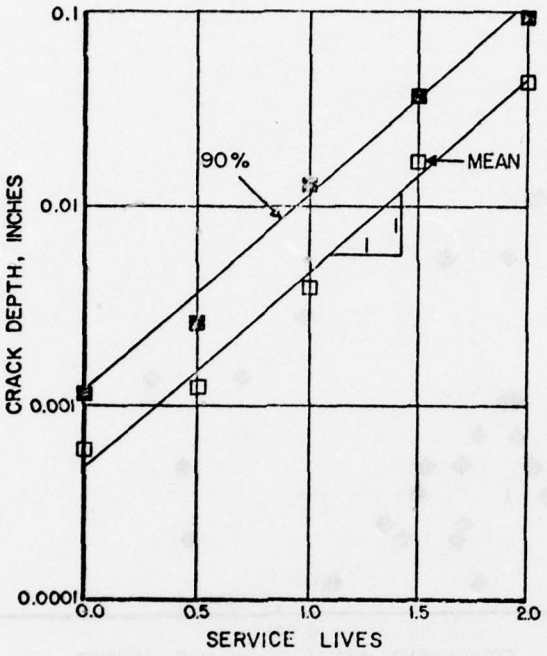


Figure 4 Crack Depth as a function of Service Lives

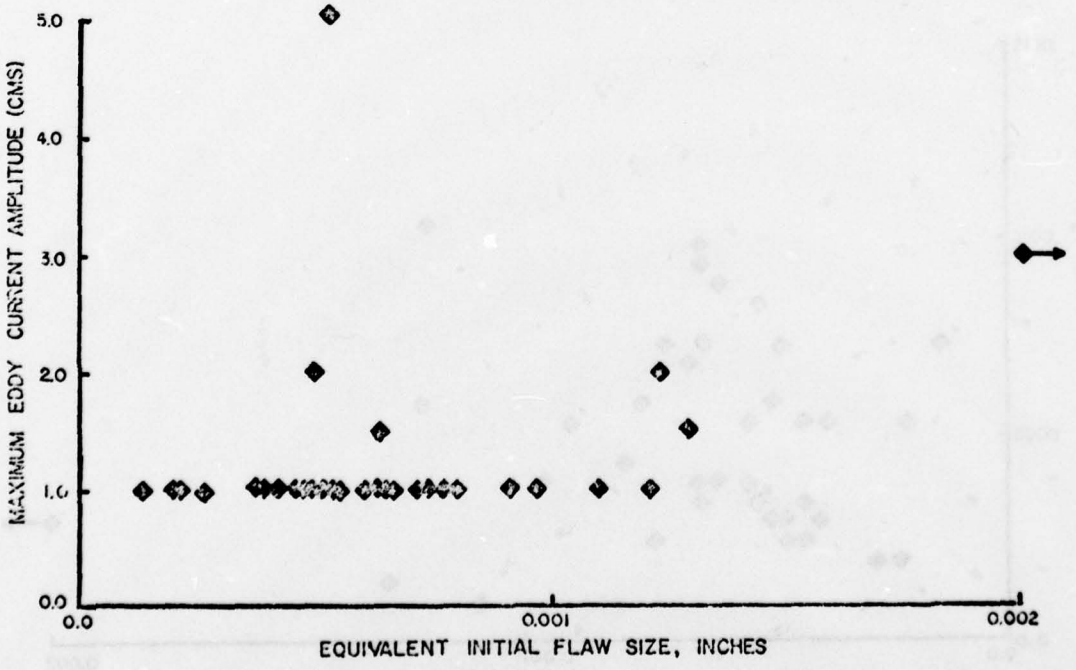


Figure 5 Correlation of Eddy Current Measurements with EIFS

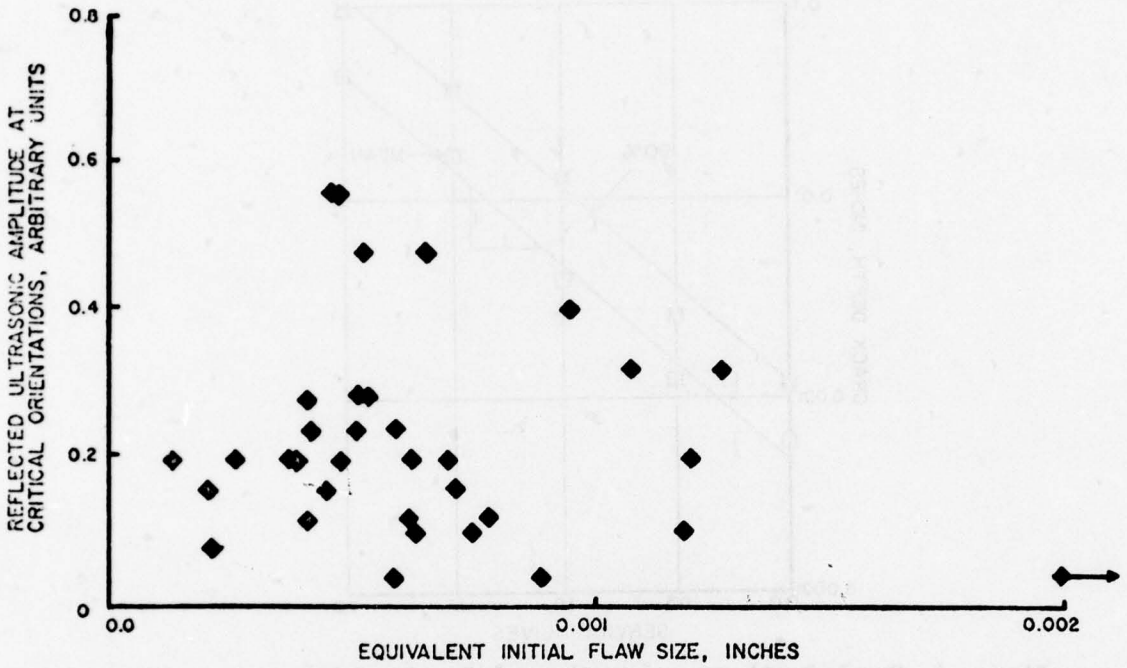


Figure 6 Correlation of Ultrasonic Measurements with EIFS

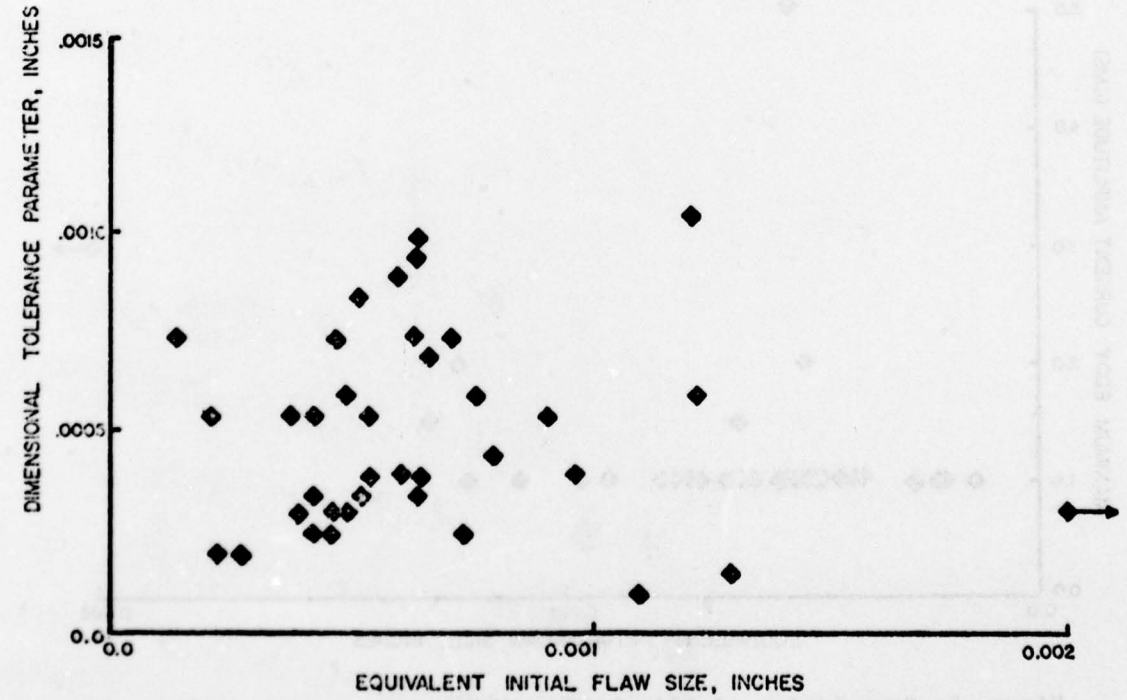


Figure 7 Correlation of Dial Bore Gage Measurements with EIFS

OPTICAL FRACTOGRAPHY

Certainly, there had been defects in the fastener holes that had been measured by the NDI methods used. The lack of correlation of those details measured by the NDI method with the equivalent initial flaw sizes means that either the EIFS process was not being properly applied or the NDI methods were not sensitive to the fastener hole details that were of importance to structural life. At this point, the failure origin of the fastener holes were closely investigated using the optical microscope. It was found that the failures typically started at locations remote from gouges, rifles, and other defects normally detected by NDI. This explains lack of correlation of the measurements made by NDI with the failure data as measured by the EIFS. The results of this investigation indicate that the hole surface defects conventionally considered to be damaging to structural integrity may not actually be important. Similar observations have been made recently by Moore (8) and Koster, Kohls, Cammett and Cornell (9).

Because of the above finding, a search was made for the source of the causes for shorter lifetimes. Using the optical microscope, the specimens with the shortest lifetimes (largest EIFS) were compared with those with the longest lifetimes (smallest EIFS). The main difference that was noticed in these two sets was that those with short lifetimes had flat initiation sites that tended to run to half or longer of the thickness of the specimen as shown schematically in Figure 8A. Those specimens with longer lifetimes had a jagged initiation site as shown in Figure 8B. The specimens that had the jagged fracture front had failure sites that had a thumbnail shaped flaw with a depth to width ratio (a/2c) of near 0.5 in value. Those specimens with flat fracture surfaces had a depth to width ratio approaching zero. For a given crack depth, the stress intensity increases substantially as the crack width along the bore of the fastener hole increases (4). Thus, a crack-like long scratch will grow much faster than a point source initiation site.

The fracture surface of the specimens with flat crack fronts were inspected with the optical microscope. Typical microphotos are shown in Figure 9. With increasing magnification it is possible to see that the cause of the initiation is a groove (Figure 9B) of very small dimension that has a "machined" appearance. The fastener hole surfaces of the specimens were found to have these grooves or scratches; some holes had many scratches extending the entire depth of the fastener hole whereas on others the scratches were shorter or nonexistent. These scratches were found to be less than 0.001 inch in radius (0.025 mm) making their discovery difficult by an conventional NDI method.

DETERMINATION OF CAUSE OF DAMAGING SCRATCHES AND SUBSEQUENT FIX

An investigation of the specimens with small EIFS indicated the presence of few, short scratches whereas those with large EIFS indicated many scratches that extended the entire fastener hole. Thus, it appears that these axial scratches were the key element to structural durability in these specimens.

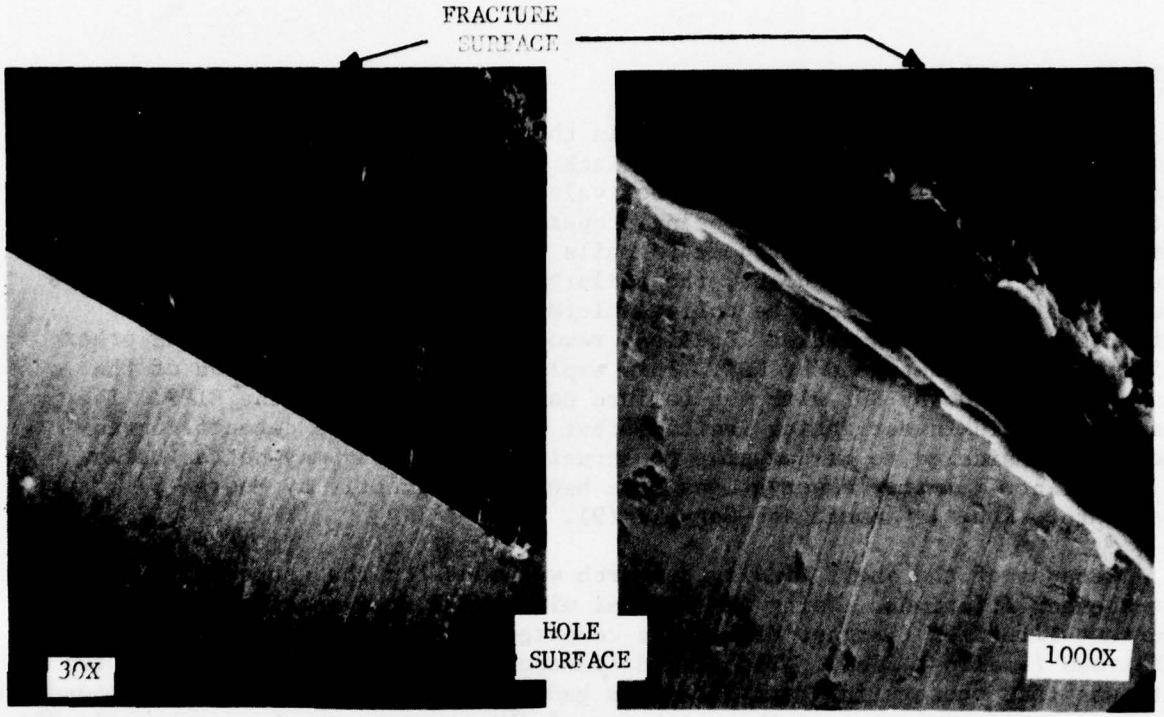


Figure 8 Scanning Electron Microscope Fractographs of Fracture Initiation Site Showing Scratch

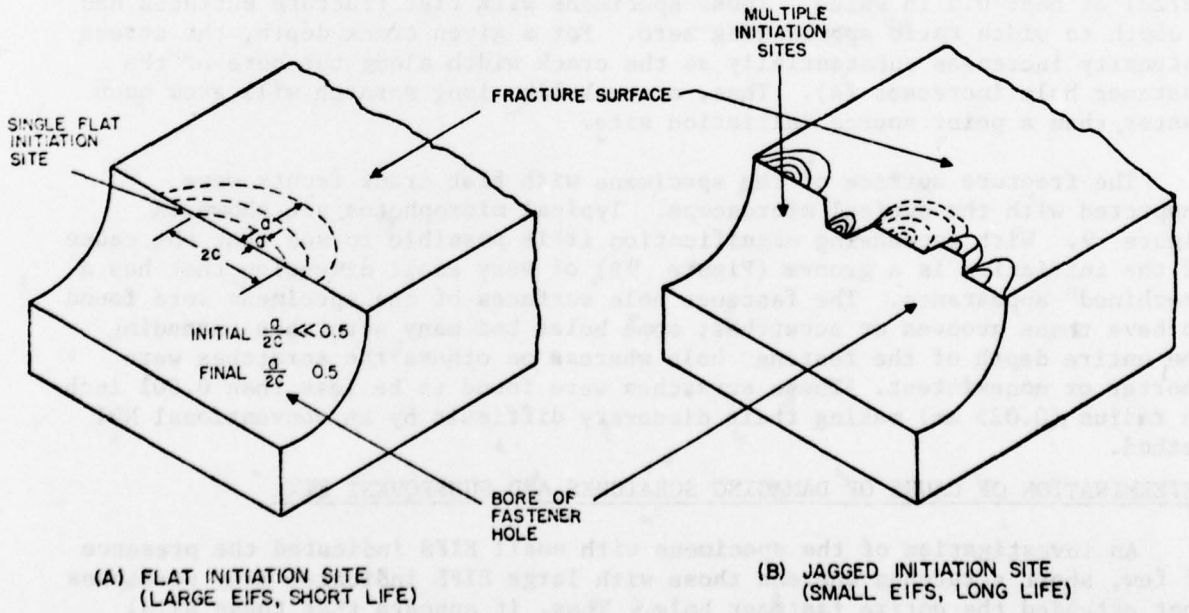


Figure 9 Schematic of Two Typical Initiation Site Types

Because of these observations, it appeared that it would be significant to identify the source of the scratches. The drilling process was investigated. It was found that the "Spacematic" tool was the cause of the problem. In the process of drilling, the tool rotates through the metal at a controlled rate. Upon reaching a preset depth, a valve in the tool resets, thus turning off all air pressure to the drill motor, directing the pressure to the retraction piston. This allows the drill motor to coast to stop. If sufficient friction exists between the drill bit and the fastener hole, the drill may stop completely during retraction. Any metal particles that adhere to the drill bit can be physically dragged through the hole. This appears to be the cause of the damaging scratches. Microscopic examinations of holes that were made when the drill was observed to be rotating through the entire period of retraction were found to be free of the axial scratches. It appears, thus, that the fastener hole scratches that are damaging to structural integrity are caused by the drill motor stopping during retraction. The solution to this problem was a simple one; change the air porting on the drill to keep the drill motor turning during retraction.

MODIFICATION FOR OTHER TOOLING

The goal of any quality program is to eliminate the occurrence of defects. In this case, the defects were determined to be due to the retraction of a non-rotating drill from a fastener hole. The defects that are significant to hole quality are small continuous scratches with a length of at least one half of the depth of the hole. Keeping the drill turning during retraction is a necessary but not sufficient condition to eliminate these defects. For example, a slow, continuously turning drill with a fast retraction mechanism will also leave the same defects. The retraction rate should be controlled so that it is less than 1/20 of the circumferential velocity of the cutting edge. It is possible also, that similar defects may be created by tooling problems such as chatter caused by flexible fixtures or insufficient cutting power since these scratches have been seen in tapered as well as straight holes.

The first step to the elimination of these damaging flaws in a structure involves their positive identification. The damaging scratches are typically less than 0.0005 inch in radius and depth. Because of their small size, the scratches are not visible without low power magnification. If such scratches are discovered, steps should be taken for their elimination by changing the drilling process.

QUALITY IMPROVEMENT

The drill motors used in this study were modified in accordance with the above instruction and an additional set of test specimens were manufactured. The equivalent initial flaw sizes that resulted from this second set of specimens are plotted in Figure 10 along with the original data. These data indicate a decrease in the mean EIFS from 0.0006 in. to 0.0003 inch (.015mm to .008 mm). Another way of looking at this is to say that 95% of these specimens had EIFS smaller than the best 50% of the original set of specimens.

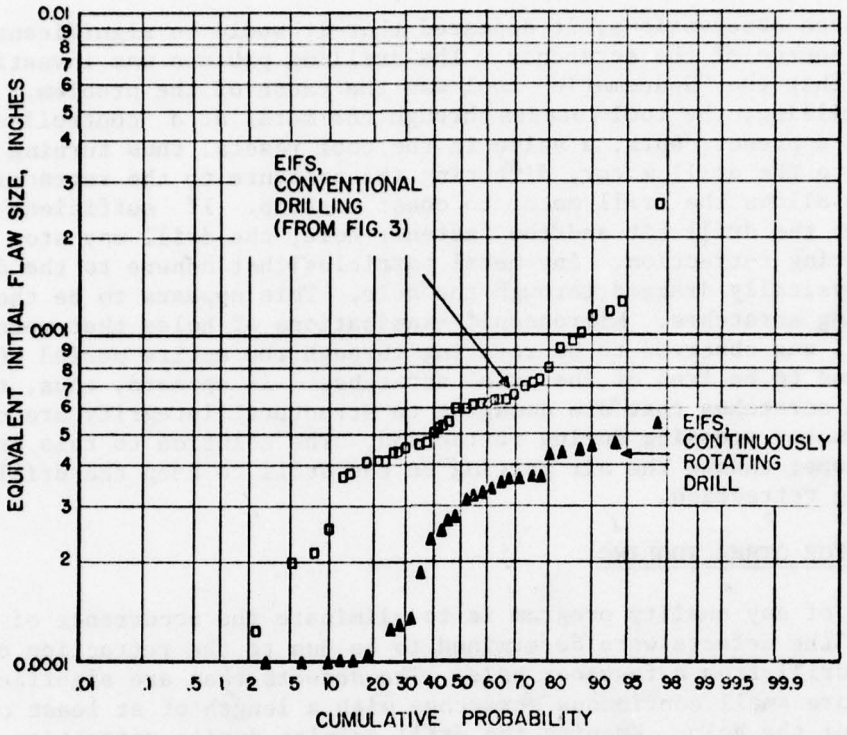


Figure 10 Comparison of EIFS for Conventional Drilling to the Continuously Rotating Drill

The improved drilling techniques results in approximately a factor of 2 decrease in the mean EIFS, with an apparent decrease in scatter. This level of decrease in EIFS can result in a one-quarter lifetime improvement (see Figure 4) in structural durability behavior compared to existing production quality. This directly affects the durability and economic lifetime levels as well as inspection intervals and maintenance and modification schedules for the airframe. This improvement in quality has tremendous potential implications to the cost of ownership of the structure in terms of reduced maintenance requirements.

DISCUSSION

Basically, the business of engineering is associated with numbers. The quantification inherent in the EIFS approach provided definition to the apparent flaw size of individual fastener holes. It is these numbers that were necessary to determine this main cause of shortened lifetimes. It may have been possible to have come to the same conclusions by some other means, but the EIFS creates the possibilities to quantifying structural durability with an efficiency not available before. The approach employed in this study

allowed for the determination of the EIFS on individual structures with a minimum of test and analysis manpower. The majority of effort necessary was fractographic analysis with emphasis on optical microscopy at crack sizes greater than 0.005 inch. Once the analysis was complete, the determination of the EIFS value consisted of sliding the analytical flaw growth template horizontally on the fractographic flaw growth curve for each specimen. There was no need for periodic surface crack length measurements during the test.

The approach taken in this study to obtain the EIFS differs from that used in both the A-7 and F-4 structural integrity audits (5). In both of these earlier cases, EIFS was determined from fastener holes that had been cut from a full scale test structure. Those structural locations investigated had significant variations in stress history, load transfer, and flaw geometry making a comparison of the data difficult. This study had the distinct advantage of being able to have multiple specimens at identical load histories, thus enabling the investigators to obtain the EIFS distributions for a consistent set of specimens without changes in stress intensity calculations from specimen to specimen. As a result, the data from this current study is representative of the hole quality for the materials, processes and load history conditions applied. In this program, the hole manufacturing process was changed and the effect on hole quality was immediately apparent. This aspect of the EIFS makes it a very powerful tool to evaluate manufacturing processes and, if desired, to compare quality from different vendors.

Using the concept of the equivalent initial flaw size, it is possible to develop a solid mechanics based durability design methodology. EIFS provides a ficticious crack size and geometry that reflects the propensity of the flaw to initiate and grow to a damaging size. For design purposes, it is more important to know the statistics of the likelihood to grow to a critical size than to be able to analyze small flaws from specific flaw geometries. The EIFS approach results in a flaw size distribution that reflects the existing hole quality in terms that integrate the initiation and small flaw crack growth behavior. Instead of developing extensive analytical efforts to characterize flaw growth at very small flaw sizes, equivalent results can be obtained using EIFS in conjunction with existing analytical methods.

CONCLUSIONS

Based on the results of this study, the following conclusions can be made.

1. Fastener hole quality and the propensity to subsequent flaw growth can be quantified in solid mechanics terms by the Equivalent Initial Flaw Size. The EIFS level is directly related to the structural durability.

2. Fastener hole flaws did not initiate at defects (i.e. gouges, rifles, etc.) that are normally considered to be damaging to structural durability. In the structures that had the largest flaws at two design lifetimes, the initiation sites were microscopically small axial scratches. NDI methods were found to be ineffective in the detection of those defects that were responsible for large flaws at two design lifetimes.

3. Manufacturing methods were found to have control over the durability of fastener holes in a structure. The axial scratches in fastener holes were determined to have been formed during drilling. The durability of these structural members was demonstrated to be increased by modification of existing drilling equipment to eliminate the axial scratches. The modifications to the drilling equipment was done such that there was no change in procedure apparent to the equipment operator.

RECOMMENDATIONS

Based on the results of this study, there are three basic general recommendations that can be made.

1. EIFS is an excellent procedure to quantify the durability of a structure. The EIFS approach provides a quantitative alternative to the assumption of a 0.005 inch corner crack requirement of MIL-A-83444 (ref. 2). The resultant procedure can be used in design and will give reliable flaw growth procedures that are simple to use.

2. Manufacturing methods should be closely inspected to determine if they are inadvertently producing axial scratches of the type found damaging in this study. If similar scratches are found, the tooling should be modified to control the retraction rate to 1/20 of the circumferential velocity of the cutting edge of the drill. Modifications to this drilling mechanism can result in a no-cost improvement to durability of a structure.

3. Consideration should be given to a reevaluation of the effectivity of manufacturing inspection in detecting defects that control structural durability. The current manufacturing inspection programs emphasize the detection of large physical defects such as gouges and rifles. These defects were determined not to be of significance to failure initiation relative to much smaller scratches caused by drilling. Emphasis should be placed on the development of methods to detect the existence of small axial scratches in fastener holes.

IMPLEMENTATION OF FINDINGS

As a direct result of this program, General Dynamics Corporation has incorporated the "Spacematic" drills, as modified in accordance with the aforementioned findings, into the F-16 production line. Further research is on-going to evaluate manufacturing process changes that have the potential of reducing manufacturing cost while increasing structural integrity. Several processes have been identified as being in this category. The equivalent initial flaw size approach will be used in evaluating the change in durability.

REFERENCES

1. Anon., "Airplane Durability Design Requirements," MIL-A-008866B(USAF), DoD, Washington, D.C. 1975.

2. Anon., "Airplane Damage Tolerance Requirements," MIL-A-83444 (USAF) DoD, Washington, D.C. 1972.

3. Gran, R.J., Orazio, F.D., Paris, P.C., Irwin, G.R., and Hertzberg, R.W., "Investigation and Analysis Development of Early Life Aircraft Structural Failures," AFFDL-TR-70-149, Air Force Flight Dynamics Laboratory, Dayton, OH, 1971.

4. Hall, L.R., Shaw, R.C., and Engstrom, W.L., "Fracture and Fatigue Behavior of Surface Flaws and Flaws Originating at Fastener Holes," AFFDL-TR-74-47, Air Force Flight Dynamics Laboratory, Dayton, OH 1974.

5. Rudd, J.L., and Gray, T.D., "Quantification of Fastener Hole Quality," Journal of Aircraft, Vol. 15, No. 3, March 1978, pp. 143-147.

6. Anderson, W.E., "Fracture Mechanics of Tiny Cracks near Fasteners," ASD-TR-74-25, Air Force Aeronautical Systems Division, Dayton, OH, 1974.

7. Wheeler, O.E., "Spectrum Loading and Crack Growth," Transactions of the ASME, Journal of Basic Engineering, 1971.

8. Moore, T.K., "The Influence of Hole Processing and Joint Variables on the Fatigue Life of Shear Joints," AFML-TR-77-167, Air Force Materials Laboratory, Datyon, OH, February 1978.

9. Koster, W.P., Kohls, J.P., Cammett, J.T., and Cornell, B.P., "Verification of Production Hole Quality," AFML-TR-77-185, Air Force Materials Laboratory, Dayton, OH, 1978.

STUDY OF STRAIN FIELDS CREATED BY A COLDWORKED FASTENER SYSTEM USING ADVANCED MOIRE TECHNIQUES

Gary Cloud
Associate Professor
Michigan State University
East Lansing, MI 48824

Dennis Corbly
Research Scientist
Air Force Materials Laboratory
Wright-Patterson AFB, OH 45433

ABSTRACT

Crack initiation and growth near fastener holes is a major cause of failure of high performance structures such as aircraft. One class of techniques for improving fatigue life is to plastically expand the hole before or during installation of the fastener. While empirical evidence shows that fatigue life is improved, the mechanism is still not completely understood, the optimum degree of coldworking is not known, and design information for different situations is not yet adequate. An investigation was undertaken to measure the residual surface strains near holes in aluminum plate which had been expanded plastically to various degrees by a proprietary process. A sophisticated Moiré technique which used only standard and inexpensive optical components was developed. Gratings were applied to each specimen with photoresist. The specimen gratings were recorded on glass photoplates before and after coldworking using high resolution techniques. Improved grating photographs with multiplication of grating frequency to obtain sensitivity multiplication were obtained using slotted apertures in the camera lens. The grating photoplates were superimposed with previously prepared submaster gratings of various spatial frequencies in a coherent optical data processing system to give sharp high-density Moiré fringe patterns with sensitivity multiplication and useful pitch mismatch. These data were digitized and then processed by computer to obtain detailed and summary maps of radial and tangential displacement and strain fields. The approach is applicable to a variety of difficult measurement problems.

INTRODUCTION

Fasteners are important components in aircraft structures in terms of component and installation costs, design effectiveness, and premature structural failure. The Air Force, aircraft manufactures, and suppliers of fastners maintain continuing programs in fastener development and evaluation.

The study described herein is part of a comprehensive Air Force program to evaluate the cost and effectiveness of a proprietary fastener system which utilizes coldworking of the fastener hole to improve structural performance under cyclic loading. One such system has been used for several years in various aircraft. It has been suggested that the system discussed here is

cheaper to buy and install, that it is as effective as the older system, and that it is more suitable for rework applications where new fasteners are to be installed in existing aircraft which are exhibiting premature structural or fastener failure.

In addition to studying a particular fastener system, this study is expected to lead to a better understanding of the coldworking process and its effects in improving fatigue life. It also yields data which are useful to designers and manufacturers in establishing load parameters and installation tolerances.

PURPOSE AND SCOPE OF INVESTIGATION

The goal of this particular investigation was to measure residual surface strain fields created by coldworking fastener holes to various degrees which might be appropriate for industrial application.

Since this effort was part of a larger and continuing program of fastener evaluation, an important auxiliary objective was to choose and develop a measurement technique which was appropriate to this complex elasto-plastic problem and which could be reduced to a procedure simple enough to be performed routinely be technical assistants while requiring little new or special-purpose equipment.

The coldworking process and apparatus marketed by J. O. King Incorporated, 711 Trabert Avenue, N.W., Atlanta, Georgia, 30318, U.S.A. is the only one considered in this study, although the results could hold for certain other processes. The spectrum of coldworking level was limited to seven magnitudes of radial interference (mandrel radius plus sleeve thickness minus hole radius) between .097 mm and .20 mm. Attention was directed mainly upon the radial strain component, but tangential strains were required for at least two levels of radial interference. The effects of remote loads upon the residual strain fields were to be established as a part of the study, and the method chosen had to accommodate that requirement.

BACKGROUND

Crack initiation and growth is a major cause of failure of high-performance structural components and a serious source of difficulty to the designer. A review of aircraft structural failures has shown that cracks which began at fastener holes were the main causes of one-third of early failures (1). The designer faces a situation where an essential component of his product - the fastener - might be responsible for its failure. It is important to lessen through improved design procedures, better understanding of crack growth, and in the development of better fastener systems, the tendency for structural failure to begin at fasteners.

One class of techniques for improving the fatigue performance of fasteners is to plastically expand the hole prior to or during installation of the fastener. Several proprietary schemes have been invented for accomplishing this coldworking of the hole in an efficient way (2). While evidence supports

the assertion that coldworking improves fatigue lives (3,4), the degree of improvement for a given amount and mode of coldworking is not clearly established.

From the designer's point of view, the problem is to establish that the fatigue life of his design is not influenced beyond a specified minimum by certain flaws at the coldworked hole. Experimental justification in every design situation is certainly not feasible. The usual approach is to develop analytical tools which can be used universally, and then to show that these tools give correct results in many different situations which can be modeled by experiments or observed through extensive service testing. Most such analytical schemes will use empirical factors which are derived from experiments on known cases. Thus are gained the benefits of optimum joining of theory, computation, and experiment.

Such design procedures for fastener holes are still in the early stages of development. It is not within the scope of this paper to discuss existing models in any detail, but mention of certain aspects of extant analytical models helps to justify and guide current efforts to measure strain fields near holes. Grandt (5) and Grandt and Gallagher (6), for example, have adapted the methods of fracture mechanics to develop procedures to account for the effect of coldworking at fastener holes. Their approach has been tested to a degree by Cathey (7) and by Grandt and Hinnerichs (8). These fracture mechanics calculations, and probably any other analysis scheme which could be devised, require knowledge of the stress field around nonflawed holes after coldworking.

Little information exists about stress fields induced by inelastic radial expansion of holes. The applicable theories remain quite untested. Noteworthy is the work of Sharpe (9) who has drawn together theoretical models and performed experiments to test them. Among other theoretical approaches, he checked the simple analytical solution developed by Potter and Grandt (10) as well as the measurements and finite difference analysis of Adler and Dupree (11). A simple experimental and analytical study of interference-fit fatigue-rated fasteners has been reported by Ford and his group (12).

The studies mentioned above are limited in one important aspect. They cover only a very limited range of degrees of coldworking. The values used are close to that (1.5 mm = 6 mils radial interference) which has been thought optimum. Only minimal evidence exists to show that this value does indeed give the best fatigue performance (3,4). Existing information about the stress-strain field near coldworked holes is not sufficient, then, to adequately test relevant theories or to serve as a data base for designers. Neither can one assess the effects of normal industrial tolerances upon either the fatigue performance or the design procedures. The experimental investigation described herein was undertaken to narrow this gap in our knowledge.

SCOPE OF PAPER

This report concentrates on the following aspects of the investigation of coldwork fasteners:

1. technical considerations leading to choice of measurement technique,
2. description of apparatus and procedures developed to satisfy the technical requirements as well as those imposed by economic, time, available equipment and technical manpower considerations, and
3. typical results.

Space limitations prohibit presentation of much technical detail, and the discussion following is of quite general nature. All details of apparatus, theory, and procedure, as well as complete results, are contained in a related Air Force technical report (13).

CHOICE OF EXPERIMENTAL METHOD

The problem of measuring strains in the vicinity of a coldworked hole is one which severely taxes the common techniques of experimental stress analysis. Characteristics of the technical problem which had to be considered when planning an approach to this problem included:

1. The strain magnitudes range from about 10% compression to about 3% tension.
2. There is considerable out-of-plane displacement near the hole.
3. Extensive "rumpling" of the surface occurs in the plastic zone.
4. The strain gradient is large in the region near the hole.
5. The area of prime interest is close to a boundary.
6. The fastener sleeve protrudes slightly from the surface.
7. A typical experiment might take place in one or more non-reversible, non-repeatable stages.
8. The procedure should be capable of yielding a whole-field map of two principal strain components (principal directions established by symmetry).

One of several modern variations of the moiré technique appeared to satisfy best the conditions of the measurement problem. The method is whole-field and noncontacting; it offers the possibility of choosing sensitivity after the raw data has been permanently recorded; and it can yield correct results in regions of high strain gradient and near boundaries.

The decision was to utilize the moiré technique with gratings of 39.4 lines per millimeter (lpm) or 1000 lines per inch (lpi) applied to the specimen using a photoresist coating. Because the specimen surface does not remain flat, a noncontacting procedure was developed which called for photographing the specimen grating before and after coldworking the specimen. The photograph replicas were superimposed with one or more submaster gratings in an optical Fourier processor in order to form separate "baseline" and "data" moiré fringe patterns. Fringe multiplication and pitch mismatch were introduced during this processing stage in order to obtain increased sensitivity and to improve the interpolation required in the subsequent computer data processing. For this processing, the moiré fringe orders and their positions along the chosen axes were obtained from the fringe photographs in digital form. Displacement and strain distributions were generated and plotted using a digital computer. Several fringe patterns were obtained with each data photograph using various

submaster gratings in the processor. The results were examined for consistency and treated statistically.

The experimental procedures used can be divided for convenience of discussion into three stages. Summary descriptions of the steps involved in each stage are given below:

CREATION OF SPECIMEN GRATING PHOTOGRAPHS

For optimum flexibility in the moiré study, it was necessary to obtain good quality photographic replicas of the specimen grating in its deformed and original states. These photos were to be superimposed with submaster photoplates which also had to be produced as part of the technique development. The requirement, then, is for sharp and contrasting specimen gratings and for high resolution photographs to produce sharp specimen and submaster grating replicas for optical processing.

PROCEDURE SUMMARY

1. Master gratings of 39.4 lpmm were obtained and reduced photographically to create a set of working submasters of various grating spatial frequencies ranging from 39.4 to about 160 lpmm.
2. After cleaning the polished specimen throughly, a thin coating of photoresist lacquer was sprayed onto its surface with an airbrush and the coating dried in low heat,
3. A submaster grating was clamped to the coated specimen and the assembly exposed to unfiltered radiation from a Mercury lamp in order to produce a contact image of the grating in the resist.
4. Fiducial marks previously scribed were touched up, highlighted, and identified.
5. The specimen was placed in a special holder and the grating photographed on glass photoplates at low magnificaition (1.3x) with high resolution.
6. The hole in the specimen was coldworked.
7. The specimen was returned to the holder and the grating, now deformed by the coldwork treatment, was photographed again.

MASTER AND SUBMASTER GRATINGS

A grating having a spatial frequency of 39.4 lpmm on a 100 mm x 100 mm glass substrate was obtained from Photolastic, Inc., of Malvern, Pennsylvania, USA, for use as a master grating for most of this study. This grating is designed for use in a Moiré camera and is not meant to serve as a master copy. Indeed, it proved to be of marginal quality for such a purpose owing to the presence of pinholes and variations of density. Submasters made from a deposited metal film grating were used in the last stages of the experiments, and they gave better results.

The making of 1:1 copies of moiré gratings has been thoroughly explored and explained by Luxmoore, Holister, and Hermann (14,15,16) and others. Their

techniques have been used in this study with certain simplifications. Contact copies were made by a method similar to that employed by Chiang (17) on Kodak High Resolution Plate (HRP) using for the light source a Durst enlarger head with a 150 mm Schneider lens at f 5.6.

Direct photographic reproduction was employed for manufacture of the several submaster gratings having various spatial frequencies which were required for optical data processing of the specimen photographs. Several of each grating having spatial frequencies clustered near 30, 60, and 90 lpmm were produced. These values are 1, 2, and 3 times the fundamental spatial frequency of the specimen grating photographs plus various frequency mismatches.

To produce these submasters, the master grating was held in a laboratory clamp base and blacklit with light from a Kodak slide projector. A ground glass plate was placed about 3 inches behind the grating to scatter the incident light. The other apparatus was the same as was used in photographing the specimen gratings and is described below. Camera to subject distances were estimated by calculation and finalized by trial to give the sought-for submaster grating frequency on the photographic plate. Focus of the grating image is absolutely critical in such a situation because of the resolution and contrast requirements.

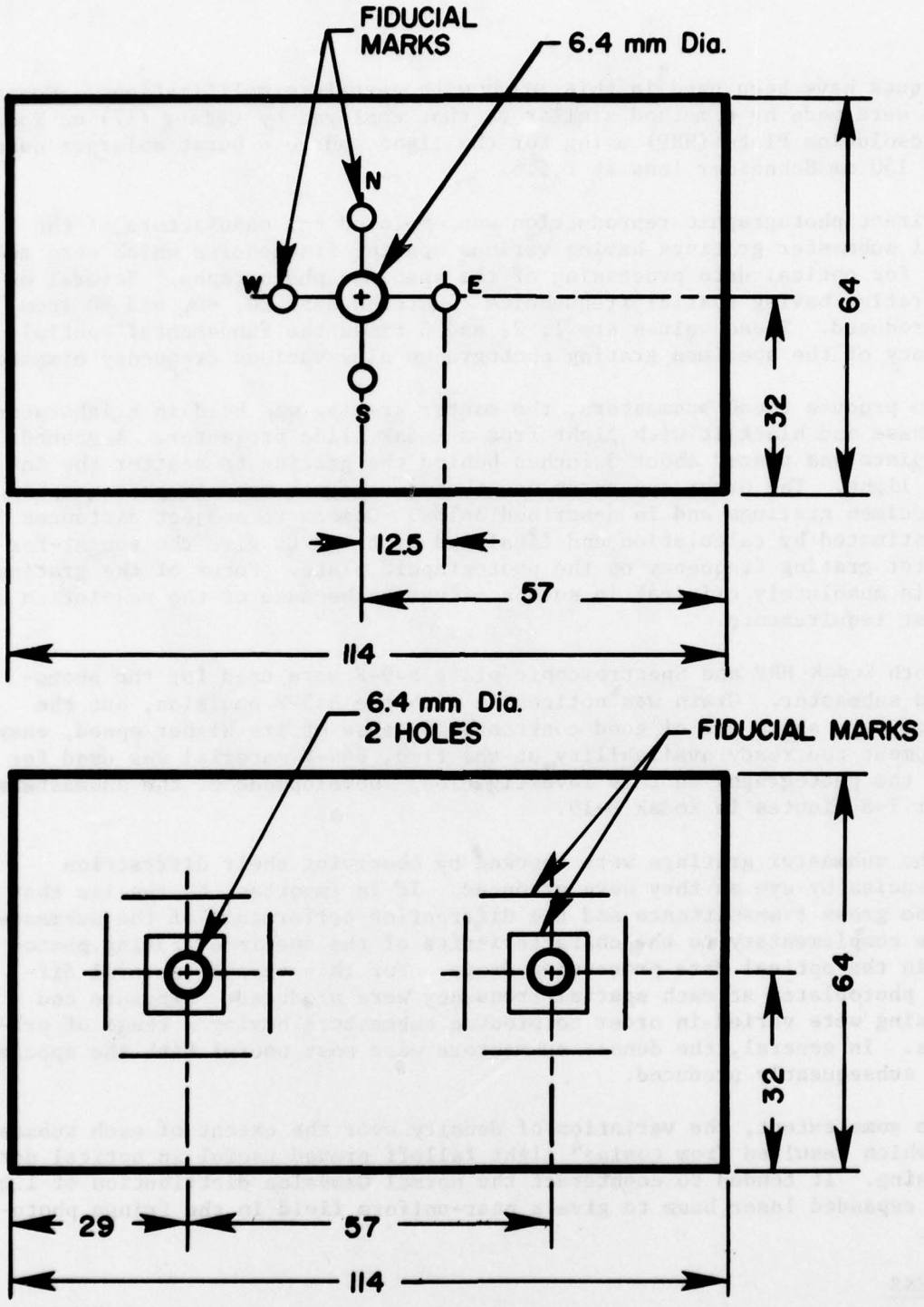
Both Kodak HRP and Spectroscopic plate 649-F were used for the photoreduced submaster. Grain was noticeable with the 649-F emulsion, but the gratings were sharp and of good contrast. Because of its higher speed, easy development and ready availability at the time, 649-F material was used for 90% of the photography in this investigation. Development of the submasters was for 7-8 minutes in Kodak D-19.

The submaster gratings were checked by observing their diffraction efficiencies by eye as they were produced. It is important to realize that both the gross transmittance and the diffraction performance of the submaster must be complimentary to the characteristics of the specimen grating photograph in the optical data processing stage. For this reason, several different photoplates at each spatial frequency were produced. Exposure and processing were varied in order to produce submasters having a range of properties. In general, the denser submasters were most useful with the specimen photos subsequently produced.

To some extent, the variation of density over the extent of each submaster plate which resulted from cosine^4 light falloff proved useful in optical data processing. It tended to counteract the normal Gaussian distribution of light in the expanded laser beam to give a near-uniform field in the fringe photographs.

SPECIMENS

Two types of specimens were used; both are pictured in Figure 1. The design with two holes was adopted as a means of saving material. Previous analytical and experimental studies suggested that the two strain fields would not interact significantly given hole separations on the order of those used.



DIMENSIONS IN MILLIMETERS

MATERIAL: 7075—T6 ALUMINUM
THICKNESS: 6.4 mm

Figure 1. Specimens used for measurement of strain near coldworked holes; typical fiducial marking shown.

In moiré work where several stages of photographic processing are used, it is important to have adequate fiducial works and identifying labels on the specimen surface. Scribed lines and self-stick lettering were utilized for this marking. Typical label patterns are included in Figure 1.

The specimens were sawn from a single plate of 7075-T6 aluminum alloy having 16.4 mm thickness. The sheet is the same stock as that used by Adler and Dupree (11), and by Sharpe (9), so direct comparisons would be valid. Preparation of the specimens was according to good standard shop practice.

SPECIMEN GRATINGS

The photoresist approach to creating gratings on the specimens was chosen because it is fairly simple, requires minimal special equipment, and offers the possibility of baking or etching the grating to make it resistant to damage. Given the severity of plastic deformation and the attendant rumpling of the specimen surface near the hole along with the potential for mechanical damage to the specimen during various stages of the experiment, the etching capability seemed important. A further potential is that etched gratings could be used for studies at temperatures above which the photoresists vaporize or burn.

The findings and techniques described by Luxmoore, Holister, and Herman (14,15,61) were adopted and adapted. The photoresist chosen was Shipley AZ1350J provided by Shipley Co., Newton, Mass., 02162, USA. This particular resist is formulated for acid resist coatings on aluminum, and its solids content is comparatively high at 30%. The companion thinner, cleaner, and developer were purchased with the resist.

Common methods of applying the resist coating in the thickness and uniformity required include spinning, dipping, wiping, spraying, and roller coating. Dipping and wiping tended to leave some buildup and sagging near the hole; that is, in the region of greatest interest. Given equipment considerations, attention settled on the spraying method. An artist's airbrush was obtained and a cleaning and spraying technique which gave satisfactory coating properties was worked out by trial and error.

The moiré grating was printed into the photoresist coating on the specimen by a simple contact procedure in which the grating submaster was clamped to the specimen and the assembly exposed to light from a mercury lamp. The procedure was unusual only in that a lamp much smaller than normal was used and several improvisations were necessary. Clamping of the submaster to the specimen was accomplished with ordinary spring-type clothespines. Lenticular effects in the submaster were reduced by using a 50% aqueous glycerine solution between the emulsion and the photoresist. Later, it was found that the fluid could be eliminated with little effect. The mercury lamp was the light source in a "Visicorder" optical chart recorder. This lamp has a power of only 100 watts, but its arc is so small that it was possible to bring the specimen to within 120 mm of the lamp without losing acuity or changing the grating pitch.

One aspect of the behavior of the photoresist deserves further comment. It is possible to balance exposure time and coating thickness to produce specimen gratings which will photograph more sharply than those one ordinarily thinks of as "good" gratings. The phenomenon utilized is that incomplete exposure and development leaves "debris" between the unexposed grating lines. It seems wiser, therefore, to use a thick coating and not try to cut through to base metal in the exposure and development. This conclusion may not apply if more uniform surfaces are produced, especially if the finish has a matte sturcture.

Figure 2 reproduces photomicrographs of typical specimen gratings in an unstrained state and after coldwork of the aluminum substrate.

COLDWORKING

In the J. O. King process, a lubricant-coated stainless steel sleeve which carries an anvil on one end is inserted into the hole. A tapered mandrel is pulled through while the sleeve is supported on the anvil. The mandrel enlarges the sleeve and expands the hole enough to cause plastic deformation of the adjacent material. The sleeve remains in the hole, but the anvil drops off.

The restriction to standard sizes of reamers, fastener sleeves, and mandrels limited the spectrum of coldworking levels to the following degrees of radial interference (mandrel radius plus sleeve thickness minus hole radius): 0.97 mm, .10 mm, .14 mm, .15 mm, .17 mm, (2 specimens), .18 mm, .20mm.

PHOTOGRAPHY OF SPECIMEN GRATING

The system devised for photographing the specimen gratings is shown schematically in Figure 3. A photograph of the apparatus appears in Figure 4. As noted earlier, this setup was similar to the one used for producing the submaster gratings. It was not of optimum quality, but it was simple and gave good results with available equipment.

The camera used was a 10 x 12.5 cm Burke and James "Orbit" monorail which was stiffened with angle iron and weighted with lead blocks and steel plate. The lens was a Goertz Red-Dot Artar Apochromat with a focal length of 24 cm and maximum aperture f9. The camera was set at full extension to give an image of the specimen which was magnified by a factor of about 1.3. The specimen in its specially designed holder, the illuminating source and the camera rested upon a Gaertner optical table.

Focus of the specimen image is very critical in such a high resolution situation. The ground glass of the camera was not satisfactory because it was too coarse and because such focus plates are often not exactly in the photoemulsion plane. For focusing, a blank plate of the same thickness and type used in the photography was developed, fixed, and mounted in a plateholder. The image of the specimen in the emulsion was examined with an Edmund 50x magnifier which had been adjusted to focus in the emulsion plane while the magnifier base rested on the opposite side of the film plate. The image

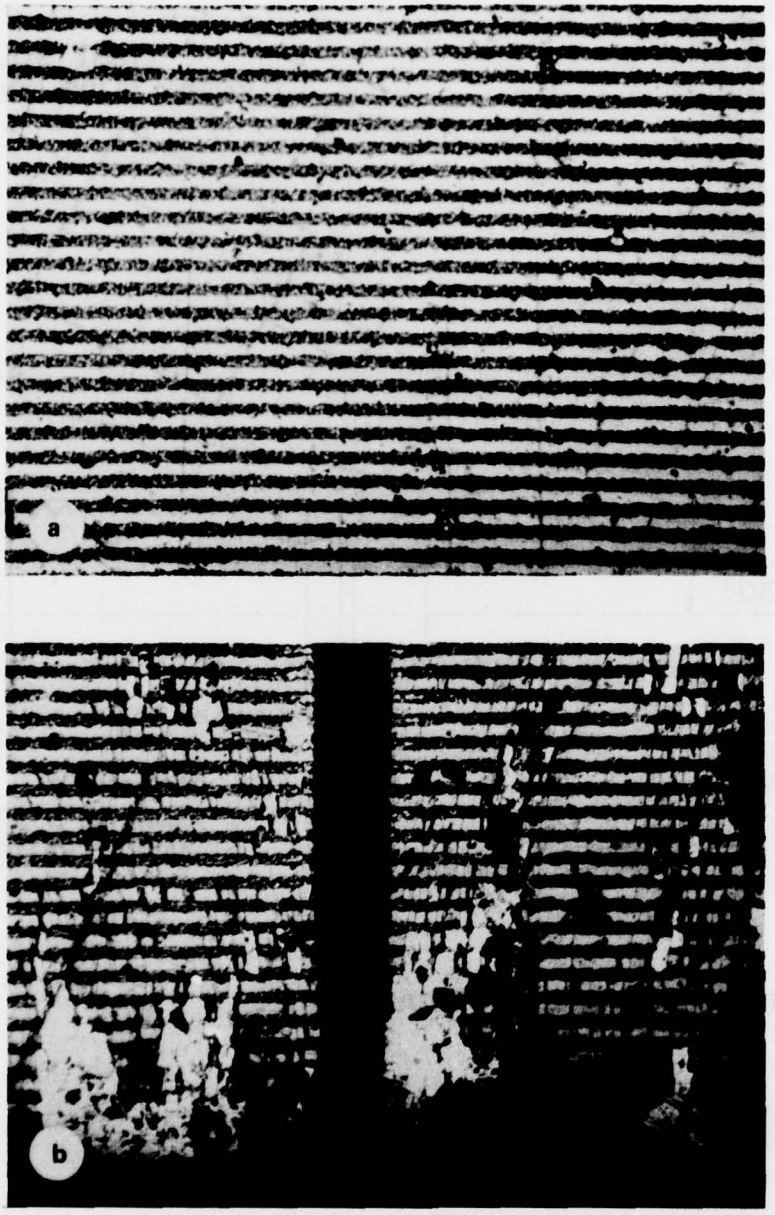


Figure 2. Photomicrographs of 39 lpmm (1000 lpi) specimen grating in photoresist:

(a) in small strain region

(b) adjacent to hole in large strain region.

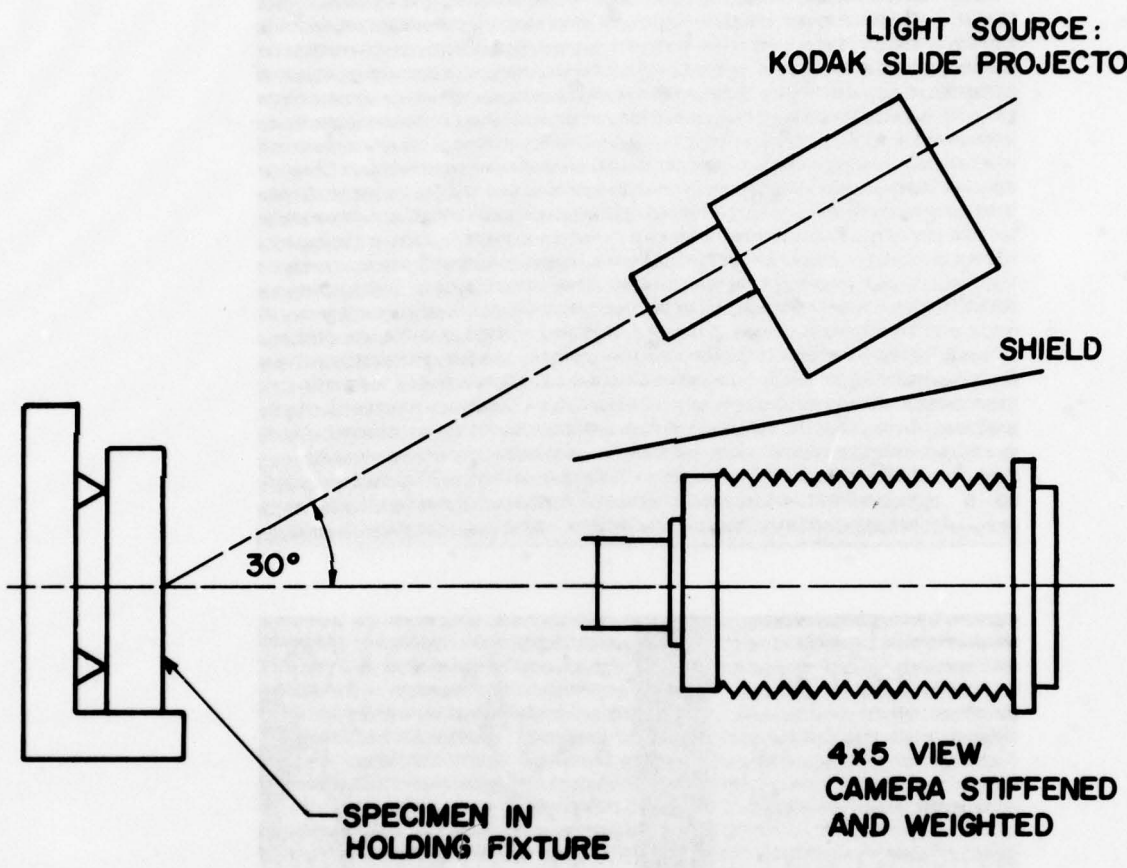


Figure 3. Sketch of apparatus for photographing specimen grating.

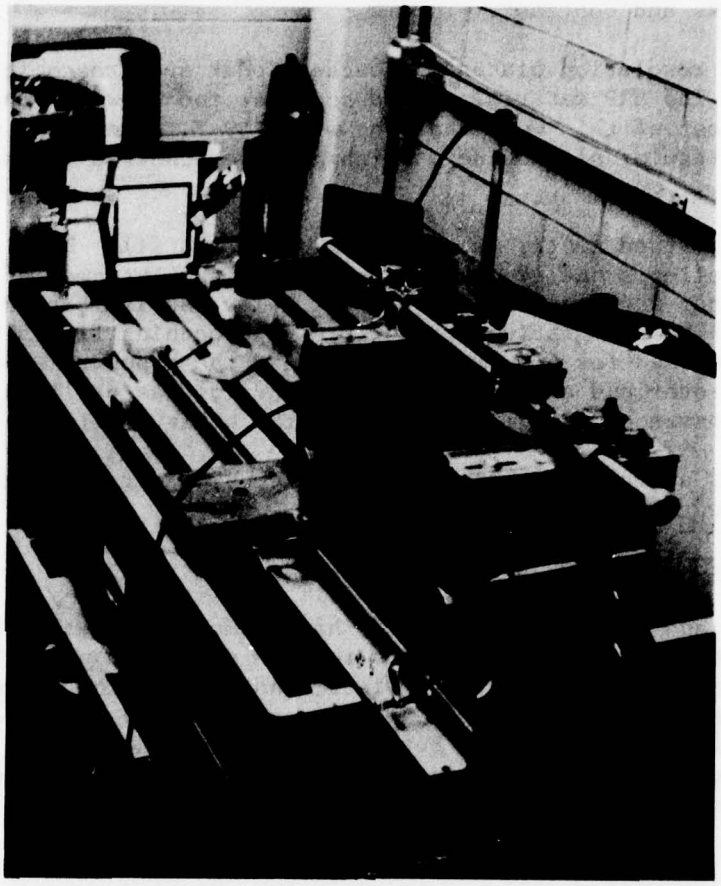


Figure 4. Photograph of apparatus for producing reduced submaster gratings and for photographing specimen grating.

of the specimen grating could be checked over the whole area of interest for maximum sharpness and contrast.

Kodak high resolution plates and backed Kodak spectroscopic 649-F plates were utilized. The HRP material proved somewhat too slow for the illumination available, so most of this work was done with 649-F. The glass photoplates were placed in regular plateholders which had been checked for matching critical dimensions.

The lens was used mostly at apertures of f9 and f11. High f-numbers gave reduced light fall-off and exposure reduction in the extremes of the field. But, the frequency response of the lens was below the limit required for photography of the 39.4 lpmm grating at apertures approaching f16. The lower f-number had to be used for proper resolution and the exposure adjusted for the best compromise over the area of interest. Dodging was utilized to even up the unequal exposure of the plate caused by the oblique illumination.

Figure 5 is a medium-contrast magnified copy of a typical grating photoplate as obtained by this procedure.

SLOTTED APERTURES IN GRATING PHOTOGRAPHY

Forno (18) and Burch and Forno (19) have demonstrated that slotted apertures can be used to tune a camera lens to give sharpened photographs of grating structures, improve depth of field, and enhance the response of a photographic system to certain spatial frequencies which might be contained in a random pattern. The work of Burch and Forno seems directed mainly towards measurement of deformation and strain through elegant but simple improvements of the moiré and speckle techniques.

Cloud (20) described an extension of the concepts which are developed and utilized in the references mentioned above. Slotted camera apertures can be used for multiplication of grating spatial frequency in moiré photography. Sensitivity of the measurement, which is often a serious problem when measuring strains with the moiré method, can be increased several fold. Depth of field is increased, and a camera lens of ordinary quality can be used to photograph the high frequency gratings. The method gives improved rendering of grating lines when sensitivity multiplication is not needed. The photography of two-dimensional arrays (grid and dot patterns) is simplified. These improvements multiply any gains which are derived from optical processing of the moiré photographs.

Forno (18) summarizes information required to design slotted aperture filter masks which will tune a given camera for photographic emphasis of particular space frequencies. These same principles can be used to obtain photographs containing gratings having frequencies which are multiples of the fundamental frequency in the specimen grating if (1) the higher frequencies are present in the structure being photographed and (2) the camera and film are capable of responding to these frequencies. The practical significance of requirement (1) is that the specimen grating be sharp and of high contrast.

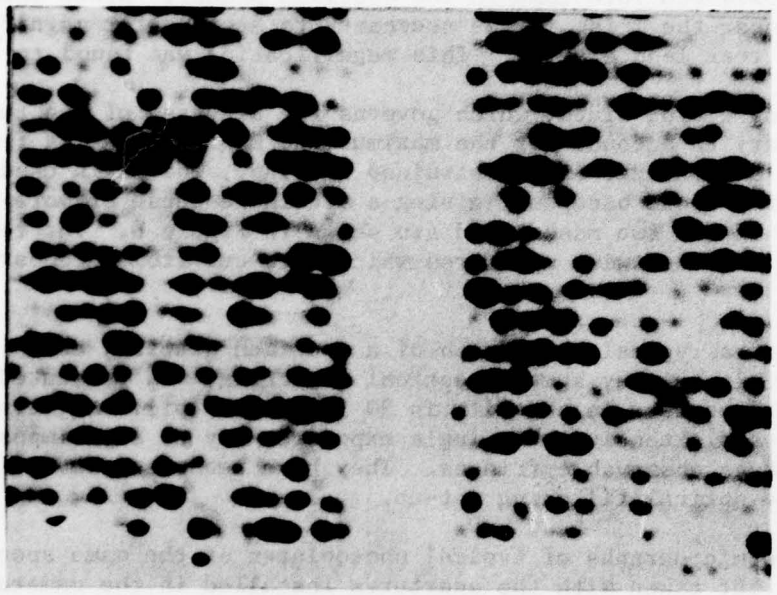


Figure 5. Photomicrograph of negative photograph of specimen grating obtained on 649-F plate at f 11 with white light and no filter mask.

The limits imposed by condition (2) are easily calculated for any camera-film combination.

Slotted apertures were designed to fit behind the iris diaphram inside the Goerz lens. Slot sizes and locations were calculated to tune the lens to spatial frequencies of 30 and 60 lpmm in the image plane for green light (corresponding to 39.4 and 78.8 lpmm in the specimen plane). Since the masks were to be placed near the iris, it was necessary to account for magnification of the mask by the rear lens element. This magnification was found to be 1.09.

In establishing a slot width, which governs the bandpass of the tuned lens, it is necessary to account for the maximum and minimum grating frequencies which will be encountered in the strained grating. The masks used were designed for a fairly broad bandpass, giving a strain response of more than $\pm$ 10%. Dimensions of the two masks used are shown in Figure 6. The results reported here were obtained with apertures which were cut from cardboard with a pocket knife.

A micrograph of a typical photograph of a specimen grating, taken at f11 in white light without any sort of optical filtering, was presented in Figure 5. Grating frequency in the film is 30 lpmm (762 lpi). Negative photos of this sort were used extensively. Single exposures may be superimposed with one another to produce observable fringes. They have been used in various combinations in the optical filtering set-up.

Figure 7 shows micrographs of typical photoplates of the same specimen used for Figure 5, but taken with the apertures installed in the camera lens. Comparison of Figures 7a and 7b, which were recorded with the 30 lpmm mask (referred to image plane) with Figure 5 suggests the degree of improvement which can be expected from using filter masks in photographing moiré specimen and master gratings. Expecially important is the delineation of the grating in the area where it cracked and flaked because of the plastic deformation of the specimen. The comparison is more suggestive if the specimen is not flat and normal to the optical axis. The depth of focus for the unmasked lens is so small that the grating will not be resolved over the whole specimen.

Figure 7c illustrates the grating frequency multiplication which can be obtained with slotted apertures inside a lens having a rather low upper frequency limit. The grating in Figure 7c is 60 lpmm on the film, which is equivalent to 78 lpmm (2000 lpi) on the specimen. Although this grating shows local non-uniformities, it produces very good moiré fringes when superimposed with an appropriate submaster.

FORMATION OF MOIRÉ FRINGE PATTERNS

Although useful moiré fringe patterns can be obtained by direct superposition of the grating photoplates with one another or with a grating submaster, such a simple procedure does not yield the best results, nor does it exploit the full potential of the information which is stored in the grating photo. Increased flexibility and control of the measurement process can be had by utilizing some of the basic procedures of optical data processing.

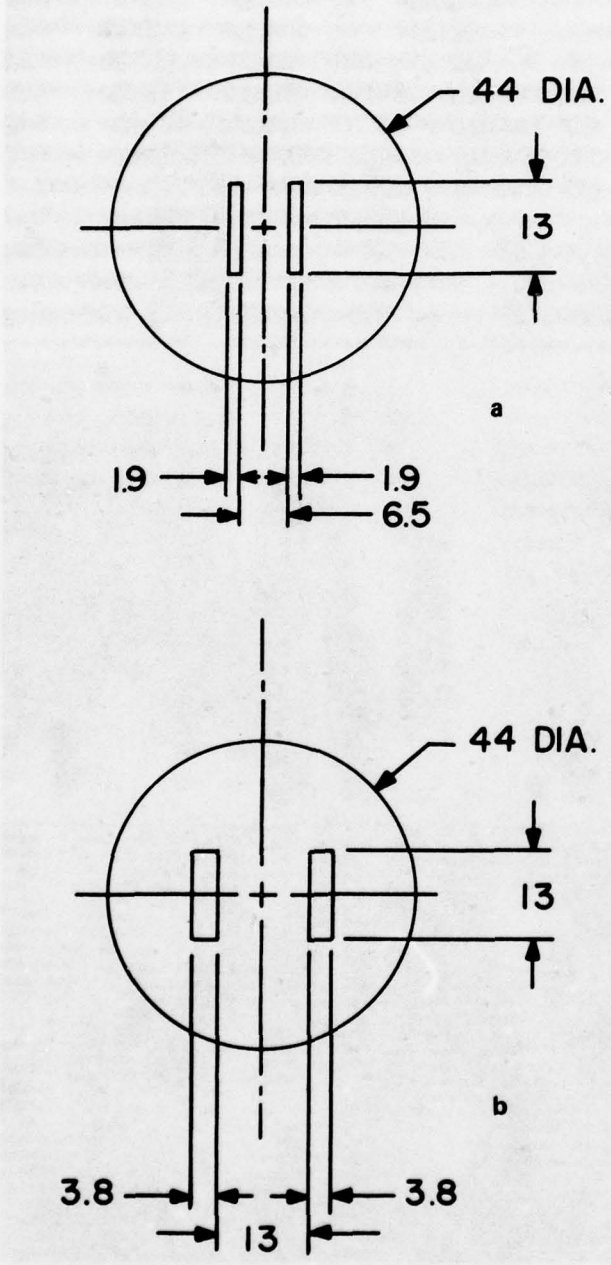


Fig. 6. Slotted aperture masks used in photographing moire gratings:

(a) mask for 39 lpmm (1000 lpi) at specimen
(b) mask for 79 lpmm (2000 lpi) at specimen

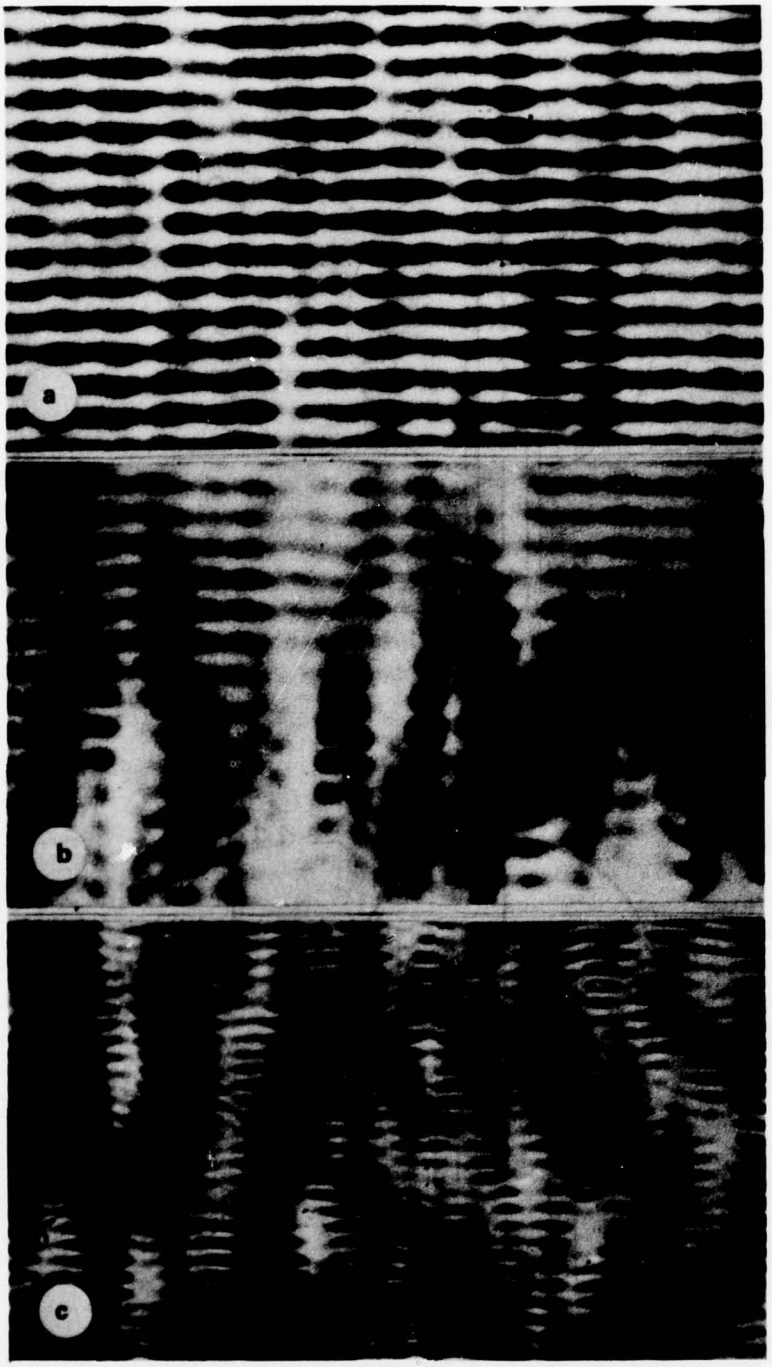


Figure 7. Photomicrographs of negative photographs of specimen grating obtained on 649-F plates with slotted aperture masks and white light.
(a) in small strain region with aperture having 39 lpmm (1000 lpi) center frequency at specimen
(b) same as (a) but in large strain region near hole
(c) in small strain region with aperture having 79 lpmm (2000 lpi) center frequency at specimen

Exploration or discussion of the relevant Fourier optics and diffraction theory are outside the scope of this paper. Of the many fine treatments in the literature, the papers of Van der Lugt (21) and Post (22,23,24) are especially useful, as is the landmark book by Guild (25).

SUMMARY OF OPTICAL PROCESSING

The grating photography stages of this experiment produced an assembly of photographic plates of the undeformed (baseline) and deformed (data) specimen gratings as well as several submaster gratings of various spatial frequencies. The steps required to produce moiré fringe photographs from these grating records were as follows:

1. A photoplate of the undeformed grid was superimposed with a submaster grating having a spatial frequency of 3 (sometimes 2) times the frequency of the magnified specimen grating plus or minus a small frequency mismatch.
2. The superimposed gratings were clamped together and placed in a coherent optical processor and adjusted to produce a correct baseline (zero strain) fringe pattern at the processor output, where it was photographed.
3. Steps 1 and 2 were repeated with the photograph of the deformed grating in order to create the "data" or "at strain" fringe pattern.
4. Steps 1-3 were repeated with other submaster gratings to produce fringe patterns having different pitch mismatch and, in some cases, different sensitivity multiplications. On the average, about 3 such pairs of baseline and data fringe patterns were produced for each coldworked specimen.
5. The fringe patterns were enlarged and printed in a size equivalent to about 7 times actual specimen dimensions with medium contrast.
6. The prints were sorted and coded for identification during the digitizing and data reduction steps.

OPTICAL PROCESSOR

The optical data processing system which was devised for moiré analysis is pictured schematically in Figure 8. This apparatus was subject to a continuing process of modification and upgrading.

The light source was a 10 milliwatt Helium-Neon CW laser made by Jodon Corporation of Ann Arbor, Michigan. The laser beam passed through a rather crude Gaertner spatial filter which converted it to a moderately clean diverging beam. This beam was directed to a sperical astronomical telescope mirror of 100 mm diameter obtained from Edmund Scientific Co. The mirror folded the beam to compensate for lack of space, and it also collimated the expanded beam. The moiré submaster grating and the photoplate of the specimen grating were placed with emulsion sides together in the optical path normal to the light beam, and they were clamped and held to an optical mount by spring-type clothespins. Trial experimentation showed that no fluid was needed between the plates. After passing through the photoplate, the beam, now containing diffraction components, was decollimated by two simple lenses (sometimes one) acting in

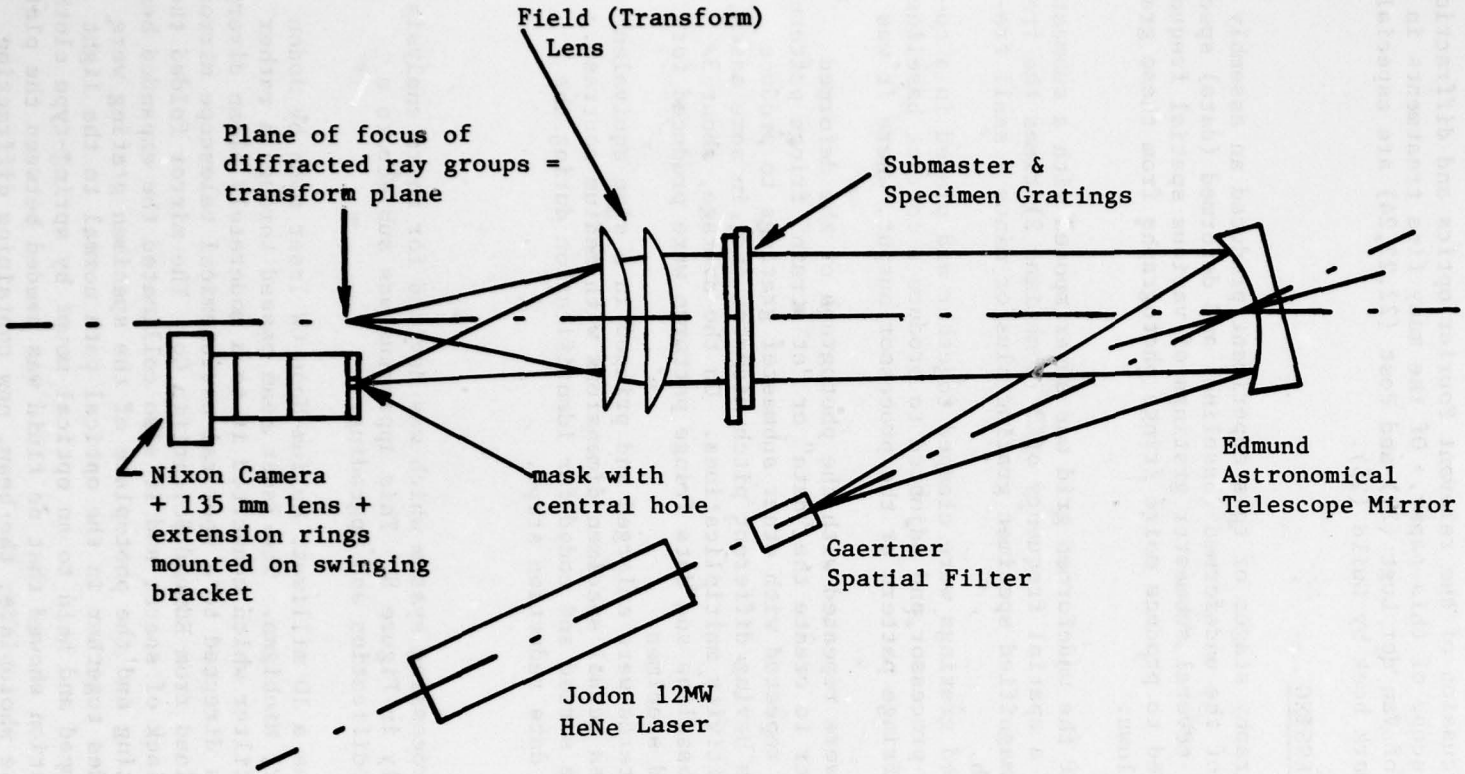


Fig. 8. Schematic of optical processing system for obtaining moire fringe photographs from specimen and submaster grating photographs.

series. These lenses were also obtained from Edmund Scientific Co. and were 102 mm in diameter with focal length of 559 mm. The focal plane of the system was found by trial with the data plates removed. In this plane, which is the transform plane of the field lens combination, was placed a black paper screen containing a hole of approximately 2.5 mm (0.1 in.) diameter. This screen was held in the filter mount of a 135 mm Nikor Lens which was mounted along with several extension rings upon a Nikon F camera. The camera was mounted on a swinging bar so that the hole in the filter mask could be made to coincide with the chosen ray group, a series of which appear as bright spots in the diffraction pattern. Selection of the proper bright patch was accomplished with the camera pointed so as to focus an image of the specimen grating plate on the camera film. The whole assembly, with the exception of the laser and spatial filter, was mounted on a simple optical bench from Ealing Optical Corp.

The camera was focused in the apparent plane of the data plate as seen through the field lens. After proper adjustment of the grating photoplates, a moiré pattern was visible upon the image of the specimen in the camera viewfinder. After final adjustment of the plates to eliminate rigid body rotation effects in the fringe pattern, the pattern was photographed on Kodak Tri-x film.

At this point in a moiré measurement the flexibility of the optical data processing procedure becomes useful. The baseline (zero strain) and deformed grating data are permanently stored on glass photographic plates. It is possible to superimpose these plates with different submaster gratings in order to gain maximum useful sensitivity multiplication and to improve subsequent fringe reading and data analysis by optimizing the spatial frequency mismatch of the superimposed grating.

In practice, it worked out that the specimen grating photographs had a spatial frequency of 30 lpmm which results with a specimen grating of 39.4 lpmm magnified 1.3 times. These plates could be superimposed with submasters of around 90 lpmm to get a sensitivity multiplication of 3, or of 60 lpmm for a multiplication of 2. The various mismatches were chosen to yield the closest fringe spacing obtainable with good fringe visibility. Most grating photoplates were processed with at least 3 mismatch levels, and sometimes with more than one sensitivity multiplication factor for checking purpose and because it was not possible to assess the quality of a dense fringe pattern through the camera viewfinder, which was used without a magnifier.

It was also possible at this stage to select by trial submasters which had density and diffraction characteristics which balanced with the properties of the specimen grating to produce the best fringe pattern. Also, the ray group which gave best fringe visibility could always be selected.

Following normal development of the 35 mm negatives of the fringe patterns in C-76 (Kodak D-76 plus Crone additive), they were sorted, cataloged, and coded. Most of them were then enlarged and printed in 200 x 250 mm size for numerical fringe analysis. Final printed image to specimen size ratio was approximately 7. Samples of typical moiré fringe patterns obtained are reproduced in Figure 9.

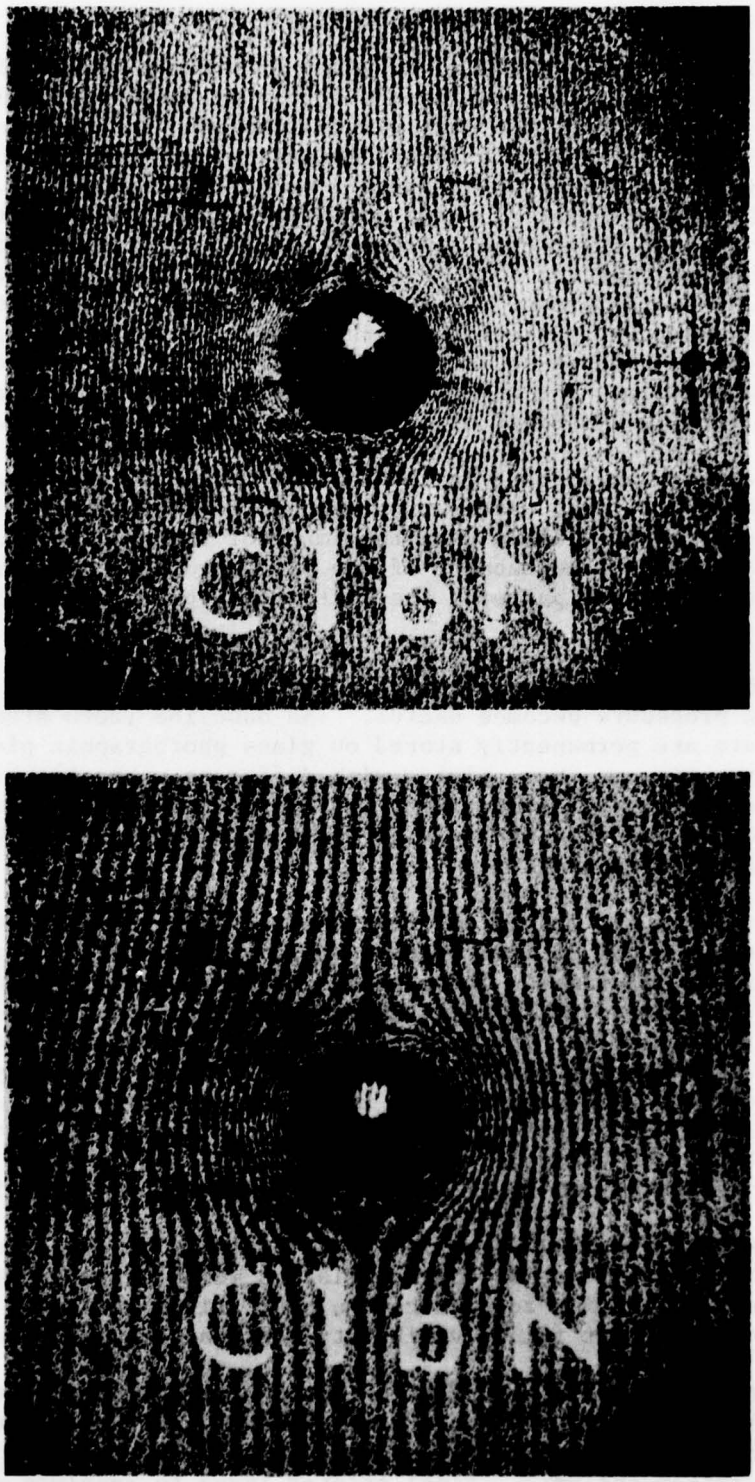


Figure 9. Typical moire fringe photographs from coldworked hole investigation; sensitivity multiplication = 3, two values of pitch mismatch.

REDUCTION OF MOIRÉ FRINGE DATA

A moiré interference fringe is a locus of points where the inplane displacement of the specimen surface normal to the grating lines, plus pitch mismatch if it exists, is a constant multiple of the pitch (period) of the grating. A picture of the inplane displacement component is constructed by plotting moiré fringe order along a given axis, subtracting mismatch (baseline) fringe orders, and dividing the remainder by the product of grating spatial frequency and the fringe multiplication factor used in the optical processing. A map of the strain component is then generated by calculating the derivative of the displacement with respect to the appropriate space variable.

The volume of moiré data accumulated made numerical processing attractive. A data reduction scheme was developed which incorporated most of the advantages of high speed computing while retaining some desirable features of cruder techniques, such as allowing examination of intermediate results and the introduction of a controlled small degree of data smoothing.

SUMMARY OF DATA REDUCTION

1. Hewlett-Packard Model 9820 desk computer with digitizing attachment was programmed to accept fringe location and scaling factors directly from fringe photographs and to compute and print fringe order along with fringe location in actual specimen dimensions.
2. The prepared enlargement of a "data" moiré pattern was taped to the table of the digitizer unit; fiducial mark locations and other data were entered as demanded by the program, and the locations of the intersections of the moiré fringes with the chosen axis were entered with the digitizer cursor.
3. Step 2 was repeated for the matching "baseline" fringe photograph.
4. The fringe location data were transferred manually to standard IBM computer cards along with the data about specimen number, interference level, moiré sensitivity, and so on.
5. A CDC 6300 digital computer with graphics facility was programmed to accept the moiré data and plot detailed graphs of the data input and to compute and plot displacement and strain as a function of distance from the hole edge.
6. After detailed analysis of each data set, various summary and statistical analysis plots were generated using computer graphics.

Certain aspects of the data reduction scheme for tangential strain differed from the procedure for radial strain measurement. These differences are ignored here.

DIGITIZING FRINGE DATA

Digitization of the fringe patterns was performed on a Hewlett-Packard Model 9820 calculator-plotter with a digitizer module attached. A one-dimensional digitizing program was prepared expecially for moiré fringe analysis. This program scaled the fringe locations to real specimen dimensions and incorporated a scale checking feature. The scaling was independent

of displacement of the cursor normal to the axis of interest, so that fiducial marks which were not on the axis under study could be used for scaling and checking.

Following initial entry of the various scaling and identification parameters requested by the program, the locations of fringe intersections with the axis under study were entered with the cursor. It was thought sufficient to enter only the integral order fringe, although the half-orders could easily have been included. The digitizer program automatically counted the fringes as they were entered.

As mentioned, the digitizing process was applied to a moiré data (after coldwork) photograph and a zero strain (before coldwork) fringe photo. These two sets of fringe data from a unit for computation and plotting of displacement and strain. Several such complete sets were obtained for each coldwork level by the use of moiré patterns obtained with different multiplication factors and pitch mismatches. In several cases, the same photos were digitized twice in order to analyze experimental errors derived from the digitizing process. Each individual run on each side of each hole was treated separately until summary plots were to be generated.

The digitized data printing by the calculator were punched on computer cards to fit the input format of the computer program for data analysis and plotting. This manual punching was rather inefficient but it did allow initial examination of the data for digitizing mistakes.

COMPUTER REDUCTION AND PLOTTING

Three computer programs for reducing data and plotting results were prepared. The first of these used a spline function smoothing, curve fitting, and interpolation algorithm to compute and plot a detailed analysis of each set of moiré data and the resulting strain and displacement maps. The second routine utilized similar procedures to prepare a summary plot of all the data for each hole. The third program constructed individual and complete statistical summary plots for any or all the coldwork levels. Because of space limitations, only a summary of the first routine is given here.

The operations performed by the detailed analysis routine were as follows:

1. Read set designation (specimen number plus other identifiers), moiré sensitivity multiplication factor from optical data processing, moiré grating spatial frequency, distance from primary fiducial mark to edge of hole, maximum fringe order to be entered, and all distances from fiducial mark to intersection of each moiré fringe for the axis under study for both baseline and data fringe patterns.
2. Generate fringe order numbers to match each fringe location entered as data.
3. Fit the baseline and coldwork data with two continuous smooth curves by means of a cubic spline smoothing routine. The degree of smoothing could be specified by the user; a minimum value was chosen for this study.

4. Interpolate the calculated curves to obtain fringe number as a function of distance from the fiducial mark at 100 points on the data and baseline curve.
5. Subtract the baseline fringe order from the coldwork hole fringe orders for each of the 100 nodes and convert the differences to radial displacement for the chosen axis.
6. Subtract the distance from the fiducial mark to the hole edge from each nodal x-value in order to have all results reported in terms of distance from the hole.
7. Compute by finite differences the first derivative of displacement with respect to distance from the hole; this result is the radial strain at each of the 100 nodes.
8. Print, of ordered by the input control cards, all values of input fringe orders, displacements and strain.
9. Scale the data and generate a plot of the input data and baseline curves. This graph shows fringe data points and the smoothed curves.
10. Plot radial displacement as a function of distance from the hole.
11. Plot radial strain as a function of distance from the hole.

Samples of each of the three graphs produced by this routine are assembled in Figure 10. A typical summary as prepared by the second routine appears in Figure 11.

The third computer program was devised to serve two purposes in the final stages of data analysis. First, it applied simple statistics to all the data obtained for each hole (or each side of a hole) and generated printout and plots showing average strain and its standard deviation at approximately 20 points on the curve. The second function of this program was to create composite summary plots of the radial strain map for all degrees of coldworking which were studied.

The data for this analysis was generated by scaling strain values at several distances from the hole from the curves previously generated for each hole. Additional data included hole label and interference level, number of points along the distance axis, the values of these distances scaled from the graphs, the number of curves which are used as data, and the radial strain from each curve at each distance. Where appropriate, opposite sides of the hole were treated first separately and then together. Also the two specimens which had identical coldwork levels were first treated separately and then combined. The flexibility of this program allowed it to be used in several different ways to fit these various situations without modification. A composite statistical plot showing the distribution of average radial strain for each of the coldworking levels appears in Figure 12. These plots constitute the final product of the investigation.

SUMMARY

The moiré technique described above, while quite sophisticated, proved to be simple and efficient enough so that large numbers of strain maps could be obtained by technicians who are not skilled in precise optical work. The results

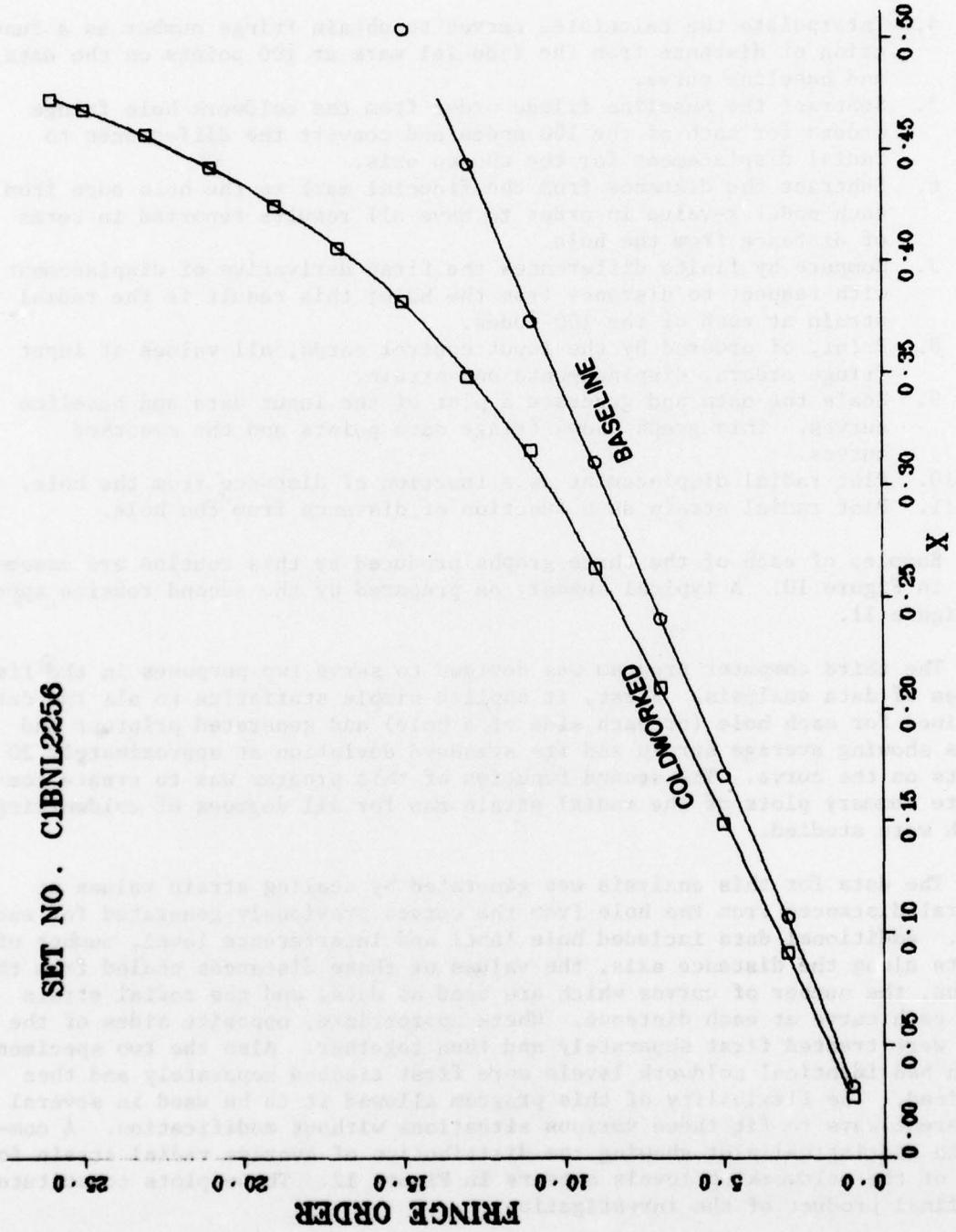


Figure 10. Typical graphs generated by detailed data reduction program: (a) typical baseline and coldworked input data from fringe photographs.

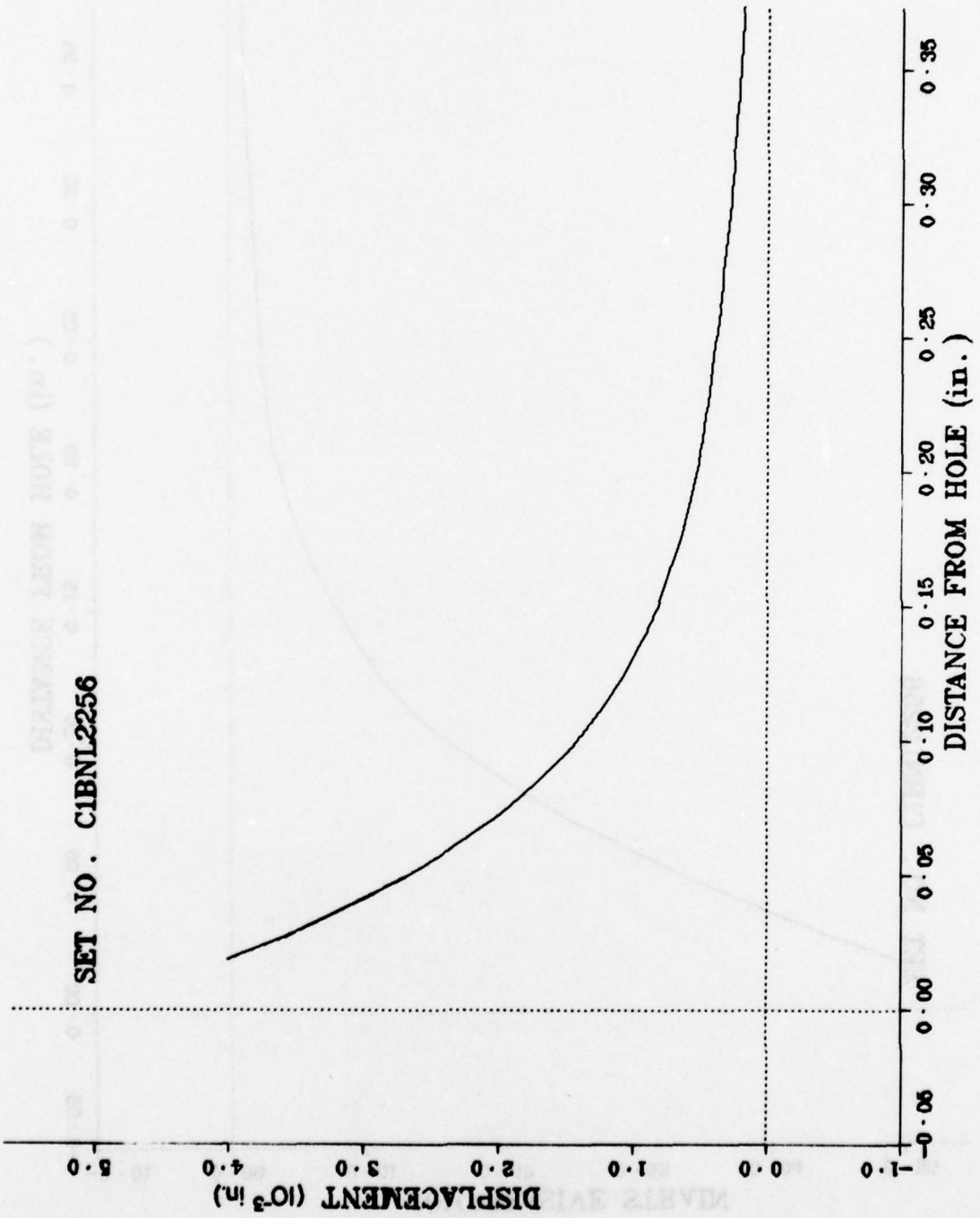


Figure 10. Typical graphs generated by detailed data reduction program; (b) typical radial displacement.

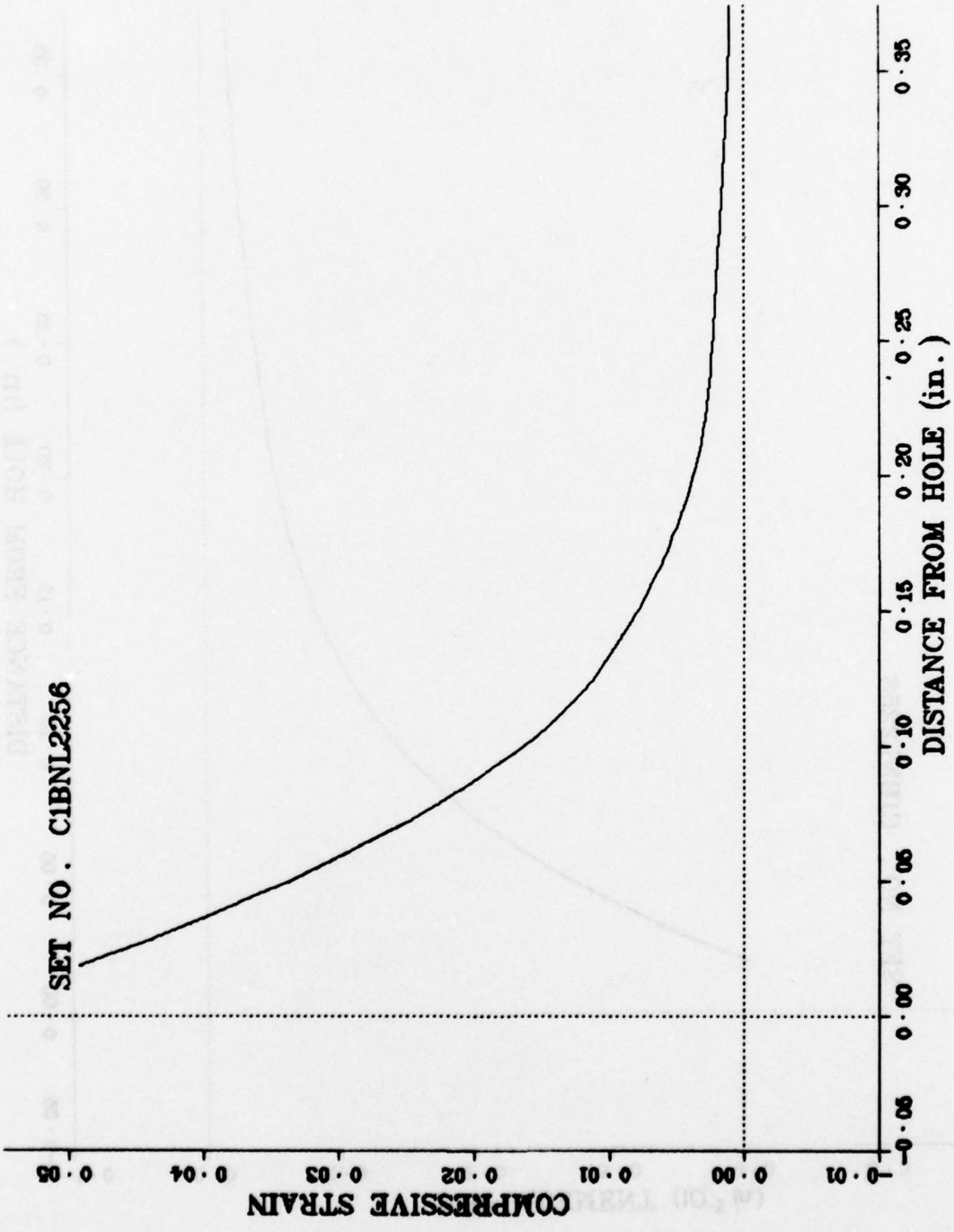


Figure 10. Typical graphs generated by detailed data reduction program; (c) typical radial strain.

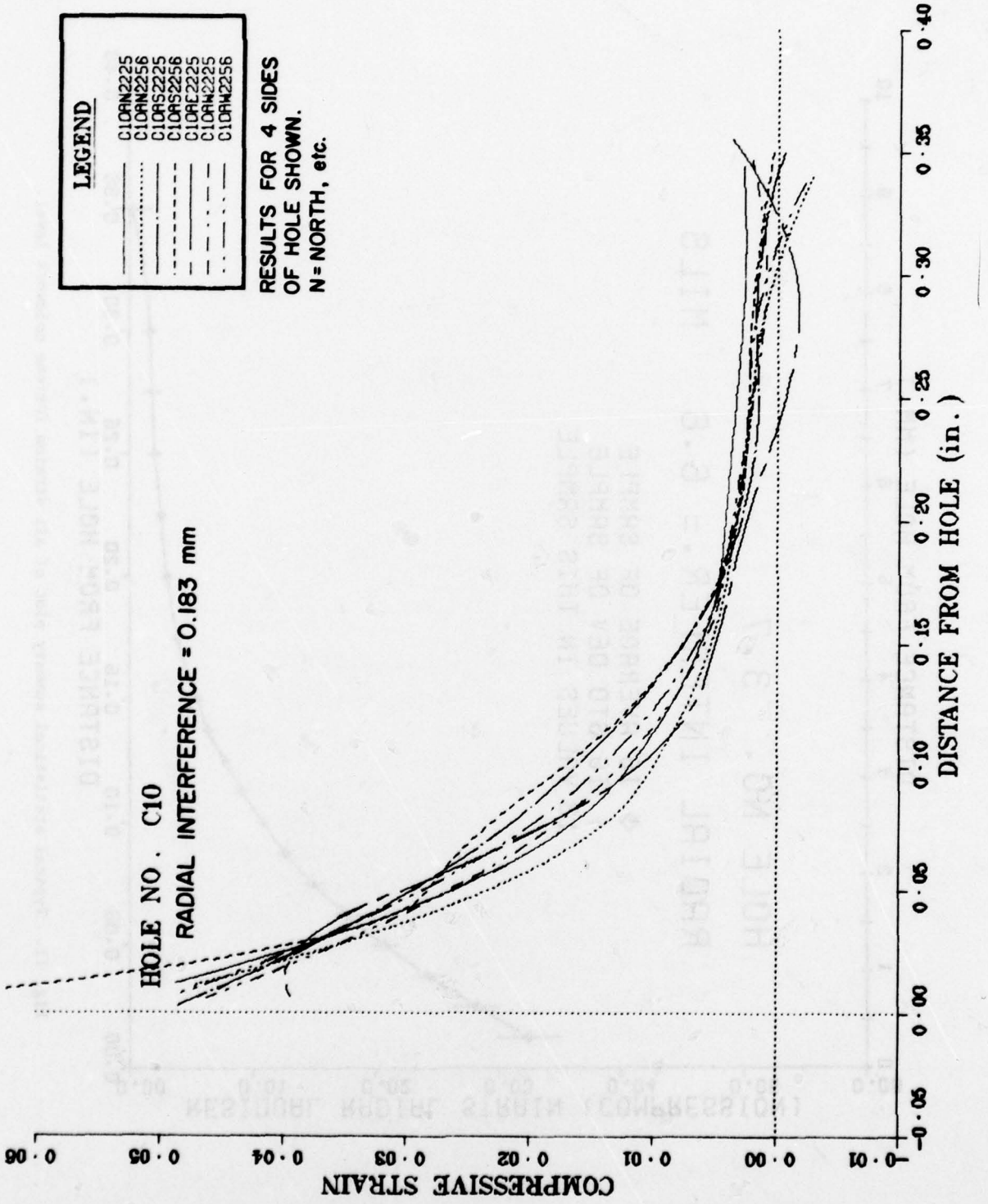


Figure 10. Typical graphs generated by detailed data reduction program; (d) typical composite radial strain for one specimen.

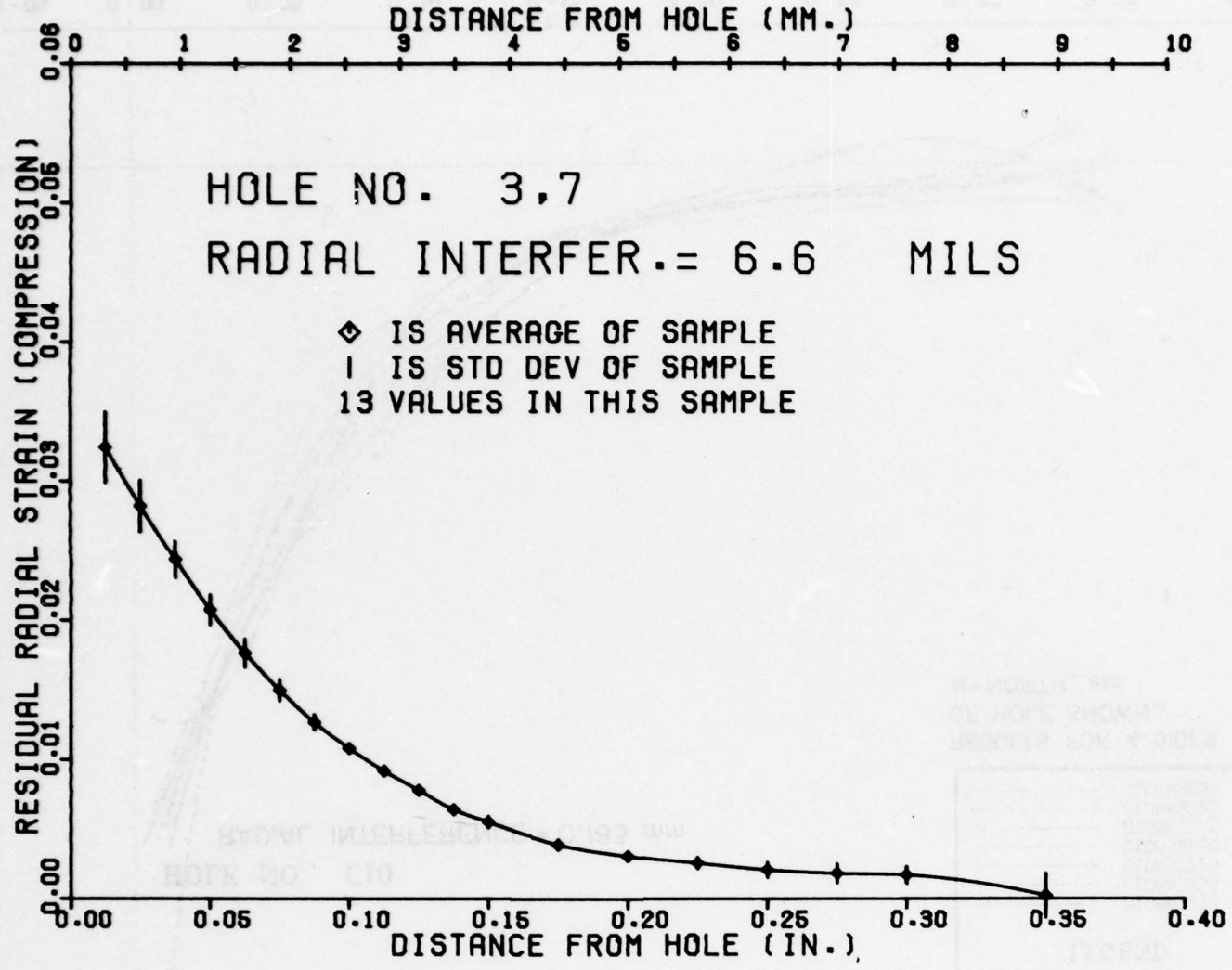


Fig. 11. Typical statistical summary plot of all strains for one coldwork level.

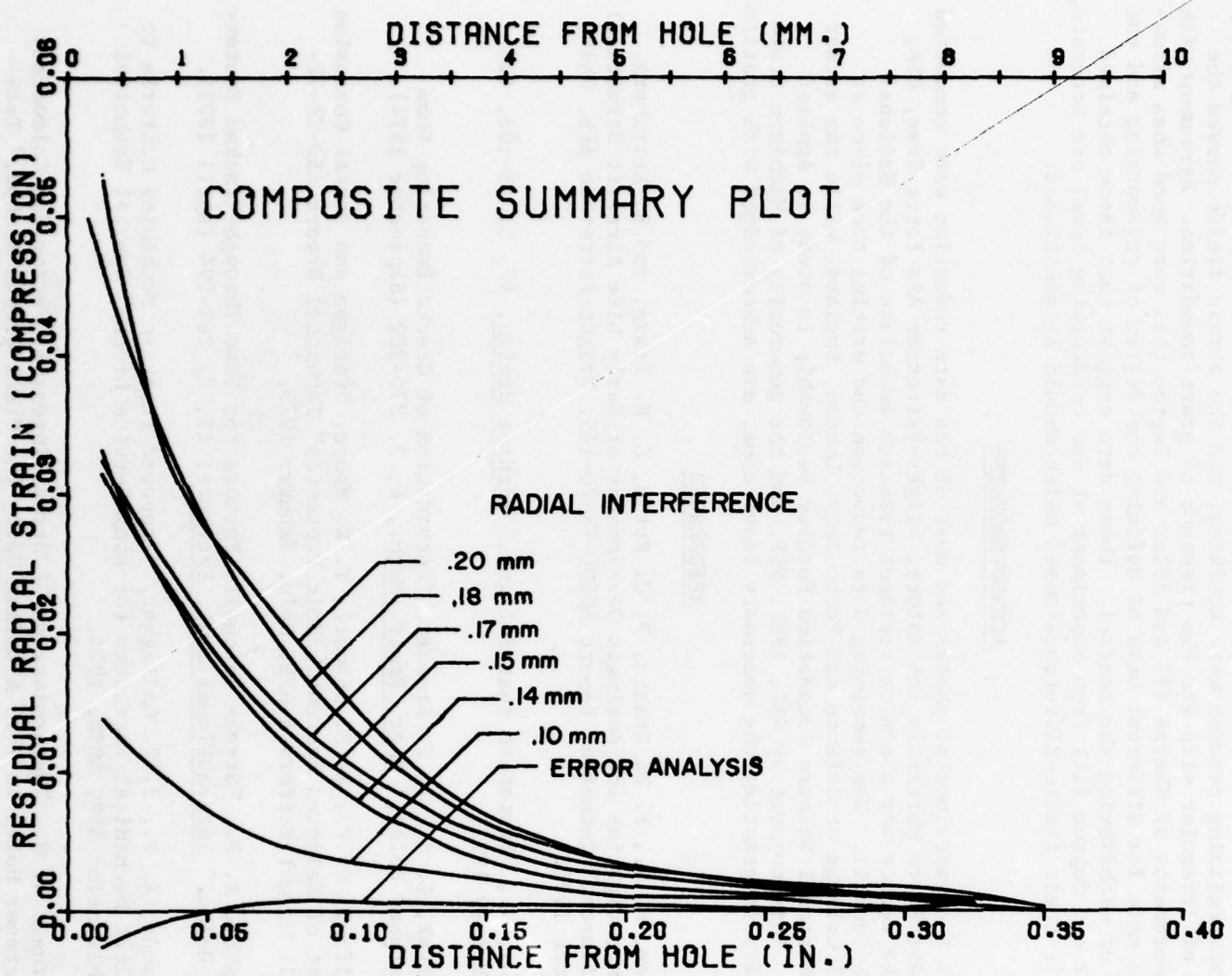


Fig. 12. Composite statistical summary plot showing average radial strains for each coldwork level.

were qualitatively consistent with expectations. The effects of non-symmetry of the mandrelizing process were striking, and the strain fields showed the effects of irregular slip and the presence of grain boundaries. Agreement with the measurements of Sharpe (9) and Adler and Dupree (11) were good when allowance was made for different ways of defining the degree of coldworking and the effects of withdrawing the mandrel. These data suggest that those obtained by Adler and Dupree (11) from experiment at one coldworking level are accurate, and it is their finite-difference model which should be questioned.

ACKNOWLEDGEMENT

All the experimental phases and most of the data reduction were conducted at the Air Force Materials Laboratory, Wright-Patterson Air Force Base, USA, while the author was a senior resident research associate of the National Research Council. The remaining data reduction and writing took place at Imperial College of Science and Technology, London, England, while the author held a National Science Foundation Faculty Fellowship to study in Applied Optics. This support by NRC, AFML, NSF, and the generosity of Michigan State University in granting the necessary leave time, are acknowledged with gratitude.

REFERENCES

1. Gran, R. J., F. D. Orazio, P. C. Paris, G. R. Irwin, and R. Hertzberg, "Investigation and Analysis Development of Early Life Aircraft Structural Failures," Technical Report AFFDL-TR-70-149, Wright-Patterson AFB, Ohio, March 1971.

2. Kohl, R., "Fasteners that Fatigue," Machine Design, 47, 5, 48-102, (20 February 1975).

3. Petrak, G. J., R. P. Stewart, "Retardation of Cracks Emanating from Fastener Holes," Engr. Fract. Mech., 6, 2, 275-282 (September 1974).

4. Tiffany, C. F., R. P. Stewart, T. K. Moore, "Fatigue and Stress Corrosion Test of Selected Fasteners/Hole Processes" Technical Report ASD-TR-72-111, Wright-Patterson AFB, Ohio, January 1973.

5. Grandt, A. F., "Stress Intensity Factors for Some Through-Cracked Fastener Holes," International Jrnl. Fracture, 11, 2, 283-294 (April 1975).

6. Grandt, A. F., J. P. Gallagher, "Proposed Fracture Mechanics Criteria to Select Mechanical Fasteners for Long Service Lives," Special Technical Publication 559, ASTM, 1974.

7. Cathey, W. H., "Determination of Stress Intensity Factor for Coldworked Fastener Holes in 7075 Aluminum Using the Crack Growth Method," Technical Report AFML-TR-74-283, Wright-Patterson AFB, Ohio, May 1975.

8. Grandt, A. F., T. D. Hinnerichs, "Stress Intensity Factor Measurements for Flowed Fastener Holes," Proc. Army Symposium on Solid Mechanics, 1974, AMMRC-MS-74-8, September 1974.

9. Sharpe, W. N., Jr., "Measurement of Residual Strains Around Coldworked Fastener Holes," Scientific Report, AFOSR Grant 75-2817, Bolling AFB, Washington, D.C., April 1976.

10. Potter, K. M., A. F. Grandt, Jr., "An Analysis of Residual Stresses and Displacements Due to Radial Expansion of Fastener Holes." ASME 1975 Failure Prevention and Reliability Conference, Washington, D.C., (September 1975).

11. Adler, W. F., D. M. Dupree, "Stress Analysis of Coldworked Fastener Holes," Technical Report AFML-TR-74-44, Wright-Patterson AFB, Ohio, (July 1974).

12. Ford, S. C., B. N. Leis, D. A. Utah, W. Griffith, S. G. Sampath, D. M. Mincer, "Interference Fit Fastener Investigation," Technical Report AFFDL-TR-75-93, Wright-Patterson AFB, Ohio (September 1975).

13. Cloud, G., D. Corbly, "Residual Surface Strain Distribution Near Fastener Holes which are Coldworked to Various Degrees," Air Force Materials Laboratory," Technical Report Wright-Patterson AFB, Ohio (In press).

14. Luxmoore, A., R. Hermann, "An Investigation of Photoresists for Use in Optical Strain Analysis." Jrnl. Strain Anal., 5, 3, 162 (July 1970).

15. Holister, G. S., A., R. Luxmoore, "The Production of High Density Moiré Grids," Exp. Mech., 8, 210 (May 1968).

16. Luxmoore, A. R., R. Hermann, "The Rapid Deposition of Moiré Grids," Exp. Mech., 11, 5, 375-377 (August 1971).

17. Chiang, F. P., "Production of High Density Moire Grids - Discussion," Exp. Mech., 9, 6, 286 (June 1969).

18. Forno, C., "White Light Speckle Photography for Measuring Deformation, Strain, and Shape," Optics and Laser Tech., 217 (October 1975).

19. Burch, J. M., and C. Forno, "A High Sensitivity Moiré Grid Technique for Studying Deformation in Large Objects," Optical Eng., 14, 2, 178 (March-April 1975).

20. Cloud, G. L., "Slotted Apertures for Multiplying Grating Frequencies and Sharpening Fringe Patterns in Moiré Photography," Optical Eng., 15, 6, 578 (Nov-Dec 1976).

21. Van der Lugt, A., "A Review of Optical Data Processing Techniques," Optica Acta, 15, 1, 1-33 (January 1968).

22. Post, D., "Analysis of Moiré Fringe Multiplication Phenomena," Appl. Opt., 6, 11, 1938 (November 1967).

23. Post, D., "New Optical Methods of Moiré Fringe Multiplication," Exp. Mech., 8, 2, 63 (Feb. 1968)

24. Post, D., "Moire Fringe Multiplication with a Nonsymmetrical Doubly Blazed Reference Grating," Appl. Opt., 10, 4, 901-907, (April 1971).

25. Guild, J., The Interference System of Crossed Diffraction Gratings, Clarendon Press, Oxford (1956).

AN EVALUATION OF THE CRACK GAGE TECHNIQUE FOR INDIVIDUAL AIRCRAFT TRACKING

T.D. GRAY
Air Force Flight Dynamics Laboratory
Wright-Patterson Air Force Base, OH 45433

A.F. GRANDT, JR.
Air Force Materials Laboratory
Wright-Patterson Air Force Base, OH 45433

ABSTRACT

This paper describes an on-going research program aimed at evaluating the "crack gage" approach as an alternate technique for meeting USAF Individual Aircraft Tracking requirements for the F-4 aircraft force. Individual aircraft tracking requirements are reviewed and the present F-4 approach is discussed. Recent developments with the crack gage technique, which employs a cracked coupon mounted to the aircraft structure as a load sensor and measurement device, are also summarized. An evaluation of this new approach presently being conducted on a full-scale F-4 fatigue test article is described and is followed by a brief discussion of the impact of a successful implementation of the crack gage tracking technique to management of the F-4 force. Cost savings for the crack gage technique have been estimated to be in excess of $7 million over a five year period.

INTRODUCTION AND DESCRIPTION OF USAF INDIVIDUAL AIRCRAFT FLEET TRACKING REQUIREMENTS

Maintaining the damage tolerance and durability of USAF aircraft structures is dependent on the capability of the appropriate Air Force Commands to perform specific inspection, maintenance, and possibly modification or replacement tasks at specific intervals throughout the service life (i.e., at specified depot or base level maintenance times and special inspection periods). Experience has shown that the actual usage of military airplanes may differ significantly from the usage assumed during design. Likewise, individual aircraft within a force may experience a widely varied pattern of usage severity as compared to the average aircraft. Thus, continual adjustments to initially determined safe crack growth intervals must be made for individual aircraft to ensure safety and to allow for modification and repair on a timely and economical basis.

Force management is the responsibility of the Air Force and is accomplished in accordance with the Force Management Tasks of MIL-STD-1530A, Aircraft Structural Integrity Program (ASIP) [1], using a data package provided by the contractor for each new aircraft system. This data package consists of the necessary data acquisition and reduction techniques and analysis methods needed to acquire, evaluate, and utilize operational usage data in order to provide a continual update of in-service structural integrity.

A basic element of the force management data package is the Individual Aircraft Tracking (IAT) program. The objective of the IAT program is to

predict potential flaw growth in critical areas of each airframe based on individual aircraft usage data. A tracking analysis method is developed to establish and adjust inspection and repair intervals for each critical structural location of the airframe. This analysis provides the capability to predict crack growth rates, time to reach crack size limits, and crack length as a function of total flight time and usage. A data acquisition system is developed which is as simple as possible and is the minimum required to monitor those parameters necessary to support the tracking analysis method.

Current practice for acquisition of IAT usage data includes recording strain, center of gravity motion parameters (e.g., normal load factor, n_z), and flight condition data (e.g. mission segment, configuration, airspeed, altitude, and gross weight). The tracking analysis method then utilizes this data to estimate crack growth from assumed initial flaws in each critical point in the structure. Initial flaw size assumptions required for new aircraft are specified in Reference 2.

PRESENT F-4 INDIVIDUAL AIRCRAFT TRACKING PROGRAM

The first IAT program for tracking crack growth in fighter aircraft was developed in conjunction with the F/RF-4 C/D and the F-4 E(S) damage tolerance assessments [3,4]. The present F-4 IAT program consists of a counting accelerometer data acquisition system and a tracking analysis methodology which is termed the "damage index and equivalent S-N curve" system. Data acquisition is accomplished by recording normal load factor exceedances via counting accelerometers installed in each aircraft. The F-4 counting accelerometers are set to record n_z counts at 3, 4, 5, and 6 g's. Extrapolation techniques are used to determine n_z counts at 7 and 8 g's. In addition, VGH data (airspeed, load factor, altitude) are recorded on approximately 13% of the force in order to develop baseline operational stress spectra.

The "damage index and equivalent S-N curve" system was developed for the F-4 to simplify the crack growth tracking process. Instead of conducting a cycle-by-cycle crack growth analysis for each critical location of each individual aircraft, only one number (the damage index) is computed for each aircraft based on individual usage. Through the damage index, crack growth at one location (the monitoring location) is determined. The amount of crack growth at other critical locations is evaluated by damage index limits that relate to the monitoring location. Individual flaw size assumptions used for all F-4 critical locations are based on the results of the previously mentioned damage tolerance assessments [3,4].

Equivalent S-N curves are used to convert individual aircraft counting accelerometer data to a damage index for each airplane. These are not the standard S-N curves for fatigue which present stress versus number of cycles to failure for constant amplitude loading. These equivalent S-N curves represent flight-by-flight crack growth at the monitoring location and were developed from crack growth curves for three usages: mild, baseline and severe (see Figure 1).

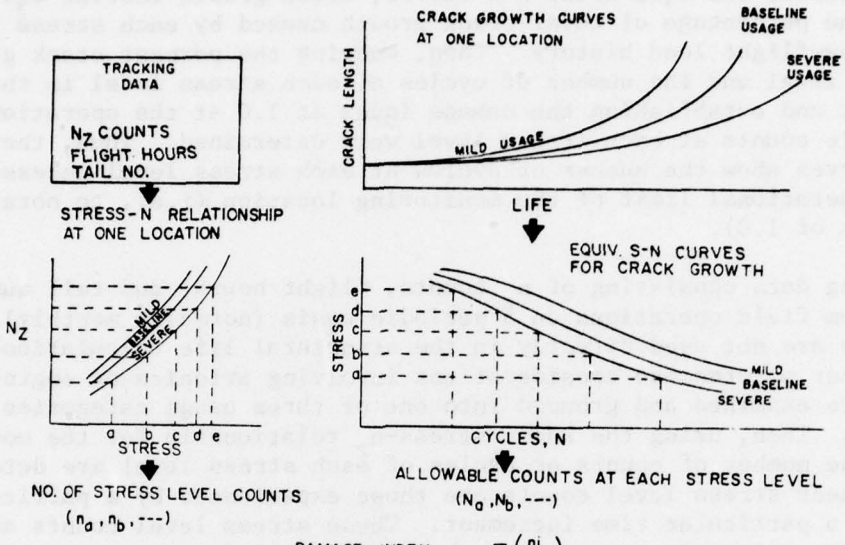


Fig. 1 Schematic representation of current F-4 tracking analysis method employing the damage index and equivalent S-N curve system.

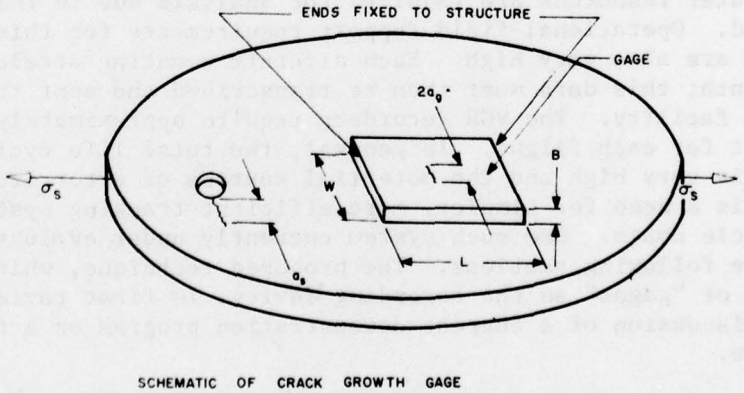


Fig. 2 Schematic view of crack growth gage attached to flawed structural component

To construct the equivalent S-N curves, crack growth testing was used to determine the percentage of total crack growth caused by each stress level in the flight-by-flight load history. Then, knowing the percent crack growth of each stress level and the number of cycles of each stress level in the operational limit and establishing the damage index at 1.0 at the operational limit, the allowable counts at each stress level were determined. Thus, the equivalent S-N curves show the number of cycles at each stress level necessary to reach the operational limit of the monitoring location (i.e., to obtain a damage index of 1.0).

Tracking data consisting of n_z counts, flight hours, and tail number are received from field operations on a periodic basis (normally monthly). Actual flight hours are not used directly in the structural life calculations but are used for other maintenance considerations involving avionics or engines. The n_z counts are examined and grouped into one of three usage categories according to severity. Then, using the known stress-n_z relationship for the monitoring location, the number of counts or cycles of each stress level are determined. Note that these stress level counts are those experienced by a particular airplane in a particular time increment. These stress level counts are then divided by the allowable counts at each stress level and summed in a Miner's type analysis to compute damage index for a particular airplane.

The F-4 IAT program is typical of the current IAT state-of-the-art in terms of cost, complexity, and accuracy and is quite adequate considering present technology. The complexity of this type of system becomes evident when one realizes the vast amount of data being recorded and the fact that reduction and analysis of this data requires many manual actions and assumptions such as screening, editing, and gap-filling for lost or bad data. Each of these manual actions and assumptions provides a potential source of error. Large amounts of computer resources are required for analysis due to the sheer mass of data involved. Operational field support requirements for this type of tracking system are also very high. Each aircraft counting accelerometer must be read each month; this data must then be transcribed and sent to the central data processing facility. The VGH recorders require approximately 45 minutes of field support for each flight. In general, the total life cycle cost of this type of system is very high and the potential sources of error are many. Clearly, there is a need for simpler, more efficient tracking systems with reduced life cycle costs. One such system currently under evaluation is described in the following sections. The proposed technique, which employs cracked coupons or "gages" as the recording device, is first reviewed, and then followed by a discussion of a current demonstration program on a full-scale F-4 test article.

CRACK GAGE TECHNIQUE FOR INDIVIDUAL AIRCRAFT TRACKING

For the past three years, the Air Force Materials and Flight Dynamics Laboratories have been conducting in-house and contractual research intended to develop an improved technique for monitoring the effect of service loads on the extension of possible preexistent structural cracks. The approach being considered consists of mounting a precracked coupon onto a load-bearing

structural member as shown schematically in Figure 2. The coupon receives the same load excursions encountered by the structure (to within a predictable scaling factor) and responds with a measurable crack extension which may be correlated with the growth of another crack assumed to be present in the structural component. One may consider the cracked coupon as an analog computer which senses the load history, determines its effect on crack growth, and responds with a measurable output (i.e., gage crack extension). The purpose of this section is to describe the general features of the crack gage method and to briefly review the developments [5-10] of this approach which led to the present evaluation program for the F-4 fleet.

OVERVIEW OF PREDICTIVE MODEL

A mathematical model for relating the crack length a_g in the coupon (crack gage) shown schematically in Figure 2 to the growth of an assumed structural flaw a_s will now be described. The initial structural flaw size and shape is based on the appropriate design criteria (i.e., Ref. 2), while the coupon geometry may be selected for a given response. The ends of the cracked gage are assumed to be fastened (e.g. adhesively bonded, riveted, welded, etc.) to the structural member so that when the structural component is subjected to some remote stress σ_s, an effective stress σ_g is transferred to the cracked coupon. This relationship between structural and gage loads can be expressed in the form

$$\sigma_g = f\,\sigma_s \qquad (1)$$

Here the load-transfer function f may depend on geometry and material properties, but not on stress level. Determining an expression for f is essentially a stress analysis problem which can be readily approached by several analytical and/or experimental techniques [5,7,8].

Now, assume that crack growth in the gage and structural materials can be described by a model of the form

$$\frac{da}{dN} = F(K) \qquad (2)$$

Here da/dN is the fatigue crack growth rate and F(K) is an appropriate function relating the stress intensity factor K, material properties, and other significant load variables. Much of the success of fracture mechanics techniques for analyzing crack growth problems lies in the fact that such crack growth models are readily available and are applicable for many structural materials. Solving Equation 2 for cyclic life N, and observing that at any instant of time the gage and structural defects receive the same number of load

cycles leads to

$$N = \int_{a_{is}}^{a_s} \frac{da}{F_s(K)} = \int_{a_{ig}}^{a_g} \frac{da}{F_g(K)} \qquad (3)$$

Here a_i and a are the initial and final crack lengths, while the subscripts s and g refer, respectively, to structural and gage quantities.

An interesting special case occurs when crack growth in the structural and gage materials can be described by the simple Paris law

$$\frac{da}{dN} = C\bar{K}^m = F(K) \qquad (4)$$

Here $\bar{K}$ is the range in cyclic stress intensity factor and C and m are empirical constants. Now, expressing $\bar{K}$ in the standard form

$$\bar{K} = \bar{\sigma}\sqrt{\pi a}\ \beta \qquad (5)$$

where $\bar{\sigma}$ is the cyclic stress, a is the crack length, and β is the usual flaw geometry dependent stress intensity factor coefficient [11-13], and combining Equations 1, 3, 4, and 5 leads to

$$N = \int_{a_{is}}^{a_s} \frac{da}{C_s(\bar{\sigma}_s\sqrt{\pi a}\beta_s)^{m_s}} = \int_{a_{ig}}^{a_g} \frac{da}{C_g(f\bar{\sigma}_s\sqrt{\pi a}\beta_g)^{m_g}} \qquad (6)$$

Note that a is the dummy variable of integration in Equation 6 and that, while f and β depend on geometric and possibly material properties, neither function depends on the load level $\bar{\sigma}_s$.

Further assuming that the gage and structural materials have the same crack growth exponent $m_s = m_g = m$ (a reasonable assumption if gage and structure are made from the same material) leads to

$$\int_{a_{is}}^{a_s} \frac{da}{C_s(\sqrt{\pi a}\beta_s)^m} = \int_{a_{ig}}^{a_g} \frac{da}{C_g(\sqrt{\pi a}\beta_g)^m} \qquad (7)$$

Note that all stress level terms effectively cancel in Equation 7. Although this expression no longer specifies the cyclic life N, it still represents a valid relationship between gage and structural quantities. Since the material properties C_s, C_g, and m can be determined from conventional baseline testing, the stress intensity factor coefficients, β, are readily available from handbooks [11-13] or are obtainable by standard analysis methods, and the initial gage and structural crack lengths a_{ig} and a_{is} are specified, Equation 7 can be integrated numerically to obtain the structural crack size a_s as a function of gage crack size a_g. Thus, measuring the gage crack length also effectively determines the growth of the initially assumed structural defect during service. Of special significance is the fact that when crack growth can be described by a simple Paris law (Equation 4), the a_s versus a_g relationship is <u>independent of loading</u>. Although this apparent load independence is one feature of the crack gage approach that seems especially attractive for crack growth based fleet tracking requirements, it may not hold true for loadings which yield crack growth rates which cannot be described by Equation 4. An alternate approach which could be employed for situations where this simple Paris law is no longer valid is described in a later section. First, however, some results of experiments conducted to evaluate the crack gage concept will be described.

EXPERIMENTAL EVALUATION OF CRACK GAGES

The encouraging results of recent in-house and contractual research programs are briefly described below. The in-house programs were designed to provide initial verification of the crack gage concept and are described in detail in References 5 to 8. In keeping with the spirit of MIL-A-83444 (Reference 2), the structural flaw geometry has consisted of a through-the-thickness radial crack emanating at the edge of a hole in a flat tension specimen. Gage geometries considered to date include adhesively bonded coupons which contained edge-cracks, center-flaws, or radially cracked holes, and the more exotic case of a second flaw intentionally placed directly in the simulated structural member.

Typical fatigue crack growth curves from two of the center crack gage tests are shown in Figure 3. Here the crack gages were 1.5 in. (3.81 cm) long (unbond length L) by 1.0 in. (2.54 cm) wide and were made from a 0.031 in. (0.079 cm) thick sheet of 7075-T6 aluminum, while the 2219-T851 aluminum structural member was 2.0 in. (5.08 cm) wide and 0.24 in. (0.61 cm) thick. Both members were precracked to the desired initial flaw sizes, and then tabs left on the ends of the small coupons were adhesively bonded to the large structural specimen with Hysol Aerospace Adhesive EA 9628 tape. Although performance of these bonds was quite satisfactory during subsequent fatigue cycling, no attempt was made to select or evaluate adhesives for long term field applications. The two assembled specimens were subjected to constant amplitude loading with an R-ratio of 0.1 (R = minimum/maximum load). The cyclic stress for Test 4 was 18 ksi (124 MPa) while that for Test 3 was 13.6 ksi (94 MPa).

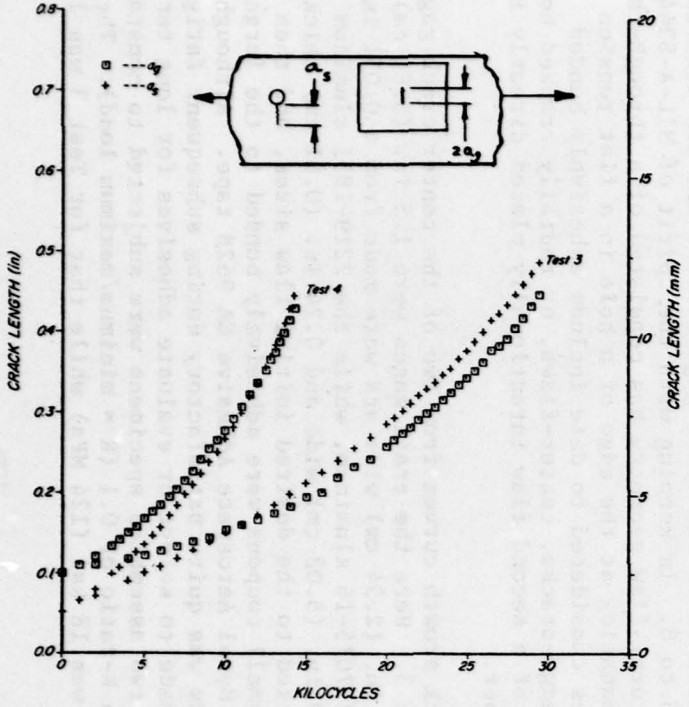


Fig. 3 Comparison of crack-length results for two specimens having equivalent initial crack lengths and being tested under different load amplitudes. The R = 0.1 cyclic stress range for Test 3 was 13.6 ksi (94 MPa) and 18 ksi (124 MPa) for Test 4.

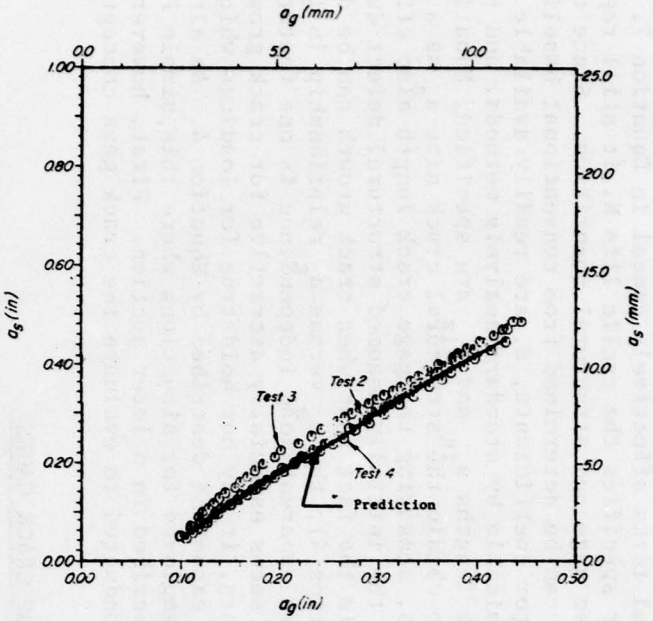


Fig. 4 Comparison of experimental data for structural crack a_s versus gage crack a_g relationship with mathematical prediction. Specimens 2 and 3 were tested at a cyclic stress of 104 MPa while specimen 4 was cycled at 138 MPa.

Note in Figure 3 that the fatigue crack growth curves for both the gage and structural defects do, of course, depend on stress level. When structural crack length a_s is plotted versus the gage flaw size a_g corresponding to the same cyclic life N in Figure 4, however, the results of tests 3 and 4 are quite similar. Figure 4 also contains data from another identical specimen (Test 2) subjected to the same loading as Test 3, and includes a prediction made by solving Equation 7 by the procedures described in Reference 7. Note that all 3 specimens gave repeatable a_s versus a_g curves and that the mathematical model predicted the behavior extremely well. It must be emphasized once more that the prediction involved no knowledge of the test loads. Other comparisons of experimental data with analysis are given in Reference 7, while a set of similar experiments and predictions for edge-cracked gages (rather than center flaws) are discussed in Reference 8. Again, repeatability, insensitivity to loading, and agreement with theory were generally observed for these other tests as well.

A word of caution regarding the load independence observed to date is in order, however, Recall that the key assumption in the analysis which allowed the loads to cancel in Equation 7 was use of Equation 4 to correlate fatigue crack growth rates. The stress level σ_s cannot be eliminated entirely when more complex crack growth models are employed (see results from calculations based on the Forman model [14] reported in Reference 6). Although use of Equation 4 may seem unduly restrictive, considerable work indicates that variable amplitude loading can often be described by this simple law. It has been shown, for example, that it may be useful to interpret σ in Equation 4 as the maximum repeating stress in a variable amplitude load history, or perhaps, as the root mean value of alternating stress [15,16]. Indeed, this approach was employed in Reference 6, where growth of two cracks located in series in a long specimen subjected to a complex load spectrum were successfully related via Equation 7. Again, no knowledge of actual loads was required for the prediction. Similar results were obtained in Reference 8 with a specimen tested to a relatively complex block amplitude loading.

Some limitations with the Paris law have, however, been observed in References 8 and 9. The results from a set of tests [8] involving two identical specimens subjected to different constant amplitude load levels are shown in Figure 5. Note that although the results of Test 5 agreed well with the load independent analysis, a_s versus a_g curve from Test 9 differed significantly. This disparity was attributed to the fact that the stress levels in the second specimen were so small that the initial K levels were approaching the threshold value of stress intensity for the test material. Crack growth rates for the small initial cracks, thus, were not described by the same Paris law applicable to Test 5. Once the crack length had grown to a size resulting in a K level compatible with the baseline da/dN versus ΔK curve, however, the results are predicted adequately by Equation 7, as indicated in Figure 5 by the short curve beginning in the latter portion of the Test 9 data.

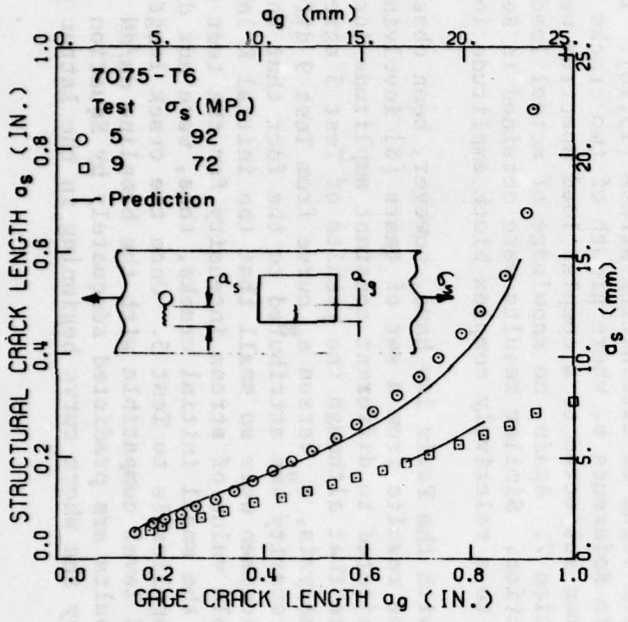


Fig. 5 Comparison of experimental data for structural crack versus gage crack with mathematical prediction for edge-cracked gage geometry. The R = 0.1 stress range for Test 5 was 13.3 ksi (92 MPa) and 10.5 ksi (72 MPa) for Test 9.

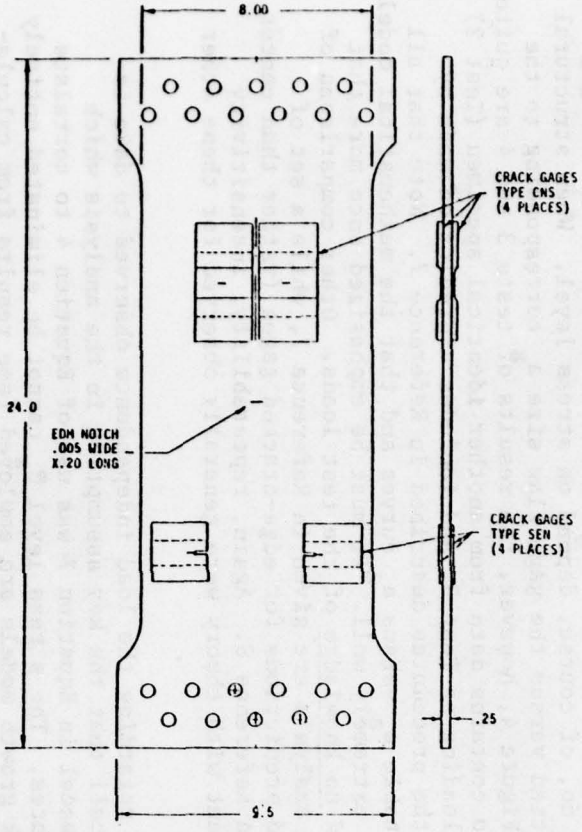


Fig. 6 Drawing of crack gage test specimens showing placement of edge-cracked coupons and reduced thickness center-crack gages on simulated structural panel (all dimensions in inches) (1 in.=25.4mm).

Further experimental studies of crack gages have been conducted under sponsorship of the AFFDL [9] and the AFML [10]. One portion of the recently completed AFFDL program with the Boeing Company sought to determine the effect of various load histories on the response of crack growth gages. Eight small coupons were precracked and adhesively bonded to large center-cracked panels as shown in Figure 6. Uniform thickness edge-cracked gages (with an unbonded length to width ratio of .375) and center-cracked coupons which had a reduced thickness over the center portion of the unbonded length were considered in this effort.

Typical fatigue crack growth curves for the center-cracked gages and the simulated structural flaw are given in Figure 7. In this test, the specimen was subjected to a variable stress history expected to occur at a given wing location in a transport aircraft. Five additional specimens were loaded with different stress histories chosen to represent other aircraft locations and missions. As seen in Figure 7, the four center-cracked coupons gave fairly repeatable fatigue crack growth curves and yielded growth rates close to that of the structural flaw. The fatigue crack growth rates for the edge-cracked coupons (not shown in Figure 7) were much slower, however, a fact which can be expected from the relatively low K levels encountered in short gage length coupons subjected to displacement controlled loading [17].

Composite gage crack versus structural crack size curves were prepared for all six tests and are summarized in Figure 8. Here the flaw lengths in the four center-cracked coupons at a given cyclic life were averaged and plotted against the corresponding structural crack size. The data from Figure 7 are designated by the composite "Wing, 4B" curve in Figure 8. Although stress intensity factor solutions were not available for the reduced thickness crack gages, and Equation 7 could not be solved for comparison, such computations are planned for future work. Note that three widely different load histories (Wing 4B, Wing 3B, and Fin 3A) gave very similar curves when plotted in the a_g versus a_s format. The results for three other loadings (Wing 3A-1, Wing 3B-1, and Wing 3A) differ significantly, however, pointing out the limitations of the Paris law based cracked gage algorithm. Another possible analysis scheme is outlined in the following section.

A LOAD DEPENDENT CRACK GAGE MODEL

The purpose of this section is to briefly describe a mathematical model which could be used to reduce crack gage data for load histories which yield fatigue crack growth rates which cannot be correlated by Equation 4. The main objective here is to present an analysis scheme which could, with a minimum of data collection and computational effort, incorporate stress level effects such as those indicated in Figures 5 and 8.

Returning to Equation 3, recall that the key assumption which led to the load independent result of Equation 7 was the choice of the simple Paris model (Equation 4) for describing fatigue crack growth. This assumption allows one to eliminate stress explicitly in subsequent development of Equation 7. The choice of more complex crack growth laws precludes cancellation of load terms

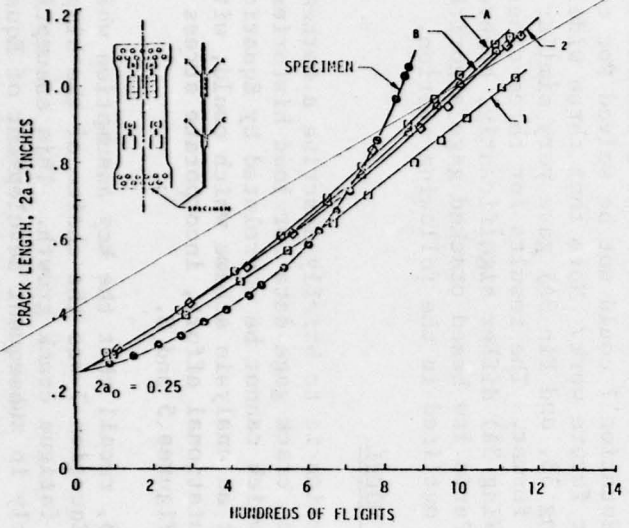


Fig. 7 Fatigue crack growth curves for simulated structural defect and four reduced thickness center-crack gages (1 in. = 25.4 mm).

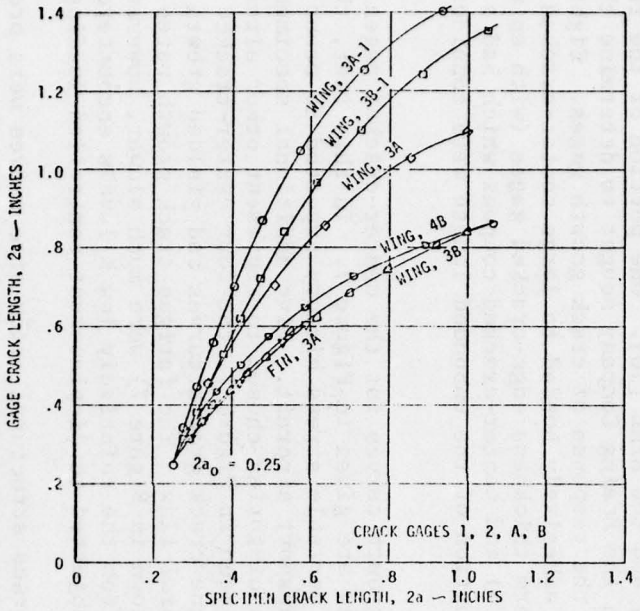


Fig. 8 Comparison of composite gage versus structural crack curves for various load histories (1 in. = 25.4 mm)

in this manner, however, and requires some measure of stress level to complete the relationship between gage and structural crack sizes. Since the desired tracking device is to be as simple as possible, the requirement for another load monitoring system (i.e., strain recorders) to reduce the crack gage data would be a severe limitation of the crack gage method for IAT. Thus, the following scheme was developed for determining the effective stress level for use with crack gage data reduction.

The major change in the proposed approach is to employ two independent crack gages at each tracking location. Now, returning to Equation 3, an analogous relationship can be written for the cyclic life of the two crack gages, giving

$$N = \int_{a_{i1}}^{a_1} \frac{da}{F_1(K)} = \int_{a_{i2}}^{a_2} \frac{da}{F_2(K)} \qquad (8)$$

where the subscripts 1 and 2 now refer to gages 1 and 2. The functions $F_1(K)$ and $F_2(K)$, relating stress intensity level with fatigue crack growth rate, are now the appropriate expressions for the gage material. Although identical materials would most likely be used for both gages, giving $F_1(K) = F_2(K)$, this requirement would not appear essential. Since the crack lengths in the gages will be recorded during service, the upper limits (a_1 and a_2) on the integrals will be known, as well as the initial crack sizes a_{i1} and a_{i2}. Thus, it is possible to introduce an effective stress level as an unknown in the expressions for F(K) in Equation 8. After solving Equation 8 for this stress term, one (or both) of the gages would again be matched wth the assumed structural flaw as in Equation 3, and solved for the structural crack size a_s. Since this procedure allows one to choose a variety of crack growth laws to characterize crack growth, including models which address threshold stress intensity factor behavior, it should be possible to analyze the apparent stress level problem described in Figure 5. Actual calculations with this algorithm remain, however, for future work.

APPLICATION OF THE CRACK GAGE TECHNIQUE TO F-4 INDIVIDUAL AIRCRAFT TRACKING

An on-going fatigue test of the full-scale F-4 C/D test article being conducted by AFFDL provides a convenient test bed for evaluating the crack gage concept for use with actual aircraft. The purpose of the F-4 C/D full-scale fatigue test is to provide full-scale test verification of several life extension modifications including those designed to extend the life to 8000 flight hours of F-4 ASIP baseline usage. To date, the equivalent of 4000 flight hours of baseline usage has been applied to the test article. At this point, the test was stopped temporarily to implement the modifications mentioned above. Thus, the test was in a hold status and provided an excellent opportunity to attach crack gages to the test structure at no additional airframe test cost.

An eighteen month long research program, including both in-house and contractor effort, was developed to evaluate the crack gage concept as a possible replacement for the present F-4 IAT program. A cooperative program between AFFDL and Ogden Air Logistics Center (ALC) was established to accomplish the effort. Funds for the program were provided by the Product Reliability, Availability, and Maintainability (PRAM) Program Office of ASD.

Ogden ALC established a contract with McDonnell Aircraft Company (MCAIR) to conduct detailed analysis and testing which would evaluate the ability of the crack gage approach to monitor potential crack growth damage in fatigue critical areas of the F-4 C/D aircraft structure. Under this contract, MCAIR is to select the three most appropriate crack growth gage locations on the lower surface of the right wing and one duplicate location on the left wing for monitoring wing fatigue critical regions of the F-4 C/D full scale test article. MCAIR will provide the crack gages, conduct engineering analysis and element testing to predict gage performance at each location, and install the gages on the test airframe. MCAIR will also establish the necessary transfer functions to relate crack growth response in the gage to potential crack growth damage in the fatigue critical region being monitored.

Under the cooperative program, AFFDL will function as the technical monitor for the MCAIR contract. Also AFFDL will be responsible for monitoring the crack growth behavior of the gages during the fatigue test. To ensure that the gages will perform as expected under actual service conditions, AFFDL will undertake an in-house program to (1) perform qualification testing of the gage to meet the requirements of MIL-STD-810C [18], which establishes uniform environmental test methods for determining the resistance of equipment to the effects of natural and induced environments peculiar to military operations, and (2) determine the most appropriate method for reading the crack growth gage data in the field. In this in-house program, AFFDL will establish (1) the crack gage sensitivity to typical environmental conditions as well as to extreme in-service environmental conditions, (2) the durability limits of the adhesive system used to attach the gages, (3) the stress limits of the device, (4) the degree of corrosion protection necessary to ensure that the gage does not degrade the structure, and (5) the degree of corrosion protection necessary to ensure continuity of easy readability throughout the expected service of the gage. To ensure field level readability of the crack gage, AFFDL will (1) develop two feasible methods for collecting crack growth data in the field, (2) conduct an evaluation of each method using ground field personnel who have ASIP responsibility, and (3) select the most appropriate method for service readings. One of these crack gage reading methods will include photomacrography of the crack gages as installed on the aircraft. The other method will utilize a replicating material known as "fax film". First, an impression of the crack in the gage will be taken using the fax film. The impression will then be measured using a microscope.

The crack gage geometry selected for this effort consists of a center-cracked coupon with a reduced thickness at the center of the unbonded gage length as shown in Figure 9. The reduced thickness effectively increases the

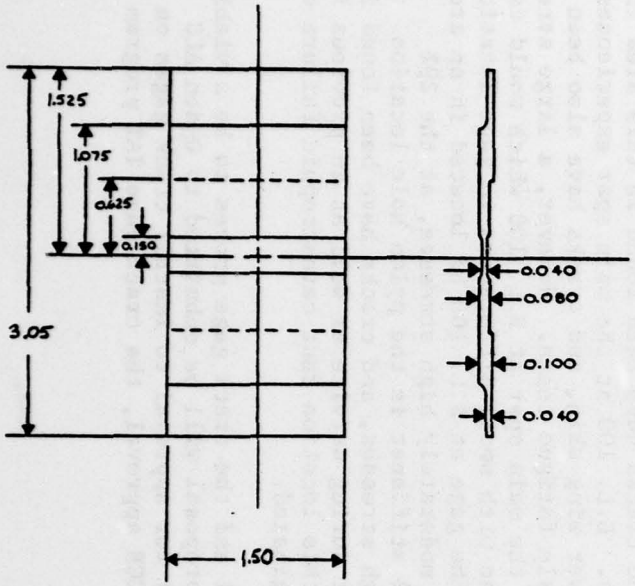


Fig. 9 Drawing of reduced thickness center-crack gage selected for evaluation on F-4 test article (all dimensions in inches) (1 in. = 25.4mm).

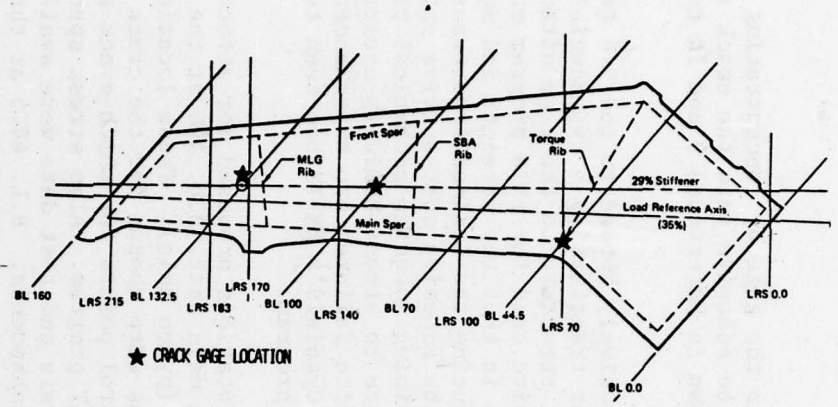


Fig. 10 F-4 lower wing station diagram (inner wing)

stress intensity factor levels in the gage by concentrating the load transferred into the coupon through the adhesive into the crack region. This reduced section approach was shown in References 9 and 10 to be a viable method for achieving desired K levels.

The crack gages will be adhesively bonded to the F-4 test article since adhesives offer the potential for transferring a reproducible and predictable amount of load from the aircraft structure to the gage without degrading structural integrity. The adhesive used for this program must meet three criteria. The first requirement is that the strength and modulus of the adhesive must be capable of producing the desired load transfer characteristics. The second requirement is that the adhesive must survive exposure at the peak service temperature while maintaining adequate mechanical properties. The third requirement is that exposure to stress-humidity cycles must not degrade the bond to the extent that service failures are experienced. Based on these three considerations, American Cyanimid's FM-73 has been tentatively selected as the adhesive for use on this program.

The three lower wing skin locations proposed for attaching the crack gages are Butt Line (B.L.) 44.5 at the main spar, B.L. 100 at the 29% stiffener, and B.L. 132.5 at the 29% stiffener (pylon hole). These locations are shown in Figure 10. These three locations were chosen for the crack gage program because they are at or near control points for which crack growth damage is calculated in the present F-4 IAT program. Also stress spectra were already developed and crack growth analysis and test data were available from the previous F-4 damage tolerance assessments. B.L. 44.5 at the main spar is the primary monitoring location in the present F-4 IAT program. It is an area of moderately high design limit stress (see design limit stress contours for the lower wing skin in Figure 11), and cracks have been found in this area in previous full-scale fatigue tests. B.L. 100 at the main spar experiences the most severe stress in the F-4 lower wing skin, and cracks have also been found in this area in previous full scale fatigue tests. However, a large stress gradient occurs in the area near the main spar at B.L. 100 which would cause large differences in gage response with small differences in gage locations. Therefore, it was proposed that the gage at B.L. 100 be located in an area of low stress gradient but still moderately high stresses, at the 29% stiffener. B.L. 132.5 at the 29% stiffener is the pylon hole location. This is also an area of moderately high stresses, and cracks have been found in this area in operational aircraft during service as well as in previous full-scale fatigue tests. It was at this location that catastrophic failure of the F-4 B/J fatigue test article originated.

If the program is successful and the crack gage proves to be a viable concept for IAT, a modification proposal will be submitted to Ogden ALC Configuration Control Board (CCB) for approval to install crack gages on all operational F-4 aircraft. Upon CCB approval, the crack gage IAT program would be implemented forcewide.

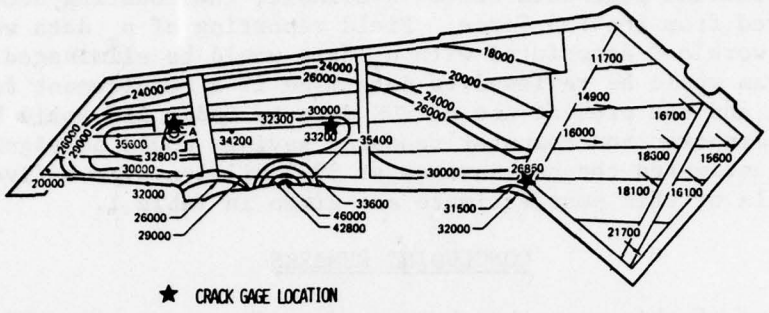


Fig. 11 Design limit stress contours for F-4 lower wing skin (stress in units of psi) (1 psi = 6.9×10^{-3}MPa)

TABLE 1. Estimated Costs of F-4 IAT Systems

Present F-4 IAT System Operating Costs	
Field/Depot Support - yearly	$ 1.3M
Equipment Replacement - 5 years	$ 3.5M
TOTAL COST - 5 years	$10.0M
Crack Growth Gage IAT System Costs	
Development	$ 0.1M
Implementation	$ 1.2M
Field/Depot Operating Support - 5 years	$ 1.0M
TOTAL COST - 5 years	$ 2.3M
NET SAVINGS - 5 years	$ 7.7M

If the crack gage IAT program were to be implemented, the potential cost savings over the present IAT program would be significant. After implementation and after the initial gage data became available, the counting accelerometers could be removed from the F-4 force. Field reporting of n_z data would cease, and Ogden ALC workload associated with n_z data would be eliminated. The VGH recorder program would be reviewed to determine if a requirement for this data still existed, and the present use of VGH data by Ogden ALC would be cancelled. The resulting manpower and computer resource savings could be significant. Ogden ALC has estimated the net savings at $7.7 million over a five year period. Details of this cost estimate are given in Table 1.

CONCLUDING REMARKS

The purpose of this paper has been to describe an on-going USAF research program aimed at demonstrating the crack gage approach for meeting Individual Aircraft Tracking requirements for the present F-4 force. As discussed previously, MIL-STD-1530A requires an IAT program for each new aircraft system. The objective of these tracking requirements is to allow force management decisions to be based on the possibility for crack growth at specific locations in individual aircraft. The crack growth analyses are to reflect the actual service usage of each aircraft. The F-4 was the first USAF fighter to employ such a crack growth based tracking system, and although an IAT program is underway, it is felt that improved tracking methods could increase accuracy while also significantly reducing total cost.

As reviewed here, the crack gage method is a relatively new technique which has been proposed to determine the effects of service loads on potential crack growth in an initially flawed structure. The approach consists of relating measured crack growth in a precracked coupon mounted on the structure with extension of the assumed structural defect. Since it is a relatively simple task to relate the gage and structural crack sizes without resorting to other expensive and cumbersome load monitoring devices, the crack gage method offers the potential for considerable cost reduction and improved system reliability. As summarized in Table 1 for example, estimated savings for the F-4 could exceed $7 million over a five year period.

Thus, the present joint program with the Air Force Flight Dynamics Laboratory, Ogden Air Logistics Center, and the McDonnell Aircraft Company was formulated to evaluate the crack gage technique for use with the F-4. Placing the cracked coupons directly onto an on-going full-scale fatigue test article allows many practical aspects of the new technique to be examined while still maintaining a relatively controlled laboratory situation. Successful completion of this effort could result in introduction of the crack gage monitoring technique to the IAT program for the F-4 force.

REFERENCES

1. "Aircraft Structural Integrity Program, Airplane Requirements," MIL-STD-1530A, Air Force Aeronautical Systems Division, December 1975.

2. "Airplane Damage Tolerance Requirements," MIL-A-83444, Air Force Aeronautical Systems Division, July 1974.

3. "Final Report, F/RF-4C/D Damage Tolerance and Life Assessment Study," Report No. MDCA2883, Vol. I, McDonnell Aircraft Company, June 1974.

4. "Model F-4E Slatted Airplane Fatigue and Damage Tolerance Assessment," Report No. MDC A3390, Vol. I, McDonnell Aircraft Co., July 1975.

5. Grandt, A.F., Jr., Crane, R.L., and Gallagher, J.P., "A Crack Growth Gage for Assessing Flaw Growth Potential in Structural Components," Fracture, Proceedings of the Fourth International Conference on Fracture, Vol. 3, Waterloo, Canada, 19-24 June 1977, pp. 39-45.

6. Gallagher, J.P., Grandt, A.F., Jr., and Crane R.L., "Tracking Crack Growth Damage in US Air Force Aircraft," Journal of Aircraft, Vol. 15, No. 7, July 1978, pp 435-442.

7. Ashbaugh, N.E. and Grandt, A.F., Jr., "Evaluation of a Crack Growth Gage for Monitoring Possible Fatigue Crack Growth," Proceedings of the ASTM Symposium on Service Fatigue Loads Monitoring, Simulation and Analysis, Atlanta, Georgia, 14-15 November 1977, (in press).

8. Ori, J.A., Grandt, A.F. Jr., "An Experimental Evaluation of Single Edge-Cracked Coupons for Monitoring Service Loads," presented at the 11th ASTM Symposium on Fracture Mechanics, Blacksburg, VA, June 1978.

9. "The Influence of Fleet Variability on Crack Growth Tracking Procedures for Transport/Bomber Aircraft," USAF/Boeing Wichita Contract No. F33615-76-C-3130.

10. "Evaluation of the Crack Gage Concept for Monitoring Aircraft Flaw Growth Potential," USAF/Boeing Wichita Contract No. F33615-77-C-5073.

11. Rooke, D.P., and Cartwright, D.J., Compendium of Stress Intensity Factors, The Hillington Press, Uxbridge, England, 1976.

12. Sih, G.D., Handbook of Stress Intensity Factors, Institute of Fracture & Solid Mechanics, Lehigh University, Bethlehem, PA, 1973.

13. Tada, H., Paris, P., and Irwin, G., The Stress Analysis of Cracks Handbook, Del Research Corporation, Hellertown, PA, 1973.

14. Forman, R.G., Kearney, V.E., and Engle, R.M., "Numerical Analysis of Crack Propagation in Cyclic Loaded Structures," Journal of Basic Engineering, Trans. of the ASME, Vol. 89, No. 3, 1967, pp. 459.

15. Gallagher, J.P., and Stalnaker, H.D., "Developing Methods for Tracking Crack Growth Damage in Aircraft," Proceedings AIAA/ASME/SAE 17th Structures, Structural Dynamics, and Materials Conference, 5-7 May 1976, pp. 486-494.

16. Rolfe, S.T., and Barsom, J.M., Fracture & Fatigue Control in Structures, Prentice Hall, Englewood Cliffs, NJ, 1977.

17. Torvik, P.J., "Applications of the Extremal Principles of Elasticity to the Determination of Stress Intensity Factors," Technical Report AFIT TR-77-3, Air Force Institute of Technology, Wright-Patterson AFB, OH, July 1977.

18. "Environmental Test Standards," MIL-STD-810C, Air Force Aeronautical Systems Division, March 1975.

PREDICTION OF DEBOND SHAPE AND SIZE IN CRACKED, ADHESIVELY BONDED STRUCTURES

MOHAN M. RATWANI
Senior Technical Specialist
Northrop Corporation, Aircraft Group
Hawthorne, CA 90250

ABSTRACT

The importance of debond shape and size in predicting crack growth behavior of cracked, adhesively bonded structures is discussed. A technique is developed for predicting debond shape and size produced during fatigue cycling. Using this technique, the debond shapes and sizes are predicted in a variety of cracked, adhesively bonded structures. The analytically predicted debond shapes and sizes are compared with those observed experimentally. The crack growth life of a two-layer, cracked, bonded structure is predicted using the debond shapes and sizes predicted analytically. It is shown that the crack growth life can be reliably predicted using analytically predicted debond shapes and sizes.

INTRODUCTION

The analysis of cracked bonded structures has attracted considerable interest in recent years due to the increased application of bonding in aerospace structures. Analysis methods for bonded structures must be available during developmental design in order to ensure satisfaction at damage tolerance requirements and to establish an allowable design stress for limiting the amount of slow crack growth. Methods must be developed to predict the sequence of events where subcritical growth causes failure of one or more individual elements prior to complete loss of the structure.

Consider a two-layer, adhesively bonded, metallic structure with a through-crack in one layer, as shown in Figure 1. The flaw in the metallic layer may initiate as a surface crack. During subsequent fatigue loads, this flaw becomes a through-the-thickness flaw and propagates longitudinally. The stress intensity factors in the bonded structure are lower than would be the case in a monolithic layer having the same remote boundary conditions due to the load transfer taking place from the cracked layer to the uncracked layer. This load transfer to the uncracked layer depends on the relative stiffness of the adhesive and adherends, the crack length, and debond size and shape in the adhesive layer. There may or may not be an initial debond in the adhesive around the surface flaw in the metallic layer. If there is no initial debond in the adhesive, a debonded area will develop in the adhesive layer and propagate during fatigue loads along with the crack in the metallic layer. As the crack in the metallic layer propagates, more load is transferred to the uncracked layer, increasing the stresses locally in the latter. Due to the stress concentration and the fatigue load, a crack initiates in the previously uncracked layer and propagates with subsequent fatigue loads. Thus,

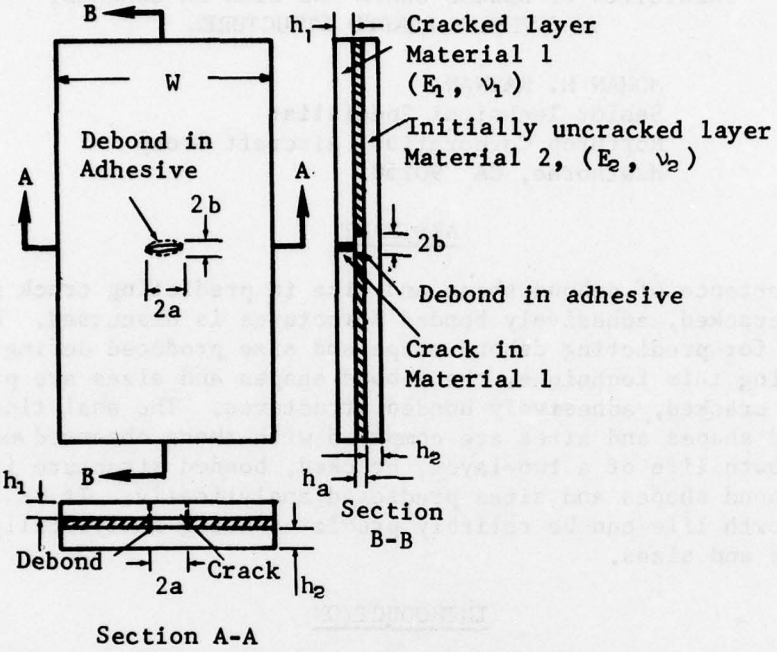


Figure 1. Two-Layer, Adhesively Bonded Metallic Structure with Through-Crack in One Layer

the analysis of a cracked, adhesively bonded structure will require availability of the following: 1) a method to obtain stress intensity factors to predict crack growth behavior, 2) a method to predict debond shape and size, and 3) a criterion for the cracking of an initially sound layer. These analytical techniques have been discussed recently in References 1 and 2, where finite element and mathematical methods of analysis have been developed. Methods to obtain stress intensity factors for cracked, adhesively bonded structures have also been discussed in References 3 through 10. A technique to predict cyclic debonding of a composite-to-metal bonded joint has been discussed in Reference 11.

The debond shape and size influence the computation of stress intensity factors in the cracked layer hence, the predicted crack growth in a bonded structure. Thus, an accurate estimate of debond shape and size is necessary for accurate crack growth life prediction. A technique for predicting debond shape and size based on failure stress of the adhesive, obtained from finite element analysis, has been discussed in Reference 12. The predicted debond shape and size based on failure stress of the adhesive will be accurate only if the debond develops under static loads. The experimental results have shown (References 1 and 2) that the debond develops and propagates under fatigue loads even though the stress in the adhesive is less than the failure

stress of the adhesive. The technique developed in References 1 and 2 for predicting the debond shape and size under fatigue loads, and its application is discussed in this paper.

ANALYSIS OF DEBOND SIZE AND SHAPE

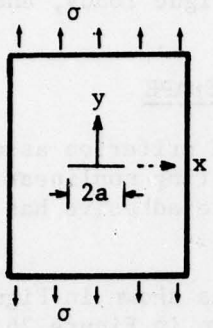
The debond shape and size are governed by the criterion associated with the failure of the adhesive. For materials exhibiting nonlinear behavior, a simple failure criterion could be assumed, that the adhesive has failed when the strain reaches a critical value.

Consider a single-layer plate with a crack, as shown in Figure 2a. Under applied loading the crack will open, as shown in Figure 2b. Next, consider a case where this plate is the cracked layer in a two-layer, adhesively bonded structure (Figure 1). In such a structure, the crack opening will be smaller than the single-layer opening, as shown in Figure 2c. The reduction in the crack opening will depend on the load transferred to the uncracked layer, which is a function of the thickness and material properties of the adhesive and adherends. Also, the presence of a crack in one layer of a bonded structure gives rise to out-of-plane bending. This load transfer to the sound layer and the out-of-plane bending will create normal and shear stresses in the adhesive.

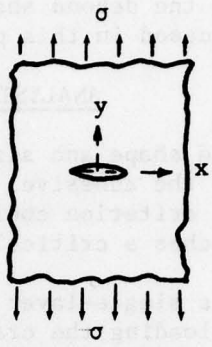
Consider the cross-section of the two-ply, bonded structure shown in Figure 2d. The displacements in the cracked and sound layer far from the crack plane will be the same, hence no load transfer through the adhesive. In the vicinity of the crack plane, the cracked sheet will undergo a large deformation compared to the sound layer, with the result that the adhesive on the surface of the cracked plate will deform more in the y direction than the adhesive on the surface of the sound layer. The difference in the deformation of the two plates will depend on the distance from the crack plane. The adhesive in the bonded structure may be looked on as discrete elements (both in the x and y directions) connecting two plates, as shown in Figure 3a. These elements are denoted by A_1B_1, A_2B_2, A_3B_3, etc. (at $x = 0$), and D_1E_1, D_2E_2..., F_1G_1... at other x locations, as shown in Figure 3b. Under applied loads, the elements will undergo deformation (Figure 3c). Points A_1B_1, A_2B_2... will displace to $A'_1B'_1$, $A'_2B'_2$..., respectively, as shown in Figure 3c, which also shows that the displacements are larger in a cracked plate. Point A_1 displaces V_{c1} and B_1 is displaced by V_{s1}. The relative displacement of the two points will be $V_{c1} - V_{s1}$.

The strain ϵ_1 in the adhesive (element A_1B_1 at $x = 0$), is given by

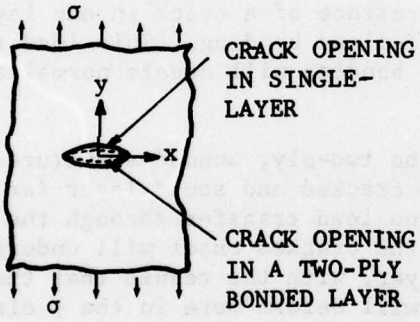
$$\epsilon_1 = \frac{V_{c1} - V_{s1}}{h_a} \quad (\text{at } y = 0) \qquad (1)$$



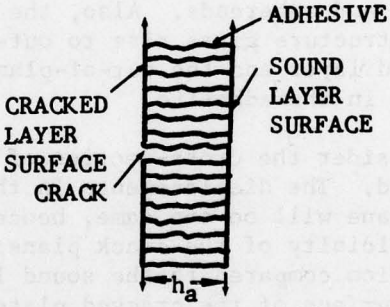
(a) Single-Layer Plate with a Crack



(b) Crack Opening in a Single-Layer



(c) Crack Opening in a Two-Ply, Adhesively Bonded Structure

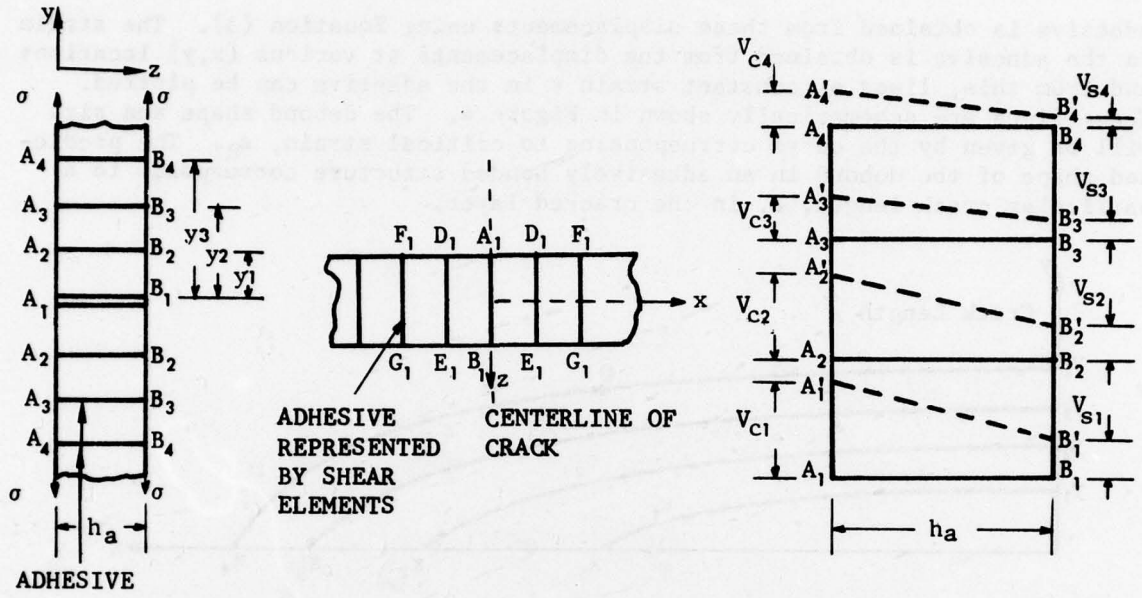


(d) Cross-Section of Adhesive in a Two-Ply, Cracked, Bonded Structure

Figure 2. Crack Surface Openings in Cracked Structures

Similarly, strains $\epsilon_2, \epsilon_3 \ldots$ in elements A_2B_2, $A_3B_3 \ldots$ (at $x = 0$) are given by

$$\epsilon_2 = \frac{V_{c2} - V_{s2}}{h_a} \; (y = y_1), \quad \epsilon_3 = \frac{V_{c3} - V_{s3}}{h_a} \; (y = y_2)$$



h_a = Adhesive thickness

(a) Cross-section showing representation of adhesive at x = 0

(b) Sectional plan at y = 0 showing representation of adhesive

(c) Displacements in plates (upper half only) (x = 0)

Figure 3. Discrete Element Representation of Adhesive

In general, the strain ϵ, at any location is given by

$$\epsilon = \frac{V_c - V_s}{h_a} \qquad (3)$$

The value of the strain will decrease as the distance from the crack plane increases. The strains at other x locations (elements $D_1 E_1$ ...Figure 3b) can be obtained in a similar manner. The adhesive will fail if the strain in the adhesive reaches a critical value ϵ_R, which is defined as the resistance of the adhesive to fracture. The ϵ_R is taken as the failure strain of the adhesive from a tensile test of the adhesive.

The displacements V_c and V_s in the cracked and sound layers are obtained from the mathematical or finite element analysis of the cracked, adhesively bonded structures at a particular crack length, a. The strain in the

adhesive is obtained from these displacements using Equation (3). The strain in the adhesive is obtained from the displacements at various (x,y) locations and from this, lines of constant strain ϵ in the adhesive can be plotted. These lines are schematically shown in Figure 4. The debond shape and size will be given by the curve corresponding to critical strain, ϵ_R. The predicted shape of the debond in an adhesively bonded structure corresponds to a particular crack length, a, in the cracked layer.

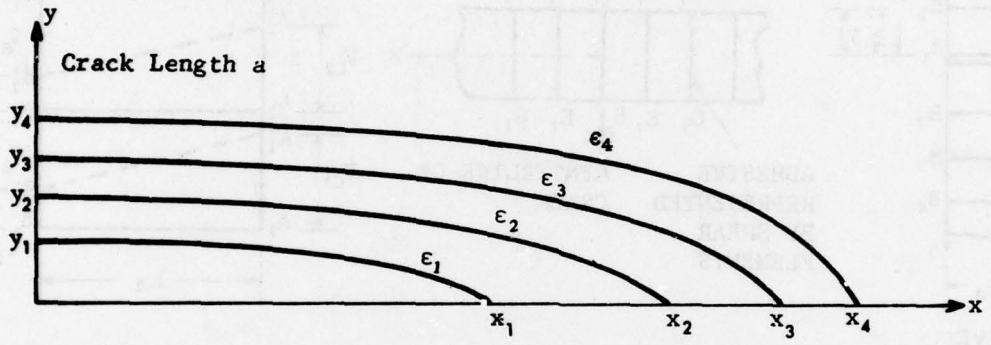


Figure 4. Lines of Constant Strain in Adhesive for a Fixed Applied Stress in a Bonded Structure (one-quarter of contours shown)

As the crack propagates under fatigue loads, the crack opening and load transfer to the sound layer will increase, hence the relative displacements between the two layers will increase, or the strain in the adhesive at various x,y locations will continue to increase. As soon as the strain at any (x,y) location in the bonded region reaches the critical strain ϵ_R, the adhesive will fail, and the size of the debond will increase. Thus, the size of debond can be determined for every crack length as the crack in the cracked layer propagates. It may be noted that the values of V_c and V_s, hence strain ϵ_R at any crack length, depend on the size of the initial debond present in the adhesive. Hence, to compute debond size at a crack length of $a + \Delta a$, the displacements V_c and V_s (Equation (3)) obtained for crack length $a + \Delta a$, assuming debond size predicted at crack length a, may be used (Reference 2). From the above criterion of debond propagation, the following points are observed.

1. The size of the debond is dependent on the adhesive thickness and properties. From Equation (3), it is seen that if the thickness of the adhesive is large, the strain in the adhesive will be small, hence the size of the debond will be small. If the adhesive thickness is very large, the size of the debond may be zero.

2. The size of the debond will depend on the applied loads (σ_{max} for fatigue loads). The large applied loads will cause large crack openings, hence large shear strain in the adhesive.

3. The size of the debond will depend on the relative elastic properties of the sound and cracked layers, as these will influence the relative displacement between the two layers.

COMPARISON OF ANALYTICAL AND EXPERIMENTAL DEBOND SIZES

The debond produced in the adhesive during fatigue crack growth in a metallic layer of a two-ply laminate was predicted analytically for a variety of crack geometries. These analytical predictions were compared with the debond sizes observed in the test verification program. The debond shape and size was predicted using the method discussed earlier. The analysis of the cracked, adhesively bonded structures was carried out using two-dimensional finite element analysis (References 1 through 4). In this analysis, the displacements V_c and V_s are assumed to be constant through the thickness of each layer, though in reality, these displacements may vary through the thickness if the thickness of the layers is large. The displacement V_c at the crack plane (crack surface displacement) in a two-layer, adhesively bonded structure (Figure 1) is shown in Figure 5 for two half-crack lengths. The

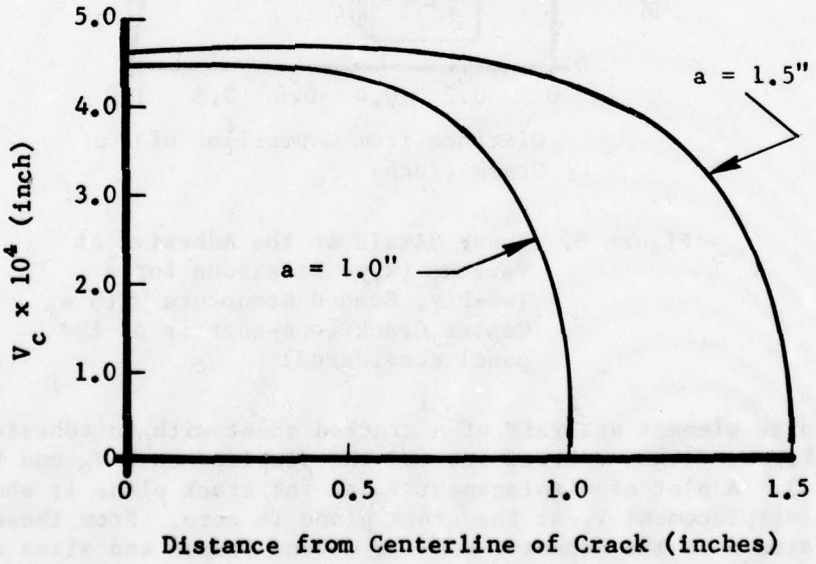


Figure 5. Displacement V_c at Crack Plane in a Two-Layer, Adhesively Bonded Structure for Various Half-Crack Lengths

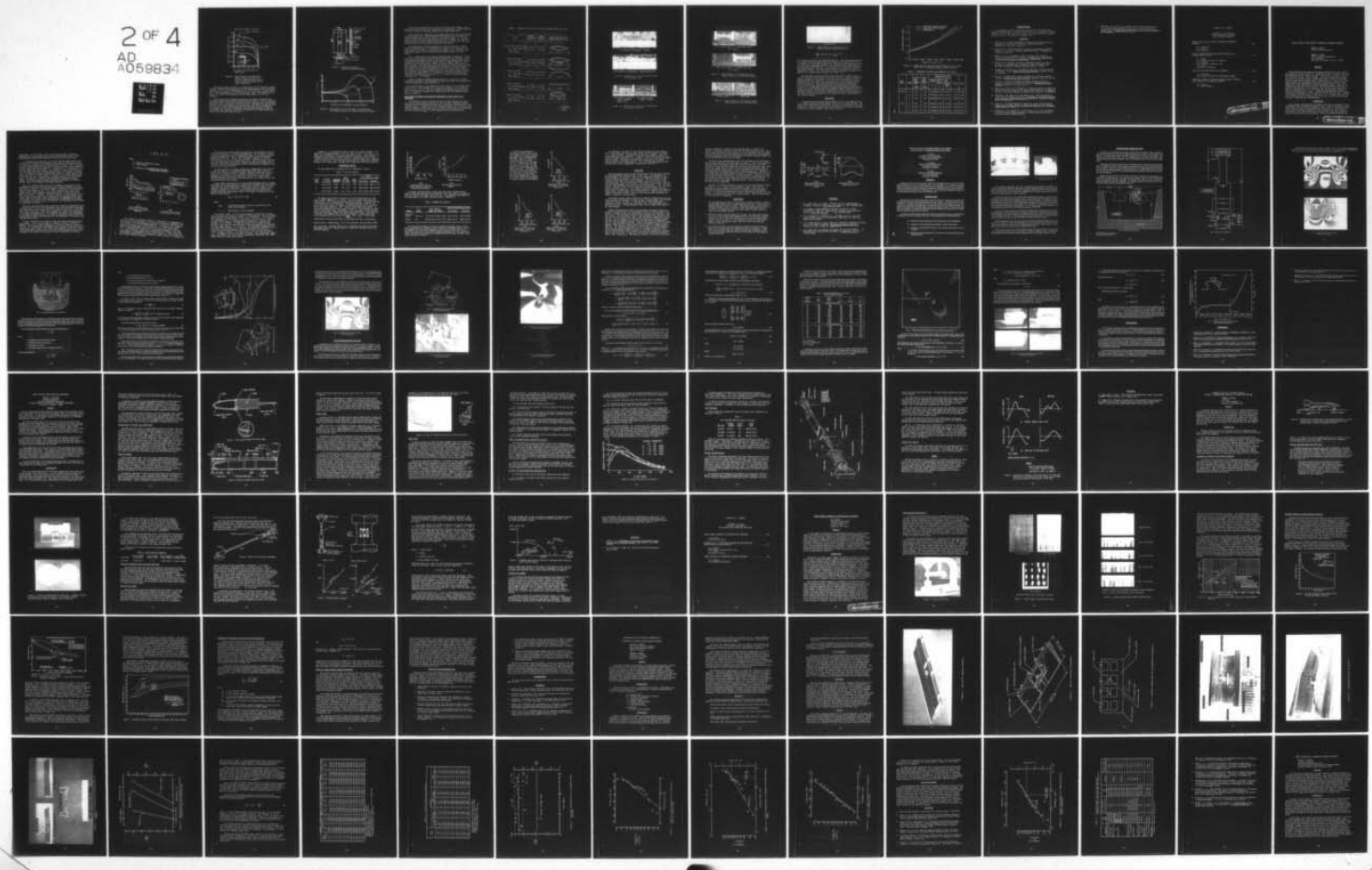
displacement V_s in the sound layer at the crack plane is zero due to symmetry. The displacements V_c and V_s away from the crack palne are obtained from the finite element analysis and from these, the strains in the adhesive at various locations are calculated using Equation (3). A typical plot of these strains is shown in Figure 6. From this plot, the constant strain lines in the adhesive can be found (Reference 2).

AD-A059 834 ARMY MATERIALS AND MECHANICS RESEARCH CENTER WATERTO--ETC F/G 20/11
PROCEEDINGS OF THE ARMY SYMPOSIUM ON SOLID MECHANICS, 1978 - CA--ETC(U)
SEP 78

UNCLASSIFIED AMMRC-MS-78-3

NL

2 OF 4
AD
A059834



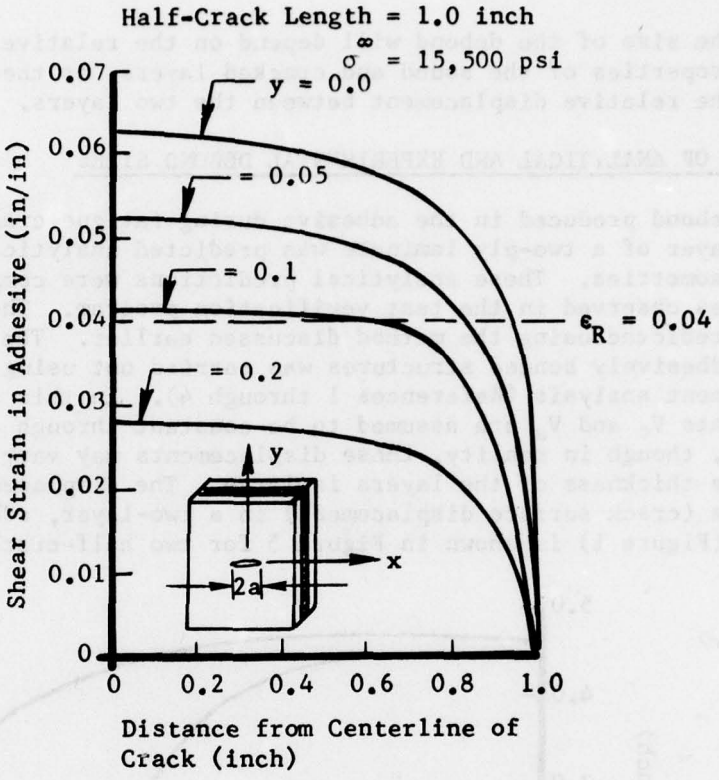


Figure 6. Shear Strain in the Adhesive at Various (x,y) Locations for a Two-Ply, Bonded Structure with a Center Crack (one-quarter of the panel considered)

The finite element analysis of a cracked sheet with an adhesively bonded stiffener (Figure 7) was carried out and the displacements V_c and V_s computed (Reference 2). A plot of displacement V_c at the crack plane is shown in Figure 8. The displacement V_s at the crack plane is zero. From these displacements, the strain in the adhesive and the debond shapes and sizes are computed.

During the course of fatigue cycling the test panels, nondestructive inspection (Harmonic Bond Tester and Ultrasonic C-scan) were used to determine the debond sizes. The results obtained by these techniques were inconsistent. Therefore, after obtaining the crack growth data, the panels were peeled apart in such a way that the debond area was marked by charring the debonded or loose adhesive. This was accomplished by heating the specimen at 375F for three hours, then removing it from the oven and driving a wedge between the plies in the area away from the crack.

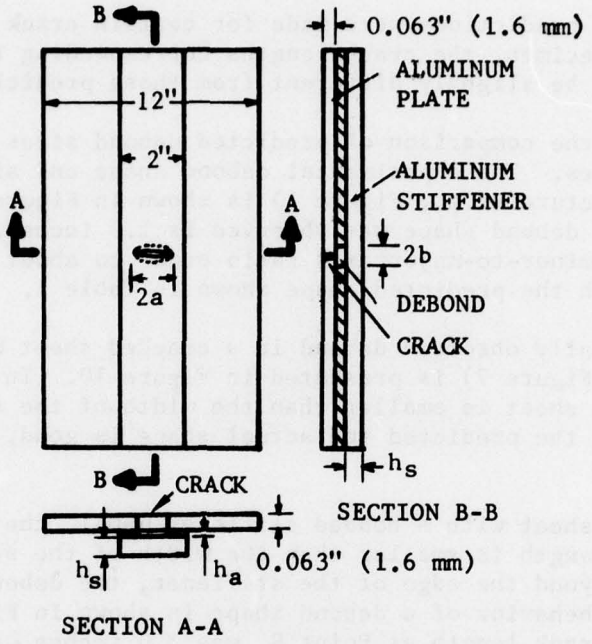


Figure 7. Cracked Plate with an Adhesively Bonded Stiffener

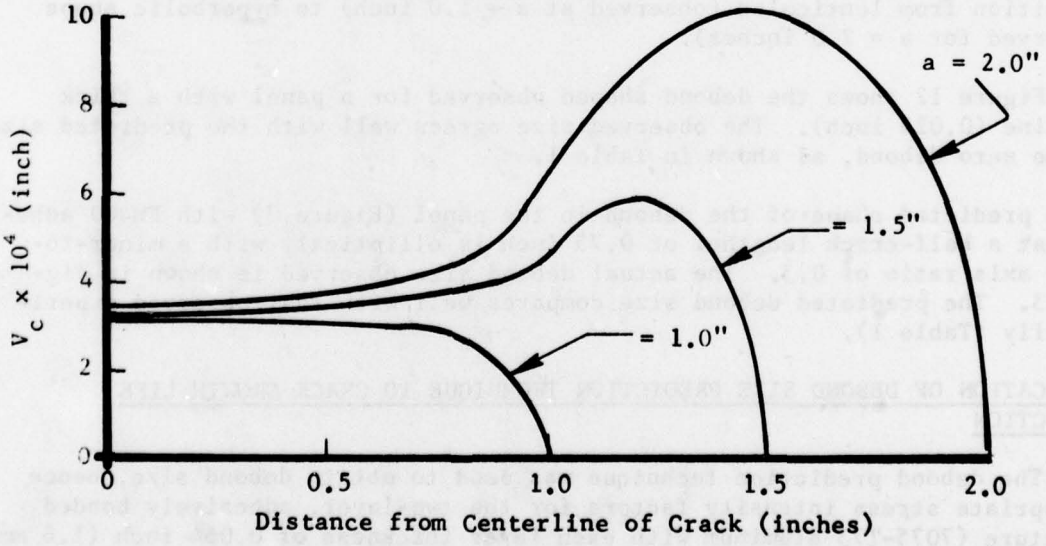


Figure 8. Displacement V_c at Crack Plane in Cracked Sheet with Bonded Stiffener for Various Half-Crack Lengths

The analytical predictions were made for certain crack lengths. After peeling the test specimen, the crack lengths corresponding to debond shape and size, were found to be slightly different from those predictions.

Table 1 shows the comparison of predicted debond sizes and experimentally measured debond sizes. The experimental debond shape and size measured in two-ply bonded structure (e.g., Figure 1) is shown in Figure 9. The crack length at which the debond shape was observed is 1.8 inches. The debond is lenticular, with a minor-to-major axis ratio equal to about 0.12. This compares favorably with the predicted shape shown in Table 1.

The experimentally observed debond in a cracked sheet with a bonded central stiffener (Figure 7) is presented in Figure 10. In this case, the crack length in the sheet is smaller than the width of the stiffener. The correlation between the predicted and actual shape is good, as noted in Table 1.

For a cracked sheet with a bonded stiffener panel, the debond is lenticular if the crack length is smaller than the width of the stiffener. As the crack propagates beyond the edge of the stiffener, the debond changes shape. An example of this behavior of a debond shape is shown in Figure 11. For Crack A, the half-crack length at Point R, was 3.0 inches, and at Point Q, was 2.2 inches. The shape and size of the debond at P and Q agrees well with that predicted for a half-crack length of 2.0 inches, as shown in Table 1. For Crack C, the half-crack length on side U is 1.4 inches, and on side S is 2.2 inches. The shape on side S and at T, compares well with the predicted shape, as shown in Table 1. The debond at U is still undergoing the transition from lenticular (observed at a = 1.0 inch) to hyperbolic shape (observed for a = 2.0 inches).

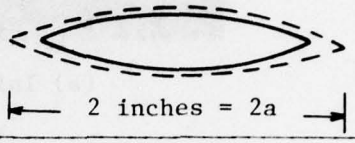
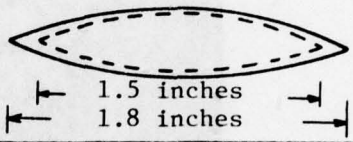
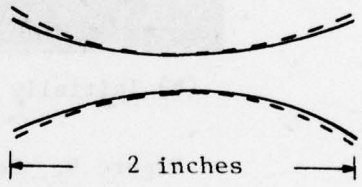
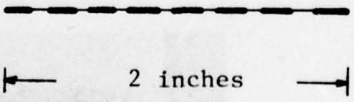
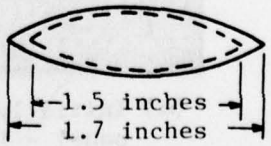
Figure 12 shows the debond shaped observed for a panel with a thick bondline (0.023 inch). The observed size agrees well with the predicted size of the zero debond, as shown in Table 1.

The predicted shape of the debond in the panel (Figure 7) with FM400 adhesive at a half-crack lengthof of 0.75 inch is elliptical, with a minor-to-major axis ratio of 0.3. The actual debond size observed is shown in Figure 13. The predicted debond size compares well with that observed experimentally (Table 1).

APPLICATION OF DEBOND SIZE PREDICTION TECHNIQUE TO CRACK GROWTH LIFE PREDICTION

The debond prediction technique was used to obtain debond size, hence appropriate stress intensity factors for the two-layer, adhesively bonded structure (7075-T73 aluminum with each layer thickness of 0.064 inch (1.6 mm)) shown in Figure 1. Using these stress intensity factors and the crack growth equation obtained from fatigue tests on a 7075-T73 monolithic layer 0.063 inch (1.6 mm) in the form (K_{max} = stress intensity factor at maximum load)

TABLE 1. COMPARISON OF ACTUAL AND PREDICTED DEBOND SHAPES AND SIZES

PANEL	DEBOND PREDICTION AT a =	DEBOND MEASURED AT a =	PREDICTED AND ACTUAL DEBOND SHAPES AND SIZES
12-inch wide center crack h_a = 0.008" (0.20 mm) FM73 Adhesive	1.00 inch (25.4 mm)	0.90 inch (22.8 mm)	
Bonded stiffener h_a = 0.003" (0.07 mm) FM73 Adhesive	0.75 inch (19.1 mm)	0.90 inch (22.8 mm)	
Bonded stiffener h_a = 0.006" (0.15 mm) FM73 Adhesive	2.00 inches (50.8 mm)	2.20 inches (55.9 mm)	
Bonded stiffener h_a = 0.023" (0.58 mm) FM73 Adhesive	0.75 inch (19.1 mm)	0.75 inch (19.1 mm)	
Bonded stiffener h_a = 0.010" (0.25 mm) FM400 Adhesive	0.75 inch (19.1 mm)	0.85 inch (21.6 mm)	

--- PREDICTED

—— ACTUAL

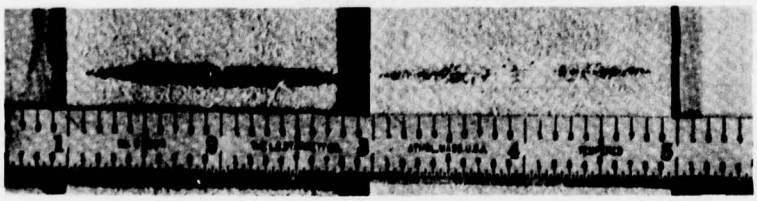


(a) Initially sound panel - inside



(b) Initially cracked panel - inside (glue line)

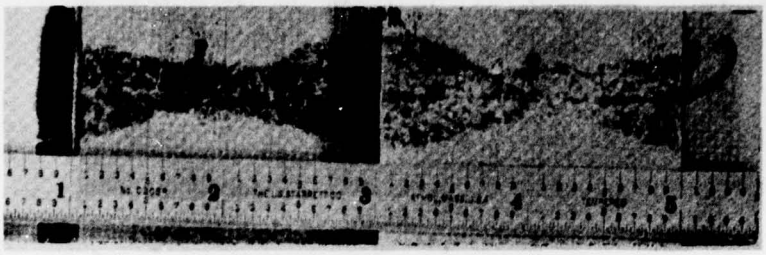
Figure 9. Debonding in a 12-inch (304.8 mm) Wide, Two-Ply Bonded Panel



(a) Initially cracked panel - inside (glue line)

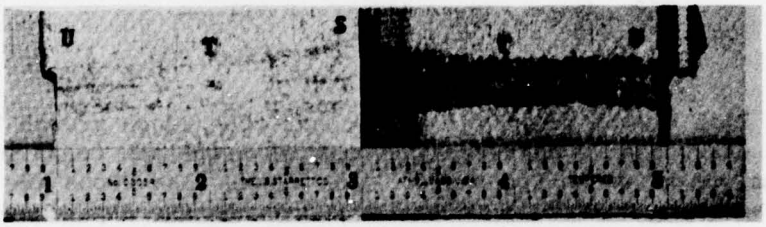
(b) Initally sound panel - inside

Figure 10. Debonding at Crack A in a Cracked Sheet with a Bonded Stiffener



total crack length = 5.2 inches (132.1 mm)

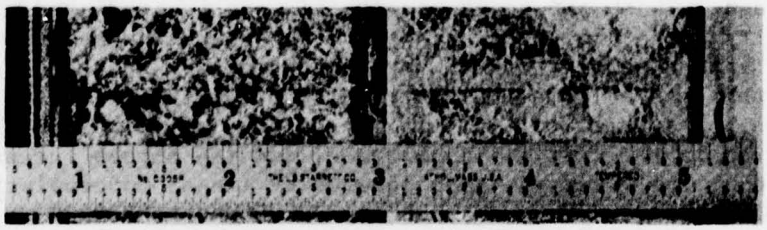
(a) Crack A



total crack length = 3.6 inches (91.4 mm)

(b) Crack C

Figure 11. Debond Shape in a Cracked Plate with a Bonded Stiffener for Large Crack Lengths



Cracked layer Sound layer

Figure 12. Debond Shape in a Cracked Plate with a Bonded Stiffener for a Thick Bondline



Cracked layer

Figure 13. Debond Shape in a Cracked Plate with a Bonded Stiffener (FM-400 Adhesive)

$$\frac{da}{dN} = 0.0169 \times 10^{-6} \, (K_{max})^{2.731}$$

the crack growth life of the panel was predicted. The crack growth behavior to propagate the crack from a half-crack length of 0.25-inch (6.35 mm) to 1.0 inch (25.4 mm) is shown in Figure 14. The figure also shows the analytical predictions assuming no debond in the adhesive and the experimentally observed crack growth behavior. It is seen that the analytically predicted crack growth based on correctly computed debond size agrees well with the experimental results. The analytical predictions, assuming no debond in the adhesive, are unconservative and predict a longer life.

The experimental and analytical crack growth life is shown in Table 2 for two test panels (each having three equal cracks), assuming no debond and predicted debond in the adhesive. Note that the crack growth life can be predicted within ten percent of the actual life if the correctly computed debond size is used. Thus, the crack growth life can be predicted with greater reliability. The predicted cycles for the crack to grow from 0.25 inch to 1.0 inch (Table 2) differ for the three cracks, as the crack growth life is predicted by numerical integration from the analytical stress intensity factors. The numerical integration is done at values of crack extensions observed in the test for each crack, and the stress intensity factors are obtained at the observed crack lengths by linear interpolation in the computer program.

CONCLUSIONS

A technique for predicting debond shape and size in the adhesive layer of a cracked, adhesively bonded metallic structure, has been developed. The debond in the adhesive has considerable influence on the prediction of crack growth life. The crack growth life can be predicted with greater reliability by using the properly computed debond shape and size.

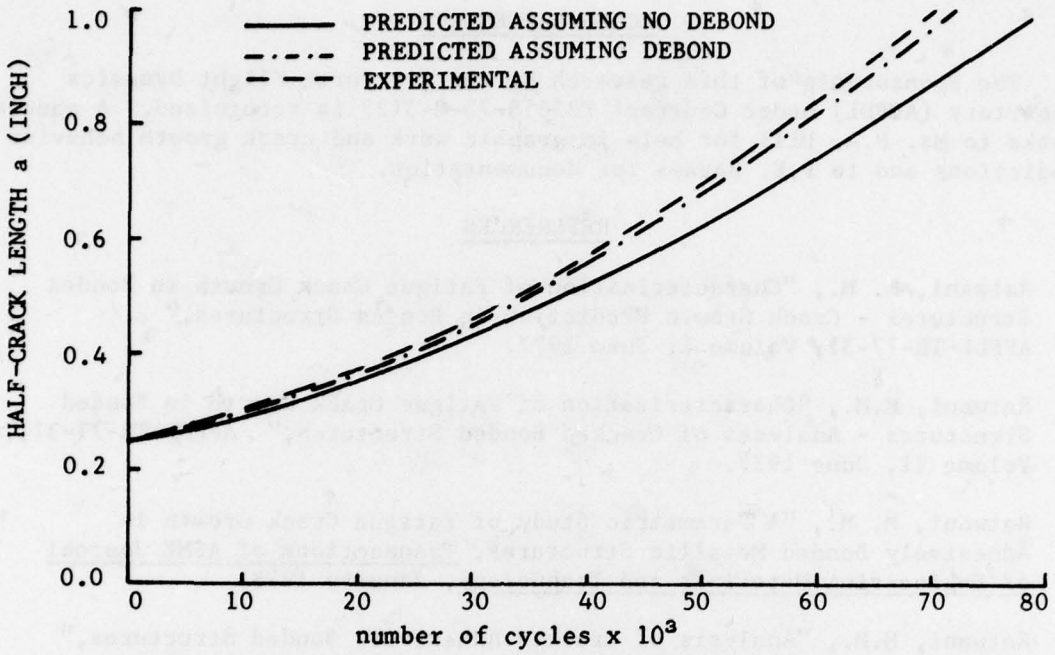


Figure 14. Comparison of Actual Life and Predicted Life for a Two-Layer (7075-T3 Aluminum-Aluminum) Bonded Structure

TABLE 2. COMPARISON OF ACTUAL AND PREDICTED LIFE CYCLES

TEST PANEL	CRACK	INITIAL HALF-CRACK LENGTH a_o (INCH)	FINAL HALF-CRACK LENGTH a_f (INCH)	ACTUAL CYCLES N_A	PREDICTED CYCLES		N_O/N_A	N_P/N_A
					ASSUMING NO DEBOND N_O	WITH PREDICTED DEBOND N_P		
II-10	A	0.25	1.00	73,048	81,279	74,551	1.113	1.020
	B	0.25	1.00	73,242	81,106	79,642	1.107	1.087
	C	0.25	1.00	78,962	85,710	78,331	1.085	0.992
I-11	A	0.25	1.00	68,927	77,056	71,063	1.118	1.031
	B	0.25	1.00	74,480	82,322	75,372	1.105	1.012
	C	0.25	1.00	70,402	79,439	72,566	1.128	1.031

ACKNOWLEDGEMENTS

The sponsorship of this research by the Air Force Flight Dynamics Laboartory (AFFDL) under Contract F33615-75-C-3127 is recognized. A special thanks to Ms. P.A. Hill for help in graphic work and crack growth behavior predictions and to P.E. Barnes for documentation.

REFERENCES

1. Ratwani, M. M., "Characterization of Fatigue Crack Growth in Bonded Structures - Crack Growth Prediction in Bonded Structures," AFFDL-TR-77-31, Volume I, June 1977.

2. Ratwani, M.M., "Characterization of Fatigue Crack Growth in Bonded Structures - Analyses of Cracked Bonded Structures," AFFDL-TR-77-31, Volume II, June 1977.

3. Ratwani, M. M., "A Parametric Study of Fatigue Crack Growth in Adhesively Bonded Metallic Structures," Transactions of ASME Journal of Engineering Materials and Technology, January 1978.

4. Ratwani, M.M., "Analysis of Cracked Adhesively Bonded Structures," Presented at AIAA/ASME 19th Structures, Structural Dynamics and Materials Conference, Bethesda, Maryland, April 3-5, 1978.

5. Erdogan, F., and Arin, K., "A Sandwich Plate with a Part-Through and a Debonding Crack," Engineering Fracture Mechanics, Volume 4, 1972, pp. 449-458.

6. Arin, K., "A Plate with a Crack, Stiffened by a Partially Debonded Stringer," Engineering Fracture Mechanics, Volume 6, 1974, pp. 133-140.

7. Arin, K., "A Note on the Effect of Lateral Bending Stiffness of Stringers Attached to a Plate with a Crack," Engineering Fracture Mechanics, Volume 7, 1975, pp. 173-179.

8. Keer, L. M., Liu, C. T., and Mura, T., "Fracture Analysis of Adhesively Bonded Sheets," Presented at the Winter Annual Meeting of the American Society of Mechanical Engineers, December 1976, Paper No. 76-WA/APM-12.

9. Anderson, J. M., Hsu, T. M., and McGee, W. M., "Characterization of Crack Growth in Bonded Structures," Proceedings of 12th Annual meeting of the Society of Engineering Science, University of Texas, at Austin, 1975, pp. 1283-1292.

10. Swift, T., "Fracture Analysis of Adhesively Bonded Cracked Panels," Transactions of ASME, Journal of Engineering Materials and Technology, January 1978, pp. 10-15.

11. Roderick, G. L., Everett, R. A., and Crews, J. H., "Cyclic Debonding of Unidirectional Composite Bonded to Aluminum Sheet for Constant-Amplitude Loading," NASA TN-D-8126.

12. Anderson, J.M., Chu, C.S., and McGee, W.M., "Growth Characteristics of a Fatigue Crack Approaching and Growing beneath an Adhesively Bonded Doubler," Transactions of ASME Journal of Engineering Materials and Technology, January 1978, pp. 52-56.

SESSION IIb: AIRCRAFT

Chairman: D. R. Mulville
Research Mechanical Engineer
Naval Research Laboratory

TENSILE LOADS IN HIGH CAPACITY LAMINATED ELASTOMERIC BEARINGS 103

D. P. Scala and
R. H. Finney
Lord Kinematics

OPTICAL FRACTURE MECHANICS AND STRESS ANALYSIS OF A TURBINE ENGINE FAN DISK 113

V. J. Parks
The Catholic University of America,
R. J. Sanford
Naval Research Laboratory, and
J. W. Dally
University of Maryland

MODEL 540 MAIN ROTOR BLADE RISK ASSESSMENT 132

A. J. Gustafson
Army Aviation Research and Development Command

PREMATURE FAILURES OF AIRCRAFT CARRIER CATAPULT "TENSION BARS" CAUSED BY ILL-CONCEIVED REDESIGN 144

T. W. Butler
U.S. Naval Academy

PRECEDING PAGE BLANK-NOT FILMED

TENSILE LOADS IN HIGH CAPACITY LAMINATED ELASTOMERIC BEARINGS

DENNIS P. SKALA
Senior Research Associate

ROBERT H. FINNEY
Senior Engineering Specialist
Lord Kinematics
1635 West 12th Street, Erie, PA 16512

ABSTRACT

Three different high shape factor bonded elastomeric disk test samples were tested to failure in tension. Characteristic of this type of test, the load-deflection curves showed a distinct "knee" which is a result of internal cavitation failure in the elastomer. Load-controlled tension fatigue tests were run on these samples to 80%, 90%, 110%, and 120% of the experimentally determined cavitation loads. Minimum load in all cases was a small tensile value. All the measured cavitation loads were roughly 2.5 times higher than those predicted by a generally accepted theory. Data is also presented for slow tensile pulls of two laminated elastomeric bearings - a spherical bearing and a thrust bearing. This is shown to be a good agreement with the disk data. It is concluded that the accepted cavitation theory is quantitatively in error. Curves are presented which enable the estimation of fatigue lives over a limited range of tensile stress. Fatigue lives ranged from 3,000 cycles to 300 cycles. It is further concluded that even relatively small oscillating tensile stresses can cause rapid fatigue failures in high capacity laminated parts.

INTRODUCTION

High capacity laminated (HCL) elastomeric bearings are composed of thin, alternating layers of rubber and metallic shims. They are utilized in situations where a relatively high compression load exists in combination with a small oscillating motion perpendicular to the compression load direction. For instance, this type of bearing is being used as a main rotor retention bearing in several military helicopters, such as the UH-60A Blackhawk and

PRECEDING PAGE BLANK-NOT FILMED

the CH-53D. The centrifugal force of the rotating blade is borne by compression of the bearing, while torsional and rotational shear of the bearing permit blade control motions at relatively low torque levels.

It is common design practice to avoid placing high shape factor (ratio of load area to bulge area) elastomeric parts, such as laminated bearings, in a service environment which includes any tensile loads, since it is well-known that the tolerance of such parts to tensile loads is low in comparison to their compression load capability. In some cases, it is impractical to entirely avoid such tensile loads. For instance, a small tension may exist in a helicopter main rotor bearing when the blade is resting on its droop stop. A disregard of design criteria might result in a bearing which could conceivably fail in tension, simply as a result of the rotor blade falling to its rest position. Alternatively, repeated landings of the helicopter cause a cycling of this tension load and possible consequent fatigue damage. The present paper presents some design guidelines for allowable tensile loads in high capacity elastomeric bearings.

Gent and Lindley [1] were the first to attempt an explanation of the phenomenon of cavitation in high shape factor bonded elastomer disks which were pulled in tension. They tested samples to ultimate failure covering a range of shape factors of 0.5 - 9.0. Their elastomers were carbon black loaded natural rubber compounds having shear moduli in the range 45 PSI - 284 PSI (0.31 MPa - 1.96 MPa). They found that the "cracking stress" (S' in their notation) was a function of modulus alone for any given shape factor sample, where the cracking stress is defined as the average tensile stress in the sample at the knee in the load-deflection curve. Tensile strength, for instance, was found to have little effect. For reference, their results are summarized in Figure 1.

Gent and Lindley explained their analytical results by hypothesizing the existance of small voids in the elastomer, which are acted upon by the negative hydrostatic stress which exists in the central portion of a high shape factor disk in tension. These cavities behave as stress risers and eventually rupture catastrophically. This hypothesis was based on the appearance of the ruptured samples (similar to craters on the moon) and by the audible popping which occurred simultaneously with the appearance of the knee in the load deflection curve.

In order to quantify this behavior, Gent and Lindley analyzed an analogue problem. This was the problem of a spherical cavity in an infinite medium, acted on by a negative hydrostatic (radially outward) pressure at infinity. An incompressible neo-Hookean strain energy function was used and large strains were allowed. The results were expressed in terms of a relation between the pressure acting at infinity and the extension ratio of the elastomer at the surface of the cavity in the circumferential direction.

$$P = \frac{G}{2}\left(5 - \frac{4}{\lambda} - \frac{1}{\lambda^4}\right)$$

where:

P = negative hydrostatic stress,
G = shear modulus,

λ = extension ratio $\left(\frac{\text{existing dia. of hole}}{\text{original dia. of hole}}\right)$

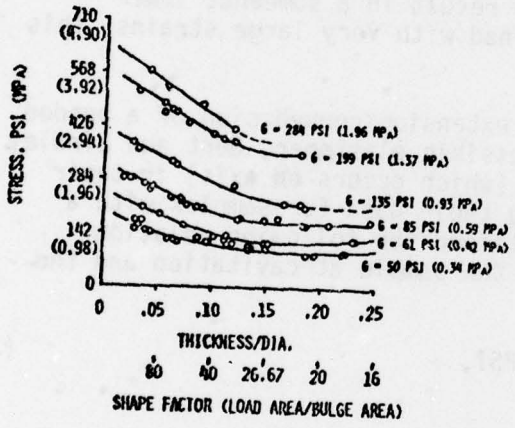


FIGURE 1
CRACKING STRESS VS THICKNESS/DIAMETER RATIO FOR SLOW TENSILE PULL OF DISK SAMPLES (FROM REFERENCE 1)

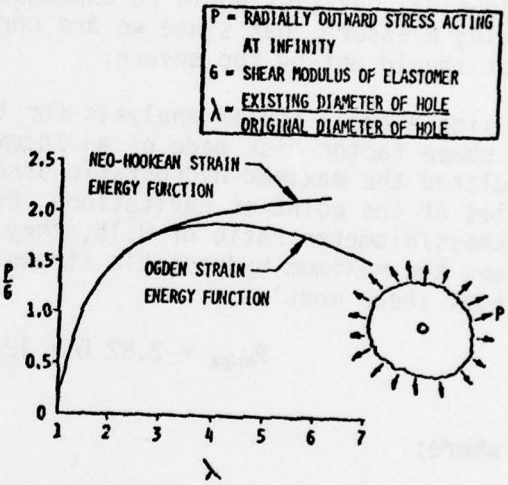


FIGURE 2
P/G VS EXTENSION RATIO FOR THE EXPANSION OF A SMALL SPHERICAL CAVITY IN AN ELASTOMER

This relation is plotted in Figure 2. Note that it is independent of the size of the cavity (which is, of course, infinitesimal compared to the entire body). For the neo-Hookean material, the pressure rises asymptotically to a value of 2.5 G at high values of λ. In other words, as the applied stress approaches 2.5 G, the size of the cavity grows without limit. Presumably this growth will be interupted somewhere in the range $4 < \lambda < 8$ by a rupture of the cavity surface material. However, even this large range of λ corresponds to only a small range of P. This accounts for the observed repeatability of the measured cracking stesses, in constrast to that of most fracture processes.

The use of strain energy functions other than the neo-Hookean does not alter the predicted $P - \lambda$ relation substantially. For instance, in Figure 2, we also indicate the results obtained by using a strain energy function proposed by Ogden [2]. This is indistinguishable from the neo-Hookean results up to $\lambda = 2.5$. In this case, P reaches a maximum of 1.9 G at $\lambda = 4.25$ and then falls off for higher values of λ. Gent and Lindley also used their own logarithmic form of strain energy function and obtained results similar in form to the neo-Hookean results, but reaching an asymptotic pressure which was about 7% lower.

The above analytical results indicate that, independent of the details of material behavior, an elastomeric body containing a small spherical cavity (flaw) should be unable to support a negative hydrostatic stress in excess of 2.5 G, where G is the classical shear modulus of the material. Nonspherical cavities would be expected to result in a somewhat lower limiting pressure, but since we are concerned with very large strains, this effect should not be too severe.

Using a small strain analysis for the extension/compression of a bonded high shape factor disk made of an incompressible elastomer, Gent and Lindley calculated the maximum hydrostatic stress (which occurs on axis) in their samples at the point of cavitation. Using their data for samples with a thickness/diameter ratio of 0.15, they obtained the following relation between the maximum hydrostatic stress in the sample at cavitation and the material shear modulus:

$$P_{max} = 2.82\ G + 12.1\ PSI, \tag{2}$$

where:

P_{max} = calculated hydrostatic stress at cavitation in the center of the sample,

G = shear modulus of the elastomer.

The constant factor, 12.1 PSI, was attributed to the effect of atmospheric pressure, which was not included in their analysis. Gent and Lindley concluded that the experimental result, i.e., equation (2), is in satisfactory agreement with their theory. We disagree. On the basis of Figure 1, one would expect P_{max} to be proportional to roughly 2.1 G, based on an assumed $\lambda = 6$ at rupture. The observed value of 2.82 is 34% too high. Moreover, they state that the same results would be obtained using the data for other shape factors. This is not so. The discrepancy becomes worse as the shape factor increases. For instance, using the data from Figure 1 on disks with a thickness/diameter ratio of 0.03 results in the P_{max} - G relation shown in Figure 3. For low G values, this curve has a slope of 7.11. It becomes non-linear for higher G values. Thus, depending on shape factor and modulus, Gent and Lindley's experimental results are 34% - 239% higher than their theory would predict.

Lindsey et. al. [3] observed similar results for urethane samples. For samples of thickness/diameter = 0.05 of a material with G = 170 PSI (1.17 MPa), their experimental values were about 40% too high. These authors also attempted to incorporate a fracture mechanics approach by balancing the release of elastic energy and the increase in surface energy for a spherical growth of the cavity. This approach proved generally unsuccessful, possibly because of the large number of simplifying assumptions which were required.

EXPERIMENTAL RESULTS

Our experimental work on bonded disks in summarized in Table I.

TABLE I DISK TEST RESULTS

Sample Type	Diameter in. (cm)	Thickness / Diameter	Shear Modulus PSI (MPa)	$\frac{\sigma max}{\sigma ave}$	Load at Cavitation, Lb. (KN)	
					Calculated	Observed
A	2.50 (6.35)	0.025	155 (1.07)	1.86	1023 (4.55)	2500 (11.12)
B	3.50 (8.89)	0.025	155 (1.07)	1.86	2006 (8.92)	5550 (24.69)
C	3.50 (8.89)	0.050	155 (1.07)	1.94	1921 (8.54)	5050 (22.46)

The samples were pulled in tension on a Tinius Olson machine at slow speed (roughly 100%/min in all cases). The test fixtures were specially constructed to avoid imposing any bending on the sample - loads were applied through spherical rod end bearings. No attempt was made to measure the actual deflection across the sample, although deflection across the entire test fixture was plotted vs. load. Three of each sample were tested. A typical load-deflection curve is shown in Figure 4. The response is linear up to the cavitation load. Subsequent to this, the sample is considerably softer and nonlinear, breaking at rather large deflections. The stress distribution in the samples was calculated by means of a generalized plane strain approach [3] to give the ratio $\frac{\sigma max}{\sigma ave}$, where σ_{max} is the maximum (hydrostatic) stress at the center of the sample and σ_{ave} is the average tensile stress. Assuming $\sigma_{max} = 2.5\ G$ at cavitation, the cavitation loads were calculated. Observed results are in agreement with Gent and Lindley's experimental results - they are about 2.5 times the calculated values for the above samples.

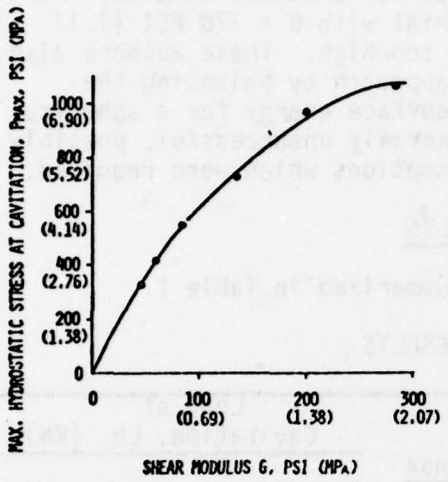


FIGURE 3
MAXIMUM HYDROSTATIC STRESS VS MODULUS FOR CAVITATION OF DISKS HAVING A THICKNESS/DIAMETER RATIO OF 0.028 (DATA FROM REFERENCE 1)

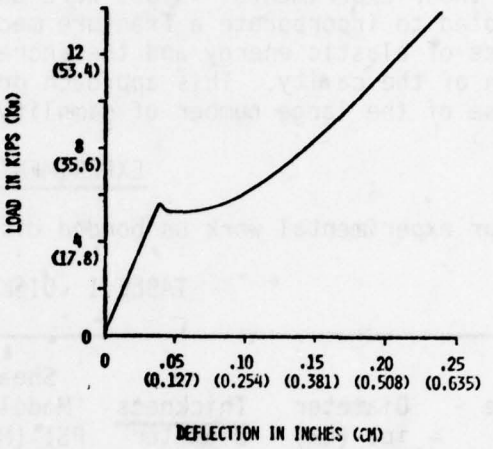


FIGURE 4
LOAD VS DEFLECTION FOR SLOW TENSILE PULL OF SAMPLE B

To support the experimental single layer disk data, production high capacity laminated bearings of the spherical thrust and thrust configuration were also tested to ultimate tensile failure. The specimens were tested in the same manner as the disks, plotting load vs. deflection.

TABLE II BEARING TEST RESULTS

Sample	S. F. Range	Shear Modulus Range, PSI (MPa)	Load at Cavitation Lb (KN)	
			Calculated	Observed
Spherical Thrust	16 to 12	75 (0.52) to 240 (1.65)	2731 (12.15)	6250 (27.80)
Thrust	16	140 (0.97) to 215 (1.48)	3074 (13.67)	6500 (28.91)

The production bearings, by design, contained elastomer layers of different shear modulus, different layer thickness and different areas. Due to the complexity of the bearing geometry, the stress distributions in the layers were calculated using finite element techniques [4]. The calculated load at cavitation was obtained by determining when the peak elastomer layer stress equaled 2.5 times G.

Using the experimentally observed cavitation loads on the disk samples as a basis, fatigue tests were run at approximately 80%, 90%, 110%, and 120% of the cavitation load in a load-controlled mode on an MTS tester at 1 Hz. Minimum load was 100# (0.44 KN) in all cases. No temperature rise was observed under these conditions. One sample was tested for each load condition. The same test fixtures were used as in the tensile break tests. Results are summarized in Figures 5-7. Here failure was defined as a complete rupture of the sample.

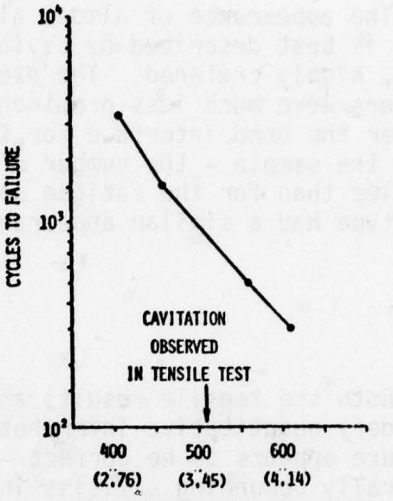


FIGURE 5
CYCLES TO FAILURE VS PEAK AVERAGE TENSILE STRESS FOR SAMPLE A. MIN. CYCLIC STRESS = 20 PSI (0.14 MPA)

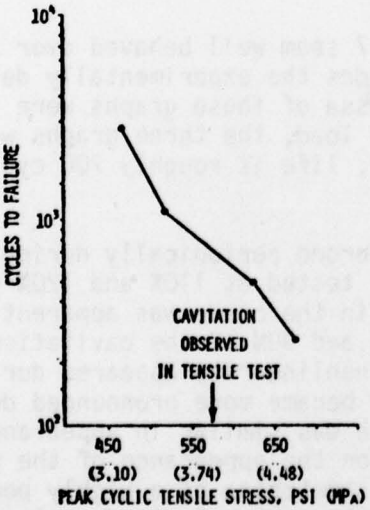


FIGURE 6
CYCLES TO FAILURE VS PEAK AVERAGE TENSILE STRESS FOR SAMPLE B. MIN. CYCLIC STRESS = 10 PSI (0.07 MPA)

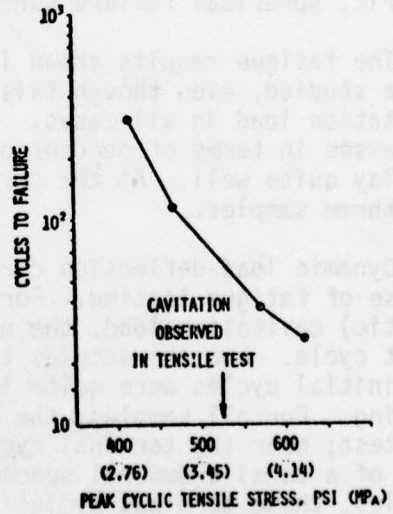


FIGURE 7
CYCLES TO FAILURE VS PEAK AVERAGE TENSILE STRESS FOR SAMPLE C. MIN. CYCLIC STRESS = 10 PSI (0.07 MPA)

The appearance of almost all the fracture surfaces was very similar - this is best described by saying they looked like the surface of the moon, i.e., highly cratered. The exception was the type A samples. Here the craters were much less prominent. In addition, the failure plane was much nearer the bond interface for these samples. The size of the craters varied with the sample - the number of craters was different for the tensile samples than for the fatigue samples. All of the fatigued samples of any one type had a similar appearance, regardless of test load.

DISCUSSION

Both the tensile results and the fatigue results are quite well behaved but defy quantitative interpretation at this time. The hypothesis for failure appears to be correct - that is the catastrophic rupture of small, naturally occurring cavities in the material. This is borne out by the fracture surface and by the audible "popping" noise which occurs at the cavitation load. The size and shape of the cavities is puzzling. They vary with thickness/diameter ratio and are in the range 0.020" - 0.050" (0.5 mm - 1.0 mm). Any naturally occurring flaws must be microscopic, i.e., less than 0.001" (0.03 mm) in size. This is borne out by other fracture work on slender tensile samples [5]. The cavities appear to represent the growth of these natural flaws in some sort of spherical sense. Some of the cavities showed an "onionskin" effect - that is individual cavities displayed concentric, spherical failure surfaces.

The fatigue results shown in Figures 5-7 seem well behaved over the load range studied, even though this range includes the experimentally determined cavitation load in all cases. If the abscissa of these graphs were expressed in terms of percent of cavitation load, the three graphs would overlay quite well. At the cavitation load, life is roughly 700 cycles for all three samples.

Dynamic load-deflection curves were recorded periodically during the course of fatigue testing. For the samples tested at 110% and 120% of the (static) cavitation load, the nonlinearity in the curve was apparent in the first cycle. For the samples tested at 80% and 90% of the cavitation load, the initial cycles were quite linear - the nonlinearity appeared during the testing. For all samples, the nonlinearity became more pronounced during the test; near the terminal cycles the curve was similar in appearance to that of a tensile dumbell specimen. Based on the appearance of the fatigued samples, these terminal cycles involve the stretching of a highly porous material - this would be like parallel tensile tests of slender strands of material. The increasing nonlinearity of the curves can be attributed to the increasing amount of material which has undergone cavitation - this process should proceed axially outward at a rate which depends on the magnitude of the load cycle. It would be interesting to continue the testing down to lower load values. There may be a distinct limit load at which the

S-N curve undergoes a change of slope, perhaps even an infinite life region. This may even turn out to be the calculated cavitation load. This would imply that the cavitation process is less catastrophic than it appears and that the observed one cycle behavior may just represent the culmination of many microscopic events which were each too minute to markedly affect the gross load-deflection curve of the sample.

The knee in the load-deflection curve for the spherical thrust bearing was not as pronounced as the knee shown in Figure 4. This was attributed to the multitude of elastomer stocks used in this HCL bearing. The intersection of the two distinct slopes was defined as the cavitation load. When the various layers were evaluated using this observed cavitation load to obtain the maximum (peak) stress, it was found that more than one-half of the layers were at a hydrostatic stress of approximately 6 G. Therefore, it is believed that the smooth change in slope in the load-deflection curve is due to the successive cavitation of the various layers. Figure 8 is a plot of the tension stress across layer 14 of the spherical thrust bearing, with the shape of a typical tension load-deflection curve for this type of bearing inserted in the upper right hand corner. The 6 G stress level is also overlaid for comparison.

The knee in the load deflection curve for the thrust bearing was similar to Figure 4, i.e., it had a distinct change in slope. This could be expected, since even though a multitude of elastomer stocks were used in this HCL bearing design, 85 per cent of the layers were of one modulus. Figure 9 is a plot of the hydrostatic tension stress pattern across the shim profile, as determined using finite element analysis. The 6 G stress level is also overlaid for comparison.

CONCLUSIONS

1. The accepted theory of Gent & Lindley which predicts internal cavitation of high shape factor parts is quantitatively incorrect. (This can be demonstrated with their own data.) Experimental data indicates that for thickness/diameter ratios of 0.025 - 0.05, the hydrostatic stress at cavitation is roughly six times the shear modulus, rather than 2.5 times, as predicted by theory.

2. Relatively small oscillating tensile stresses can cause rapid fatigue failures in high capacity laminated bearings. For instance, a tensile stress cycle of 0 - 400 PSI (2.76 MPa) on a disk having a thickness/diameter ratio of 0.025 will cause complete failure in 3,000 cycles. Under a similar compression cycle, the life of the disk would be virtually infinite.

3. The cavitation point for high capacity laminated production bearings agrees with the experimentally determined value of 6 times G. Therefore, the cavitation data and tension fatigue data obtained on flat circular disks may be applied directly to the design of high capacity laminated bearings.

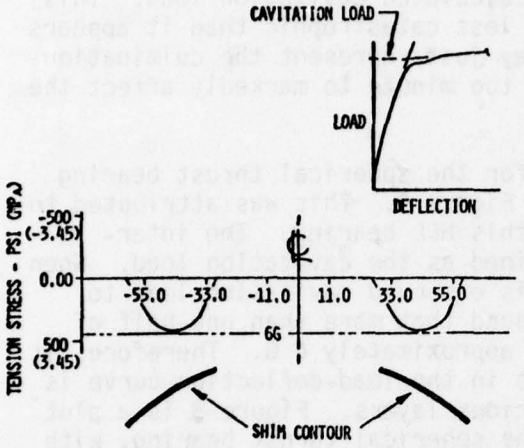


FIGURE 8
SPHERICAL THRUST BEARING STRESS PATTERN AT CAVITATION LOAD OF 6250 POUNDS (27.8 KN) IN LAYER 14

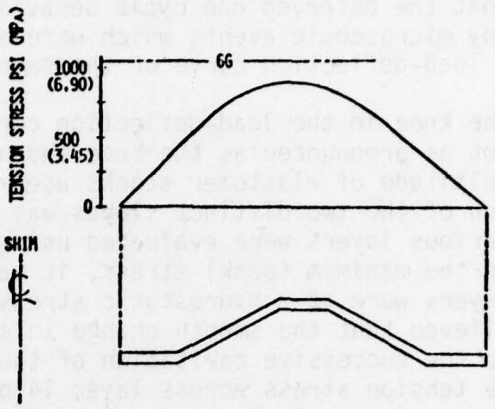


FIGURE 9
THRUST BEARING STRESS PATTERN AT CAVITATION LOAD OF 6500 POUNDS (28.91 KN)

REFERENCES

1. A. N. Gent and P. B. Lindley, "Internal Rupture of Bonded Rubber Cylinders in Tension," Proc. Roy. Soc. Lond. A, v.249, 195-205 (1958).

2. R. W. Ogden, "Large Deformation Isotropic Elasticity - on the Correlation of Theory and Experiment for Incompressible Rubberlike Solids," Proc. Roy. Soc. Lond. A, v.326, 565-584 (1972).

3. G. H. Lindsey, R. A. Schapery, M. L. Williams, and A. R. Zak, "The Triaxial Tension Failure of Viscoelastic Materials," ARL Technical Report 63-152 (1963).

4. R. H. Finney and B. P. Gupta, "Design of Elastomeric Components by Using the Finite Element Technique," The Shock and Vibration Bulletin, Bulletin 47, Part 1, Page 177, (Sept. 1977).

5. G. J. Lake and P. B. Lindley, "Cut Growth and Fatigue of Rubbers. - II. Experiments on a Noncrystallizing Rubber," J. Appl. Poly. Sci. 8. 707-721 (1964).

OPTICAL FRACTURE MECHANICS AND STRESS ANALYSIS OF A TURBINE ENGINE FAN DISK

V. J. Parks
Professor of Civil Engineering
The Catholic University of America
Washington, DC 20064

R. J. Sanford
Head, Structural Reliability Section
Naval Research Laboratory
Washington, DC 20375

J. W. Dally
Professor of Mechanical Engineering
University of Maryland
College Park, MD 20742

ABSTRACT

Photoelastic analysis of the dovetail joint region of the third-stage fan disk in the TF-30 turbojet engine indicates that the stress concentration factor at the critical fillet is 5.2. Redesign of the fillet using the photoelastic model as a guide reduced the stress concentration factor by 27%. Photoelastic models with simulated cracks were analyzed to determine the mixed-mode stress intensity factors for the crack growth path observed in the prototype part. A new method was developed to analyze the photoelastic fringe loops around the tip of the simulated crack.

INTRODUCTION

Early failures in the TF-30 turbojet engine, used in the Navy's F-14 aircraft, have resulted from fatigue cracks in the lugs of the third stage fan section shown in Figure 1. The cracks initiate at or near the junction of the fillet and bearing area of the disk lug, extend upward across the lug until they encounter the compressive stress field near the upper fillet and then turn through an angle of 45 degrees and propagate across the upper region of the lug as illustrated in Figure 2. Cracks in many lugs have been observed in third stage fan disks during periodic maintenance inspections and the cracked disks are retired after relatively short service life.

A stress and fracture mechanics analysis was conducted to determine the cause of the failures and to redesign the junction to increase the service life. The investigation had the following objectives:

(1) determine the stress concentration factors associated with the existing design;

(2) determine the stress profile along the direction of observed crack growth;

(3) redesign by contouring the fillet region to lower the peak tensile stress in the critical region;

(4) determine the stress intensity factor at the crack tip as it extends along the known crack growth path.

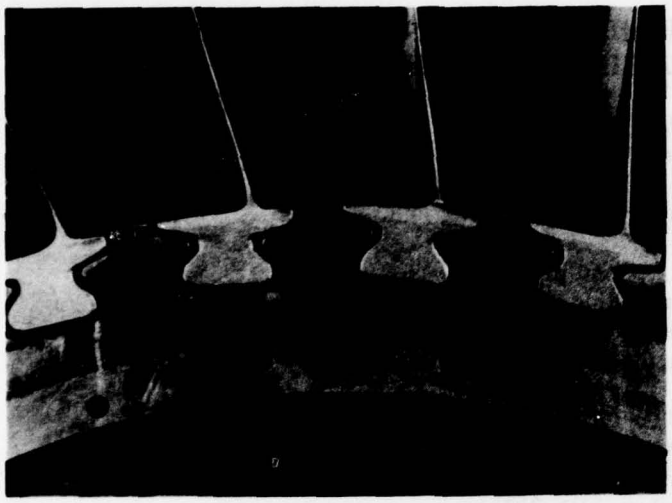


Fig. 1 — TF-30 third stage blade/disk dovetail region



Fig. 2 — Path of fatigue crack growth from disk removed from service

Two experimental approaches were used: photoelasticity and photoelastic holography. Isochromatic and isoclinic patterns were obtained using a sodium diffused-light polariscope of conventional design. Isopachic patterns were obtained using a holographic polariscope [1] which facilitates absolute retardation measurements. Either method gives sufficient data for a complete stress analysis [2]; however, it was found more efficient to use both methods.

Isoclinics and isochromatics were obtained from conventional photoelasticity. Isoclinics give the directions of the principal stresses throughout the field. The isochromatics give the difference of principal stresses over the field and the tangential stresses on all free boundaries. The isopachics, obtained from holography, give the sum of the principal stresses throughout the field. Half of the sum of the isochromatics and isopachics gives one principal stress, and half of the difference gives the other. Thus, the complete stress field in two-dimensions, i.e., both principal stresses and their direction, can be determined at any point from the isochromatics, isopachics, and isoclinics.

The fracture mechanics analysis was conducted by utilizing the same model which was used in the photoelastic analysis. It was found that the crack growth path (see Fig. 2) corresponded to mixed mode crack propagation. The analysis showed that a significant forward shear mode (K_{II}) occurred together with the opening mode (K_I). In order to determine the stress intensity factors K_I and K_{II} from the observed isochromatic fringe loops, it was necessary to develop a new analysis method.

Primary consideration in this case study is given to the loads produced by centrifugal forces as the disk and its 36 blades are rotated. The centrifugal force exerted by each blade must be carried by the blade surfaces which are in contact with the mating surfaces on the disk. These surfaces are subsequently termed either load-bearing surfaces or simply bearing surfaces.

Other in-service loads acting on the disk-blade assembly that might contribute to cracking, but were considered less important, are the gas loads on the blades, centrifugal forces on the disk both above and below the bearing surfaces, thermal gradients, and low-level vibratory stresses on the disk.

PHOTOELASTIC STRESS ANALYSIS

To represent the disk/blade dovetail region, two disk slots were modeled. Figure 3 shows the disk model; it represents the disk lug in the region between the slots. Figure 4 shows the blade model geometry. The blade models simulate the blade cross section in the area below the platform. The region above the platform was made uniform for a sufficient length, and then a reduced width shank region was added for calibration purposes. An area for clamping was left at the far end of the blade model.

Model dimensions are shown in Figs. 3 and 4; these dimensions are 3.409 times the actual dimensions. To simplify the loading, the disk model was dimensioned so that the loads acting along the blade axes were parallel to each other. This simplification eliminates the 5° angle between blade and disk lug axes but does not introduce significant error into the analysis. The parallel distance between the blade axes for the model was scaled from the circumferential distance between the blade axes at the centerline of the bearing area.

Models were machined from 1/4-in. (6-mm) thick sheets of Homalite 100* and Plexiglas II† by routing with a precision template. The models were each loaded in a small universal testing machine where the centrifugal forces were simulated. The Homalite 100 model was used to provide isochromatic fringes in a conventional polariscope. The Plexiglas model gave isoclinic fringes in the polariscope and isopachic fringes in the holographic polariscope.

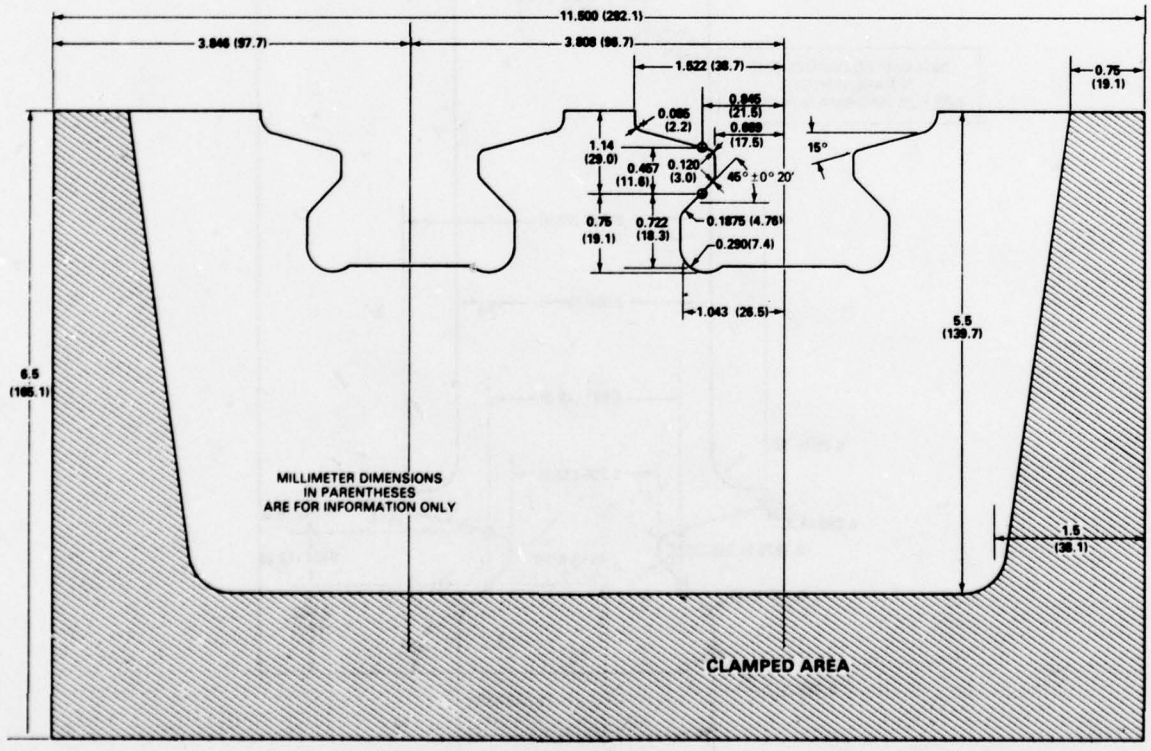


Fig. 3 — Dimensions of the disk model

*Homalite Corporation, Wilmington, Del.
†Rohm and Haas, Philadelphia, Pa.

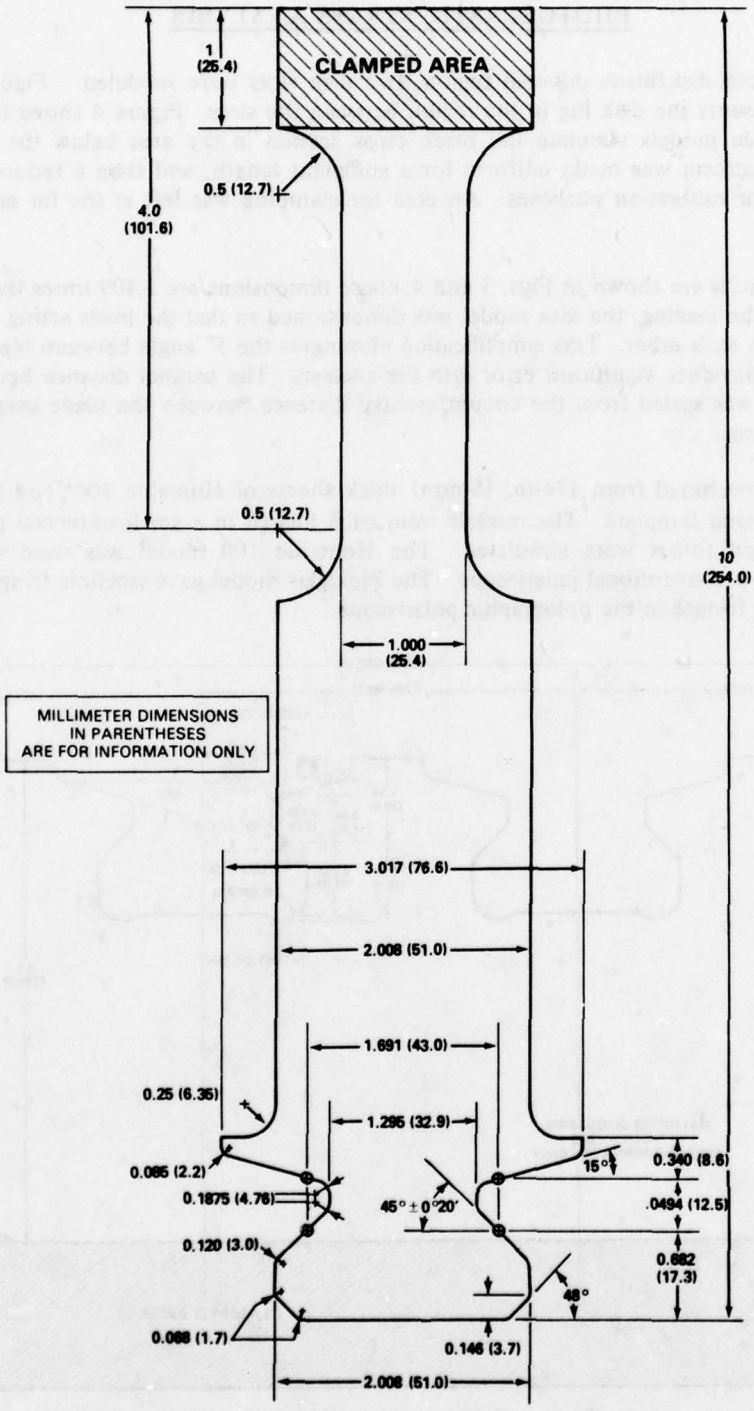


Fig. 4 — Dimensions of the blade model

Representative fringe patterns are illustrated in Figures 5 and 6. The dark-field isochromatic pattern of the center lug at 640 lb (2850N) is presented in Fig. 5. The isopachic pattern for the blade and lug is shown in Fig. 6. The isoclinic composite for the blade is presented in Fig. 7.



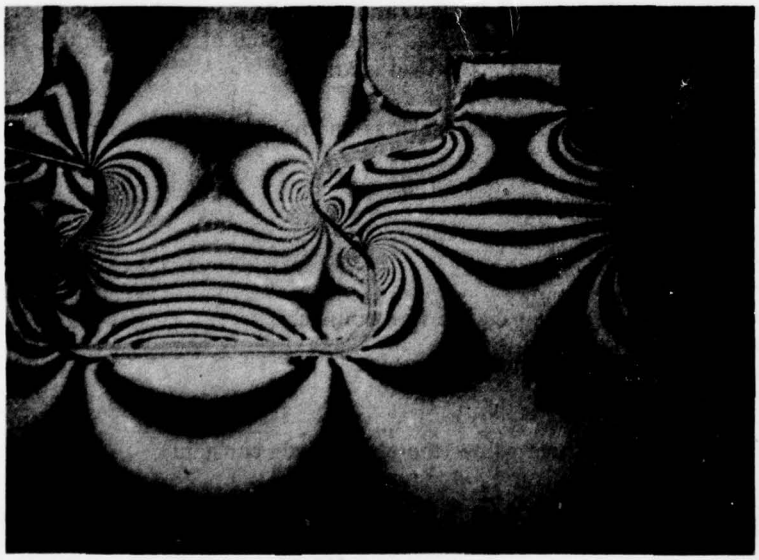


Fig. 6 — Holographic pattern (isopachics) of model of blade/disk dovetail region

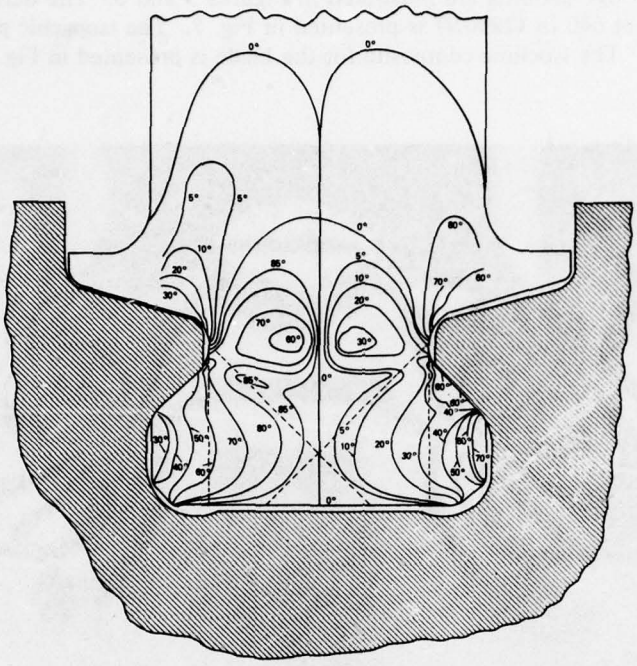


Fig. 7 — Composite isoclinic pattern of the blade model

The isochromatic patterns provide data to determine the stress concentration factor in the fillet of the disk lug. The choice of a definition for the stress concentration factor (SCF) is somewhat arbitrary and will be defined here as the ratio of the maximum tensile stress along the fillet edge to the average stress in the minimum section of the disk lug. Since the area of the minimum section is known, this average stress can always be calculated if the load is known.

The stress-optic law for uniaxial stress such as on an unloaded boundary is:

$$\sigma = \frac{Nf_\sigma}{h} \tag{1}$$

where:

σ is the stress at a point on the free boundary

N is the fringe order at the same point

h is thickness of the model

f_σ is the material fringe value (the photoelastic constant).

The corresponding SCF is

$$\frac{\sigma}{\sigma_{av}} = \frac{Nf_\sigma A}{Ph} \tag{2}$$

where

σ_{av} is the average stress in the disk neck

A is the minimum disk lug area ($A = hw$)

P is the total vertical load on the disk lug (also on the blade)

w is the width of the minimum section of the lug.

In determining the SCF's every attempt was made to keep the blade loads equal and in individual tooth loads equal and symmetric. It was possible to obtain symmetric patterns over most of the model, but in the regions of the bearing surfaces, this was impossible. Each contact region possessed an individual pattern associated with how the contact was made. The individual fillet fringes varied slightly with the variation of magnitude, position, and direction of the contact loads. In determining SCF's the average of the fringes in all four fillets was used to obtain a value of 5.2.

To illustrate the SCF in terms of stresses, consider a blade revolving at 10,500 rpm that weighs 0.738 lb (3.28 N) and has a centroid at $r_o = 10.75$ in. (273 mm) from the axis of the disk. The force due to the weight of the blade will be

$$F = \frac{\text{weight}}{g} \omega^2 r_o, \tag{3}$$

where g is the acceleration of gravity, 386 in/sec^2 (9.80 m/sec^2) and ω is the speed of rotation in radians/sec. Therefore,

$$F = \frac{0.738}{386}\left[10,500\ \frac{2\pi}{60}\right]^2 (10.75) = 24,900 \text{ lb } (110.7 \text{ kN}) \tag{4}$$

The net section of the disk just below the fillet has an area of 1.138 in.^{2} (734 mm^2). The average stress in the net section is then 24,900/1.138 = 21,900 psi (151 MPa).

The estimated maximum stress in the fillet of the disk is

$$\sigma_D = (21,900)\ (5.2) = 114,000 \text{ psi } (786\text{MPa}) \tag{5}$$

Note that any variation in the engine speed will vary the stresses by the square of the speed change. Thus, if the speed is increased 10% the stress will increase by 21% = 100 ($1.1^2 - 1$).

The stress distribution along the entire free boundary of the fillet can be obtained just as the SCF's were obtained. The tangential stress distribution along the fillets of the disk is shown in Fig. 8. Notice that the tensile stress tangential to the boundary at the lower edge of bearing area has a SCF in excess of 4. This stress has an important effect on the initiation of fretting fatigue cracks.

Stresses away from the free boundaries were determined by combining the isochromatic and isopachic data. Results showing the normalized isopachics $(\sigma_1 + \sigma_2)/\sigma_{av}$, the normalized isochromatics $(\sigma_1 - \sigma_2)/\sigma_{av}$, and the normalized principal stresses σ_1/σ_{av} and σ_2/σ_{av} are shown as a function of position in Fig. 9. Other stress distributions are reported in Reference 3.

These stress distributions indicate a rather sharp dropoff of the maximum principal stress in directions normal to the fillet boundaries, as opposed to the gradual dropoff of the fillet stress along the free boundary as shown in Fig. 8. This is typical of fillet stress distributions.

With the fringe pattern of Fig. 5 serving as a guide, the original disk lug template was modified in the two central fillet regions. The original model was then rerouted following the modified template,

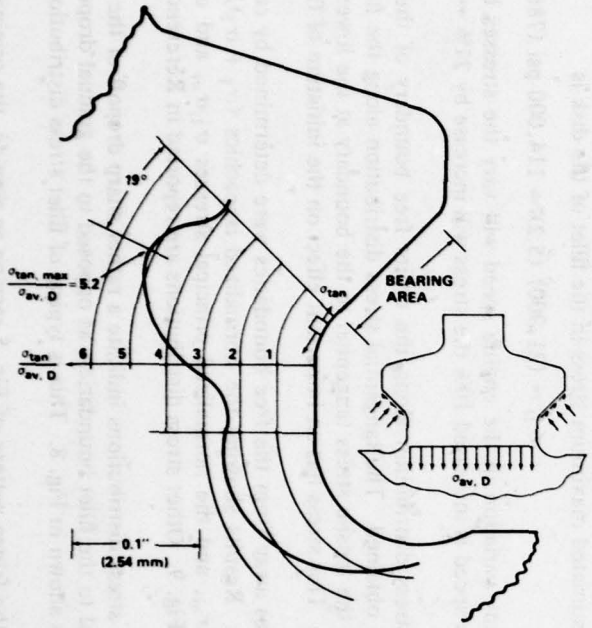


Fig. 8 — Tangential boundary stress in fillet of disk

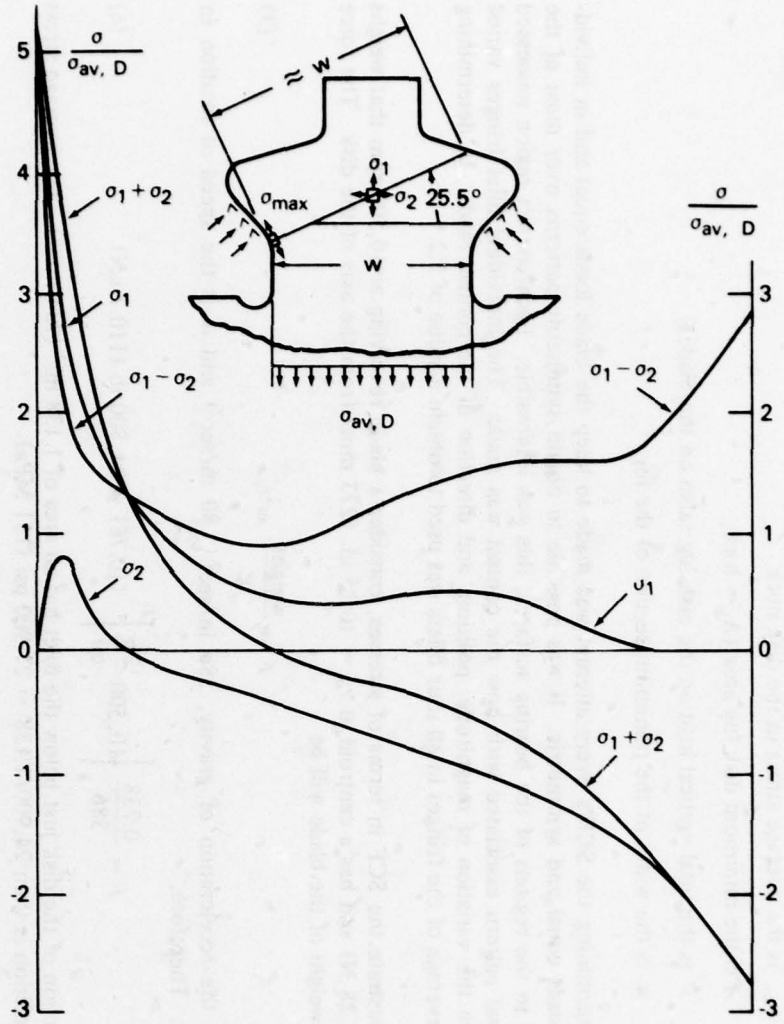


Fig. 9 — Principal stresses along a line through the point of maximum tensile stress in the disk fillet (average of left and right sides)

and isochromatic patterns of the rerouted model were photographed. The process was repeated and the photoelastic results indicated that the fillet geometry was nearly optimum. The modified fillet radius was measured and a new template was prepared to the optimized dimensions. Note that all of the fillet modifications were made in the clearance region between the blade and the disk and are thus applicable to existing disks by reworking the slots between the disk lugs.

The isochromatic pattern of the modified fillet model for the same load as that in Fig. 5 is shown in Fig. 10. The SCF from the pattern of Fig. 10, determined as previously described, was found to be 3.8. The stress distribution along the optimized fillet is presented in Fig. 11. A comparison between the original and modified fillets (Fig. 8 and Fig. 11) shows a reduction of 27% in the maximum stress in the fillet and a reduction of about 50% in the tensile stresses at the edge of the bearing area. It is believed that these reductions in stress, associated with the modified design, will result in an increased fatigue life by about an order of magnitude.



Fig. 10 — Dark field isochromatic pattern of disk lug with modified fillet radius

FRACTURE MECHANICS ANALYSIS

A crack along the line of failure was simulated in the Homalite model by cutting with a fine-pitched jeweler's saw and then sharpening the crack tip with a file. The model was loaded in a sodium diffused-light polariscope and isochromatic fringe patterns were photographically recorded. The crack was extended incrementally by sawing and filing; then the loading and photographing sequence was repeated. A total of 18 combinations of load and crack length were analyzed.

Typical isochromatic fringe patterns obtained for three different lengths of cracks are illustrated in Fig. 12 and an enlargement of the fringe loops at the crack tip is presented in Fig. 13. Inspection of these fringe patterns shows that the loop tilt angles θ_m (defined in Fig. 14) and the maximum radii, r_m,

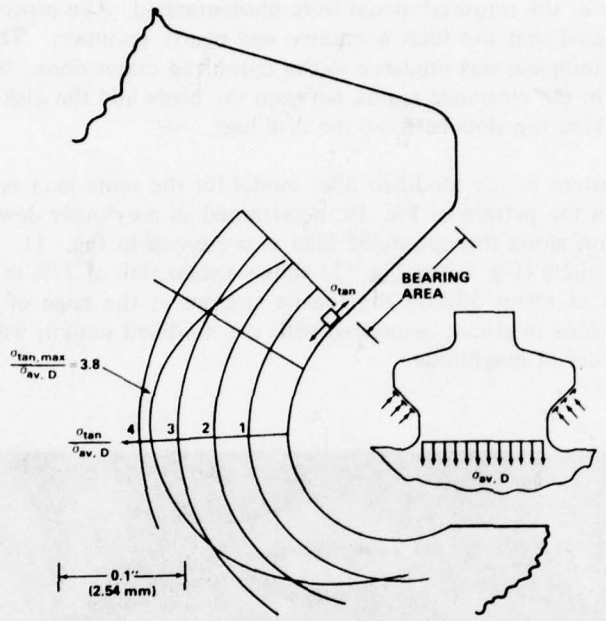


Fig. 11 — Tangential boundary stress in fillet of disk with improved design geometry



Fig. 12 — Typical isochromatic fringes for crack extension in disk lug

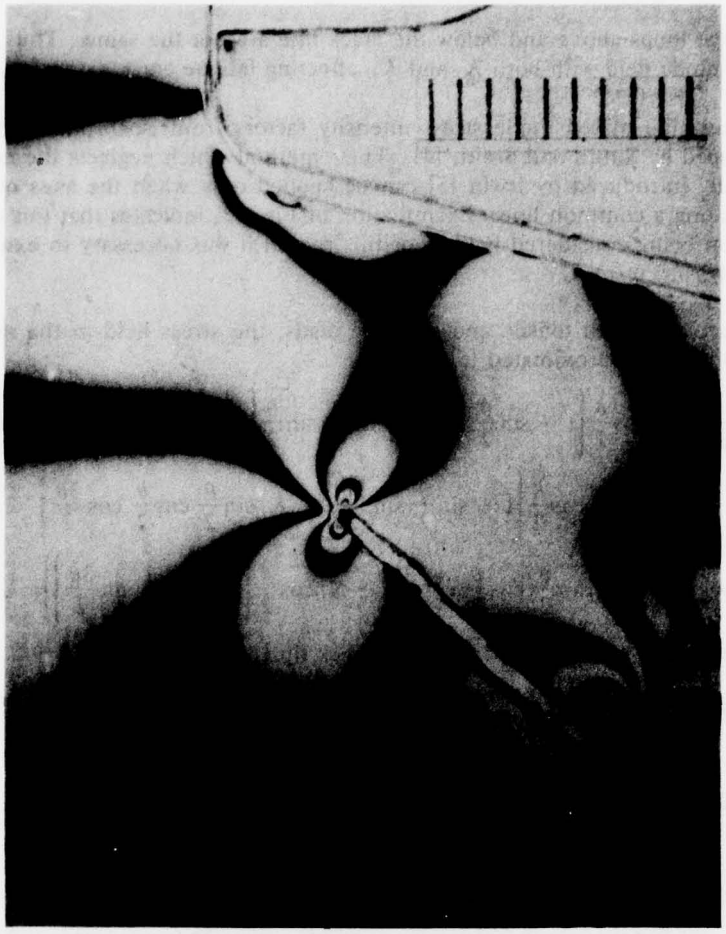


Fig. 13 — Enlargement of isochromatic fringe pattern showing detail of fringe loops at the simulated crack tip

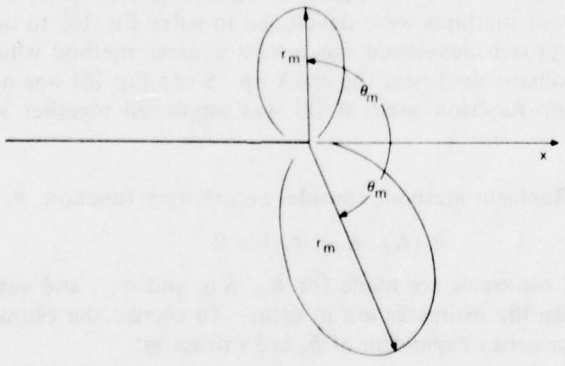


Fig. 14 — Characteristic shape of upper and lower fringe loops for mixed-mode loading

associated with the fringe loops above and below the crack line are not the same. Thus, the cracks are propagating in a mixed mode field with both K_I and K_{II} affecting fatigue crack extension.

A method to determine mixed mode stress intensity factors from isochromatic fringe loops has previously been developed by Smith and Smith [4]. Their method which neglects the non-singular far-field stress σ_{ox} originally introduced by Irwin [5] can be applied only when the axes of the upper and lower fringe loops lie along a common line. Examination of Fig. 13, indicates that this condition is not satisfied for the problem being considered here. For this reason it was necessary to extend the method of analysis to include the σ_{ox} term.

For a crack subjected to both tensile and shearing loads, the stress field in the neighborhood of the crack tip ($r << a$) can be approximated [6] as:

$$\sigma_x = \frac{1}{\sqrt{2\pi r}}\left\{K_I \cos\frac{\theta}{2}\left[1 - \sin\frac{\theta}{2}\sin\frac{3\theta}{2}\right] - K_{II}\sin\frac{\theta}{2}\left[2 + \cos\frac{\theta}{2}\cos\frac{3\theta}{2}\right]\right\} - \sigma_{ox}$$

$$\sigma_y = \frac{1}{\sqrt{2\pi r}}\left\{K_I\cos\frac{\theta}{2}\left[1 + \sin\frac{\theta}{2}\sin\frac{3\theta}{2}\right] + K_{II}\sin\frac{\theta}{2}\cos\frac{\theta}{2}\cos\frac{3\theta}{2}\right\}$$

$$\tau_{xy} = \frac{1}{\sqrt{2\pi r}}\left\{K_I\sin\frac{\theta}{2}\cos\frac{\theta}{2}\cos\frac{3\theta}{2} + K_{II}\cos\frac{\theta}{2}\left[1 - \sin\frac{\theta}{2}\sin\frac{3\theta}{2}\right]\right\}. \quad (6)$$

where the co-ordinates r and θ are measured from the crack tip.

The Cartesian components of stress are related to the isochromatic fringe order by:

$$(Nf_\sigma/h)^2 = (\sigma_y - \sigma_x)^2 + (2\tau_{xy})^2 \quad (7)$$

Substituting Eq. (6) into Eq. (7) gives

$$(Nf_\sigma/h)^2 = \frac{1}{2\pi r}\left\{[K_I \sin\theta + 2K_{II}\cos\theta]^2 + [K_{II}\sin\theta]^2\right\}$$

$$+ \frac{2\sigma_{ox}}{\sqrt{2\pi r}}\sin\frac{\theta}{2}\,[K_I \sin\theta(1 + 2\cos\theta) + K_{II}(1 + 2\cos^2\theta + \cos\theta)] + \sigma_{ox}^2. \quad (8)$$

Equation (8) is the basis of all the methods to determine stress intensity factors from isochromatic patterns. In this generalized form the equation is non-linear in terms of K_I, K_{II}, and σ_{ox}. In this investigation several different methods were developed to solve Eq. (8) to determine K_I, K_{II}, and σ_{ox} (see Ref. 7). The best approach developed was a least squares method which fit Eq. 8 to a large number of points in the isochromatic field near the crack tip. Since Eq. (8) was non-linear, a numerical technique based on the Newton-Raphson method [8] was employed together with the least squares approach.

To describe the Newton-Raphson method, consider an arbitrary function, h_k of the form:

$$h_k(K_I,\ K_{II},\ \sigma_{ox}) = 0 \quad (9)$$

where $k = 1, \ldots, M$. If initial estimates are made for K_I, K_{II}, and σ_{ox}, and substituted into Eq. (9), the equality is not satisfied since the estimates are in error. To correct the estimates, a series of iterative equations based on a Taylor series expansion of h_k are written as:

$$(h_k)_{i+1} = (h_k)_i + \left(\frac{\partial h_k}{\partial K_I}\right)_i \Delta K_I + \left(\frac{\partial h_k}{\partial K_{II}}\right)_i \Delta K_{II} + \left(\frac{\partial h_k}{\partial \sigma_{ox}}\right)_i \Delta\sigma_{ox}, \quad (10)$$

where the subscript i refers to the i th iteration step. ΔK_I, ΔK_{II} and $\Delta\sigma_{ox}$ are corrections to the previous estimates. The corrections are determined so that $(h_k)_{i+1} = 0$, and thus, Eq. (10) gives:

$$\left[\frac{\partial h_k}{\partial K_I}\right]_i \Delta K_I + \left[\frac{\partial h_k}{\partial K_{II}}\right]_i \Delta K_{II} + \left[\frac{\partial h_k}{\partial \sigma_{ox}}\right]_i \Delta\sigma_{ox} = -(h_k)_i. \tag{11}$$

Rewriting Eq. (8) in a form suitable for use with the Newton-Raphson method gives:

$$g_k(K_I, K_{II}, \sigma_{ox}) = \frac{1}{2\pi r_k}\left\{[K_I \sin\theta_k + 2K_{II}\cos\theta_k]^2 + [K_{II}\sin\theta_k]^2\right\}$$

$$+ \frac{2\sigma_{ox}}{\sqrt{2\pi r_k}} \sin\frac{\theta_k}{2}\left[K_I \sin\theta_k(1 + 2\cos\theta_k) + K_{II}(1 + 2\cos^2\theta_k + \cos\theta_k)\right]$$

$$+ \sigma_{ox}^2 - (N_k f_\sigma/h)^2 = 0 \tag{12}$$

where N_k is the fringe order corresponding to the point (r_k, θ_k).

Applying the iteration scheme suggested in Eq. (11) to $M(>3)$ equations of the form given in Eq. (12), results in an overdetermined set of linear equations in terms of the unknowns ΔK_I, ΔK_{II} and $\Delta\sigma_{ox}$ of the form

$$\begin{bmatrix} g_1 \\ g_2 \\ \cdot \\ \cdot \\ g_M \end{bmatrix}_i = - \begin{bmatrix} \frac{\partial g_1}{\partial K_I} & \frac{\partial g_1}{\partial K_{II}} & \frac{\partial g_1}{\partial \sigma_{ox}} \\ \frac{\partial g_2}{\partial K_I} & \frac{\partial g_2}{\partial K_{II}} & \frac{\partial g_2}{\partial \sigma_{ox}} \\ \cdot & \cdot & \cdot \\ \cdot & \cdot & \cdot \\ \frac{\partial g_M}{\partial K_I} & \frac{\partial g_M}{\partial K_{II}} & \frac{\partial g_M}{\partial \sigma_{ox}} \end{bmatrix}_i \begin{bmatrix} \Delta K_I \\ \Delta K_{II} \\ \Delta\sigma_{ox} \end{bmatrix} \tag{13}$$

for brevity rewrite the matrices in Eq. (13) as

$$[g] = [a]\,[\Delta K] \tag{14}$$

It can be shown that ΔK in Eq. (14) can be determined in the least squares sense by multiplying both sides from the left by $[a]^T$, where $[a]^T$ is the transpose of $[a]$, i.e.

$$[a]^T[g] = [a]^T[a]\,[\Delta K] \tag{15}$$

or

$$[d] = [c]\,[\Delta K] \tag{16}$$

where

$$[d] = [a]^T[g]$$

$$[c] = [a]^T[a].$$

Finally,

$$[\Delta K] = [c]^{-1}[d]$$

where $[c]^{-1}$ is the inverse of $[c]$

The solution of Eq. (17) gives ΔK_I, ΔK_{II}, and $\Delta\sigma_{ox}$ which are used to correct initial estimates of K_I, K_{II}, and σ_{ox} to obtain a better fit of the function g to the M data points. Utilizing the matrix operations available in BASIC, a computer program [7] was written to determine K_I, K_{II}, and σ_{ox} using data from 10 points over the fringe field.

Data read from negatives showing the isochromatic fringe loops were processed on the computer to determine K_I, K_{II}, and σ_{ox}. Ten data points were used for each determination, 5 from an upper loop and 5 from a lower loop. When more than 10 data points were available, different combinations of data sets were employed and several estimates of K_I, K_{II}, and σ_{ox} were made. In these instances, averages of the individual determinations were taken. The mean values of K_I, K_{II}, and σ_{ox} are presented in Table I.

Table I — Summary of Results for K_I, K_{II}, and σ_{ox} from the Photoelastic Model

Number of Readings	P Load lbs	Crack Length in.	K_I psi $\sqrt{in}$	K_{II} psi $\sqrt{in}$	σ_{ox} psi
Before the crack turns					
(1)	800	.096	573	-569	2482
(1)	1000	.096	693	-706	2974
(1)	200	0.122	439	-216	327
(1)	200	0.185	475	-159	238
(5)	200	0.241	348	-219	377
(6)	200	0.357	318	-285	357
(7)	200	0.466	512	-203	298
(7)	200	0.622	539	-281	318
(5)	200	0.710	549	-221	134
(3)	200	0.843	392	-334	152
(5)	200	0.955	351	-444	213
After the crack turns					
(1)	200	.100	793	-365	370
(3)	150	.190	782	-184	431
(1)	200	.190	1038	-198	533
(2)	100	.296	815	-86	131
(1)	100	.296	786	-163	154
(1)	100	.410	1044	244	-326
(1)	100	.518	1196	347	-519

1 psi = 6.895 kPa
1 psi $\sqrt{in.}$ = 1.099 kPa $\sqrt{m}$
1 in. = 25.4 mm

An example of the ability of the least squares method to give accurate estimates of the mixed-mode stress intensity factors is illustrated in Fig. 15. This figure shows a computer plot of the isochromatic pattern generated from Eq. (8) using the values of K_I, K_{II} and σ_{ox} determined with this method. The crosses are the original input data. It is evident that the fit is excellent.

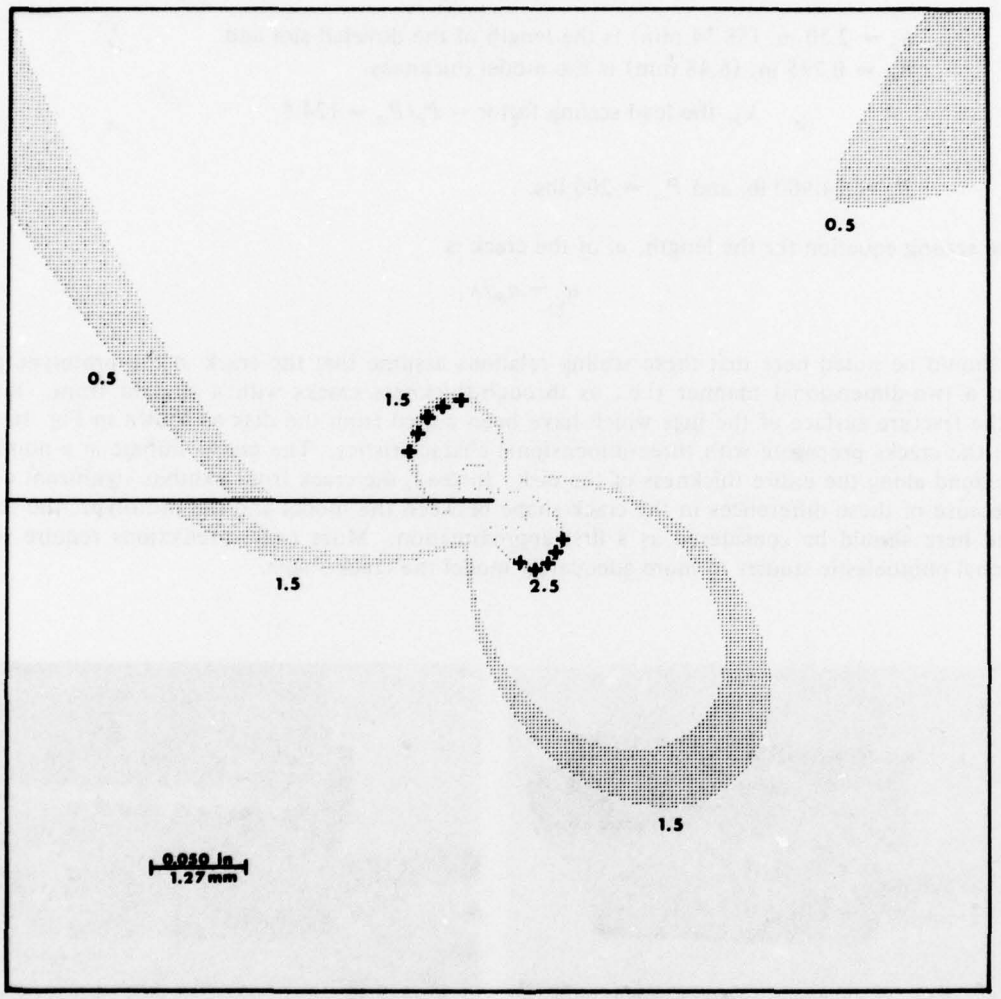


Fig. 15 — Theoretical mixed-mode fringe pattern for K_I = 319 psi $\sqrt{\text{in.}}$, K_{II} = 293 psi $\sqrt{\text{in.}}$, and σ_i = 355 psi (crosses denote data points used to compute the stress intensity factors)

Conversion of the results from the photoelastic model of the turbine disk to results which correspond to the actual prototype, requires the use of a scaling relationship. The scaling equation for K_I or K_{II} is:

$$(K_{I,II})_p = \sqrt{\lambda_1}\,\lambda_2\,\lambda_3 (K_{I,II})_m \tag{18}$$

where subscripts p and m refer to the prototype and model respectively. The terms λ_1, λ_2, and λ_3 in Eq. (18) are scaling factors defined below:

$$\lambda_1, \text{ the in-plane scaling factor} = w_m/w_p = 3.409 \tag{19}$$

where:

w_m the center to center dimension between two adjacent blades on the model is 3.808 in. (96.7 mm), and the corresponding dimension of the prototype w_p = 1.117 in. (28.28 mm).

$$\lambda_2, \text{ the thickness scaling factor} = h_m/h_p = 0.111 \tag{20}$$

where:

h_p = 2.30 in. (58.34 mm) is the length of the dovetail slot and
h_m = 0.255 in. (6.48 mm) is the model thickness.

$$\lambda_3, \text{ the load scaling factor} = P_p/P_m = 124.5 \tag{21}$$

where

P_p = 24,900 lb. and P_m = 200 lbs.

The scaling equation for the length, a, of the crack is

$$a_p = a_m/\lambda_1 \tag{22}$$

It should be noted here that these scaling relations assume that the crack in the prototype propagates in a two-dimensional manner (i.e., as through-thickness cracks with a straight front. Inspection of the fracture surface of the lugs which have been pulled from the disk as shown in Fig. 16 indicate that the cracks propagate with three-dimensional characteristics. The cracks initiate at a point and do not extend along the entire thickness of the disk. Instead, the crack front exhibits significant curvature. Because of these differences in the crack shape between the model and the prototype, the results presented here should be considered as a first approximation. More exact predictions require three-dimensional photoelastic studies to more adequately model the crack shape.

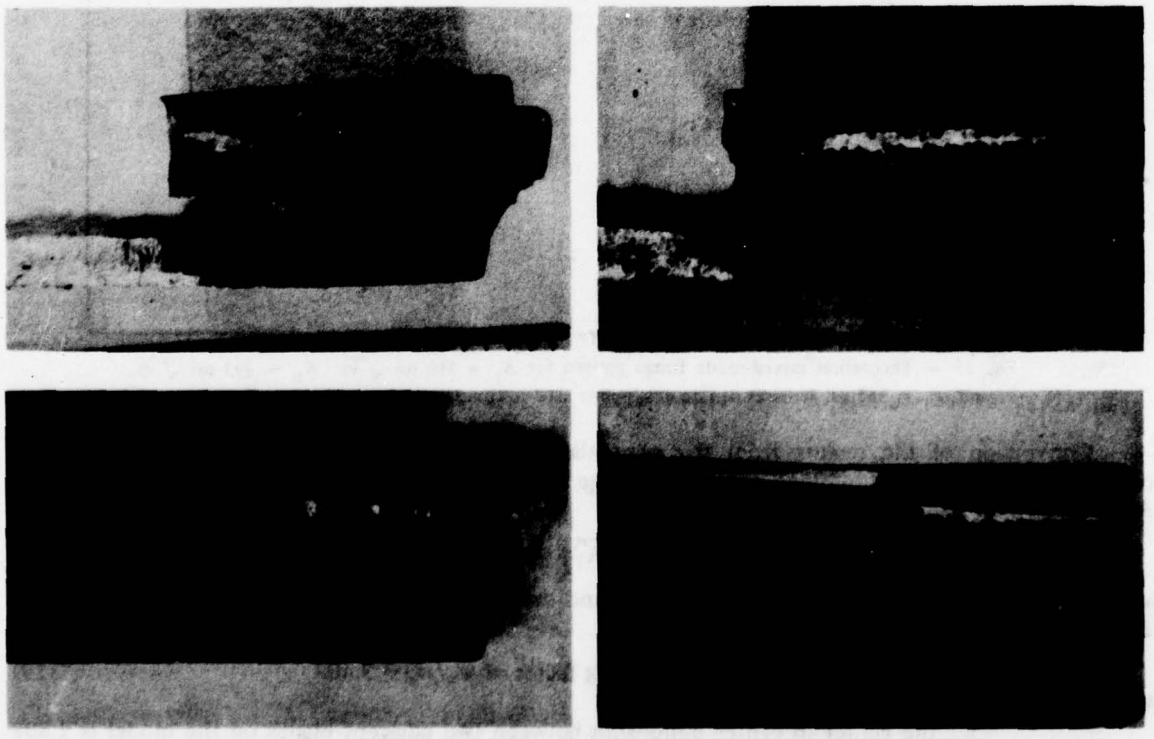


Fig. 16 — Typical fracture surfaces showing three-dimensional characteristics of fatigue crack

To assess the influence of the combined effect of K_I and K_{II}, it is appropriate to consider the total strain energy release rate $\mathcal{G}$ which is given by:

$$\mathcal{G} = \mathcal{G}_1 + \mathcal{G}_{II} \tag{23}$$

where, for plane strain:

$$\mathcal{G}_1 = \frac{1 - \nu^2}{E} K_I^2 \tag{24}$$

$$\mathcal{G}_{II} = \frac{1 - \nu^2}{E} K_{II}^2$$

and E = modulus of elasticity and ν = Poisson's ratio.

Substituting Eq. (24) into Eq. (23) gives

$$\mathcal{G} = \frac{1 - \nu^2}{E} K_{eff}^2 \tag{25}$$

where

$$K_{eff} = \sqrt{K_I^2 + K_{II}^2} \tag{26}$$

The effective stress intensity factor K_{eff}, which governs the rate of crack propagation da/dN, increases from zero to a value of about 14 ksi $\sqrt{\text{in.}}$ (15.4 kPa $\sqrt{\text{m}}$) as the crack extends to a depth of about 0.100 in. as shown in Fig. 17. Continued crack extension from 0.100 to 0.280 in. (2.54 to 7.11 mm) occurs at nearly constant K_{eff}. As the crack approaches the upper fillet of the lug where the stress field is compressive, the volume of K_I decreases and $|K_{II}|$ increases until the crack turns through an angle of 45 degrees. After turning, K_I becomes dominant and K_{eff} increases markedly with further crack extension. The rate of crack propagation increases rapidly after the crack turns.

CONCLUSIONS

A stress analysis using photoelasticity and photoelastic holography showed that early failures were due to a sharp fillet which exhibited a SCF = 5.2. Using photoelasticity the fillet was redesigned to lower the stress concentration factor to 3.8 providing a 27% reduction in the maximum stress level. It is believed that fatigue life can be extended by a factor of 10 if the optimized fillets are employed in reworked disks.

A new method of analysis was developed using a combined least squares, Newton-Raphson numerical method to determine K_I, K_{II}, and σ_{ox} from an isochromatic representation of a mixed mode field. Results of the fracture mechanics analysis showed that K_{eff} was nearly constant as the fatigue crack extended into the lug (prior to turning). This fact implies that da/dN remains constant during the early propagation phase. Since da/dN is relatively small the cracks grow slowly permitting operation of the engine after crack initiation.

The results presented here are part of an overall materials and mechanics study into the origin of the failures in the third-stage fan of the TF-30 engine. The emphasis in this paper has been on the optical mechanics aspects of the solution to the problem and was intended to demonstrate that these methods can provide valuable information to an overall failure investigation.

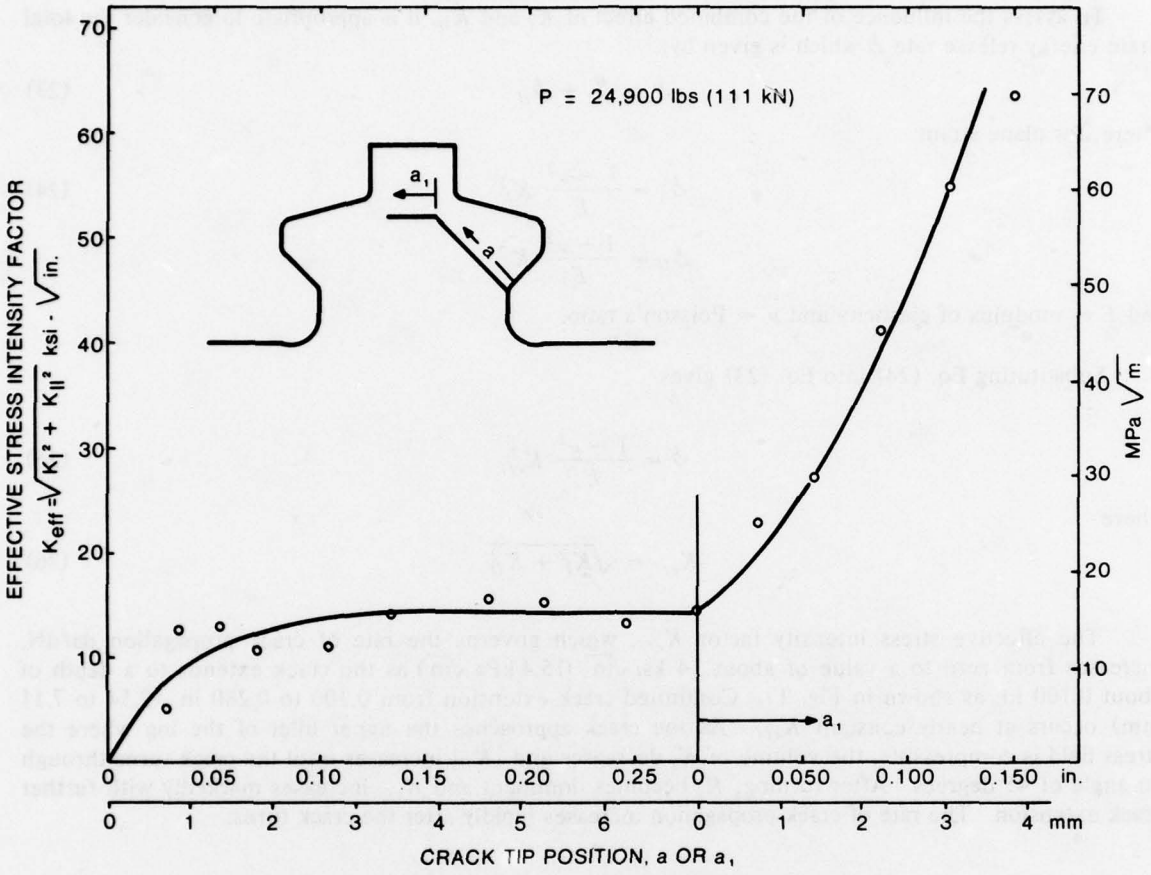


Fig. 17 — Effective stress intensity factor K_{eff} as a function of crack length for the prototype disk.

REFERENCES

1. Fourney, M. E. and Mate, K. V., "Further Applications of Holography to Photoelasticity," *Experimental Mechanics,* Vol. 10, No. 5, May 1970, 177-186.

2. Sanford, R. J., "A General Theory of Polarization Holography And Its Application to Photoelastic Analysis," *Engineering Applications of Holography*, SPIE, Redondo Beach, CA, 1972, 331-343.

3. Parks, V. J. and Sanford, R. J., "Experimental Stress Analysis of the TF-30 Turbine Engine Third-Stage Fan-Blade/Disk Dovetail Region," Naval Research Laboratory Report, NRL 8149, August 1977.

4. Smith, D. G. and Smith, C. W., "Photoelastic Determination of Mixed Mode Stress Intensity Factors," *J. of Engineering Fracture Mechanics*, Vol. 4, No. 2, 1972, 357-366.

5. Irwin, G. R., "Discussion of: The Dynamic Stress Distribution Surrounding a Running Crack — A Photoelastic Analysis," *Proc. SESA*, Vol. 16, No. 1, 1958, 93-96.

6. Paris, P. C. and Sih, G. C., "Stress Analysis of Cracks," *Fracture Toughness Testing and Its Applications*, ASTM STP 381, Philadelphia, 1965, 30-81.

7. Sanford, R. J. and Dally, J. W., "Stress Intensity Factors in the Third Stage Fan Disk of the TF-30 Turbine Engine," Naval Research Laboratory Report, NRL 8202, May 1978.

8. Kelly, L. G., *Handbook of Numerical Methods and Applications*, Addison Wesley Publishing Co., Reading, Mass, 1967, 99.

MODEL 540 MAIN ROTOR BLADE RISK ASSESSMENT

ARTHUR J. GUSTAFSON
Aerospace Engineer
Applied Technology Laboratory
US Army Research & Technology Laboratories (AVRADCOM)
Ft Eustis, Virginia 23604

ABSTRACT

The all-aluminum Bell Model 540 main rotor blade, with an allowed life of 1100 flight hours, is used on several helicopter models, including the AH-1G, UH-1C, and UH-1M. The occurrence of catastrophic helicopter accidents due to structural failure of this blade triggered an investigation by an AVRADCOM-appointed Risk Assessment Team.

The Risk Assessment Team's first task was to define the scope of the problem, which was accomplished by conducting interviews with field personnel and analyses of the failed structure. A failure analysis was conducted for the Team by the US Army Materials and Mechanics Research Center, which included metallurgical and chemical tests of the failure surface and residues found on the surface. These examinations showed the probable cause of failure to be fretting fatigue between the spar and spar spacer in the areas of disbond between these elements.

A new safe life for the Model 540 rotor was calculated using the known failure rate and population distribution using the censored population analysis due to A.M. Stagg. Also, nondestructive techniques were reviewed for applicability to detecting disbonds between the spar and spar spacer. An ultrasonic shear-wave technique was selected.

A substantiation of the new safe life was made by fatigue testing three full-scale Model 540 blades. Each blade had a varying bond/disbond condition and accumulated flight hours. The approach taken in this test was to apply the same load spectrum as that used during the original substantiation of the Model 540 blade fatigue life conducted by Bell Helicopter Company. Existing inspection techniques for bond/disbond detection were used and evaluated, with emphasis placed on nondestructive test techniques.

It was concluded that a fully bonded Model 540 blade is flightworthy for 1100 flight hours; blades with accumulated disbonds less than 3 feet long are flightworthy for 550 flight hours.

INTRODUCTION

The all-aluminum Model 540 Bell Helicopter Company main rotor blade, with a safe fatigue life of 1100 hours, is used on several Army helicopters and one Navy model, including the AH-1G, UH-1C, UH-1M, and the AH-1J (Navy). Seven Model 540 rotor blades developed structural failures in the time period from April 1968 to December 1973. Four were Army helicopters and three were Navy. Two of these failures were catastrophic, two had cracked spars, and

three had cracked skin just aft of the spar with no spar cracks. All exhibited a disbond between the spar and the spar spacer, with some evidence of fretting in that area.

In response to direction from the Commanding General, US Army Materiel Development and Readiness Command (DARCOM), the US Army Research and Technology Laboratories (USARTL) conducted a technical risk assessment to determine the cause of the Model 540 rotor blade failures on the AH-1 and UH-1 aircraft and to recommend corrective action. A team of engineering specialists from several Army agencies and NASA conducted the assessment.

The investigation of these failures by the Risk Assessment Team included (1) determination of the cause of the failures, (2) examination of stress states in the spar and skin for a bonded and a debonded spar spacer, (3) review of blade loads, (4) evaluation of nondestructive inspection techniques as applied to the Model 540, and (5) development and substantiation of a new safe fatigue life. These actions are described in greater detail below.

DESCRIPTION OF THE MODEL 540 ROTOR BLADE

The Model 540 rotor blade is approximately 19 feet (5.79 meter) long with a 27-inch (.69 meter) chord and 9-1/3% thick symmetrical airfoil. The spar is made from a C section extrusion of 2024 aluminum alloy and forms the basic profile of the airfoil leading edge. The spar spacer (see Figure 1) is also a 2024 aluminum extrusion and, when bonded in place, it controls airfoil thickness. The lips of the spacer engage the shallow grooves inside the "C" spar, converting the C section to a D section. The tolerance of the spar in its free state and the spacer range from .035-inch (.00089 meter) clearance to .265-inch (.0067 meter) interference, excluding bonding adhesives. The blade from the spar aft is composed of aluminum honeycomb and skins bonded to the spar and to an extruded aluminum trailing edge piece. The spar is tapered chordwise between stations 80 and 140 (see Figure 2), the section being constant outboard of this point. The trailing edges are also tapered, this taper being the only difference between two Model 540 blade types.

CAUSE OF FAILURE

The Risk Assessment Team, as a first step, investigated the cause of failure of each rotor blade. This was accomplished by interviewing the accident investigation personnel at Corpus Christi for the Army and at Pensacola, Florida, for the Navy. Personnel at Bell Helicopter Company had also assisted in diagnosis of the accident cause(s), so the results of their analysis were also reviewed. All failures had been classed as fatigue failures and were identified tentatively as the result of stress corrosion. Minimum fractography or chemical examination had been performed.

Fortunately, specimens of the fracture surface were still available from three of the failed blades. These specimens were examined by personnel of the US Army Materials and Mechanics Research Center (AMMRC). The results of their examination clearly indicated that these failures were caused by fretting fatigue. Further examination revealed that all failures occurred in

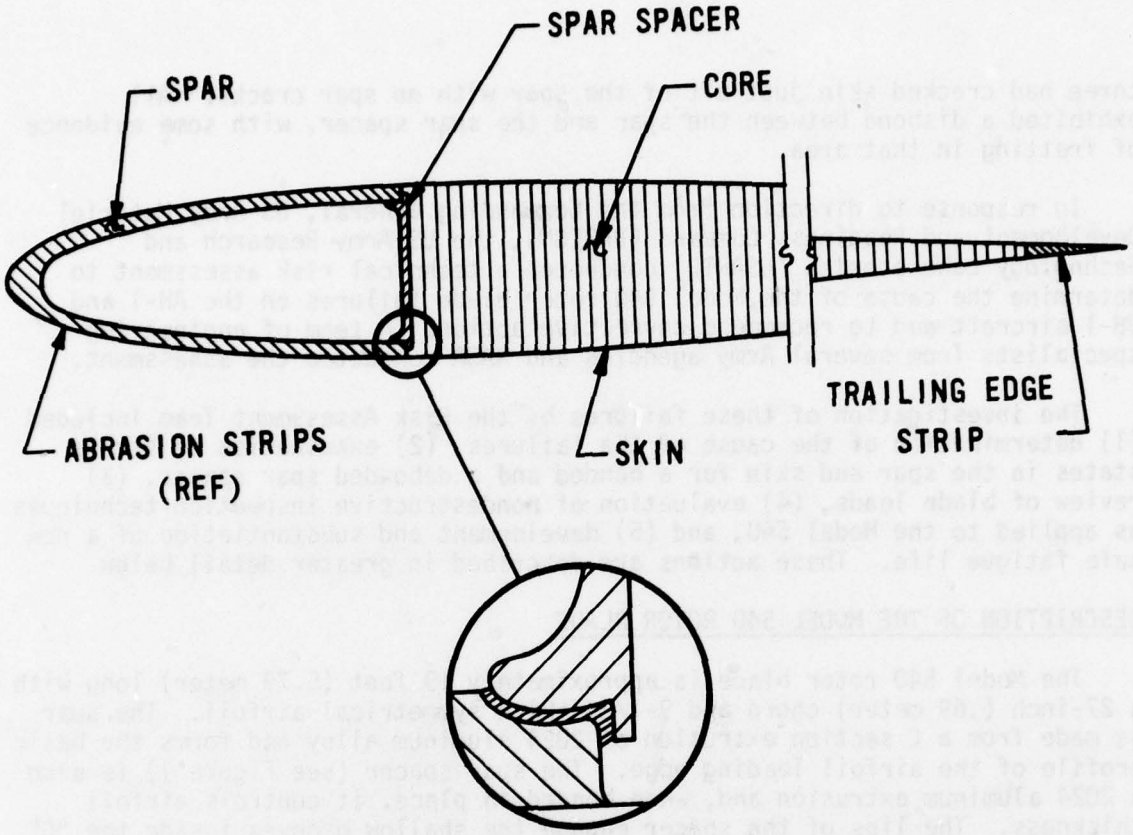


Figure 1. Cross Section Model 540 Rotor Blade

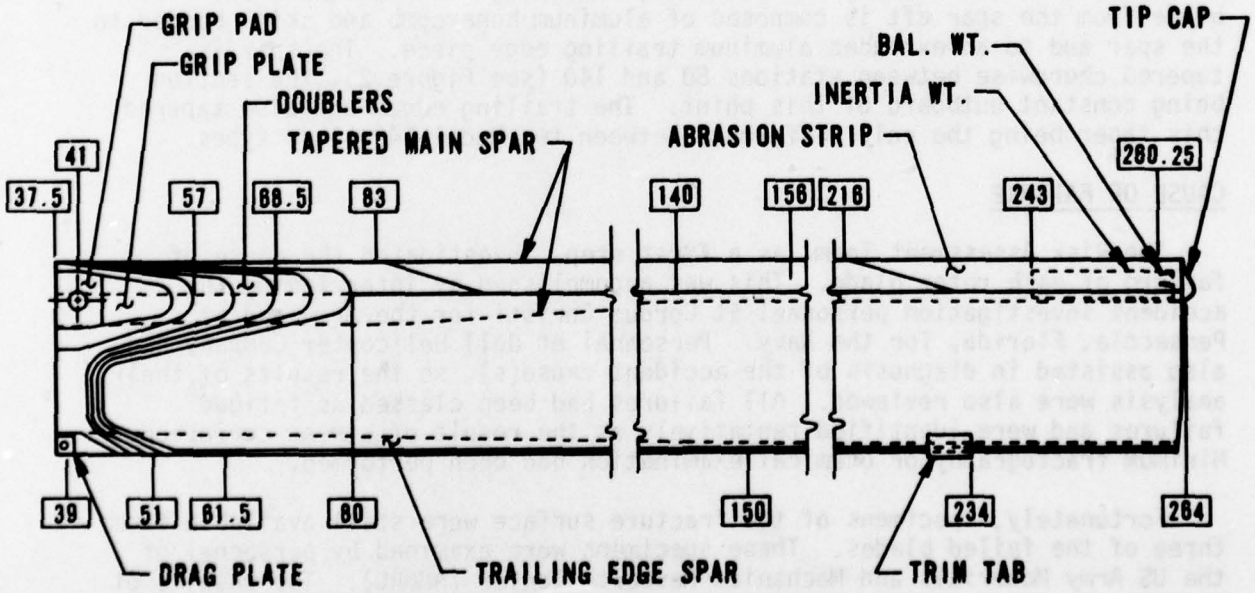


Figure 2. Planform of Model 540 Rotor Blade

regions of disbond along the spar/spar spacer bond line. This area is shown in Figure 1.

The macroscopic appearances of fractured "C" spars and their mating closures are respectively similar. Figure 3 illustrates the origin of a fracture in the spar of blade S/N A2-723 (Ft Sill) which failed catastrophically. In this illustration, a series of radial marks eminate from the upper left corner of this fracture. The origin can be found by determining the location at which these vestigial radial marks intersect--near the concave surface. This location is the interface of the spar, spar spacer, and bond where fretting had occurred.

BLADE STRESS

A stress analysis of the Model 540 was made by AMMRC analysts except for the bond between the spar and spar spacer, which was analyzed by the Applied Technology Laboratory/Langley personnel. These analyses were made as a check on the original stress analysis performed by Bell Helicopter Company.

AMMRC found that, in the absence of unusual conditions, e.g., fretting, corrosion, etc., the "C" spar should not fail in fatigue regardless of whether the spar spacer remains bonded or not. On the other hand, the trailing aluminum skin does become marginal with respect to fatigue after loss of bond at the spar spacer.

The analysis also showed that debonding of the spar and spacer for the full length of the blade would drastically reduce blade torsional stiffness, resulting in a noticeable change in flight characteristics. However, in most of the reported blade failures, debonding was noted to be localized in the region of the fracture initiation. This would have little effect on the overall blade stiffness and flight characteristics. Consequently, blade damage occurred insidiously during flight operations. Interim flight visual inspection would reveal damage only after cracks appeared in the skin, which may or may not have occurred prior to initiation of spar fracture.

A finite element analysis was made by the Applied Technology Laboratory/Structures Lab of three possible bond-line configurations based on tolerance of the spar and spar spacer. All configurations analyzed were observed on cross sections of actual spars and are considered to be typical. The stress concentration factor varied from 2.0 on a good uniform bond, to 3.5 and 5.5 on nonuniform bonds. When these stress concentrations are applied to the average and alternating stresses in the bond line for the AH-1J and AH-1G, then failure may occur by normal loads which produce stresses beyond the ultimate strength and/or by normal loads which produce stresses beyond the fatigue limit. These conditions are slightly worse for the AH-1J because of the higher normal loads. The Applied Technology Laboratory/Structures Lab found that the bond between the spar and spar spacer was not adequate because of the high probability of stress concentration in the bond. These stress concentrations may be caused by several factors: thin bond lines created in manufacture; poor adhesion to the spar and/or spacer because of

inadequate surface preparation of the adherents; and voids in the bond allowing metal-to-metal contact of the spar and spar spacer.

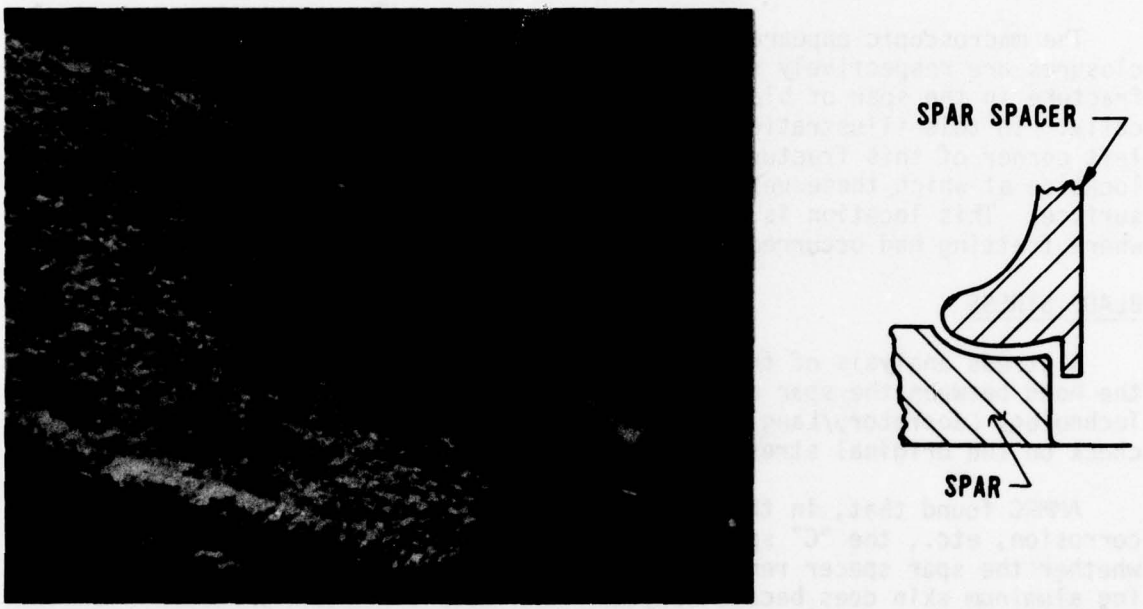


Figure 3. Origin of Fracture on the Spar of Blade S/N A2-723

BLADE LOADS

A review was made of a Bell Helicopter Company report on the 540 rotor system and an Applied Technology Laboratory/USARTL study which reassesses the flight loads and fatigue life of several rotor components for the AH-1G, Reference 1. There was no indication that fatigue loads were greater than those used for design of the rotor system. The gross weight of the aircraft, flown in combat, tends to be heavier than design gross weight, and this increases the mean loads. The alternating loads were less, however, because of reduced airspeed throughout the flight regime. Reference 1 suggests that these two factors are offsetting, resulting in only a small change from the fatigue life of the rotor which was calculated during blade design.

The analysis reported in Reference 1 is based on flight loads measured in Southeast Asia (SEA) by Technology Inc. during the period August 1968 to April 1969 under Contract DAAJ02-77-C-0076 for the Applied Technology Laboratory/USARTL. The reconstructed mission profile presented in Reference 2 is probably a good representation of flight operations of the AH-1G in SEA. It probably is more severe than that encountered in Continental United States (CONUS) operations. However, it cannot be stated with assurance that the aircraft which had the defective rotors were flown within the mission profile described in Reference 1. Although one cannot discount the possibility that each of these aircraft experienced a damaging load sufficient to fail the spar closure and initiate fretting, this is

considered unlikely. The number of flight hours on each aircraft falls in a relatively narrow range (659 to 867.4 hours), which is indicative of fretting fatigue starting on each blade at the same relative time. If the fretting fatigue was induced by an overload, one would not expect this load to occur at the same relative time in each aircraft.

It was concluded from the foregoing studies that:

(1) Cracked spars were caused by fretting fatigue of the spar and spar spacer in the bond line.

(2) There are three possible causes of failure on the bond sufficient to allow fretting; these are listed in decreasing order of probability below. Any combination of the factors is possible.

(a) Metal-to-metal contact occurs during manufacture because of the scraping of the adhesive upon the insertion of the spar spacer in the spar and/or cold flow of the adhesive under pressure created by the spring action of the spar on the spar spacer.

(b) Weak bonds are created during manufacture by an unfavorable combination of dimensions of the spar and spar spacer or inadequate treatment of the bonded surfaces.

(c) Blades experience overloads which cause debonds that eventually induce fretting fatigue conditions.

MODEL 540 NONDESTRUCTIVE INSPECTION CRITERIA

The Model 540 rotor system was designed using safe-life design procedures. Safe-life design requires that a service life in operational hours be established and that the component be removed from service at or before this elapsed time to reduce the probability of catastrophic failure to a very low level. The advent of the failures described in this paper requires that the safe life be drastically shortened because a fretting fatigue condition exists that was not considered in setting the current safe life of 1100 hours. Nondestructive inspection procedures had to be developed to detect spar-to-spacer debonds that are large enough to allow fretting fatigue of the spar and spar spacer.

Various inspection procedures were reviewed by AVRADCOM, the Navy, and Bell Helicopter Company. The Risk Assessment Team selected an ultrasonic technique for detecting disbond between the spar and spar spacer as the best overall technique for blade inspection.

FATIGUE LIFE DEVELOPMENT AND SUBSTANTIATION

To calculate a safe life for the blade, three things were required:

(1) The number of blades in the fleet susceptible to the fretting fatigue failure.

(2) The distribution of times to failure which would occur if all susceptible blades were flown until they failed by the fretting fatigue mode at the spar-to-spacer bond line.

(3) A criterion specifying the risk of failure that is acceptable.

The information that was available and the assumptions that had to be made for each of the above items are discussed below.

(1) Fleet Size - Based on teardown inspections of blades removed from service for reasons other than fretting fatigue failure, it was determined that not all blades in the fleet showed evidence of spar-to-spacer debond and associated fretting fatigue. From the results of these inspections, it was estimated that perhaps only 2500 of the 18,481 blades manufactured would develop the debond. Since the number of blades susceptible to the fretting fatigue failure mode was not known exactly, several population sizes were assumed in order to determine the sensitivity of the failure distribution parameter estimates to fleet size.

(2) Failure Distribution - As in practically all instances in which a safe life is to be calculated, the type of distribution was assumed and the parameters of the distribution were estimated from the information available. In this case, the times to failure were assumed to be lognormally distributed. Also, since the actual distribution of high flight time blades that had no fretting fatigue was unknown, several failure distributions were assumed. These assumed distributions are illustrated in Figure 4.

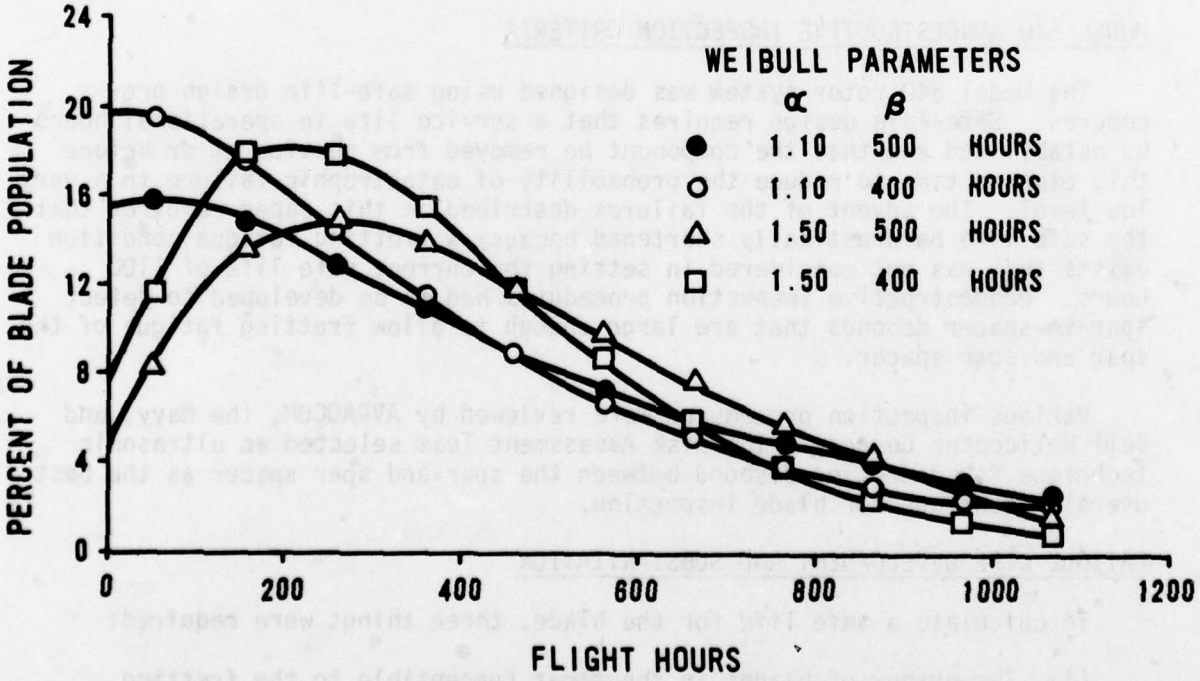


Figure 4. Assumed Population Distributions

The method used to estimate the failure distribution parameters is described in Reference 2. The results of applying this method yielded a safe life of 500 flight hours with a risk criterion of one failure on the average in a fleet twice as large as the one under consideration.

In order to confirm the foregoing, as well as to establish an inspection criterion and inspection interval for these blades, a fatigue test of three blades was conducted. The details of this fatigue test are given below.

TEST SPECIMENS

Three blades were selected for the test program; their conditions are presented in Table I.

TABLE I

TEST SPECIMEN CONDITION PRIOR TO TESTING

SER. NO.	DEBOND STATION	FLIGHT HOURS	BLADE TYPE
IHB-3057	100-112	105	540-011-250-1
IHB-3298	no debond	89	540-011-250-1
A2-2822	no debond	608	540-011-001-5

These test specimens were modified slightly for testing purposes. On a production blade, a lead weight is embedded near the blade tip to increase the local inertia. A 22-inch section from the tip, including the tip weight, was removed to accommodate the end fitting. Also, a laminated stepped aluminum doubler was installed by Bell Helicopter Company similar to the one used by Bell Helicopter Company in the original fatigue-life substantiation of the 540.

FATIGUE TESTING MACHINE

The Applied Technology Laboratory rotor blade fatigue test machine (see Figure 5) was used to fatigue test the specimens. This machine is approximately 44 feet (13.41 meter) long, 10 feet (3.04 meter) wide, 12 feet (3.67 meter) high, and it can accept specimens up to 25 feet (7.62 meter) long. Initially, it could apply only centrifugal force (C.F.) and bending loads; upon modification of the machine for this test, its load application capability was expanded to include torsional loads. The loads were applied on the specimen by two actuators, one located at each end of the test section of the machine.

By controlling the frequency of excitation, the blade-grip system was made to resonate near its first bending mode natural frequency. As the forcing frequency approached the blade-grip natural frequency, the blade's

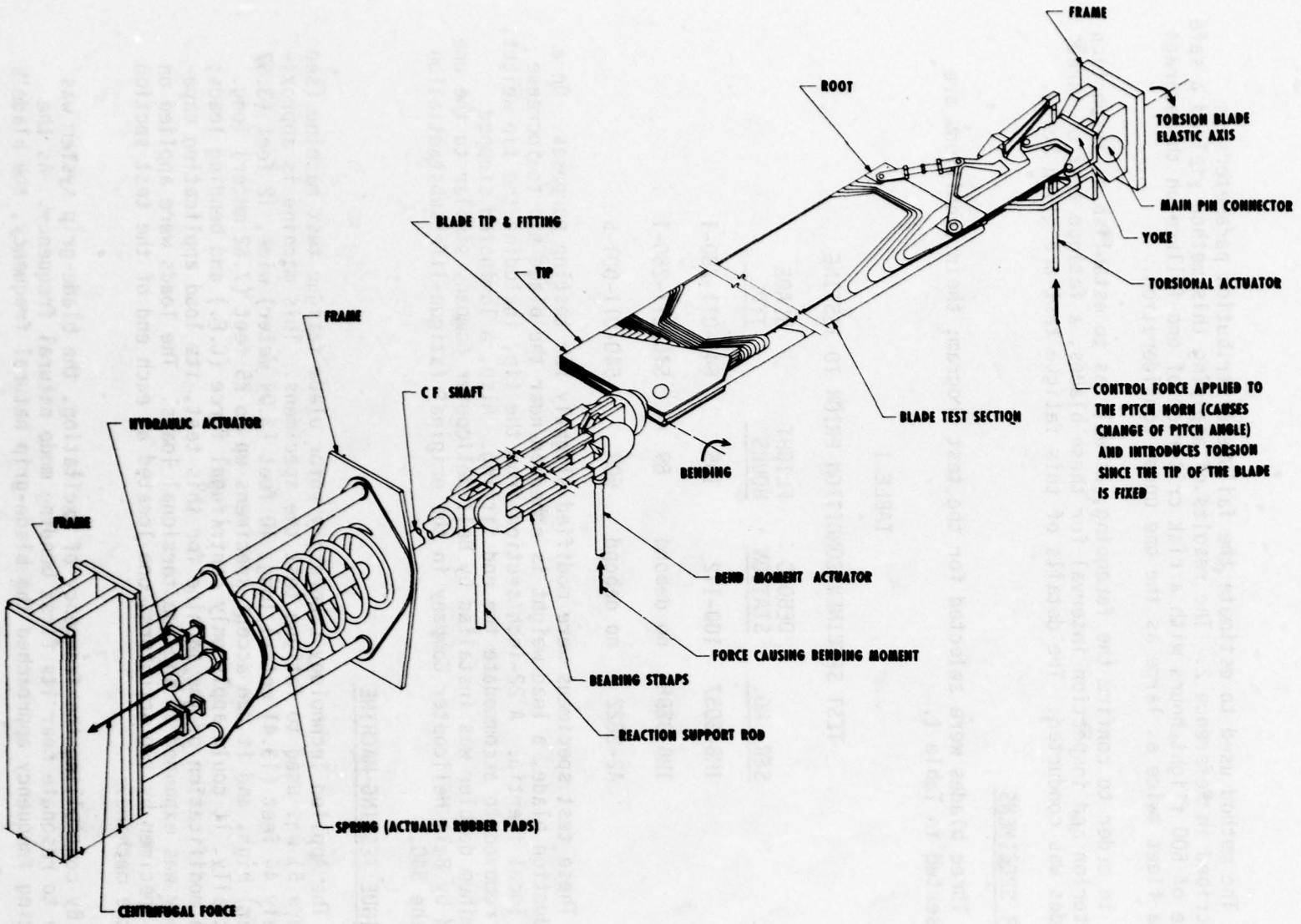


Figure 5. Schematic of Rotor Blade Test Machine

center span amplitude became larger. The beam bending moment was controlled in this fashion.

The loads used for the test were furnished by Bell Helicopter Company and were identical to the load spectrum used by Bell Helicopter Company in their original fatigue-life substantiation of the Model 540 blade. The in-plane loading (due to drag force) has a negligible effect on the spar spacer fatigue life of the blade and, therefore, was not applied.

The load spectrum and its rate of application was considered an important parameter in this test. Bell Helicopter Company provided flight load data which shows the interrelationship of the bending and torsional loads, as well as the wave shape of each. Figure 6 indicates the trace of loads applied during flight and during fatigue testing.

The load spectrum furnished by Bell Helicopter Company represented approximately one flight hour, and included 15 different load segments which encompassed the entire beam and torsion spectrum.

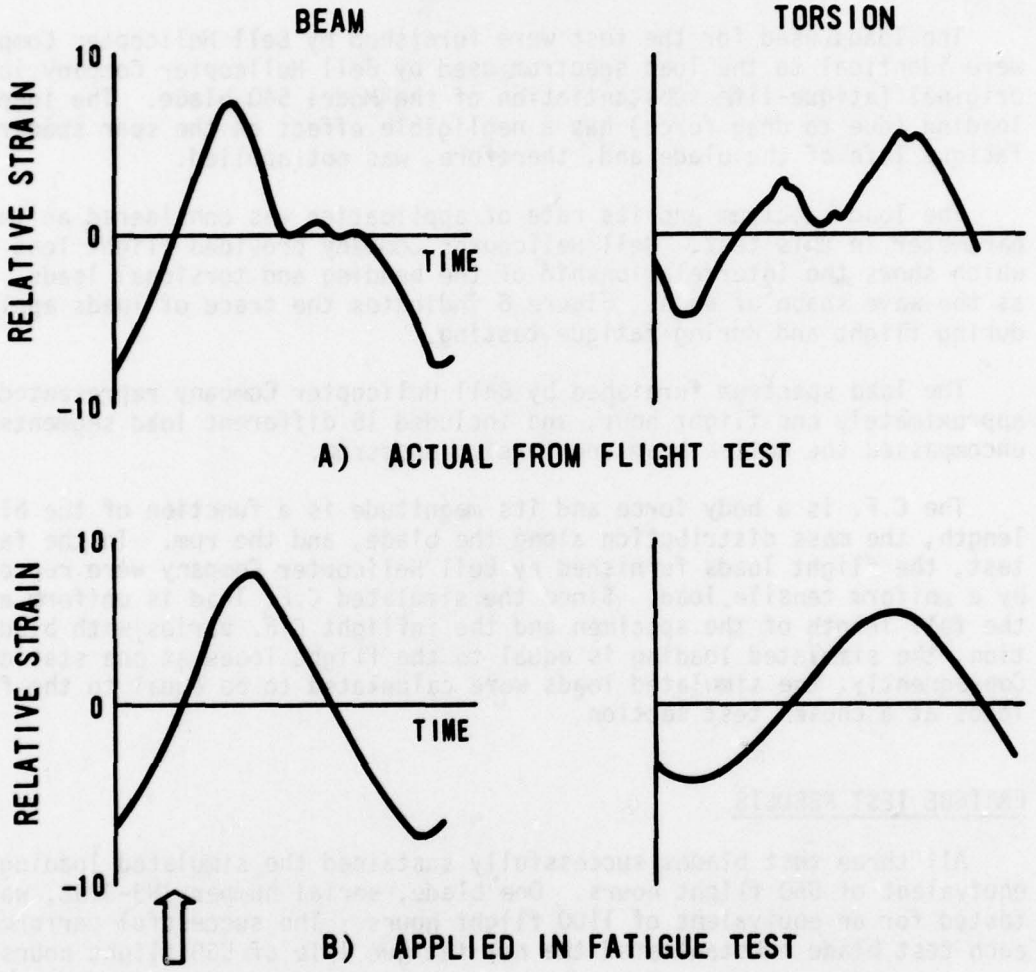
The C.F. is a body force and its magnitude is a function of the blade length, the mass distribution along the blade, and the rpm. In the fatigue test, the flight loads furnished by Bell Helicopter Company were represented by a uniform tensile load. Since the simulated C.F. load is uniform along the full length of the specimen and the inflight C.F. varies with blade station, the simulated loading is equal to the flight loads at one station only. Consequently, the simulated loads were calculated to be equal to the flight loads at a chosen test section.

FATIGUE TEST RESULTS

All three test blades successfully sustained the simulated loading for an equivalent of 550 flight hours. One blade, serial number IHB-3298, was tested for an equivalent of 1100 flight hours. The successful performance of each test blade substantiated the new fatigue life of 550 flight hours.

SUMMARY

The Risk Assessment Team, in a space of 11 months, established the cause of the Model 540 failure, recommended an inspection technique that was applied to the entire stockpile of Model 540 blades, calculated a new safe life, and substantiated this life by full-scale fatigue tests. These accomplishments required the combined skills and talent of many people throughout the Army, Navy, NASA, and Bell Helicopter Company, and dramatically illustrates the far-reaching consequences of structural deficiencies in operational aircraft.



NOTE:

540-011-250 MAIN ROTOR BLADE
1.0 V_H LEVEL FLIGHT @ 314 RPM
7100 LBS G.W. FWD. C.G. 3000 FT.

Figure 6. Comparison of Relative Strain that Occurs in Flight with that Which was Applied During the Fatigue Test for Beam and Torsion Loads for One Rotation of the Rotor

REFERENCES

1. Glass, Max E., et al., "AH-1G Design and Operational Flight Loads Study," USAAMRDL Technical Report 73-41, January 1974.

2. Stagg, A.M., "Parameter Estimation for the Log-Normal Parent Population of Fatigue Failures From a Sample Containing Both Failed and Non-Failed Members," Royal Aircraft Establishment Report 70145, August 1970.

PREMATURE FAILURES OF AIRCRAFT CARRIER CATAPULT "TENSION BARS" CAUSED BY ILL-CONCEIVED REDESIGN

THOMAS W. BUTLER
Professor
U. S. Naval Academy
Annapolis, Maryland 21402

ABSTRACT

A frangible hold back bar is used as part of a release mechanism for aircraft being catapulted from aircraft carriers. When this bar was redesigned to save machining costs, the redesigned bars were found to break prematurely in service with serious consequences. The only substantive difference between the old and new hold back bars (whose cross-sectional areas are equal) was an axial hole through the original bar. This paper outlines an analysis of the failures which demonstrated that the redesign did not take into account the reasons for the axial hole in the original hold back bar.

INTRODUCTION

Although landing aircraft on aircraft carriers is commonly thought of as a hazardous operation, the launching of aircraft from carriers has not been without its problems.

The common method used to launch aircraft from carrier decks uses a release mechanism to restrain the airplane from forward motion while the catapult and the aircraft engines are developing thrust. This paper discusses a problem which arose when a seemingly innocuous redesign was made of the frangible hold back bar which was used as the release mechanism. The problem arose because the redesign failed to take into account the reasons for certain features of the original design. The author of this paper became involved in the problem at the request of the Naval Air Systems Command after the new style hold back bars had been introduced into the fleet and premature failures of these bars had caused the loss of aircraft.

LAUNCHING OF AIRCRAFT FROM AIRCRAFT CARRIERS

In order to allow aircraft to be accelerated sufficiently for take-off from a carrier, catapults are used to assist the aircraft engines. Typically, the nose gear of the aircraft is connected by means of a launch bar to the shuttle of the catapult. While force in the catapult is being built up, the aircraft is held back from forward motion by the hold back or "tension bar". When the forces on the hold back bar reach the level necessary to break the bar, the bar fractures resulting in the aircraft being catapulted from the carrier deck.

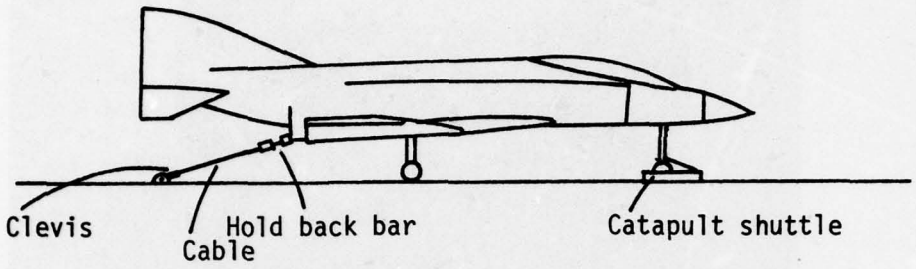


Figure 1 - Sketch of an airplane about to be catapulted from an aircraft carrier deck. Thrust due to engine and catapult causes hold back bar to break, releasing aircraft.

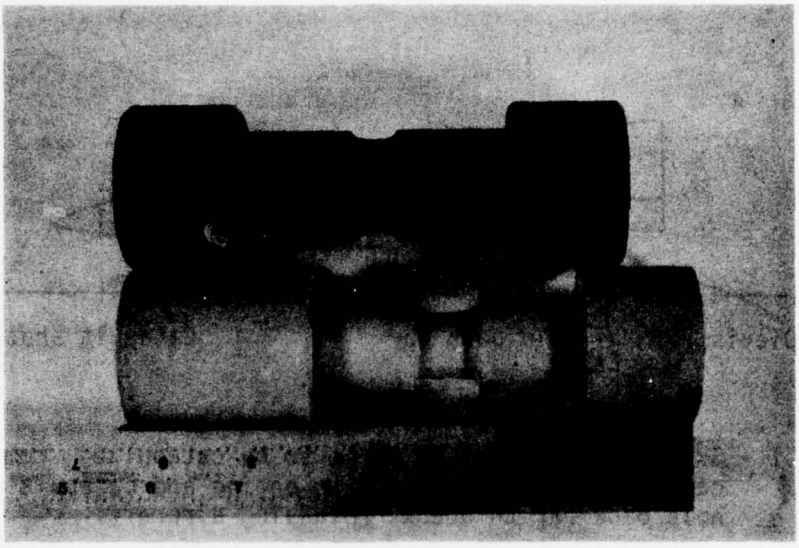
Figure 1 is a drawing of the arrangement used which was involved in the case discussed here. The cable shown allows for ease in attaching the hold back bar to the carrier deck.

ORIGINAL AND REDESIGNED HOLD BACK BARS

The specification for hold back bars, MIL-T-23426A(AS) - "MILITARY SPECIFICATION-TENSION BARS AIRCRAFT LAUNCHING," includes specifications for bars with breaking forces from 17,500 lb (78kN) to 75,000 lb (334 kN). The specified breaking force depends upon several variables including the type of aircraft being catapulted. Due cautions are emphasized in the specifications regarding the workmanship required when manufacturing the bars (section 3.8):

> The items covered by this specification are used in launching military aircraft from aircraft carrier and shore-based catapults. These items were designed with a minimum margin of safety and are subject to critical loading applications. Premature failure of any bar can easily result in loss of life and destruction of the aircraft and constitute a servicing impediment to fleet readiness.

a.



b.

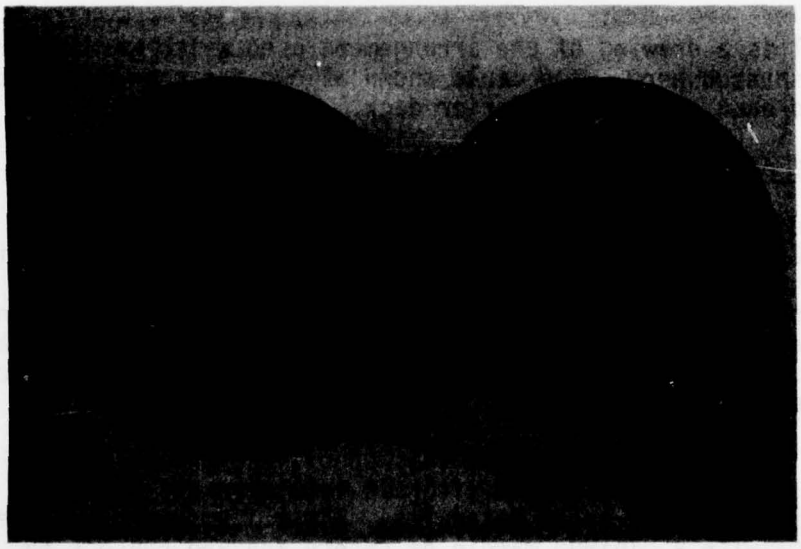


Figure 2 - Original and Redesigned Hold Back Bars. Original (hollow) hold back bar is darker colored bar. Note nominal maximum load of 63,000 lb (280 kN) stamped on end of each bar.

The original hold back bar is the darker colored bar shown in Figure 2. This hollow original bar has a minimum outside diameter in the reduced section of 1.000 in (25.4 mm) and an inside diameter of 0.661 in (16.8 mm). Stamped on the end of the bar is the nominal maximum load the bar can carry, 63,000 lb (280 kN), as well as other marks required by the specification. The minimum cross-section area of the original bar is 0.442 in^2 (285.2 mm^2); consequently, the nominal axial ultimate tensile stress is 142,500 psi (982.5MN/m^2).

In an attempt to save machining costs, a solid bar with the same cross-sectional area made of the same material was substituted as a replacement for the hollow bar. The diameter of the lighter colored, solid bar shown in Figure 2 is 0.750 in (19.1 mm) which gives it the same cross-sectional area as the hollow bar. The end of this bar is also stamped with the nominal maximum load of 63,000 lb (280 kN). Specifications call for breaking loads within 3 percent of the nominal maximum load.

Properties of the hollow and solid hold back bar cross-sections are shown in Table I.

TABLE I - Cross-Section Properties

	O.D., in (mm)	I.D., in (mm)	Area, in^2(mm^2)	J, in^4 (mm^4)
Hollow Bar	1.000 (25.4)	0.661 (16.8)	0.442 (285.2)	0.0794 (33 100)
Solid Bar	0.750 (19.1)	--------	0.442 (285.2)	0.0310 (12 900)

PROBLEMS ENCOUNTERED WITH SOLID HOLD BACK BARS

When solid hold back bars were substituted for the hollow bars which had been previously used, the solid bars reportedly broke before the catapult had developed enough force to enable aircraft to be successfully launched. Since both the hollow and solid bars were designed to break at 63,000 lb, it was thought that the solid bars were "faulty". Consequently, the use of the original hollow bars was resumed until the cause of the problem could be determined. Unfortunately, none of the bars which failed prematurely were recovered. An investigation could uncover no flaws in the solid hold back bars; bars from the same lot broke well within specifications in laboratory tension tests.

ANALYSIS OF FAILURE

When the present author was presented with this problem, it was made clear to him that no metallurgical problems had been found. He was told that one theory which showed some promise of explaining the premature failures involved the differences in the peak stresses caused by stress wave propagation in the hollow and solid bars due to geometry differences during the relatively rapid build-up of force in the bars. Another more basic factor was actually found to be the reason for the premature

failures experienced when the solid bars were used.

Since the solid hold back bars broke well within specifications in laboratory tension tests, attention was then focused on the type of loading experienced by the "tension bars". When a hold back bar is pulled in tension by a cable in series with it, the twisted strands making up the cable tend to untwist. The cable used aboard the carrier was not special non-spinning hoisting cable.

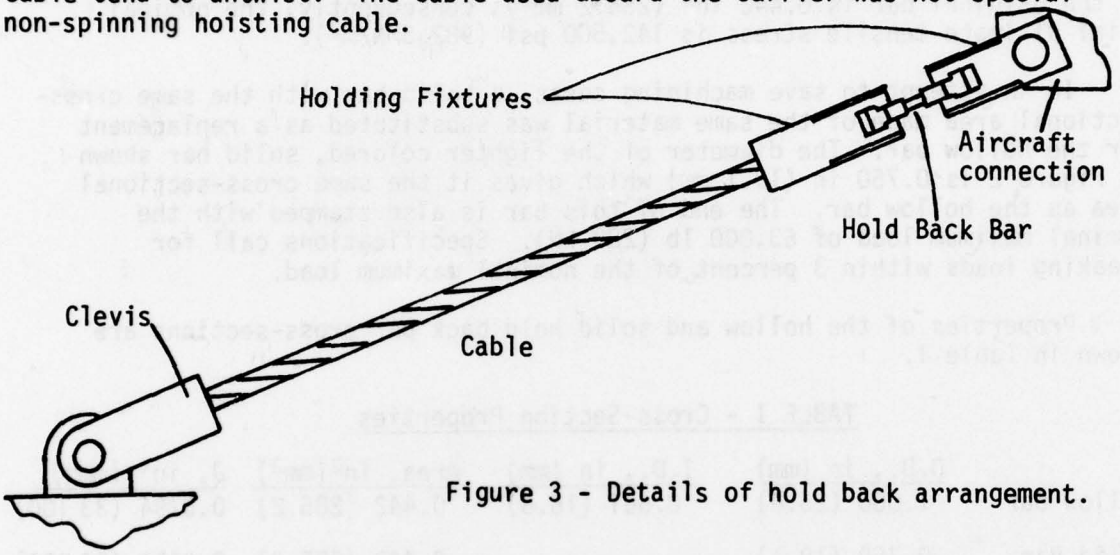


Figure 3 - Details of hold back arrangement.

Figure 3 shows the cable arrangement in some detail. The clevis end of the cable is restrained so that it cannot rotate. Similarly, the holding fixture attached to the aircraft cannot rotate. Since neither end can rotate and friction keeps the hold back bar from rotating in the fixtures, a torque is induced in the hold back bar by the untwisting cable. This torque exists whether the bar being loaded is hollow or solid. However, the shear stress due to torque applied to a shaft is inversely proportional to the polar moment of inertia, J, of the cross-section and directly proportional to the distance from the shaft's axis, ρ. If a hollow tube and a solid bar of the same cross-sectional area are loaded in torsion with the same applied torque, the hollow tube will have a smaller maximum shear stress since it has a larger J/ρ ratio. This combined stress state with a larger shear stress would then in principle cause the solid bar to break at a lower axial load.

To determine the magnitudes of the stresses involved to see if the untwisting of the cable introduces a significant effect, a simple stress analysis using electrical resistance strain gages was performed. A cable was used in these tests which is identical with those on the aircraft carriers involved. Two rectangular, three-gage, 45° strain gage rosettes were mounted on opposite sides of the reduced area section of a solid hold back bar and wired in series.

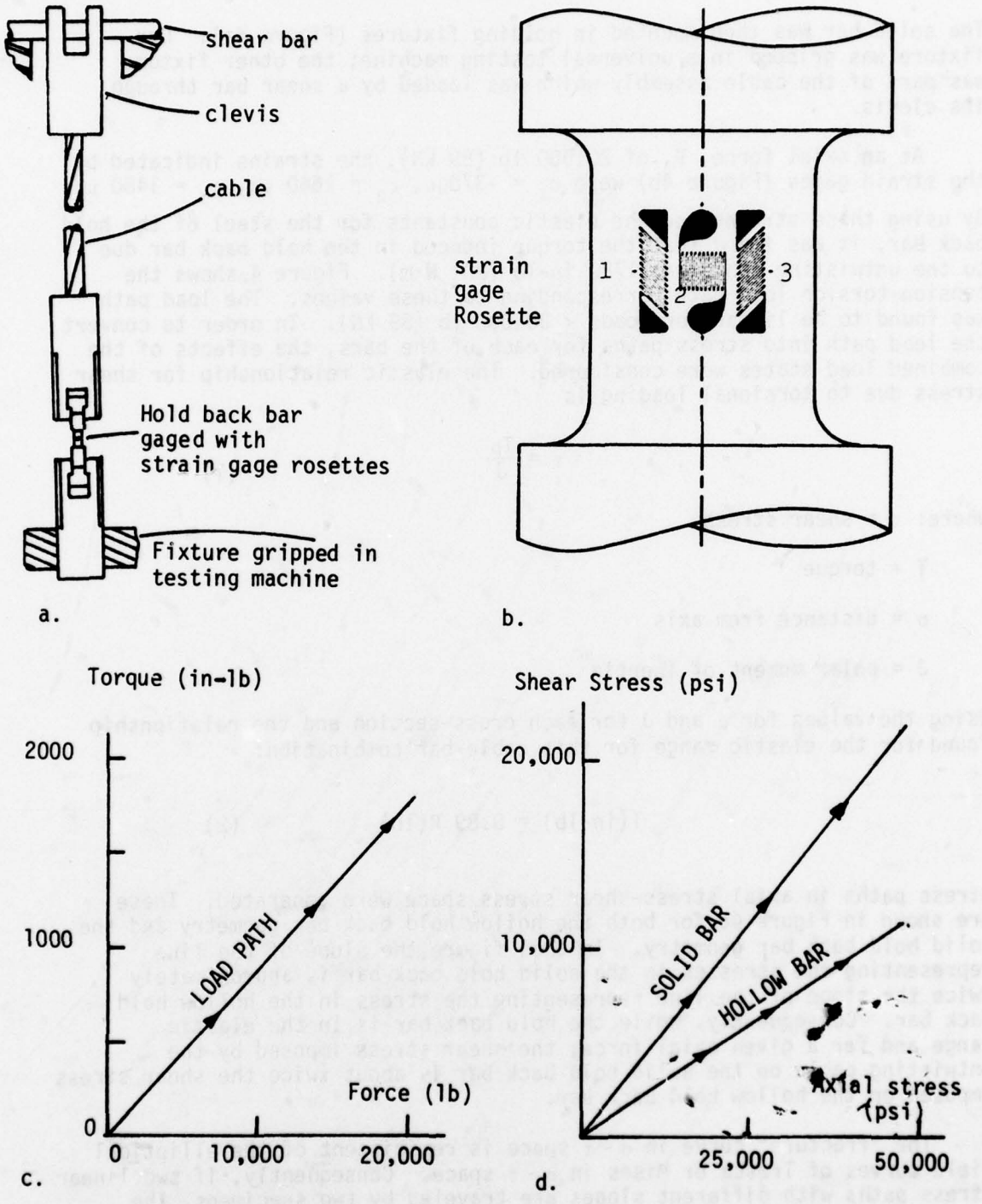


Figure 4 - Stress Analysis Figures

The solid bar was then mounted in holding fixtures (Figure 4a). One fixture was gripped in a universal testing machine; the other fixture was part of the cable assembly which was loaded by a shear bar through its clevis.

At an axial force, P, of 20,000 lb (89 kN), the strains indicated by the strain gages (Figure 4b) were $\varepsilon_1 = -370\mu\varepsilon$, $\varepsilon_2 = 1640\ \mu\varepsilon$, $\varepsilon_3 = 1480\ \mu\varepsilon$. By using these strains and the elastic constants for the steel of the hold back bar, it was found that the torque induced in the hold back bar due to the untwisting cable was 1780 in-lb (201 N·m). Figure 4 shows the tension-torsion load path corresponding to these values. The load path was found to be linear for loads $\leq$ 20,000 lb (89 kN). In order to convert the load path into stress paths for each of the bars, the effects of the combined load states were considered. The elastic relationship for shear stress due to torsional loading is

$$\tau = \frac{T\rho}{J} \qquad (1)$$

where: τ = shear stress

T = torque

ρ = distance from axis

J = polar moment of inertia

Using the values for ρ and J for each cross-section and the relationship found for the elastic range for this cable-bar combination:

$$T(\text{in-lb}) = 0.89\ P(\text{lb}) \qquad (2)$$

stress paths in axial stress-shear stress space were generated. These are shown in Figure 4d for both the hollow hold back bar geometry and the solid hold back bar geometry. In this figure the slope of the line representing the stresses in the solid hold back bar is approximately twice the slope of the line representing the stress in the hollow hold back bar. Consequently, while the hold back bar is in the elastic range and for a given axial force, the shear stress imposed by the untwisting cable on the solid hold back bar is about twice the shear stress imposed on the hollow hold back bar.

The "fracture" curve in $\sigma - \tau$ space is reminiscent of the elliptical yield curves of Tresca or Mises in $\sigma - \tau$ space. Consequently, if two linear stress paths with different slopes are traveled by two specimens, the specimen loaded along the stress path with the steeper slope will fracture at a lower axial load than will the other. The solid hold back bar was

pulled to fracture with a cable in series and instead of fracture occuring at 63,000 lb (280 kN), the bar fractured at 54,400 lb (242 kN), 13.7% less than the 63,000 lb figure.

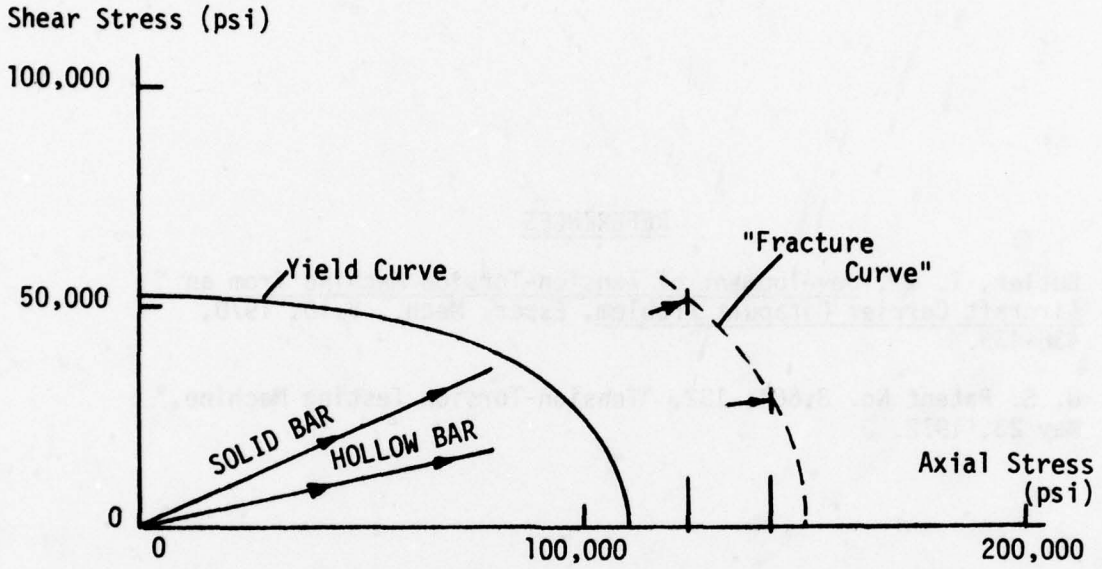


Figure 5 - Schematic description of effect of increased shear stress on axial load at fracture

Figure 5 shows that, because of the shape of the fracture curve, the axial fracture load reduction due to a solid bar as opposed to a hollow bar of the same cross-sectional area is much larger than might be expected.

LESSON TO BE LEARNED

It is clear that the hollow bar was chosen by the designer of the original hold back bar because he apparently knew what effect the untwisting cable has on the stress state. However, when the solid bar was allowed to be substituted, the effects of the cable had apparently been forgotten or perhaps not known by the "redesigner". It also may be that the title of the military specification "TENSION BARS AIRCRAFT LAUNCHING" and the commonly used name "tension bar" mislead the redesigner. It is clear that in this case bars loaded in series with a standard cable experience a significant torque as well as tension.

The obvious lesson to be learned from this analysis of these premature hold back bar failures if that before a redesign is implemented, the reasons for original design features must be understood. Subsequent to the problems involved with the cable-hold back bar system, an entirely

new system which utilizes no cable was developed and is now in use. The author, realizing that testing machines which generate combined states of stress are of use in materials testing, designed and built a simple tension-torsion testing machine utilizing an "untwisting" cable (1, 2).

REFERENCES

1. Butler, T. W., Development of Tension-Torsion Machine from an Aircraft Carrier Catapult Problem, Exper. Mech., V.10, 1970, 438-439.

2. U. S. Patent No. 3,664, 182, "Tension-Torsion Testing Machine," May 23, 1972.

SESSION IIc: AIRCRAFT

Chairman: R. Foye
Aerospace Technologist
Army Research and Technology Laboratory

IMPACT DAMAGE TOLERANCE OF GRAPHITE/EPOXY LAMINATES 155

N. M. Bhatia
Northrop Corporation

REPRODUCIBILITY OF STRUCTURAL STRENGTH AND STIFFNESS FOR GRAPHITE-EPOXY AIRCRAFT SPOILERS 167

W. E. Howell
NASA-Langley Research Center, and
C. D. Reese
University of Kansas

DAMAGE TOLERANCE OF LIGHTWEIGHT AIRCRAFT STRUCTURE 188

D. F. Haskell
Army Armament R&D Command

IMPACT DAMAGE TOLERANCE OF GRAPHITE/EPOXY LAMINATES

N.M. BHATIA
Engineering Specialist
Northrop Corporation
Aircraft Group
Hawthorne, CA 90250

ABSTRACT

In this paper, the results of an experimental program to evaluate impact damage susceptibility and residual strength capability of graphite/epoxy structures are presented. Monolithic and sandwich all-graphite laminates and hybrid laminates of graphite-glass and graphite-Kevlar were evaluated. It is shown that graphite composites are readily damaged and lose significant strength capability even at low impact energies. It is also shown that damage resistance of graphite composites can be improved by increasing laminate thickness or by using graphite-glass hybrid laminates. Design procedures for impact damage tolerant structures are developed. Finally, a case study is described involving the application of these design procedures to an advanced aircraft wing/fuselage structure.

INTRODUCTION

The ability to resist impact damage is an important design consideration for military aircraft structures. Impact damage can occur during ground handling, landing, take-off, and in flight due to foreign object damage (FOD). Extensive data on FOD incidents obtained during the last several years have indicated the severity of this problem on aircraft structures. Since applications of advanced composite materials are currently undergoing a transition from secondary to increasing use on primary, that is, safety-critical components, impact damage susceptibility of advanced composites is receiving increasing attention. Furthermore, graphite/epoxy, which is a widely used advanced composite material because of its high strength and stiffness properties, is more susceptible to impact damage than conventional metal structures, because it is relatively more brittle. Therefore, characterization of impact damage resistance of graphite structures has become of immediate concern.

Many aspects of impact damage are continuing to be investigated and reported in the literature. The objective of this program was to evaluate the damage susceptibility and residual strength capability of graphite/epoxy aircraft structural components and to develop design guidelines for improved impact damage resistant structures. The parameters considered in the test program were: all-graphite and hybrid laminates with E-glass and Kevlar-49, laminate thickness and orientation, nonsandwich and sandwich construction, damage modes and strength, and impact energy levels. Impact damage may be caused by hard objects (e.g., tool drops and runway rocks) and soft objects (e.g., bird impacts that occur at low altitudes during landing and takeoff). In the present investigation, only hard object impacts that generally cause localized damge to structural components are considered.

PRECEDING PAGE BLANK-NOT FILMED

IMPACT DAMAGE SUSCEPTIBILITY

The low-velocity hard-object impact to graphite composites can cause laminate damage including surface denting, ply delamination, matrix cracking, and fiber failures spreading out from the impact point. In the present study, the impact damage susceptibilities of monolithic and sandwich AS/3501-5 graphite/epoxy laminates and hybrid laminates of graphite with E-glass and Kevlar-49 were evaluated. All laminates were fabricated of $\pi/4$ orientation. Impact tests were conducted on 9-inch by 6-inch panels using the impact device shown in Figure 1. The specimens were supported on the cylindrical base of the impact device and impact damage was caused by dropping a 4.0-pound steel bar on the flat end of the impactor shown in the figure. The steel bar was guided in a graduated cylindrical tube and dropped from selected heights to provide the desired impact energy.

Each panel was impact-damaged at 16 locations using eight impact energy levels that were selected from initial screening tests. The damage levels varied from no visible failures to significant fiber failure. The typical impact-damaged panel and its C-scan record are shown in Figure 2. Typically, the back faces of the panels showed considerably more damage than the front faces. Also, for the lowest impact energy levels when the front and back faces showed no visible surface damage, the C-scan records indicated some internal damage. The impact-damaged sandwich panel with the adhesively bonded honeycomb core is shown in Figure 3. The photomicrographs of the damaged cross-sections show significant localized core crushing adjacent to the

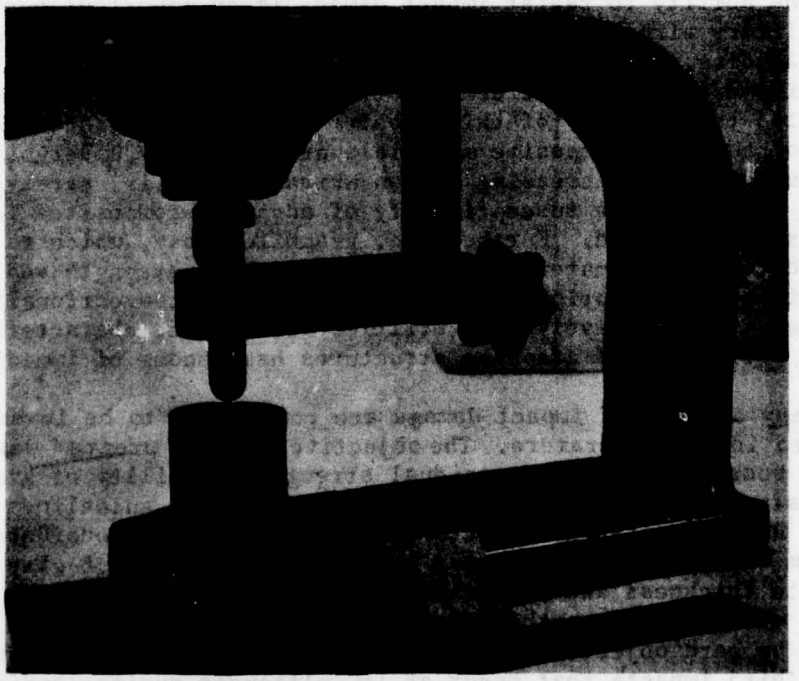
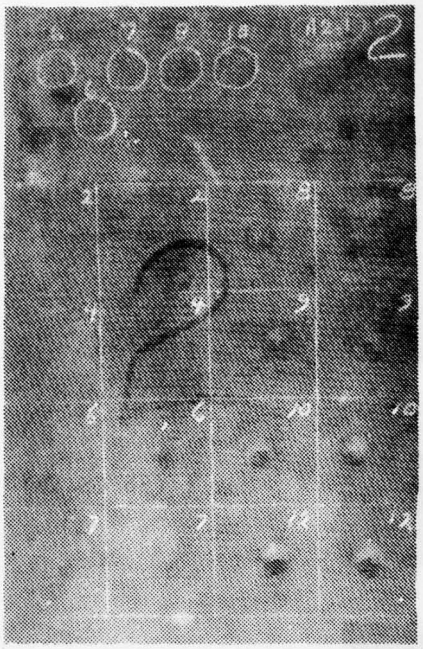
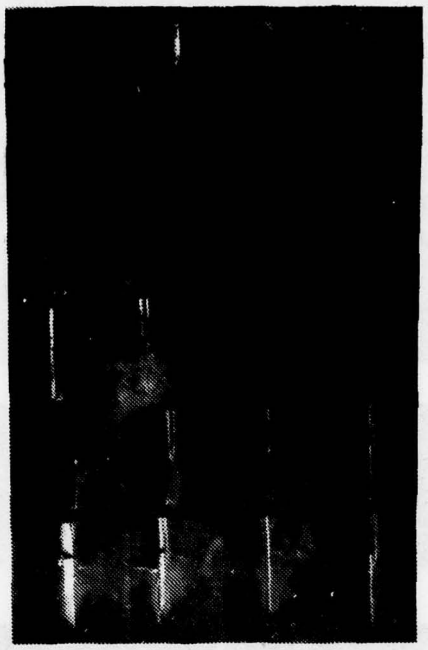


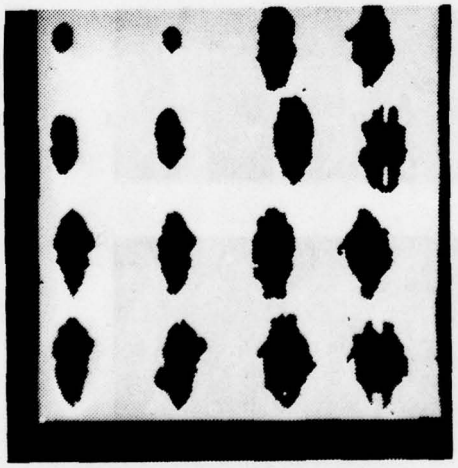
Figure 1. Impact Test Device



(a) Front Face



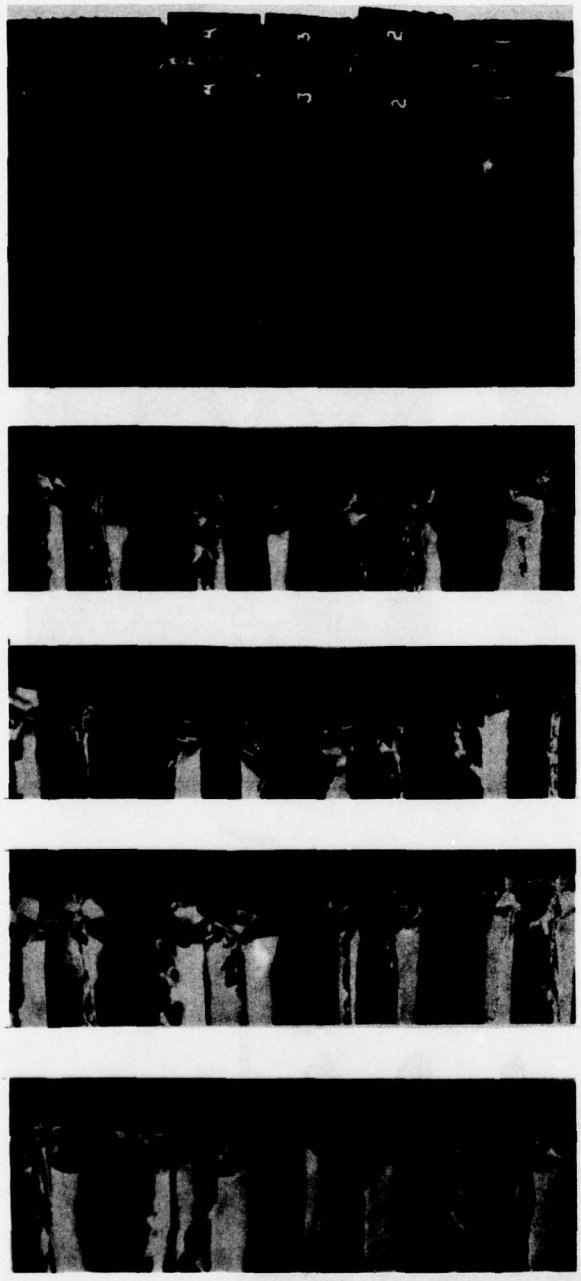
(b) Back Face



(c) C-Scan

AS/3501-5 (RTD), 8-ply $(0/90/\pm45)_s$ Laminate

Figure 2. Impact-Damaged Graphite/Epoxy Panel



AS/3501-5 (RTD), 8-ply $(0/90/\pm45)_s$ Laminate, FM-123 Adhesive
Core: 4.5 pcf, 1/8-5056-0.001, 0.625 inch thick

Figure 3. Impact-Damaged Graphite/Epoxy Sandwich Panel

skins and interlaminar failure of the skin. The adhesive layer remained attached to the core. For the test panels, the observed levels of surface damage and C-scan records were used to establish damage levels and damage size versus impact energy relationships. The detailed results are documented in Reference 1. In this paper, those results are used to establish design curves for laminate thickness versus impact energy for visual threshold of fiber failure and are presented on a log-log plot in Figure 4. These curves show that the impact energy required to cause a visual threshold level of damage increases with laminate thickness; furthermore, that generally, it is not a linear function of thickness. The figure also shows that graphite-glass hybrids with glass plies on the back face provide the best damage resistance capability.

The curves presented in the figure may be used to establish the minimum skin thicknesses required to achieve impact damage tolerant designs for specified impact energy levels. To demonstrate the use of these curves, consider a composite structure that is subjected to a potential threat of 48 in-lbs impact energy (based on a 4-foot drop of a one-pound tool, or a 200-ft/sec impact of a 0.5-inch diameter rock with a density of 0.1 lb/in^3). To prevent the occurrence of fiber failures at this impact energy, the minimum skin thicknesses determined from Figure 4 are 0.110 inch for the graphite laminate, 0.082 inch for the graphite sandwich laminate, and 0.058 inch for the graphite-glass hybrid laminates. These results show that for structural applications requiring thin skin laminates where durability requirements dictate laminate thickness, the use of graphite-glass hybrids can result in significant weight savings.

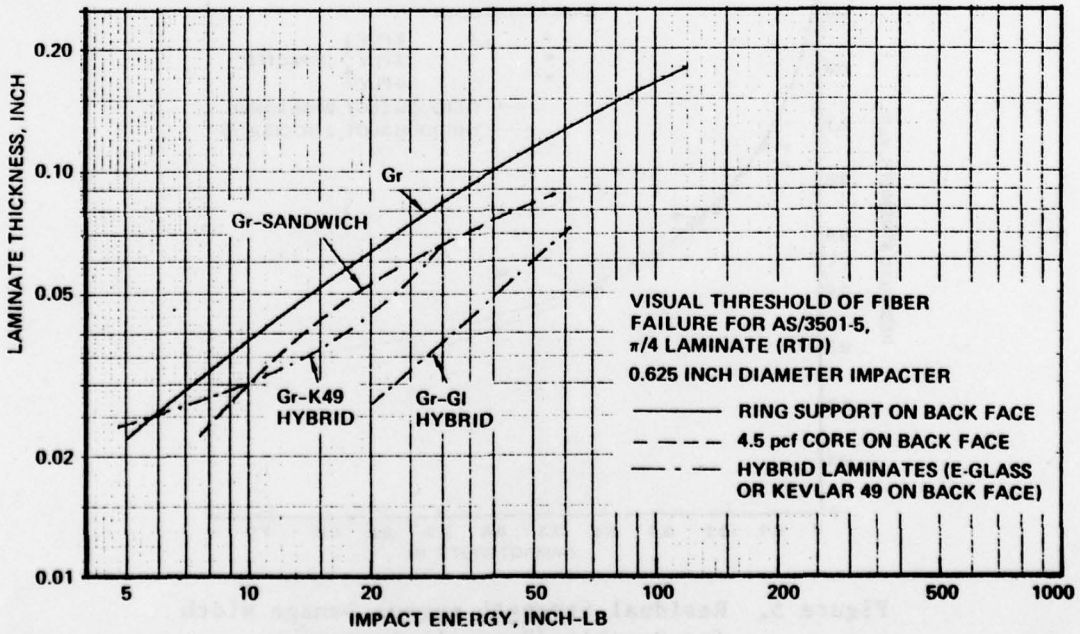


Figure 4. Laminate Thickness versus Impact Energy for Graphite/Epoxy Laminates

RESIDUAL STRENGTH OF IMPACT-DAMAGED LAMINATES

Strength reduction caused by impact damage is also an important design comsideration to satisfy the safety-of-flight requirements for aircraft structures. To evaluate residual tensile strength capability of impact-damaged laminates, 2 inches by 8 inches, coupons of AS/3501-5 graphite/epoxy and hybrid laminates of graphite-glass and graphite-Kevlar were tested. Specimens were impact-tested with back faces supported with aluminum honeycomb core to simulate sandwich skins. A group of impact-damaged specimens was static tested to failure and a second group with identical impact damages was subjected to two lifetimes of tension-dominated fatigue exposure before static testing to failure. For the fatigue test specimens, the impact-damaged areas were measured before and after fatigue on the laminate front and back faces and from C-scan records. This was done to measure possible growth of the damaged areas caused by fatigue exposure.

Test results for residual strength versus flaw size are presented graphically in Figure 5, and results for residual strength versus impact energy in Figure 6. These results show that graphite composites undergo significant strength loss even at very low impact energies when the front surface shows no damage. The fatigued specimen data are not separately shown

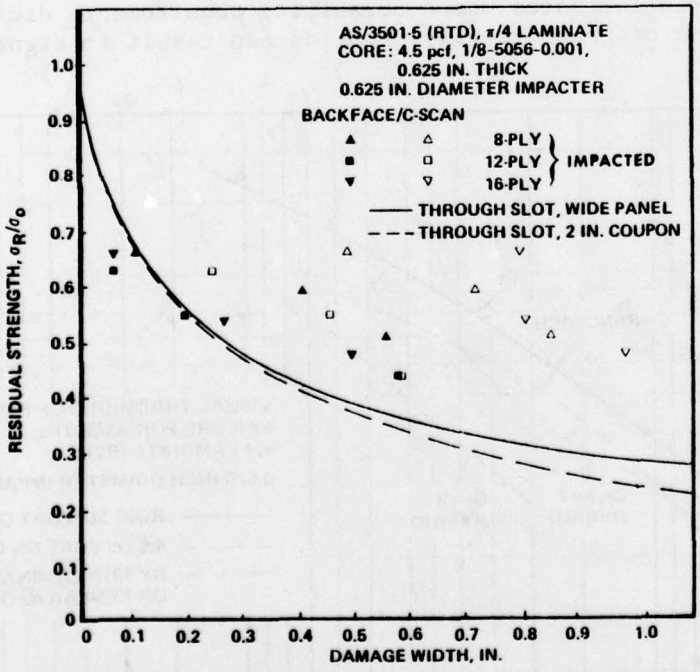
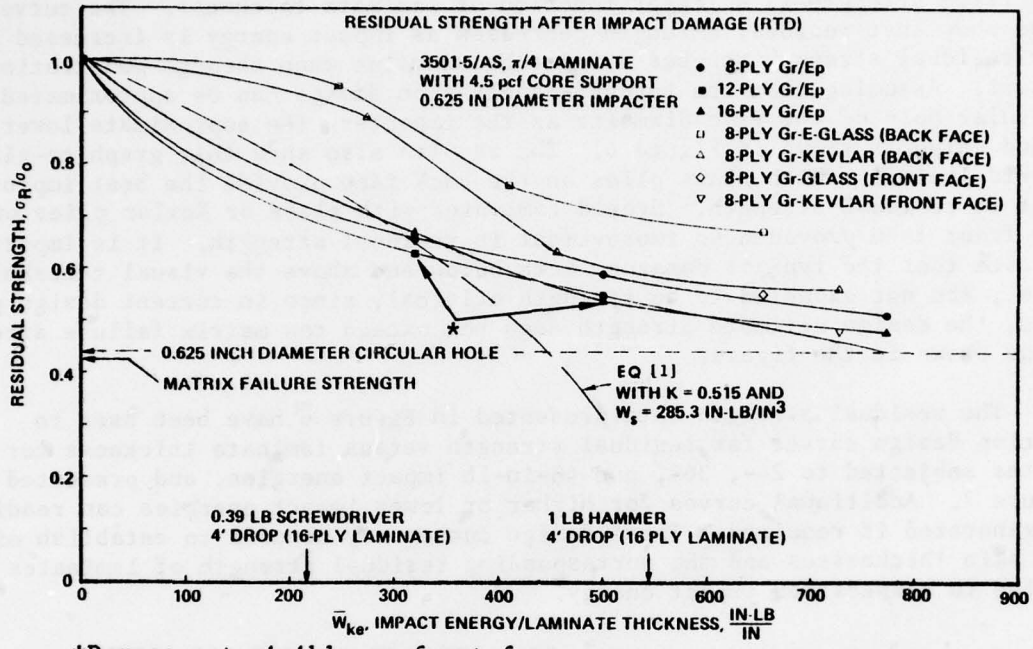


Figure 5. Residual Strength versus Damage Width for Graphite/Epoxy Laminates



*Damage not visible on front face.

Figure 6. Residual Tensile Strength of Impact-Damaged Graphite Composite Laminates

since the residual strengths were nearly identical to those of the unfatigued specimens. Also, the measured damage size did not appear to grow during fatigue exposure. The present results, showing that fatigue exposure does not further degrade the residual strength of impact-damaged laminates, is significantly different from previous results reported by Verette and Labor[2] for identical tests on nonsandwich laminates. In those results, further strength loss due to fatigue exposure was noted indicating possible growth of the damaged area due to fatigue exposure. This important difference in the impact behavior of nonsandwich and sandwich laminates needs further investigation.

In Figure 5, the residual strength of the π/4 laminate with a through-slot is also presented. Comparison shows that for damage sizes larger than 0.25 inch, the impact damage is not as severe as a through-slot in reducing laminate strength. This difference is due to the fact that for impact damages, the crack length varies through the laminate thickness and is generally largest on the back face. The C-scan observations show larger damage sizes because this method detects fiber failures, as well as ply delaminations which typically cover a larger area.

The residual tensile strength data plotted as functions of impact energy per laminate thickness in Figure 6, provide the following characteristics of impact-damaged laminates. For the all-graphite laminates of three laminate thicknesses, residual strength curves are nearly coincident. This indicates that at least for the range of the considered thickness, impact energy for a

specified strength is a linear function of laminate thickness. The curves also show that residual strength decreases as impact energy is increased and the residual strength reaches a lower bound value when through-penetration occurs. Assuming that the through-penetration damage can be approximated by a circular hole of the same diameter as the impacter, the approximate lower bound value is shown in Figure 6. The results also show that graphite-glass hybrid laminates with glass plies on the back face provide the best improvement in residual strength. Hybrid laminates with glass or Kevlar plies on the front face provided no improvement in residual strength. It is important to note that the typical damages, both below and above the visual threshold level, are not expected to be strength critical, since in current design practice, the design ultimate strength does not exceed the matrix failure strength value shown in the figure.

The residual strength data presented in Figure 6 have been used to develop design curves for residual strength versus laminate thickness for laminates subjected to 24-, 36-, and 48-in-lb impact energies, and presented in Figure 7. Additional curves for higher or lower impact energies can readily be generated if required. These design curves may be used to establish minimum skin thicknesses and the corresponding residual strength of laminates subjected to a specified impact energy.

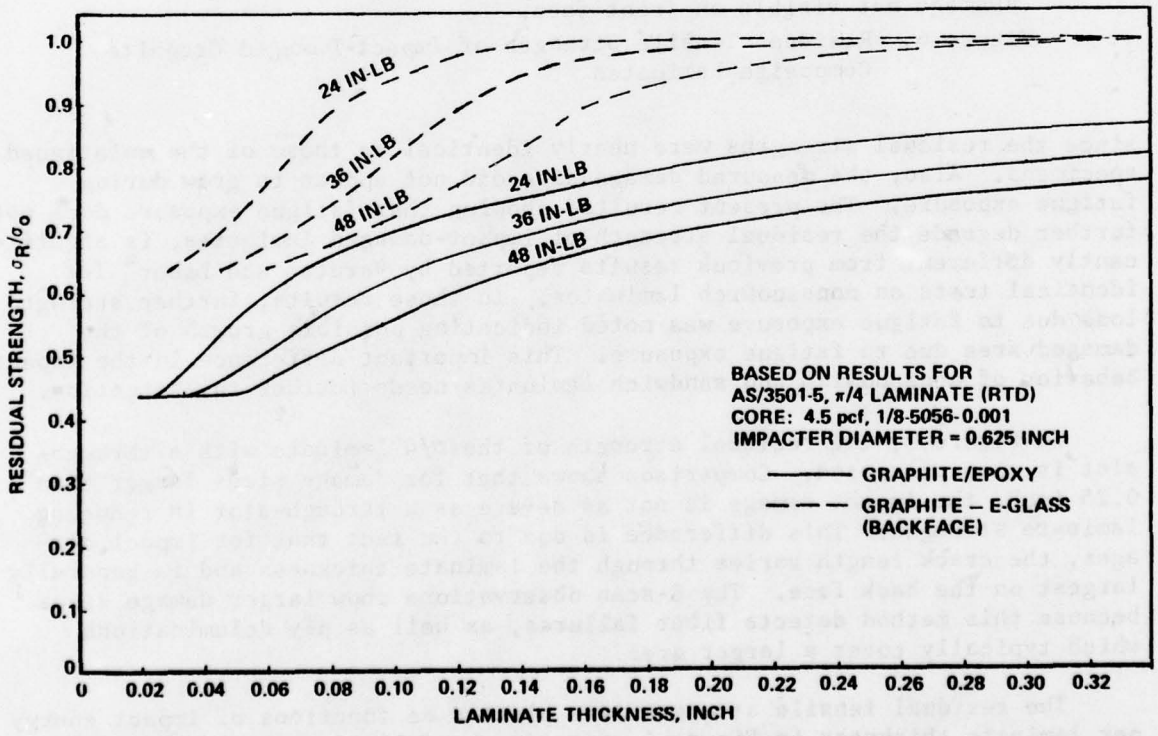


Figure 7. Residual Strength versus Laminate Thickness after Impact Damage

COMPARISON OF STRENGTH DATA WITH ANALYTICAL PREDICTIONS

Numerous analytical approaches have been described in the literature for predicting residual strength of impact-damage laminates. Two approaches that are based on linear elastic fracture mechanics consideration of an idealized through-crack simulating the impact-damaged area, are evaluated for applicability to the present experimental data. For predicting residual strength from the size of the damaged area, Awerbuch and Hahn[3] considered an idealized through-slot to represent impact damage. However, for graphite/epoxy laminates with through-slots and impact damages, the strength versus damage size data presented in Figure 5 show poor correlation. Therefore, using an idealized through-slot to predict the residual strength of impact-damaged laminates would, at best, provide a crude approximation of residual strength. An improved analytical model needs to be developed that could account for through-the-thickness variation of damage size.

An analytical model for predicting residual strength as a function of impact energy was developed by Husman, Whitney, and Halpin.[4] In this approach, an analogy was considered between damage inflicted by a single-point, hard particle impact, and damage caused by a through-crack of known dimensions in a static tensile coupon. The analytical model was represented by the following equation

$$\frac{\sigma_R}{\sigma_o} = \sqrt{\frac{W_s - K\bar{W}_{ke}}{W_s}} \qquad (1)$$

where

- σ_R is the residual strength
- σ_o is the unflawed laminate strength
- W_s is the strain energy required to break the unflawed laminate under static load ($= \sigma_o^2/2E_L$ for linear stress-strain response).
- $\bar{W}_{ke}$ is the impact energy per unit laminate thickness imparted to the specimen
- K is the effective damage constant determined by fitting the test data to the theory at one value of impact energy.

Good correlation was shown between the predicted and test results for residual strength as a function of impact energy for relatively low impact energies that caused much less than through-penetration damage. For the present test data, the predicted residual strength curve based on Equation (1) is shown in Figure 6. The values of W_s and K were calculated using the undamaged and damaged laminate strength data. For the undamaged all-graphite $\pi/4$ laminates, the average strength and modulus values were

$$\sigma_{avg} = 63.1 \text{ ksi}$$

and

$$E_L = 6.98 \times 10^6 \text{ psi}$$

Therefore, $W_s = \sigma_o^2/2E_L = 285.3$ in-lb/in^3. The value of K, calculated using one data point in Figure 6 is

$$K = 0.515 \text{ in}^{-2}$$

Comparison of the predicted strength curve with test data shows that the analytical model is not valid for relatively large impact energies that are still well below the through-penetration energy. The current data did not go to impact energies low enough to provide a comparison with the predicted strength.

DESIGN OF IMPACT DAMAGE TOLERANT STRUCTURES

The results presented above have demonstrated that graphite composites are susceptible to impact damage by hard objects. The extent of impact damage can vary considerably from barely visible skin dents to extensive indentation and skin punctures. The extent of damage depends on the geometry of the aircraft structure and the size, shape, and velocity of the impacting object. During the service life of the aircraft, impact damages that exceed a specified size and depth must be repaired. The objectives of a damage-resistant design, that satisfies the durability and safety-of-flight requirments imposed on aircraft structures, are to minimize the need for repeated repair of damage resulting from the most frequently occurring impacts, and to prevent the occurrence of catastrophic failures.

To evaluate the potential for impact damage, the ground servicing requirements for a specific aircraft system may be investigated to establish the probability of occurrence and the severity of the impact threat for specific areas of the aircraft. In the absence of specific criteria, or extensive service experience, judgments may be made to define low, medium, or high probability threats. For example, the low probability threat may be assumed to occur once per lifetime per aircraft. The medium probability threats may be assumed to occur up to 10 times per lifetime per aircraft. The high probability threats may be assumed to result from the most frequent ground servicing, which occurs for each flight. These may involve refueling, ground electrical and hydraulic power connections, servicing of the oxygen system, ammunition replacement, etc.

This approach was used to assess the potential for impact damage to the wing/fuselage components being analyzed at Northrop under the Air Force contract "Wing/Fuselage Critical Component Development Program."[5] The aircraft surfaces were zoned on the basis of the potential for impact damage by the

various types of threats. Since specific criteria based on service experience were not available, threats were defined using engineering judgment. Each threat was assigned a maximum potential impact energy value. For example, in the equipment service areas of the wing upper surface, these ranged from a 4-ft-lb medium probability threat from dropped hand tools to a 50-ft-lb low probability threat from installation or removal of fuel pump or hydraulic motor and gear box. For the 4-ft-lb threat, the minimum skin thickness determined from Figure 4 for the all-graphite laminate is 0.11 inch. Since the design thicknesses in this area ranged from 0.16 inch to 0.224 inch, the 4-ft-lb impacts will not cause fiber failures requiring repairs. Furthermore, Figure 6 shows that the 4-ft-lb impact is not going to be strength critical because the design ultimate stress does not exceed the matrix failure strength value shown in the figure. The 50-ft-lb impact is expected to cause significant fiber failures of the impacted area. However, since this may occur possibly once per service life of the aircraft, it is more economical to repair or replace the damaged component instead of designing it to be impact damage tolerant for this potential threat.

CONCLUSIONS AND RECOMMENDATIONS

Results presented above have demonstrated that relatively thin graphite/epoxy laminates are susceptible to foreign object damage even at low impact energies. Damage occurs in the form of matrix and fiber failures and the damaged panels undergo a significant tensile strength degradation. Therefore, composite structures that are exposed to foreign object impacts should be designed to resist damage and strength degradation. The significant conclusions and recommendations of this investigation are:

1. Impact damage resistance of laminated composites increases with thickness.

2. Back faces of graphite laminates generally undergo more severe damage than the front faces.

3. The use of honeycomb core provides some improvement in damage resistance of face sheets, however, core crushing and disbonding are additional damage modes encountered.

4. The use of E-glass plies on the back faces of graphite laminates provides significantly improved resistance to impact damage.

5. Residual tensile strength of impact-damaged specimens decreases as the size of the damaged area increases, which in turn, increases with impact energy levels.

6. Visual inspection indicates only the size and extent of surface damage, whereas, C-scan inspection indicates the overall size of the damaged area.

7. For sandwich panel skins, fatigue loading does not appear to increase the size of the damaged area and does not appear to reduce residual static tensile strength of damaged laminates. This differs from previous results, which showed that for nonsandwich laminates, fatigue loading reduces residual static tensile strength of damaged laminates.

8. Typical ground handling impact damage that goes undetected is not likely to cause catastrophic failure, because, in the current design practice for advanced composites, relatively low design ultimate strength values are specified. Therefore, the safety-of-flight is less of a concern than the durability requirement to minimize the need for repeated repairs.

The above conclusions have been based on results for relatively thin $\pi/4$ laminates up to 16 plies. Impact damage behavior of thick laminates and laminates with discrete stiffeners was not considered and is being investigated under an ongoing NADC program being conducted at Northrop. Residual tensile strength of impact-damaged laminates was investigated under the present program. Behavior of impact-damaged laminates under compression and shear loading and the influence of environmental exposures also needs to be investigated.

ACKNOWLEDGMENT

The work reported herein was conducted as part of Northrop Corporation's IR&D activity.

REFERENCES

1. Bhatia, N.M., "Impact Damage Characteristics of Graphite/Epoxy Laminates," Northrop Corporation, Aircraft Division, Report No. NOR76-186, June 1977.

2. Verette, R.M. and Labor, J.D., "Structural Criteria for Advanced Composites," AFFDL-TR-76-142, March 1977.

3. Awerbuch, J. and Hahn, H.T., "Hard Object Impact Damage of Metal Matrix Composites," J. of Comp. Materials, v. 10, July 1976, 231 - 257.

4. Husman, G.E., Whitney, J.M., and Halpin, J.C., "Residual Strength Characterization of Laminated Composites Subjected to Impact Loading," ASTM STP568, American Society of Testing and Materials, 1975.

5. Noyes, J.V., et al., "Wing/Fuselage Critical Component Development Progran," Second Interim Report, AFFDL Contract F33615-77-C-5078, Northrop Corporation, Aircraft Group, NOR78-23, February 1978.

REPRODUCIBILITY OF STRUCTURAL STRENGTH AND STIFFNESS FOR GRAPHITE-EPOXY AIRCRAFT SPOILERS

WILLIAM E. HOWELL
Structural Materials Engineer
NASA Langley Research Center
Hampton, Virginia

CHARLES D. REESE
Associate Professor
University of Kansas
Lawrence, Kansas

ABSTRACT

Structural strength reproducibility of graphite-epoxy composite spoilers for the Boeing 737 aircraft was evaluated by statically loading fifteen spoilers to failure at conditions simulating aerodynamic loads. Spoiler strength and stiffness data were statistically modeled using a two-parameter Weibull distribution function. Shape parameter values calculated for the composite spoiler strength and stiffness were within the range of corresponding shape parameter values calculated for material property data of composite laminates. This agreement showed that reproducibility of full-scale component structural properties was within the reproducibility range of data from material property tests.

NOMENCLATURE

Values are given in both U.S. Customary and SI Units. Measurements and calculations were made in U.S. Customary Units. Factors relating the two systems are given in reference 1.

F = Failure load
$P()$ = Probability distribution function
S = Structural stiffness
X = Random variable
α = Weibull shape parameter
μ = Statistical mean
σ = Standard deviation

Superscript
$\hat{}$ = Weibull scale parameter

INTRODUCTION

Several flight service programs are being conducted with composite components on transport aircraft. These include Kevlar 49-epoxy fairing components on Lockheed L-1011 aircraft (ref. 2), boron-epoxy-reinforced wing-box structures on U.S. Air Force C-130 aircraft (ref. 3), graphite-epoxy rudder section on McDonnell Douglas DC-10 aircraft (ref. 4), and

graphite-epoxy spoilers on Boeing 737 aircraft (ref. 5). These components are being carefully monitored to determine their ability to withstand the normal day-to-day aircraft environment.

The Boeing 737 composite spoiler (ref. 5), which is the component discussed in this paper, is in flight service with several airlines. To date approximately one million hours of flight time have been accumulated.

Even though considerable composite material property data are in the literature, usually, only one-of-a-kind structural components have been tested. Insufficient data are available for adequate confidence in designs which minimize structural weight. A broader statistical base would aid in this respect. The statistical distribution functions that are normally employed for strength and structural reliability are discussed in references 6 to 10. One of these functions is the Weibull distribution which is described in greater detail in reference 11. In reference 12, this distribution function is used to develop a reliability plan for composite materials static strength based on the macroscopic material properties.

The purpose of the present paper is to report the results of an initial portion of a structural reproducibility evaluation of a composite aircraft component. The entire program consists of structural tests of the component and static tensile, compression, and interlaminar shear tests of the same material as used in the component construction. This paper is restricted to reporting the structural component tests. Fifteen components were evaluated by loading to structural failure. This is the first series of structural strength tests with sufficient replicates for a statistical analysis of a builtup composite structural component fabricated on a production basis. Component stiffness and strength data are examined statistically and are shown to fit a two-parameter Weibull distribution. The two parameters, the shape and scale factors, were computed. In addition, some initial comparisons are made of the Weibull shape parameter for the component tests with shape parameters for material property test data from several NASA contracts.

MATERIALS

The composite materials discussed in this paper were combinations of graphite or aramid fibers and epoxy resins. The specific materials were:

Thornel 300 graphite fibers, manufactured by Union Carbide Corporation

AS graphite fibers, manufactured by Hercules Incorporated

Kevlar 49 aramid fibers, manufactured by E. I. duPont de Nemours & Co., Inc.

Narmco 5209 epoxy resin, manufactured by Narmco Materials, a subsidiary of Celanese Corporation

3501 epoxy resin, manufactured by Hercules Incorporated

EA 9628 epoxy adhesive, manufactured by Hysol, a division of Dexter Corporation.

Identification of commercial products in this report is to adequately describe the materials and does not constitute official endorsement, expressed or implied, of such products or manufacturers by the National Aeronautics and Space Administration.

TEST COMPONENTS

The test articles (fig. 1) were graphite-epoxy aircraft spoilers that were developed for and are being evaluated in the flight service program previously discussed (ref. 5). Spoiler construction was similar to the standard aluminum production spoilers on the Boeing 737 transport aircraft except that graphite-epoxy skins were substituted for the aluminum skins (fig. 2). These composite skins were fabricated from Thornel 300/Narmco 5209 prepreg and were bonded to the substructure with EA 9628 adhesive. The structure was designed for a stiffness criterion and design limit load [3,790 lb (16,858 N)] and design ultimate load [5,685 lb (25,287 N)] criteria were also satisfied. The spoilers tested in this investigation were among the last 25 of a production run of 140 items. Fifteen of these spoilers were loaded to failure. The remaining 10 spoilers will be used in other tests. All spoilers used in this evaluation were new and flight qualified.

PROCEDURES

Spoilers were loaded with a whiffletree arrangement which applied a distributed load to simulate aerodynamic loading. Spoiler loading pads are shown in figure 3 and the test setup, mounted on a rigid backstop, is shown in figure 4. The load was applied to the spoilers by a hydraulic cylinder pulling down on the crossbeam below the spoiler. Through this arrangement, the spoilers were loaded to failure and the values of load, strain, and displacement were recorded on magnetic tape throughout the tests. Strain gage locations and the three points along the trailing edge of the spoiler where displacements were measured are shown in figure 3. The strain gages were located on the upper and lower surfaces near the corners of the hydraulic actuator attachment box where the maximum strains were expected to occur. Displacements were measured using weighted strings turning calibrated, 10-turn, variable resistors. Failure was taken to be the point of maximum load which was also the point at which catastrophic structural failure occurred. Figure 5 shows a failed spoiler in the test rig.

RESULTS

All fifteen spoilers appeared to fail in the same mode. The lower skin (compression side) buckled around the actuator attachment frame and the upper skin (tension side) failed at one or both of the frame aft corners. These failures are shown in figure 6. Trailing edge deflection at the corners of the spoiler at failure was approximately 2.7 in. (69 mm). A typical load-deflection curve is shown in figure 7 and the failure loads and deflection

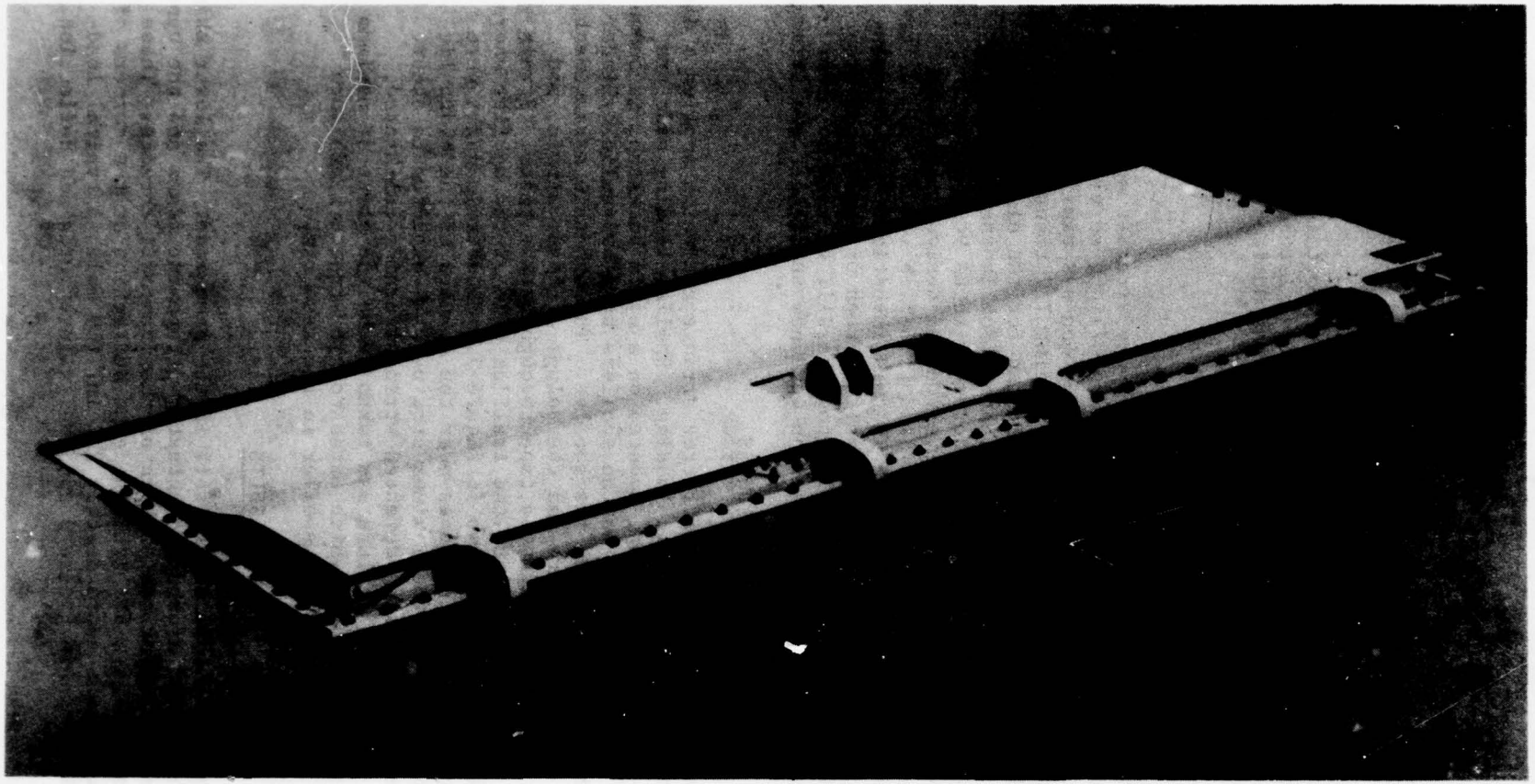


Figure 1. - Boeing 737 composite spoiler.

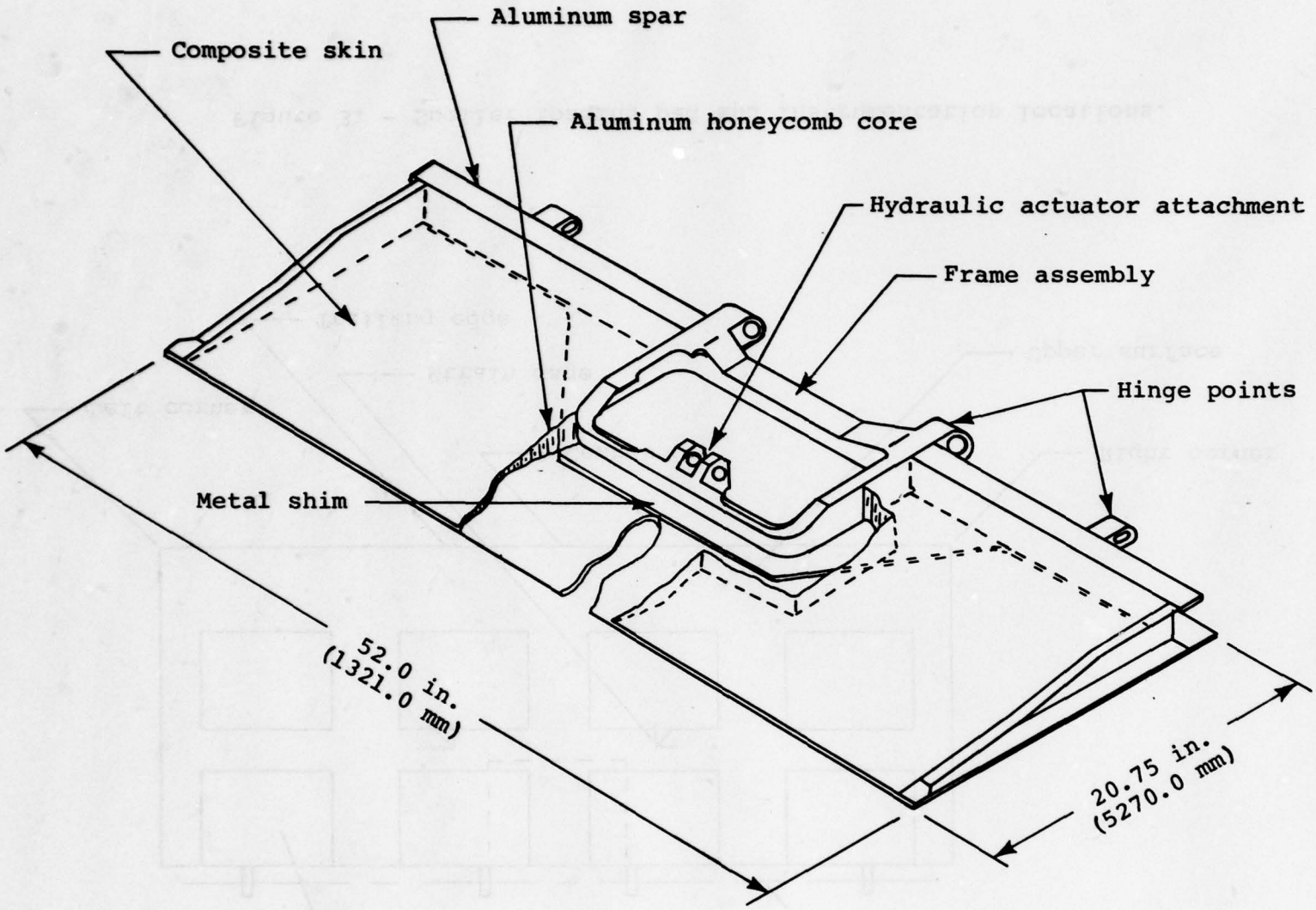


Figure 2. - Spoiler structural arrangement.

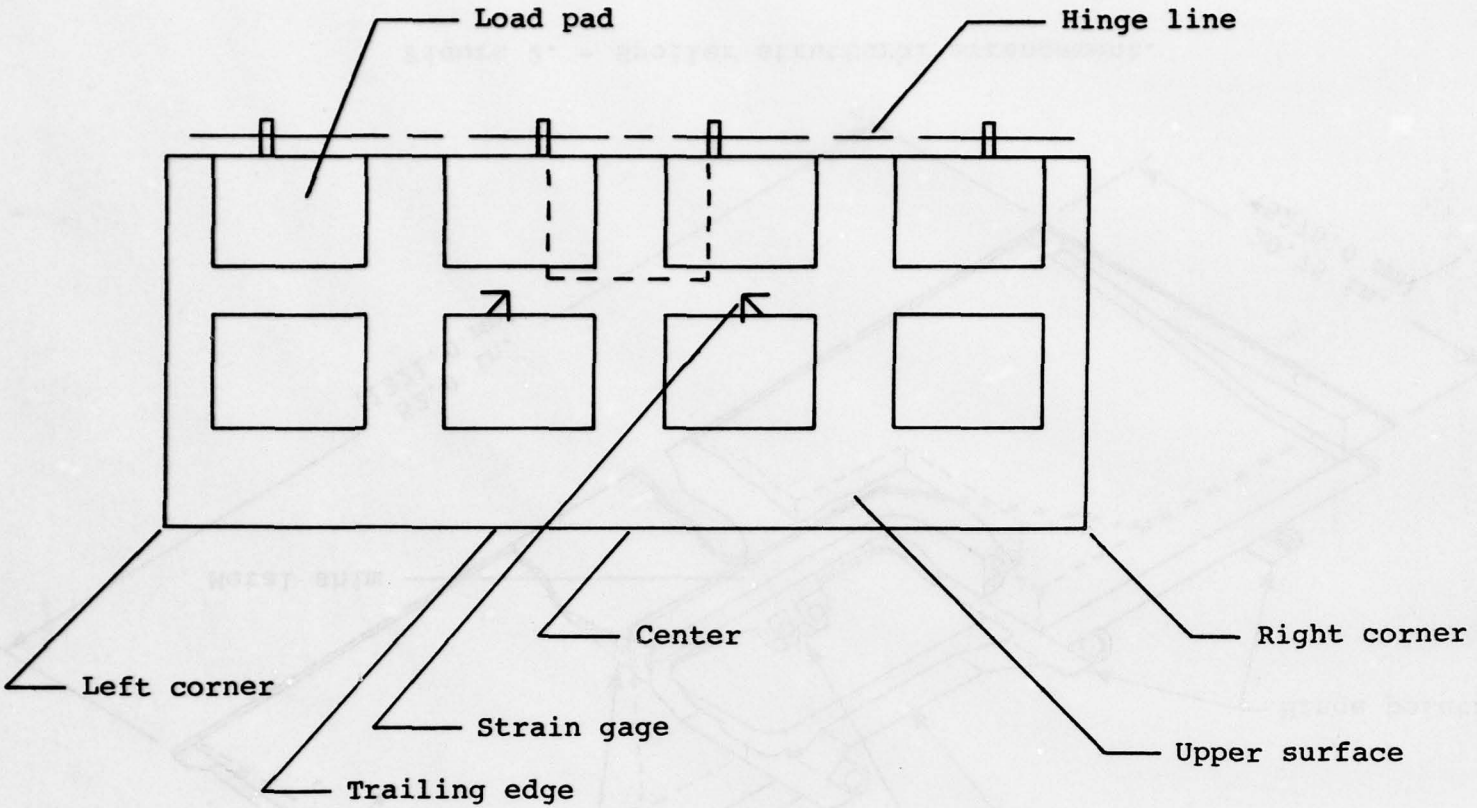


Figure 3. - Spoiler loading pad and instrumentation locations.

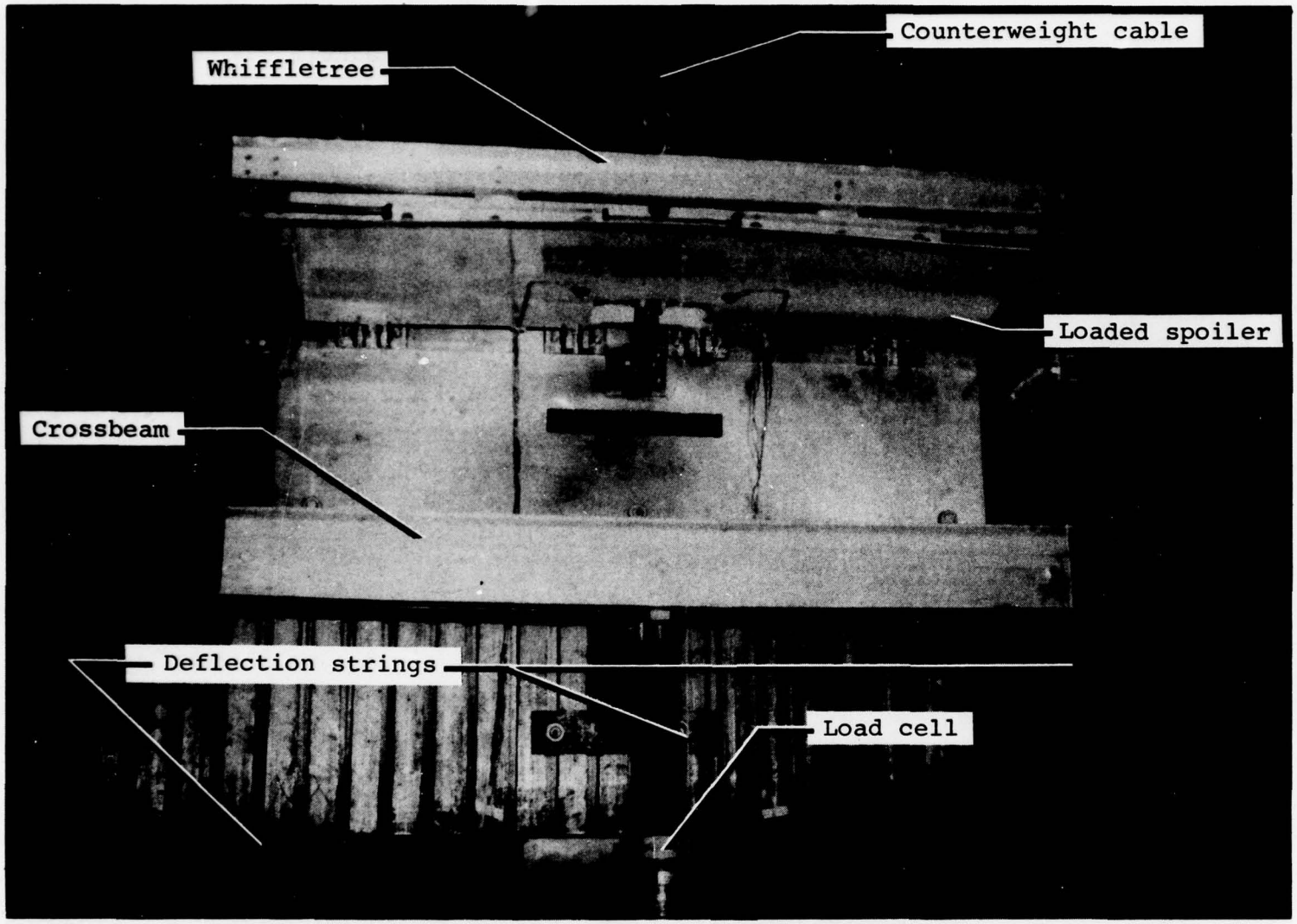


Figure 4. - Spoiler during loading in test rig.

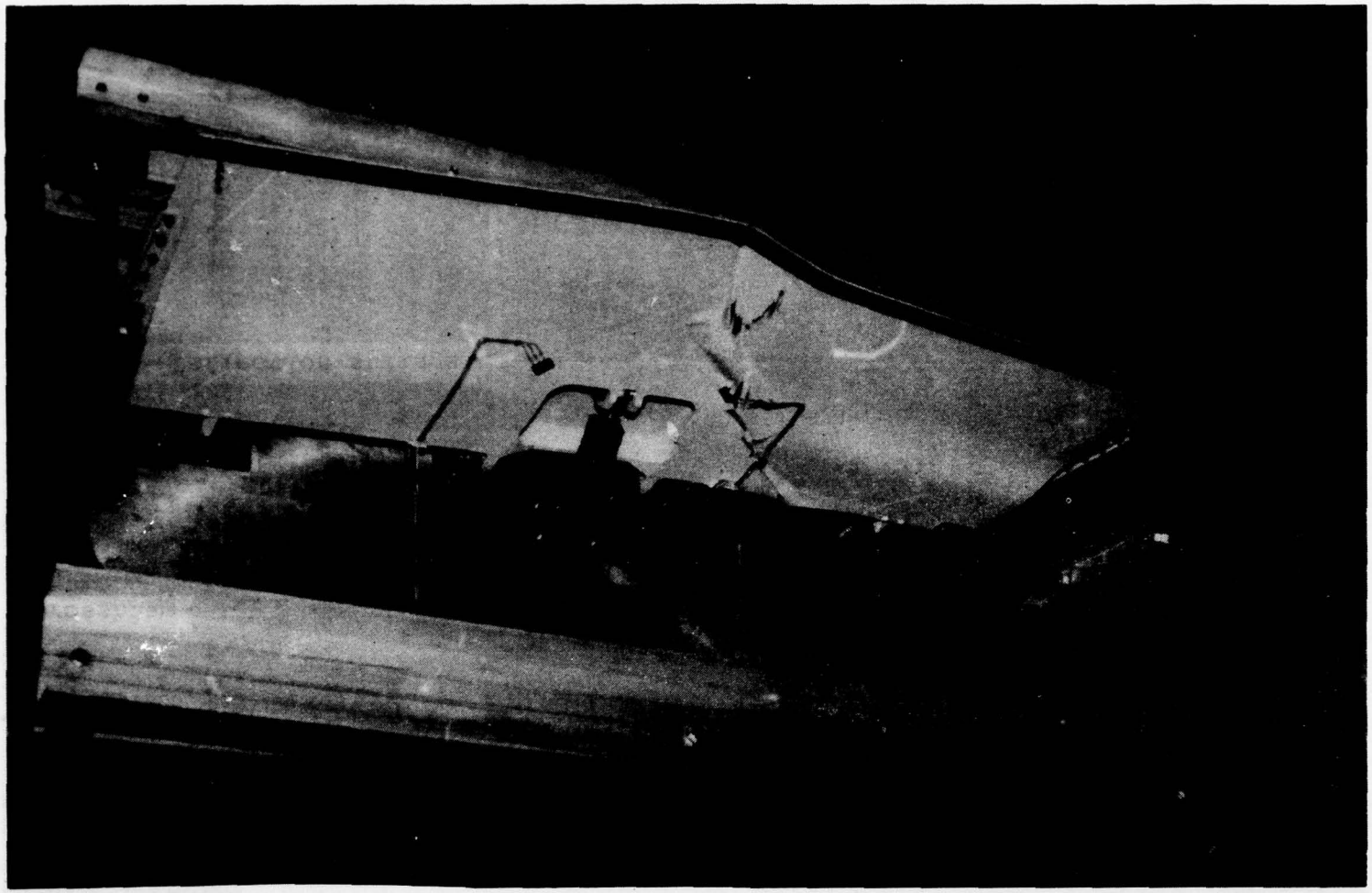


Figure 5. - Structural failure of spoiler.

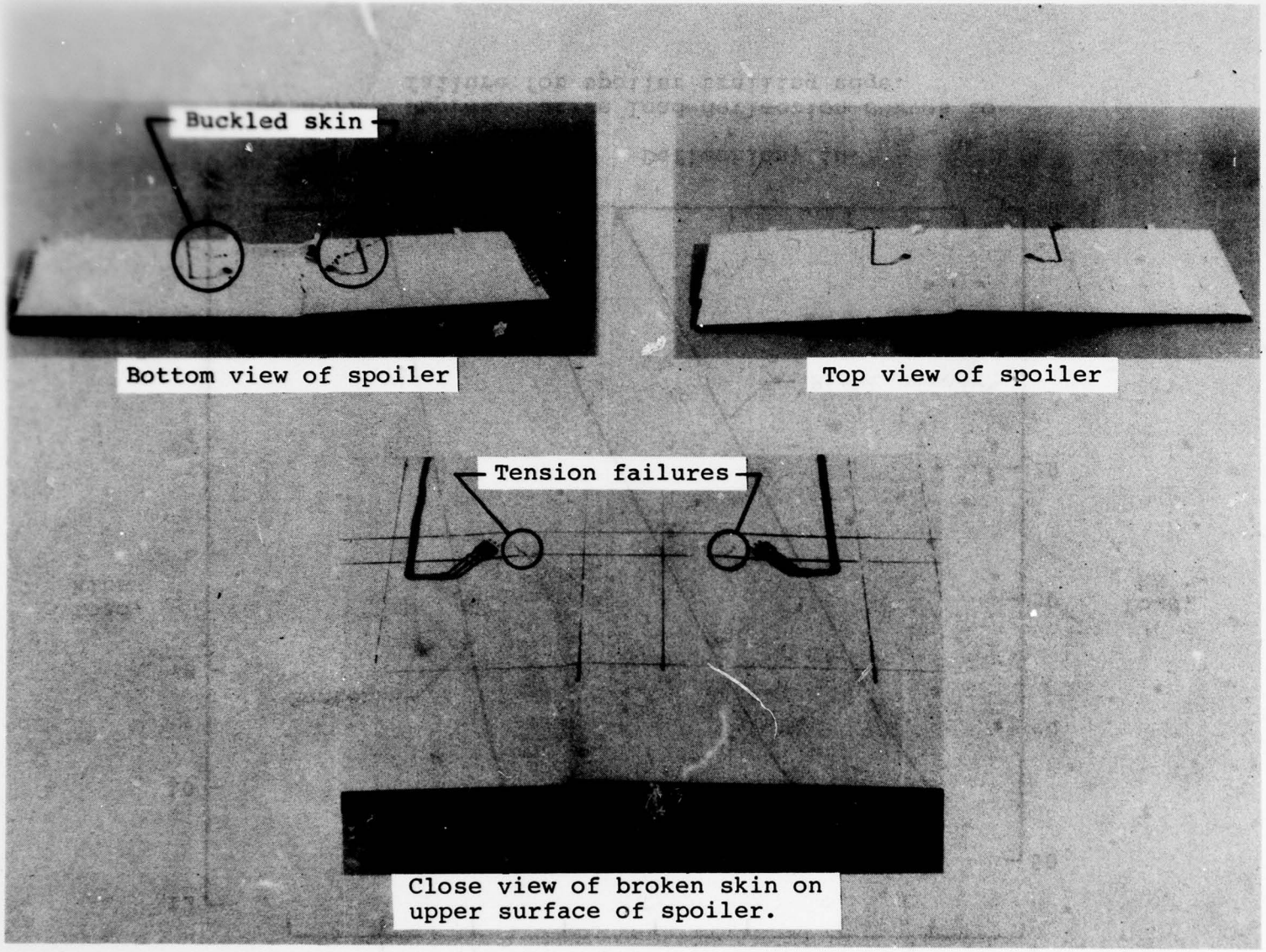


Figure 6. - Views of failed spoiler showing extent of damage.

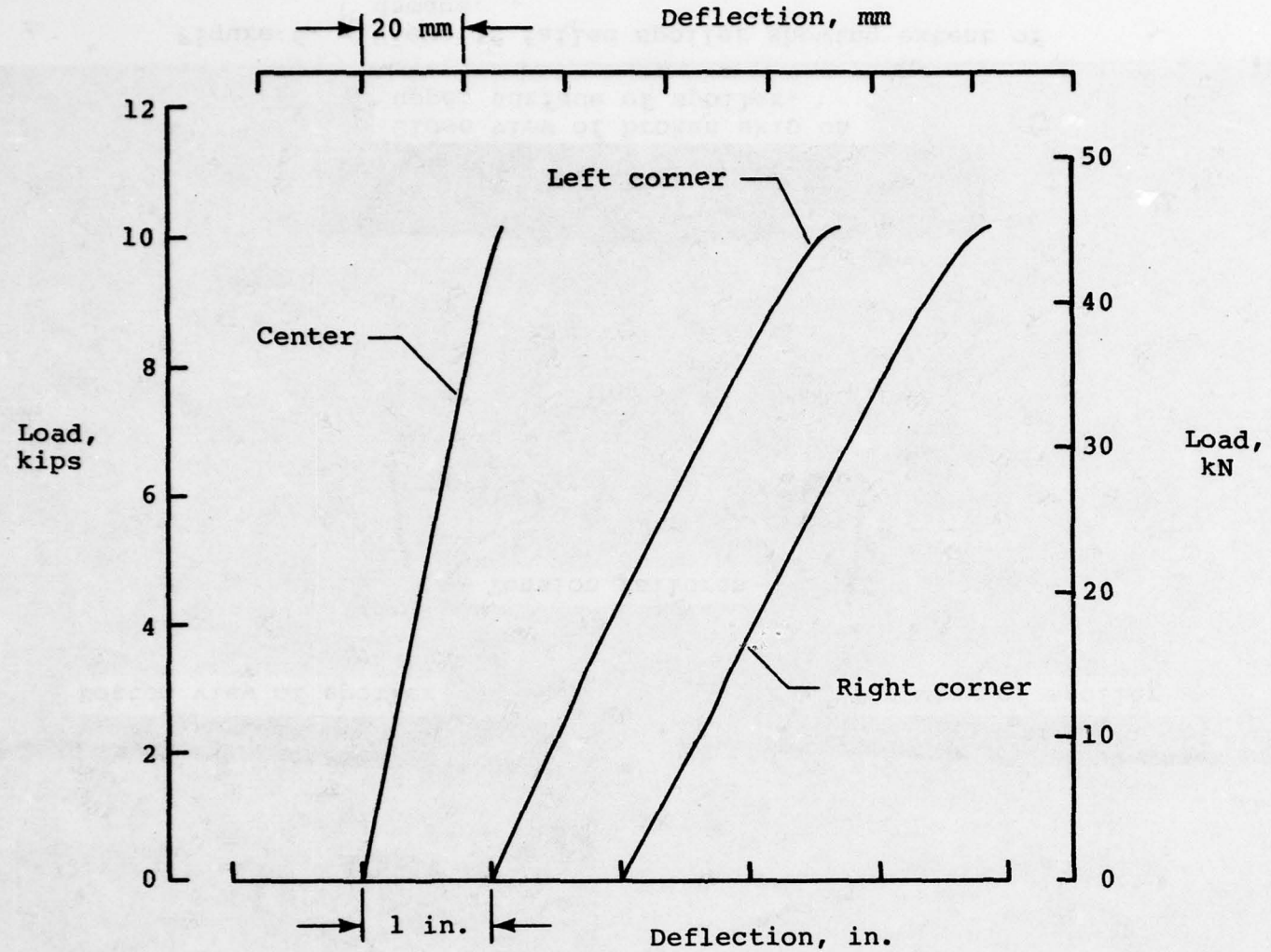


Figure 7. - Representative load-deflection curves to failure for spoiler trailing edge.

data are given in table 1. Using load-deflection data, comparative initial stiffness values (table 2) were computed. These stiffness values were obtained by dividing the applied load by the associated deflection.

Failure loads of the 15 spoilers are plotted in figure 8 in the sequence tested. The solid line represents the mean failure load of 10,190 lb (45,325 N) for all the tests. The two dashed lines represent an arbitrary ±10 percent band. All of the data are within this band except for two points which are 12.9 and 14.5 percent below the mean failure load of the spoilers. The lowest failure load of 8,709 lb (38,708 N) is 53 percent above the design ultimate load of 5,685 lb (25,287 N). As indicated in table 1, the standard deviation of the load data is 673 lb (2,994 N).

A test was made for normal distribution of the failure loads by plotting the data on a normal probability scale. If they are normally distributed, the data should fit a straight line. In figure 9, failure loads are plotted in this manner where the ordinate represents the probability of survival. A straight line based on the computed mean and standard deviation is not a good fit of the data.

As previously discussed, references 11 and 12 indicate that experimentally measured parameters may be described by the two-parameter Weibull distribution function

$$P(X) = \exp\left[- \left(\frac{X}{\hat{X}}\right)^{\alpha} \right] \qquad (1)$$

where X is the random variable such as failure load, $\hat{X}$ is the scale parameter, and α is the shape parameter. The parameter $\hat{X}$ is the characteristic value or estimate of the mean and α gives the shape of the distribution and some measure of dispersion or scatter. Large values of α are indicative of small scatter in the data. $P(X)$ is the probability of survival and $1-P(X)$ the probability of failure.

The failure load data are replotted in figure 10 on ordinate and abscissa scales such that a Weibull distribution lies along a straight line. The solid line is a least square fit of the data with a slope, α, of 14.70 and a scale parameter, $\hat{F}$, of 10,532 lb (46,846 N). The parameter $\hat{F}$ is an estimate of the mean failure load.

Comparative initial stiffness values (table 2) are plotted on a normal probability scale in figure 11. The data fit a straight line based on the computed mean and standard deviation. These results indicate that the computed initial stiffness data, which have very little scatter, are normally distributed.

TABLE I. - Failure loads and trailing edge deflections of spoilers.

Test number	Failure load		Displ. of left corner		Displ. of Center		Displ. of right corner	
	lb	N	in.	mm	in.	mm	in.	mm
1*	9946	44242	-	-	-	-	-	-
2	9543	42449	2.404	61.06	0.907	23.03	2.350	59.69
3	10921	48579	2.993	76.02	1.181	30.00	3.060	77.72
4	10848	48254	2.939	74.65	1.074	27.28	2.887	73.33
5	10736	47756	2.938	74.63	1.180	29.97	2.953	75.01
6	8709	38740	2.178	55.32	0.878	22.30	2.261	57.43
7	10153	45163	2.698	68.53	1.064	27.03	2.867	72.82
8	10296	45799	2.663	67.64	1.027	26.09	2.657	67.49
9	10404	46279	2.817	71.55	1.088	27.64	2.753	69.93
10	10304	45834	2.727	69.27	1.084	27.53	2.685	68.20
11	10400	46261	2.867	72.82	1.048	26.62	2.979	75.67
12	10813	48099	2.881	73.18	1.195	30.35	3.008	76.40
13	10408	46297	2.644	67.16	1.048	26.62	2.727	69.27
14	10549	46924	2.694	68.43	0.963	24.46	2.790	70.87
15	8875	39478	2.161	54.89	0.818	20.78	2.281	57.94

Mean failure load = 10190 lb (45325 N)
Standard deviation = 673 lb (2994 N)
Weibull shape parameter = 14.7
Mean corner deflection at failure = 2.711 in. (68.85 mm)
* No deflection data on first test

TABLE II. - Spoiler trailing corner stiffness

Test number	Stiffness					
	Left corner		Right corner		Mean	
	lb/in.	kN/m	lb/in.	kN/m	lb/in.	kN/m
1*	-	-	-	-	-	-
2	4153	727	4212	738	4183	733
3	4259	746	4160	729	4209	737
4	4194	734	4338	760	4266	747
5	4160	729	4198	735	4179	732
6	4389	767	4224	740	4307	754
7	4320	757	4012	703	4166	730
8	4197	735	4299	753	4248	744
9	4273	748	4304	754	4289	751
10	4216	738	4430	776	4323	757
11	4191	734	4093	717	4142	725
12	4392	769	4154	727	4273	748
13	4397	770	4302	753	4350	762
14	4337	760	4099	718	4218	739
15	4357	763	4101	718	4229	741

Mean stiffness = 4242 lb/in. (743 kN/m)
Standard deviation = 63 lb/in. (11 kN/m)
Weibull shape parameter = 69.2
* No deflection data on first test

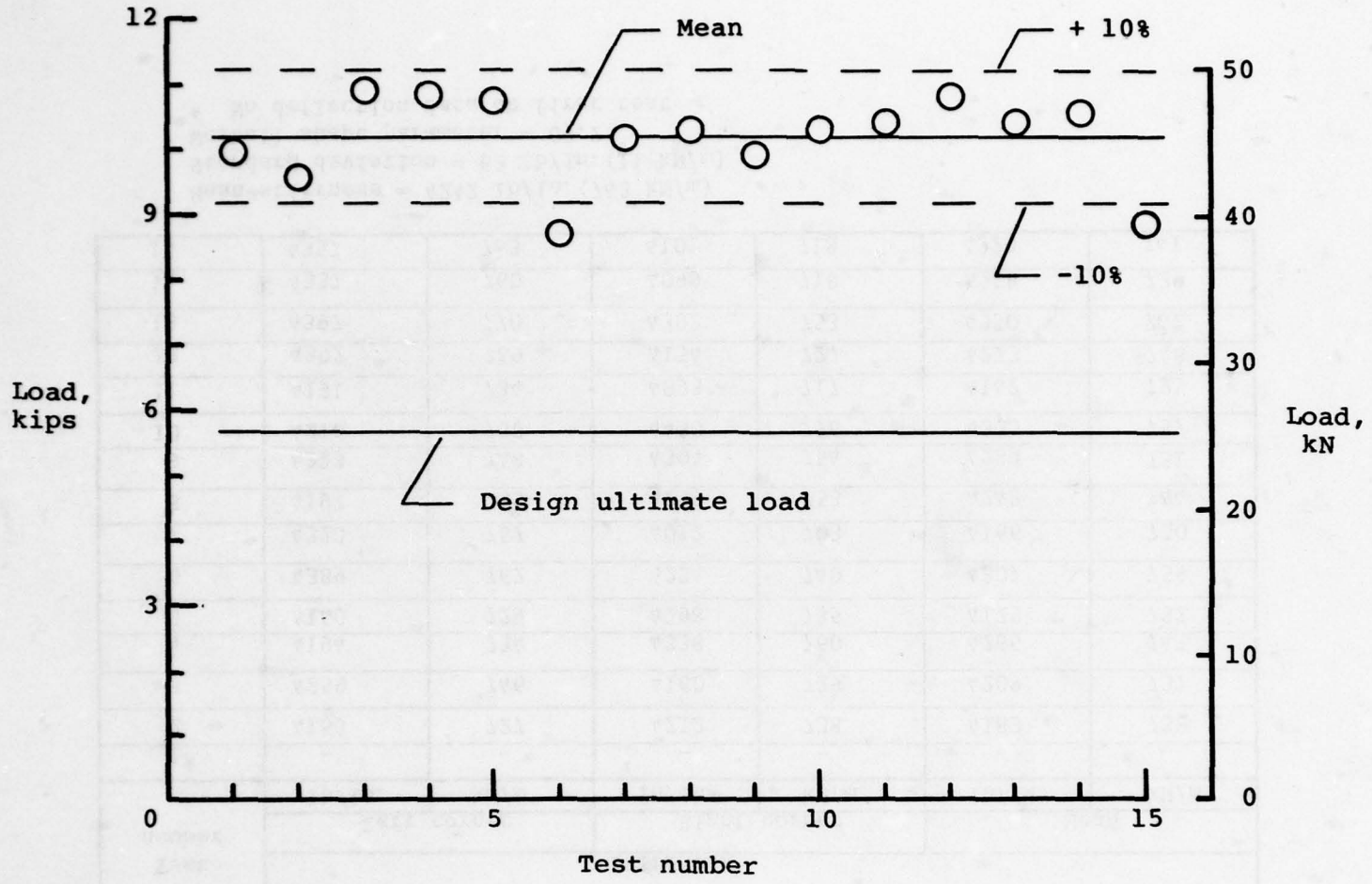


Figure 8. - Strength reproducibility of graphite-epoxy spoilers.

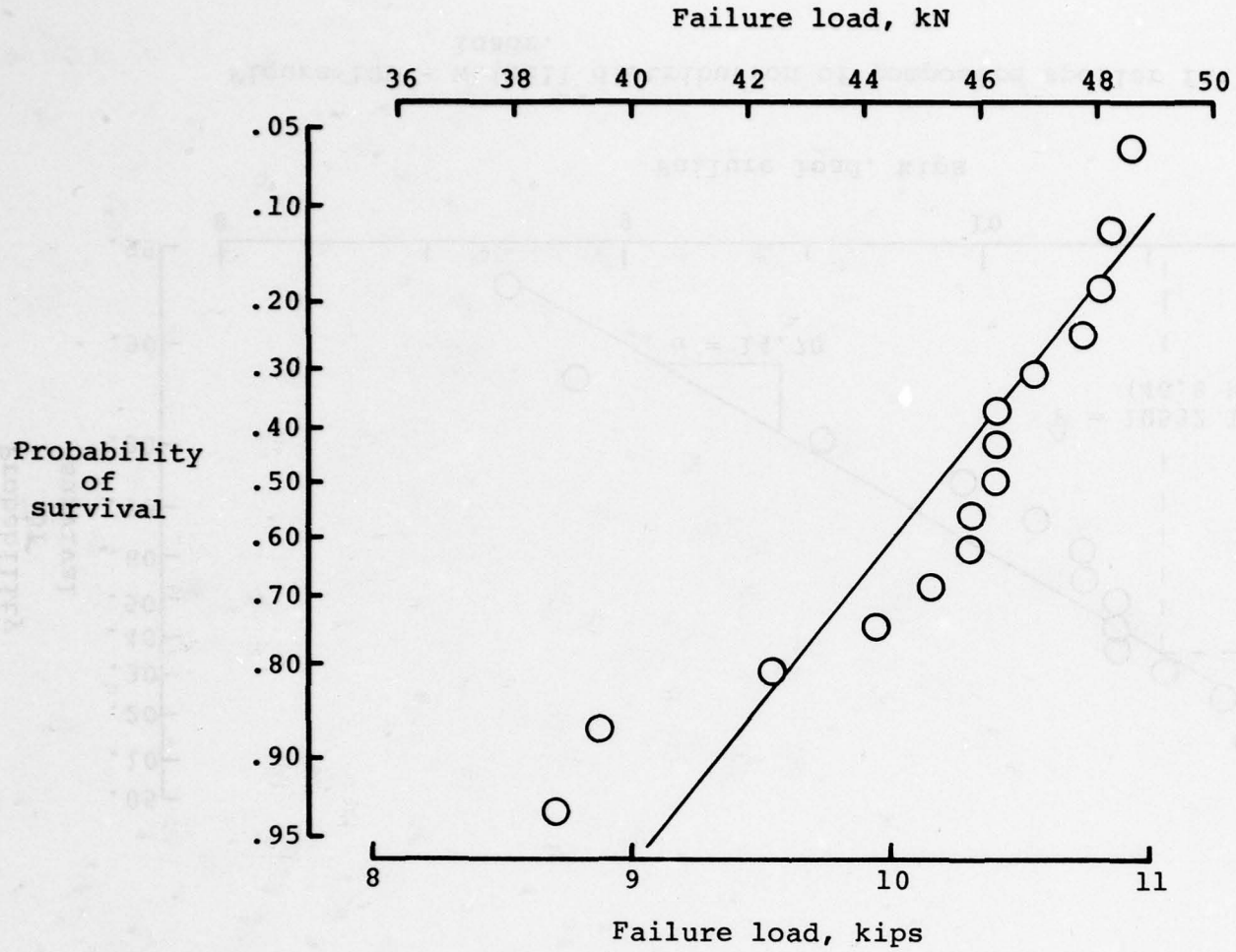


Figure 9. - Test for normal distribution of composite spoiler strength data.

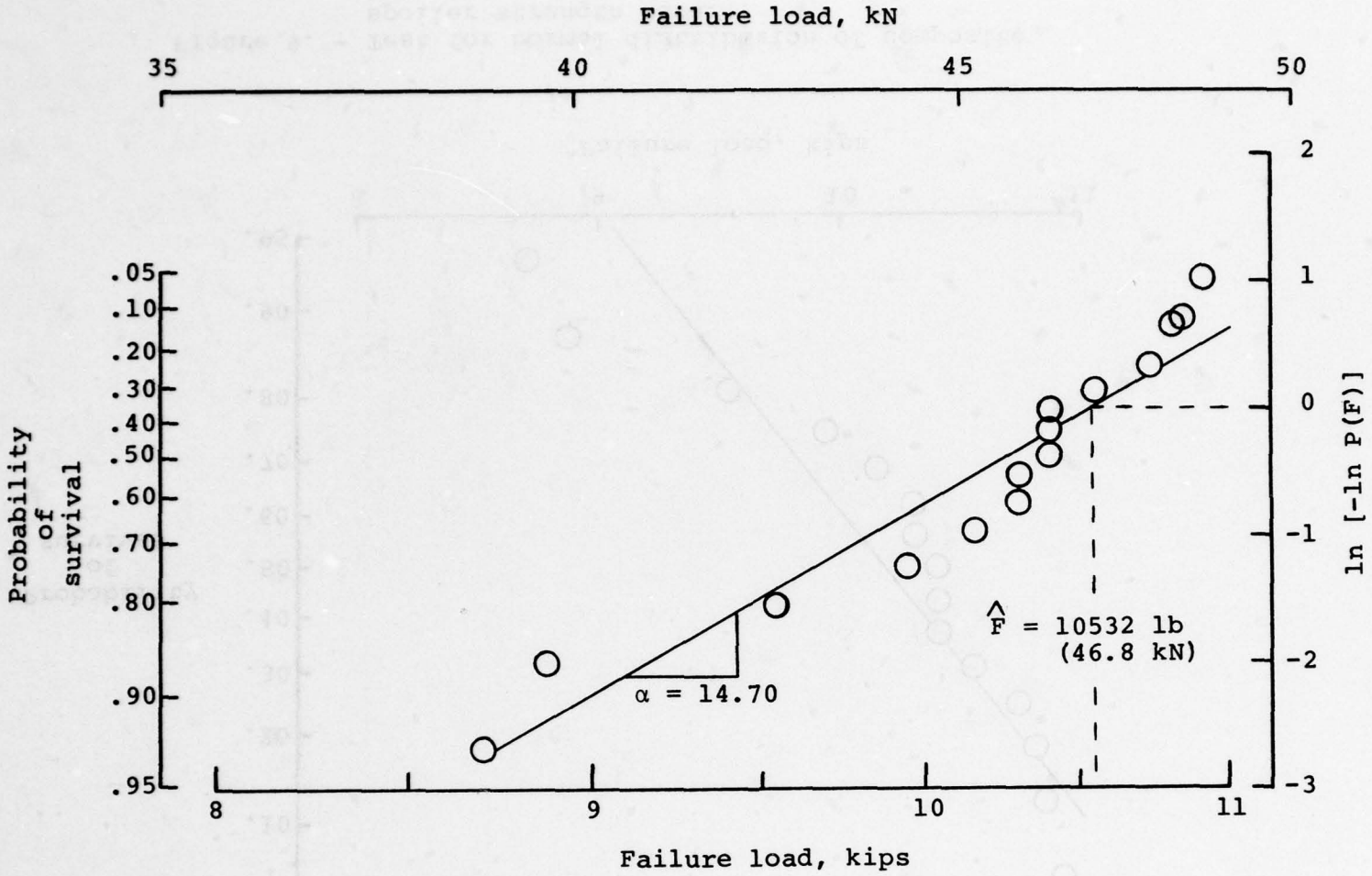


Figure 10. - Weibull distribution of composite spoiler failure loads.

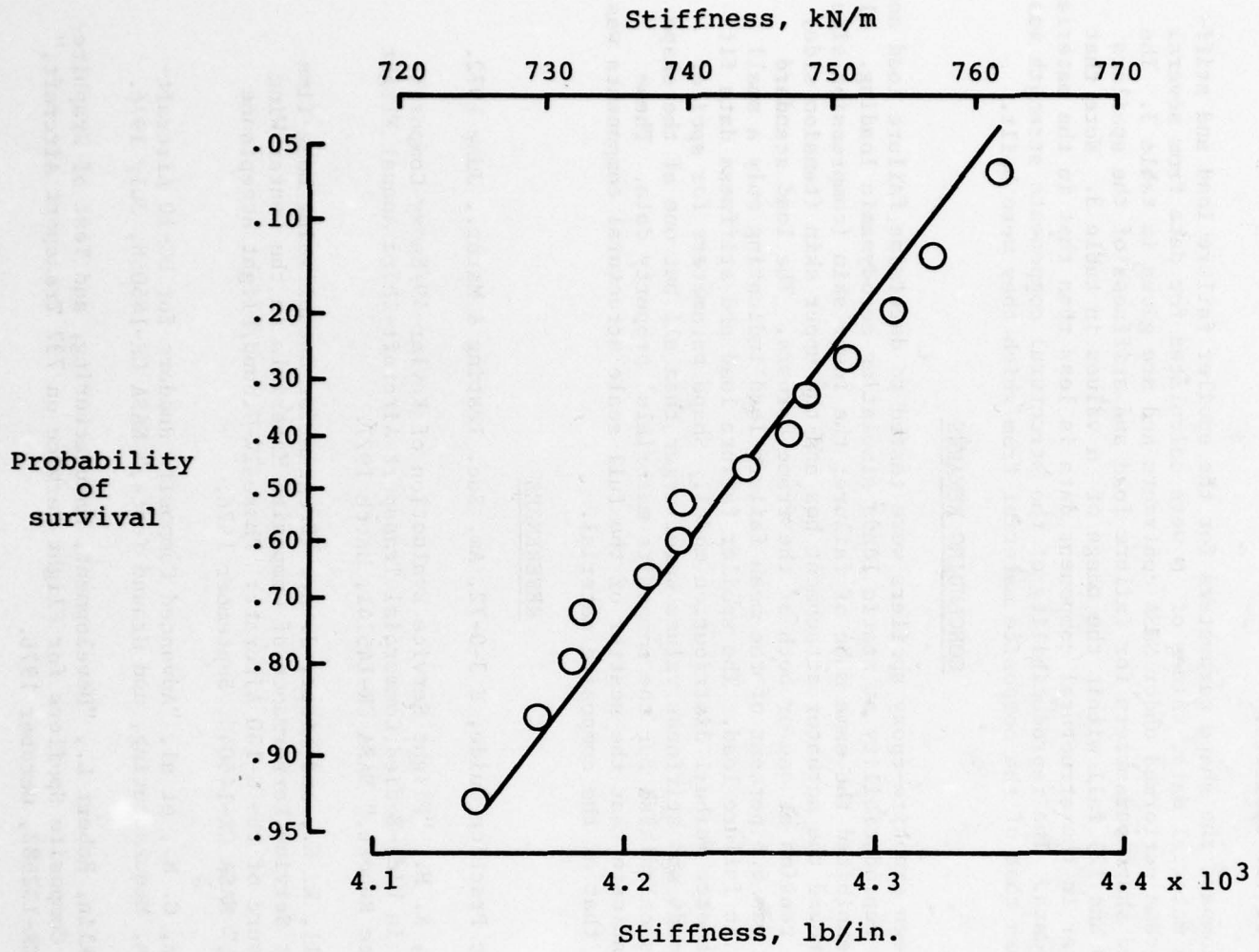


Figure 11. - Test for normal distribution of composite spoiler stiffness data.

Figure 12 is a Weibull plot of the stiffness data. The shape parameter value of 69.19 is indicative of a small amount of scatter in the initial stiffness of the spoilers.

To compare the shape parameters for the spoiler failure load and stiffness with material data, values of α were calculated for data from several test programs performed under NASA contracts and are given in table 3. The calculated shape parameters for failure load and stiffness of the spoilers (figs. 10 and 12) fall within the range of α values in table 3. Note that the scatter in the structural component data is less than that in the material property data. The reproducibility of the structural components strength was better than that of the composite material from which they were built.

CONCLUDING REMARKS

Fifteen graphite-epoxy spoilers were tested to determine failure load and stiffness reproducibility at static loads simulating aerodynamic loading. All spoilers exhibited the same mode of failure; the lower skin (compression side) buckled around the actuator attachment box and the upper skin (tension side) failed in tension at one or both of the frame corners. The load standard deviation was 6.6 percent of the mean failure load indicating only a small variation in failure load. The spoiler failure load and stiffness data fit a two parameter Weibull distribution model. Shape parameters for spoiler failure loads and stiffness values were larger than all but one of the shape parameters calculated for the composite materials' property data. These results indicate that the scatter of the full scale structural components was less than that of the composite material.

REFERENCES

1. Metric Practice Guide, E 3-0-72, Am. Soc. Testing & Mater., June 1972.

2. Stone, R. H., "Flight Service Evaluation of Kevlar-49/Epoxy Composite Panel in Wide-Bodied Commercial Transport Aircraft-Third Annual Flight Service Report," NASA CR-145141, March 1977.

3. Harvill, W. E., and Kizer, J. A., "Program for Establishing Long-Time Flight Service Performance of Composite Materials in the Center Wing Structure of the C-130 Aircraft: Phase IV-Ground/Flight Acceptance Tests," NASA CR-145043, September 1976.

4. Lehman, G. M., et al, "Advanced Composite Rudders for DC-10 Aircraft-Design, Manufacturing, and Ground Tests," NASA CR-145068, July 1976.

5. Stoecklin, Robert L., "Development, Manufacturing, and Test of Graphite-Epoxy Composite Spoilers for Flight Service on 737 Transport Aircraft," NASA CR-132682, October 1976.

6. Lemon, G. H., "Statistical Considerations for Structural Reliability Analysis," Colloquium on Structural Reliability: The Impact of Advanced

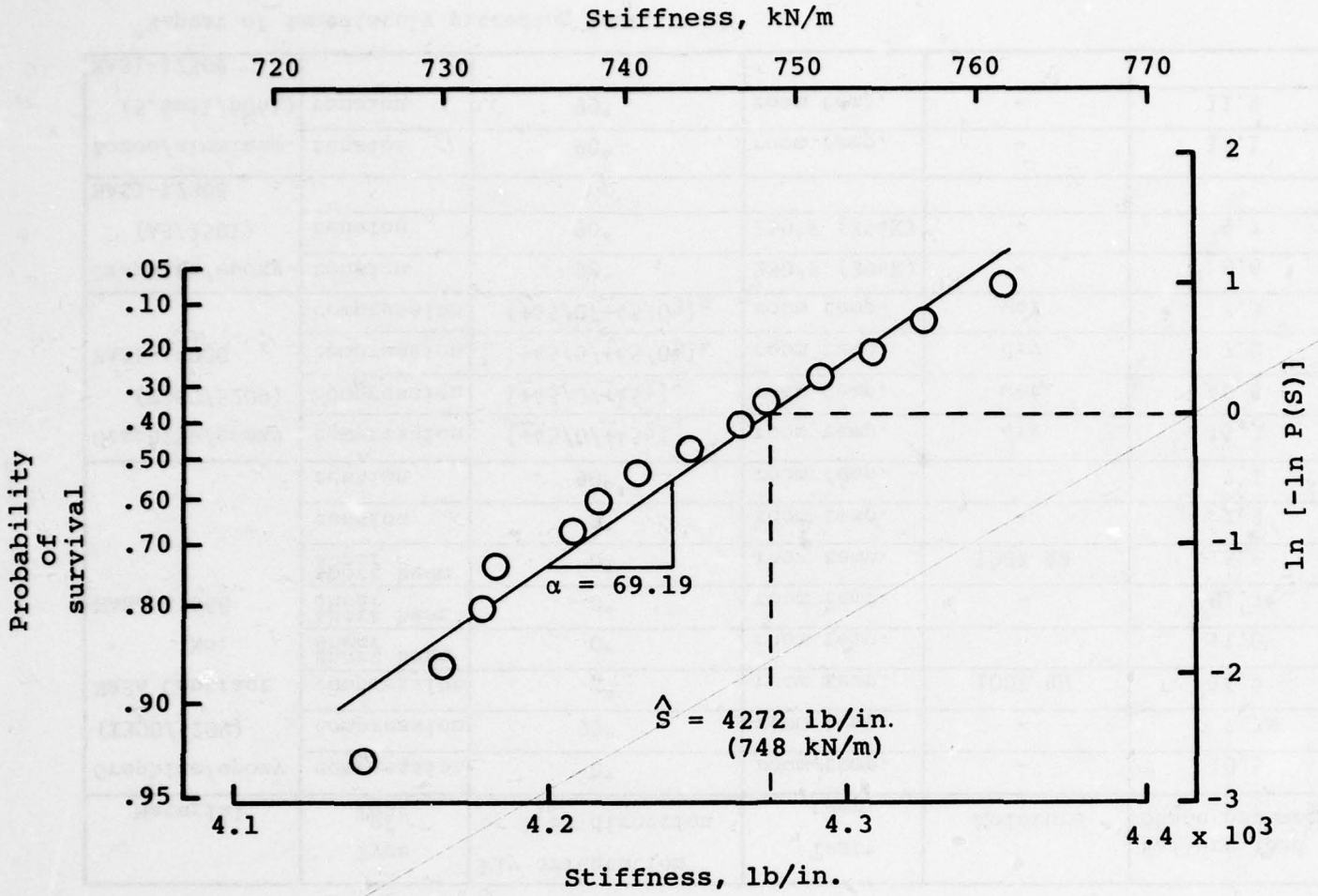


Figure 12. - Weibull distribution of composite spoiler corner stiffness.

TABLE III. - Material property test conditions and shape parameters (Tests performed under NASA contracts).

Material	Type of Test	Ply orientation or load direction	Test temp.	Moisture	Failure load shape parameter
Graphite/epoxy (T300/5209) NASA Contract No. NAS1-11668	compression	0°	room temp.	-	10.5
	compression	90°	room temp.	-	7.7
	compression	0°	room temp.	100% RH	16.9
	short beam shear	0°	room temp.	-	11.0
	short beam shear	0°	room temp.	-	81.7*
	short beam shear	0°	room temp.	100% RH	15.2
	tension	0°	room temp.	-	7.3
	tension	90°	room temp.	-	7.4
Graphite/epoxy (T300/5209) NAS1-14000	compression	$[\pm 45/0/\pm 45_2]_s$	room temp.	dry	15.3
	compression	$[\pm 45/0/\pm 45_2]_s$	room temp.	wet	40.6
	compression	$[\pm 45/0/\pm 45/0_3]_s$	room temp.	dry	7.0
	compression	$[\pm 45/0/\pm 45/0_3]_s$	room temp.	wet	7.5
Graphite/epoxy (AS/3501) NAS1-12308	tension	90°	250°F (394K)	-	8.6
	tension	90°	250°F (394K)	-	9.7
Boron/aluminum (5.6mil/6061) NAS1-12308	tension	90°	room temp.	-	12.1
	tension	90°	room temp.	-	11.9

*Repeat of immediately preceding test.

Materials on Engineering Design, Carnegie-Mellon University, Pittsburgh, PA, October 9-12, 1972, Proceedings, 35-85.

7. Heller, R. A., "Extreme Value Methods in Reliability Engineering," Colloquium on Structural Reliability: The Impact of Advanced Materials on Engineering Design, Carnegie-Mellon University, Pittsburgh, PA, October 9-12, 1972, Proceedings, 104-135.

8. Robinson, E. Y., "Estimating Weibull Parameters for Composite Materials," Colloquium on Structural Reliability: The Impact of Advanced Materials on Engineering Design, Carnegie-Mellon University, Pittsburgh, PA, October 9-12, 1972, Proceedings, 462-526.

9. Singpurwalla, N. D., "Statistical Failure Models - A Survey," Colloquium on Structural Reliability: The Impact of Advanced Materials on Engineering Design, Carnegie-Mellon University, Pittsburgh, PA, October 9-12, 1972, Proceedings, 86-103.

10. Saunders, S. C., "The Treatment of Data in Fatigue Analysis," Colloquium on Structural Reliability: The Impact of Advanced Materials on Engineering Design, Carnegie-Mellon University, Pittsburgh, PA, October 9-12, 1972, Proceedings, 136-155.

11. Weibull, W., "A Statistical Distribution Function of Wide Applicability," J. Applied Mechanics, v. 18, no. 3, September 1951, 293-297.

12. Halpin, J. C., Keph, J. R., and Goldberg, W., "Time Dependent Static Strength and Reliability for Composites," J. Composite Materials, v. 4 October 1970, 462-474.

DAMAGE TOLERANCE OF LIGHTWEIGHT AIRCRAFT STRUCTURE

DONALD F. HASKELL
Mechanical Engineer
Ballistic Research Laboratory
US Army Armament Research and Development Command
Aberdeen Proving Ground, Maryland 21005

ABSTRACT

The tolerance of lightweight aircraft structure to damage inflicted by high-explosive projectile has been studied. Test results of both US Army Cobra and Huey helicopter tail booms damaged while under flight load by bare explosive charges and/or high-explosive projectile fire are presented and discussed in terms of the tolerance of these structures to the incurred damage. In this study the Ballistic Research Laboratory developed and demonstrated by test a simple, low cost tail boom modification for the current fleet of Cobra and Huey helicopters that very significantly reduces their vulnerability to the severe, Soviet 23mm high-explosive projectile. The tests have demonstrated that, without the modification, the tail booms fail when hit in various critical regions by a single 23mm HEI-T projectile. However, with the modification, the tail booms can survive multiple hits in adjacent bays.

INTRODUCTION

In combat the tail boom of a helicopter, because of its relatively high presented area, can be expected to receive a high percentage of the fire directed at the helicopter. This factor, combined with earlier work at the Ballistic Research Laboratory by W. Vikestad, J. Foulk and R. Mayerhofer that indicated the potential vulnerability of the Huey and Cobra tail booms to small caliber, high explosive projectile, formed the impetus for the present effort. The object of this particular study was to develop a simple, low cost tail boom modification for the current Army fleet of Huey and Cobra helicopters to reduce their vulnerability to the severe Soviet 23mm high explosive projectile threat.

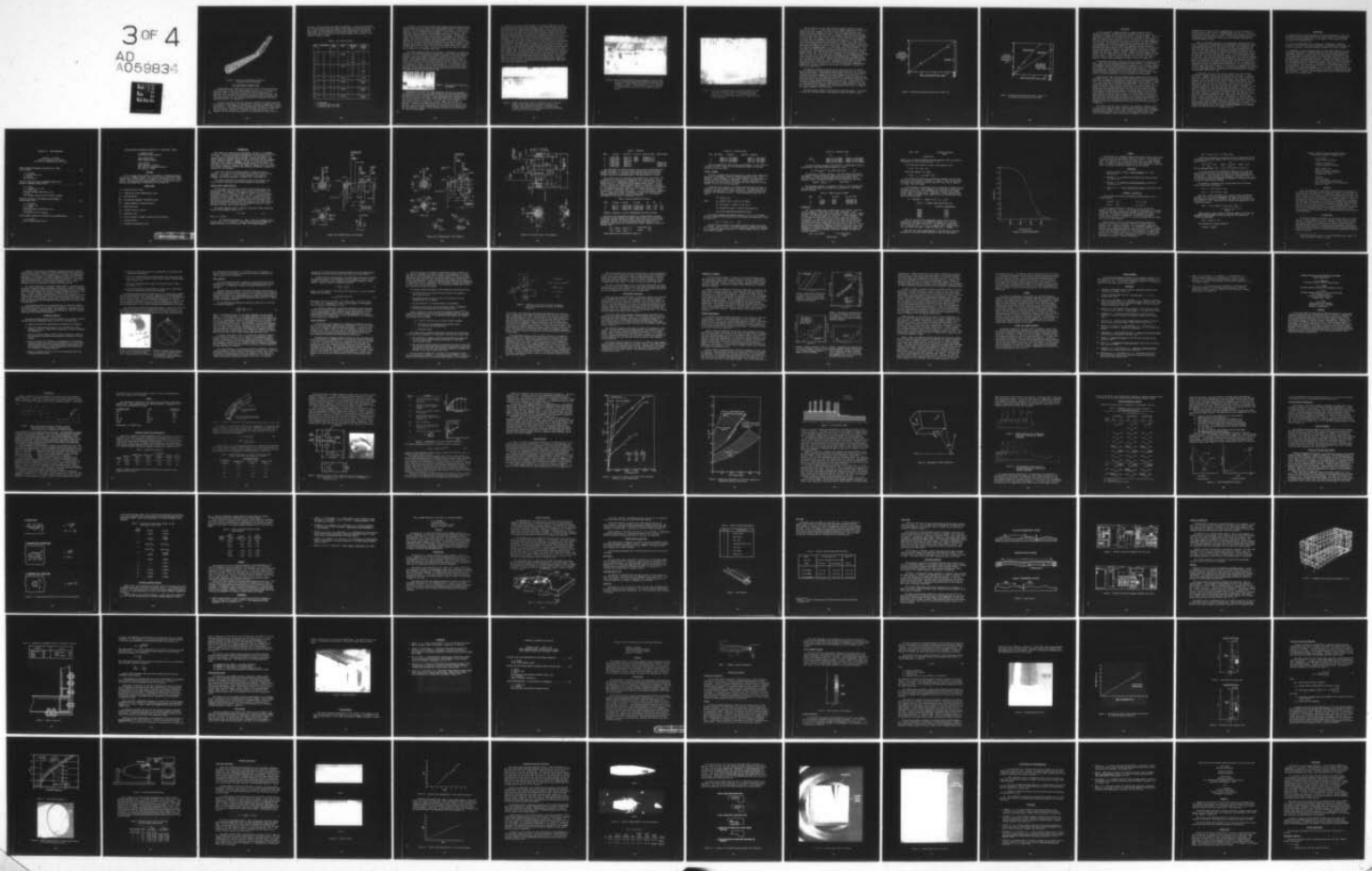
In this paper, test results of both Huey and Cobra (see Figure 1) helicop tail booms damaged while under flight load by bare explosive and/or small-caliber, high explosive antiaircraft projectile fire are presented and discussed in terms of the tolerance of these structures to the incurred damage. Such knowledge of damage tolerance may be employed in the design process, both in the design of damage tolerant aircraft as well as in the design of antiaircraft munitions. It can also be used to assess the vulnerability of existing or proposed aircraft as well as in the vulnerability reduction of existing aircraft. In addition, a modification conceived, developed and tested by BRL for these tail booms is described that very significantly reduces their vulnerability to the Soviet 23mm HEI projectile. This modification has been proposed as a product improvement for both the Cobra and Huey helicopters.

AD-A059 834 ARMY MATERIALS AND MECHANICS RESEARCH CENTER WATERTO--ETC F/G 20/11
PROCEEDINGS OF THE ARMY SYMPOSIUM ON SOLID MECHANICS, 1978 - CA--ETC(U)
SEP 78

UNCLASSIFIED AMMRC-MS-78-3

NL

3 OF 4
AD
A059834



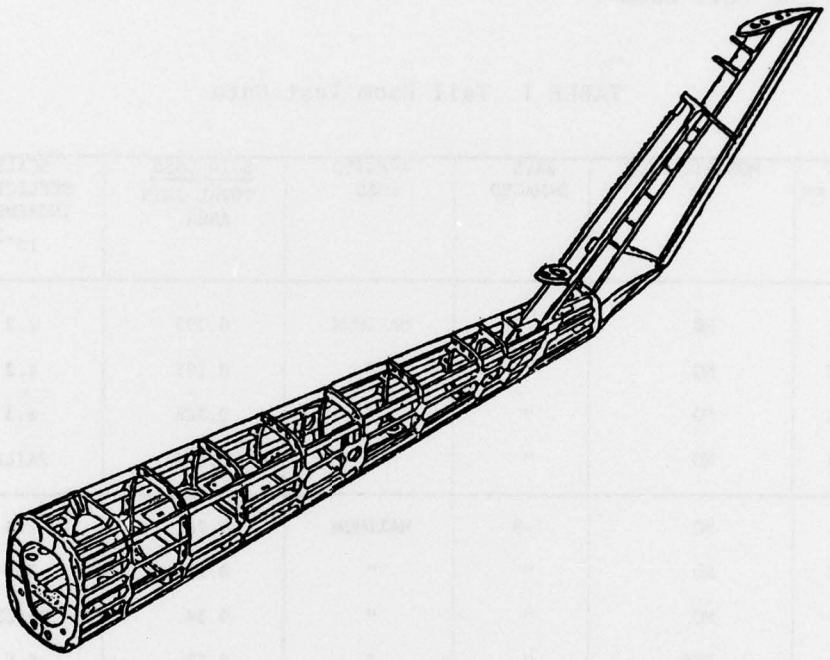


Figure 1 Cobra Tail Boom Showing Stiffening Arrangement with Skin Removed.

TAIL BOOM DAMAGE TOLERANCE TESTS

Semimonocoque tail booms from the current fleet of Army Cobra and Huey helicopters were tested. Both were roughly the same size. The Cobra tail boom, see Figure 1, consisted of eight bays along its length plus its empennage. This tail boom was essentially an all-aluminum alloy boom. The Huey tail boom consisted of ten bays plus empennage, with an aluminum alloy stiffening system. Its top and bottom skins were of aluminum alloy with a magnesium alloy for its side skins.

In some of the tests these tail booms were modified with additional external longerons and stringers to determine their influence on reducing tail boom vulnerability. These longerons and stringers were obtained from other, untested Huey tail booms. Identical longerons and stringers were used in the modifications of both tail boom types. One Cobra tail boom was modified. Two longerons and two stringers were added to the predominately tension side of

the boom. Two of the Huey tail booms were modified. In this case two longerons and two stringers each were added to both sides of the Huey tail booms. In all, a total of seven booms were tested: three unmodified and one modified Cobra booms, and one unmodified and two modified Huey booms. (See Table I). Rivets were used in all cases to attach these longerons and stringers to the exterior of the tail booms.

TABLE I Tail Boom Test Data

TEST NO. **	MODIFICATION	BAYS DAMAGED	APPLIED LOAD	SKIN LOSS / TOTAL SKIN AREA	SCALED DEFLECTION INCREMENT, 10^{-3}
A1-1	NO	4-5	MAXIMUM	0.093	2.2
A1-2	NO	"	"	0.193	4.2
A1-3	NO	"	"	0.305	6.3
A1-4	NO	"	"	0.351	FAILED
A4	NO	7-8	MAXIMUM	0.05	1.8
A1-5	NO	"	"	0.11	3.2
A2	NO	"	"	0.34	FAILED
A3	YES	"	"	0.35	6.5
B1	NO	3-4	.63 MAX	*	FAILED
B2-1	YES	2-3	MAXIMUM	*	SUSTAINED LOAD
B3-1	YES	"	"	*	"
B2-2	YES	3-4	MAXIMUM	*	SUSTAINED LOAD
B3-2	YES	"	"	*	"
B3-3	YES	4-5	MAXIMUM	*	SUSTAINED LOAD

* NOT MEASURED
** A indicates Cobra tail boom
B indicates Huey tail boom

In order to test these tail booms while loaded, they were bolted at their manufacturing joint to a rigid fixture and deadweight-loaded at their elevator and tail rotor attachment points as illustrated by Figure 2. As shown, the boom axis in this arrangement was horizontal. In all tests but one, the tail booms were loaded to simulate their maximum flight load conditions. These conditions were different for the two types of tail booms. The maximum flight load condition for the Cobra helicopter corresponds to 130 knot level flight. This condition imposes a 560 lb force downward at the tail boom elevator and 652 lb to the right (looking forward) at the tail rotor attachment point. The maximum flight load condition for the Huey helicopter is also 130 knot level flight. This condition imposes a force equal to 842 lb in the downward direction on the Huey tail boom at the elevator and a 582 lb force to the right at the tail rotor. In one test the Huey tail boom was loaded to only 63 percent of its maximum flight load.

Two types of damaging agents were employed, a 0.0395-pound (18-gram) bare spherical 50/50 Pentolite explosive charge and a Soviet 23mm, high explosive projectile. The bare charges were statically detonated at various standoff distances from the helicopter structure to achieve the desired levels of damage. These charges were all detonated within the tail boom interior at points located midway between adjacent frames of the bays tested. The projectile was fired so as to strike the boom normal to its longitudinal axis at the longitudinal midpoint of the selected target bay. The striking speeds were approximately equal to 60, 67, and 100 percent of the projectile muzzle velocity. All projectiles detonated within the interior of the tail booms. The aimpoints were varied from test to test.



Figure 2 Tail Boom Test Fixture and Arrangement.

Measurements of overall tail boom deflection and skin loss were made. Two surveyor's transits located roughly along the tail boom longitudinal axis and about 40 feet (12.2 m) behind the tail boom were used to measure deflection at the tail end of the booms. These measurements were made both after the load was applied to the boom and then after the boom was damaged by the bare explosive charge or projectile. In this manner, the increase in deflection caused by the damage was obtained. Gross skin loss was also measured. Included in this measurement was the total area of the skin that was blown away or otherwise removed from the structure by the damaging agent. The area removed by fragments that perforated the skin was not included in the skin loss measurements.

Figures 4, 5, and 6 are photographs of tail booms damaged by the 23mm HEI projectile while under load. In Figures 4 and 5 the tail booms were struck by the projectile in approximately the same region. These figures show the left side of the tail boom, or the side opposite that struck by the high explosive round. The whole left side of the tail boom in Figure 4 was severed under the combined action of the projectile detonation and the tail rotor torsional load causing the aft portion to be practically twisted free from the remainder of the tail boom. This situation would represent a kill of the helicopter. The tail boom pictured in Figure 5 was modified by the addition of longitudinal straps prior to the test. In contrast, this tail boom sustained considerably less damage than the unmodified tail boom shown in Figure 4 and was able to carry the applied load with little additional deflection. The straps not only increased the tail boom stiffness but served as crack stoppers. They stopped cracks that would otherwise form and propagate around the tail boom circumference. In this manner they restricted the damage to a relatively small region. This modification shown in Figure 5 consists of four longitudinal straps that can be rivetted to the outside of the tail boom, two to each side, in the field or manufacturing facility for about $1000. Total added weight is 9.7 lb or about 4.5% of the present tail boom weight. Figure 6 shows an overall view of a tail boom with added longerons and stringers that continues to carry the full, maximum applied load with three 23m HEI shots fired into three adjacent bays.

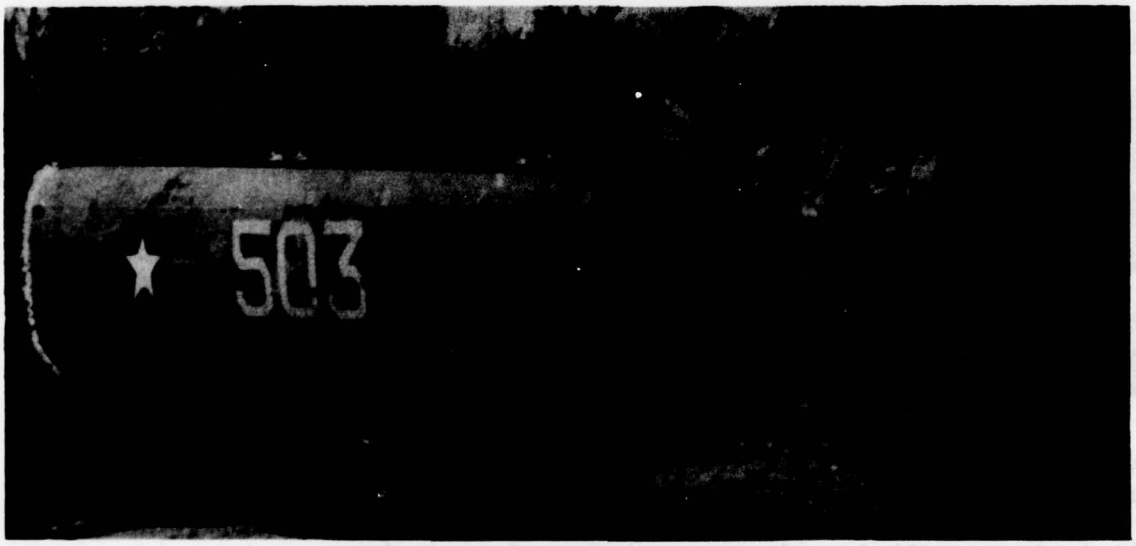


Figure 4 Damage inflicted on a Huey tail boom by a single 23mm HEI projectile hit while the tail boom was loaded to its maximum flight condition statically. The damage shown (complete severance of one side) would cause the helicopter to be killed if it were in flight.

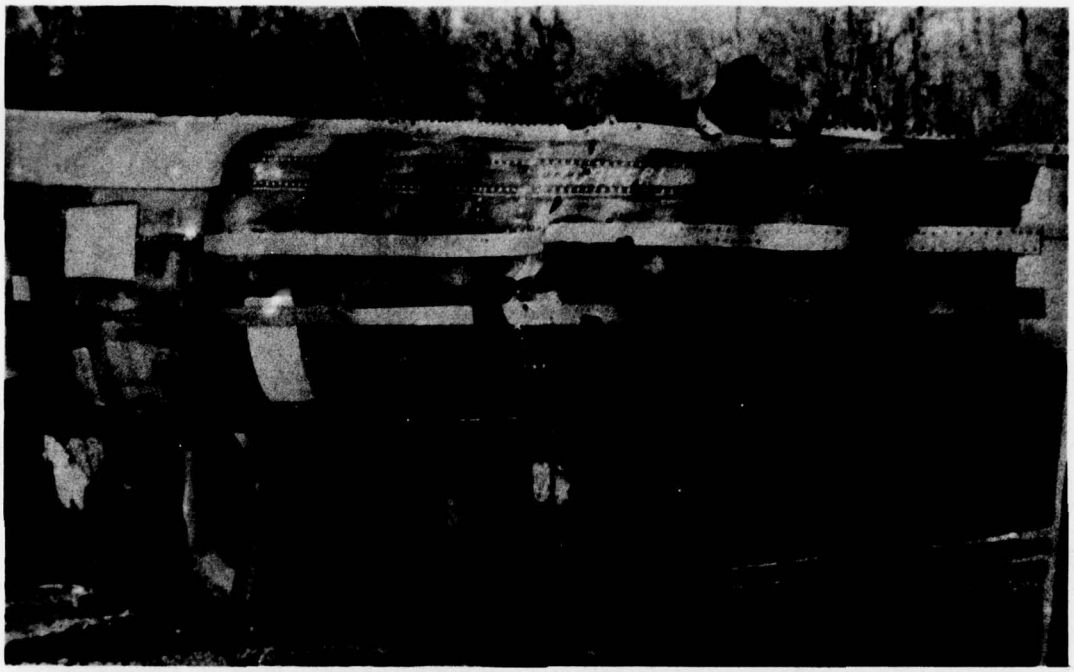


Figure 5 Huey tail boom modified with longitudinal straps, loaded to its 130 knots maximum flight condition statically and damaged by a single 23mm HEI projectile in the same area as shown in Figure 4. This modified tail boom sustained its maximum flight load while in the damaged condition shown.

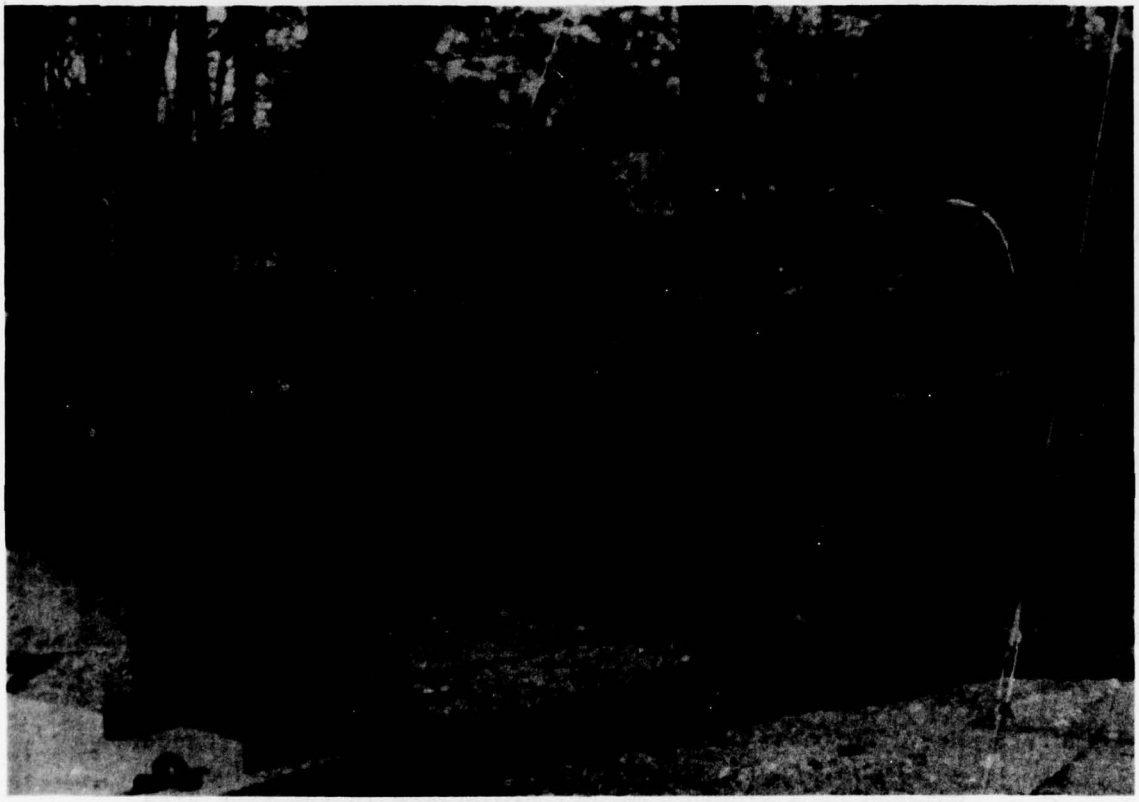


Figure 6 Tail boom with added external longerons damaged by three 23mm hits in adjacent bays. This modified tail boom continued to carry the full 130 knot forward flight load statically applied during and after damage incurred by the 23mm hits.

The test results of these bare charge and dynamic projectile firings are given in Table I. In this table the test number, modification (yes or no), applied load, bays damaged, skin loss-to-total skin affected ratio, and scaled deflection increment are listed. The test number indicates the type of boom (A for Cobra and B for Huey), the number of the boom tested (given by the first digit after the letters A or B), and the number of the test performed on the boom. For example, A1-2 refers to type A tail boom, the number 1 tail boom, and the second test firing into boom number A1. A total of five test firings were performed on boom number A1. Four of these were in bay 4-5 (tests A1-1 through A1-4), and one test firing was made in bay 7-8 (test A1-5). Bare explosive charges were used in these tests. The high explosive projectile was used as the damaging agent in all the other tests listed in Table I. In this table the applied load is listed as maximum flight load for all the tests except test B1. The applied load employed in test B1 was 63 percent of the maximum flight load. The extent of skin damage to the structures is listed in Table I as the ratio of skin that was lost because of the damaging agent to the total skin area in all bays affected by the damaging agent. Damage to the skin in terms of skin actually removed from the structure generally occurred over more than the target bay. The two adjacent bays generally suffered some skin loss as well as the target bay. Consequently, the total skin area affected was either the skin area in one, two, or three bays, depending upon whether skin loss was confined to only one bay or extended to a second or third bay, respectively.

The measures of damage tolerance used in these tests are: (1) whether the tail boom failed or sustained the applied load under fire, and (2) scaled deflection increment. Scaled deflection increment is the ratio of deflection caused by the incurred damage to the overall length of the tail boom. As described previously, this additional deflection is obtained by measuring the deflection after a test and subtracting from it the deflection of the tail boom under the applied load measured before the firing test. Scaled deflection increment is proportional to the maximum strain in the structure and as such is considered in this study as a good measure of damage tolerance. The lower the scaled deflection increment for a given amount of skin loss, the higher is the damage tolerance of the structure.

The data listed in Table I are discussed in the next section. The deflection data for the Cobra (type A) tail booms are shown in Figures 7 and 8.

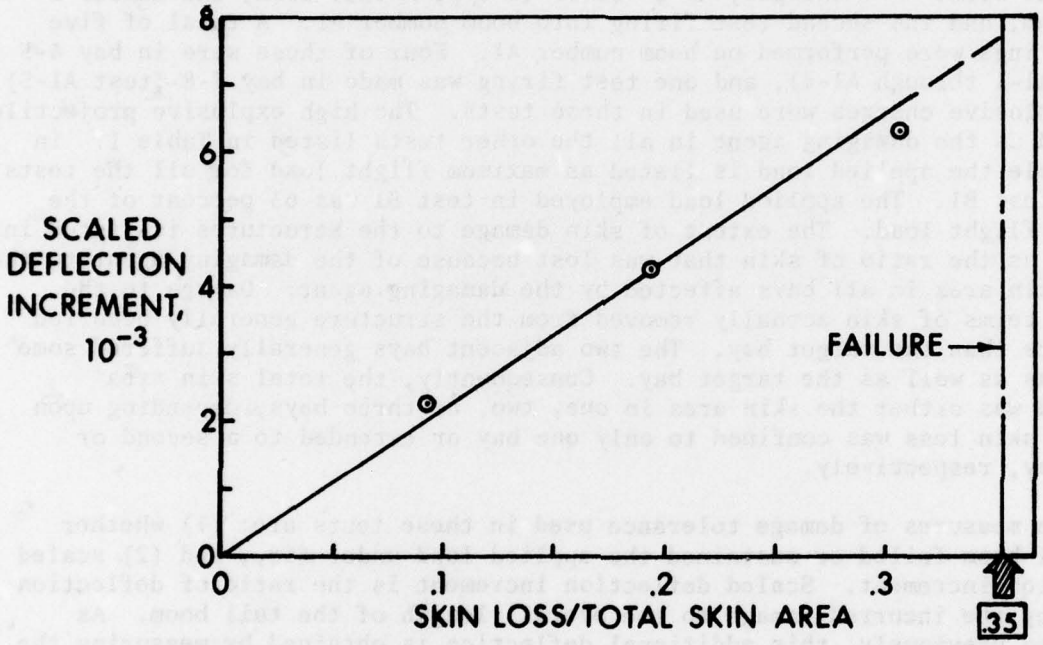


Figure 7 Deflection Incurred by Skin Loss in Bays 4-5.

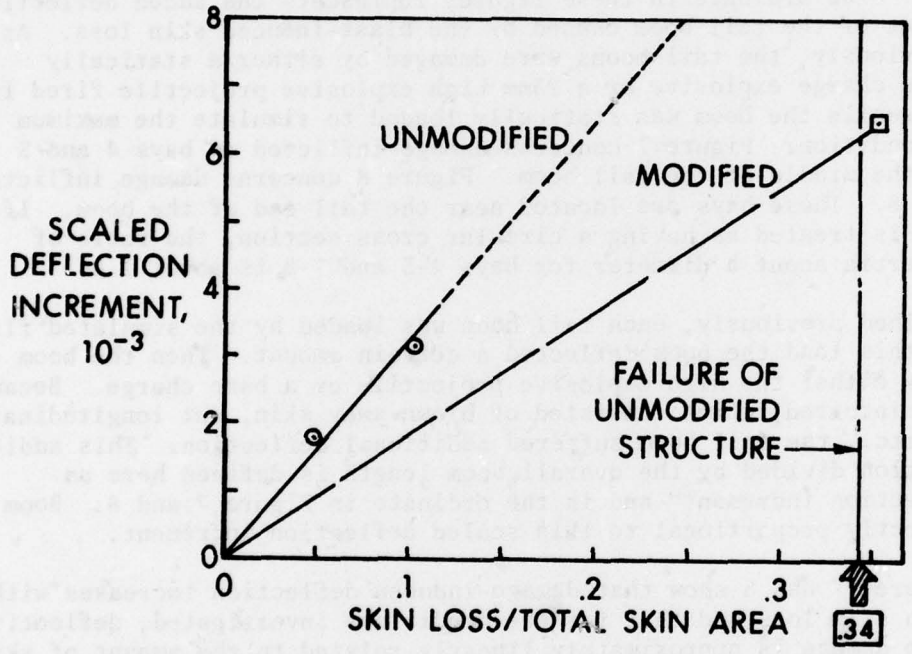


Figure 8 Deflection Incurred by Skin Loss in Bays 7-8 for Unmodified and Modified Tail Booms.

DISCUSSION

In this discussion, damage tolerance is characterized by scaled deflection increment. Scaled deflection increment is used to gauge the tolerance of the complete helicopter tail boom to structural damage. The test data listed in Table I for two separate bays of the Cobra, or type A, tail booms are shown plotted in Figures 7 and 8. The abscissa in these figures is skin loss from blast divided by the total area of skin in all bays damaged by the explosion. The ordinate in these figures represents the added deflection at the endpoint of the tail boom caused by the blast-induced skin loss. As described previously, the tail booms were damaged by either a statically detonated bare charge explosive or a 23mm high explosive projectile fired into the tail boom while the boom was statically loaded to simulate the maximum flight load condition. Figure 7 concerns damage inflicted on bays 4 and 5 located near the middle of the tail boom. Figure 8 concerns damage inflicted on bays 7 and 8. These bays are located near the tail end of the boom. If the tail boom is treated as having a circular cross section, the ratio of moments of inertia about a diameter for bays 4-5 and 7-8 is about 1.8.

As described previously, each tail boom was loaded by the simulated flight load. Under this load the boom deflected a certain amount. Then the boom was damaged by either the high explosive projectile or a bare charge. Because of the damage incurred, which consisted of blown-away skin, cut longitudinals, bent frames, etc., the tail boom suffered additional deflection. This additional deflection divided by the overall boom length is defined here as ""scaled deflection increment" and is the ordinate in Figure 7 and 8. Boom strain is directly proportional to this scaled deflection increment.

Both Figures 7 and 8 show that damage-induced deflection increases with an increase in skin loss and that for the conditions investigated, deflection caused by skin damage is approximately linearly related to the amount of skin lost. The intent here of presenting the data shown in these figures is purely to indicate trends and is not meant to be definitive. The vertical line labeled "failure" in both figures corresponds to the relative amount of skin removed by the bare charge or projectile in those tests in which the boom failed under the applied flight load. The skin loss associated with these failures does not necessarily represent the minimum amount of skin that has to be removed to cause the boom to fail. This value should be fairly well represented by the failure line of Figure 7 since the nearest data point, at skin loss/total skin area equal to about 0.3, is fairly close to the failure line where skin loss/total skin area equals 0.35. However, the modified structure failure line of Figure 8 at skin loss/total skin area - 0.34 is far removed from the next nearest data point at skin loss/total skin area equal to about 0.1.

The slope of the data line in Figure 7 corresponding to damage in bays 4 and 5 is 0.022 while the slope of the modified boom data line in Figure 8 corresponding to damage in bays 7 and 8 is 0.032, indicating that the damaged structure of bays 4 and 5 is 1.45 times stiffer than that of bays 7 and 8. This is understandable, particularly since the moment of inertia in the

undamaged state of bays 4 and 5 is approximately 1.8 times the moment of inertia of bays 7 and 8 in their undamaged condition, that is, the bulk of the structure in bays 4 and 5 is located farther from the boom cross section neutral axis than that of bays 7 and 8. This fact that damage tolerance increases with an increase in section size and structural stiffness was predictable before testing.

Figure 8 illustrates the result of longitudinally stiffening the tail boom. In this case two longerons and two lightweight stiffeners were added to the predominately tension side of the tail boom. These longerons and stiffeners were identical to those used in the original, unmodified tail boom. The resultant slope of the modified structure deflection-skin loss line is 0.018. This represents a 44 percent increase in stiffness over the original unmodified tail boom structure. Also, as indicated on the figure, at a skin loss to total skin area ratio equal to 0.34, the unmodified tail boom failed. (This value may actually be high since tests were not performed at skin loss/total skin area values between about 0.1 and this 0.34 figure.) However, the modified tail boom was able to carry the maximum flight load while sustaining skin loss/total skin area equal to 0.35 -- essentially the same value at which the unmodified tail boom failed. So, the additionally stiffened tail boom, with 35 percent of the skin in two adjacent bays lost due to blast damage, was able to sustain its load while an unmodified tail boom with the same damage failed. Furthermore, the stiffeners added 44 percent to the rigidity of the tail boom.

As described in the test description section, the effect of added stiffening on damage tolerance was also evaluated on the Huey, or type B, tail booms. Longerons and stringers identical to those used to modify the Cobra tail booms were employed on the Huey booms. Two longerons and two stringers each were added to both sides of the Huey booms whereas they were added to only one side of the Cobra booms. Three of the Huey tail booms were tested. One was used as a control and was tested in its original unmodified condition. The other two booms were tested as modified. A total of seven projectile firings were made into these booms. As indicated by Table I, a single shot into the unmodified tail boom caused it to fail, and this occurred with only 63 percent of maximum flight load applied to the tail boom. However, the modified tail booms, hit at the same point by the same type of projectile under the same firing conditions, were able to sustain the full, maximum flight load. Furthermore, as shown in Table I, a total of three projectiles each were fired into both of the modified tail booms -- both of which sustained the full, maximum flight load. Therefore, it may be seen that the added stiffening allowed the Huey tail booms to carry their maximum flight load while sustaining <u>multiple hits</u> in adjacent bays, whereas the unmodified tail boom failed at only 63 percent of its maximum flight load from the action of a <u>single</u> projectile.

CONCLUSIONS

1. Damage tolerance of the helicopter tail booms investigated in this study have been found to be proportional to the section modulus of the undamaged section and inversely proportional to the amount of skin removed from the structure by the damaging agent.

2. It has also been shown that an increase in longitudinal stiffening, achieved in this particular study by addition of longerons and stringers, can provide an increase in structural damage tolerance of at least 44 percent.

3. Furthermore, it has been demonstrated that the simple addition of a few lightweight longitudinal stiffening members can mean the difference between catastrophic failure of a helicopter tail boom from the damage caused by a single high explosive projectile and a tail boom that can continue to carry its maximum flight load with multiple hits in the same critical area by the same projectile. The longitudinal strap is a simple, low weight, low cost, and test proven modification applicable to both the Huey and Cobra helicopters. This modification consists of four longitudinal straps that can be rivetted to the outside of the tail booms in the field or by a manufacturing facility for about $1000. Total added weight is 9.7 lb or 4.5% of the present tail boom weight. The tests have demonstrated that, without the modification, the tail booms fail when hit in various critical regions by a single Russian 23mm HEI-T projectile. However, with the modification, the tail booms can survive multiple hits in adjacent bays.

SESSION III: OTHER EQUIPMENT

Chairman: M. Wright
Director of Materials Division
University of Tennessee Space Institute

STRESS-STRENGTH-STRUCTURAL RELIABILITY OF A ROAD WHEEL SPINDLE 203

J. E. Bilikam
B. Bordenkircher, and
J. Hendriks
FMC Corporation

DESIGN OF EXPLOSIVE BLAST CONTAINMENT VESSELS FOR EXPLOSIVE ORDNANCE DISPOSAL UNITS 215

B. D. Trott
J. E. Backofen, Jr., and
J. J. White, III
Battelle-Columbus Laboratories, and
J. Petty
Army Armament Research and Development Command

INTEGRITY ANALYSIS OF THE SEWARD STATION NUMBER 5 STEAM TURBINE ROTOR. 229

C. W. Marschall
A. T. Hopper, and
S. H. Smith
Battelle-Columbus Laboratories, and
W. J. Moll
Pennsylvania Electric Company

FINITE ELEMENT ANALYSIS OF THE MAGIS IAC ADP/COMM SHELTER 248

C. M. Blackmon
Naval Surface Weapons Center

STRESS-STRENGTH-STRUCTURAL RELIABILITY OF A ROAD WHEEL SPINDLE

J. EDWARD BILIKAM
Senior Reliability Engineer

BRUCE BORDENKIRCHER
Senior Design Engineer

JOHAN HENDRIKS
Staff Engineer - Analysis
FMC Ordnance Engineering Division
San Jose, CA 95108

ABSTRACT

This is a study of part design. The problem is fluctuating fatigue stresses on a roadwheel spindle. The solution chosen evolved thru three designs toward a final design with a median life of 58,229 cycles of wheel loading. The predicted life was accomplished from application of stress analysis and extended with a prediction of life dispersion.

NOMENCLATURE

S_t = nominal tensile stress

K_t = theoretical stress concentration factor

I/c = section modulus

σ_a = alternating component fluctuating stress

σ_m = steady component fluctuating stress

k = modifying factor

S_n = fatigue stress at N cycles

S_e = endurance limit

θ = scale parameter of Gumbel extreme value distribution

v = variance factor

R = reliability functional value

PRECEDING PAGE BLANK-NOT FILMED

INTRODUCTION

This report is a case study of part design. The part is a roadwheel spindle of a tracked vehicle being developed by the FMC Corporation for the U. S. Army. The design features are evidenced as the discussion of the progress toward an improved design proceeds. Because the spindle is an active suspension component taking the load of the vehicle during roadwheel travel, the main concern is fatigue. The goal is to keep the spindle at low weight while increasing the predicted reliability of the design. Reliability is expressed in terms of the number of fatigue cycles til failure. This, however cannot be predicted with certainty, therefore, a probability measure will be introduced.

In the first section the design changes in three steps will be described. The steps are three different parts 11672817, 12250918, and 12258631. The spindle is a steel forging machined to two bearing diameters (for roller bearings), a shoulder, etc. (See Figure 1).

The fatigue properties are enhanced by material improvements and stress relief in the area of the critical section of the spindle.

SPINDLE STRESS CHARACTERISTICS

Stress analysis across various sections of the spindle under four loading conditions shows that the critical section of the spindle is at the shoulder. This diameter is finished to a minimum 1.970" in step 1 design and changes to a minimum of 1.999" in step 3. The bending moment of 80,652 lb-in occurs here under load. This is a combined side wheel loading and vertical impact. The reverse stress condition applies when the vehicle is just settling on the torsion bars in a semi-static load. Then the bending moment obtains 26,720 lb-in adjusted to a lower value for torsion bar preset. The torsion bars are attached to the wheel spindle indirectly thru the road arm (and trunnion).

The typical bending stress is tension in the outer fibers, where the formula for the nominal stress, S_t is

$$S_t = Mc/I \qquad (1)$$

Here $I/c = \pi\, d^3/32$

for appropriate diameter d. Table I shows the parameter values for eacn step 1, 2, 3 in design. Stress values are given in pounds per square inch (psi) or million Pascals (1MPa = 10^6 newton's/meter^2).

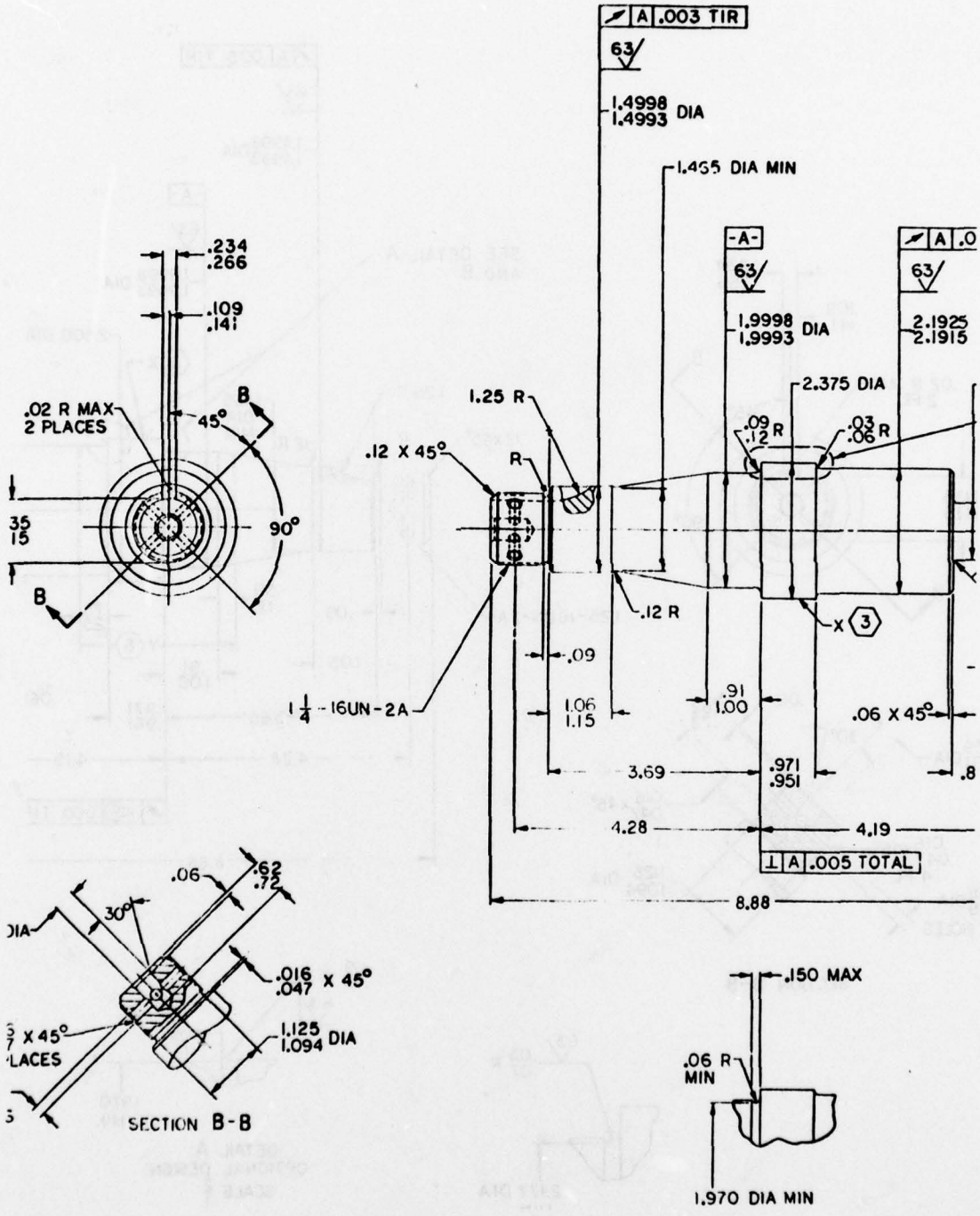


Figure 1(a). Spindle Detail (P/N 11672817)

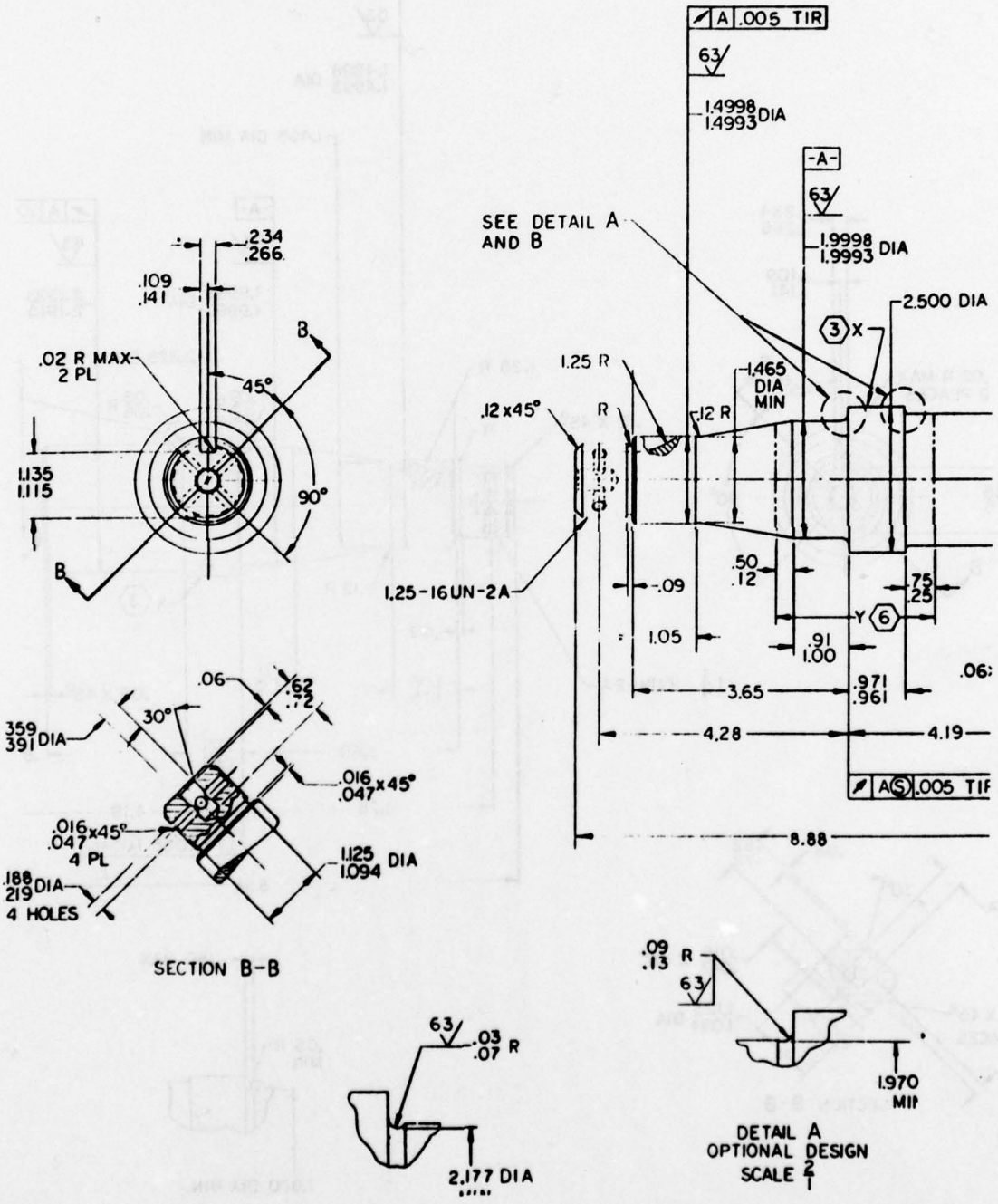
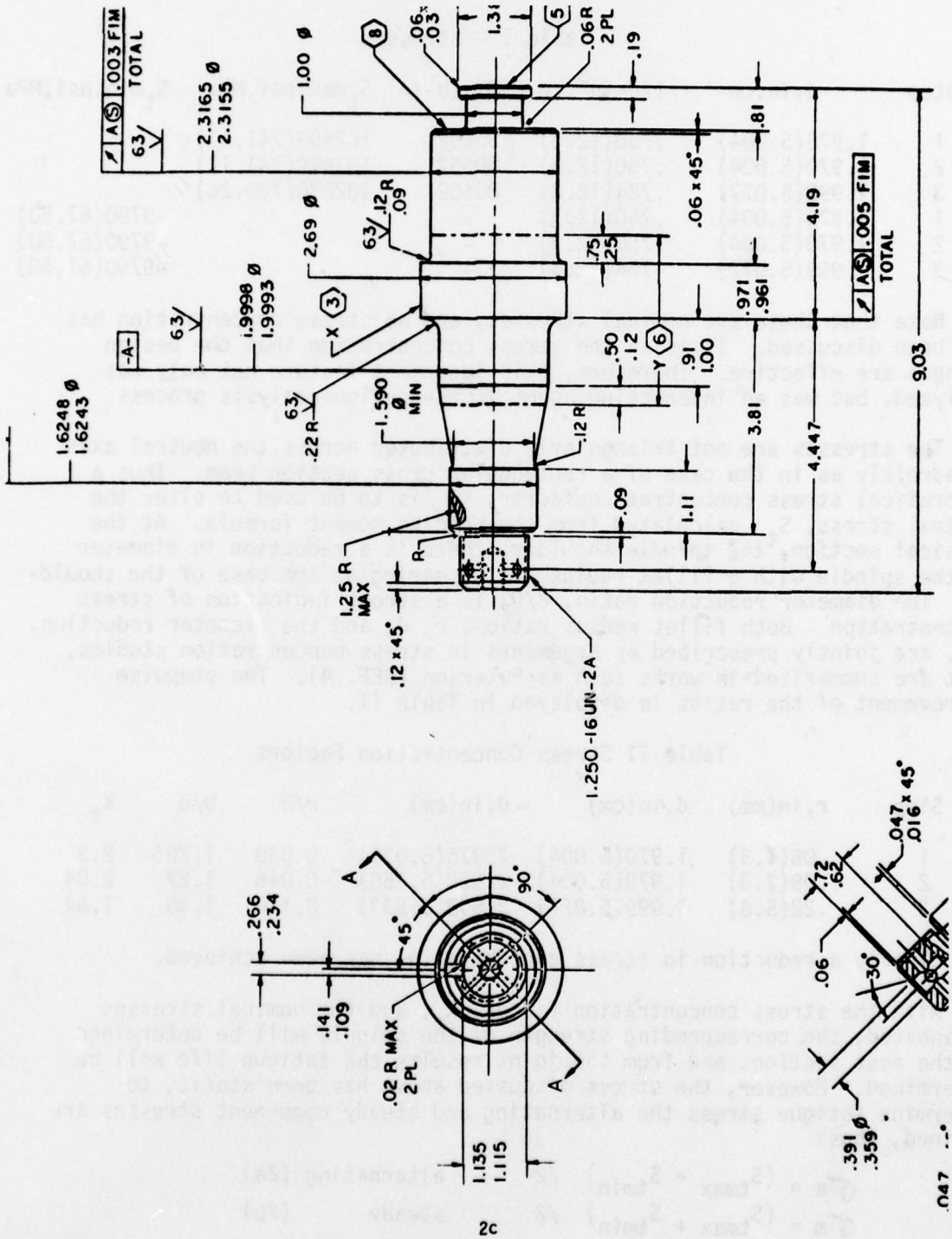


Figure 1(b). Spindle Detail (P/N 12250918)



2c

Figure 1(c). Spindle Detail (P/N 12258631)

Table I - Stresses

Step	d,in,cm	$I/C\text{-in}^3$,cc	M, lb-in	$S_t$max,psi,MPa	$S_t$min,psi,MPa
1	1.970(5.004)	.750(12.3)	80652	107499(741.17)	
2	1.970(5.004)	.750(12.3)	80652	107499(741.17)	
3	1.999(5.077)	.784(12.8)	80652	102870(709.26)	
1	1.970(5.004)	.750(12.3)	-		-9790(67.50)
2	1.970(5.004)	.750(12.3)	-		-9790(67.50)
3	1.999(5.077)	.784(12.8)	-		-9790(67.50)

Note that these are nominal stresses, and no stress concentration has yet been discussed. It is in the stress concentration that the design changes are effective. Therefore, this important feature not only was analyzed, but was an interacting agent in the design-analysis process.

The stresses are not triangularly distributed across the neutral axis as adroitly as in the case of a rectangular cross section beam. Thus a theoretical stress concentration factor, K_t is to be used to alter the nominal stress, S_t calculated from the bending moment formula. At the critical section, the spindle shoulder, there is a reduction in diameter of the spindle with a fillet radius, r, appearing at the base of the shoulder. The diameter reduction ratio, d/D, is a strong indication of stress concentration. Both fillet radius ratio , r, d, and the diameter reduction, d/D, are jointly prescribed as arguments in stress concentration studies, that are summarized in works such as Peterson (REF. 4). The stepwise improvement of the ratios is displayed in Table II.

Table II Stress Concentration Factors

Step	r,in(mm)	d,in(cm)	D,in(cm)	r/D	D/d	K_t
1	.06(1.5)	1.970(5.004)	2.375(6.033)	0.030	1.205	2.3
2	.09(2.3)	1.970(5.004)	2.500(6.350)	0.046	1.27	2.04
3	.22(5.6)	1.999(5.077)	2.690(6.833)	0.110	1.35	1.64

Clearly a reduction in stress concentration has been achieved.

With the stress concentration factor, K_t, and the nominal stresses delineated, the corresponding strength of the spindle will be determined in the next section, and from the joint results the fatigue life will be determined. However, the stress discussed above has been static, to determine fatigue stress the alternating and steady component stresses are defined, thus:

$$\sigma_a = (S_{tmax} - S_{tmin})/2 \qquad \text{alternating} \quad (2a)$$

$$\sigma_m = (S_{tmax} + S_{tmin})/2 \qquad \text{steady} \quad (2b)$$

These quantities are displayed in Table III.

Table III - Fatigue Stress

Step	σ_m Steady Component	σ_a Alter. Component
1	48855 psi (336.84MPa)	58644 psi (404.33MPa)
2	48855 psi (336.84MPa)	58644 psi (404.33MPa)
3	46540 psi (320.88MPa)	56330 psi (388.38MPa)

When the probabilistic definitions are considered, in the reliability section, the stress levels will be represented as modes, or the most frequently occurring values.

FATIGUE STRENGTH

The basic strength comes from the material, 4142H, 4145H, 8645H steel, where the "H" designates H steels of known hardenability band. 32-37 Rockwell C steel throughout is specified but further local properties are derived from flame or induction hardening. Induction hardening was accomplished only after step 1, the surface was later specified at 45-50 Rockwell C, to a 0.12 inch minimum depth.

Beyond the basic material, the fatigue endurance limit furnishes an insight to the life characteristics of the part. The endurance limit is evaluated from modifying "k" factors applied to a standard rotating beam specimen, with endurance limit Se'. The relationship, Shigley (REF 3) gives:

$$Se = k_a k_b k_c k_d \, Se'$$

where k_a; Surface factor = 0.89 for 63 finish

k_b; Size factor = 0.85 for $0.3" \leq d < 2"$

k_c; Reliability factor = 0.85 for 95% durability

k_d; Stress concentration modifying factor

The stress concentration modifying factor $k_d = 1/K_f$, is a defined quantity related to notch sensitivity q and the stress concentration factor K_t (table II).

$$K_f = 1 + q\,(K_t - 1) \qquad (3)$$

Because of the hardness of the material and the large fillet radius r, q=1 here. Thus $k_d = 1/K_t$. It is only required to render the endurance Se' to a numerical value to obtain Se. Shigley suggests that Se' is half the ultimate strength.

Table IV - Endurance Limit

	Se	Su
Step 1	19360 psi(133.48MPa)	140000 psi(965.26MPa)
2	22060 psi(152.10MPa)	140000 psi(965.26MPa)
3	39200 psi(270.27MPa)	200000 psi(1378.94MPa)

The actual fatigue strength of the spindle is represented as the S-N relationship, a well known log-log formula for steel:

$$N = 10^6 (S_N/Se)^M \quad \text{for } 10^3 < N < 10^6 \text{ cycles} \qquad (4)$$

The exponent $M = 3/\log_{10} (Se/.9S_u)$. The fluctuating stress condition imposes a restriction on the point failure, S_N, after N cycles, the restriction is actually a design prediction of the spindle life in endurance cycles. The Modified Goodman failure criteria has the form:

$$\sigma_a/S_N + \sigma_m/S_u = 1 \qquad \text{restriction}$$

The predicted strength is presented in Table V, this strength value will represent the mode of the probability distribution of the random material strength.

Table V - Modal Fatigue Strength

Step	1/M	N,cycles	S_N, psi, MPa
1	-.27116	34476	90078(621.06)
2	-.252255	37827	90078(621.06)
3	-.22066	58229	73413(506.16)

RELIABILITY

The stress exceeding the strength causes local failure. When the failure is general, the spindle is no longer serviceable. Over increased endurance cycles the working stresses cumulate and the strength declines - at some point there is a crossover of stress-strength. This is indicated by a point where the S-N curve crosses the cumulative stress curve. In the discussion above, the changes were evaluated in a parametric way, where it was noted that the predicted failure stress and predicted failure strength were not exact point at which failure must occur, but the most frequently occurring values at failure. In the appendix the probabilistic treatment of failure is derived. Under the assumptions of extreme value distributions of strength and stress, the parameters θ_1 and θ_2 are related to the modal strength and stress by the power formulas:[2]

$$\ln\theta_1 = S_e (10^{-6}N)^m \qquad \text{S-N relationship (mode)}$$

(decreasing)

$$\ln\theta_2 = A\,N^L$$

cumulative stresses (mode)

(increasing)

where A is a constant determined from the crossover point (S_N, table V). The exponent m = 1/M and the exponent L = 1.3.

The reliability function is shown in the appendix to be:

$$R(N) = 1/(1 + \theta_2 / \theta_1).$$

After some algebra it is found:

$$R(N) = 1/\ 1 + \exp(BN^m - CN^L)$$

The reliability function was evaluated by computer, for the final design only, the function is plotted in Figure 2. The first two steps of design, have reliability function that are to the left of Figure 2 on a lower scale (not shown).

In the appendix, the derivation of the reliability includes only two parameters, θ_1 and θ_2. These parameters are sufficient to locate the crossover point S_N but not to determine the variation of the random variate number of fatigue cycles. Therefore, a linear function of the nominal number of fatigue cycles, 58229 cycles, was derived empirically from the following data:

$$N' = (N-58229)\ \ v + 58229 \text{ for } 10^3 \leq N' \leq 10^6$$

Table VI - Computer Generated Reliability

v	Percentile Range/Median
.00020	0.271
.00010	0.539
.00008	0.679
.00006	0.872
.00004	~1.3

Values of the percentile range/median ratio in Table VI were compared with some data in the ASM Metals Handbook Vol 1, Ref. No. 1, on dispersion of fatigue data points. The percentile range/median ratio is defined as $N'_{.95} - N'_{.05}/ N'$ median, with a value of about .9 in the dispersion data. It was concluded that v = 0.00006.

Note that the linear transformation is such that $N' \neq 0$, but this corresponds to the band limited condition of the S-N relationship.

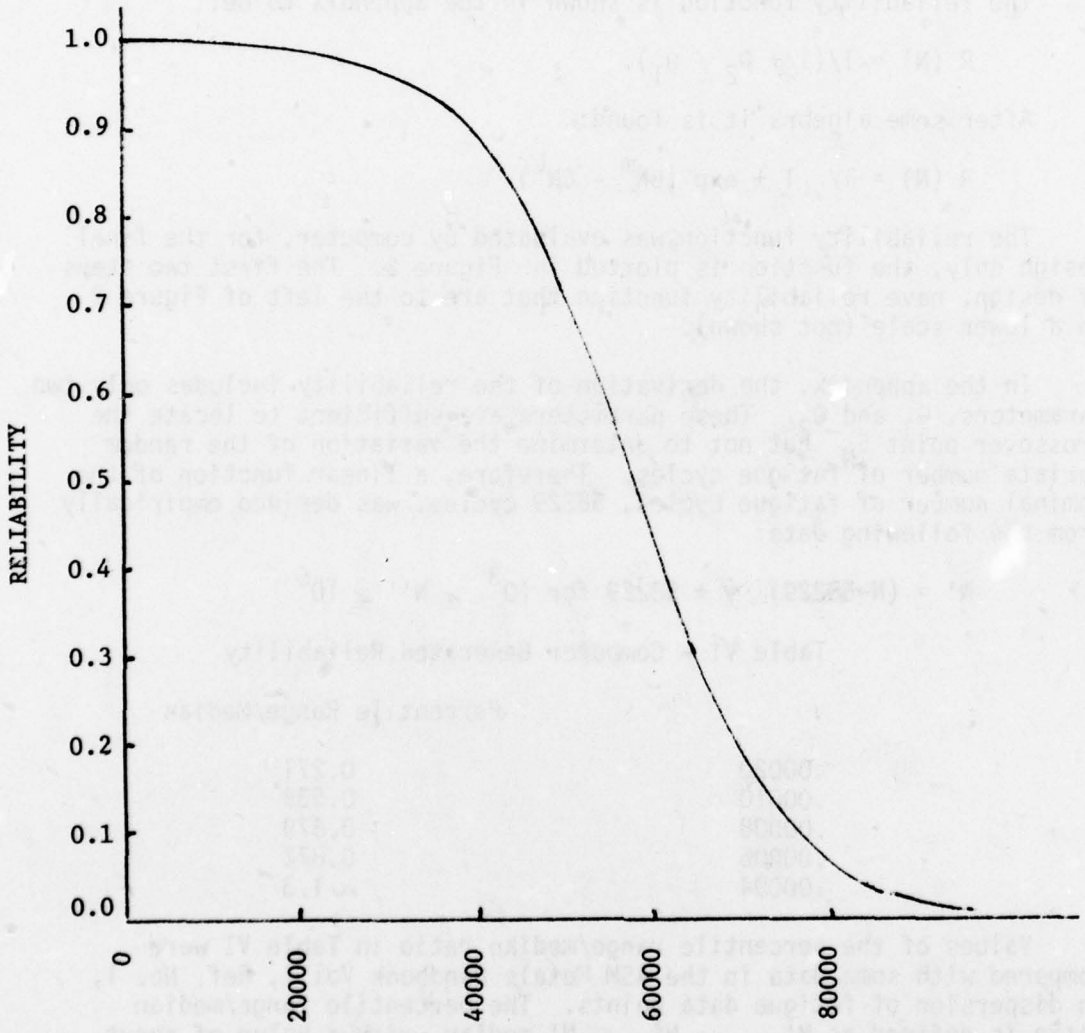


Figure 2. SPINDLE RELIABILITY

SUMMARY

Three designs of a roadwheel spindle have evolved from the interaction of stress analysis-design change-reliability analysis. The changes proceeded thru material specification and stress relief to a much improved part. The predicted life in endurance cycles range from 34476 to 58229. There is, however, considerable dispersion in the predicted life represented by the fatigue reliability function of the final design.

REFERENCES

1. American Society of Metals, Metals Handbook, Vol 1, 8th Edition 1967

2. Bilikam, J. E., "Strength-Stress-Reliability" Working Paper, FMC TR3218, 1977

3. Shigley, J. E., Mechanical Engineering Design, McGraw Hill 3rd Edition 1977

4. Peterson, R. E., Stress Concentration Factors, John Wiley & Sons, 1974

APPENDIX - RELIABILITY

Both strength and stress are considered random processes with random variates:

Strength: $X(t)$ ... d.f. $F_t(x|y)$

Stress: $Y(t)$ ... d.f. $G_t(y)$

The strength distribution function $F_t(x|y)$ is conditional probability $P(X(t) \leq x \mid Y=y)$, it is necessarily conditioned on the stress because the physical realization of strength is only found when a stress is applied. Thus material strength test is conducted at a known stress level y, applied to the material and then the strength is inferred from the type of failure (i.e., yield, ultimate, elastic strain, etc.) that has been observed.

Failure occurs locally in the material where the strength is exceeded by the stress in magnitude. However, reversed stress are possible, that is negative stresses (i.e., compression) and positive stresses (i.e., tension) are present. The reliability function is then the set function determined from the event that $X(t) < y < o$, the strength is less than the negative stress (i.e., more compressive strength than stress) and in the event that $X(t) > y \geq o$, the strength, is greater than the stress (i.e., more tensile strength than stress). The two events are mutually exclusive. Thus the reliability:

$$R(t) = P\ (X \geq y \mid y \geq 0\ ) + P\ (X \leq y \mid y \leq 0)$$

A reduction of notation is now used to obtain an expression for the reliability in Stieltjes integral form, for $F_t\ (x|y)$ write $F(x)$ and for $G_t(y)$ write $G(y)$.

$$R(t) = \int_0^{\infty} 1 - F(y) \quad dG(y) + \int_{-\infty}^{0} F(y) \quad dG(y) \quad \text{(A-1)}$$

with no reversed stress, $G(y) = o$ (A-2) for negative values of y.

It is now clear that the distribution functions of X(t) and Y(t) contain the theory that will be used here to evaluate the reliability function R(t). These distribution functions will have parameters that are monotonic in the continuous time parameter t (the age or life). In the sections to follow the monotonic age parameters correspond to working stresses and deteriorating strength.

The integrals in equation (A-1) are evaluated here for the two given extreme value distribution:

$$F(x) = 1 - \exp\ ((-\exp x) / \theta_1)$$

$$G(y) = 1 - \exp\ ((-\exp y\ ) / \theta_2)$$

Note that a single parameter only is given for each distribution function F, G. This must be compensated for when the variability of the strength and stress are considered. The mode of the extreme value distributions is $\ln\theta$. Substituting the formula into Equation (A-1) the reliability obtains:

$$R(t) = 1 - \exp\ (-1/\theta_2) + 2 \exp\ (-1/\theta_1 - 1/\theta_2) - 1$$

$$(\theta_2/\theta_1 + 1)$$

Applying Taylor series analysis estimation methods, with $\ln\theta$, and considered large (20,000) so that θ_1 and θ_2 are very large, the reliability approaches

$$R(t) = 1/(\theta_2/\ \theta_1 + 1).$$

The estimate has a Landau function:

$$O((1/\theta_1 + 1/\theta_2)^2).$$

DESIGN OF EXPLOSIVE BLAST CONTAINMENT VESSELS FOR EXPLOSIVE ORDNANCE DISPOSAL UNITS*

B. DALE TROTT
Senior Research Scientist

JOSEPH E. BACKOFEN, JR.
Principal Research Scientist

JOHN J. WHITE, III
Principal Research Scientist
Battelle, Columbus Laboratories
Columbus, OH 43201

JON PETTY
Project Engineer
U.S. Army Armaments R&D Command
Large Caliber Weapon Systems Laboratory
Dover, NJ 07801

ABSTRACT

This paper describes an experimental and analytical investigation of the design and performance of closed spherical vessels for containment of explosive blast for application by explosive ordnance disposal teams. The design criteria for the spherical shell, port reinforcing ring, and internally overlapping door are discussed. An extensive program to evaluate the performance of eight vessels was completed. Good agreement was obtained between dynamic strain gage records and elastic-plastic model predictions of a thin shell for the first cycle response to the high explosive 50/50 Pentolite in 3.0-ft (91-cm) and 4.5-ft (137-cm) diameter vessels. Agreement was also good between the model and plastic deformations observed on 2.0-ft (61-cm) diameter vessels. The ultimate failure mode for bare charges appears to be from the "static" internal pressure from the detonation product gas.

INTRODUCTION

The Battelle Ordnance Technology Group has been involved for several years in a program sponsored first by the Army and more recently by the Navy for the development of portable, affordable, and reliable explosion containment vessels. The primary goal has been to provide explosive ordnance disposal teams with a convenient and safe means of transporting hazardous explosive devices in built-up urban areas. Additional applications include various aspects of explosive device manufacture and disposal (demilitarization).

---

*Research supported by the U. S. Army Picatinny Arsenal, Dover, N.J. under Contract No. DAAA21-72-C-0129.

Spherical vessels have the advantage of biaxial strain for efficient energy absorption and an absence of sharp corners, where shock loading can be greatly intensified. The requirements for a portable, low usage device have lead to the selection of a design capable of several percent plastic deformation as the result of a single design-limit explosion. Two of the more challenging aspects concern vessel material selection for low service temperatures and control of high velocity fragments. Both of these aspects are topics of research in progress not reported here.

The vessels discussed in this paper demonstrated an acceptable design approach for explosion blast containment. Since then a number of additional requirements have been addressed with vessels employing a variety of steels and door closure designs, but the basic design principles have held up quite well. The early vessels were mounted in cradles or had four casters. Figure 1 shows a prototype trailer-mounted, 3-ft (91-cm) diameter, 0.72-inch (1.83-cm) wall thickness vessel with an externally hinged door, which is a direct result of the research reported here. Guidance and information from Picatinny Arsenal and the FBI Bomb Data Program concerning this vessel have been published.[1,2]

The following sections of this paper discuss the analytical, design, and experimental efforts of the initial Army program. A brief overview of the current program is also provided. The emphasis has been given to principles of explosion containment design and development. Specific engineering details are available in Reference 3.

DESIGN AND ANALYSIS

The general design procedure that has emerged for a spherical, totally-enclosed explosion containment vessel involves the following steps:

- Analyze and refine the engineering and operational requirements.
- Select the vessel material based on cost, availability, yield strength, ductility, lowest service temperature, fracture toughness, and weldability.
- Select the vessel diameter and door closure mechanism in light of the operational requirements and engineering experience with door designs.
- Select the vessel wall thickness in consideration of the maximum explosive charge anticipated, the configuration of the most severe design explosive device, the maximum allowable vessel weight and the permissible amount of plastic deformation in the vessel wall as the result of a single detonation.
- Design a compatible vessel door and port reinforcing ring using procedures outlined below.

- Design the door closure system in consideration of structural and operational requirements.
- Perform a detailed design, specifying welds, door stops, door support, door closure mechanism, charge support system, lifting rings, doubler plates, etc.
- Design the transportability items, such as the trailer, cradle, or casters, etc.
- Iterate the general design procedure at least once to approximate practical optimization within the constraints.

The general design procedure originated with the initial Army program[3] and has been refined by recent projects. Feasibility at room temperature was the initial concern. Hot pressed hemispheres of A537 or A516 steel were selected primarily from cost and availability considerations. Figure 2 gives a schematic side view of a 4.5-ft (137-cm) diameter, 1.0-inch (2.5-cm) wall thickness vessel with a single-pin door support mechanism, which is a design representative of the vessels evaluated experimentally for the Army.

For the explosive ordnance disposal application, a relatively large port is required for insertion of the potentially odd-shaped bomb package. We have limited the port size to not greater than the vessel radius for practical reasons. The resulting vessel radius has been large enough that the

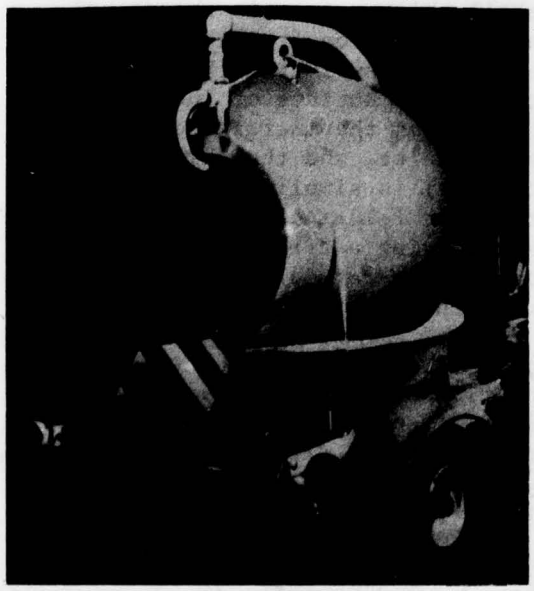


FIGURE 1. Trailer-mounted containment vessel with an externally hinged door. Vessel weighs 900-lbs (409-kg).

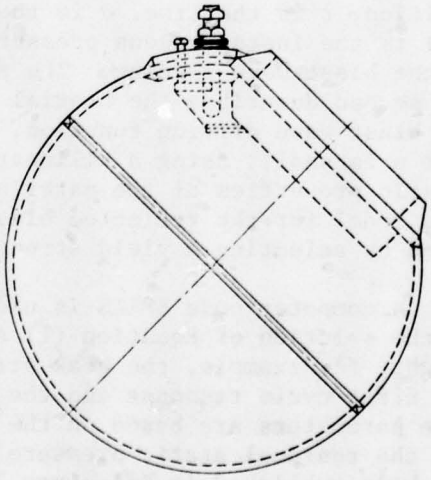


FIGURE 2. Schematic side view of a 4.5-ft (137-cm) diameter spherical containment vessel with a single-pin door support mechanism (U. S. Patent 4,056,212).

only remaining design analysis is to determine the wall thickness. In general, however, the analysis outlined can be used to determine both vessel radius and wall thickness.

SHELL ANALYSIS

In this section we discuss a design tool used for selection of the spherical shell dimensions for a given size of explosive device, amount of explosive to be contained, and type of material selected for the structure.

Although subsequent motions of the shell are quite complicated due to the asymmetric mass distribution, the first cycle response of the explosion containment vessel shell to the detonation of a centrally located spherical charge of explosive is well approximated by the radial "breathing" mode of a simple thin shell. This problem was adequately described by W. E. Baker[4] and will be summarized briefly.

The one-dimensional differential equation of motion for a unit area of the shell is given by:

$$\rho h \frac{d^2u}{dt^2} + \frac{2h\sigma}{a} = p(t), \qquad (1)$$

where ρ is the mass density, h is the shell thickness, a is the vessel radius, u is the displacement in the radial direction from the initial position, t is the time, σ is the tangential stress in the thin shell, and p(t) is the instantaneous pressure on the inside surface of the shell due to the blast wave loading. The first term gives the inertial effect, the second describes the biaxial stress restraint, and the third expresses the blast wave driving function. Equation (1) is simplified by assuming that u is small, using a bilinear constitutive relation for the elastic-plastic properties of the material, and employing a triangular pressure-time model for the reflected blast wave. Strain rate effects are approximated by selecting a yield strength larger than the static value.

A computer code SPLAS is used to calculate the significant aspects of the solution of Equation (1) as a function of the explosive charge weight, for example, the peak stress, strain, and time of occurrence of the first cycle response and the resulting residual strain. The shock wave parameters are based on the synthesis of data on Pentolite by Goodman[5] and the residual static pressure results of Proctor.[6] Further explanation has been published in Reference 7.

The vessel thickness is principally selected by examining a parametric output from SPLAS to insure that the single shot response of the vessel will not exceed a specified user criterion, for example, a peak first cycle stress equal to some fraction of the yield stress (e.g., 50 percent) or perhaps a particular incremental residual strain (e.g., 1/2 percent).

Accuracy of the elastic-plastic response predictions can be improved using experimental results from an earlier vessel made of the same material.

It was found from log-log plots of the peak first cycle stress σ versus the explosive weight w, the thickness h, and the diameter ϕ that a simple, accurate scaling law could be obtained for the elastic response of steel vessels. Using the elastic constitutive relation:

$$\sigma = \frac{E}{1-\nu}\varepsilon = \frac{E}{1-\nu}\frac{u}{a}, \tag{2}$$

where ε is the strain, $E = 30 \times 10^6$ psi (207 GPa) and $\nu = 0.28$, we obtained graphically the formula

$$\sigma = c_o w^{0.768} h^{-1.0} \phi^{-1.324}. \tag{3}$$

Expressing σ in psi, w in pounds, h in inches, and ϕ in feet, we found $c_o = 9.80 \times 10^4$. Expressing σ in MPa, w in kilograms, h in centimeters, and ϕ in meters, we determined $c_o = 653$.

An important design point concerns the significant weight advantage possible if an elastic-plastic response of the vessel shell is selected. It is straightforward to show using the impulse approximation[7] that an elastic-plastic design translates into a weight advantage ratio over a conservative elastic design ($\varepsilon_{max} = 0.2\varepsilon_y$) varying from 5 to 35 depending on the frequency of intended use.

DESIGN DISCUSSION

As described in the introduction, a spherical geometry was selected for the blast containment chambers under development. To meet the requirements of the explosive ordnance disposal application, a relatively large access port is needed to allow for the easy insertion of shapes such as attache´ cases. Such a port will require a reinforcing ring at its edge to prevent a large stress concentration in the spherical vessel shell when internally pressurized by the detonation product gas.

Considerations of maximum strength, desired low cost, and high reliability indicated in our judgment that the closure door should be designed to overlap the inside edge of the port reinforcing ring over the full 360° of the port. Practical considerations suggested that the maximum port opening diameter in the spherical vessels should not appreciably exceed the radius of the vessel. Following these guidelines design techniques described in this section were developed which have proven to work satisfactorily when fabricated from tough, ductile materials. However, certain aspects of the design, for example, the configuration of the door cross section, have not yet been fully optimized from a minimum weight standpoint.

Due to the nearly total absence of experimental data on vessels for the complete containment of explosive blasts at the beginning of this program and the relatively high cost of complete dynamic analysis of a blast containment vessel equipped with the desired large port, a relatively simple design technique based on static internal pressure loading of the vessel and port was developed. To keep the analysis simple and allow the generation of experimental data for comparison, the vessel wall thickness was restricted to 1/20 or less of the vessel radius. This constraint allowed use of thin shell analysis with some confidence.

The concepts behind the design of the reinforcing ring and door were:

- The deflection of the sphere and the ring were to be equal at their weld junction.
- The maximum stress in the door was to be no greater than the maximum stress in the sphere.
- All eccentricities of load paths were to be minimized.
- Adequate bearing area to prevent premature plastic deformation was used in the overlap area of the ring and door.

Elastic analyses for static loading from handbook formulas[8,9,10] for stresses and deflections were used to derive expressions for the pertinent quantities as shown in Figure 3. The meaning of the symbols not defined by the figure are as follows:

σ_s = stress in the shell due to static pressure loading.

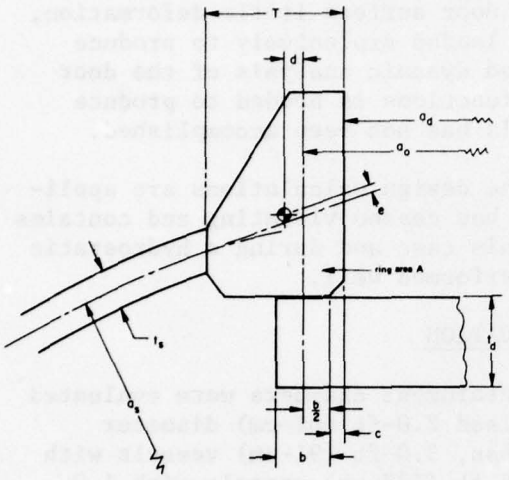
σ_b = the lower of the compressive yield-stress values for the door and ring materials.

ν = Poisson's ratio.

This figure and its equations were used to iterate the cross section of the ring from rectangular to a trapezoidal cross section in order that:

- The transition or change in cross section between the sphere and the ring could be made as smooth as possible to avoid large stress concentrations.
- The sum of the moments caused by the bearing load from the door and the loading by the sphere could be made as near equal to zero about the centroid of the ring cross section as possible to minimize the tendency of the ring to twist under load.

The use of static design for a structure to be dynamically loaded cannot be defended in principle. In this application, however, it led to a good practical design for the ring and perhaps somewhat of an overdesign



$$b = (\sigma_s/\sigma_b)(a_o/a_s)t_s,$$

$$t_d = \left[\frac{3}{4}(3+\nu)\,a_o^2/(a_s/t_s - \frac{1}{2}(\frac{3+\nu}{1-\nu}))\right]^{1/2}$$

$$A = \frac{a_s t_s}{(1-\nu)} \cos\phi_o \sin\phi_o,$$

where

$$\phi_o = \sin^{-1}(a_o/a_s),$$

$$e = d\frac{a_o}{a_s}.$$

FIGURE 3. Geometry of the junction between the sphere, port reinforcing ring, and door, and design equations.

for the door. The large mass concentration represented by the ring and door in comparison to the spherical shell means that they move more slowly under the impulsive blast load. There appear to be two major results of this inertial mismatch. One is that the ring and door deform plastically much less than the spherical shell at points away from the ring. The elastic deflection matching technique employed for the ring design meant that the ring was designed to operate at somewhat lower stresses since it is primarily in uniaxial tension leading to a lower effective modulus. This design approach would be expected to produce smaller strains in the ring as well. This feature for the ring has been retained in subsequent designs because it better retains the overlap of the door after plastic deformation of the vessel.

The other major result is that the vessel responds in an asymmetric manner leading to the generation of bending modes of vibration near the ring-shell interface. These bending modes focus at the pole of the shell opposite the port after several cycles of vibration of the fundamental "breathing" mode of the shell. This focusing action leads to up to five times the first quarter cycle maximum surface strain at this location for small, otherwise elastic impulsive loadings of the shell. These large localized surface strains could lead to a fatigue failure in this area after repeated loadings, although this possibility has not yet been investigated in depth. At larger loads when the shell is slightly deformed plastically, the plastic deformation appears to damp out the vibrations leading to these large late-time strains.

The design thickness for the door presented here is quite conservative. In practice, it has been observed that the door suffers little deformation, if any, even when the spherical chamber is loaded explosively to produce significant plastic deformation. A detailed dynamic analysis of the door using realistic blast loading and support functions is needed to produce a minimum weight door design. To date, this has not been accomplished.

The static loading formulas used in the design calculations are applicable to the state of the chamber after it has ceased vibrating and contains the high pressure gaseous products. For this case and during a hydrostatic test of one chamber, the stated criteria performed well.

EXPERIMENTAL EVALUATION

Eight spherical experimental blast containment chambers were evaluated in the programs reported here. They comprised 2.0-ft (61-cm) diameter vessels with 0.5-inch (1.3-cm) wall thickness, 3.0-ft (91-cm) vessels with 0.72-inch (1.83-cm) wall thickness, and 4.5-ft (137-cm) vessels with 1.0-inch (2.5-cm) wall thickness. A total of 117 charges were detonated in the vessels, comprising five explosive compositions and three principle charge configurations. In a limited series of tests the air in the vessels was partially replaced by experimental shock attenuating materials. All charges were detonated in the center of the vessels.

All of the vessels were completely enclosed using doors which overlapped the port rings from the inside. Three different types of door closure mechanisms were employed. They were: an internally hinged door with hinge pins vertical; a subsequently patented mechanism (see Figure 2), which supported the door on a single vertical pin penetrating the vessel wall to allow external operation of the door; and the external hinge design shown in Figure 1.

Two principal diagnostics were used to measure the performance of the vessels. One was foil-type strain gages bonded to the vessels at various points. These served to monitor the dynamic performance of the vessels during explosive loading and the residual plastic strains at low values of strain. Specialized techniques[3] were required to maintain the integrity of the gage adhesive bond and associated wiring during the large impulsive loads encountered.

The second principal diagnostic consisted of a number of gage lengths between adjacent reference marks on the vessel surface. These were generally arranged along three orthogonal great circles. Measurement of these gage lengths between experiments produced data reducible to the plastic strain distribution over the vessel surface, and allowed calculation of the average vessel strain.

HYDROSTATIC RESPONSE

A 4.5-ft (137-cm) diameter, 1.0-inch (2.54-cm) wall thickness vessel was filled with liquid, sealed, and pressurized to obtain a calibration of the strain gage response with internal pressure. The investigation served to verify the dynamic results, as well as showing something of the vessel material properties. The pressure readings were obtained with a BLH SR-4 pressure transducer.

Figure 4 gives an example of the data for strain gage 3 located at the pole position opposite to the door. The hydrostatic test was conducted in three cycles of pressurizing as indicated. The data was linear with no hysteresis up to 1500 psi (10.34 MPa) on the first cycle, which corresponds to no significant plastic deformation for stresses up to 20 ksi (137.9 MPa). Pressurization on the second cycle was terminated at 2725 psi (18.79 MPa) when creep became noticeable. On the subsequent depressurization and repressurization, plastic deformation was confirmed and some work-hardening demonstrated. The pressure was taken to 2885 psi (19.89 MPa) during the third cycle, corresponding to 39,700 psi (273 MPa) biaxial stress or 80 percent of the minimum 50 ksi (345 MPa), 0.2 percent offset yield strength expected for this A-537 material. Further details on the creep data are available.[3]

DYNAMIC MEASUREMENTS

The results obtained included measurements of the effects of explosive charge weight, composition, and configuration on both the dynamic and residual plastic strain of the vessels under explosive loading. The attenuating effects of experimental vessel-fill-materials were also obtained. Of these we report only selected results of the effects of charge weight here to illustrate verification of the design methodology. The complete results of all tests are given in Reference 3.

Figure 5 shows the comparison of the first cycle maximum strains measured from the dynamic strain gage records with the same quantity calculated from the analysis for the 4.5-ft (137-cm) diameter vessels. The predicted curve was calculated using the data for full density 50/50 Pentolite.[5] Our data were taken using low-density, 0.73-0.80 g/cc, granular Pentolite which produces a much lower initial shock pressure.[11] We ascribe the difference between the predicted curve and the curve fitted to the data shown in Figure 5 to this effect. A nearly identical comparison between theory and experiment was obtained in a 3.0-ft (91-cm) diameter vessel, thus verifying the scaling relationships as well.

Figure 6 shows the maximum strains observed, independent of their time of occurrence, taken from the same data set plotted as first-cycle response in comparison. The occurrence of the large maxima shown, are explained by the generation of a flexural mode oscillation at the port-vessel skin interface, where the ring and door respond less rapidly to the impulsive load than the vessel skin due to their higher masses. This flexural mode wave is

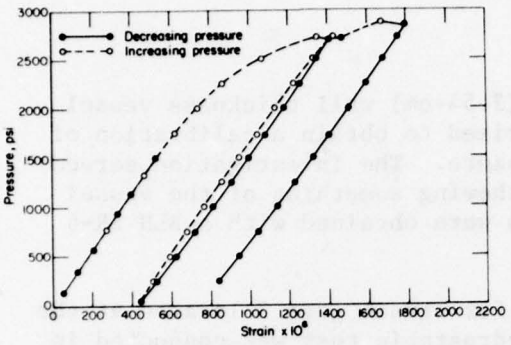


FIGURE 4. Hydrostatic Pressure Versus Strain for a 4.5-ft (137-cm) Diameter, 1.0-inch (2.54-cm) Wall Thickness, Spherical Vessel with a Single Pin Door Design.

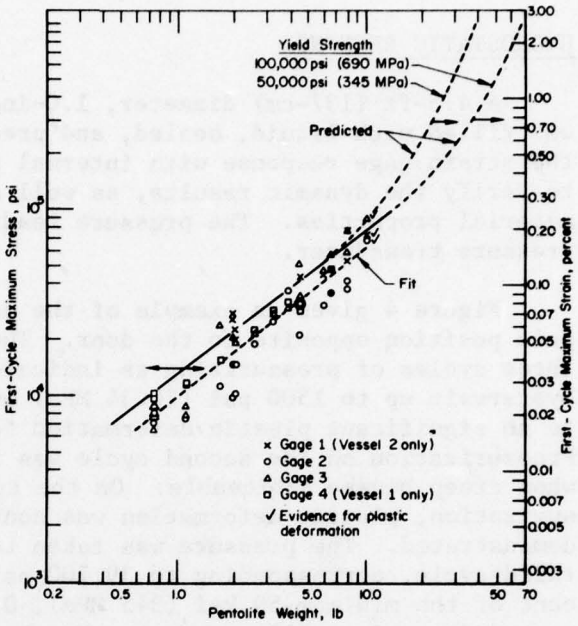


FIGURE 5. Experimental and Theoretical First-Cycle Response of 4.5-ft (137-cm) Diameter, 1-inch (2.54-cm) Wall Thickness Spherical Vessels to Compact Pentolite Charges.

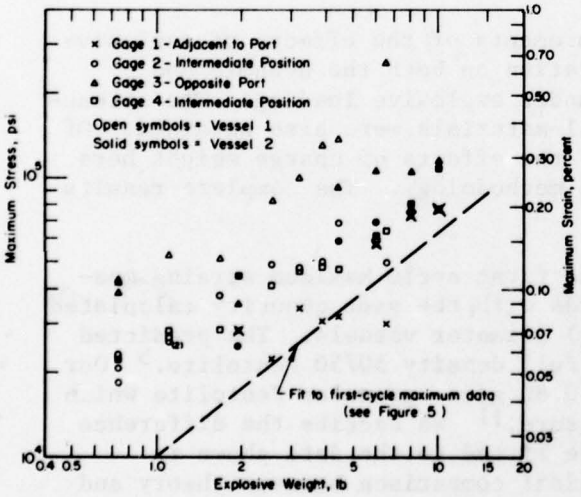


FIGURE 6. Maximum response of the 4.5 ft (137-cm) Diameter, 1-inch (2.54-cm) Wall Thickness Spherical Vessels to Compact Pentolite Charges.

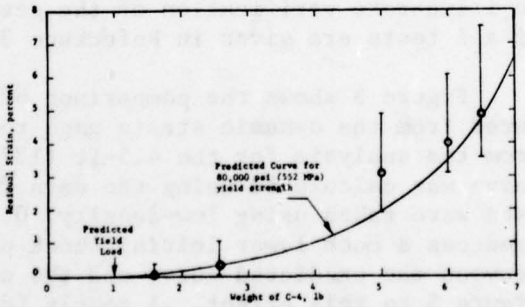


FIGURE 7. Comparison of Predicted and Observed Residual Strains from Detonation of Spherical Charges of Composition C-4 Explosive in new 2.0-ft (61-cm) Diameter, 0.52-inch (1.26-cm) Wall Thickness Spherical Vessels.

constrained to a small amplitude near the ring, as evidenced by the fact that the gage 1 records do not show large maxima. As the wave propagates around the vessel, the maximum observed strain occurs later in time and with larger amplitude as observed on the dynamic records. Figure 6 shows the increasing amplitude of this wave through gages 2 and 4, reaching a maximum at gage 3 as the wave converges at the pole opposite to the port. Huffington and Robertson[12] calculated a similar phenomenon using the PETROS 3.5 finite difference computer program for an explosively loaded hemisphere.

As shown in Figure 6, dynamic, oscillatory surface strains up to 0.65 percent were recorded, which most certainly caused at least local plastic deformation, although no permanent strain was detected using gage length measurements on the vessel surface, with a precision of at least 0.1 percent. Static strain gage measurements showed random compressive and residual strains of only 0.01 percent following shots with maxima above 0.3 percent strain. The point of this observation is that vessel designs intended for the containment of many repeated detonations must be carefully evaluated for the possibility of fatigue failures due to these high amplitude oscillatory stresses which may be seen to reach five times the amplitude of the primary first cycle maximum stresses. To date our programs have not been concerned directly with this problem, as the explosive ordnance disposal application is infrequent in nature and is more concerned with the containment of large charges where general plastic deformation of the vessel is expected to be the primary failure mode.

Before passing on to the effects of overall plastic deformation, it should be noted that appreciable effects due to charge configuration were also observed. In general, non-spherical or non-compact charges, such as rectangular prisms or rods, produce the largest effects normal to the charge's longest dimension and largest flat surface. This effect, as measured by the ratio of peak first cycle stresses for non-compact versus compact charges increases with increasing charge weight. In this program[3], for the largest charges fired, 10 lbs (4.5 kg) in a 4.5-ft (137-cm) diameter vessel, this ratio reached a value slightly in excess of three. Thus, non-spherical charges are more difficult to contain due to large localized strains than spherical charges.

Figure 7 shows the comparison between observed and calculated residual plastic strains for spherical charges of Composition C-4 plastic explosive in 2.0-ft (61-cm) diameter vessels. Except for the two smallest deformations shown, each of these data points was obtained on a new, undeformed vessel. The SPLAS-calculated curve was based on an assumed 80-ksi (582-MPa) dynamic yield strength, the shock wave parameters[5] for 50/50 Pentolite and the static gas pressure loading calculated[6] for a composition similar to Composition C-4. The plotted points represent the average surface strain from 13 gage lengths on the vessel surface. The error bars show the range of surface strains measured from individual gage lengths. The measuring accuracy of gage length was 0.06 percent strain. The material used for these vessels was A-516, grade 70, which had a static (0.2 percent offset) yield strength of 53 ksi (365 MPa) and an ultimate strength of 75 ksi

(517 MPa) for the lot. An additional vessel tested with 7.0 lbs (3.2 kg) of C-4 suffered catastrophic failure with all fractures showing essentially full-shear ductile fracture. The calculated confined explosion gas pressures for this charge and the largest successfully contained charge of 6.5 lbs (3.0 kg) led to calculated static stresses in the vessel walls which bracket the ultimate static strength of the vessel material. Thus we conclude that the plastic deformation can be reasonably calculated and that the ultimate failure mode for vessels of the class represented here appears to be due to static stresses generated by the confined detonation product gas.

SUMMARY

This paper has summarized an innovative U.S. Army R&D program to demonstrate the explosive blast containment capability of closed spherical vessels. The results confirm the conclusion that closed spherical vessels fabricated from high fracture toughness material and designed for a small number of elastic-plastic responses provides a safe, high performance, transportable, and weight efficient solution for the explosive ordnance disposal application. The present design methodology is straightforward and reliable, however it is conservative and could be improved upon by a dynamic analysis of the ring and door response to explosive loading. Analysis of the large body of experimental data has shown that fiducial mark readings and first cycle responses of dynamic strain gages can be consistently related to mechanical properties, thus making it possible to perform scaling calculations for alternative designs. Limited destructive testing by intentional explosive overload suggests that the principal failure mode results from the initial contained static gas pressure exceeding the ultimate strength of the vessel.

RECENT AND CURRENT RESEARCH

Development progress for explosive blast containment vessels since the initial Army program has concentrated on improved door design from an operational standpoint, fragment restraint systems, and dynamic fracture resistance of materials in the plastic strain regime. This work[7,13] has been conducted primarily at Battelle under sponsorship of the Naval Explosive Ordnance Disposal Facility at Indian Head, Maryland. Additional publications are planned. The most recent progress[14] concerns the design, fabrication, and evaluation of 3-1/2-ft (107-cm) diameter, 0.88-inch (2.24-cm) thick vessels based on HY-80 steel alloy and using a cable and spider support mechanism to achieve door closure. These vessels can withstand repeated detonations of 10 lbs (4.54 kg) of Composition C-4 explosive at a service temperature of -30F (-34.4C).

ACKNOWLEDGEMENTS

The authors acknowledge the support of the Picatinny Arsenal for the work reported herein, conducted under Contract No. DAAA21-72-C-0129. Dr. J. H. Brown, Jr., Mr. J. G. Dunleavy (deceased), and Mr. H. W. Mischler are thanked for their many helpful contributions.

REFERENCES

1. "Explosive Confinement Vessel," General Information Bulletin 76-9, FBI Bomb Data Program, 1976, 1-12.

2. "Total Containment Bomb Trailer," Int. Def. Rev., v. 10, no. 6, December 1977, 1183.

3. Trott, B. D., Backofen, J. E., and White, J. J., "Design of Explosion Blast Containment Vessels for Explosive Ordnance Disposal Units," Final Report to Picatinny Arsenal, Contract No. DAAA21-72-C-0129, Battelle, Columbus Laboratories, June 1975.

4. Baker, W. E., "The Elastic-Plastic Response of Thin Spherical Shells to Internal Blast Loading," J. Appl. Mech., v. 27, March 1960, 139-44.

5. Goodman, H. J., "Compiled Free-Air Blast Data on Bare Spherical Pentolite," Ballistic Research Laboratories, Report 1092, February 1960.

6. Proctor, J. F., "Internal Blast Damage Mechanisms Computer Program," Naval Ordnance Laboratory Report, NOLTR 72-231, August 1972.

7. White, J. J., Trott, B. D., and Backofen, J. E., "The Physics of Explosion Containment," Physics in Technology, v. 8, no. 3, May 1977, 94-100.

8. Timoshenko, S., and Woinowsky-Krieger, S., Theory of Plates and Shells, Second Edition, McGraw-Hill, New York, 1959.

9. Flugge, W., Stresses in Shells, Fourth Printing, Springer-Verlag, New York, 1967.

10. Roark, R. J., Formulas for Stress and Strain, Fourth Edition, McGraw-Hill, New York, 1965.

11. Johansson, C. H., and Persson, P. A., Detonics of High Explosives, Academic Press, London and New York, 1970, 36.

12. Huffington, N. J., and Robertson, S. R., "Containment Structures Versus Suppressive Structures," Ballistic Research Laboratories, Mem. Report 2597, February 1976.

13. Trott, B. D., Backofen, J. E., White, J. J., and Wolfson, L. J., "Trailer-Mounted Chamber for Containment of 40 Pounds of TNT," Minutes of the 17th Explosives Safety Seminar, Denver, Colorado, September 14-16, 1976, DoD Explosives Safety Board, Washington, D. C., v. I, 1976, 229-263.

14. Trott, B. D., "The Construction and Evaluation of Prototype Blast Containment Chambers," Final Report to Naval Explosive Ordnance Disposal Facility, Contract No. N00174-77-C-0372, Battelle, Columbus Laboratories, in preparation.

INTEGRITY ANALYSIS OF THE SEWARD STATION NUMBER 5 STEAM TURBINE ROTOR

C. W. MARSCHALL
Principal Scientist, Metal Science Section

A. T. HOPPER
Associate Manager, Applied Solid Mechanics Section

S. H. SMITH
Principal Research Scientist, Structural Materials and Tribology Section
Battelle Columbus Laboratories
Columbus, Ohio 43201

W. J. MOLL
Project Mechanical Engineer
Pennsylvania Electric Company
Johnstown, Pennsylvania

ABSTRACT

A rotor with suspected flaws found by NDI was subjected to a structural integrity investigation that included measurement of fracture toughness and tensile properties, thermal and mechanical stress analyses under various start-up and shut-down conditions, and a fracture mechanics analysis that included both fatigue and residual strength considerations. Miniature compact tension specimens in conjunction with a J-integral method permitted measurement of K_{Ic} without destruction of the rotor. Measured values of K_{Ic} were considerably greater than minimum literature values and led to larger permissible flaw indication sizes being acceptable in the fracture mechanics analysis. The investigation indicated that none of the suspected flaws would reach critical size in an additional 1100 start-up and shut-down cycles, including an annual overspeed test.

INTRODUCTION

During a nondestructive investigation of Pennsylvania Electric Company's Seward Station No. 5 low pressure turbine rotor, nine holding indications were found by ultrasonic inspection. These suspected flaws were located in the body of the rotor and were at or near the bore wall as shown in Figure 1. Also shown

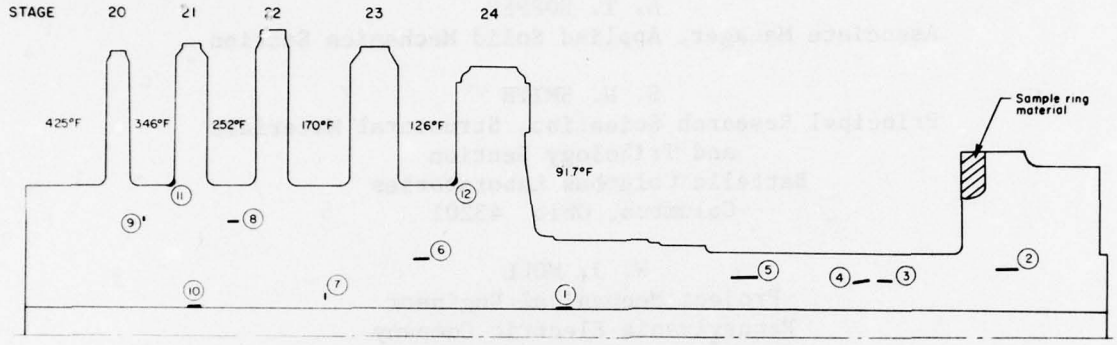


Figure 1. Rotor Flaw Locations; Flaws 1 Through 9 are NDI Indications While 10 Through 12 are Hypothetical Flaws Introduced at the Regions of Greatest Stress.

is the temperature of the steam entering each stage. An investigation designed to assess the structural integrity of the rotor was undertaken which consisted of several interrelated activities. First, the fracture toughness, tensile properties, and hardness were determined. These data provided support for a thermal and mechanical stress analysis of the rotor under various start-up and shut-down conditions. Finally, a fracture-mechanics analysis was performed which involved fatigue-crack growth analysis for 1100 start-up and shut-down cycles with periodic overspeed cycles.

The determination of the structural integrity and reliability of the rotor was intimately linked with the fracture toughness and the flaw dimensions. For components manufactured prior to the development of fracture mechanics, the discovery of flaws raises serious doubts about structural integrity because of the lack of fracture toughness data for the specific component. Were such data available, it would be possible to define combinations of stresses and flaw sizes that would permit continued safe operation of the component.

The use of miniature fracture toughness specimens in combination with recently developed J-integral methods offers promise of providing fracture toughness data in an essentially nondestructive manner. In contrast with conventional methods for obtaining K_{Ic} values, based on ASTM E 399-74 Method of Test for Plane-Strain Fracture Toughness of Metallic Materials [1] which require relatively large test specimens, the new method can employ specimens weighing only a few grams. For many components, this means that test specimens can be removed without compromising subsequent performance.

Recently, exploratory studies were conducted on the use of miniature specimens to measure K_{Ic} of large steel rotating components. In one case, trepanning was used to remove a cylindrical sample several inches long by 3/4-inch diameter. In the present case study, a ring of 3/4-inch square cross section

was removed from a noncritical region. Details of the test procedures and analyses are given in the following.

UNITS

The investigation described in this paper was conceived and conducted in English units. Thus, English units are used exclusively. Conversion to SI units can be accomplished as follows:

To Convert From	To	Multiply By
inch	mm	25.4
psi	Pa	6895
ksi	MPa	6.895
ksi $\sqrt{in}$	MPa $\sqrt{m}$	1.1
lb/in	N/m	175

Additionally, $°C = \frac{5}{9} (°F - 32)$.

MECHANICAL PROPERTIES DETERMINATION

Tests were conducted to measure hardness, tensile properties, and fracture toughness of the ring of material removed from the outside diameter of the generator rotor. The ring had an arc length of approximately 80 inches and a cross section measuring approximately 3/4-inch square. It was taken from the coupling end of the rotor. Two samples labled AB and DE, each approximately 4-3/4 inches long were sawed from the ring at diametrically opposite locations. They displayed similar strength and hardness properties as tabulated below.

Table 1. Mechanical Properties

Sample	Hardness, R_B	Upper Yield Point, ksi	Lower Yield Point, ksi	0.2% Offset Yield Strength, ksi	Tensile Strength, ksi	Elong., pct in 1/2 in.
AB	94-95	80.5	78.6	79.2	97.5	19
DE	93-96	78.5	78.3	78.8	97.9	18

Fracture toughness specimens were machined from the two samples as shown schematically in Figure 2.

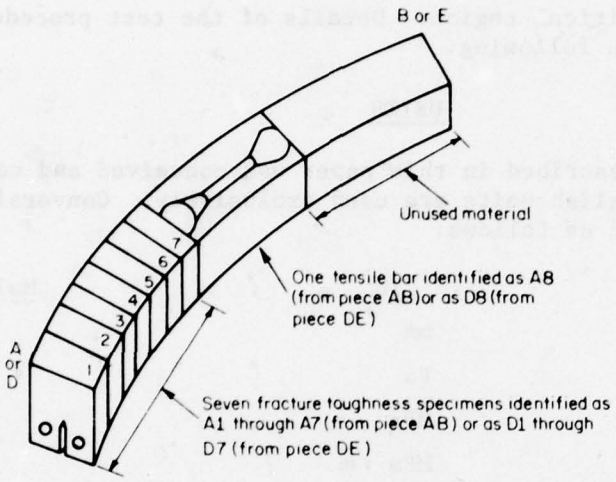


Figure 2. Pattern For Machining Test Specimens From Sample Ring of Rotor Steel

The amount of rotor material available was inadequate for conducting valid fracture toughness (K_{Ic}) tests, as described in ASTM E399. According to the ASTM specification, the minimum thickness (B), width (W), and height (2H) of compact tension specimens are governed by the yield strength (σ_y) and K_{IC} through the empirical relationships

$$B \geq 2.5 \left(K_{IC}/\sigma_y\right)^2 \qquad (1)$$

where $W = 2.5\ B$
$2H = 2.4\ B$

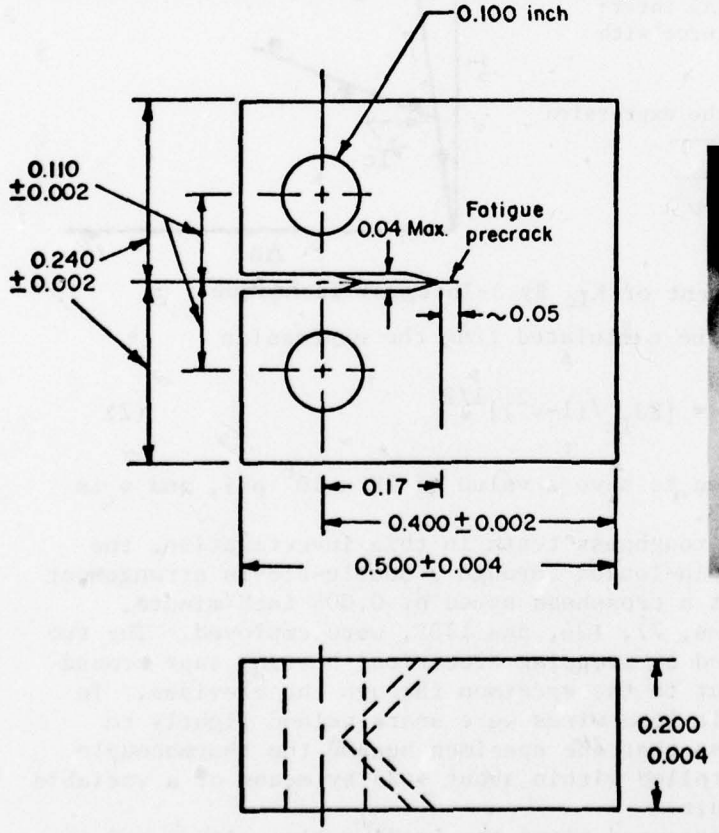
Shown in Table 2 are the minimum dimensions for compact tension specimens of the rotor steel, assuming a value of 80 ksi for σ_y and various values for K_{Ic}. Note that even for the lowest assumed K_{Ic} value of 50 ksi$\sqrt{in.}$, the minimum specimen size is approximately 2.5 inches square by 1-inch thick.

Table 2 Minimum Dimensions for Compact Tension Specimens Based on ASTM E399 and Assuming σ_y = 80 ksi

Assumed K_{Ic}, ksi$\sqrt{in.}$	Minimum Dimensions		
	Thickness (B) inch	Width (2.5B) inch	Height (2.4B) inch
50	1.0	2.5	2.4
75	2.2	5.5	5.3
100	3.9	9.8	9.4
125	6.1	15.3	14.6

Recently developed J-integral techniques permit the use of smaller compact tension specimens [2]. In these techniques, specimen dimensions; a (crack length), b (uncracked ligament), and B (thickness) must equal or exceed the quantity 25 J_{Ic}/σ_f, where σ_f is the flow stress and can be taken as the average of yield and ultimate strengths. The specimen design selected for this investigation is shown in Figure 3. According to the most recent developments in J-integral testing, a specimen of this size is capable of measuring K_{Ic} values of at least 135 ksi$\sqrt{\text{in.}}$, assuming b = 0.16 inch and σ_f = 89 ksi.

The J-integral technique required a graph of load versus load-line displacement for several nominally identical specimens, each loaded to a different level of displacement, as shown schematically in Figure 4. After unloading from a specified level of displacement, the specimen was heated at 600F in air for about 30 to 45 minutes to oxidize the crack surfaces, including the preexisting fatigue crack and any newly created crack surface. The specimen was then cooled in dry ice to make it brittle and is broken open to reveal any crack extension (Δa) that occurred in the initial step. A graph of J versus Δa was prepared and a best fit line was drawn through the data points. The intersection of this line with the blunting line (see Figure 4) is termed J_{Ic}.



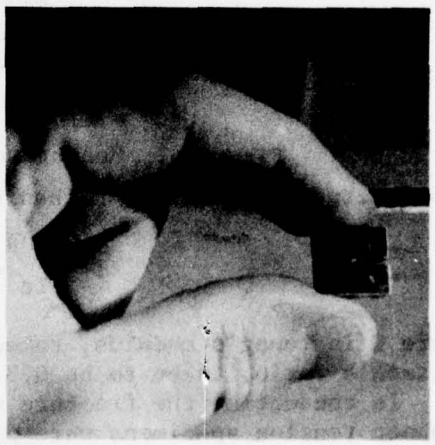


Figure 3. Miniature Compact Tension (MCT) Specimen for Measurement of J_{Ic}
Note: Dimensions are in inches; to convert to millimeters, multiply by 25.4.

STEP NO.	PROCEDURE
(1)	Load MCT specimens to displacement levels 1, 2, 3, or 4 and then unload
(2)	Compute $J_I = 2A/Bb$, where B = thickness and b = uncracked ligament
(3)	Heat tint at ~ 600°F to oxidize crack surface
(4)	Break specimens open at low temperature to reveal any crack extension, Δa
(5)	Plot J_I versus Δa
(6)	Obtain J_{Ic} by locating intersection of J-vs-Δa curve with blunting line
(7)	Calculate K_{Ic} from the expression $K_{Ic} = \sqrt{\frac{EJ_{Ic}}{(1-\nu^2)}}$

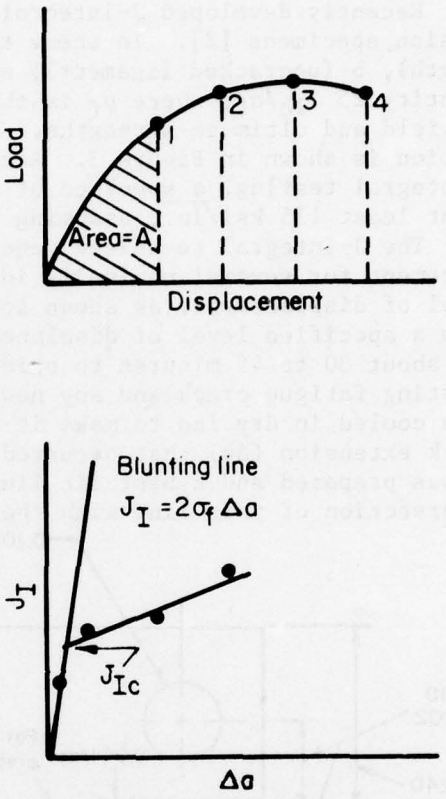


Figure 4. Measurement of K_{Ic} By J-Integral Technique

The fracture toughness can then be calculated from the expression

$$K_{Ic} = [EJ_{Ic}/(1-\nu^2)]^{1/2} \qquad (2)$$

where E is Young's modulus, taken to have a value of 29×10^6 psi, and ν is Poisson's ratio, taken to be 0.3.

In conducting the fracture toughness tests in this investigation, the compact tension specimens were pin-loaded through a double-clevis arrangement in an Instron testing machine at a crosshead speed of 0.005 inch/minute. Three different test temperatures, 77, 126, and 170F, were employed. The two higher temperatures were achieved by wrapping electrical heating tape around the pull rods and conducting heat to the specimen through the clevises. To monitor temperature, thermocouple lead wires were spark welded lightly to opposite faces of the specimen so that the specimen became the thermocouple junction. Temperature was controlled within about $\pm$ 2F by means of a variable transformer in the heating circuit.

Specimen displacement was measured along the loading line with a rod-in-tube extensometer arrangement that transmitted the displacement outside the hot-zone where it was measured with a standard Instron extensometer.

Results of J-integral tests are shown graphically in Figure 5. The intersection of the J versus Δa curve with the experimental blunting line was defined as J_{Ic}. J_{Ic} values at each temperature are indicated in Figure 5, along with K_{Ic} values calculated from Equation 2. These K_{Ic} values are plotted in Figure 6 as a function of test temperature. For comparison, valid K_{Ic} data from other rotor forgings are included in Figure 6.

K_{Ic} was seen to be strongly dependent on temperature, i.e., it increased sharply with increasing temperature over the temperature range investigated. This behavior was similar to that reported in Reference (3) for other Ni-Mo-V rotor steels, shown as a band in Figure 6. It should be noted that valid K_{Ic} data at relatively high toughness levels involve some finite amount of crack growth, whereas K_{Ic} data derived from J_{Ic} tests are based on crack initiation. Thus, K_{Ic} values obtained in this investigation could reasonably be expected to be somewhat less than those reported in Reference (3).

As noted earlier, the material tested in this study was taken from a noncritical region of the rotor forging. Thus, there is no assurance that the toughness values reported here are representative of the entire forging. However, in limited tests conducted on a failed rotor, Clark, Kramer, and Tu (5) reported only relatively small differences in K_{Ic} for specimens taken at two radial positions (0.8 inch and 4.0 inch). Furthermore, the K_{Ic} values reported by Clark, et al for material containing scattered small indications from ultrasonic inspection were similar to those for clean material. This provides some basis for assuming that the toughness values reported here are typical of the entire forging.

STRESS ANALYSIS

In order to perform a crack-growth analysis of the suspected flaws in the turbine rotor, an accurate knowledge of the stresses, stress gradients, and distributions that would tend to propagate the flaw was required. Handbook stress analysis methods are not sufficiently accurate for this problem due to the complexity of the turbine geometry and loading. Therefore, stresses in the turbine rotor were determined by finite element stress analysis techniques.

Because the turbine rotor was a solid of revolution, an axisymmetric finite element analysis was performed. The axisymmetry condition implies that field quantities such as temperatures, pressure loads, stresses, etc., are not dependent upon angular orientation with respect to the axis of symmetry. This allows geometrical treatment of the structure in two dimensions using radial (R) and axial (Z) coordinates, thus simplifying the problem. The well-tested and proven computer code AXISOL by E. L. Wilson was used in the analysis.

The finite element model of the turbine rotor is shown in Figure 7. The model, with 893 elements and 956 nodes, considers half of the turbine since

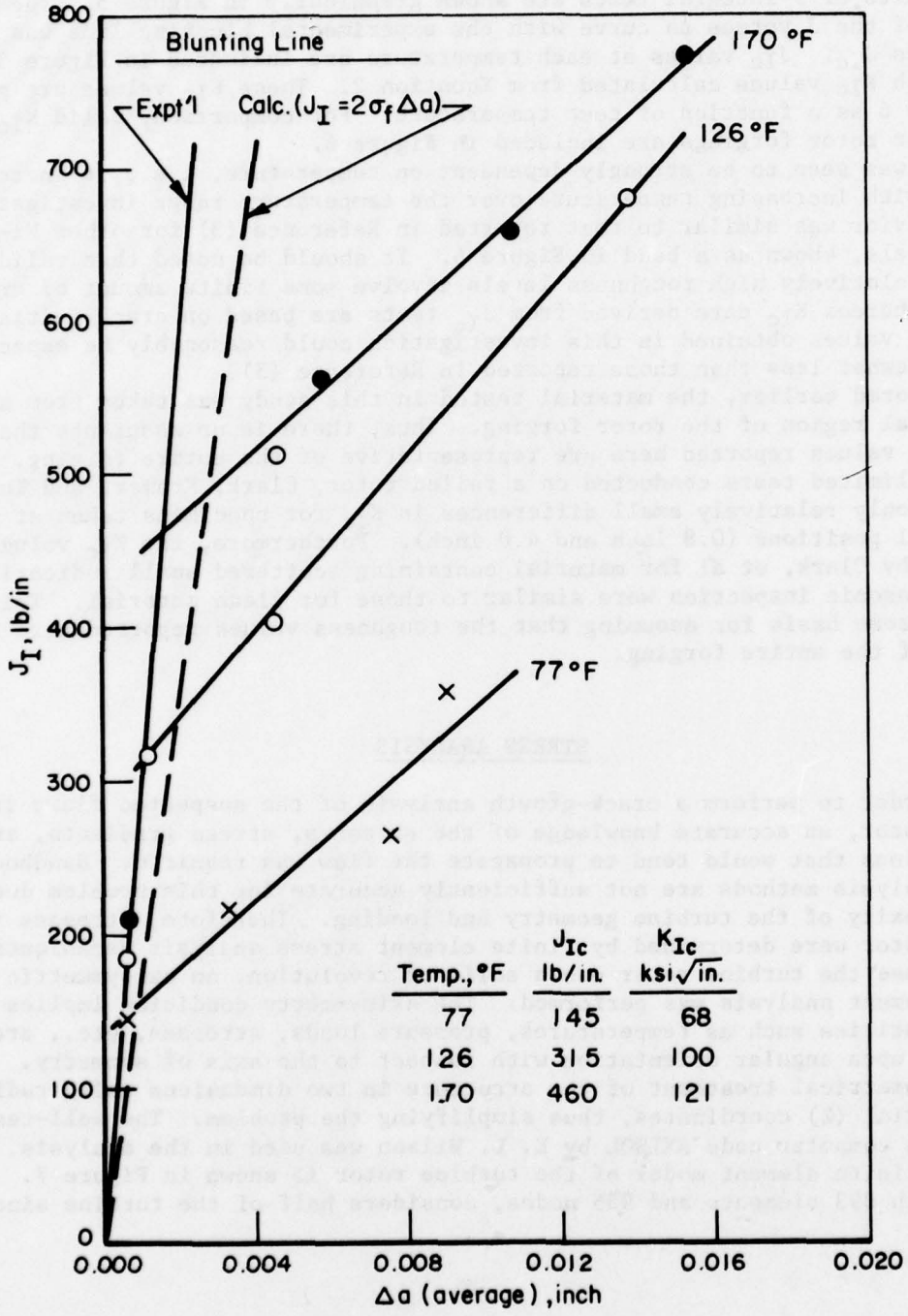


Figure 5. Curves of J_I Versus Δa For Rotor Steel Specimens Tested at Several Temperatures

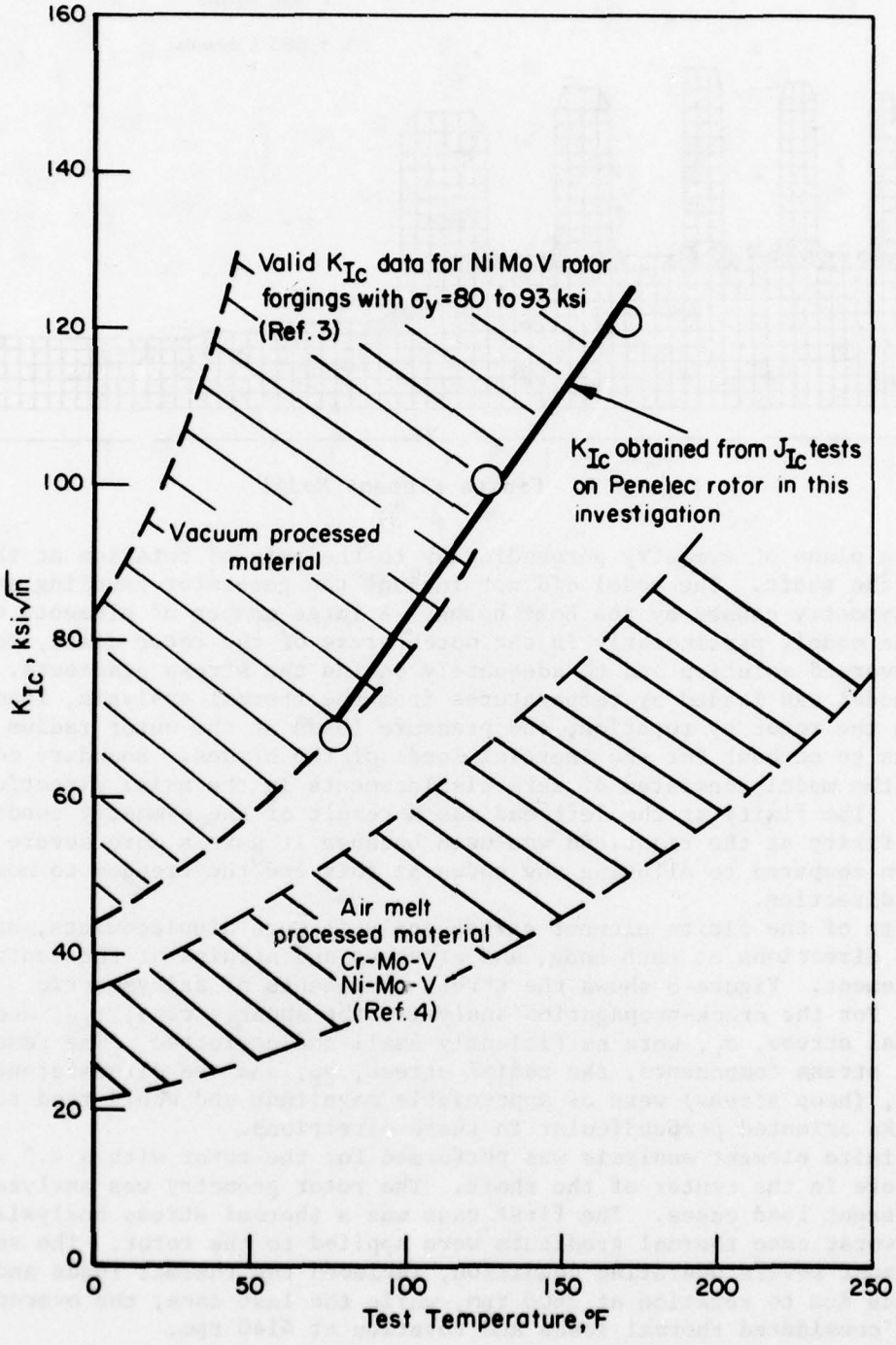


Figure 6. Temperature Dependence of Fracture Toughness For Pennsylvania Electric Rotor Steel

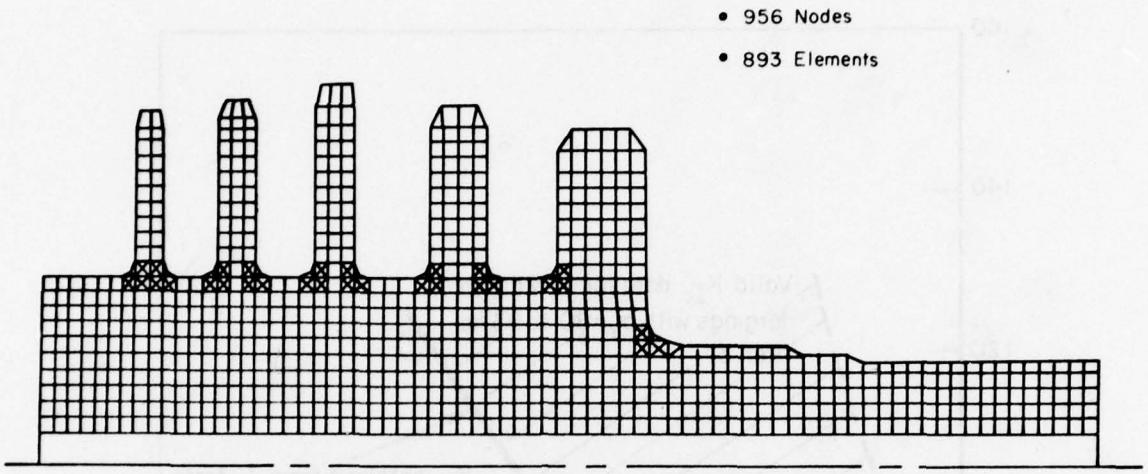


Figure 7. Finite Element Model

there was a plane of symmetry perpendicular to the axis of rotation at the center of the shaft. The model did not include the generator coupling end due to nonaxisymmetry caused by the bolt holes. A large number of elements were used in the model, particularly in the notch areas of the rotor disks, to ensure a converged solution and to adequately define the stress gradients.

The model was loaded by temperatures from the thermal analysis, loads induced in the rotor by rotation, and pressure loads at the outer radius of the rotor disks to account for the inertial loads of the blades. Boundary conditions for the model consisted of zero displacements in the axial direction at both ends. The fixity at the left end was a result of the symmetry condition, while the fixity at the right end was used because it gave a more severe stress state, when compared to allowing the nodes at this end the freedom to move in the axial direction.

Results of the finite element stress analysis were displacements, axial and radial directions at each node, and stresses and strains at the centroids of each element. Figure 8 shows the stress components of axisymmetric analysis. For the crack-propagation analysis, the shear stress, τ_{rz}, and the axial normal stress, σ_z, were sufficiently small and neglected. The ramaining two normal stress components, the radial stress, σ_r, and the circumferential stress, σ_c, (hoop stress) were of appreciable magnitude and would tend to propagate cracks oriented perpendicular to these directions.

The finite element analysis was performed for the rotor with a 4.5 inch diameter bore in the center of the shaft. The rotor geometry was analyzed with three different load cases. The first case was a thermal stress analysis in which the worst case thermal gradients were applied to the rotor. The second case, the most severe operating condition, included the thermal loads and mechanical loads due to rotation at 3600 rpm, while the last case, the overspeed condition, considered thermal loads and rotation at 4140 rpm.

The radial thermal stresses were generally small, except in the notch areas of the rotor disks. At the worst case thermal gradient condition, relatively large temperature differences exist on either side of the disks; hence,

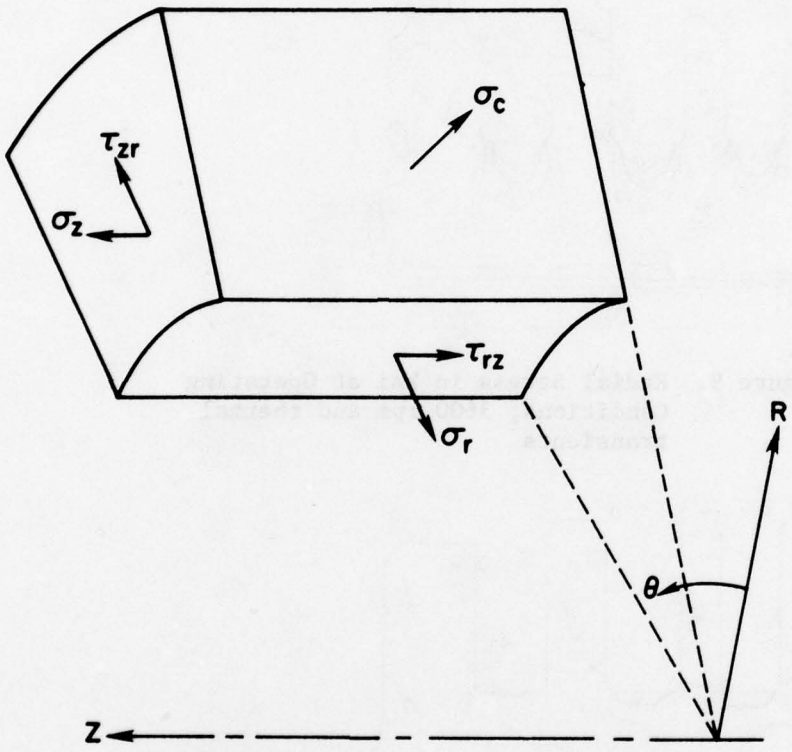


Figure 8. Axisymmetric Stress Components

large localized stresses develop at the notches. On the hot side of the disk, there was tension, while on the cooler side, there was compression, indicating some bending of the disks. Figures 9 and 10 show the radial and circumferential stresses at operating conditions. At the bore wall, the stress was zero, rising to a peak value rather rapidly, then dropping off toward zero at the diameter where the rotor disks were attached.

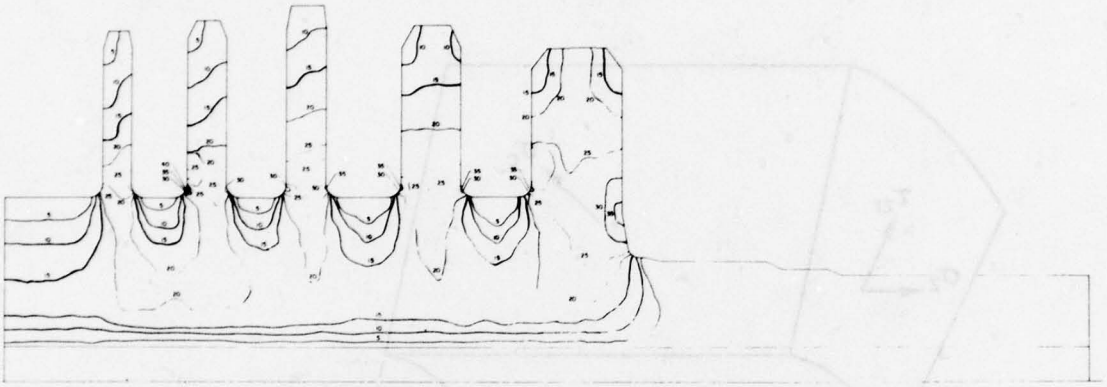


Figure 9. Radial Stress in ksi at Operating Conditions; 3600 rpm and thermal transients

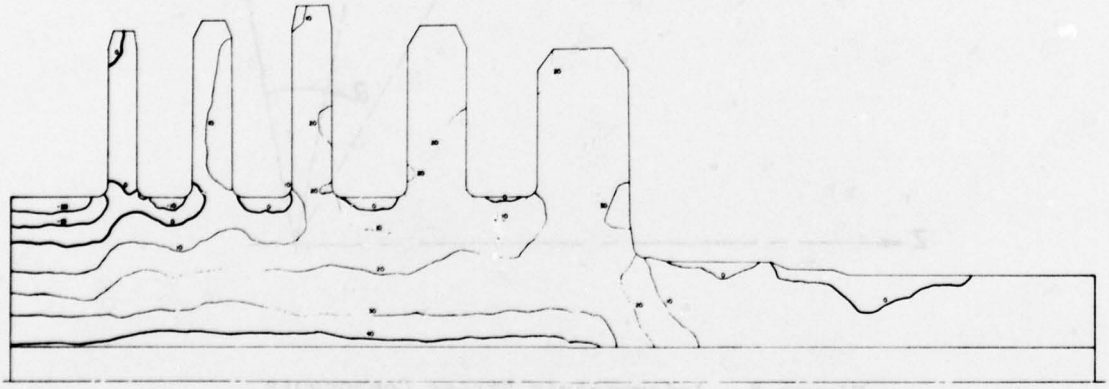


Figure 10. Circumferential Stress in ksi at Operating Conditions; 3600 rpm and thermal transients

The circumferential stresses due to a combination of the mechanical rotating loads of the shaft and blades, and large thermal gradients in the rotor during a starting with a cold turbine, are quite low except near the longitudinal midpoint of the shaft which is at the left end of the axisymmetric half section of the rotor depicted in Figure 7. In several areas, the circumferential stress is compressive, which would tend to close cracks in those

areas of the rotor. The circumferential stresses at operating condition start at a peak at the bore wall and decrease while moving radially outward.

FRACTURE-MECHANICS ANALYSIS

Table 3 has been compiled to summarize the stresses at the flaw

Table 3. Summary of Stresses at Flaw Locations For Operating Conditions

	4.5-Inch Bore					
	Hot Start		Cold Start		Hot Overspeed	
Flaw Number	σ_r, psi	σ_c, psi	σ_r, psi	σ_c, psi	σ_r, psi	σ_c, psi
1	0. (92.)[a]	26000.	0. (85.)	21930.	0. (92.)[a]	33870.
2	--	--	6380. (80.)	9820.	--	--
3	843. (85.)	2078.	869. (80.)	2096.	1118. (85.)	2754.
4	844. (85.)	2078.	869. (80.)	2055.	1119. (85.)	2754.
5	885. (85.)	2294.	851. (83.)	1591.	1173. (85.)	3040.
6	[15262.] (126.)	22491.	[17995.] (104.)	25335.	[20217.] (126.)	29956.
7	11057. (170.)	[30070.]	14710. (117.)	[40200.]	14697. (170.)	[39950.]
8	11664. (252.)	17129.	15020. (207.)	12073.	15204. (252.)	22126.
9	8700. (346.)	12495.	14310. (286.)	5827.	11760. (346.)	16556.
10[b]	0. (299.)	[29883.]	0. (176.)	[51400.]	0. (299.)	[39343.]
11[b]	24450. (346.)	20196.	[43950.] (299.)	21040.	32390. (346.)	26756.
12[b]	[35519.] (126.)	29239.	38410. (126.)	29000.	[47019.] (126.)	38699.

(a) Temperature, F
(b) These are hypothetical flaws

indication locations. The table presents the radial and circumferential stress, as well as the temperature at each flaw indication for a hot and cold turbine rotor condition during start-up and overspeed. The cold start conditions include the thermal gradients from the thermal analysis, while the hot condition considers only the mechanical rotational loading. No hot start data were reported for the flaw 2 location since it was in an area of neglible thermal gradients. In all cases, the stress magnitudes are less than 78 ksi to 81 ksi measured yield stress of the rotor forging material.

The fracture-mechanics analysis consisted of cyclic fatigue-crack growth and residual-strength analysis. The main objectives and assumptions are listed below.

(1) Assume a critical flaw geometry for the nine original nondestructive testing indications
(2) Three additional flaw geometries were assumed at the three highest-stressed locations in the turbine rotor
(3) Incremental fatigue-crack-growth behavior was determined for all flaws. The fatigue stress spectrum was developed for 1100 start-ups and shutdowns with an annual overspeed for test purposes.
(4) The ratio of critical crack length to actual flaw length was determined for all initial flaws.

Figure 11 shows schematically the fundamental concepts of fracture-mechanics analysis. The residual strength curve, Figure 11a, shows the applied stress level, σ, versus crack length, a, which is defined for the critical condition by K_{Ic}. At instability, the critical applied stress was σ_{cr} and the corresponding critical crack size was a_{cr}. The fatigue-crack-growth curve, Figure 11b, shows crack length, a, versus applied stress cycle, N. The total

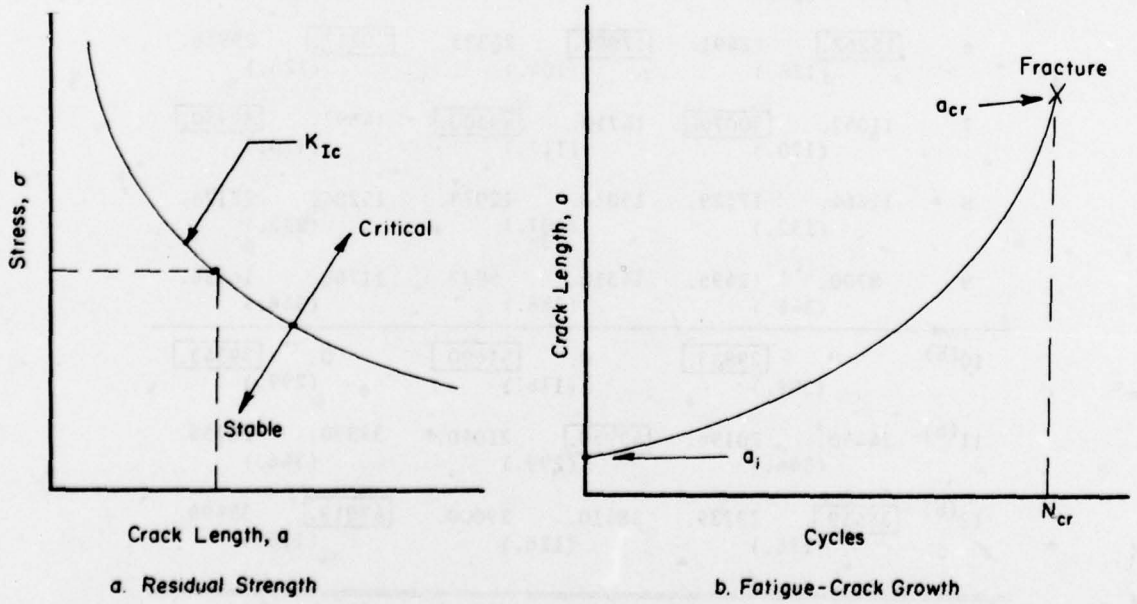


Figure 11. Fracture-Mechanics Analysis

curve was determined from the initial flaw size, a_i, to fracture instability as determined by a_{cr} at the maximum applied stress level.

STRESS-INTENSITY FORMULATION

Three types of flaws were assumed to determine the appropriate stress-intensity solution, K_I, for use in residual strength determinations. Figure 12 shows the types of flaws assumed. A surface flaw, with aspect ratio a/ℓ, is shown with the K_I solution in Figure 12a. This solution was utilized extensively in treating surface flaw/crack growth fracture mechanics problems. Figure 12b shows the embedded flaw geometry and stress intensity solution. This stress intensity solution is presented in a form for total flaw width, a, not for a/2 as is sometimes customary. When $a = \ell$, the solution reduces to the stress intensity solution for a circular embedded disk as shown in Figure 12c. For $a/\ell = 1.0$ in Figure 12b, $\phi = \pi/2$, and the K_I solution reduces to that shown in Figure 12c.

SERVICE SPECTRUM

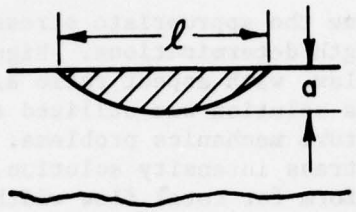
The fatigue-crack-growth behavior of the NDI flaws in the rotor turbine was determined for an applied service spectrum which was generated based on the past operational history of the turbine. In summary, the turbine was subjected to 353 start-ups and shutdowns in 195 months of operational time, an average of 22 start-ups per year. Although the actual annual overspeed test occurs at a level less than 110% of rated speed (3600 rpm), for the purposes of a conservative fracture-mechanics analysis an overspeed condition of 115% of the rated speed was applied once per year in the service spectrum. The average yearly service spectrum was developed in the form of applied stress, σ, versus cycles for each flaw. The stress magnitudes were those determined from the stress analysis at the flaw location.

RESULTS ON FATIGUE-CRACK GROWTH

Fatigue-crack-growth calculations for the service spectrum were performed using the AFFDL "CRACKS III" computer program [6]. This computer program contained the stress-intensity solutions and β-options for the required analysis of the flaws in the turbine rotor. The β parameter accounts for modifications in the applied stress to consider the flaw propagating in a nonuniform stress field. Cycle-by-cycle incremental fatigue-crack growth was determined for the cold start/cold overspeed service spectrum. Forman's fatigue-crack-growth equation was used in the integration. Linear accumulation of damage was performed to minimize the load or stress interaction effects of the overspeed stresses. Thus, the results were essentially the same for any application of the overstress within a 1 year span.

Table 4 shows the incremental fatigue-crack-growth results for the 12 flaws. The table defines the flaw number and the incremental growth in terms of Δa and $\Delta \ell$ for 1100 start-ups and shutdowns. The 1100 cycles include the overspeed cycles. The growth analysis assumed that flaws 3 and 4 were joined to consider the most severe case. The results of the analysis show that ΔK developed by flaws 3-4 and 5 were below the threshold ΔK_{th} of 5.0 ksi $\sqrt{in}$.

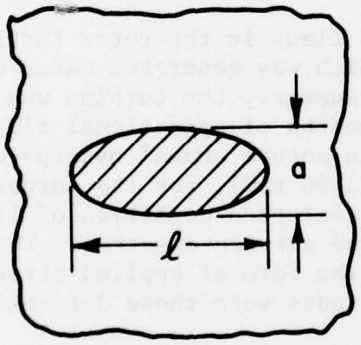
a. Surface flaw



$$K_I = \frac{1.1\beta\sigma\sqrt{\pi a}}{[Q]^{\frac{1}{2}}}$$

$$[Q]^{\frac{1}{2}} = \phi = f\left(\frac{a}{\ell}\right)$$

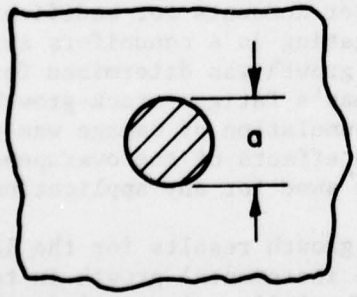
b. Embedded flaw, elliptical disk



$$K_I = \frac{\beta\sigma\sqrt{\pi a}}{\sqrt{2}\ \phi}$$

$$\phi = f(a/\ell)$$

c. Embedded flaw, circular disk



$$K_I = \frac{2}{\pi\sqrt{2}}\ \beta\sigma\ \sqrt{\pi a}$$

Figure 12. Stress-Intensity Solutions for Flaw Size Equivalency

Of the existing flaws, flaws 6 and 7 showed the largest amount of growth in 1100 cycles, whereas flaw 11 was predicted to show the most growth for the hypothetical flaws. None of the flaws grew to a critical length in this analysis.

Table 4. Incremental Fatigue-Crack Growth in 1100 Start-Ups (4.5-in. Bore)

Flaw Number	Δa, in.	$\Delta \ell$, in.
1	0.00225	0.00450
2	--	0.0005
	0.00007	0.00041
3-4	--	--
	Below ΔK_{th}	Below ΔK_{th}
5	--	
	Below ΔK_{th}	Below ΔK_{th}
6	--	0.00416
	0.00227	0.01135
7	--	--
	0.00472	0.00661
8	--	0.00277
9	--	0.00115
10	0.01539	0.03078
11	0.01069	0.0338
12	0.00394	0.00788

RESIDUAL STRENGTH ANALYSIS

Flaws 6 and 7 were identified as the most critical flaws and were treated as embedded elliptical disks where the applied stress, σ, is perpendicular to the disk. The β-parameter shown in Figure 12 reflects changes in the applied stress due to stress gradients in the rotor when flaws of various lengths are considered.

Based on the K_{Ic} data presented earlier, a lower bound room temperature K_{Ic} of 65 ksi $\sqrt{\text{in.}}$ was selected for residual strength analyses of flaws 6

and 7. Each was considered at room temperature even though the thermal analysis showed the material temperature to be slightly higher.

Table 5 shows the critical applied stresses at each flaw location which would cause the flaw to propagate in an unstable mode of fracture. The ratio of critical stress to applied stress as determined in the rotational stress analysis is also shown. The applied maximum stresses are for a 15% cold overspeed.

Table 5. Critical Applied Stresses at Each Flaw Location

Flaw Number	Flaw Depth, a, inch	Aspect Ratio, a/ℓ	σ_{cr}, ksi	$\frac{\sigma_{cr}}{\sigma_{applied}}$
6	0.625	0.2	63.0	1.863
	0.75	0.25	60.0	1.775
	0.875	0.30	58.0	1.715
7	0.775	0.58	75.0	1.399
	0.90	0.75	76.0	1.418
	1.075	0.95	78.0	1.455

SUMMARY

The application of the J-integral technique to the measurement of the fracture toughness of the rotor material has been shown to be a valuable tool in an overall integrity evaluation. The technique was nondestructive and conservative in the estimate it gives for K_{Ic}. In this case study, the measured lower bound of 65 ksi $\sqrt{in}$. would have had to have been replaced with a value of 40 ksi $\sqrt{in}$. if only the literature had been available as a source of fracture toughness data. However, the higher actually measured values of K_{Ic} led to larger permissible flaw indication sizes being acceptable without reaching the estimated larger critical crack size.

Stress and fracture mechanics analyses were conducted on the rotor. Calculated stresses were applied to the detected and assumed flaws in order to calculate the fatigue-crack growth which would occur in 1100 start-ups and shutdowns. Analytically, none of the flaws showed growth to a critical size. In addition, a residual strength analysis was conducted on the most critical flaws for the overspeed condition. It was shown that these flaws (flaw 6 and 7) would not propagate in an unstable fashion under this loading.

REFERENCES

1. ASTM, "Standard Method of Test for Plane-Strain Fracture Toughness of Metallic Materials," Designation E399-74, 1974 Annual Book of ASTM Standards, ASTM, Philadelphia, 432.

2. Landes, J. D. and Begley, J. A., "Test Results from J-Integral Studies, An Attempt to Establish a J_{Ic} Test Procedure," Fracture Analysis, ASTM STP 660 (1974) 170-186.

3. Greenberg, H. D., Wessel, E. T., and Pryle, W. H., "Fracture Toughness of Turbine-Generator Rotor Forgings," Engineering Fracture Mechanics, 1, 1970, 653-674.

4. Kramer, C. D., Tu, L. K., and Clarke, G. A., "Reliability of Steam Turbine Rotors RP502 Material Mechanical Properties Measurement Phase I," Semi-Annual Report, Westinghouse/EPRI Preliminary Report.

5. Clarke, G. A., Kramer, L. D., and Tu, L. K., "Reliability of Steam Turbine Rotors," Westinghouse, Semi-Annual Report No. 2 on EPRI Contract RP502-4, April 19, 1977.

6. Engle, R. M., Jr., "Cracks III - Users' Manual", AFFDL-TM-74-173, 1976.

FINITE ELEMENT ANALYSIS OF THE MAGIS IAC ADP/COMM SHELTER

C. M. BLACKMON
Aerospace Engineer
Naval Surface Weapons Center
Dahlgren, Virginia 22448

ABSTRACT

The Marine Air to Ground Intelligence System (MAGIS) consists of several components, one of which is the Intelligence Analysis Center (IAC). The IAC itself consists of a data processing and communication shelter (ADP/COMM) and one or more analyst shelters. The shelters to be used were 8' x 8' x 20' (2.44 x 2.44 x 6.1m) and were originally designed for approximately 9000 pounds (4082kg) gross weight. The equipment to be used in the ADP/COMM brought the gross weight to approximately 14,500 pounds (6577kg), a significant increase. This paper describes the design requirements, structural analysis using the finite element method, and subsequent modification of the MAGIS IAC ADP/COMM shelter.

INTRODUCTION

The Marine Air to Ground Intelligence System (MAGIS) consists of several components, one of which is the Intelligence Analysis Center (IAC). The IAC itself consists of a data processing and communication shelter (ADP/COMM) and one or more analyst shelters. Data is received from various types of observations, processed in the ADP/COMM and passed to the analyst where data is interpreted and given to tactical commanders.

The shelters to be used were 8' x 8' x 20' (2.44 x 2.44 x 6.1m) and were originally designed for approximately 9000 pounds (4082kg) gross weight. The equipment to be used in the ADP/COMM brought the gross weight to approximately 14,500 pounds (6577kg). No significant weight change occurred in the analyst shelter. For all new structures and those in which significant changes have been made, an analysis should be done to insure the structural integrity of the item.

This paper describes the design requirements, structural analysis and subsequent modification of the ADP/COMM shelter. There were two basic objectives to be met. First, to determine if the shelter would be structurally sound with the current design requirements and new equipment suite; second, if the shelter was not sound, develop modifications to preserve integrity.

SHELTER STRUCTURE

The ADP/COMM shelter is manufactured by Craig Systems Corporation, Lawrence, Massachusetts. Difficulty was encountered in ascertaining the complete structural makeup of the bare shelter. The documentation package on this shelter had not been purchased originally and thus was not available, and since the drawings contained proprietary information, Craig Systems was reluctant to release the drawings. They were willing however, to allow plant visits and answer questions by telephone. Through visiting, X-Raying, dismantling and using some drawings available, it is believed that sufficiently accurate structural detail for use in the analysis was obtained.

The ADP/COMM shelter is composed of six basic panels with cutouts for doors, air conditioning, power plugs, etc., as required. While the dimensions of the individual parts are not identical, the construction of each panel is typical. An outer skin is spot welded to extruded hat sections, which make up the main stiffening members of the panel. Wood spacers are bonded to the top of the hat sections and, in turn an inner skin bonded to wood spacers. The wood spacers serve as a thermal barrier. The entire perimeter of each panel is closed by a box extrusion to which the skins and hat sections are welded. All voids in the panels are filled with urethane foam. The six panels are then assembled into the 8' x 8' x 20' (2.44 x 2.44 x 6.1m) shape with closure angles. These closure angles are pop riveted to the perimeter box extrusions with 3/16" (4.763mm) rivets.

The floor panel has, in addition to the main floor beams (hat extrusions), intercostal beams running perpendicular to the floor beams. These intercostals are comprised of box sections and are welded to the floor beams. The intercostals are arranged in a pattern evidently suited to the original equipment for which the shelters were designed. Figure 1 shows a cutaway of a floor panel.

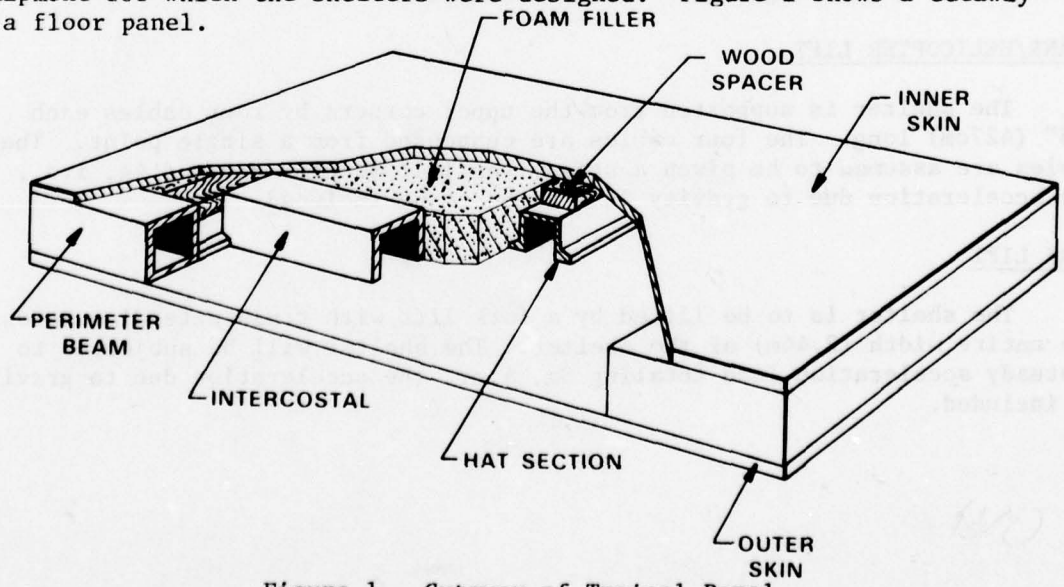


Figure 1. Cutaway of Typical Panel

The skins, beams and intercostals in the structure are all comprised of only one material type, that being 5053-H36 aluminum.

The entire shelter is mounted on two skids manufactured by the Barry Division of the Barry Wright Corporation, Burbank, California. The top and bottom structures of the skid are 6061-T6 aluminum with elastomer elements set between them. A section of the skid is shown in Figure 2.

When necessary to transport the shelter, a set of wheels, or mobilizers, is mounted forward and aft converting the shelter into a trailer. A modified A/M 32U-15 end-mount mobilizer is used for the MAGIS IAC.

DESIGN CRITERIA AND LOADS

The shelter must be designed to maintain structural integrity for the specified requirements as shown in Table 1. The basic mobility requirements are defined by Type V specifications of MIL-M-8090F. All drops are made from a height of 12 inches (30.48cm).

The following paragraphs give a brief description of each of the load conditions.

DROP TESTS

For the corner drops, one corner is placed on a 12" (30.48cm) timber, then the opposite corner is raised to a level position and allowed to drop onto a concrete surface. For the edge drops, one side of the shelter is supported at a 12" (30.48cm) height and the opposite side allowed to drop. The flat drop is performed by lifting the shelter to a height of 12" (30.48cm) and releasing onto a concrete surface.

CRANE/HELICOPTER LIFT

The shelter is supported from the upper corners by four cables each 168" (427cm) long. The four cables are suspended from a single point. The cables are assumed to be given a steady vertical acceleration of 4g, i.e., the acceleration due to gravity is assumed to be included.

FORK LIFT

The shelter is to be lifted by a fork lift with tines extending across the entire width (2.44m) of the shelter. The shelter will be subjected to a steady acceleration load totaling 3g, i.e., the acceleration due to gravity is included.

Table 1. Shelter Design Requirements

Test	Description
1	Corner Drops
2	Edge Drops
3	Flat Drop
4	Crane/Helicopter Lift
5	Fork Lift
6	Rail Hump
7	Rough Road

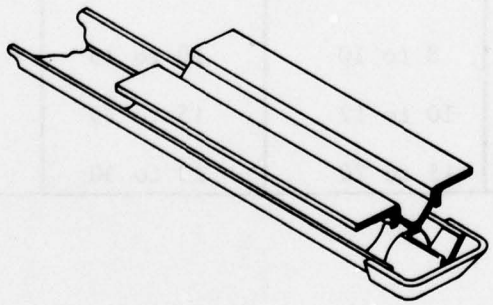


Figure 2. Skid Section

RAIL HUMP

The shelter will be placed on a rail flat car. It will be secured by wooden timbers around its lower perimeter and cables stretched from the upper corners to the rail car floor. The assembly will then be accelerated to a speed of 8-10 miles/hour (12.87-16.09KPH) and allowed to impact another rail car. Table 2 is a summary of accelerations based on measurements made with filtered piezioelectric accelerometers mounted to the base of a series of shelters tested at Aberdeen Proving Grounds, Maryland.* The horizontal and vertical accelerations are considered to act simultaneously.

Table 2. Shelter Accelerations From Rail Hump

Impact Velocity (MPH)	Acceleration (g)		Duration (MSEC)
	Vertical	Longitudinal	
8 (12.87KPH)	8 to 10	10 to 15	10 to 30
9 (14.48KPH)	10 to 12	15 to 25	10 to 30
10 (16.093KPH)	15 to 20	20 to 30	10 to 40

* McKay P., "Private Communication," Aberdeen Proving Grounds, Maryland, December 1976.

ROUGH ROAD

There are four types of rough road courses the shelter must traverse without failure, i.e., the six-inch (15.24cm) washboard, the Belgian block, the radial washboard, and the gravel road. Profiles of the first three courses are shown in Figure 3.

The six-inch (15.24cm) washboard profile approaches a sine wave with a double amplitude of six inches (15.24cm) and a complete cycle occurring every six feet (1.83m) for a distance of 800 feet (244m). The course surface is concrete. The Belgian block course consists of a cobblestone road which provides an irregular and bumpy surface. The individual cobblestones average approximately five inches (12.7cm) in width. The course irregularities, which not only vary along the length (3936 feet, 1200m) of the course but also across its width, have crests of about three inches (7.62cm). The crests are such that a vehicle traveling over them is subjected to both pitching and rolling motions.

Two 90 degree (1.5705rad) radial turns make up the radial washboard course along with symmetrical bumps which vary from two (5.08cm) to four (10.16cm) inches in height and from one (.3m) to six feet (1.83m) from crest to crest. The course is 255 feet (78m) long and 20 feet (6.1m) wide.

STRUCTURAL ANALYSIS

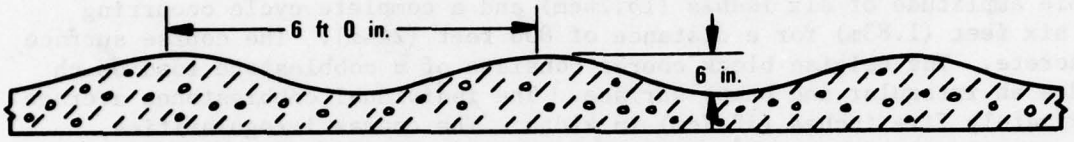
The structural analysis of the shelter comprises many pages of data. In fact, a detailed summary of all analysis would in itself be quite lengthy. This section includes a general description of the analysis methods, a relative comparison between the two finite element programs used, and a description of the changes needed as indicated by the analysis.

Initially, a conventional manual component by component stress analysis was begun using as a baseline the equipment suite as shown in Figures 4 and 5. This was going to be a lengthy and laborious process. It was also evident that the possibility of human error in evaluating all the loading conditions was quite high. However, these analyses indicated failures in many of the welded joints, particularly the intercostal to floor beam and floor beam to perimeter beam welds.

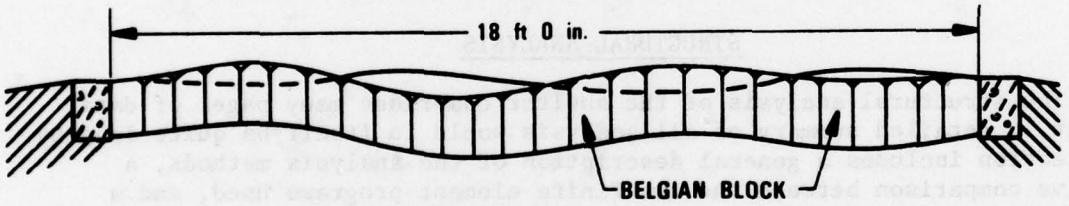
The failures indicated by the manual analysis led to a decision to employ the finite element technique to get a detailed stress analysis of the entire shelter structure.

The Naval Surface Weapons Center let contracts with the Center for Building Technology of the National Bureau of Standards (NBS) and the David Taylor Naval Ship Research and Development Center (DTNSRDC) to perform two simultaneous finite element analyses. These analyses were done concurrently so as to provide a check since no testing would be possible except on the completed system.

SIX-INCH WASHBOARD COURSE



BELGIAN BLOCK COURSE



RADIAL WASHBOARD COURSE

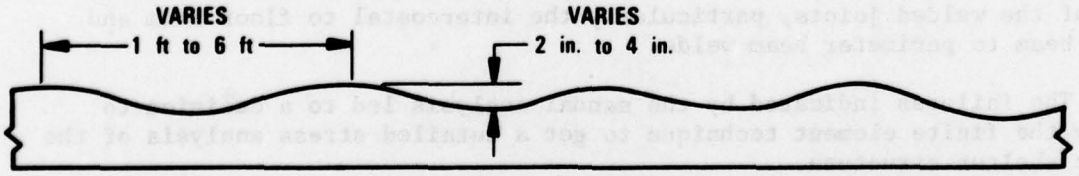


Figure 3. Road Courses

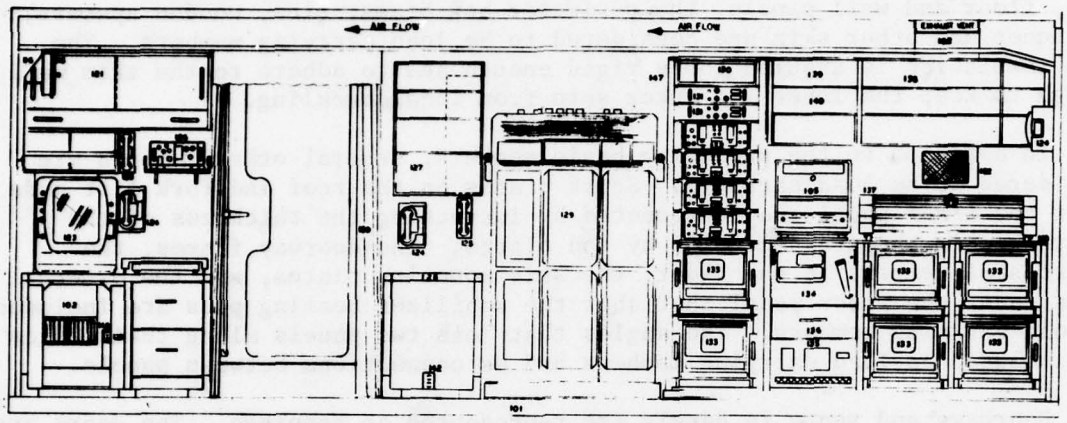


Figure 4. Shelter Internal Arrangement Main Door Side

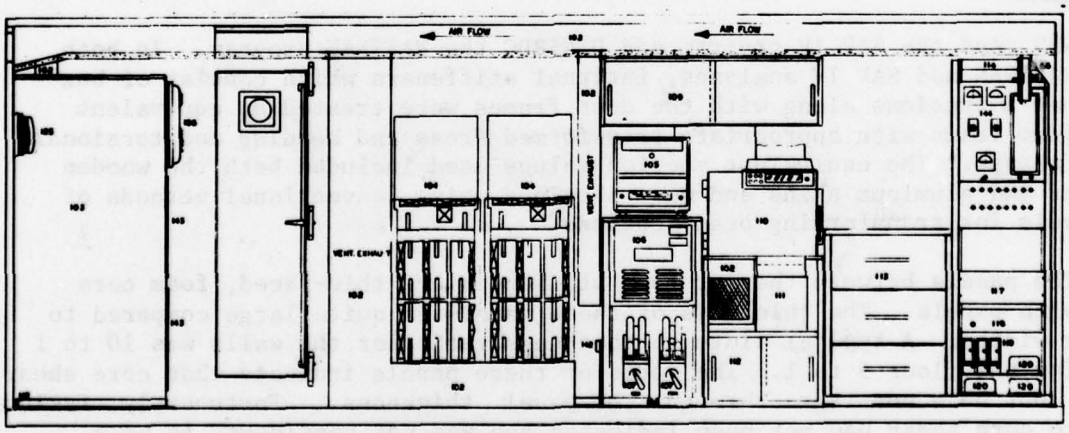


Figure 5. Shelter Internal Arrangement Emergency Door Side

MODELING ASSUMPTIONS

Identical data is supplied to the participants for the analyses. In the roof, floor and wall panels, the perimeter box beams, ribs, wooden spacers, and inner and other skin are considered to be load carrying members. The foam insulation is assumed to be rigid enough and to adhere to the skin well enough to keep the inner and outer skin from local buckling.

In addition to the preceding basic members, several other members are considered to be load carrying. Scuff plates on the roof and fork lift pads under the floor panel are represented by increasing the thickness of the outer skin in the area occupied by the plates. The doorway frames, the intercostal members in the floor, the skid mounting plates, and the external beams under the floor panel that abut the mobilizer bearing pads are included as load carrying members. The angles that join two panels along their edges are included as load carrying members and as connections between panels.

Doorways and vents in panels are represented as openings. The doors are considered to carry no load, however their mass is included. Also, the following are not included as load carrying members: the shoe plates of the skids, since they are attached by flexible mounts; and the ventilation and lighting suspension, since they are not mounted firmly to the shelter.

The internal equipment is represented as nonload carrying members attached to the floor or wall as required.

ANALYSIS

NBS used the SAP IV program and DTNSRDC the NASTRAN program. In both the NASTRAN and SAP IV analyses, internal stiffeners which consist of box and hat extrusions along with the door frames were treated as equivalent aluminum beams with appropriate transformed areas and bending and torsional stiffnesses. The equivalent section values used included both the wooden spacer and aluminum skins and were obtained using conventional methods of analysis for transforming beam sections.

The panels between the internal stiffeners are thin-faced, foam core sandwich panels. The thickness of these panels is quite large compared to their widths. A typical width to thickness ratio for the walls was 10 to 1 and for the floor 5 to 1. The ratio of these panels indicate that core shear will not be a constant through the panel thickness. Fortunately, failure due to core shear had not been indicated and was not considered to be a problem. Only the relative magnitude of the in plane stresses were considered to be important since failures were expected at beam joints. The typical plate element used in both analyses span the nominal distance (22", 55.9cm) between frame sections and has an aspect ratio of 1 to 1.

The CQUAD1 element of NASTRAN was used for sandwich panels and for SAP IV an equivalent plate of constant thickness used. This was done by transforming the cross-section geometry and material properties of the sandwich panel

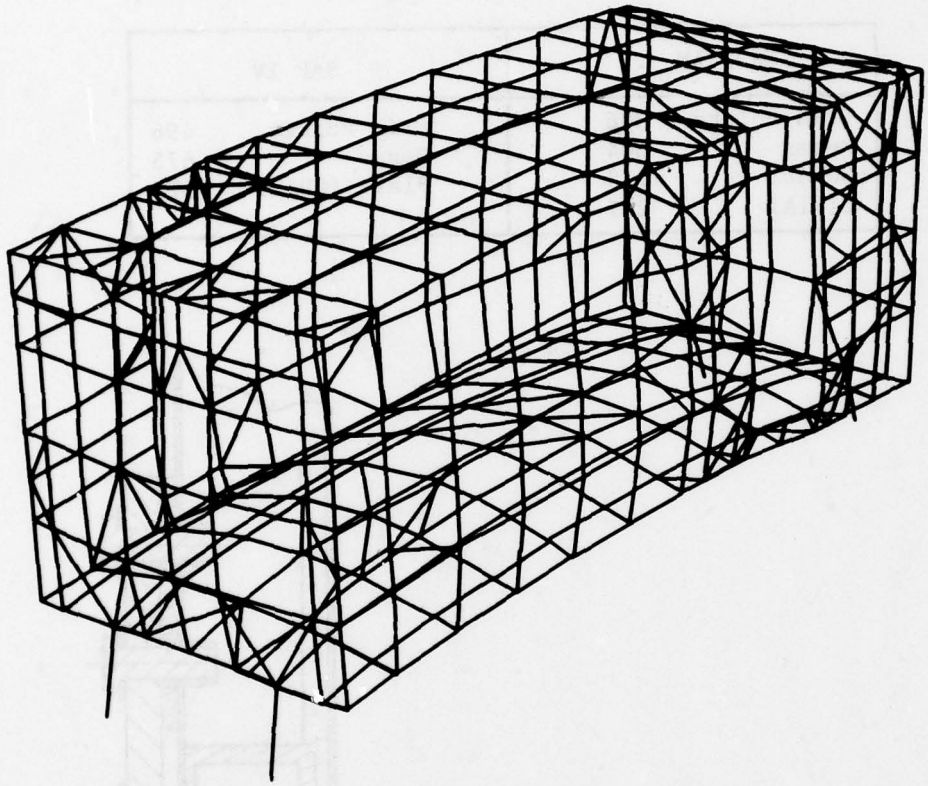


Figure 6. Fundamental Mode Shape from NASTRAN, 11.5 Hz

Table 3. Comparison of NASTRAN and SAP IV for Shelter Structure

NASTRAN		SAP IV	
Grid Points	386	Grid Points	496
Beams	804	Beams	675
CQUAD1	218	Plate (QUAD)	573
CTRIA1	207		

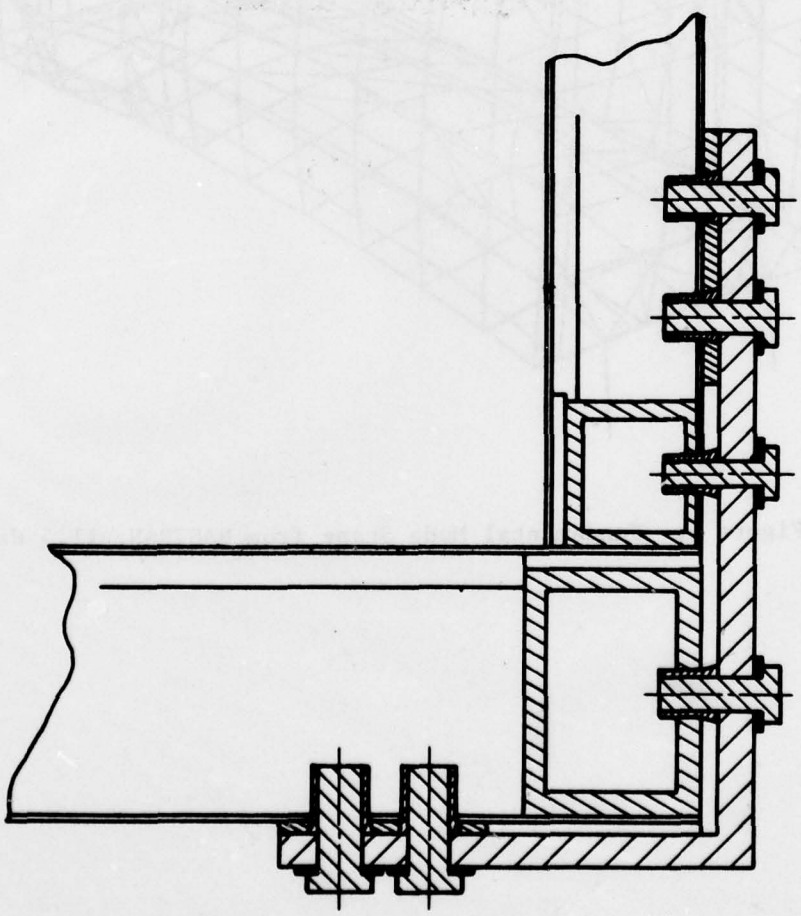


Figure 7. Typical Corner Fix

to those of an equivalent cross section for an anisotropic plate of constant thickness. (1) The thickness for the equivalent plate h_e is given in terms of the face plate thickness, t_f and distance between face plates, d by

$$h_e = \sqrt[3]{6t_f d^2}$$

The shear modulus, G_e for the equivalent plate is given in terms of the core shear modulus, G_e. This relationship assumes complete restraint against warping as indicated in reference 2.

$$G_e = \frac{dG_c}{h_e}$$

The relationship between elastic modulus and Poisson ratio for the equivalent plate and face material is given by

$$\frac{E_e}{1-\mu_e^2} = \frac{E_f}{1-\mu_f^2}$$

Table 3 shows the major types and finite element used in both the NASTRAN and SAP IV models.

After creation of the model the next step in the analysis of the shelter was to determine natural frequencies so that the type of reaction to excitations of various frequencies could be anticipated.

The boundary conditions for the load conditions fall into two classes. In considering the rail hump and flat drop, the shelter is sitting on the skids. However, for the road tests, the shelter is mounted on a mobilizer. The mobilizer units are being designed under separate contract and their characteristics are not known. A conservative approach was taken and was assumed that a rigid link connects the shelter to the point of rotation on the present mobilizer, thus neglecting any attenuation of the mobilizer spring-shock system.

NBS calculated a fundamental frequency of 34 hertz for the skid support condition while the frequency for a mobilizer type support was calculated by DTNSRDC as 11.5 hertz. Figure 6 shows the fundamental mode shape from the DTNSRDC model.

A discussion was held with the test and evaluation group* at Aberdeen Proving Grounds, Maryland pertaining to the relative severity of the test conditions. In general it had been found that if a shelter passed the rail hump and flat drop it would survive the road course tests.

Based on the above information, it was decided to limit the analysis to the rail hump and flat drop conditions. A static analysis would be done

*McKay. P.. "Private Communication" Aberdeen Proving Grounds, MD, August 1977.

using a combination of 20g vertical with 30g horizontal (see Table 2) for the rail hump and 20g vertical, 0g horizontal for the vertical drop. A recent report by Yancey[3] of NBS, which data from the work by Ostrem [4] is included indicates the values used for rail hump will be conservative. A shock spectra envelope for a coupling speed of 11 mph and a damping ratio of C/C_c = .03 indicates the maximum acceleration for a shelter with a natural frequency of 34 Hz will be on the order of 10g. The damping ratio C/C_c = 0.03 is indicative of nonshock isolated cargo according to Ostrem [4] and Foley [5].

The results of the analyses indicated points of probable failures. Extensive failure patterns were found throughout the floor, and areas of failure in the ceiling. The failures are not in the beams or skins themselves but their connections. The failures are of the following basic types:

(a) failure of floor beams to perimeter beam welds,
(b) failure of intercostal to floor beam welds,
(c) failure of ceiling beam to perimeter beam welds, and
(d) failure of floor and ceiling beam to exterior skin spot welds.

SHELTER MODIFICATION

The solution to the probable failures consisted of several modifications. First, additional beams were installed running longitudinally between the equipment and existing inner floor. This serves two purposes; the first is to spread the load, the second is to raise the neutral axis thus reducing the tensile weld failures induced by bending. A larger closure angle was incorporated to provide mechanical fastening between the floor/ceiling beam and perimeter beam. This relieves a portion of the load on the weld and also corrects a moment transfer failure in the existing angles. Figure 7 shows this fix. Failure of spot welds in the exterior floor/ceiling skins was taken care of by providing rivets between existing spot welds.

The results of the two original analyses agreed within 5 to 10 percent so the verification of the redesign was done only by DTNSRDC on their NASTRAN model. During the course of the analysis, the NASTRAN output including its graphical capabilities was found to be much easier to correlate to the original structure than SAP IV. All fixes were verified by the reanalysis. A modified shelter is shown in Figure 8.

TEST PROGRAM

Structural testing of the shelter was carried out in two phases. The mobility and transportation tests were carried out at Aberdeen Proving Grounds, Maryland. These tests consisted of traversing the road courses and performing the rail hump. The second phase was drop testing done at NSWC. Between these tests the shelter was taken to DTNSRDC for strain gaging. A crane lift was done and test data taken. This data will be compared to a

similar condition done on the finite element model. The shelter with a full suite of equipment has undergone all structural testing with no failure found.

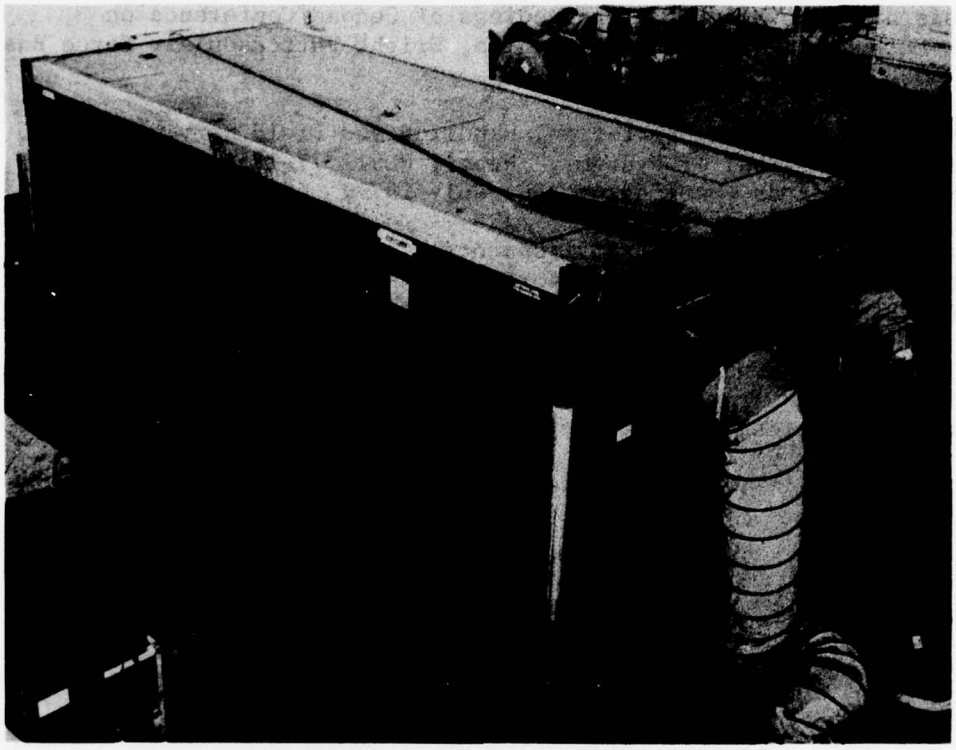


Figure 8. Modified Shelter

ACKNOWLEDGEMENT

The author expresses appreciation for the efforts of all members of the team who performed the various aspects of this analysis. The members of this team included Oliver J. Huey, NSWC; Petro Matula, DTNSRDC; and James R. Shaver, NBS.

REFERENCES

1. Shaver, J. R., "Finite Element Model for the S-552/T Shelter," Draft Report, National Bureau of Standards, Washington, DC, May 1978.

2. Clough, R. and Felippa, C., "A Refined Quadrilaterial Element for Analysis of Plate Bending," Proceedings of Second Conference on Matrix Methods in Structural Mechanics, Wright-Patterson Air Force Base, Ohio, 1968.

3. Yancey, C. W. C., "Transportation, Handling and Field Service Loads for Air Mobility Shelter Systems," Report NBSIR 77-1254, National Bureau of Standards, Washington, DC, July 1977.

4. Ostrem, F. E., "A Survey of Environmental Conditions Incident to the Transportation of Materials," Report PB-204-442, General American Transportation Corporation, Nile, Illinois, October 1971.

5. Foley, J. T. and Gens, M. B., "Environment Experienced by Cargo During Normal Rail Truck Transport-Complete Data," Report SC-M-77-0241, Sandia Laboratories, Albuquerque, New Mexico, August 1971.

SESSION Va: ORDNANCE AND MISSILES

Chairman: CAPT. J. Miceli, USN
Deputy Program Manager, Guided Missiles (Navy)
Army Armament Research and Development Command

CRITICAL SIZE FLAW INVESTIGATION OF THE HIFRAG PROJECTILE 265

C. B. Palmer
Naval Surface Weapons Center

DESIGN OF XM-753 ROCKET MOTOR TO BULKHEAD JOINT UTILIZING PINS. 285

J. Adachi
M. Benicek, and
T. Tsui
Army Materials and Mechanics Research Center, and
G. A. Benedetti
Sandia Livermore Laboratories

CRACK INSPECTION MAPS - AN APPLICATION TO COPPERHEAD. 307

J. I. Bluhm, and
C. E. Freese
Army Materials and Mechanics Research Center

CRITICAL SIZE FLAW INVESTIGATION OF THE HIFRAG PROJECTILE

CHARLES B. PALMER
Aerospace/Mechanical Engineer
Naval Surface Weapons Center
Dahlgren, VA 22448

ABSTRACT

This report presents a theoretical analysis and a preliminary verification of the defect which the 5-inch/54 Mark-82 (Hifrag) projectile will tolerate before brittle failure occurs due to gunfire loads. Using a finite element analysis, the highest tensile stressed region that the projectile experiences during gunfire was determined. Various size semielliptical surface defects were placed in this region and two gunfire tests to date confirm the analysis; however, further tests are needed to prove the validity of any proposed correlation between theoretical and experimental results.

INTRODUCTION

The phenomenon of structural failure by catastrophic crack propagation (fracture) at average stresses well below the yield strength has been known for many years. Brittle failures have occurred with increasing frequency as the strength and size of our engineering structures have increased. Army and Navy requirements for very high strength, lightweight hardware have given added importance to the problem of brittle fracture and greatly emphasized the need for a quantitative approach to the general problem of crack tolerance in structures.

In the past few years, special steels have been utilized in projectile designs to produce desired fragmentation characteristics. The Naval Surface Weapons Center (NAVSURFWPNCEN) recently completed development of the 5-inch/54 Mark-82 (Hifrag) projectile in which the high fragmenting steel HF-1 is used. The Hifrag is of two-piece construction, having a press-fit joint as shown in Figure 1. The tangential stress around the joint, due to the press-fit[1], makes this round very susceptible to fracture during gunfire. With the aid of the ZPI-1 finite element computer code[2] the tangential stress in the joint was determined. Based on plain strain fracture theory, a critical flaw (a defect that propagates catastrophically during gunfire) was determined. Various size semielliptical surface flaws were placed in the joint. The flawed rounds were gunfired at a service charge condition of approximately 13,000 g's acceleration. The work described in this paper attempts to correlate experimental data obtained from gunfire tests with analytical results.

PRECEDING PAGE BLANK-NOT FILM

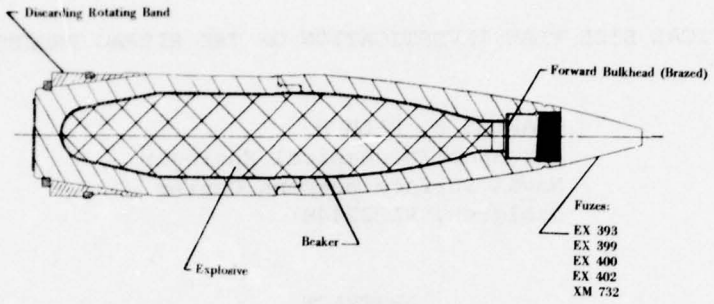


FIGURE 1. SCHEMATIC OF 5"/54 HI-FRAG PROJECTILE

ANALYTICAL APPROACH

PROJECTILE DESCRIPTION

The 5-inch/54 Mark-82 (Hifrag) projectile design is shown in Figure 1. The body is of two-piece construction, weighing approximately 69 pounds (31.3 kgf). The projectile is forged from HF-1 steel that has the following properties: 150 ksi (1,034 M Pa) minimum yield strength, 198 ksi (1,365 M Pa) ultimate tensile strength, 8.9 percent elongation, and a fracture toughness of 35 ksi$\sqrt{in}$ (39 M Pa$\sqrt{m}$). The explosive load is approximately 6.6 pounds (3 kgf) of PBXW-106 castable plastic bonded explosive [loading density of 0.059 lbs/in^3 (1,630 kg/m^3)]. The explosive is cast as a billet in a plastic beaker. The maximum chamber pressure under proof condition is 63.2 ksi (436 M Pa) which corresponds to a maximum acceleration of 15,500 g's for the Hifrag projectile. The flawed projectiles were gunfired at a service charge condition of approximately 13,000 g's acceleration.

METHOD

The finite element method was chosen for the stress analysis of the projectile because of its accuracy in the analysis of complex shaped and loading conditions. The ZPI-1 code was chosen over other available codes due to its user oriented nature and accuracy in the elastic-plastic analysis of axisymmetric shapes. This code is a modified version of the ZP-26 code[3] which was written by Dr. Gifford at the David W. Taylor Naval Ship Research and Development Center. The ZPI-1 code was modified by Dr. Lindeman at the Naval Surface Weapons Center to include stress analysis of interference fits. In addition to interference fits, the ZPI-1 program can perform static, elastic-plastic analyses of axisymmetric structures containing contact surfaces. The structure may gap or slide along these surfaces.

The major advantage of this program lies in the fact that only the geometry of the two members and the material properties are needed for input. Unlike other methods used in the analysis of interference fits, neither the interference pressure not final deformation of the two members must be assumed.

FINITE ELEMENT PROGRAM

Since the press-fit interference influences the stress state of the Hifrag projectile, test rounds were selected with approximately the same radial interference [0.008 inch (0.20 mm)]. A stress analysis was then performed on the Hifrag projectile, with this radial interference, using the ZPI-1 finite element computer program[2]. Using St. Venant's principle, only a small portion of the projectile around the press-fit joint was modeled as shown in the finite element mesh (Figure 2). This allows for greater element detail of the joint without affecting the stress distribution.

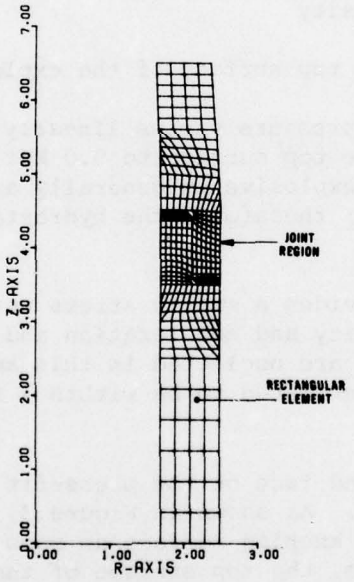


Figure 2. Mesh Used for Joint Analysis

LOADING CONDITION

In performing the analysis an acceleration of 13,000 g's was assumed for the projectile gunfired at service charge conditions. As it turned out, the two projectiles tested had peak accelerations of 13,260 g's and 13,300 g's. All loads were assumed to be axisymmetric, or unchanging in the circumferential direction.

The force exerted by the forward portion of the projectile not shown in Figure 2 was assumed to be uniformly distributed on the top flat surface of the model. The value was estimated by multiplying the mass forward of this surface by the acceleration and dividing by the cross-sectional area. The magnitude determined by this method was 28.96 ksi (200 M Pa). The bottom surface of the model was fixed from moving in the longitudinal direction.

The explosive load was assumed to behave as a liquid during gun launch. The pressure acts in a direction normal to the projectile wall and has a varying magnitude, P, given by

$$P = \rho g h \qquad (1)$$

where

P = explosive pressure
ρ = explosive mass density
g = acceleration
h = distance below the top surface of the explosive

The magnitude of explosive pressure varies linearly in the axial direction from 5.5 ksi (38 M Pa) at the top surface to 9.0 ksi (62 M Pa) at the bottom surface of the model. The explosive is generally assumed to be imcompressible (Poisson's ratio = 0.5); therefore, the hydrostatic assumption is valid for small deflections.

The computer model provides a static stress analysis of the projectile. The effect of angular velocity and acceleration and the dynamic effects due to acceleration body forces are neglected in this analysis. The accuracy of this type of analysis was estimated to be within 4 to 5 percent of the true stresses[1].

The effects of a knurled face on the press-fit surface of the Hifrag projectile was also studied. As shown in Figure 3, the male press-fit joint has a knurled surface. The knurled surface as such could not be modeled by the computer code; therefore, the top surface of the knurl was modeled as a smooth surface. Strain gauges were placed in the hoop direction on the outside diameter of nine forward Hifrag projectile noses near the joint to determine the accuracy of this assumption. The noses were then pressed onto the bases. Figure 4 shows the comparison of measured values of hoop strain with that predicted by the computer model, and that the knurling has an upper bound equivalent to a solid surface. Thus, the computer results can be considered as the upper limit or worst case under any loading situation.

Using the mesh shown in Figure 2, an elastic-plastic stress analysis for a radial interference of 0.008 inch (0.20 mm) was obtained. Figures 5 and 6 show that the female joint section is a high stressed region with a maximum Von Mises stress of 155 ksi (1,069 M Pa) and a maximum tensile hoop

stress of 94 ksi (648 M Pa) in region A. A flaw would most likely propagate in a high tensile stressed region. Therefore, region A was chosen as the appropriate area for incorporating a flaw in the projectile hardware used in the experimental portion of this study.

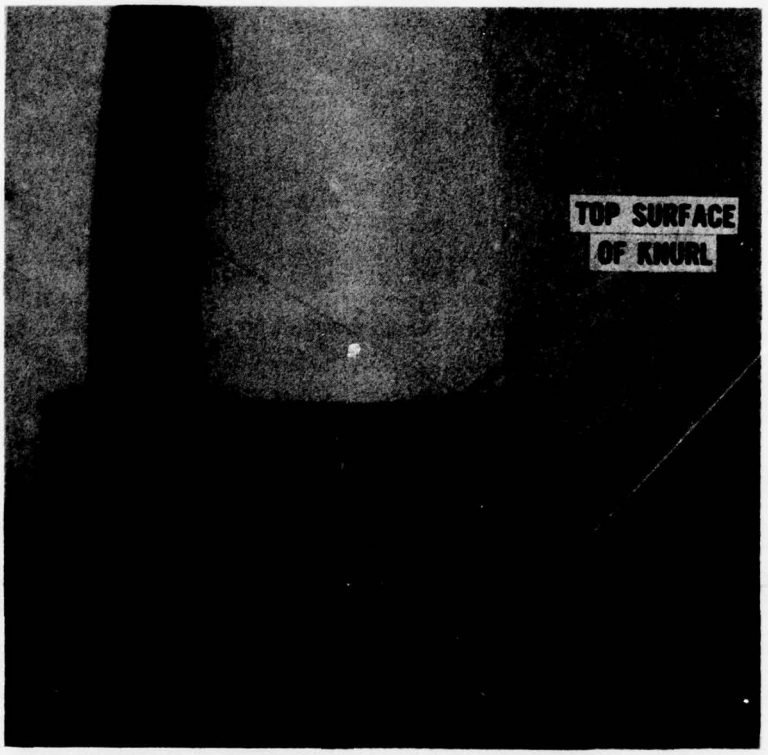


Figure 3. Knurled Press-Fit Joint

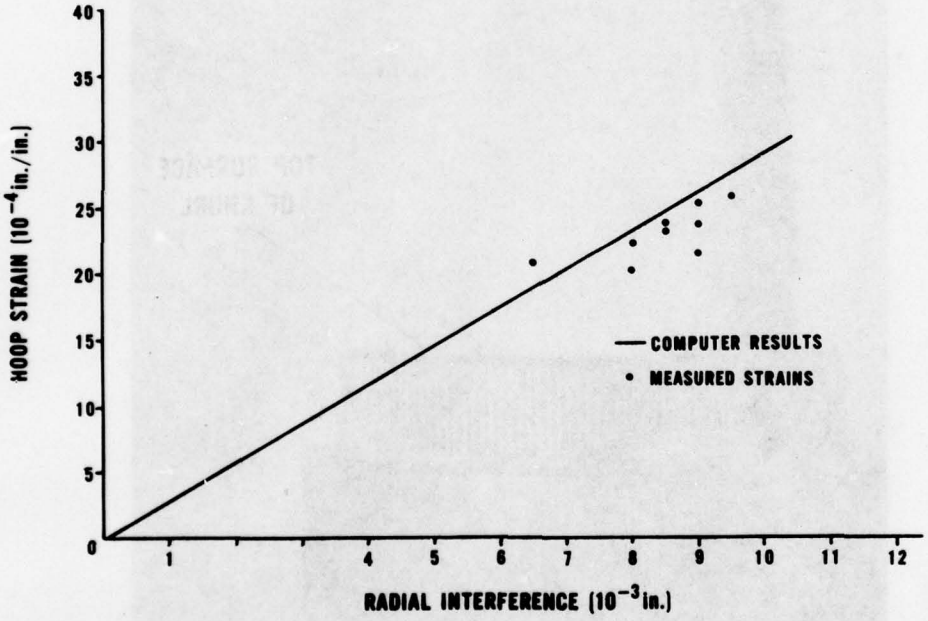


Figure 4. Measured Hoop Strain Versus Radial Interference on 5-Inch/54 Hifrag Projectiles

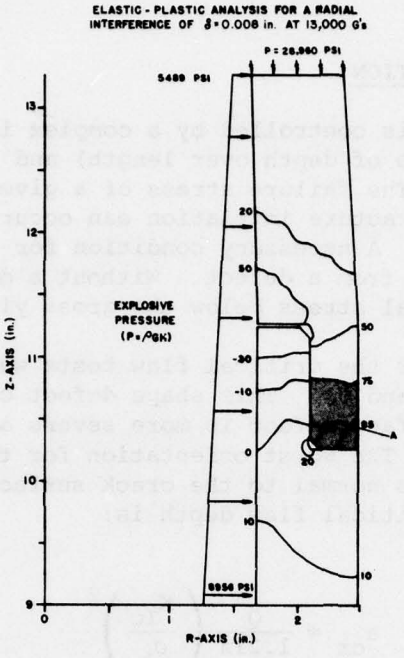


Figure 5. Hoop Stress Contours (ksi)

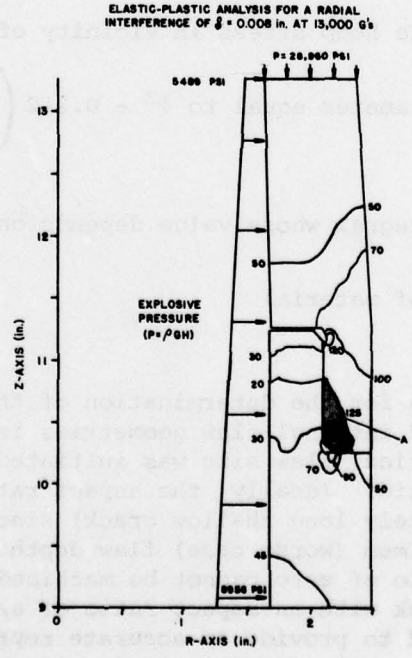


Figure 6. Von Mises Stress Contours (ksi)

CRITICAL FLAW SIZE ESTIMATION

Fracture initiation is controlled by a complex interrelationship between defect size (ratio of depth over length) and stress state in the vicinity of the defect. The failure stress of a given defect will depend primarily on its size. Fracture initiation can occur at nominal stress levels below gross yielding. A necessary condition for this to occur is that the fracture must emanate from a defect. Without a defect present, failure will not occur at a nominal stress below the gross yield stress.

The defect chosen for the critical flaw tests was a semielliptical surface flaw (Figures 7, 8, and 9). This shape defect can be easily machined into a projectile. A surface defect is more severe and more likely to occur than an embedded defect. The worst orientation for this flaw is such that the tensile hoop stress is normal to the crack surface. The equation[4,5] used for estimation of critical flaw depth is:

$$a_{cr} = \frac{Q}{1.21\pi}\left(\frac{K_{Ic}}{\sigma_h}\right)^2 \qquad (2)$$

where

K_{Ic} = plane strain fracture toughness

σ_h = average tensile hoop stress in vicinity of crack

Q = flaw shape parameter equal to $\Phi^2 - 0.212\left(\frac{\sigma_h}{\sigma_y}\right)^2$

and where

Φ = elliptical integral whose value depends on the shape of the crack (aspect ratio)

σ_y = yield stress of material

A graphical solution for the determination of the flaw-shape parameter Q for various surface and internal-flaw geometries is presented in Figure 7.[5] The determination of critical flaw size was initiated with the selection of an appropriate aspect ratio. Ideally, the aspect ratio for the flaw would be zero (i.e., an infinitely long shallow crack) since this type of configuration would yield a minimum (worst case) flaw depth. However, since a crack with an aspect ratio of zero cannot be machined into the joint region of the projectile, a crack with an aspect ratio of a/2c = 0.1 was chosen. This ratio has been found to provide an accurate representation of the most severe types of cracks normally found in projectile bodies.[6]

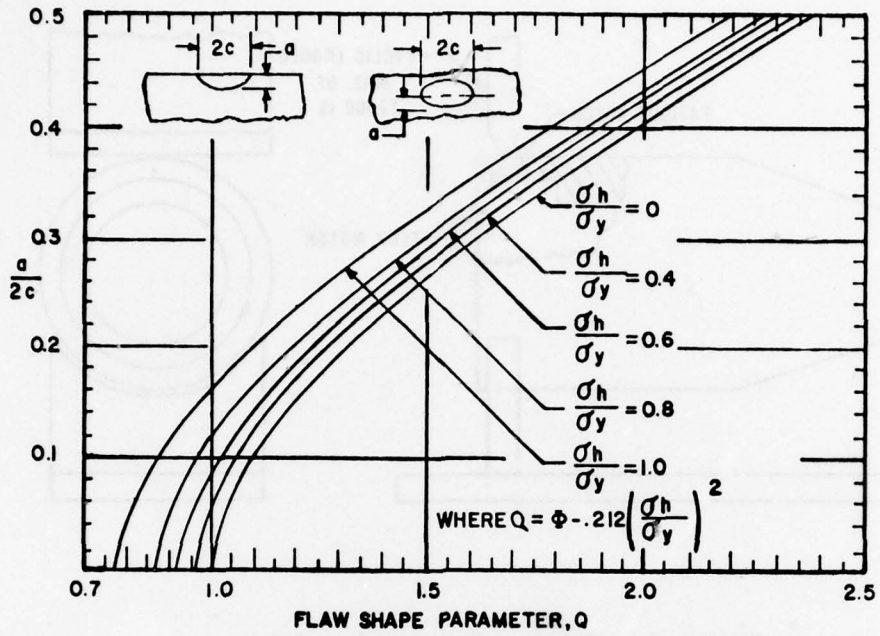


Figure 7. Flaw Shape Parameter, Q

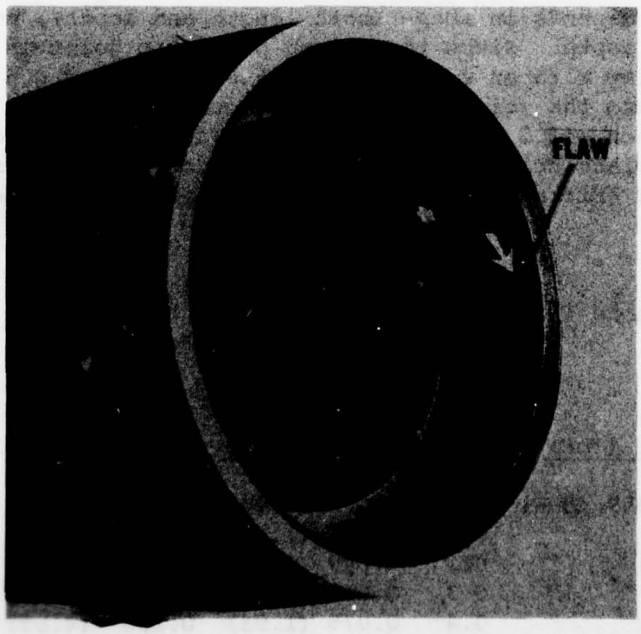


Figure 8. Typical Placed Defect in Forward Body Section of 5-Inch/54 Hifrag Projectile

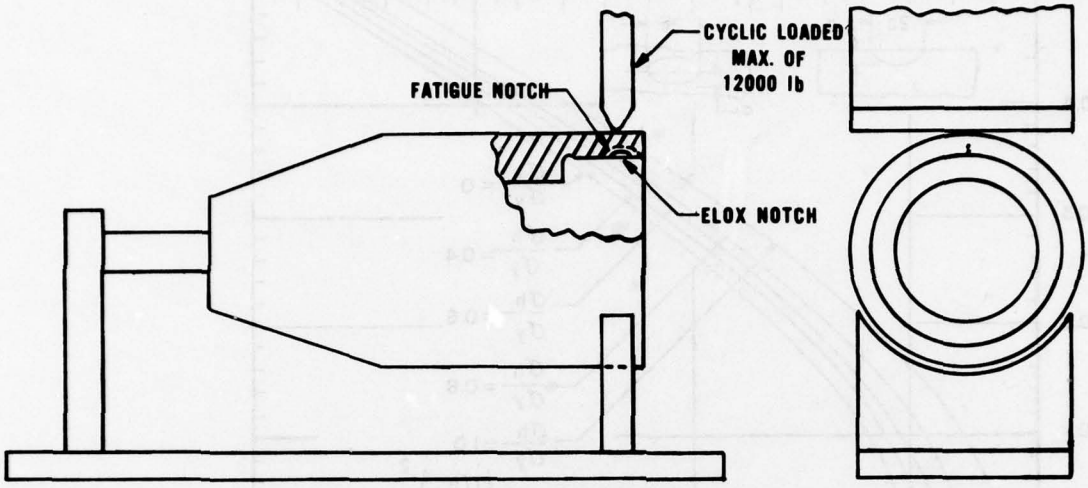


Figure 9. Fatigue Precracking Setup

For a 0.008-inch (0.20-mm) radial interference at 13,000 g's and a fracture toughness of K_{Ic} = 35 ksi$\sqrt{in}$ (39 M Pa$\sqrt{m}$) for HF-1 steel, the critical flaws for region A of highest tensile stress are shown in Table I. For surface flaws with a/2c ratios ranging from 0.0 to 0.5, Table I shows that the critical flaw depends on shape (both length and depth), not on a single dimension such as depth. Since the Hifrag press-fit joint is only 1-inch (25-mm) long, a flaw with an aspect ratio between 0.1 and 0.5 may be purposely machined into the joint without being critical as long as the length is between 0.41 inch (10.0 mm) and 0.184 inch (4.7 mm), respectively. The next step was to place critical and larger than critical flaws in region A of several Mark-82 (Hifrag) projectiles and gunfire them to verify the analytical results.

Table I Critical Surface Flaw at 0.008 inch (0.20 mm) Radial Interference

[ksi (M Pa)]	a/2c	a_{cr} [in (mm)]	2c [in (mm)]
80.659 (556)	0.0	0.037 (0.94)	∿
" "	0.1	0.041 (1.04)	0.410 (10.41)
" "	0.2	0.049 (1.24)	0.245 (6.22)
" "	0.3	0.061 (1.55)	0.203 (5.16)
" "	0.4	0.076 (1.93)	0.190 (4.83)
" "	0.5	0.092 (2.34)	0.184 (4.67)

HARDWARE PREPARATION

FLAW SIZE INITIATION

Flaws can be induced during manufacture of the projectile components. The flaws may be the result of the forging process, tempering or material impurities. Such flaws cause weaknesses that can lead to structural failure during gunfiring. Naturally flawed components for testing are difficult to obtain so artificially flawed components must be generated. This was done by machining notches and cyclic stressing the flaw to induce fatigue cracks that simulate natural flaws. Although "fatigue" cracks will be mentioned throughout the text that follows, the reader should bear in mind that there is no "fatigue" problem associated with projectile manufacture and use and that the discussion is really centered on manufacturing defects or "flaws".

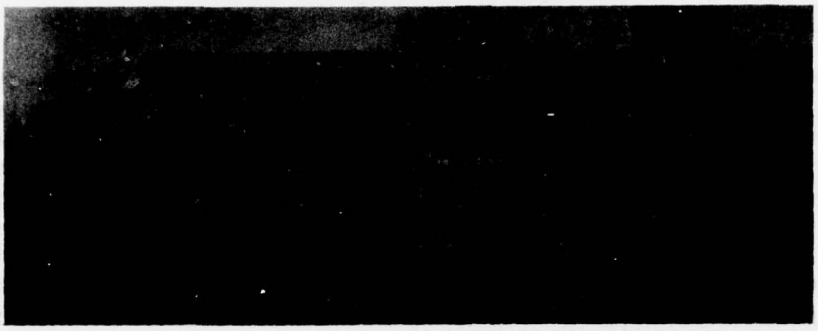
A small elliptical notch was generated in region A in several Hifrag projectiles (Figure 8) with the use of an electrical discharge machine (EDM). The depth of the notch ranged between 0.0196 inch (0.498 mm) and 0.0230 inch (0.584 mm), and the length ranged between 0.315 inch (8.001 mm) and 0.345 inch (8.763 mm).

In linear elastic fracture mechanics, the calculation of flaw sizes is based on the assumption of a sharp crack [root radius $\leq$ 0.005 inch (0.13 mm)]. Therefore, the EDM notch was cyclic loaded to generate a sharp fatigue crack approximately 0.05 inch (1.3 mm) beyond the notch, as recommended in ASTM E399.[7] Figure 9 shows how fatigue cracks were generated, and Figure 10 shows two fatigue cracks that resulted. Length and depth measurements were taken of seven fatigued cracks, and Figure 11 shows a least-squares fit of this data in a linear curve of depth versus length. The equation of this curve is:

$$D = -0.0480 + 0.3112L \qquad (3)$$

To verify the assumption that a linear relationship was valid, length and depth measurements were taken of seven fatigued HF-1 steel test specimens. Figure 12 shows that this linear relationship does indeed exist. These ring specimens were cut from 5-inch (127-mm) bar stock that was heat-treated to the same Rockwell hardness as Hifrag projectiles, 39 $\pm$ 3. The forging of the HF-1 steel in Figure 11 probably was the reason for the slight change in slope of the two curves.

The linear curves of depth versus length in Figures 11 and 12 show very good agreement with the actual measurements of the fatigue cracks. The percentage difference between the actual fatigue cracks and that of the curves ranged between 0.0 and 11.8 percent. Based on the above result, the depth of a fatigue notch in the test projectile was determined by substituting the known length of the cracks into equation (3). Measurements of length were taken with a microscope.



Flaw 1



Flaw 2

Figure 10. Fatigue Cracks

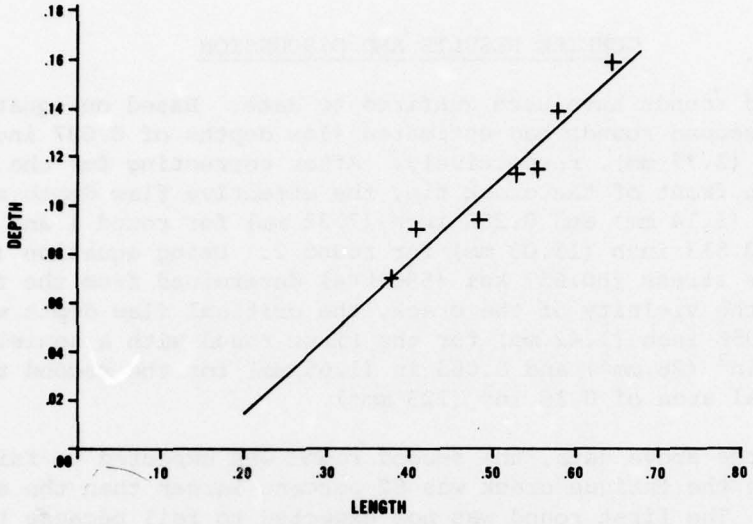


Figure 11. Fatigue Crack Measurements in the Hifrag Projectile

Ultrasonic measurements were taken of the fatigue cracks in Figure 11 before the cracks were sectioned. These measurements failed to detect some cracks and grossly overestimated the size of others.[8] Most nondestructive inspection methods can fail to detect cracks or defects that are tight (fatigue crack) or in an inconvenient orientation; and, human error must also be expected. Therefore, in the selection of rounds to be gunfired, the estimated flaw depth was determined solely from equation (3).

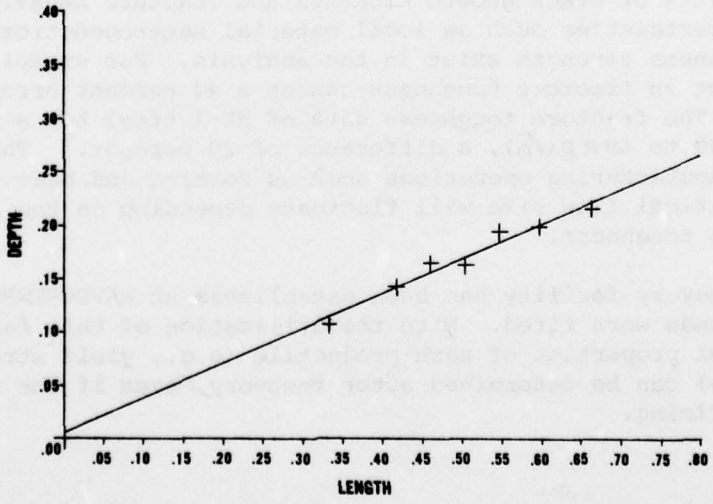


Figure 12. Fatigue Crack Measurements in Ring Test Specimens

GUNFIRE RESULTS AND DISCUSSION

Two flawed rounds have been gunfired to date. Based on equation (3), the first and second rounds had estimated flaw depths of 0.037 inch (0.94 mm) and 0.109 inch (2.77 mm), respectively. After correcting for the small plastic zone in front of the crack tip, the effective flaw depth and length was 0.045 inch (1.14 mm) and 0.288 inch (7.32 mm) for round 1 and 0.118 inch (3.00 mm) and 0.513 inch (13.03 mm) for round 2. Using equation (2) and the average tensile stress [80.657 ksi (556 M Pa) determined from the finite element code] in the vicinity of the crack, the critical flaw depth was calculated to be 0.056 inch (1.42 mm) for the first round with a semielliptical area of 0.041 in^2 (26 mm^2) and 0.065 in (1.65 mm) for the second round with a semielliptical area of 0.19 in^2 (123 mm^2).

Based on the above data, the second round was expected to fail during gunfire because the fatigue crack was 82 percent larger than the expected critical flaw. The first round was not expected to fail because the fatigue crack was 20 percent below the estimated critical flaw. Only the second round with a flaw depth of 0.118 inch (3.00 mm) failed (Figure 13). The gunfire results along with other data such as chamber pressure and acceleration are shown in Table II. Much more testing is necessary before any true comparison can be made between the experimental data and analytical results, but the two gunfire results show promise.

As mentioned earlier, ultrasonic inspection of the small fatigued EDM flaws was not accurate. Another nondestructive test, such as a proof pressure test, should be considered. Pressurizing the projectile to loads slightly higher than at gun launch with no fracture occurring will ensure that no failure occurs during gunfire.

Precise analysis of crack growth kinetics and fracture behavior is difficult because uncertainties such as local material heterogenetics, residual stresses and toughness strength exist in the analysis. For example, an error of 20 percent in fracture toughness causes a 44 percent error in critical flaw depth. The fracture toughness data of HF-1 steel has a range of 35 to 45 ksi$\sqrt{in}$ (39 to 49 M Pa$\sqrt{m}$), a difference of 29 percent.[9] This range may result from manufacturing operations such as forming and heat treatment. Therefore, the critical flaw size will fluctuate depending on the actual values of fracture toughness.

A gunfire recovery facility has been established at NAVSURFWPNCEN since the two flawed rounds were fired. With the utilization of this facility, the actual material properties of each projectile (e.g., yield stress and fracture toughness) can be determined after recovery, even if the round fractures during firing.



Round 1



Round 2

Figure 13. Gunfired Flawed Rounds, 25 Feet from Muzzle

Table II Gunfire Results

Rnd	Intrf [in(mm)]	Projectile Weight [lbf (kgf)]	Chamber Pressure [ksi(MPa)]	Accel (g's)	Estimated Flaw Depth [in (mm)]	Critical Flaw Depth [in (mm)]	Expected Gunfire Results	Gunfire Results
1	.008(.2)	69.20(31.4)	55.6 (383)	13,300	.045(1.14)	.056(1.42)	No Failure	Did Not Break Up
2	.008(.2)	69.15(31.4)	55.4 (382)	13,260	.118(3.00)	.065(1.65)	Failure By Fracture	Nose Sect Broke Up

The actual shape of the flaw can be determined before gunfiring if a quarter-shape flaw (half of a semiellipse) is used instead of a semielliptical flaw. The procedure involves the placement of a semielliptical notch in an extended Hifrag joint (Figure 14). The notch is then fatigued and the extended joint is machined until only half of the semiellipse remains (Figure 14). Both sides of the quarter-shape flaw are then visible and can be polished; and, measurements of length and depth can be taken with the aid of a microscope. Magnified pictures of the polished sides will also reveal the actual dimensions (Figures 15 and 16).

By conducting the flawed tests this way, no uncertainties exist as to the shape of the flaws before gunfiring, or as to material properties after gunfiring. With most of the uncertainties controlled, a good comparison between experimental data and calculated results can be properly made.

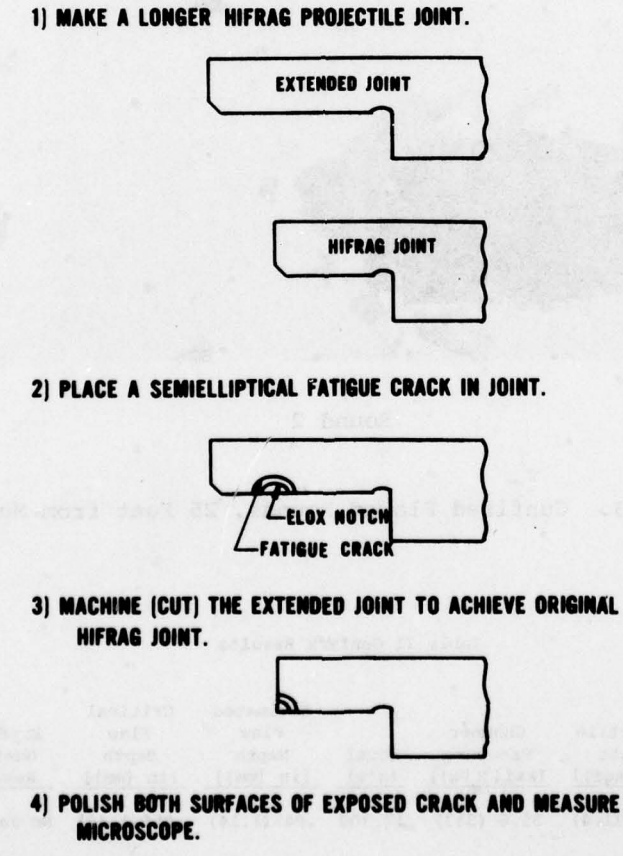


Figure 14. Procedure in Determining Quarter-Shape Flaw Dimensions

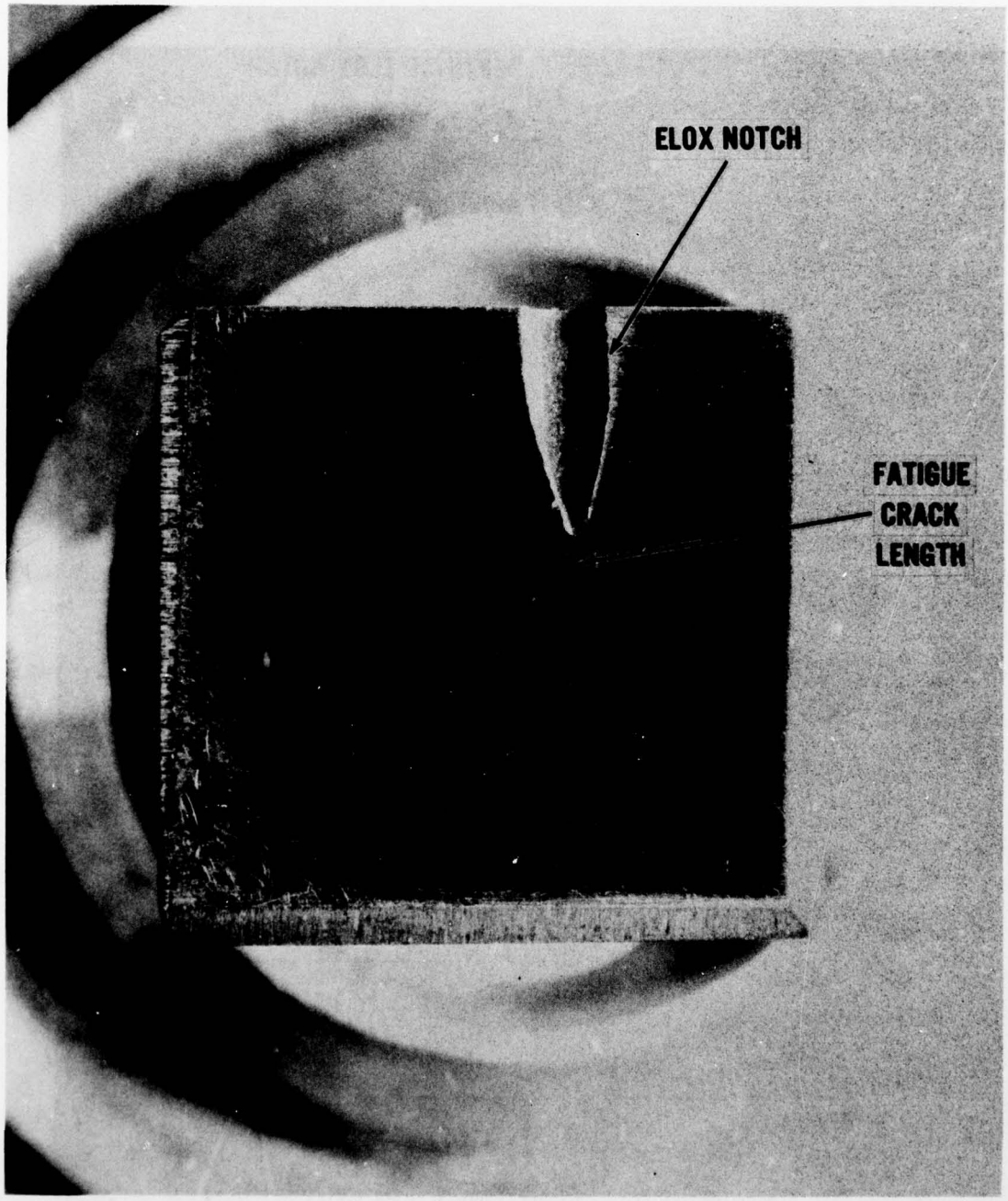


Figure 15. Quarter-Shape Flaw, Top Surface

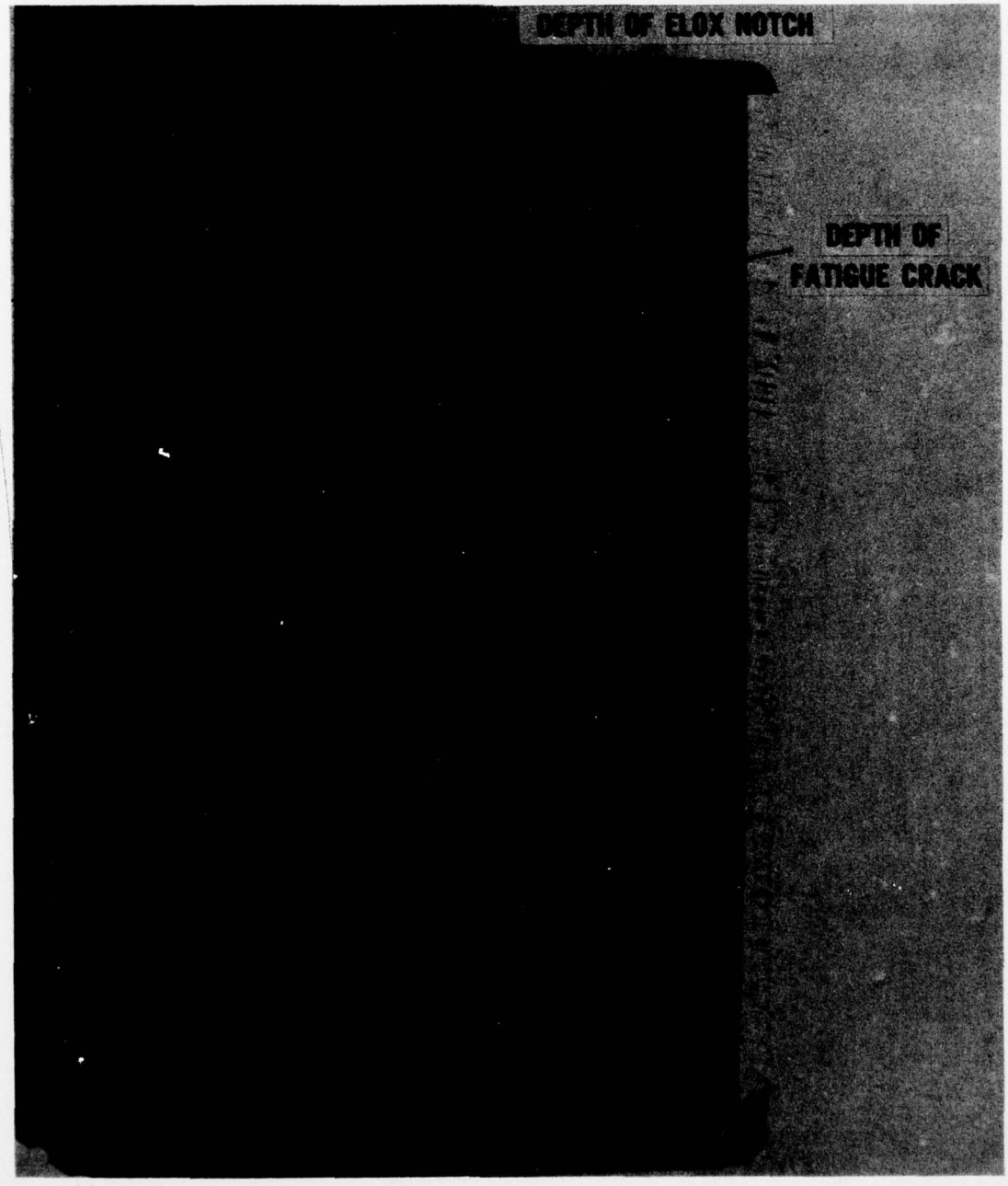


Figure 16. Quarter-Shape Flaw, Cut Surface

CONCLUSIONS AND RECOMMENDATIONS

1. No conclusion as to critical flaw size was reached, as this study was based on only two tests. However, it appears that the upper and lower bounds are known for the 13,000-*g* load and that further tests should be conducted to determine the critical flaw size.

2. These additional tests to determine critical flaw size should use some form of projectile recovery to enable the failed area to be more thoroughly analyzed.

3. The use of a quarter-shaped flaw over a semielliptical flaw has the definite advantage in that the flaw dimensions are known, and should therefore be considered in future tests.

4. Behavior of PBXW-106 explosive during setback should be determined from experimental tests.

5. The possibility of replacing the ultrasonic inspection with a proof pressure test should be considered when examining projectiles for critical size flaws.

REFERENCES

1. Lindeman, R. A., *Critical Evaluation and Stress Analysis of the 5-Inch/54 Hifrag Projectile*, Naval Surface Weapons Center/Dahlgren Laboratory Technical Report, NSWC/DL TR-3164, Dahlgren, VA July 1974.

2. Lindeman, R. A., *Finite Element Computer Program for the Solution of Nonlinear Axisymmetric Contact Problems with Interference Fits*, Naval Surface Weapons Center/Dahlgren Laboratory Technical Report, NSWC/DL TR-3148, Dahlgren, VA, June 1974.

3. Gifford, N., Jr., *Finite Element Analysis for Arbitrary Axisymmetric Structures*, David W. Taylor Naval Ship Research and Development Center Report, NSRDC AD-835243, Bethesda, MD, March 1968.

4. Kobayaski, A. S. and Moss, W. L., *Stress Intensity Magnification Factors for Surface-Flawed Tension Plate and Notched Round Tension Bar*, Proceedings of the Second International Conference on Fracture, Brighton, England, 1968.

5. *Progress in the Measurement of Fracture Toughness and the Application of Fracture Mechanics to Engineering Problems*, Materials Research and Standards, 4 (3), 107, March 1964.

6. Parrish, J. A., *Critical Flaw Size Calculations for 9260 Steel, 76-mm Projectiles*, Naval Surface Weapons Center/Dahlgren Laboratory Technical Note TN-E-17/73, Dahlgren, VA, October 1973.

7. *Metals: Mechanical, Fracture, and Corrosion Testing, Part 10*, Annual Book of ASTM Standards, American Society for Testing and Materials, 1916 Race Street, Philadelphia, PA, 1975.

8. Buckingham, R. D., *Hifrag Faulty Unit Flaw Size Measurements*, Naval Surface Weapons Center/Dahlgren Laboratory memo EPA:RDB:lmc, Dahlgren, VA, 19 November 1974.

9. Hall, J. D., *Picatinny Arsenal and Pitmann-Dunn Laboratory, Frankford Arsenal; trip report of visit to*, Naval Surface Weapons Center/Dahlgren Laboratory memo EJMQ:JAH:min, Dahlgren, VA, 09 July 1974.

DESIGN OF THE XM-753 ROCKET MOTOR TO BULKHEAD JOINT UTILIZING PINS

JIRO ADACHI
Research Team Leader

MILOSLAV BENICEK
Mechanical Engineer

TIEN-YU TSUI
Mechanical Engineer
U.S. Army Materials & Mechanics Research Center
Watertown, Massachusetts 02172

and

G. A. BENEDETTI
Technical Staff Member
Sandia Livermore Laboratorires
Livermore, California

ABSTRACT

Because of the failure of the JFF-1 EDT projectile in December 1976 the threaded joint between the rocket motor and the bulkhead of the XM-753 projectile was redesigned. The successful solution of this joint problem employed a pinned joint with snap rings to retain the pins.

Specific design requirements included structural integrity under launch, barrel exit and inflight loads, and disassembly and reassembly in the field without damage to components.

The new pin joint developed has been installed and test fired without incident in ten XM-753 test projectiles at normal and overtest g levels.

The easy assembly and disassembly of the snap ring assemblies in these projectiles shows that final design requirement also was met.

INTRODUCTION

Because of the failure of the first of a series of advanced development test projectiles in December 1976 the threaded joint joining the rocket motor to the aft bulkhead of the XM-753 projectile was redesigned. The successful solution of this joint problem employed a pinned joint with snap rings to retain the pins and was the result of a combined effort involving contributions from ARRADCOM, Sandia Livermore Laboratories and AMMRC. This paper briefly discusses the analysis of the failure, the redesign studies and the design resulting from the studies.

BACKGROUND

The XM-753 is an 8" nuclear projectile. Its conventional ammunition counterpart is the XM-650. Both projectiles utilize a rocket assist system requiring the connection of a rocket motor to the aft bulkhead of the XM-753 and to the warhead of the XM-650. The early versions of these projectiles utilized the threaded joint shown on the XM-650 projectile in Figure 1.

In a threaded joint the large torsional forces, which result from the rotational acceleration imparted to the projectile through engagement of the rotating band with the gun tube rifling twist, are transmitted primarily by friction forces on the contact interfaces of the joint. These surfaces are usually knurled to increase the friction coefficient. However during assembly the act of tightening the joint tends to smooth out the knurling and produces a dilemma in which tightening of the threaded joint to produce higher normal contact force to increase friction force also tends to reduce the friction force by smoothing out the contact surface. The actual friction resistance available is therefore uncertain at best. At worst, it is possible for the joint contact surfaces also to be lubricated accidentally by cutting oil, thread locking compounds or moisture which further reduces the friction coefficient and the available resisting friction force to unsafe levels.

The projectile failure which led to the redesign of the joint occurred as a relative rotation of the mating components of the joint through 350° resulting in stripping of the threads, functional failure of internal systems and reduced range. Although it was apparent that the resisting friction force had not been large enough to carry the applied torque, post-failure examination proved inconclusive as to the exact cause of the failure - whether excessive torsion load, deficient frictional resistance, or a combination of the two. Only traces of friction-reducing foreign substance were found in the interface. Also rotational accelerations were not measured.

In order to maintain firing schedules reinforcing pin retrofits were designed for the remaining projectiles in the test series and these were tested successfully. In addition, because of the uncertain torsion-carrying ability of the threaded joint, the design of the pinned joint was undertaken.

DESIGN REQUIREMENTS

The principal requirements which the pin joint must satisfy were as follows:

STRUCTURAL INTEGRITY

Structural integrity under the following conditions with ample safety margin was necessary

1. At Launch

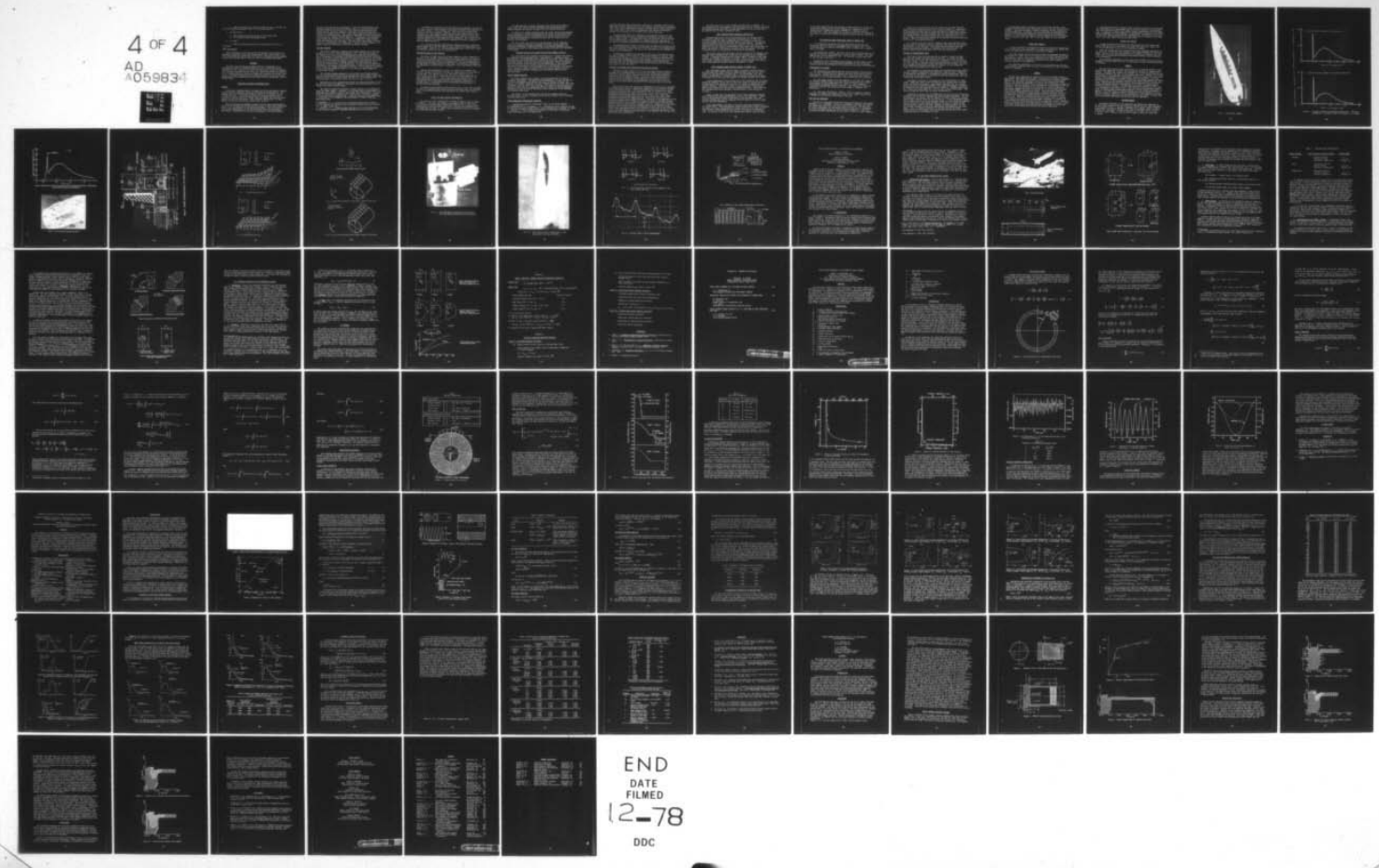
    a. Combined axial load and torque (10,400 g).

AD-A059 834 ARMY MATERIALS AND MECHANICS RESEARCH CENTER WATERTO--ETC F/G 20/11
PROCEEDINGS OF THE ARMY SYMPOSIUM ON SOLID MECHANICS, 1978 - CA--ETC(U)
SEP 78

UNCLASSIFIED AMMRC-MS-78-3

NL

4 OF 4
AD
A059834



END
DATE
FILMED
12-78
DDC

b. Impulsive torque only (free run condition) due to 260,000 rad/sec^2 peak angular acceleration with 0.5 millisecond duration.

2. At Barrel Exit

a. 2000 g negative setback acting on rocket motor mass
b. Pin retention under centrifugal forces.

3. In Flight

a. 3000 psi internal pressure with rocket motor on for 2.5 to 4 seconds.

OTHER REQUIREMENTS

The interference fit of the pins must not produce out of plane local deformation (bulging) of the seal surface greater than .00025 inches. For field disassembly and assembly the pins must be extractable without damaging the pin hole surfaces and at a pull out load not exceeding 5000 pounds.

APPROACH

The short time available precluded elaborate 3-D mathematical or experimental analyses of candidate designs in all of which the critical problems were 3-D. However, an earlier 3-D photoelastic analysis of another joint had been performed and the stress data from that analysis was adapted to the current problem to obtain an estimate of the stress levels that could occur. In addition selected tests on simplified models of the joints were performed and these demonstrated failure modes and gave approximate values of failure loads.

ANALYSIS OF FAILURE OF THREADED JOINT

GENERAL

It has been standard practice to assume that axial and angular accelerations acting on a projectile during gun firing occur simultaneously. This presumes that the rotating band of the projectile is in contact with the rifling initially. In the JFF projectile the rotating band may not be initially in contact with the rifling; axial and angular acceleration consequently may not be simultaneous. This condition could result in a high angular acceleration and torsion without axial set-back.

The joint failure was probably caused in part by this non-simultaneity of the axial and angular accelerations which occur at early times (within the first 2 to 4 milliseconds) in the launch environment. The JFF projectile could travel approximately 1" axially before the rotating band engaged the rifling. Associated with the axial displacement is an axial velocity

and axial acceleration of the projectile. Since the rotating band is not initially engraved into the tube rifling, there is no rotational motion associated with the axial motion until the rotating band encounters the rifling and the projectile suddenly experiences a torsional load which results in an angular motion. The initial large angular acceleration causes a large inertial torque to be generated at a time when the axial acceleration is relatively low (perhaps 2000 to 3000 G's). Consequently, an abnormally large coefficient of friction is required to transmit the inertia torque across the threaded joint interface. Once the rocket motor begins to rotate relative to the bulkhead, the coefficient of static friction decreases to a dynamic value and the relative rotations can further increase.

FREE RUN ANALYSIS

The study by Benedetti[1] computed the torsional impulse for a free-run distance of 1.0" with a spin-up distance of .40". (The spin-up distance is the length of the scar at the leading edge of the engraved rotating band and is a measure of the distance travelled from the initiation of rotational motion to the time at which the projectile motion exactly follows the rifling twist.) The force producing rotation is provided by the gradually increasing resistance of the band as it engages, presenting increasingly more area against the forward thrust of the projectile. The peak torsional impulse is determined by the ability of the band material to provide the required force, which ability is assumed in Benedetti's analysis. This assumption in addition to the rigid body assumption results in the torsional impulse magnitude being an upper bound.

The torsional impulse computed by this analysis was 425,000 rad/sec^2 with .27 millisecond direction for an assumed sine-squared impulse shape and 360,000 rad/sec^2 with .27 millisecond duration for a sine impulse shape. The resulting angular acceleration curves are shown in Figs. 2a and 2b.

Modification of the rotating band reduces the free-run distance to .090" for which the torsional impulse is predicted to be 60,000 rad/sec^2 for the assumed sine-squared impulse shape.

The study by Schmidlin[2] performed a dynamic analysis of the projectile using the "Super Scepter" technique. For torsional motion the projectile is represented by a dynamic system of four masses and three springs. For axial motion the projectile is assumed to be a rigid body. Free-run is assumed to be one-inch for the original band. "Spin-up" distance and maximum torque is determined by the strength of the band material in shear during the engraving process.

---

1. Benedetti, G. A., "Estimates for the Minimum Coefficients of Static Friction Required at the Rocket Motor Bulkhead Interface Joint for the W79". S. L. L. Memo, 12 May 1977.
2. Schmidlin, A. E., "Computer-Aided Simulation of In-Tube XM-753/XM-650 8-Inch Projectile Dynamics", ARRADCOM (LCM-NAD) Study II, June 1977

In Schmidlin's computations the band material was assumed to be able at all times to provide the resistance to projectile movement which produces the torsional impulse. In this respect this analysis gives an upper bound similar to the first analysis. However, since this analysis models the projectile as a multi-degree dynamic system, which is more realistic than assuming rigid body response, this analysis can be expected to give more accurate predictions of the impulsive forces produced. The accuracy of the analysis appears to be substantiated by agreement obtained in experiments with the XM-650 projectile.

For a one-inch free-run condition this analysis predicts a torsional impulse magnitude of 260,000 rad/sec^2 with a duration of approximately 0.5 multiseconds. (See Fig. 3) For the modified band with a free-run of .090" the analysis predicts a peak of 62,000 rad/sec^2.

CONCLUSIONS FROM FAILURE ANALYSIS

The effect of high levels of torsional impulse on other components in addition to the probable contributions of torsional impulse to the failure of the test projectile led to the decision to modify the rotating band to eliminate the free-run condition in unworn guns. This was accomplished by cutting down the leading section of the band. The resulting band geometry was adopted for the XM-753 and is referred to as the "new" band or the "cut" band.

However, the possibility of a free-run condition of somewhat less severity arising in worn guns or because of copper deposits in the bore of any gun tube still remains and it was considered necessary for the joint design to be able to carry some level of torsional impulse at low axial acceleration levels. Since these levels are unknown and are now being determined by test, the joint was tentatively assumed to be satisfactory if it could safely survive the torsional acceleration of 260,000 rad/sec^2 with duration of 0.5 milliseconds corresponding to a one-inch free-run condition.

To avoid the uncertainties of the friction force at the joint interface and thus give assurance that similar failures would not occur, the threaded joint in the XM-753 projectile was replaced by the pinned joint shown in Figure 4.

FINAL PIN JOINT DESIGN CONFIGURATION

The final pin joint configuration is shown in Figure 4 and, in detail in Figure 5. The joint uses sixteen 12 mm diameter pins of 4340 steel, Rc 35 hardness, equally spaced around the projectile and in line with the forward pins of the bulkhead-to-case joint. The pins are assembled with an interference of .0001" to .0005" and are retained in place by a standard 1/2" snap ring and groove system.

A C-ring seal with a tightly compressed coil spring core provides a static vapor seal against out-gassing vapors from the propellant and a dynamic pressure seal against the gases from the burning propellant.

In addition to strength analysis under all loads, analysis and engineering was necessary to limit the magnitude of the bulges on the bulkhead seal surface produced by the pin interference and to ensure reliability of the pin-snap ring sytem both in retaining the pins and for trouble free disassembly and reassembly.

The use of soft pins (Rc 35) for joining harder (Rc 45) components serves to concentrate the material damage in the pin during launch and during pin extraction, thereby protecting the structural components and eliminating the need for refinishing holes during disassembly and reassembly in the field.

STRENGTH ANALYSIS FOR LAUNCH SET-BACK AND TORQUE, 10,400 g

The joint between the bulkhead and warhead case is located less than an inch forward of the redesigned joint. (See Figure 4). Because of their proximity each can affect and can be affected by the other. Also, since both were pinned joints of similar basic form and structural function located in zones with similar stress distributions and magnitudes, it was anticipated that the analyses and test results of the earlier forward joint would contribute to and expedite the development of a safe redesign of the present joint. Because of these two factors the forward joint analyses and test results provided important information to the redesign effort and are described below.

FINITE ELEMENT ANALYSIS

The finite element stress analysis utilized extensively was that of Callabrese and Murphy.[3] The analysis was axisymmetric, did not include the 3-D joint configuration and omitted the effect of torque. However, the behavior of internal components was well represented and the stress data were considered valid for use in this redesign. This analysis had been used as a source of stress data for combination with the results of three-dimensional photoelastic study to predict the actual stress conditions in the bulkhead-to-structural case joint.

The results of this analysis were used for the present study, as described below, to obtain estimates of the stress condition in the bulkhead-to-rocket motor joint.

THREE-DIMENSIONAL PHOTOELASTIC ANALYSIS

A photoelastic analysis by Benicek[4], early in the XM-753 program,

3. Callabrese, M. C., and Murphy, L. M., "Preliminary Stress Analysis for the 79 Artillery Projectile" SAND 75-8247, Sandia Laboratories, Livermore, CA (SRD).
4. Benicek, M., "Three-Dimensional Analysis of a Pin Joint by Scattered Light Photoelasticity" (in preparation)

utilized scattered light photoelastic techniques to determine locations and magnitudes of high stress in the pin joint between the bulkhead and structural case. This type of experimental analysis provides elastic stress concentration factors which can be used in conjunction with general mathematical analysis of the projectile to estimate local stress conditions.

Of great significance and usefulness to the present studies were the stress distributions and stress concentration magnitudes as shown in Table 1 and in Figures 6 and 7. The quantities shown are the ratios of the stresses at the various points to the nominal or average stress at a distance in the axial (y) direction beyond the stress-flow disturbing effect of the pin.

The distributions in Figure 6 clearly show the effect of rotation of the pin in the vertical plane of its axis resulting in high stress concentrations and stress gradients in three directions not predictable by the mathematical analysis in two dimensions.

Of additional interest and usefulness is the stress distribution along the joint interface shown in Fig. 8. The marked reduction in contact stress directly below the pin is a direct result of the transfer of load from the structural case through the pin into the bulkhead. Locating the pins of the new rocket-motor-to-bulkhead joint directly below the pins through the structural case has the advantage of the reduced contact stress to minimize the stresses in the new joint.

ESTIMATE OF MAXIMUM JOINT STRESSES FOR SETBACK AND TORQUE

The finite element analysis of the new joint area (which by necessity excluded the 3-D complications of the pins) was combined with the photoelastically derived stress concentration factors to provide estimates of setback and torque induced stresses. These were then combined variously with the stresses produced by centrifugal force or pin interference to obtain engineering estimates of the magnitudes and locations of critical stresses in the joint and an estimate of the structural safety of the new joint.

Since the new joint was similar in configuration to the earlier bulkhead-to-structural-case joint, an approximate comparison of the relative strength of the two joints was made. This was accomplished by assuming that stress concentration factors and stress gradients in the new joint with its longer (compared to diameter) pin would be, at worst, only as severe as those obtained by the 3-D photoelastic study for the older joint. These stress concentration factors were applied to the stress values obtained by the Callabrese, Murphy finite element analysis. Estimates of the magnitudes of the stresses (assuming elastic behavior) distributed along the horizontal plane through the top of the pin (where the highest stresses occur) were obtained. These are shown for both joints in Figures 9 and 10. Comparison of the stress values of the two cases show the estimated peak stresses and the average stresses to be generally lower in the present pin joint than in the earlier joint. Since the earlier joint had a history of successful firings at 12,000 g using the same components more than once, it was expected that the new joint would also prove satisfactory.

The final proof lies in test firings and load tests to failure. To date examination of test components and pins fired at up to 12,000 g have shown no measurable damage except for a slight deformation of the soft pins which was expected and, in fact, designed to occur.

JOINT STRENGTH UNDER TORSIONAL IMPULSE LOAD

Although modification of the rotating band has, as discussed above, eliminated an obvious cause of free-run, the possibility of free-run occurring through some other mechanism makes it necessary for the joint to be strong enough to survive some level of torsional impulse. Although the impulse levels from some other cause were expected to be less than that associated with the original rotating band, since those other levels were not known, the ability of the joint to survive the 260,000 rad/sec^2 torsional acceleration peak 0.5 milliseconds in duration was determined.

Earlier pin tests using the soft Rc 35 pins joining RC 45 components had shown pin shear strength to be 15,500# with an estimated yield strength of 13,700#. A torsional acceleration of 260,000 rad/sec^2 produces a peak shear load per pin (sixteen 12 mm pins) of 14,200#. Thus, over the short period of the pulse, yielding of the pins can occur and would produce, at worst, a small inconsequential permanent plastic deformation in shear.

JOINT STRENGTH UNDER NEGATIVE SETBACK AT BARREL EXIT

This requirement arises from an impulsive negative set-back effect on the projectile that results from the sudden pressure drop off and elastic recovery of the projectile at barrel exit. For the present joint this effect is equivalent to a negative 2000 g acceleration acting on the mass (61 pounds) aft of the joint and produces an average load per pin of 7625#.

A brief examination of the problem led to the conclusion that the three-dimensional behavior of the joint in this case cannot be ignored and cannot be approximated with sufficient accuracy by a simple two-dimensional mathematical analysis. Therefore a series of test specimens simulating the tensile load condition on the pins were designed and used. Four double-pin test configurations were eventually required before a final design was attained.

Figure 11 shows the test specimens for the final candidate configurations including the design configuration used in the projectiles. Except for the non-cylindrical shape of specimens, which were made flat, the detailed configuration and the important behavior modes of the joint under tensile load were reproduced.

Strain measurements were made at key points and were extrapolated to the extreme fiber. These measurements showed extreme fiber strains (excluding the effect of stress concentration) to reach yield levels at loads on the order of 8500 to 9000 pounds per pin and well in excess of the expected load. The failure of the final joint design under tensile load was found

to be 15,500 pounds per pin and occurred by shear failure of the soft pin. The maximum strength of the joined components was measured at 18,450 pounds per pin accompanied by gross deformation. Complete failure did not occur. Thus the strength of the joint in this case was limited by pin shear as desired and exceeded the expected applied load by a factor of two.

PIN RETENTION UNDER CENTRIFUGAL FORCE AT BARREL EXIT

It is necessary to prevent the pins from being ejected from the projectile under the effect of centrifugal force at barrel exit. For a 12 mm steel pin 0.9" long the centrifugal force at barrel exit is approximately 750 pounds.

Two methods were studied. The first was to use an interference fit to provide the resistive force required to hold the pins in place. The other approach was to use a mechanical lock - in this case a simple snap ring - to lock the pin in the hole.

Reliability, ease of assembly and disassembly, and the effect of the pin retaining devices or pin installation procedure on the surrounding structure and on the performance of the projectile were major considerations.

INTERFERENCE FIT METHOD

The interference fit method had been used successfully and routinely by S.L.L. for the bulkhead-to-structural-case joint of the XM-753 and for other devices. However certain conditions in the present joint made it inadvisable to use the same technique. These conditions were as follows:

(1) The longer length of the pin compared to the short pin length of the bulkhead-structural-case joint made the pin extraction force significantly higher for the interference fit (.0006" to .0012" diametral interference) recommended for pin retention. This higher force made pin extraction difficult and extraction without damage to components an uncertainty.

(2) The large interference, .0006" to .0012" on diameter, produced bulging of the nearby seal surface in excess of the .00025" specified as a maximum for satisfactory functioning of the seal.

SNAP RIN PIN RETENTION

The use of a snap ring evolved from discussions among the three groups ARRADCOM, S.L.L. and AMMRC. Initially a "standard" 12 mm snap ring design was adopted and installed on two test rounds for firing. The snap ring, the groove dimensions, and the special groove cutting tool as recommended by a snap ring manufacturer were used for these projectiles. Pins were inserted with small interference on the order of .0002" to .0004" diametral.

Only one of the projectiles was test fired since 15 snap rings and eight pins were ejected at barrel exit as shown in Figure 12. Examination of the projectile showed that the snap ring grooves as fabricated to the specified depth with the special groove tool were not sufficiently deep nor well enough formed to provide assurance that the centrifugal force of the pin pressing on the snap ring would not force the snap ring out of its groove. Figure 13 shows groove dimensions as obtained by Castone impression projected on a Shadowgraph projector.

As a result of the test failure a special snap ring retention system and procedure was designed using an "oversized" .500 inch snap ring normally specified for a .500 inch pin. This system assured adequate snap ring groove fabrication and rendered it impossible for the snap ring to be ejected without shearing the metal lip of the snap ring groove.

MAXIMUM PIN INTERFERENCE LIMIT

This limit arises from the necessity to maintain a vapor and high pressure seal between the propellant and the pins. A specific flatness specification on the seal seat limited out-of-flatness of the seal seat to less than .00025". Since the insertion of interference fit pins into holes near the seal surface produces local bulging of the seal surface, the limit on the magnitude of bulging, specified at .00025", in turn limited the amount of pin interference that could be used.

To determine the relationship between pin interference and seal surface bulging a combined experimental and analytical study was made. Comparison of experimental measurements to mathematical prediction provided a check on the accuracy of the analysis to allow the use of the analysis for other pin diameter and interference values.

Experiments consisted of inserting pins with interferences of .0003", .0006", .0009" and .0012" in sets of four into the sixteen holes of rocket motors and simulated bulkheads. Measurements were made over each section using a sensitive, specially designed, strain gaged displacement transducer. An example of the trace obtained is seen in Figure 14. Readout sensitivity was 2 inches pen displacement for .001 inch seal surface displacement. Each trace was repeated three times to ensure reproducibility.

Mathematical analysis was two-dimensional and utilized both collocation techniques and collocation combined with finite element techniques. The only shortcoming of the analysis was the inability of plane analyses to consider varying edge distances along the axis of the pin - a three dimensional effect. Since an edge step occurs on the bulkhead because of the seal groove geometry, exact predictions of the bulging produced on the seal lip, where sealing actually occurs, could not be made. However, as shown in Figure 15, the two extremes reasonably bracket the experimental measurements as one would expect. Thus, it appears reasonable to conclude that for non-three dimensional cases the analysis will give accurate prediction of the surface bulging produced by interference fit pins.

The analytical curves in Figure 5 were a guide for fairing a curve through the experimental bulge measurements made on the seal surface of the bulkhead. This curve provides a usable relationship between interference and bulge magnitude. In general, the bulge magnitude is approximately 35 percent of the interference magnitude for this particular configuration. Therefore to stay within the limit of .00025" bulging the pin interference must be limited to less than .0007" (less than .0005" to be on the safe side.)

FIRING TEST RESULTS

To date ten XM-753 test projectiles with the new pin joint design have been assembled and fired successfully at normal and overtest g. levels with no loss of snap rings or pins and no indication of damage.

After the firings the pins extracted showed some permanent deformation in the form of a .001" step at the location of the radial interface of the mating parts. However, this type of deformation was expected and indicates that the "soft" pin is yielding and absorbing strain which otherwise would be absorbed by the components.

The successful performance of the total of 160 separate pin and snap ring assemblies indicates that the joint is performing in a safe, controlled fashion as designed.

SUMMARY

The pin joint connecting the rocket motor to the bulkhead required a many faceted study embracing the gamut from exploratory research to hardware manufacture. The effort was aided by the availability of advanced mathematical and analytical techniques for most of the problems that arose. However, for certain key problems it was found that sufficiently accurate or effectively usable techniques, either mathematical or experimental, were not available. For these problems it was necessary to resort to practical engineering judgment and selective testing and it was extremely fortunate that timely workable solutions were found. These particular problems involved three-dimensional elastic-plastic structural behavior which is a characteristic of joints in advanced highly stressed projectile systems. For efficient handling of problems of this type it is necessary to have better tools. These can be three-dimensional computer codes or combined three-dimensional photoelastic-finite element treatments, in advance, of a large family of typical problems that may be expected to arise. Whatever, there is a definite need for preparation in anticipation of the next series of problems (which may be even more difficult and urgent) to ensure that they can be solved efficiently and with the desired timeliness.

The analytical curves in Figure 5 were a guide for fairing a curve through the experimental bulge measurements made on the seal surface of the bulkhead. This curve provides a usable relationship between interference and bulge magnitude. In general, the bulge magnitude is approximately 35 percent of the interference magnitude for this particular configuration. Therefore to stay within the limit of .00025" bulging the pin interference must be limited to less than .0007" (less than .0005" to be on the safe side).

FIRING TEST RESULTS

To date ten XM-753 test projectiles with the new pin joint design have been assembled and fired successfully at normal and overtest g. levels with no loss of snap rings or pins and no indication of damage.

After the firings the pins extracted showed some permanent deformation in the form of a .001" step at the location of the radial interface of the mating parts. However, this type of deformation was expected and indicates that the "soft" pin is yielding and absorbing strain which otherwise would be absorbed by the components.

The successful performance of the total of 160 separate pin and snap ring assemblies indicates that the joint is performing in a safe, controlled fashion as designed.

SUMMARY

The pin joint connecting the rocket motor to the bulkhead required a many faceted study embracing the gamut from exploratory research to hardware manufacture. The effort was aided by the availability of advanced mathematical and analytical techniques for most of the problems that arose. However, for certain key problems it was found that sufficiently accurate or effectively usable techniques, either mathematical or experimental, were not available. For these problems it was necessary to resort to practical engineering judgment and selective testing and it was extremely fortunate that timely workable solutions were found. These particular problems involved three-dimensional elastic-plastic structural behavior which is a characteristic of joints in advanced highly stressed projectile systems. For efficient handling of problems of this type it is necessary to have better tools. These can be three-dimensional computer codes or combined three-dimensional photoelastic-finite element treatments, in advance, of a large family of typical problems that may be expected to arise. Whatever, there is a definite need for preparation in anticipation of the next series of problems (which may be even more difficult and urgent) to ensure that they can be solved efficiently and with the desired timeliness.

ACKNOWLEDGEMENT

Of greatest importance to the successful and expeditious completion of the work described herein was the spirit of team work and hard work engendered by the program leaders C. Spinelli, ARRADCOM, and D. Bohrer, Sandia Livermore Laboratories, and carried through by the teams at ARRADCOM, Sandia Livermore Laboratories, and AMMRC. Notable individuals on the teams were R. Favale, A. Calvino, and B. Stang; J. Vieira, and R. Demo; W. Foster, D. Doyle and R. Breen.

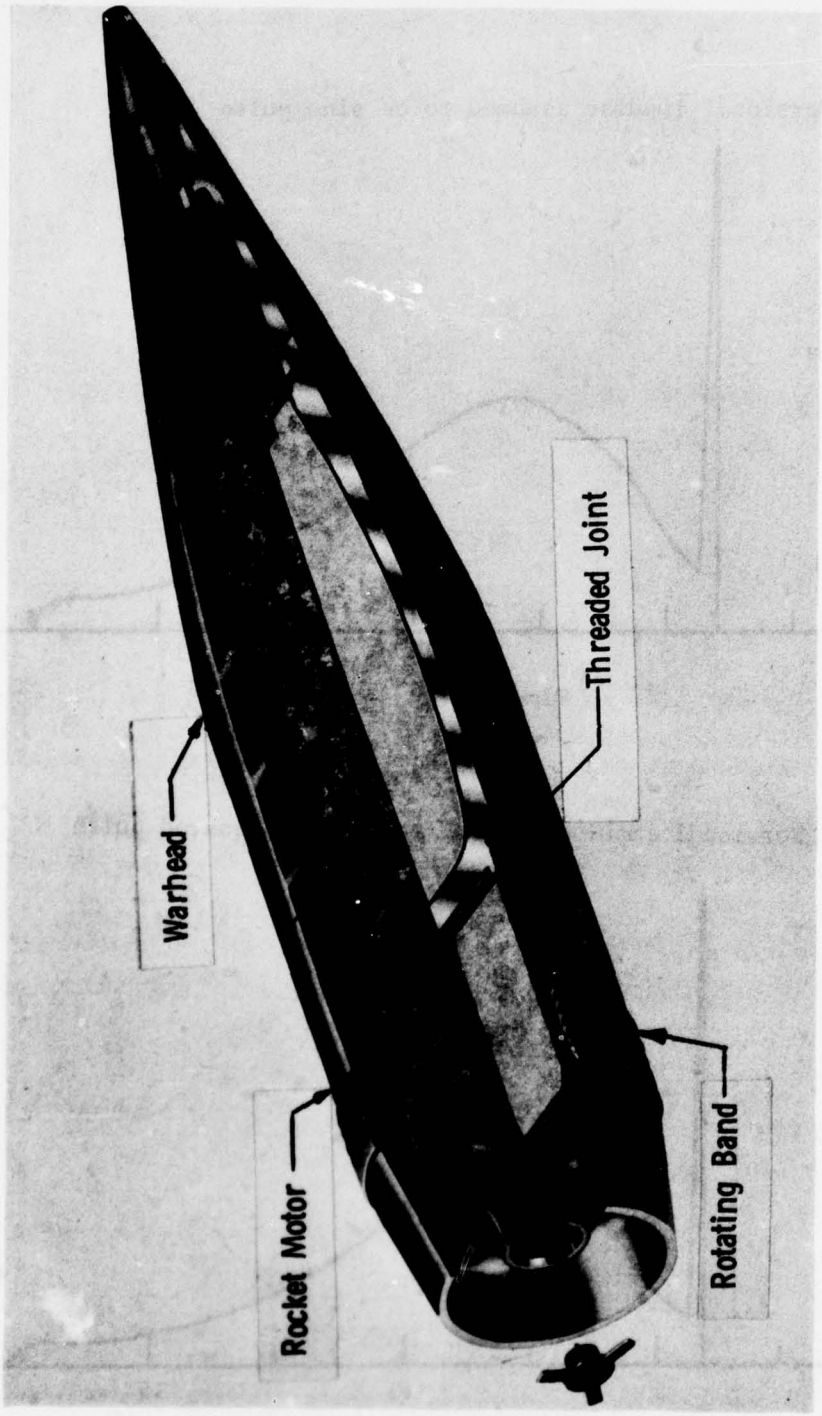


FIG. 1. 8-INCH RAP, XM650E5

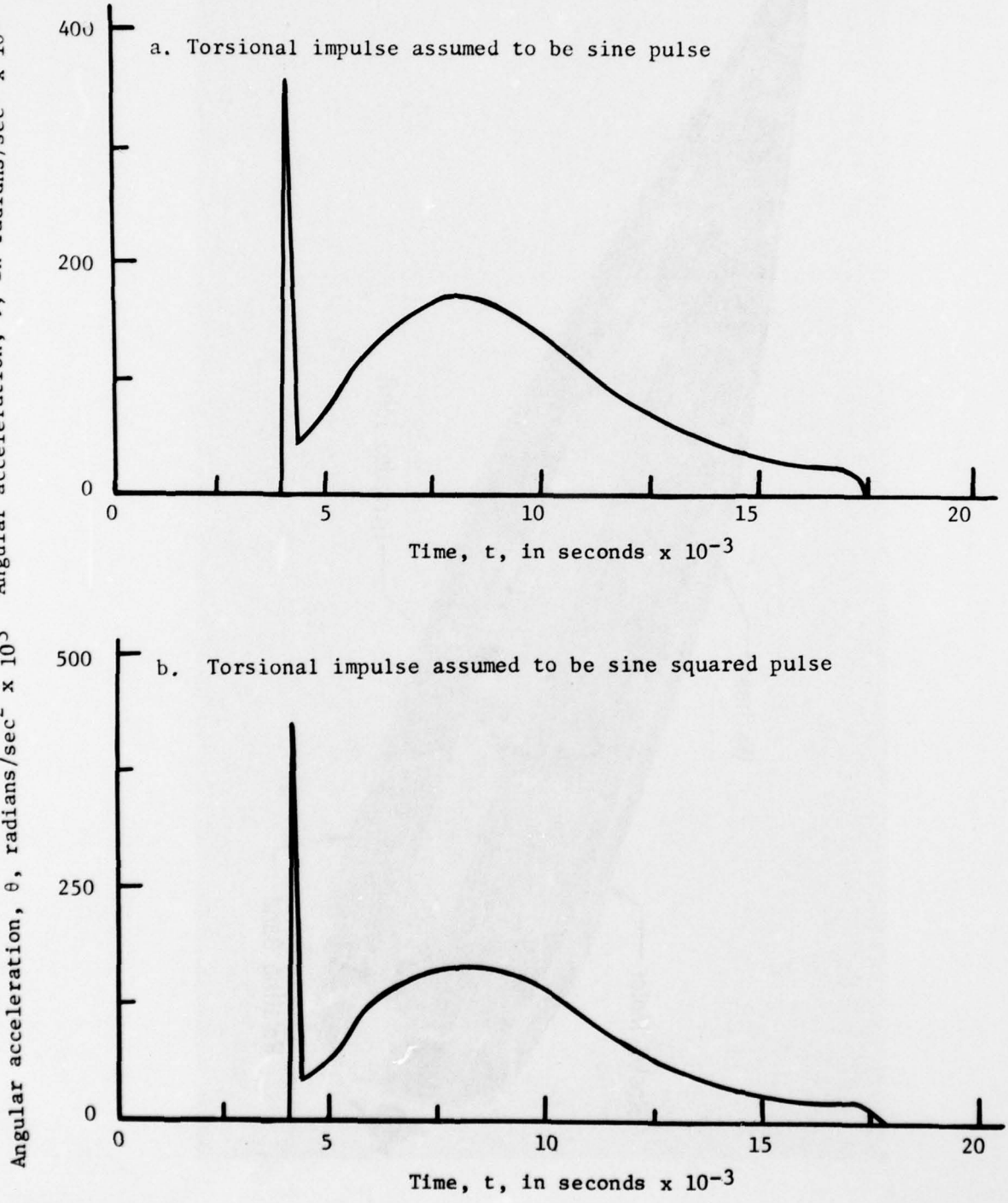


FIGURE 2 - PROJECTILE ANGULAR ACCELERATION VERSUS TIME. "FREE RUN" DISTANCE IS 1.0 INCHES; "SPIN UP" DISTANCE IS 0.4 INCHES.

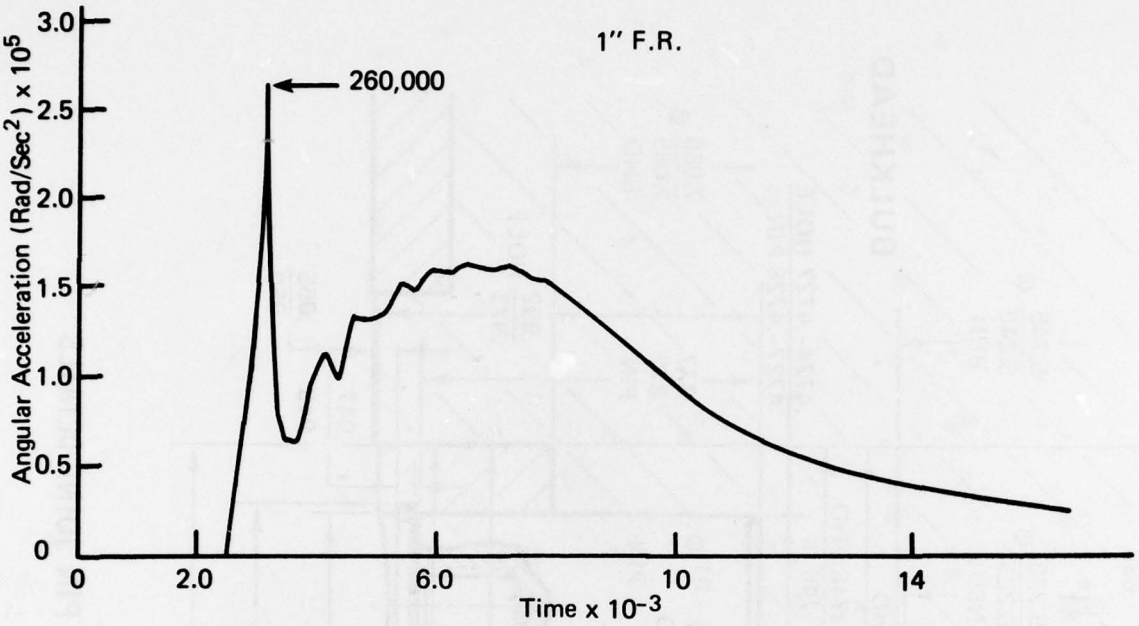


Figure 3. PROJECTILE ANGULAR ACCELERATION VERSUS TIME FOR 1" FREE RUN, INCLUDING PROJECTILE DYNAMICS

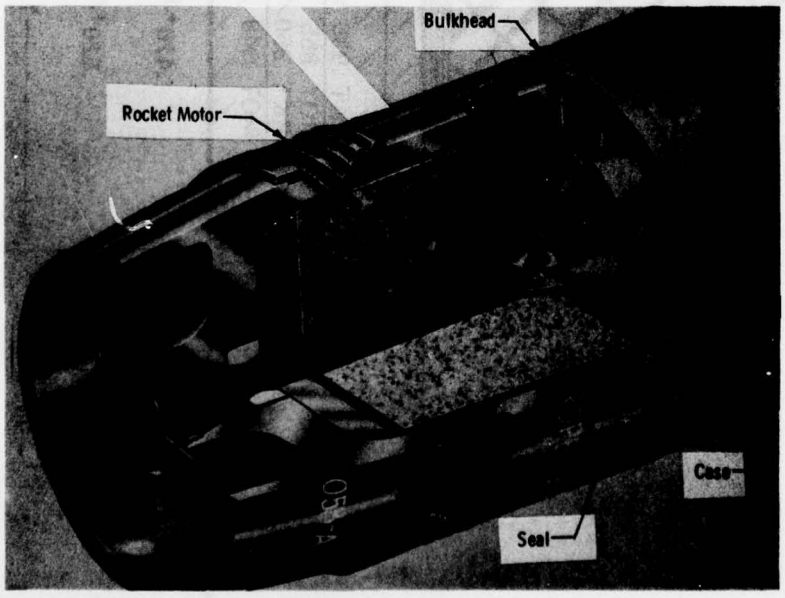


FIGURE 4. XM-753 ROCKET MOTOR / BULKHEAD / CASE JOINTS

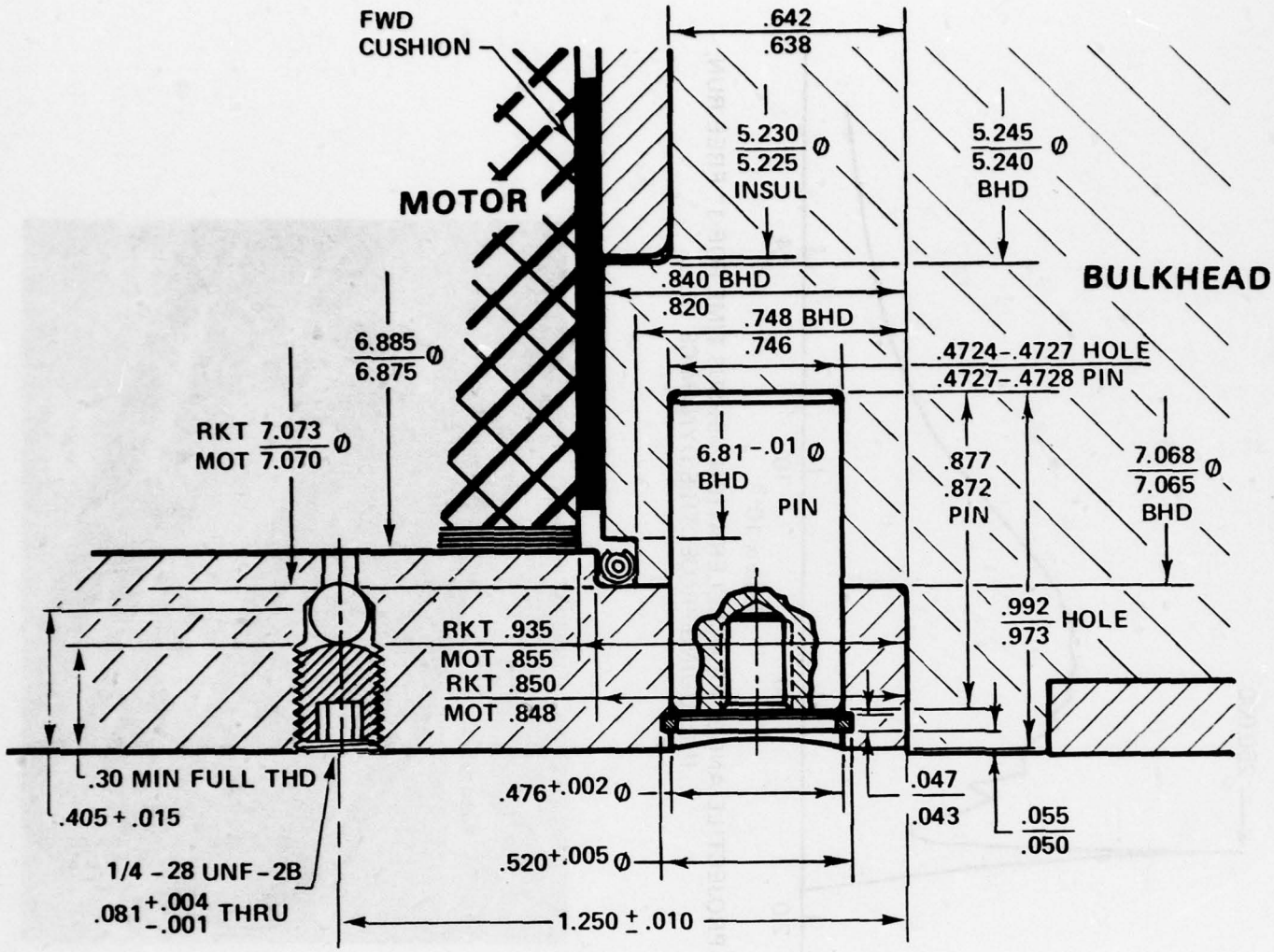


Figure 5. ROCKET MOTOR/BULKHEAD PIN JOINT DETAILS

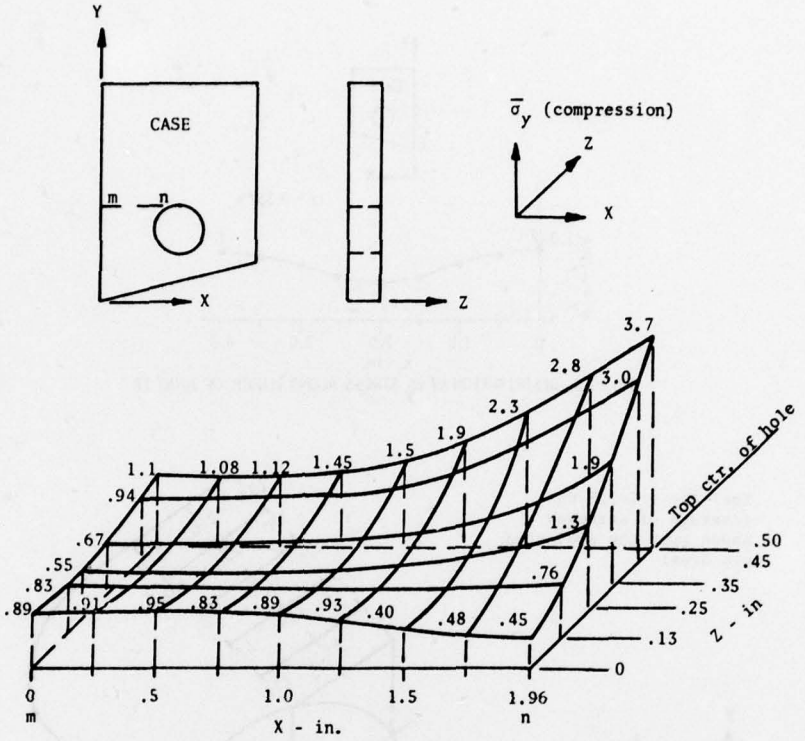


FIG. 6. $\bar{\sigma}_y$ STRESS CONTOURS ALONG LINE mn

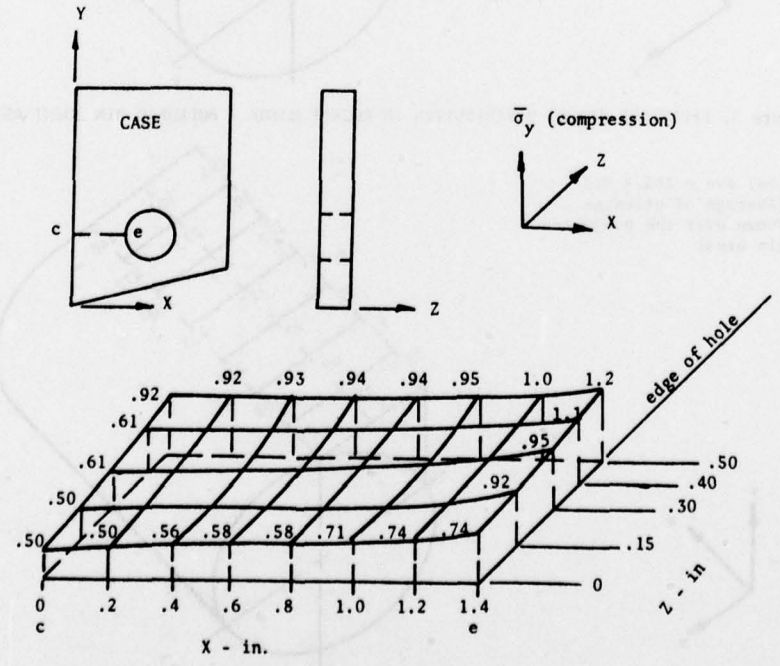


FIG. 7. $\bar{\sigma}_y$ STRESS CONTOURS ALONG LINE ce

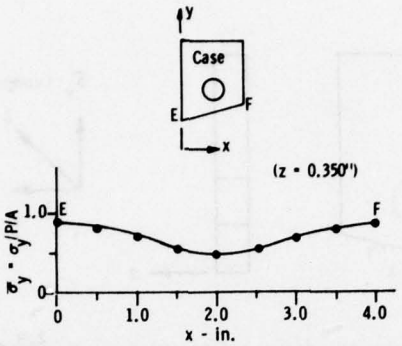


Figure 8. DISTRIBUTION OF $\bar{\sigma}_y$ STRESS ALONG LENGTH OF JOINT EF

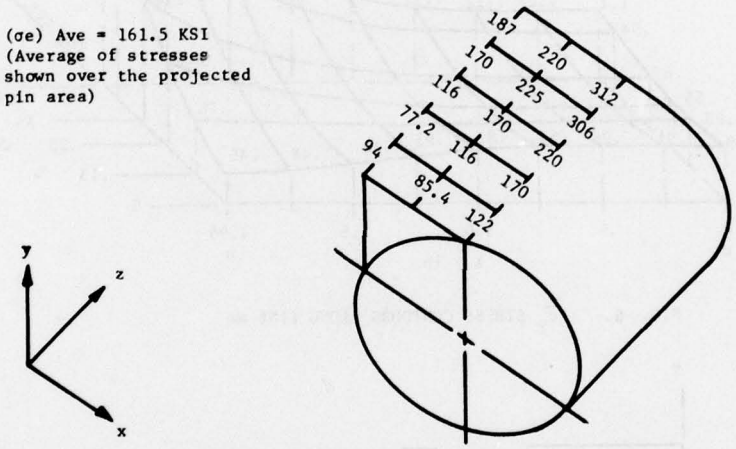


Figure 9. EFFECTIVE STRESS DISTRIBUTION IN ROCKET MOTOR - BULKHEAD PIN JOINT REGION

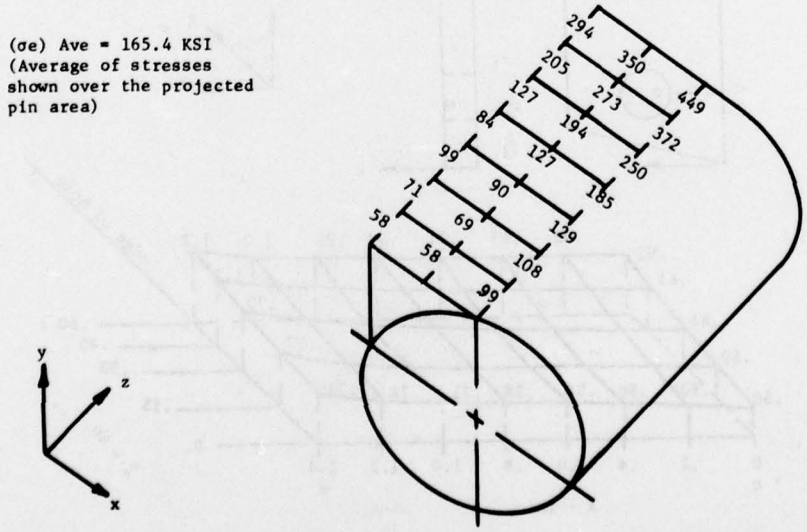


Figure 10. EFFECTIVE STRESS DISTRIBUTION IN CASE STRUCTURE - BULKHEAD PIN JOINT REGION

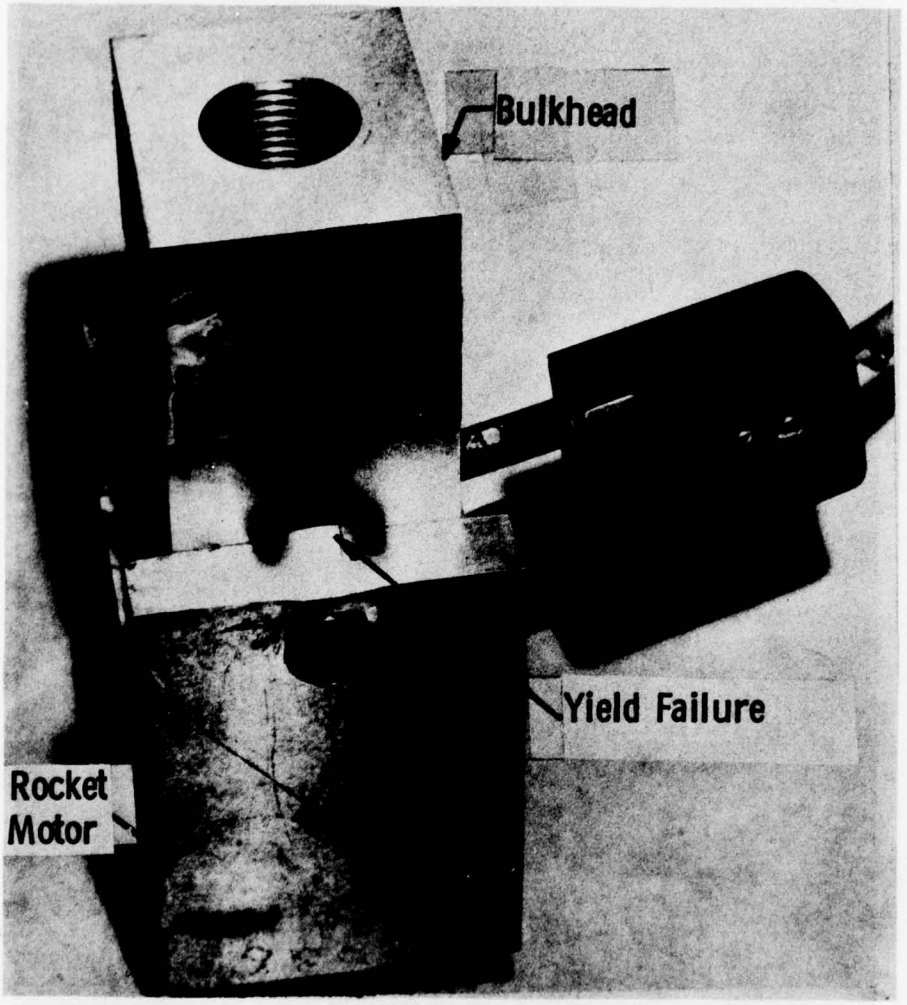


Fig. 11. TEST SPECIMEN FOR DETERMINING STRENGTH OF PIN JOINT UNDER TENSION (NEGATIVE SET-BACK)

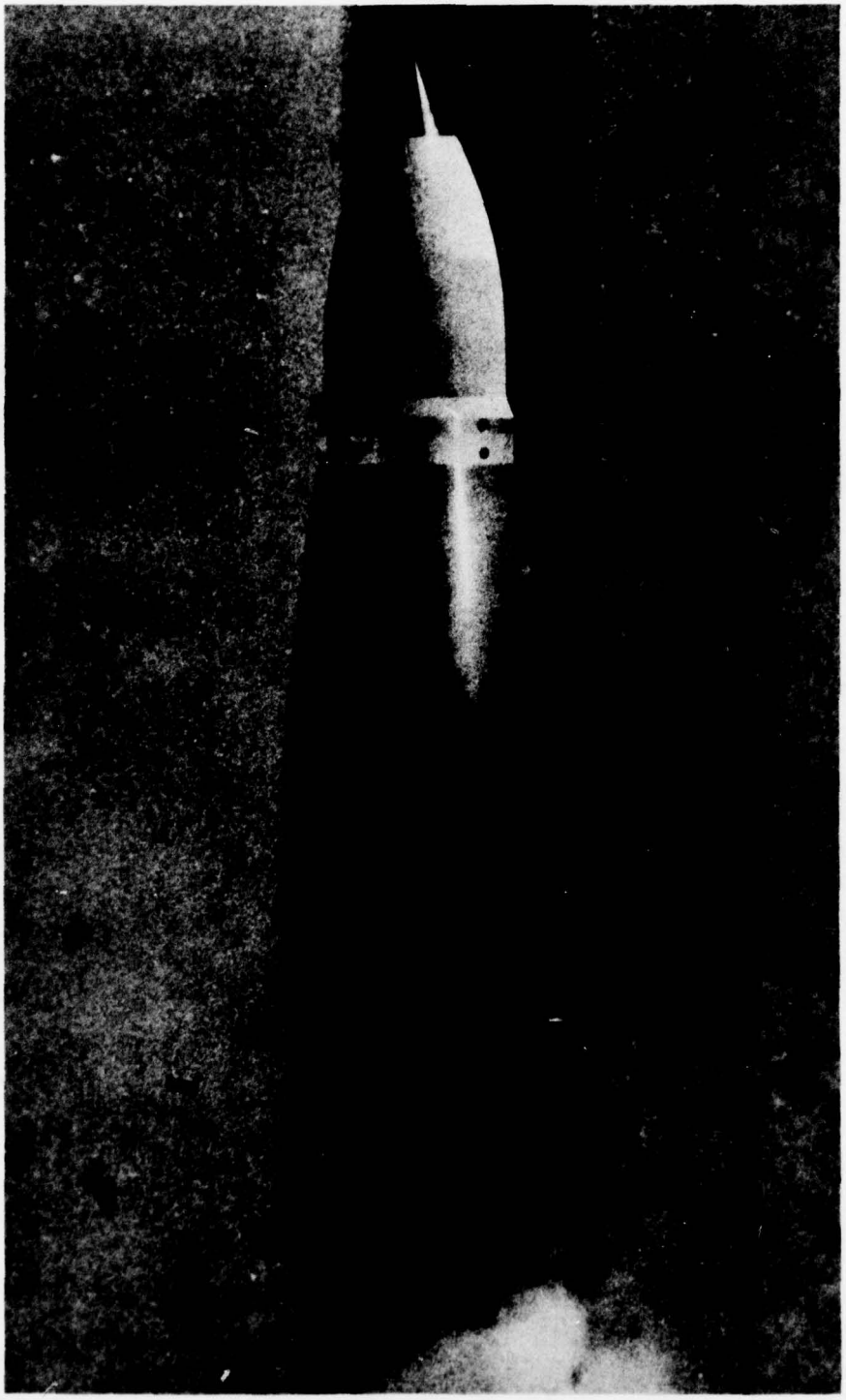
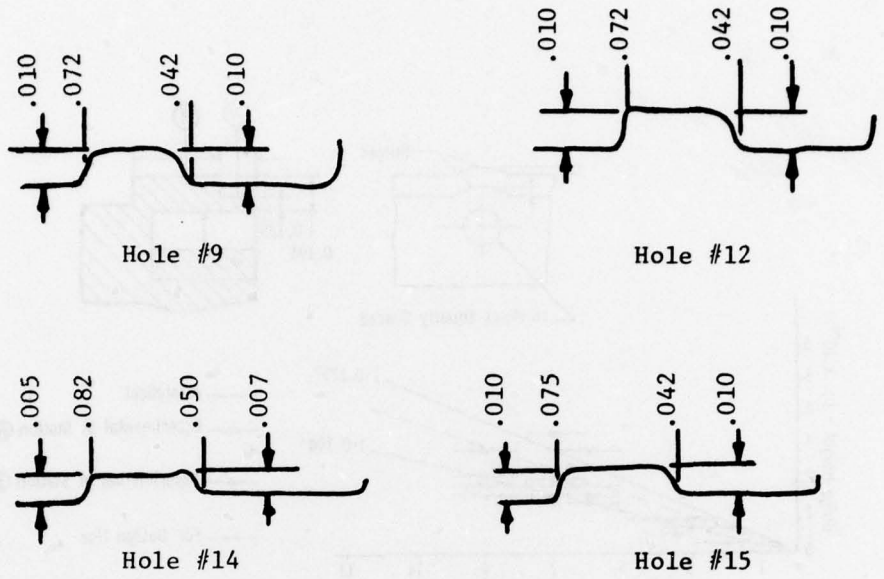


FIG. 12. TEST FIRING OF XM-753 PROJECTILE w. PIN JOINT USING SNAP RING RETAINERS



From Failed Test Projectile

FIG. 13 - TYPICAL SNAP RING GROOVES USING STANDARD 12 MM RING, GROOVE AND TOOL.

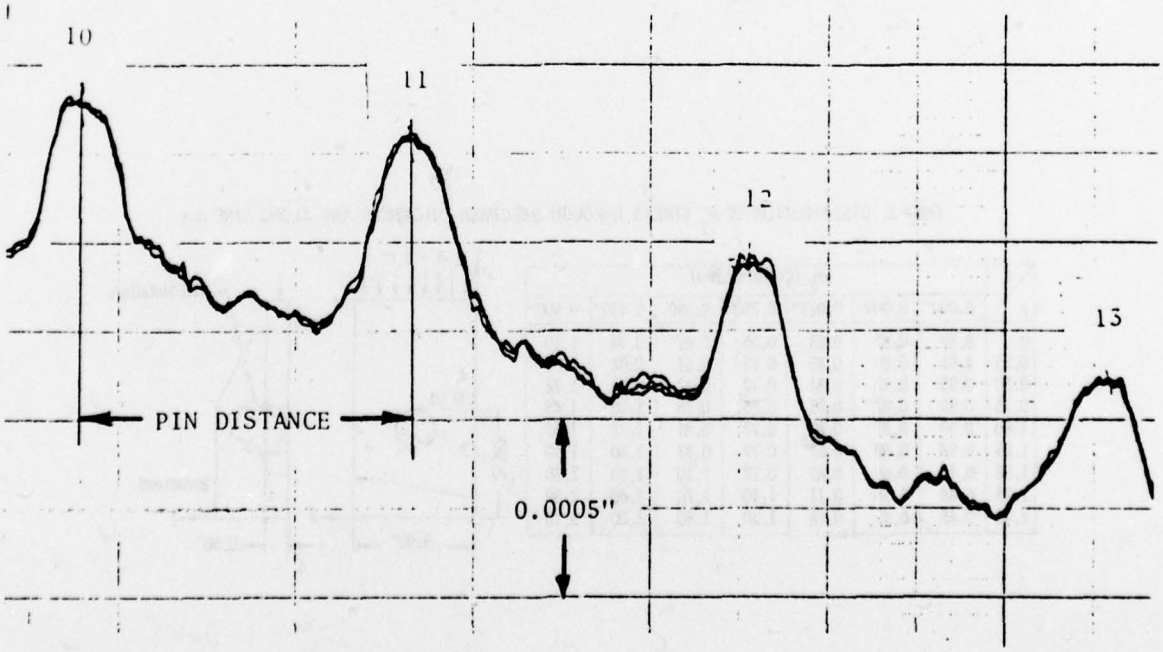


FIG. 14 - TYPICAL TRACE OF BULGE MEASUREMENTS

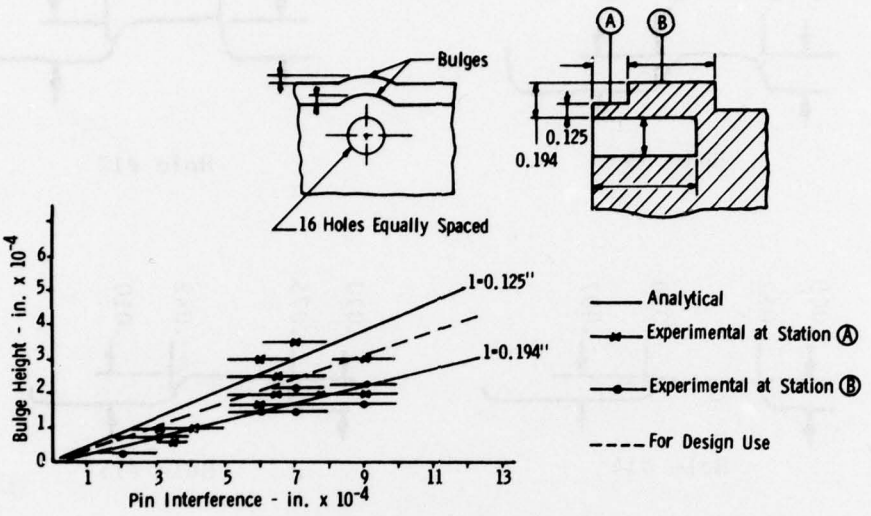
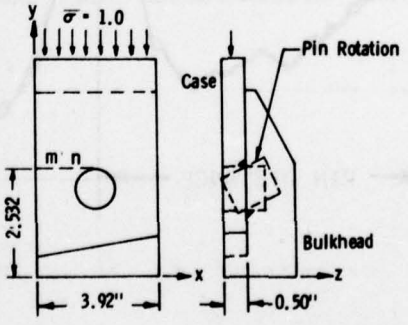


Figure 15. SEAL SURFACE BULGE VERSUS PIN INTERFERENCE XM 753

Table 1. DISTRIBUTION OF $\bar{\sigma}_y$ STRESS THROUGH SPECIMEN THICKNESS AND ALONG LINE mn

x \ z	$\bar{\sigma}_y$ (Compression)						
	0.000"	0.060"	0.013"	0.250"	0.350"	0.450"	0.500"
0	0.89	0.87	0.83	0.55	0.67	0.94	1.10
0.25	0.91	0.89	0.85	0.55	0.67	0.92	1.08
0.50	0.95	0.92	0.81	0.72	0.72	0.96	1.12
0.75	0.83	0.82	0.81	0.75	0.75	1.20	1.45
1.00	0.89	0.87	0.81	0.72	0.81	1.20	1.50
1.25	0.93	0.89	0.81	0.77	0.87	1.60	1.90
1.50	0.40	0.60	0.85	0.72	1.10	1.80	2.30
1.75	0.48	0.58	0.77	1.10	1.70	2.40	2.80
1.96	0.45	0.55	0.76	1.30	1.90	3.00	3.70



CRACK INSPECTION MAPS - AN APPLICATION TO COPPERHEAD

JOSEPH I. BLUHM
Research Mechanical Engineer

COLIN E. FREESE
Mechanical Engineer
Army Materials and Mechanics Research Center
Watertown, Massachusetts 02172

ABSTRACT

Exploitation of Fracture Mechanics in the design process requires the integration of three factors: a stress analysis; a measure of the fracture toughness; and the capability of inspecting for cracks. The immediate goal of the inspection process is to render decisions as to acceptability of the component based upon general consideration of those factors and more specifically upon the size of crack like defects relative to a critical size. Since however the critical crack size is a function of the stress levels as well as the type and orientation of the crack, this critical crack size in general will vary from point to point in a component. The Crack Inspection Map (CIMAP) is being developed to assist the inspector in sorting out critical crack sizes throughout the component. In its present state of conceptual development, CIMAP can be visualized as a graphical display of the structural component divided into regions, each of which is identified with a critical crack length and type.

In the present illustrative application to Copperhead, a Cannon Launched Guided Projectile (CLGP), the stress fields are predominately compressive (associated with launch). The role of these large compressive stresses has stimulated some interesting considerations; fracture mechanics generally has not been considered pertinent to situations of compression dominated stress fields. Nevertheless it is shown that these stress fields, by virtue of the induced shear and/or tensile stresses, can in fact cause fracture; the applicability of conventional fracture mechanics under such loading is illustrated and included in the CIMAP concept.

I INTRODUCTION

The elements of Fracture Mechanics are well documented elsewhere, e. g. Broek[1] or Knott[2]. The reader is well advised to consult these if further background is desired. Review and digestion of these 'elements' of fracture mechanics leads to the observation that exploitation of fracture mechanics entails three thrusts; (a) a stress analysis, (b) characterization of the material (primarily toughness) and (c) inspection for cracks.

In the present paper we attempt an integration of these thrusts aimed at (a) providing an inspector with a map or guide to facilitate identification of 'critical' cracks and (b) illustrating the extended role of fracture mechanics to load states which are predominately compressive.

As a vehicle for pursuing these objectives, we will consider "Copperhead",* a Cannon Launched Guided Projectile (CLGP). Copperhead is a projectile which can be launched from a standard 155 mm artillery howitzer and subsequently guided via a laser homing system to a (moving) point target. Fig. 1 shows CLGP being launched. Fig. 2 is a line drawing identifying its major components. We shall limit the emphasis of this presentation to the Control (Section) Housing though the concepts should be generally applicable to any structural component. Fig. 3 is a sectioned view of the Control Housing. Basically it is an intermediate thickness circular cylinder which houses the fins, wings and the control actuating system. This housing, the principal axial load carrying member, is designed to sustain the large launch "g" loads. The rotational continuity of the housing is interrupted by two sets of 4 each longitudinal slots to permit deployment of the fins and wings after launch.

II THE CRACK INSPECTION MAP (CIMAP)

1. Motivation and Concept: A most useful product of a 'fracture mechanics analysis' is the calculated value of the critical (i.e., maximum allowable) crack size. The structural integrity phase of product inspection is geared in general first to the detection of these critical cracks and then to an ultimate accept/reject decision. Obviously intelligent decisions demand an effective means of communicating the critical crack sizes from analyst to inspector. The Crack Inspection Map (CIMAP) is proposed as a visual aid in implementing this communication.

For components where weight is not critical and stress analysis not available, it may suffice to assume a constant maximum tensile stress level throughout the structure and to calculate a conservative single valued "critical crack size" without regard for such factors as orientation**; placement**; crack type**or the complexities of the stress state. This "worst case" calculation (Fig. 4(a)) leads to an inordinately small allowable crack size.† A somewhat less conservative approach taking into account the crack type is shown in Fig. 4(b).*** Either of these approaches could be used if a stress

*It had been anticipated that the stress analysis of Copperhead would have been available to the present authors in time to incorporate the results in this paper. That analysis is not yet completed. Nevertheless in order to provide a timely and concrete illustration of the concepts of the present paper, we have arbitrarily selected as a vehicle for demonstration a thick-walled hollow cylinder under a combination of internal and external pressure.

**These terms relate to the angular orientation, the location of the crack relative to other discontinuities, and the class of crack, i.e., surface crack, edge crack, corner crack, etc., respectively.

†See Appendix A, Level I(a), analysis.

***See Appendix A, Level I(b), analysis.

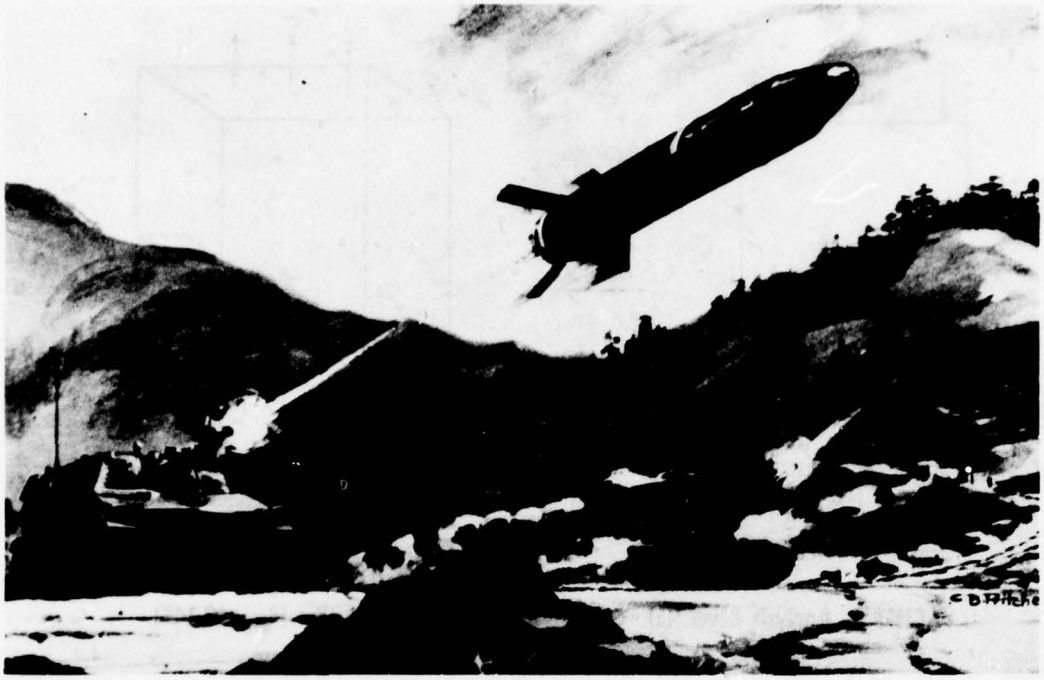


Figure 1. CLGP Being Launched

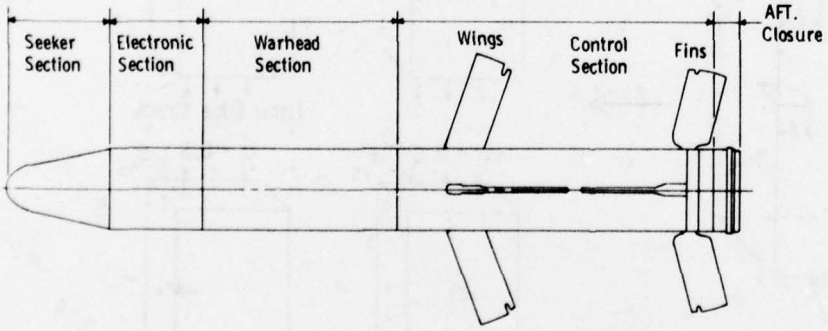


Figure 2. CLCP Structural Configuration

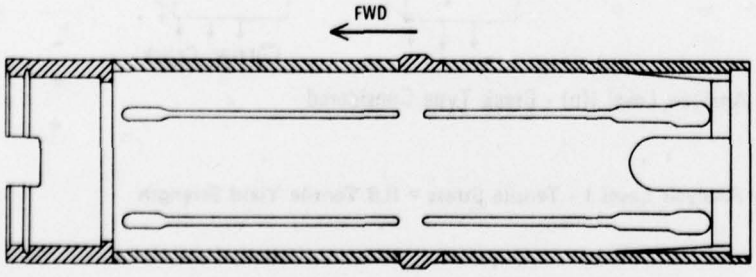
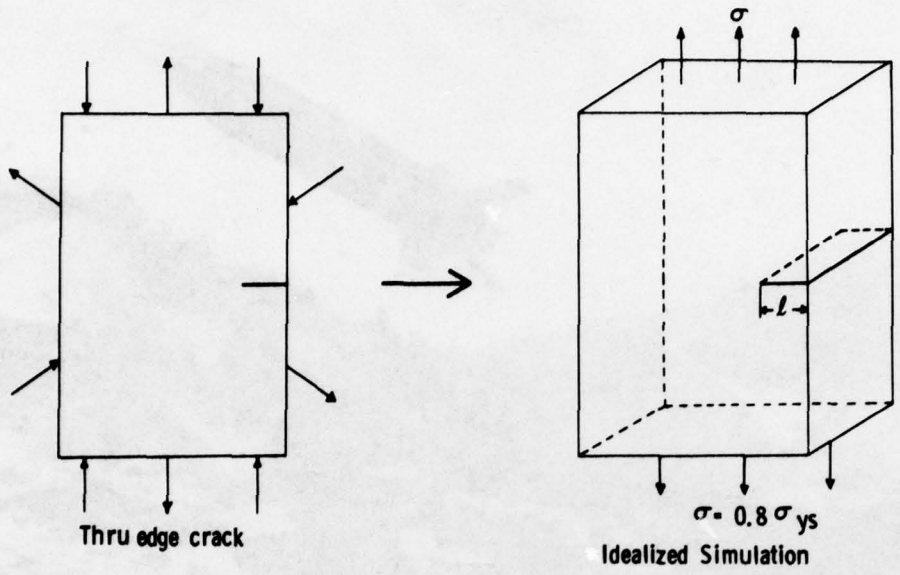
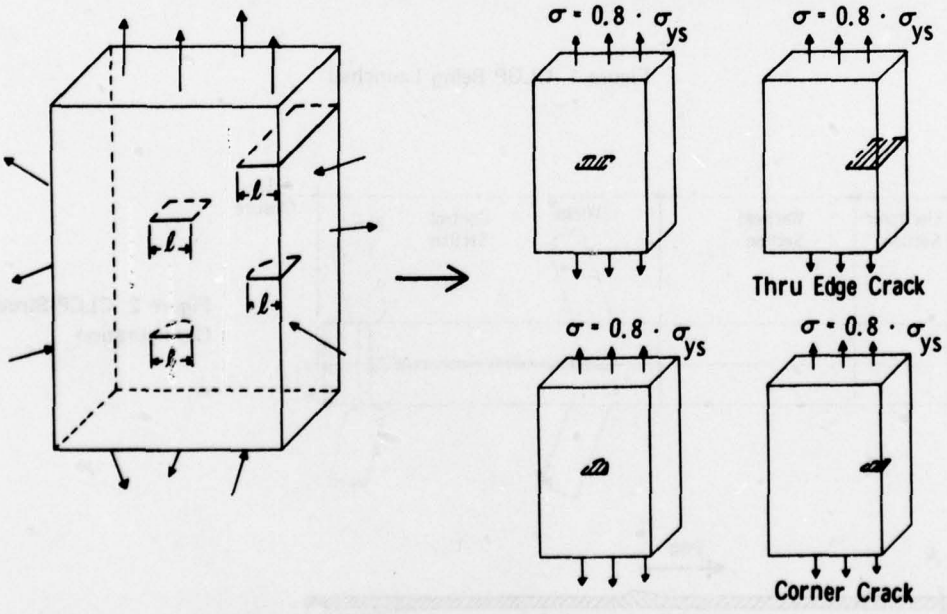


Figure 3. Control (Section) Housing



a) CIMAP - Analysis Level I(a) - Single Valued Critical Crack Size ($\ell_{all} \simeq 0.14''$)



b) CIMAP - Analysis Level I(b) - Crack Type Considered

Figure 4. CIMAP - Basis for Analysis Level I - Tensile Stress = 0.8 Tensile Yield Strength

analysis were not available but the results would be expected to be overly conservative. For weight critical components, such conservative approach could seriously compromise the design. Generally stress states and stress intensities vary spatially and the "critical crack size" can not be treated as unique even for a given crack type. Rather, it becomes essential to specify these critical sizes taking these factors into consideration. Immediately following we shall consider two of these factors in detail; crack type and stress state.

2. Crack Type: It being recognized that the nature (configuration) of a crack significantly influences the critical crack size, it is therefore necessary to qualify each critical crack size, by the crack type. For pragmatic reasons we shall consider, in this paper, only several basic (and idealized) types;

(a) Isolated* through cracks in an infinite plate

(b) Isolated edge through cracks in a semi-infinite plate (or a long surface scratch)

(c) Isolated surface (semi-elliptical) cracks in an infinite plate

(d) Isolated corner cracks in a square tension member.

In general cracks may not be isolated; they may originate in sharp fillets or from boundaries of holes, etc. Surface cracks may not be ideally semi-elliptical. Cracks will occur in components which can not be construed as being a plate. Nevertheless we shall for the purposes of illustrating the CIMAP concept restrict our attention to the above idealized configurations.

3. Stress States: In projectiles, the dominating loads are compressive and arise from the large 'set back' or longitudinal accelerations of the launch. We shall see momentarily how such compressive loads may lead to fracture. Furthermore it will be implied that the methods of fracture mechanics which usually treat fracture as a tension or shear field phenomena can also be applied to this compression load regime. We first consider, at least briefly, both the tensile and shear mode of fracture but will emphasize the lesser appreciated role of compressive stress fields.

Fracture inducing tensile and/or shear stresses may arise in a loaded component in either a direct or induced (parasitic) fashion as summarized in Table I. A plate under uniformly distributed uniaxial tensile loading experiences both the obvious direct tensile stresses and an induced or parasitic shear stress; likewise shear loadings give rise to direct shear stresses as well as parasitic tensile (and compressive stresses).

*"Isolated" in the sense used in this paper means remote from any significant effects of neighboring discontinuities, i.e., holes, fillets, etc.

TABLE I FRACTURE MODE IDENTIFICATION

Remote Loading	Local Fracture Initiation Stress	Fracture Mode
Tension	(Direct) Tension	I
	(Parasitic) Shear	II, III
	(Parasitic) Compressive	Benign, N/A
Shear	(Parasitic) Tension	I
	(Direct) Shear	II, III
	(Parasitic) Compressive	Benign, N/A
Compression	(Parasitic) Tension	I
	(Parasitic) Shear	II, III
	(Direct) Compressive	Benign, N/A

To complete the pattern we note significantly that compression loading leads not only to direct compressive stresses but to parasitic tension and shear stresses. The direct compressive stresses are benign with respect to fracture. However both parasitic tensile and parasitic shear stresses induced by the compressive loading are potential fracture initiation causes. If the loaded structure contains for example a through hole, then parasitic tensile stresses are induced at certain regions of the hole boundary; the magnitude of these tensile stresses may be of the same order as the applied compressive stresses. However since fracture associated with critical cracks in these parasitic tensile stress fields may be treated essentially as for the direct tensile stress fields we will not consider them further. In developing a CIMAP for a predominately compression loaded structure such as Copperhead, we shall emphasize the role of the parasitic shear stresses.

It is clear that critical crack sizes throughout a projectile must be computed not only for those regions stressed in tension (direct or parasitic) but also for those regions stressed in shear particularly compression induced shear. Fracture by this induced shear may be either a Mode II (in-plane) shear fracture or a Mode III (out of plane) shear fracture. We will later (Part III) discuss the pertinent K_{II} determination. We will not dwell on K_{III} determination.

4. Representations of CIMAPS - Resume: In paragraph 1 above we described two elementary models of CIMAP, Level I, and qualified their general utility. We are now in a better position to consider alternative (see Appendix B) to those limited models exploiting varying levels of sophistication.

The elementary CIMAP models above (Fig. 4 - Level I of Appendix B) represent essentially the lowest levels of sophistication and are intended to represent only interim CIMAPS pending the acquisition of appropriate stress analyses.

The ultimate level of sophistication (Level III of Appendix B) requires first, extensive structural/elasticity/plasticity competence so that necessary 'cracked structures' stress analyses can be carried out and appropriate K's determined and secondly that the material be adequately characterized with respect to the various fracture mode toughness levels K_{Ic}, K_{IIc} and K_{IIIc} and with respect to their interaction in defining a fracture envelope. With this level of sophistication one can also incorporate the alleviating influence of friction in apparently augmenting the critical value of K_{II} or K_{III} under compression loading. Unfortunately much of the background data needed for this approach is not currently available.

Between these two extremes lies a useful compromise, (Level II of Appendix B). For this compromise we presume (a) that the results of a non-crack stress analysis are available (i.e., one which neglects the crack in the basic analysis), (b) that cracks exist in the worst orientation (i.e., normal to tensile fields or at 45° to compressive fields), (c) K_{IIc} is taken equal to K_{Ic} pending acquisition of specific data, (d) the coefficient of friction μ is taken as zero, and (e) that there is no interaction between K_I and K_{IIc} or K_{II} and K_{Ic}. It is further presumed that the relevant stress intensity factor may be approximated where necessary from 'off the shelf' crack solutions of idealized specimens using as the pertinent remote stress some measure of the local stresses taken from the stress analysis. Representative and idealized crack types are considered. An obvious disadvantage of this compromise approach is that it is highly dependent on the judgement and experience of the analyst. This however must of course be weighed against its relative simplicity.

It should be evident now that the allowable crack size ℓ_a* will depend not only on the crack type and orientation but also upon the stress state. How can this information be presented pragmatically to the inspector? To simplify an otherwise complex multidimensional problem we restrict our CIMAP to a 2-D model and consider only crack size and crack type; we include crack orientation by assumption that the crack is always oriented in the worst way relative to the stresses. With the problem now reduced to the 2 variables, crack size and type, we proceed with the preparation of a CIMAP per Level II, Analysis.

Fig. 5(a) shows a quadrant of a loaded thick wall cylinder (TWC) which we use as a vehicle for illustrating the preparation of a CIMAP. As indicated the TWC has a wall thickness ratio W = D/d = 2 and is subjected to internal and external pressure of 200 and 100 ksi respectively. It is assumed that the fracture toughness $K_{Ic} = K_{IIc} = 40$ ksi $\sqrt{in}$ corresponding to fracture modes I and II.† A simple stress analysis, e.g., per Timoshenko[4] leads to principal stress contours. Figs. 5(b) and 5(c) portray typical sets of these representing the maximum and minimum principal stresses. Note these contours are concentric circles. Each contour line has been identified with its stress level. For each region between contour lines, the allowable "through the thickness" crack length has been determined assuming conservatively that the

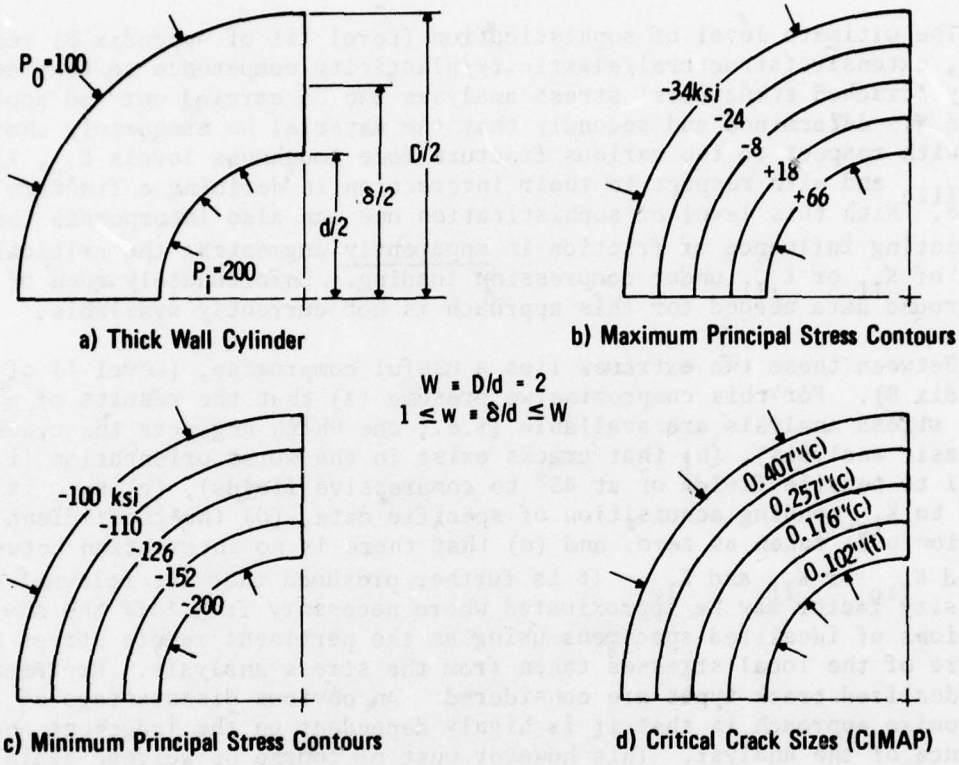


Figure 5. Construction of a CIMAP from Principal Stress Contours

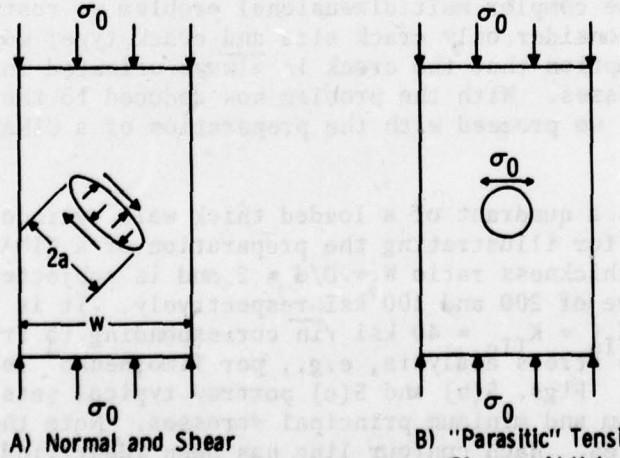


Figure 6. Stresses Induced by Compressive Loading σ_0
(Crack shown exaggeratedly open)

crack is oriented in the most critical direction relative to the stress fields. The crack sizes and governing stress states (t) tension, (c) compression shown in Fig. 5(d) are the result of such calculations. For other than "through the thickness" cracks, correction factors should be used.

III FRACTURE MECHANICS IN THE COMPRESSIVE REGION

1. Background: Here we are concerned principally with the determination of K_{II} induced by compressive loading. Table I identifies fracture modes stemming from different gross or remote loadings. As indicated earlier, fracture is usually identified with tensile stresses. However as illustrated in Table I and discussed earlier, fracture can also occur by direct shear or shear induced tension and/or by compression induced tension or compressive induced shear. In projectiles compressive stresses frequently dominate the high stress regions. Copperhead is no exception to this and it is necessary therefore to treat these compressive stresses as potential fracture initiators. We will not consider the induced or parasitic tensile stresses since they may frequently be treated in a conventional manner. However the short range nature of these induced tensile stresses may significantly complicate even this case. In this section, we exploit the concepts of conventional fracture mechanics to calculate critical crack sizes in materiel which is loaded predominantly in compression. Figs. 6a and 6b show the induced shear and tension stresses induced under compression; as indicated above we shall not consider the case of induced parasitic tensile stresses, Fig. 6(b). Although the present development will highlight Mode II fracture, the rationale holds equally for Mode III fracture. We assume for simplicity that fracture occurs at a critical value of $K_{II} = K_{IIc}$ and is not influenced by the K_I producing load component. (Actually the appropriate K_I, K_{II} failure envelope should be ascertained and used.)

2. Analysis: Referring to Fig. 6(a), note that the stress state in the vicinity of the crack tip is defined at most by the two stress intensity factors K_I and K_{II} and the effective coefficient of friction μ between the crack surfaces. Here K_I and K_{II} refer to the normal mode and the in-plane shear modes of loading respectively (relative to the crack plane).

---

*For purposes of the present paper, all allowable crack lengths have been calculated with nominal limitations imposed by plasticity considerations. Two guidelines have been used: (a) the crack tip plastic zone size calculated should be very small relative to the thickness of the component and (b) the nominal net section stress should not exceed 0.8 times the yield strength. Maximum allowable crack sizes in regions where the nominal stress exceeds this value are taken as the same as though stressed to 0.8 times the yield strength.

†As indicated earlier it is assumed here that K_{Ic} is independent of K_I and vice-versa. However this is not essential to the concept discussed and appropriate data should be used as made available. The yield strength of the cylinder is taken as 250 ksi.

If friction is ignored, (i.e. $\mu = 0$) and the crack is small, (i.e. $2a << W$) it is readily ascertained by superposition (see Fig. 7) that the K_{II} value applicable to the compressively loaded crack of Fig. 6(a) is identically equal to that of the corresponding tension case, (with sign reversed), i.e.

$$K_{IIC} = -K_{IIG} \text{ (since } K_{IIF} = 0) \qquad (1)$$

Fortunately solutions for the required tensilely loaded case (Fig. 7(b) are either generally available in the literature or readily computed. By contrast solutions for compressively loaded inclined cracks are both sparce and difficult to obtain because of the inherent crack closure problem. Inclusion of friction effects would be expected to lead to (a) a decrease in the effective stress intensity factor K_{II} or alternatively (b) an associated apparent increase in the fracture toughness K_{IIc}; hence neglecting friction tends toward a conservative prediction of fracture.

For edge cracks, the asymmetry associated with the proximity of the boundary leads to $K_{IIF'} \neq 0$ and the superposition model, Fig. 8; in this we obtain

$$K_{IIC'} = -K_{IIG'} - K_{IIF'} \qquad (2)$$

We observe here that though solutions for $K_{IIG'}$ are available in the literature[3] at least over a limited range of parameters, the complementary solution for case F' is neither available nor readily obtained because of the crack closure problem. Freese[5] solved for case C' directly rather than for the two superposable components. Fig. 9 compares his results for $K_{IIC'}$ with the tension case (Case G'). As will be noted the asymmetry effects are quite pronounced.

IV SUMMARY

The concept of a Crack Inspection Map (CIMAP) has been presented and illustrated for several levels of technical complexity or sophistication. The lowest levels of sophistication are only of interim interest in the design/inspection process since they merely replace actual stress distributions with constant amplitude stresses uniformly distributed. Nevertheless one modification of this approach was applied to Copperhead and led to an enumeration of maximum allowable crack lengths associated with different types of cracks. Higher levels of CIMAP sophistication could not be applied to Copperhead at this time since the stress analysis was not yet available; however a Level II CIMAP was illustrated for a thick-walled cylinder.

The authors have highlighted the applicability of Fracture Mechanics to compressively loaded structures. This load regime is of particular concern in projectiles during the launch period, but has not generally been identified with fracture initiation. The role of compressive stresses in fracture is illustrated at the Level II CIMAP prepared for the cylindrical model.

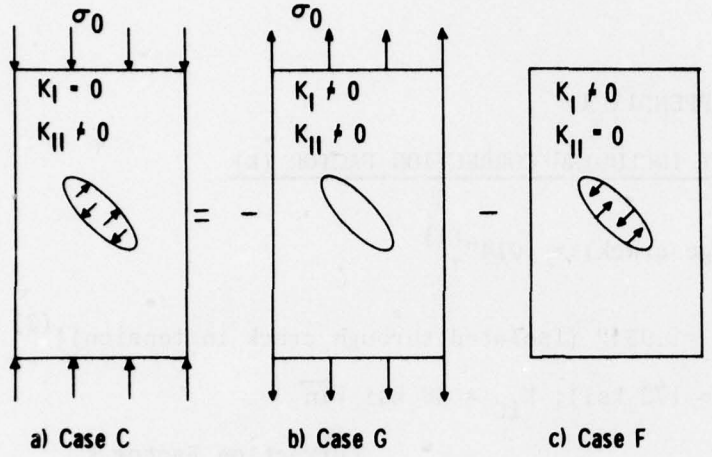


Figure 7. Superposition Model for Isolated Thru Crack ($\mu = 0$) (Crack shown exaggeratedly open)

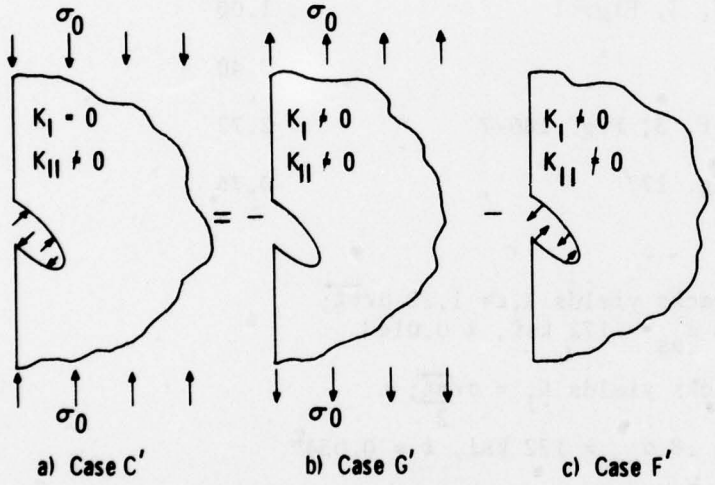


Figure 8. Superposition Model for Edge Thru Crack ($\mu = 0$) (Crack shown exaggeratedly open)

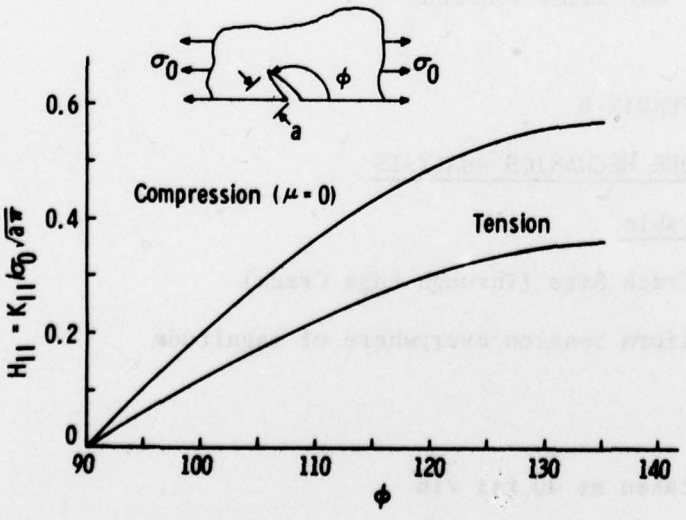


Figure 9. Stress Intensity for Short Inclined Edge Thru Cracks

APPENDIX A

LEVEL I ANALYSIS, SUMMARY INCLUDING CORRECTION FACTOR (k)

Level I (a)

ℓ_a (through edge crack) = .014"[1]

Level I (b)

$\ell_a = k\,\ell_o$ [ℓ_o = .034" (Isolated through crack in tension)][2]

Tension [(σ = .8 σ_{ys} = 172 ksi); K_{IC} = 40 ksi $\sqrt{in}$

Crack Loading and Type	Correction Factor k
Isolated through Crack, Ref. 3, Fig. 1	1.00
Edge Crack, Ref. 3, Fig. 55	0.40
Surface Crack (ℓ/c = 5), Ref. 3, Fig. 186-7	2.77
Corner Crack[3], Ref. 3, Fig. 177	0.76

---

(1) Ref. 3, Fig. 55 for small cracks yields $K_I = 1.12\,\sigma\sqrt{\pi\ell}$;
for K_{IC} = ksi $\sqrt{in}$ and σ = .8 $\sigma_{\mu s}$ = 172 ksi, ℓ 0.014"

(2) Ref. 3, Fig. 1 for small cracks yields $K_I = \sigma\sqrt{\frac{\pi\ell}{2}}$;
for K_{IC} = 40 ksi $\sqrt{in}$ and σ = .8 $\sigma_{\mu s}$ = 172 ksi, ℓ = 0.034"

(3) Quarter Circle Crack in Square Bar under Tension

APPENDIX B

LEVELS OF FRACTURE MECHANICS ANALYSIS

Level I - No Stress Analysis Available

(a) Single Valued Critical Crack Size (Through Edge Crack)

Stress assumed to be uniform tension everywhere of magnitude .8 x yield strength

(σ = 8 $\sigma_{\mu s}$ = 172 ksi)

Fracture Toughness K_{IC} taken as 40 ksi $\sqrt{in}$

(b) Multi Valued Critical Crack Sizes (Depending upon Crack Type)

Correction Factors (k) for Crack Type other than Isolated Through Cracks

Stress assumed to be either uniform tension everywhere as in Level I(a) above.

Fracture Toughness K_{IC} taken as 40 ksi $\sqrt{in}$

Level II - Crack Free Stress Analysis Available

'Isolated Through Crack' taken as reference crack

Correction factor for other crack configuration

Compression induced fracture considered

Coefficient of friction $\mu = 0$

K_{IC} = 40 ksi $\sqrt{in}$ - No interaction of K_I with K_{IIC} or K_{II} with K_{IC}

Level III - Cracked Body Stress Analysis Required

Interaction affects considered

Compression induced fracture considered

Coefficient of friction effect evaluated

Plasticity effects considered

REFERENCES

1. Broek, D., Elementary Engineering Fracture Mechanics, Noordhoff International Publishing, Leydon, Holland, 1974.

2. Knott, J. F., Fundamentals of Fracture Mechanics, Butterworths, London, 1973.

3. Rooke, D. P. and Cartwright, D. J., Compendium of Stress Intensity Factors, Hillington Press, Uxbridge, Middlesex, England, 1976.

4. Timoshenko, S., Strength of Materials, Vol. II, D. Van Nostrand Company, Inc., 1941.

5. Freese, C., Unpublished results.

SESSION Vb: ORDNANCE AND MISSILES

Chairman: P. Munafo
Leader, Mechanical Metallurgy Group
NASA-Marshall Space Flight Center

PLANE STRAIN RESPONSE OF A CYLINDER TO BLAST LOADING 323

N. J. Huffington, Jr.
Army Armament Research and Development Command

SENSITIVITY ANALYSIS OF FATIGUE LIFE ESTIMATES IN CANNON BORES 343

M. Shinozuka, and
R. Vaicaitis
Modern Analysis, Incorporated, and
E. M. Lenoe
Army Materials and Mechanics Research Center

FINITE ELEMENT STRESS ANALYSIS OF U. S. NAVY MARK 83 BASE DETONATING FUZE BODY. 365

O. H. Griffin, Jr. and
C. M. Blackmon
Naval Surface Weapons Center

PRECEDING PAGE BLANK-NOT FILMED

PLANE STRAIN RESPONSE OF A CYLINDER TO BLAST LOADING

NORRIS J. HUFFINGTON, JR.
Supervisory Mechanical Engineer
U.S. Army Ballistic Research Laboratory
U.S. Army Armament Research and Development Command
Aberdeen Proving Ground, Maryland 21005

ABSTRACT

The structural integrity of solid propellant rocket motors subjected to transverse air blast loading has been investigated. For long, slender motors it is appropriate to consider the response of a cylindrical body in a state of plane strain. An analytical modal solution was derived as a supplement to a previously reported numerical analysis and comparisons were made between predictions by the two approaches. Results from such calculations reveal the highly nonlinear dependence of maximum deflection on internal pressurization (such as that produced by propellant combustion) for a fixed blast loading and suggest a possible procedure for enhancing the survivability of rocket motors when subjected to long duration air blast.

NOMENCLATURE

E = Young's modulus
I = Integral defined by Equation (18)
M_θ = Circumferential bending moment/unit length
R = Outside radius of motor case
U = Shock front velocity
a = Mid-surface radius of motor case
$f_{n,s}$ = Natural frequencies of cylinder
h = Thickness of motor case
k = $(h/a)^2/12$
n = Circumferential wave number
p_e = External (blast) pressure
p_i = Internal pressure
p_o = Ambient pressure
p_n = Coefficient of n^{th} term of series for p_e
p_r = Reflected peak overpressure
p_s = Side-on overpressure
q = $(1-\nu^2)p_i a/(Eh)$
s = Mode family identifier
t = Time
t_a = Time of arrival of shock front
v = Circumferential component of displacement
w = Radial component of displacement

PRECEDING PAGE BLANK-NOT FILMED

w_n = Amplitude of n^{th} term in series for w

$\alpha = \frac{12(1-\nu^2)a^4}{Eh^3}$

$\beta = \frac{Eh}{(1-\nu^2)\rho h a^2}$

$\bar{\varepsilon}_\theta$ = Circumferential membrane strain

θ = Circumferential angular coordinate

λ = Blast wave decay coefficient

ν = Poisson's ratio

ρ = Mass density

σ_o = Yield stress

τ = Dummy time variable in convolution integrals

$\tau_{n,s}$ = Period of the (n,s) mode

ω = Circular frequency

INTRODUCTION

At the request of the U.S. Army Harry Diamond Laboratories and the Missile Research and Development Command the Ballistic Research Laboratory has undertaken to provide appropriate methodology for assessing the vulnerability of solid propellant rocket motors to lateral air blast loading, especially that produced by nuclear weapons detonation. A two-fold approach to this task was undertaken: (1) a contractual effort designed to provide maximum compatibility with two-dimensional finite element analyses presently in use by the design community and (2) an in-house study employing the PETROS 3.5 response code [1] which provides numerical solutions for finite amplitude elastoplastic deformation of shell structures by the finite difference method. In its present form the PETROS 3.5 code can model an entire rocket motor case but can treat the propellant only through a lumped-mass approximation. To provide comparison with results to be produced under the contractual effort the PETROS 3.5 code was applied to the plane strain problem of response of a transverse cross section of the rocket motor during and following envelopment by an air blast shock wave. Results from this numerical analysis were presented at the 48th Shock and Vibration Symposium [2].

In addition to the foregoing, the author has derived an analytical solution for the plane strain cylinder problem which, while restricted to small amplitude elastic response, provides useful insight into the meaning of certain phenomena revealed by the numerical analysis. In this paper details of this hitherto unreported analysis model are given, results obtained therefrom are compared with numerical data derived by use of the PETROS 3.5 code, and conclusions regarding possible vulnerability reduction and enhanced structural integrity are drawn.

THE ANALYSIS MODEL

Although several alternate versions were considered it appears that the simplest theoretical development which contains the desired effects can best be presented as a generalization of Flügge's equations [3] for the buckling of cylinders. When Flügge's formulation is particularized to the case of plain strain and augmented by the addition of inertia and load terms the resulting differential equations of motion become:

$$(1 + q)\left(\frac{\partial^2 v}{\partial \theta^2} + \frac{\partial w}{\partial \theta}\right) = \frac{1}{\beta}\frac{\partial^2 v}{\partial t^2} \tag{1}$$

$$\frac{\partial v}{\partial \theta} + w + k\left(\frac{\partial^4 w}{\partial \theta^4} + 2\frac{\partial^2 w}{\partial \theta^2} + w\right) + q\left(\frac{\partial v}{\partial \theta} - \frac{\partial^2 w}{\partial \theta^2}\right) + \alpha k p_e(\theta,t) = -\frac{1}{\beta}\frac{\partial^2 w}{\partial t^2} \tag{2}$$

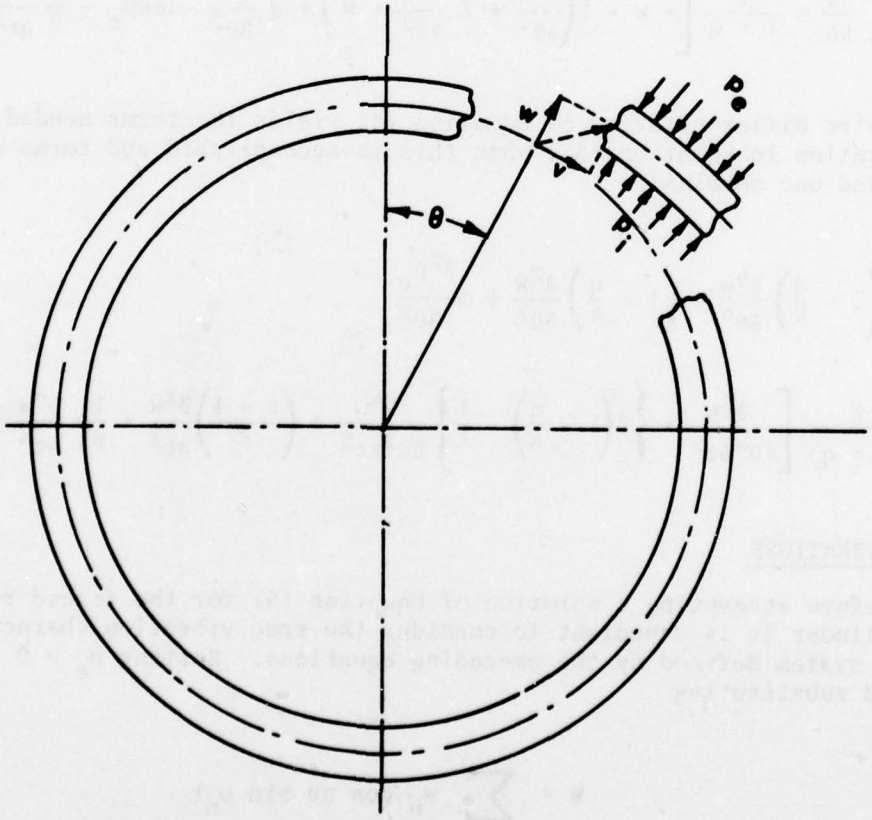


Figure 1. Sign Conventions for Displacements and Loads

The symbols employed in these equations are defined in the Nomenclature and the sign conventions for positive values of displacements and loads are indicated in Figure 1. The effects of transverse shear deformation and rotatory inertia are neglected in this formulation but the buckling terms necessary to represent the effect of internal pressurization produced by propellant combustion are included. It should be reiterated that this formulation is valid only for elastic, small deflection response.

If desired, one can eliminate the tangential displacement v and obtain a single differential equation for the radial displacement w. To achieve this, Equation (1) is differentiated with respect to θ and Equation (2) is solved for $\frac{\partial v}{\partial \theta}$:

$$(1 + q)\left(\frac{\partial^3 v}{\partial \theta^3} + \frac{\partial^2 w}{\partial \theta^2}\right) = \frac{1}{\beta}\frac{\partial^3 v}{\partial \theta \partial t^2} \tag{3}$$

$$\frac{\partial v}{\partial \theta} = \frac{1}{1 + q}\left[- w - k\left(\frac{\partial^4 w}{\partial \theta^4} + 2\frac{\partial^2 w}{\partial \theta^2} + w\right) + q\frac{\partial^2 w}{\partial \theta^2} - \alpha k p_e - \frac{1}{\beta}\frac{\partial^2 w}{\partial t^2}\right] \tag{4}$$

Successive differentiation of Equation (4) yields the terms needed for substitution in Equation (3); when this is accomplished and terms are collected one obtains:

$$\frac{\partial^6 w}{\partial \theta^6} + \left(2 - \frac{q}{k}\right)\frac{\partial^4 w}{\partial \theta^4} + \left(1 - \frac{q}{k}\right)\frac{\partial^2 w}{\partial \theta^2} + \alpha\frac{\partial^2 p_e}{\partial \theta^2}$$

$$= \frac{1}{\beta(1 + q)}\left[\frac{\partial^6 w}{\partial \theta^4 \partial t^2} + \left\{2\left(1 - \frac{q}{k}\right) - \frac{1}{k}\right\}\frac{\partial^4 w}{\partial \theta^2 \partial t^2} + \left(\frac{1 + k}{k}\right)\frac{\partial^2 w}{\partial t^2} + \frac{1}{\beta k}\frac{\partial^4 w}{\partial t^4} + \alpha\frac{\partial^2 p_e}{\partial t^2}\right] \tag{5}$$

FREE VIBRATIONS

Before attempting a solution of Equation (5) for the forced response of the cylinder it is expedient to consider the free vibration characteristics of the system defined by the preceding equations. Setting $p_e = 0$ in Equation (5) and substituting

$$w = \sum_n w_n \cos n\theta \sin \omega_n t \tag{6}$$

demonstrates that the function cos nθ is an eigenfunction* and leads to the frequency equation:

$$\omega_n = \left[\frac{\beta}{2}\left\{ 1 + (1 + 2q)n^2 + k(1 - n^2)^2 \right.\right. \pm \left.\left. \left[(1+n^2)^2 + 4(2+q)qn^2 + 2k(1-n^2)^3 + k^2(1-n^2)^4\right]^{\frac{1}{2}}\right\}\right]^{\frac{1}{2}} \tag{7}$$

Equation (7) reveals that there are two natural frequencies associated with each value of n. Consequently in the sequel the frequencies will carry two subscripts; e.g., $\omega_{n,s}$, where s = 1 or 2. Further, it should not be assumed that the v and w components of displacement are independent. If the radial component of the n^{th} mode is assumed to be

$$w_n = \cos n\theta \; (w_{n,1} \sin \omega_{n,1}t + w_{n,2} \sin \omega_{n,2}t) \tag{8}$$

where $w_{n,1}$ and $w_{n,2}$ are arbitrary amplitude coefficients, then the tangential displacements in the same mode must have the form

$$v_n = \frac{\sin n\theta}{2(1+q)n}\left\{\left[(n^2-1)\{1-k(n^2-1)\} - \left\{(n^2+1)^2 + 4(2+q)qn^2 - 2k(n^2-1)^3 + k^2(n^2-1)^4\right\}^{\frac{1}{2}}\right]w_{n,1} \sin \omega_{n,1}t + \left[(n^2-1)\{1-k(n^2-1)\} + \left\{(n^2+1)^2 + 4(2+q)qn^2 - 2k(n^2-1)^3 + k^2(n^2-1)^4\right\}^{\frac{1}{2}}\right]w_{n,2} \sin \omega_{n,2}t\right\} \tag{9}$$

*n takes on only integral values. The sin nθ is also an eigenfunction but, since we are concerned only with modes symmetric with respect to θ = 0, no use will be made of this function.

in order that v_n, w_n satisfy Equations (3) and (4) simultaneously. Since either of the amplitude coefficients $w_{n,1}$ or $w_{n,2}$ can be taken to be zero, it is clear that there are two distinct families of modes having frequencies $\omega_{n,1}$ and $\omega_{n,2}$, the lower frequency family being identified with s = 1.

Certain useful characterizations of these two families of vibration modes can be achieved by substitution of their individual displacement components into the expressions for circumferential membrane strain

$$\bar{\varepsilon}_\theta = \frac{1}{a}\left(\frac{\partial v}{\partial \theta} + w\right) \tag{10}$$

and for circumferential bending moment

$$M_\theta = \frac{Eh^3}{12(1-\nu^2)a^2}\left(\frac{\partial^2 w}{\partial \theta^2} + w\right) \tag{11}$$

For the s = 1 modes with $n \geqslant 2$ the membrane strains are insignificantly small while the bending moments are appreciable. Thus, this lower frequency set of modes can be identified as the family of inextensional bending modes of a cylinder. The special cases for n = 0 and n = 1 (for s = 1) are not vibratory modes; n = 0 corresponds to a static expansion or contraction of the cylinder while n = 1 represents a rigid body translation of the cylinder cross section along the $\theta = 0$ axis.

Turning to the s = 2 family of vibratory modes and making use of Equations (10) and (11), it may be deduced that this is an extensional set of modes which, in general, also entail flexural stresses. The n = 0 mode of this set is the axisymmetric breathing mode of the cylinder.

FORCED VIBRATIONS

The response of the plane strain cylinder to the prescribed blast loading has been analyzed in the classical manner, representing both the applied loading and the radial deflections by infinite series in the free vibration eigenfunctions:

$$p_e(\theta,t) = \sum_{n=0}^{\infty} p_n(t) \cos n\theta \tag{12}$$

$$w(\theta,t) = \sum_{n=0}^{\infty} w_n(t) \cos n\theta \tag{13}$$

The coefficients for the load series may be determined from

$$p_o(t) = \frac{1}{\pi} \int_0^{\pi} p_e(\theta,t)d\theta \tag{14}$$

$$p_n(t) = \frac{2}{\pi} \int_0^{\pi} p_e(\theta,t) \cos n\theta \, d\theta \quad \text{for} \quad n \geq 1 \tag{15}$$

When the expressions for p_e and w given by Equations (12) and (13) are substituted into Equation (5) to effect a separation of variables the following ordinary differential equations for the coefficients $w_n(t)$ are obtained:

$$\ddot{\ddot{w}}_n + \beta k\left[n^4 - \left\{2\left(1 - \frac{q}{k}\right) - \frac{1}{k}\right\}n^2 + \left(\frac{1+k}{k}\right)\right]\ddot{w}_n$$

$$+ \beta^2 k(1 + q)n^2\left\{n^4 - \left(2 - \frac{q}{k}\right)n^2 + 1 - \frac{q}{k}\right\}w_n = -\alpha\beta k\left\{\ddot{p}_n + \beta(1 + q)n^2 p_n\right\} \tag{16}*$$

$$n = 0,1,2,3,.....$$

These equations were solved in the conventional manner employing the Laplace transform technique, imposing the initial conditions of zero displacement and velocity at t = 0 for both radial and tangential components of displacement. Since the tangential displacement v was eliminated in the derivation of Equation (5) (at the expense of raising the order of the differential equation for w) it was necessary to have recourse to Equations (1) and (2) to establish initial values of $\ddot{w}_n$ and $\dddot{w}_n$ which would ensure that

*A dot over a variable indicates differentiation with respect to time.

$v(\theta,t) = 0$ and $\frac{\partial v}{\partial t}(\theta,t) = 0$. When the solutions for the individual $w_n(t)$ are inserted in Equation (13) the total radial response component is obtained:

$$w(\theta,t) = -\frac{1}{\rho h}\left[\frac{1}{\omega_{0,2}}\int_0^t p_0(t-\tau)\sin\omega_{0,2}\tau\,d\tau\right.$$

$$+\frac{\cos\theta}{\omega_{1,2}}\left(1-\frac{\beta(1+q)}{\omega_{1,2}^2}\right)\int_0^t p_1(t-\tau)\sin\omega_{1,2}\tau\,d\tau$$

$$+\sum_{n=2}^{\infty}\frac{\cos n\theta}{\omega_{n,2}^2-\omega_{n,1}^2}\int_0^t p_n(t-\tau)\left\{\frac{\beta(1+q)n^2-\omega_{n,1}^2}{\omega_{n,1}}\sin\omega_{n,1}\tau\right. \qquad (17)$$

$$\left.\left.+\frac{\omega_{n,2}^2-\beta(1+q)n^2}{\omega_{n,2}}\sin\omega_{n,2}\tau\right\}d\tau\right]$$

$$-\frac{\beta(1+q)}{\rho h\omega_{1,2}^2}\cos\theta\int_0^t p_1(t-\tau)\,\tau\,d\tau$$

The last term in this equation is a non-vibratory term which represents the rigid body translation of the rocket motor section in the direction of the $\theta = 0$ axis produced by the transverse blast loading. It may be omitted if one is only concerned with the deformation of the section relative to its moving mass center. The circular frequencies appearing in Equation (17) are the free vibration eigenfrequencies defined by Equation (7). If the tangential displacements $v(\theta,t)$ are also desired they may be readily obtained by substituting the result for $w(\theta,t)$ from Equation (17) into Equation (4) and performing a single integration with respect to θ.

A digital computer program has been written to facilitate the use of Equation (17). This program evaluates the convolution integrals appearing therein by numerical integration for prescribed pressure coefficients $p_n(t)$ This formulation is quite satisfactory provided $w(\theta,t)$ is to be evaluated for only a few values of time. However, if w is to be calculated for numerous

values of t (e.g., to obtain data for a time-wise plot of w) the evaluation of the convolution integrals over the range $0 \leqslant \tau \leqslant t$ becomes costly and wasteful. This difficulty can be circumvented by use of the following computational algorithm. Equation (17) contains numerous integrals of the type

$$\left.\begin{aligned} I(t) &= \int_0^t p(t-\tau)\, \sin \omega\tau\, d\tau = \int_0^t p(\tau)\, \sin \omega(t-\tau)\, d\tau \\ &= \sin \omega t \int_0^t p(\tau)\, \cos \omega\tau\, d\tau - \cos \omega t \int_0^t p(\tau)\, \sin \omega\tau\, d\tau \\ &= I_c(t)\, \sin \omega t - I_s(t)\, \cos \omega t \end{aligned}\right\} \quad (18)$$

where

$$I_c(t) = \int_0^t p(\tau)\, \cos \omega\tau\, d\tau \quad (19)$$

$$I_s(t) = \int_0^t p(\tau)\, \sin \omega\tau\, d\tau \quad (20)$$

The integral of Equation (18), when evaluated at a time Δt later than above, becomes

$$I(t + \Delta t) = I_c(t + \Delta t)\, \sin \omega(t + \Delta t) - I_s(t + \Delta t)\, \cos \omega(t + \Delta t) \quad (21)$$

But,

$$I_c(t + \Delta t) = \int_0^{t+\Delta t} p(\tau)\, \cos \omega\tau\, d\tau = I_c(t) + \int_t^{t+\Delta t} p(\tau)\, \cos \omega\tau\, d\tau \quad (22)$$

Defining

$$\Delta I_c(t+) = \int_t^{t+\Delta t} p(\tau) \cos \omega\tau \, d\tau \tag{23}$$

$$\Delta I_s(t+) = \int_t^{t+\Delta t} p(\tau) \sin \omega\tau \, d\tau \tag{24}$$

one obtains:

$$I(t + \Delta t) = \left\{I_c(t) + \Delta I_c(t+)\right\} \sin \omega(t + \Delta t) - \left\{I_s(t) + \Delta I_s(t+)\right\} \cos \omega(t + \Delta t) \tag{25}$$

Consequently, it is only necessary to evaluate the expressions of Equations (23) and (24) (by numerical integration unless the interval Δt is taken so small that a cruder approximation suffices) and to accumulate the values of $I_c(t)$ and $I_s(t)$ by incremental additions. The computer program which was developed for evaluation of Equation (17) has been modified to incorporate this algorithm.

APPLICATION OF ANALYSIS

The foregoing modal analysis of cylinder response to air blast has been applied to the same configuration for which the PETROS 3.5 calculations cited in the Introduction were made. This configuration (see Figure 2), while not corresponding to any specific rocket motor, is a generic one having parameters representative of several current tactical and stategic missile systems.

ROCKET MOTOR PARAMETERS

In addition to the geometric data shown on Figure 2 the material properties listed in Table I were employed in the plane strain response calculations. For the PETROS 3.5 calculations the steel motor case was modeled as being elastoplastic with linear strain hardening but no strain-rate effects. However, since the modal analysis is only applicable to elastic response, comparisons with the numerical solutions will only be made where the

Table I
Material Properties

Motor Case (Steel		
Young's modulus	E_c	= 200 GPa = 29 × 10^6 psi
Poisson's ratio	ν_c	= 0.3
Yield stress	σ_o	= 483 MPa = 70,000 psi
Mass density	ρ_c	= 7850 kg/m^3 = 0.000735 lb sec^2/in^4
Propellant (Viscoelastic Solid)		
Young's modulus	E_p	= 689 MPa = 100,000 psi
Poisson's ratio	ν_p	= 0.472
Mass density	ρ_p	= 1660 kg/m^3 = 0.000155 lb sec^2/in^4

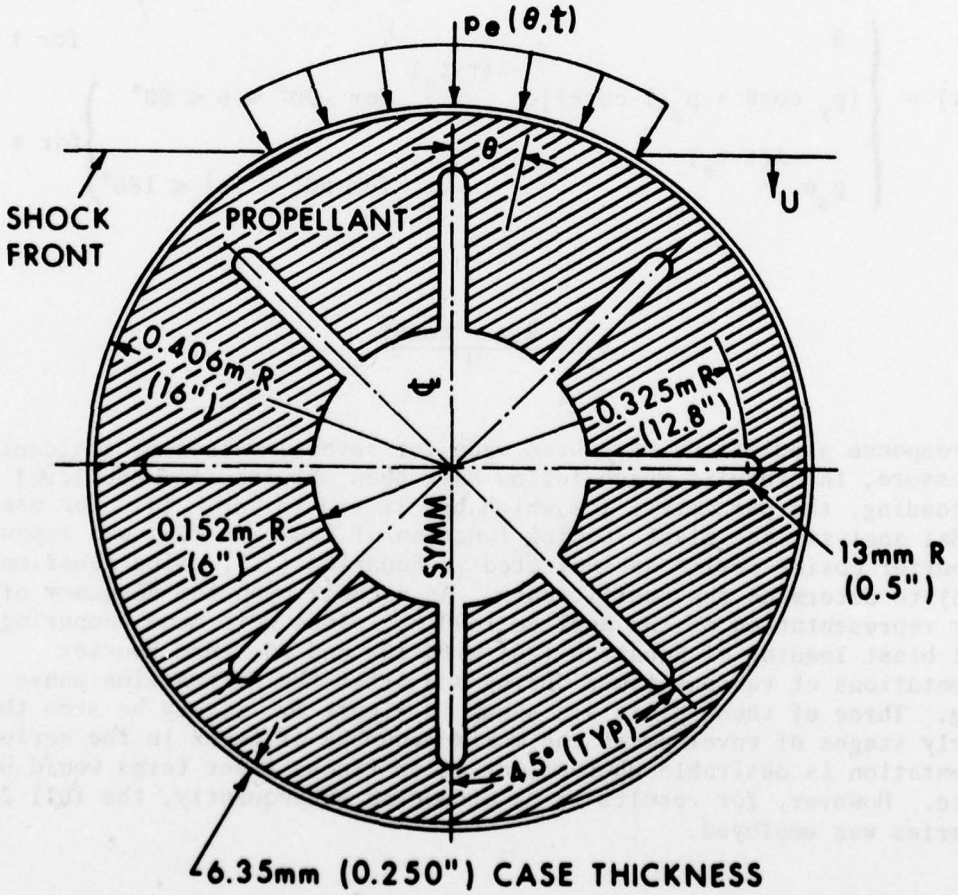


Figure 2. Rocket Motor Cross Section

response remains elastic. Although the propellant is being modeled as a viscoelastic material in the cited contractural effort, the lumped mass treatment of the propellant in the PETROS 3.5 calculations and the modal analysis required use of only the propellant density. The resistance of the propellant grain to deformation is also neglected in this modeling, an approximation which may not be too serious owing to the relatively low strength of the propellant in comparison to that of the steel motor case (see Table I) and the weakening effect of the slots in the propellant grain.

LOADS DEFINITION

The blast loading was introduced as a plane shock wave having an exponentially decaying tail, moving down from above as shown in Figure 2. Although surface overpressures $p_e(\theta,t)$ obtained experimentally or by refined hydrodynamic calculations can be readily employed it was convenient to employ the following functional representation for the blast loading which includes the essential aspects of wave reflection, diffraction, and post-envelopment drag loading:

$$p_e(\theta,t) = \begin{cases} 0 & \text{for } t < t_a \\ \left.\begin{array}{ll} [p_r \cos\theta + p_s(1-\cos\theta)]e^{-\lambda(t-t_a)} & \text{for } -90° \leqslant \theta \leqslant 90° \\ p_s e^{-\lambda(t-t_a)} & \text{for } 90° < |\theta| \leqslant 180° \end{array}\right\} & \text{for } t \geqslant t_a \end{cases} \tag{26}$$

$$t_a = \frac{R(1 - \cos\theta)}{U} \tag{27}$$

While response predictions have been made for several values of incident overpressure, the results which follow have been obtained for one level of blast loading, the parameters for which are listed in Table II. For use in the modal analysis the blast loading function of Equation (26) was expanded in a Fourier cosine series as indicated in Equation (12), using Equations (14) and (15) to determine the coefficients. As a check upon the adequacy of the Fourier representation of the applied loading, plots were made comparing the initial blast loading of Equation (26) with 10- and 20- term Fourier representations at various times during and after the diffraction phase of loading. Three of these plots are shown in Figure 3. It may be seen that at the early stages of envelopment the maximum number of terms in the series representation is desirable whereas, at later times, fewer terms would be adequate. However, for results to be presented subsequently, the full 20-term series was employed.

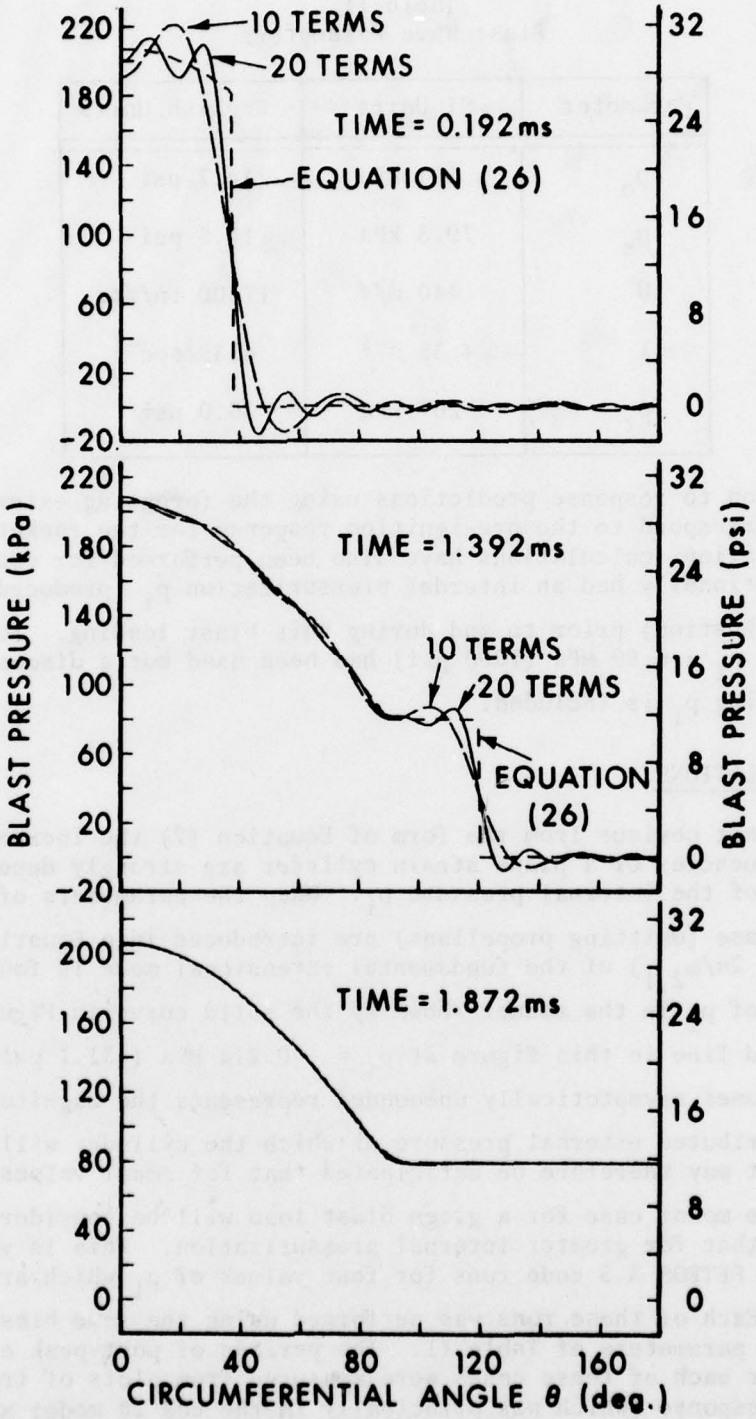


Figure 3. Fourier Representations of Pressure Distributions

Table II
Blast Wave Parameters

Parameter	SI Units	English Units
p_o	101 kPa	14.7 psi
p_s	79.3 kPa	11.5 psi
U	440 m/s	17300 in/sec
λ	4.35 s^{-1}	4.35 sec^{-1}
p_r	207 kPa	30.0 psi

In addition to response predictions using the foregoing external loading, which would correspond to the pre-ignition response for the rocket motor stage under consideration, calculations have also been performed for cases where the motor additionally had an internal pressurization p_i (produced by propellant combustion) prior to and during this blast loading. For the most part the value p_i = 6.89 MPa (1000 psi) has been used but a discussion of the effect of varying p_i is included.

CYLINDER OSCILLATIONS

Although not obvious from the form of Equation (7) the inextensional vibration frequencies of a plane strain cylinder are strongly dependent upon the magnitude of the internal pressure p_i. When the parameters of the generic rocket motor case (omitting propellant) are introduced into Equation (7) the period $\tau_{2,1}$ ($= 2\pi/\omega_{2,1}$) of the fundamental extensional mode is found to vary as a function of p_i in the manner shown by the solid curve in Figure 4. The vertical dashed line in this figure at p_i = - 0.214 MPa (-31.1 psi) where the $\tau_{2,1}$ curve becomes asymptotically unbounded represents the magnitude of uniformly distributed external pressure at which the cylinder will buckle statically. It may therefore be anticipated that for small values of p_i the response of the motor case for a given blast load will be considerably enhanced over that for greater internal pressurization. This is verified by the results of PETROS 3.5 code runs for four values of p_i which are presented in Figure 5. Each of these runs was performed using the same blast loading, defined by the parameters of Table II. The periods of post-peak elastic oscillation for each of these cases were measured from plots of transient displacement response (which was principally in the cos 2θ mode) and the values are shown as circled points in Figure 4. For the larger two values of

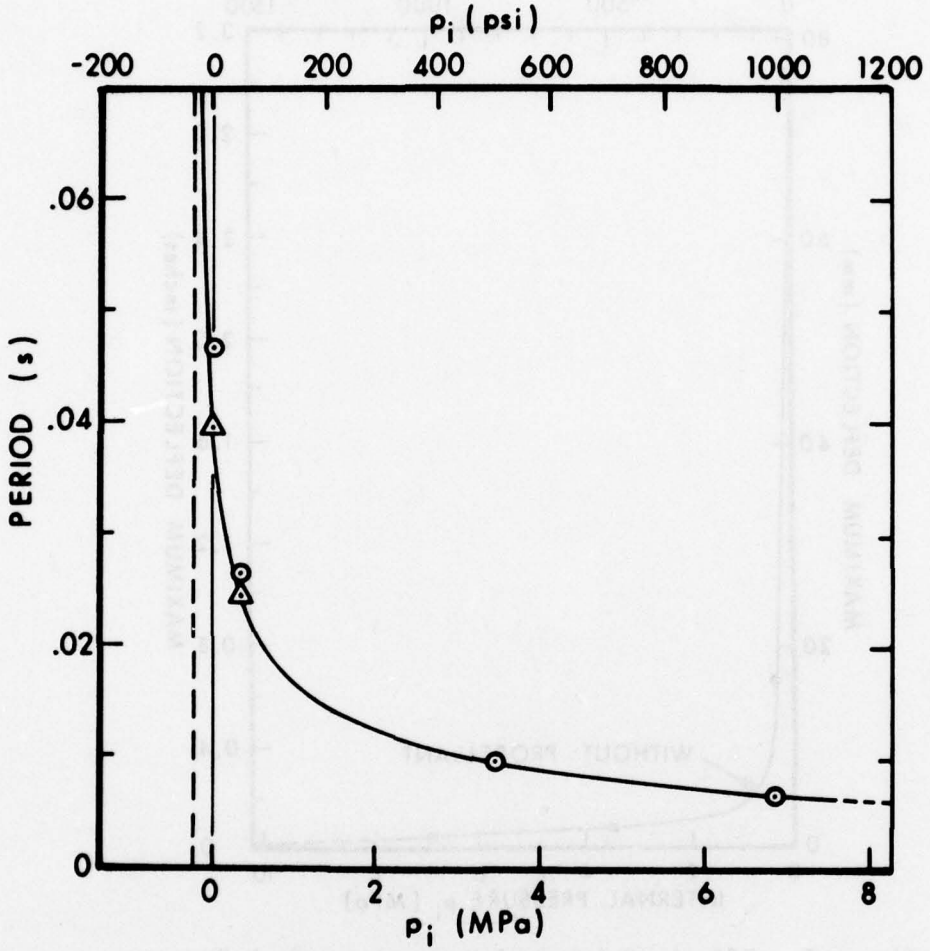


Figure 4. Effect of Internal Pressure on Period of Fundamental Inextensional Mode

p_i the agreement between these points and the curve derived from Equation (7) is amazingly good. The fact that the other two points lie somewhat above the theoretical curve may be attributed to the large amplitude of the response for these cases and to an effective (but unplotted) reduction in the value of p_i due to the non-uniformly distributed external blast pressure. To test this hypothesis, these two cases were re-run at the same values of p_i but with greatly reduced blast loading and the values of free vibration periods plotted within triangles were obtained. Thus there is excellent agreement between the theoretical predictions and the numerical analysis for all cases where the theory should be valid.

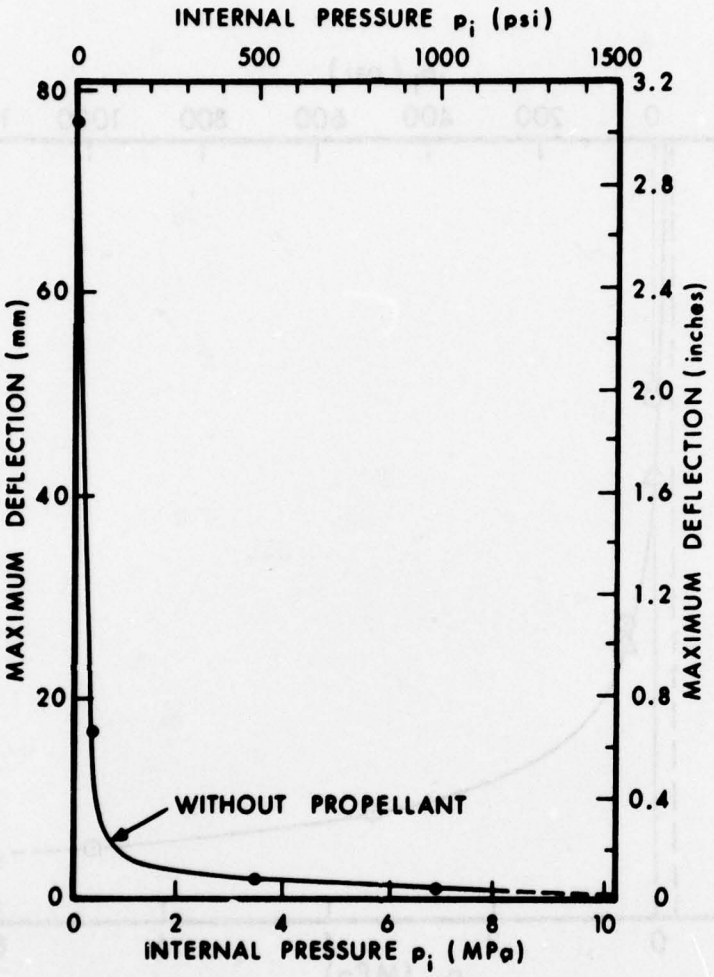


Figure 5. Effect of Internal Pressure on Peak Response

It might be assumed that the extensional family (s = 2) of modes, which exhibit only a slight dependence on internal pressurization, make little contribution to the response of a rocket motor. However, examination of Figure 6, which is a plot of the radial acceleration at $\theta = 0$ for an unpressurized motor including propellant obtained with the PETROS 3.5 code, reveals that this is not necessarily correct. Frequencies for this case derived by use of Equation (7) are listed in Table III. It may be seen that the acceleration response of Figure 6 consists of contributions from modes having frequencies in the range of the extensional modes listed in the table whereas the contribution from the fundamental inextensional mode is imperceptible. The explanation is simple: relatively low amplitude extensional modes when amplified by the square of their large circular frequencies (as is effectively done when calculating accelerations) can become dominant in the manner illustrated in Figure 6.

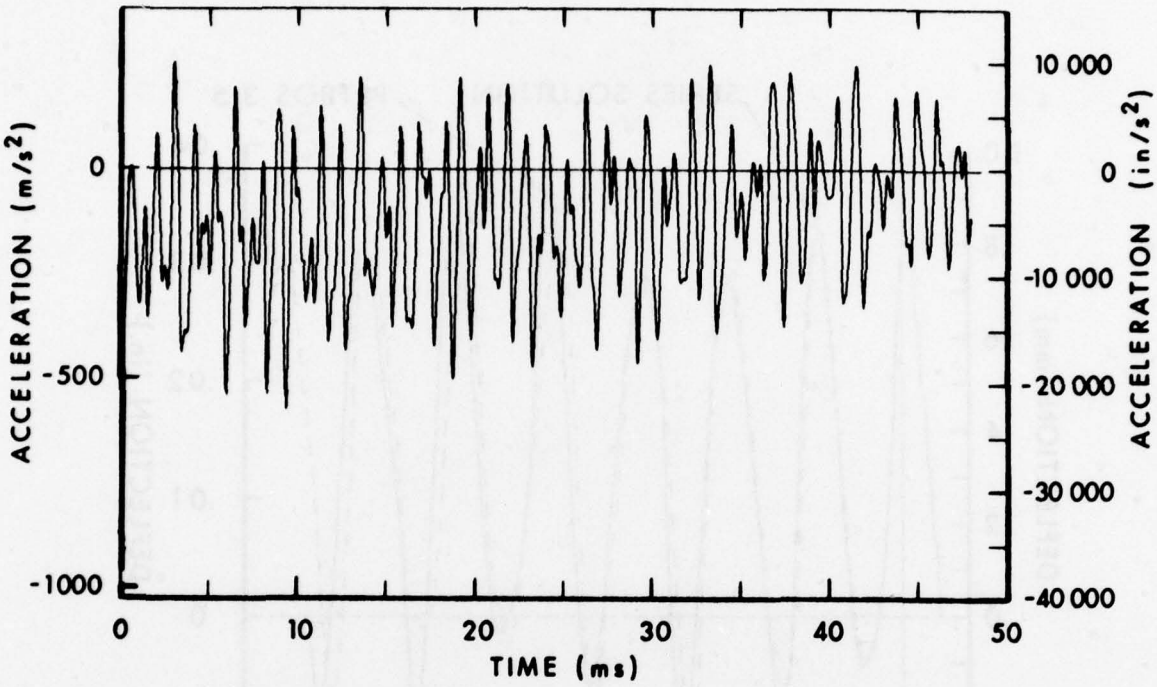


Figure 6. Acceleration at $\theta = 0°$ for Unpressurized Motor Case Containing Propellant

Table III
Frequencies of Unpressurized Rocket Motor

n	$f_{n,1}$ (Hz)	$f_{n,2}$ (Hz)
0	0	838.3
1	0	1185.5
2	10.2	1874.5
3	28.9	2651.0

TRANSIENT RESPONSE CORRELATIONS

A comparison of deflections at $\theta = 0$ obtained with the PETROS 3.5 code and Equation (17) of the analytical solution is shown in Figure 7 for a bare motor case with $p_i = 6.89$ MPa (1000 psi). The portion of the solution shown in negative time represents the PETROS 3.5 calculation for the establishment of the state associated with the static internal pressurization, i.e., the radial expansion of 0.803 mm (0.0316 inches) and the associated strains and stresses, and the damping out of the oscillations associated with this quasi-static calculation. The standard blast wave (parameters of Table II) then

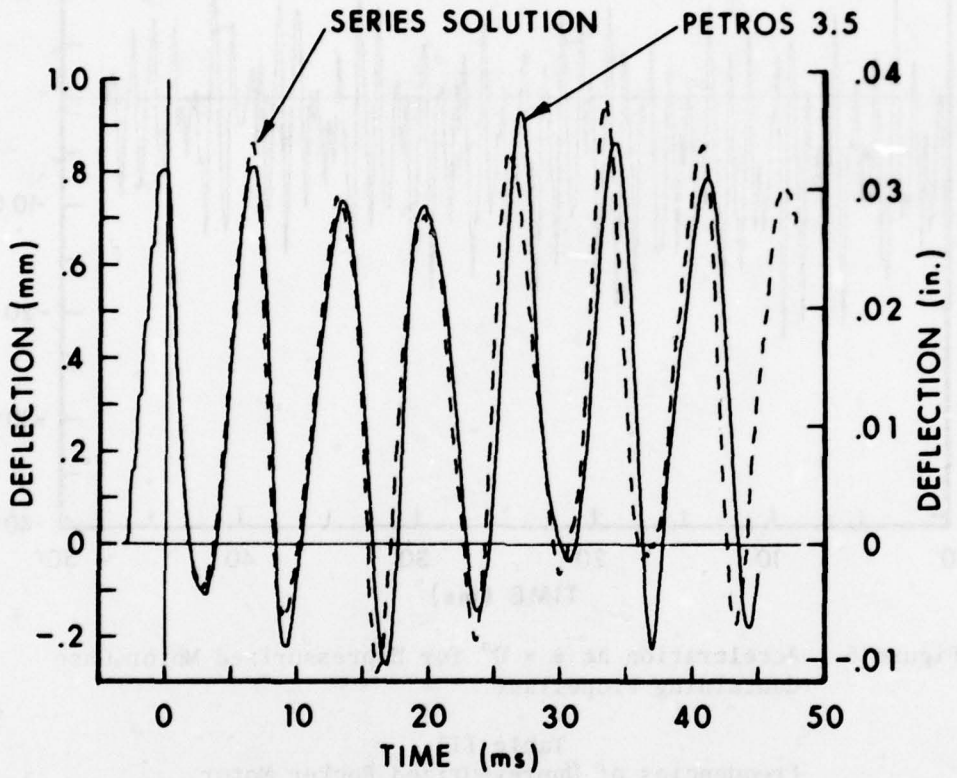


Figure 7. Comparison of Predicted Responses of Motor Case for p_i = 6.89 MPa (1000 psi)

arrives at t = 0, driving the shell at θ = 0 inwards and exciting the vibratory response which follows. It may be seen that the agreement between the two solutions is quite satisfactory for engineering purposes for this case of small amplitude response where the linear elastic analysis should be valid. In fact, the analytical solution should give accurate results for all values of p_i to the right of the "knee" of the curve in Figure 5. Conversely, one would not expect it to provide accurate results where the amplitude of response is large and this is borne out by the comparison of responses for p_i = 0 shown in Figure 8.

CONCLUDING REMARKS

The foregoing analysis of solid propellant rocket motor response to air blast loading was restricted to the plane strain case partly to conform to present design practice and also because it was desired to proceed in an

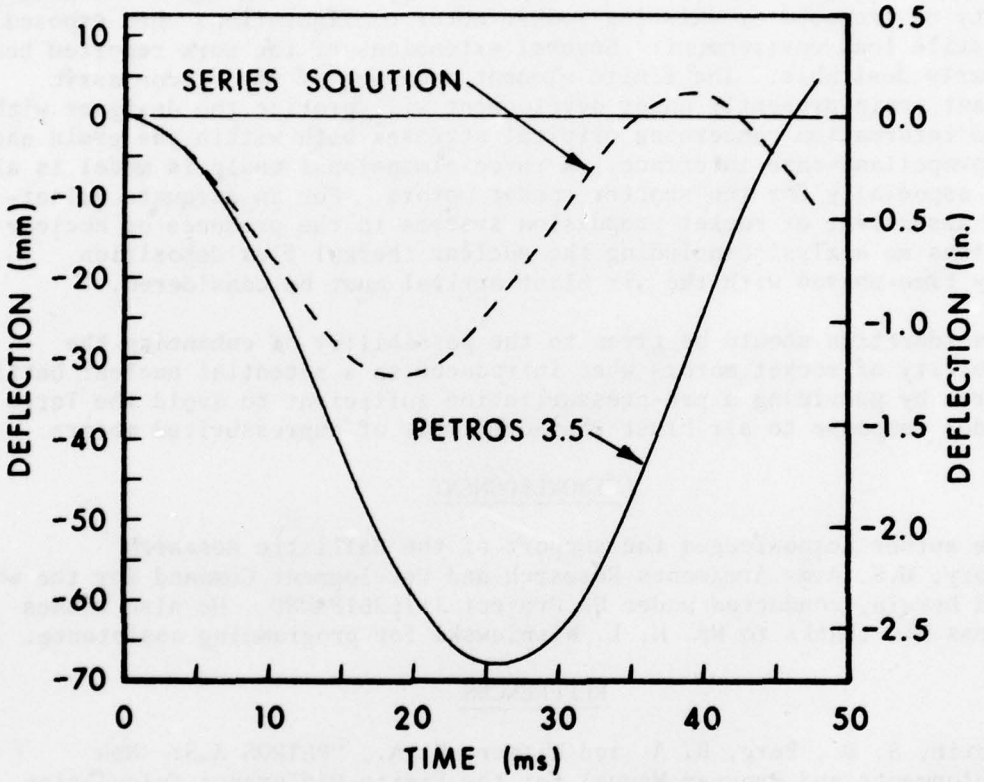


Figure 8. Comparison of Predicted Responses of Motor Case for $p_i = 0$

evolutionary manner. While this restriction limits the applicability of its results to long slender motors the failure mechanisms revealed will certainly have to be considered when more general, three-dimensional analyses are performed. The analytical model provides insight into response behavior even where certain assumptions made in its derivation are violated; e.g., the large amplitude response of the unpressurized motor when the blast loading approaches the critical buckling load. In addition to providing an independent check on the validity of the PETROS 3.5 solution, the modal series solution is preferred for long term response both for economy and because it does not entail the progressive discretization error of the time-marching numerical analysis. Of course, it is appreciated that neither of these approaches models the dissipative mechanisms which are present in physical rocket motor structures but they can certainly provide an upper bound to the response parameters.

The combination of the PETROS 3.5 and modal series methodologies provides the designer with a useful approach for assessing the structural integrity of proposed or existing rocket motor configurations when exposed to a hostile load environment. Several extensions of the work reported herein are clearly desirable. The finite element modeling of the viscoelastic propellant grain presently under development will provide the designer with required information concerning critical stresses both within the grain and at the propellant-case interface. A three-dimensional analysis model is also needed, especially for the shorter rocket motors. For an adequate vulnerability assessment of rocket propulsion systems in the presence of nuclear detonations an analysis including the nuclear thermal flux deposition properly time-phased with the air blast arrival must be considered.

Consideration should be given to the possibility of enhancing the survivability of rocket motors when introduced to a potential nuclear battlefield area by providing a pre-pressurization sufficient to avoid the large amplitudes response to air blast characteristic of unpressurized motors.

ACKNOWLEDGMENT

The author acknowledges the support of the Ballistic Research Laboratory, U.S. Army Armaments Research and Development Command for the work reported herein, conducted under DA Project 1L162618AH80. He also wishes to express his thanks to Mr. H. L. Wisniewski for programming assistance.

REFERENCES

1. Pirotin, S. D., Berg, B. A. and Witmer, E. A., "PETROS 3.5: New Developments and Program Manual for the Finite-Difference Calculation of Large Elastic-Plastic Transient Deformations of Multilayer Variable-Thickness Shells," U.S. Army Ballistic Research Laboratories Contract Report No. 211, February 1975.

2. Huffington, N. J., Jr. and Wisniewski, H. L., "Rocket Motor Response to Transverse Blast Loading," The Shock and Vibration Bulletin No. 48 (to be published).

3. Flugge, W., Stresses in Shells, Second Edition, Springer-Verlag, 1973, p. 448.

SENSITIVITY ANALYSIS OF FATIGUE LIFE ESTIMATES IN CANNON BORES

MASANOBU SHINOZUKA, President; RIMAS VAICAITIS, Research Consultant
Modern Analysis, Inc. Ridgewood, New Jersey

EDWARD M. LENOE
Supervisory Mechanical Engineer, Army Materials and Mechanics Research Center
Watertown, Massachusetts

ABSTRACT

The objective of this study is to develop practical computational procedures for fatigue crack growth and life estimations for gun tubes. Accordingly, two general aspects of these procedures are investigated. First, deterministic calculations are completed for several commonly used crack growth equations. The deterministic estimates varied by a factor of two for the formulations considered. Second, a probabilistic formulation to predict failure of gun tubes is explored. This is achieved by assuming appropriate distribution functions for selected random variables in the crack growth model and then employing the Monte Carlo technique. Numerical results are presented for geometries representative of 175-mm gun tubes for both deterministic and probabilistic life estimates. A direct comparison with experimental data is also included.

NOMENCLATURE

A,B=Empirical constants, function of material properties and crack shape
a, a_0, a_c=Crack size, initial and critical crack sizes (semiminor axis of elliptic crack)
a_f=Value of a for which da/dn approaches infinity
$C=\beta/(EK_{IC}\sigma_y)$
C_1, C_3, C_5, C_6=Proportionality constants in crack growth equation
c=Crack size (major axis of elliptic crack)
d=a/c=Ratio of crack dimensions
E=Young's modulus
E(k)=Complete elliptic integral of the second kind
K_I=Stress intensity factor
K_c, K_{IC}=Critical stress intensity factor
K_{max}=Maximum stress intensity factor
$M_c(\theta)$=Curvature correction factor
$M_{KS}(\theta)$=Stress magnification factor
m=Exponent in crack growth equations
N_{cr}(int), N_{cr}(ext)=Total number of cycles for crack to grow from a_0 to critical internal and external crack size a_c
$N_f=N_{cr}+N_n$=Total failure cycles
N_n=Number of cycles for a crack to grow from a_c to a_f
n=Number of load cycles
p=Exponent in crack growth equations
P_i=Internal pressure
R=Stress ratio; ratio of minimum stress to maximum stress
$\bar{R}$=Residual stress capacity
R_i, R_0=Internal and external radii of gun tube
R_u=Ultimate strength
$r=R_0/R_i$
β=Empirical constant, function of material properties
$\Delta K, \Delta K_{TH}$=Range of stress intensity factor and the same at threshold
θ=Angle (see Fig. 3)
λ=Empirical parameter, function of crack size and residual stress
$\mu_\lambda, \sigma_\lambda$=Mean value and standard deviation of λ
σ_0, S=Hoop stress and maximum bore stress
σ_y=Yield strength

INTRODUCTION

Gun tubes are an important system whose life must be estimated with a high degree of accuracy in order to establish reasonable retirement limits. Typically, a heat check pattern develops on the inside surface of the tube near the breech end (see Fig. 1). Once the cracks are started, they become larger with continued firing. Rate of crack growth is influenced by numerous factors in design, materials and fabrication, as well as actual firing conditions. The mechanisms of cracking, erosion, wear and failure have been the subject of continuing studies (see, for example, References 1 through 5).

While these mechanisms are understood in a general sense, there are many remaining areas of uncertainty, particularly with regard to wear and erosion phenomena. An historically important objective in gun tube performance has been to achieve a balance between wear and erosion and fatigue resistance. In this regard, each gun tube type and munition must be considered in detail. Fig. 2, for instance, suggests in a general way that condemnation limits of certain cannons are related to the specific system and its requirements. In this paper, wear and erosion aspects are not considered. Our intention is to explore the problem of fatigue crack growth in detail in order to comprehend the status of such life estimating procedures.

In the spring of 1966 a 175-mm M113 gun tube (Serial #733) fractured in Viet Nam. When the tube was sectioned, it was shown that the mechanical properties varied significantly along its length. Subsequently 38 gun tubes were sectioned and certain of their mechanical and fatigue properties evaluated. These data as well as the extensive information on gun tube properties generated by Watervliet Arsenal presented an opportunity to compare predicted and observed behavior of gun tubes under fatigue conditions. Therefore, the following tasks are completed.

First, in order to gain insight into procedures for fatigue life estimations, deterministic integration of several different crack growth formulations for the cases of internal and external cracks in thick-walled cylinders are studied. Four specific crack growth equations are treated and tube stress capacity and fatigue crack growth estimates are completed for the simple case of cyclically pressurized cylinders. The importance of these deterministic calculations is to establish the relative behavior of the different crack growth equations.

Second, a probabilistic formulation to predict failure of gun tubes is explored since fatigue life is obviously a random variable and a statistically based estimate of fatigue life has to be completed in order to make a comparison to experimental observations. This is accomplished by assuming appropriate distribution functions for selected random variables in the crack growth model and applying Monte Carlo techniques to calculate fatigue lives.

INFLUENCE OF THE CRACK GROWTH EQUATION

To investigate the influence of the crack growth equation on life estimation, the problem of semielliptic internal (pressurized) and external (not



Figure 1 Typical Heat Check Patterns in an Eroded Cannon Section.

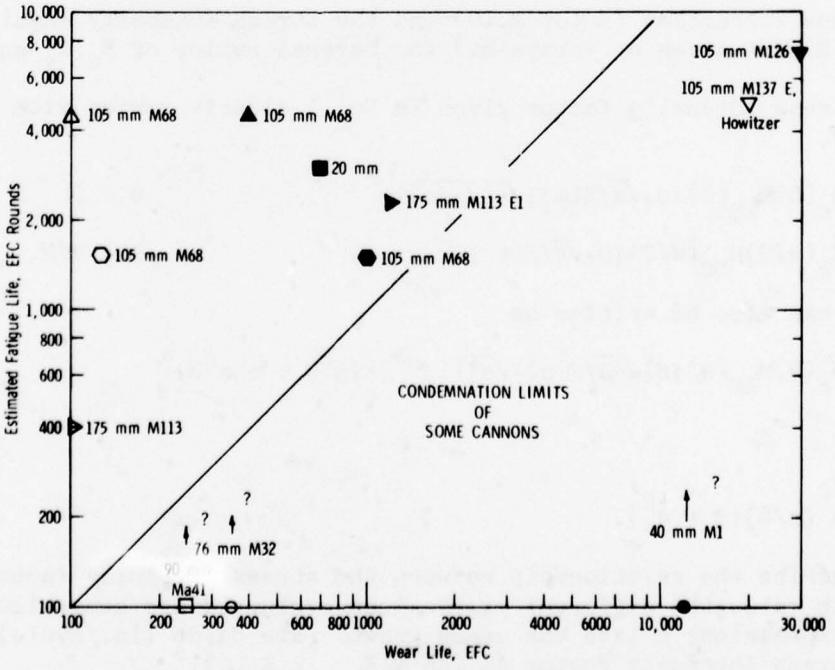


Figure 2 Condemnation Limits of Some Cannons.

pressurized) cracks in thick-walled cylinders was studied. The shape of the cracks is depicted in Fig. 3, and as shown in the detail, the major axis is 2c and semiminor axis is a. The ratios of the outside to the inside diameter for the cylinder is taken to be more than 1.2 so that the developed stress gradients can be expressed by Lame's equations from the theory of elasticity. Internal pressures considered range from 30 to 50 ksi. The general behavior of fatigue crack growth is shown schematically in Fig. 4.

The relationship between the stress intensity factor K_I at a point along the crack tip and the crack size a in a pressurized cylinder can be written as[6]

$$K_I = M_c(\theta)M_{KS}(\theta)[\sigma_0\sqrt{\pi}/E(k)]\sqrt{a/c}(c^2\sin^2\theta + a^2\cos^2\theta)^{1/4} \quad (1)$$

where the point is specified by the angle θ as shown in Fig. 3

$$\sigma_0 = 2P_iR_0^2/(R_0^2 - R_i^2) \quad (2)$$

and E(k) is the complete elliptic integral of the second kind;

$$E(k) = \int_0^{\pi/2}[1 - (1 - a^2/c^2)\sin^2\theta]d\theta$$

$$\simeq \pi/[2\{1 - (1/4)(1 - a^2/c^2) - (3/64)(1 - a^2/c^2) - \ldots\}]$$

$$\simeq 3\pi/8 + (\pi/8)(a^2/c^2). \quad (3)$$

The curvature correction factor $M_c(\theta)$ and the stress intensity magnification factor $M_{KS}(\theta)$ are given by Kobayashi[6] for several ratios of R_0/R_i and a/c.

The stress intensity factor given in Eq. 1 clearly varies with angle θ. For example,

$$K_I = M_c(0)M_{KS}(0)[\sigma_0\sqrt{\pi}/E(k)]\sqrt{a}(\sqrt{a/c}), \qquad \theta = 0 \quad (4)$$

$$K_I = M_c(\pi/2)M_{KS}(\pi/2)[\sigma_0\sqrt{\pi}/E(k)]\sqrt{a}, \qquad \theta = \pi/2. \quad (5)$$

Equation 1 can also be written as

$$K_I = M_c(\theta)M_{KS}(\theta)[\sigma_0\sqrt{\pi d}/E(d)]\sqrt{a}[(1/d^2)\sin^2\theta + \cos^2\theta]^{1/4} \quad (6)$$

where

$$d = a/c \quad (7)$$

$$E(d) = (\pi/8)(3 + d^2). \quad (8)$$

To describe the relationship between the stress intensity factor and the crack growth rate, the different expressions evaluated are summarized in Table I. These expressions relate the crack growth rate da/dn (in./cycle) to the range of stress intensity factor ΔK ($\Delta K = K_{max} - K_{min}$).[7]

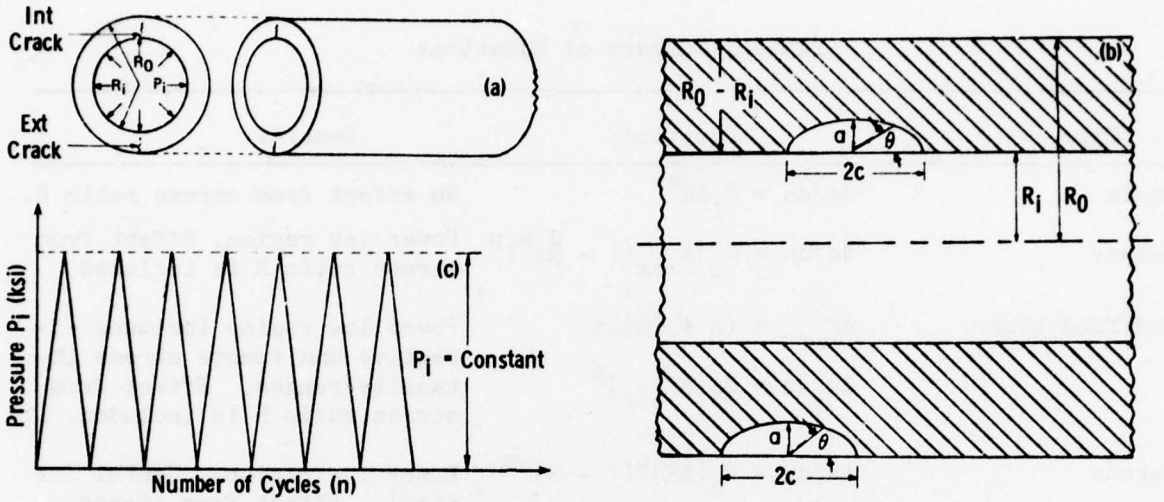


Figure 3 Geometry of Cylinder, Cracks, and Internal Pressure Variation.

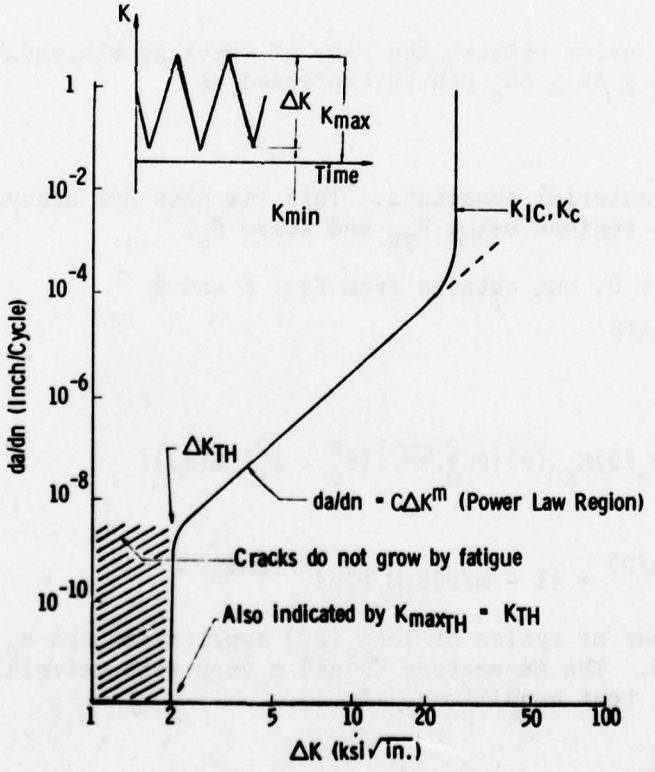


Figure 4 Schematic of Fatigue Crack Growth Behavior for Zero-Tension Loading.

Table I Summary of Equations

Type	Equation	Remarks
Paris	$da/dn = C_1 \Delta K^m$	No effect from stress ratio R.
Walker	$da/dn = C_3[K_{max}(1 - R)^m]^p$	Power law region. Effect from stress ratio R is included
Modified Elber	$\Delta K_{eff} = (A + BR)\Delta K$ $da/dn = C_5(\Delta K_{eff})^p$	Power law region includes effective and remote stress intensity ranges. Effect from stress ratio R is included.
Barsom	$da/dn = C_6(\Delta K)^p(1 - R)^{-\frac{1}{2}}$	Power law region. Useful for steel. Effect from stress ratio R is included.

THE PARIS EQUATION

The primary behavior between the rate of crack growth and ΔK in the power law region for $\Delta K_{TH} \leq \Delta K \leq \Delta K_c$ can be expressed as

$$da/dn = C_1 \Delta K^m \tag{9}$$

where C_1 and m are material constants. This law does not account properly for crack growth in the regions below K_{TH} and above K_c.

Assuming $K_{min} = 0$, one obtains from Eqs. 6 and 9

$$da/dn = C_1 M^m P_i^m a^{m/2} \tag{10}$$

where

$$M = M(\theta,d) = M_c(\theta)M_{KS}(\theta)[2R_0^2\sqrt{\pi d}/\{(R_0^2 - R_i^2)\, E(d)\}] \tag{11}$$

Solving Eq. 10,

$$a(n) = \{a_0^{(1-m/2)} + (1 - m/2)C_1 M^m P_i^m n\}^{2/(2-m)} \tag{12}$$

where n is the number of cycles of load (P_i) application and a_0 is the initial crack size at n = 0. The parameters C_1 and m vary with material property, temperature, humidity, test conditions, etc.

THE WALKER EQUATION

The Walker equation can be written as

$$da/dn = C_3[K_{max}(1 - R)^m]^p. \tag{13}$$

This equation does take the stress ratio R (= minimum stress/maximum stress) into consideration but does not have the modification for the high crack growth acceleration. From Eqs. 6 and 13, one obtains

$$da/dn = C_3 M^p P_i^p [(1 - R)^m]^p a^{p/2}. \tag{14}$$

Solving for a(n),

$$a(n) = \{a_0^{(2-p)/2} + (1-p/2)C_3 M^p P_i^p [(1 - R)^m]^p n\}. \tag{15}$$

THE MODIFIED ELBER EQUATION

A generalized linear equation that relates the effective and remote stress intensity ranges, ΔK_{eff} and ΔK, respectively, can be written as

$$K_{eff} = (A + BR)\Delta K \tag{16}$$

with A and B determined experimentally. Then,

$$da/dn = C_5(\Delta K_{eff})^p. \tag{17}$$

From Eqs. 6, 16 and 17, one obtains

$$a(n) = \{a_0^{(2-p)/2} + (1-p/2)(A + BR)^p M^p C_5 P_i^p n\}^{2/(2-p)} \tag{18}$$

THE BARSOM EQUATION

$$da/dn = C_6(\Delta K)^p (1 - R)^{-\frac{1}{2}} \tag{19}$$

where

$$R \geq 0,\ 6.4(1 - 0.85R) \leq K < 0.04\sqrt{E\sigma_y} \tag{20}$$

in which σ_y is yield strength and E is modulus of elasticity. From Eqs. 6 and 19, the solution for a(n) is obtained as

$$a(n) = \{a_0^{(2-p)/2} + (1-p/2)(1 - R)^{-\frac{1}{2}} M^p C_6 P_i^p n\}^{2/(2-p)} \tag{21}$$

NUMERICAL EXAMPLES

The following data are used for the numerical calculations: a_0 = 0.03 in. (initial crack size), $C_1 = C_3 = C_5 = C_6 = 3.6 \times 10^{-10}$ (proportionality constant), R_i = 8 in. (internal radius of the cylinder), $R_0 = 1.5R_i$ (external radius of the cylinder), P_i = 30 ksi (internal pressure), $\theta = \pi/2$ (location of the front crack), m = 3 (exponent for the Paris law), p = 3, m = 1 (exponents for Walker equation), p = 3 (exponent for Elber equation), p = 3 (exponent for Barsom equation), K_c = 75 ksi$\sqrt{\text{in.}}$ (critical stress intensity factor), R_u = 120 ksi (ultimate strength of material), d = 0.2 (semielliptic crack size ratio), and R (stress ratio = 0).

Numerical results are obtained for cracks located on the internal and on the external surfaces of the cylinder. Two types of results, namely the crack depth a, and the ratio of the residual tube strength to the ultimate material

strength $\bar{R}/R_u$, are plotted against number of cycles N_n

The values for N_n are defined as cycles after an initial critical crack size a_c is reached and the cylinder stress capacity starts to decrease. The N_{cr}(int) and N_{cr}(ext) indicate the total number of cycles for a crack to grow from a specified initial crack a_0 to the critical crack size a_c for internal and external cracks, respectively. The relationship between the remaining strength $\bar{R}$ and the fatigue crack a is obtained from Griffith-Irwin type equation.

$$\bar{R}(N_n)/R_u = [a_c/a(N_n)]^{\frac{1}{2}}, \text{ for } a(N_n) \geq a_c \tag{22}$$

where the critical crack a_c can be calculated from

$$a_c = (2/\pi)(K_c/R_u)^2. \tag{23}$$

The crack size $a(N_n)$ and the ratio $\bar{R}(N_n)/R_u$ are plotted in Figure 5 using the various solutions for $a(N_n)$. In general it can be seen that a crack initiated on the external surface of the cylinder propagates more rapidly than a crack on the internal surface. This is due to the fact that the stress intensity magnification factor M_{KS} and the curvature correction factor M_c given in Ref. 6 are larger for outer cracks for the data chosen in this study. Similar results were obtained for Paris, Walker, Elber and Barsom crack growth formulas. Depending on the particular parameters chosen for each of these models, crack growth is sensitive to the type of predictive model used. Table II lists the results obtained and indicates that the Barsom and Elber equations essentially span the range of cycles to failure.

Table II Summary of Estimated Cycles to Failure

Equation	Internal	External
Paris	4204	2092
Walker	5766	2869
Elber	8210	4085
Barsom	3988	1984

DETERMINISTIC FATIGUE OF 175-MM GUN TUBES

In this case failure cycles are calculated from $N_f = N_{cr} + N_n$, where N_{cr} is the number of cycles for a crack to grow from initial crack a_0 to the critical crack a_c, and N_n is the number of cycles for a crack to grow from a_c to the failure crack a_f. The failure crack a_f is defined as that value of a at which da/dn becomes practically infinite.

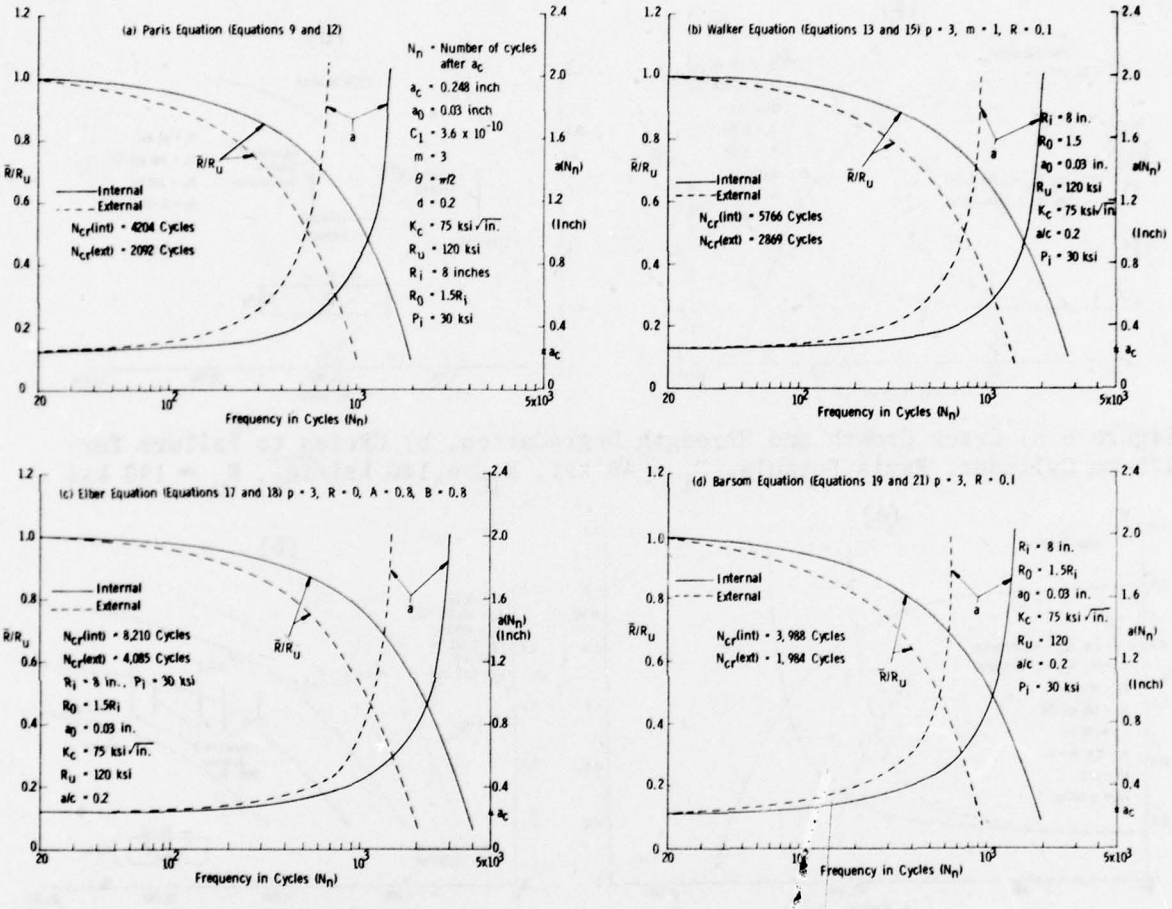


Figure 5 Crack Growth and Strength Degradation Based on a) Paris, b) Walker, c) Elber, and d) Barsom Equations.

The numerical results are obtained for a_0 = 0.03 in., R_i = 3.575 in., $R_0 = 2R_i$, P_i = 48 ksi and P_i = 50 ksi, K_c = 140 ksi√in. and K_c = 110 ksi√in., R_u = 190 ksi and R_u = 150 ksi. In Figure 6a the crack size a and the strength ratio $\bar{R}/R_u$ are obtained using the Paris crack propagation law for a specified crack size ratio a/c. Results corresponding to other a/c ratios are determined and life cycles N_f are calculated. These results are shown in Figure 6b. Experimental results from References 8 and 9 are indicated in this and other figures for a/c ratios in the vicinity of 0.6 for the semielliptic cracks. All the experimental results are for cracks on the internal surface of the cylinder. Similar results are given in Figures 7a and 7b for Elber-type crack growth equation. In Figure 7b the life cycles N_f are plotted for several values of parameter A (see Equation 16) and the stress ratio R = 0. Different values of A

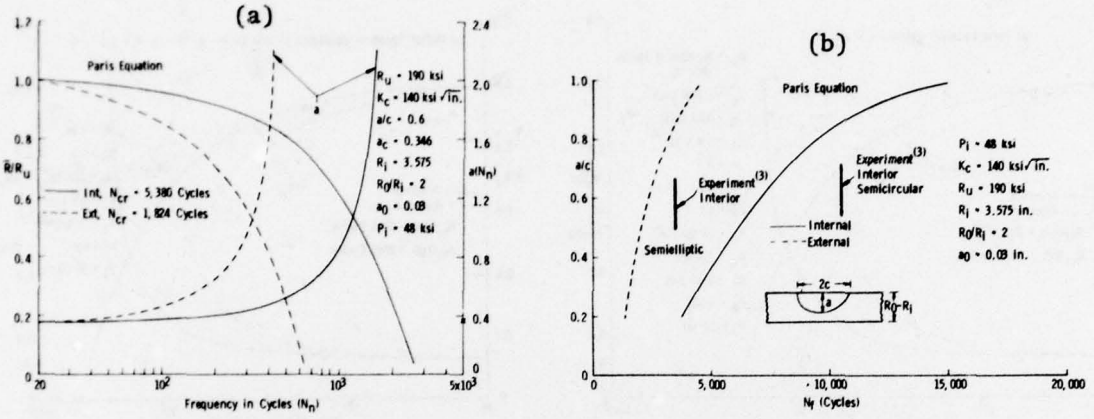


Figure 6 a) Crack Growth and Strength Degradation, b) Cycles to Failure for 175-mm Cylinder, Paris Formula, P_i = 48 ksi, K_{IC} = 140 ksi√in., R_u = 190 ksi

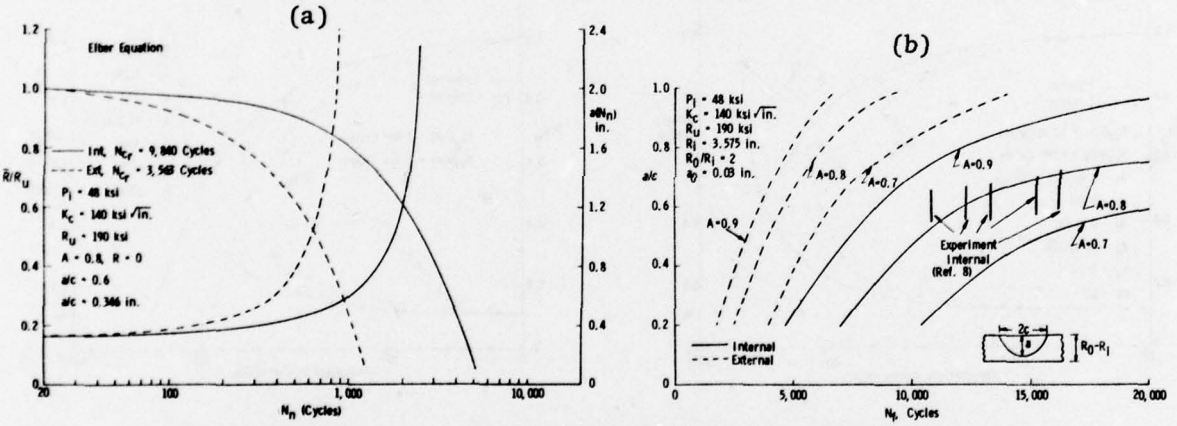


Figure 7 a) Crack Growth and Strength Degradation, b) Cycles to Failure for 175-mm Cylinder, Elber Equation, P_i = 48 ksi, K_{IC} = 140 ksi√in., R_u = 190 ksi.

could account for the autofrettage effect in the gun tube. Results corresponding to internal pressure P_i = 50 ksi, critical stress intensity factor K_c = 140 ksi√in. and ultimate strength R_u = 190 ksi are shown in Figure 8a and 8b. Similar results, but for K_c = 110 ksi√in. and R_u = 150 ksi, are plotted in Figures 9a and 9b. From these results it can be observed that the life of a gun tube due to cyclic pressure is very sensitive to the values of constant A, crack size ratio a/c, and the magnitude of internal pressure P_i. In all the calculations completed thus far, the Paris and Barsom formulas for crack growth were found to result in shortest life estimates. The Paris formulation offers simplicity in numerical computations. Referring to Figures 7, 8, and 9, it appears that different values of A give better fits to the experimental observations. For instance, a value of A = 0.8 yields reasonable approximation to the data of Reference 8. Figure 8b suggests that A = 0.7 is a best fit to the data of Reference 9, and a value of A slightly larger than 0.5 is reasonable for the data shown in Figure 9b.

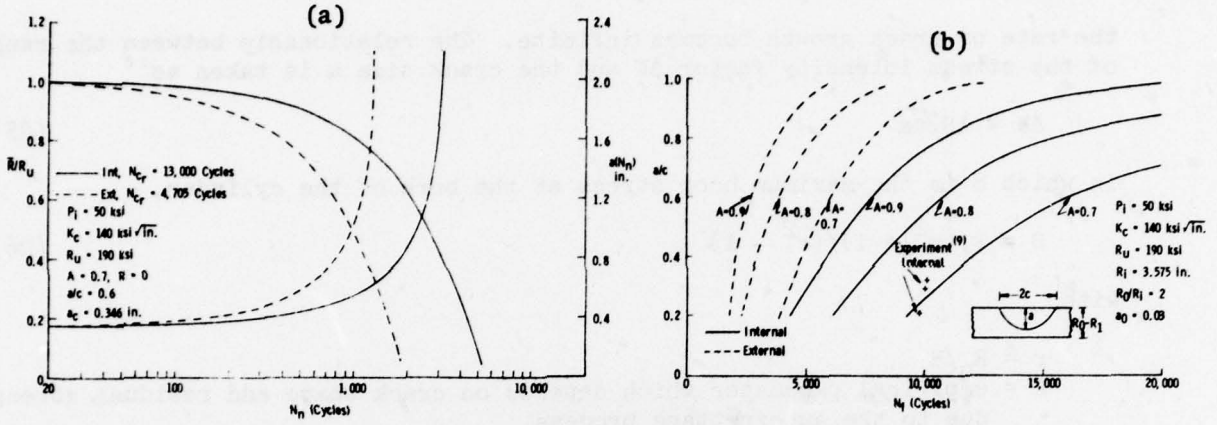


Figure 8 a) Crack Growth and Strength Degradation, b) Cycles to Failure for 175-mm Cylinder, Elber Equation, P_i = 50 ksi, K_{IC} = 140 ksi√in., R_u = 190 ksi.

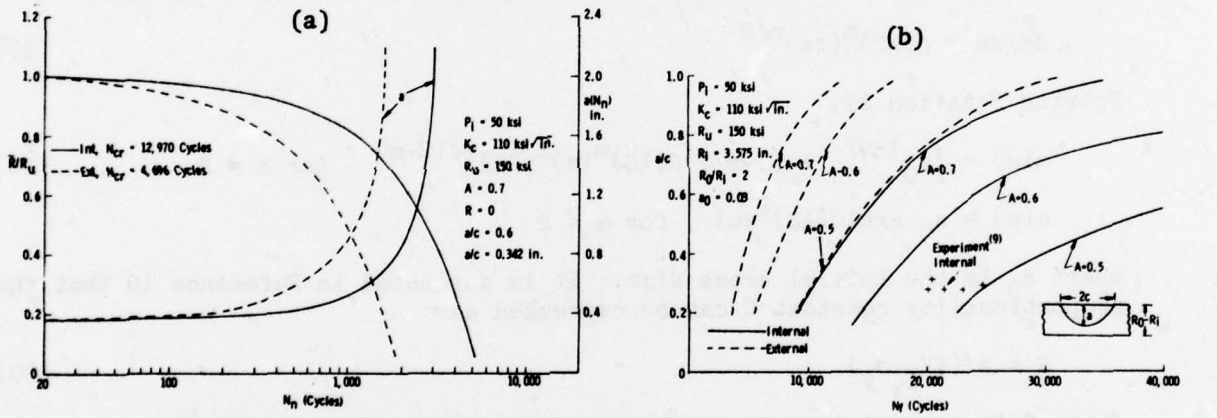


Figure 9 a) Crack Growth and Strength Degradation, b) Cycles to Failure for 175-mm Cylinder, Elber Equation, P_i = 50 ksi, K_{IC} = 110 ksi√in., R_u = 150 ksi.

PROBABILISTIC ESTIMATES OF FATIGUE LIFE

Considering the relatively conservative life estimates which resulted from the Paris equation it is reasonable to adopt this formula for our calculations. Accordingly, to construct a probabilistic model for fatigue life of cylinders under cyclic internal pressure loading, we assumed that the rate of crack growth per cycle da/dN can be related to the range of stress intensity factor ΔK in the power law region $\Delta K_{TH} \leq \Delta K < K_{IC}$ by the Paris equation

$$da/dn = C\Delta K^m \qquad (24)$$

where C and m are material constants, ΔK_{TH} is the range of the stress intensity factor at threshold, and K_{IC} is the critical stress intensity factor at which

the rate of crack growth becomes infinite. The relationship between the range of the stress intensity factor ΔK and the crack size a is taken as[10]

$$\Delta K = \lambda S\sqrt{\pi a} \tag{25}$$

in which S is the maximum hoop stress at the bore of the cylinder,

$$S = P_i(r^2 + 1)/(r^2 - 1) \tag{26}$$

with

$r = R_0/R_i$
λ = empirical parameter which depends on crack shape and residual stresses due to the autofrettage process.

In deriving Equation 25 it is assumed that R = 0 (hence $K_{min} = 0$) and that P_i is the maximum internal pressure. From Equations 24 and 25 we obtain

$$da/dn = C(\lambda S)^m(\pi a)^{m/2} \tag{27}$$

Solving Equation 27,

$$a(n) = \{a_0^{1-m/2} + (1-m/2)C(\lambda S)^m(\pi)^{m/2}n\}^{2/(2-m)} \quad \text{for } m \neq 2 \tag{28}$$

$$a(n) = a_0 \exp\{C(\lambda S)^2\pi n\} \quad \text{for } m = 2$$

where a_0 is the initial crack size. It is suggested in Reference 10 that the proportionality constant C can be expressed as

$$C = \beta/(EK_{IC}\sigma_y) \tag{30}$$

where β is an empirical constant depending on material properties and varies with m to maintain dimensional homogeneity, E is Young's modulus, and σ_y is the yield strength of the material.

Solving Equations 28 and 29 for n and using Equation 30, the number of cycles to reach a specified crack size a is determined as

$$n = [2E\sigma_y K_{IC}/\{\beta(\lambda S\sqrt{\pi})^m(m-2)\}](a_0^{1-m/2} - a^{1-m/2}) \quad \text{for } m \neq 2 \tag{31}$$

$$n = [E\sigma_y K_{IC}/\{\beta(\lambda S)^2\pi\}]\ell n(a/a_0) \quad \text{for } m = 2. \tag{32}$$

Failure of the gun tube occurs when the crack depth a is either equal to the thickness of the cylinder $(R_0 - R_i)$ or is equal to the critical crack size a_f at which the crack growth becomes unstable. Such unstable growth in cylinders occurs at[10]

$$a_f = (A/\pi)\ K_{IC}/(\lambda S)^2 \tag{33}$$

where A is an empirical constant which is a function of material properties

and crack shape. The failure cycle or the fatigue life N_f is obtained from Eqs. 31 and 32 with a replaced by the smaller of a_f and $R_0 - R_i$.

The fatigue life N_f of a cylinder under cyclic internal pressure is a function of many system parameters. For the present study we assume that all the system parameters are constant within a given cylinder, but vary statistically from cylinder to cylinder. Furthermore, only the parameters a_0, λ, K_{IC}, σ_y, and m are taken as <u>independent</u> random variables. The yield strength σ_y is related to the critical stress intensity factor K_{IC} by[10]

$$\sigma_y = 334 - 1.39K_{IC}. \tag{34}$$

Since K_{IC} is a random variable, σ_y is also a random variable through Eq. 34.

The probability distribution of fatigue life N_f is estimated from Eqs. 31 and 32 using a Monte Carlo simulation procedure. This is accomplished by estimating first the distribution functions for random variables a_0, λ, K_{IC}, σ_y and m. Using these distributions and a digital random number generator, sample values of a selected size for each of the five random variables are obtained. Substituting these parameters into Eqs. 31 and 32, sample values of the same size for the fatigue life N_f are determined from which statistical information on N_f is obtained in the form of mean, standard deviation and probability distribution. These results are then compared to the results determined from the experimental data on gun tube failure.

DISTRIBUTION FUNCTIONS FOR SYSTEM PARAMETERS

To determine the probability distribution of fatigue life N_f, it is necessary to know the forms of the distribution functions for the five selected random variables. For this purpose, available data for 175-mm M113 and 105-mm gun tubes are utilized. In Table III, the fatigue data for critical stress intensity factor K_{IC}, the yield strength σ_y (calculated from Eq. 34), and the fatigue life N_f are given.[2] From these data, probability density and the cumulative distribution are constructed for K_{IC} and σ_y, and are shown in Fig. 10. The mean value and the standard deviation are found to be, respectively, $\mu_{K_{IC}}$ = 111.60 ksi$\sqrt{\text{in.}}$ and $\sigma_{K_{IC}}$ = 12.12 ksi$\sqrt{\text{in.}}$ for the critical stress intensity factor. K_{IC}, and μ_{σ_y} = 178.89 ksi and σ_{σ_y} = 16.85 ksi for the yield strength σ_y. A two-parameter lognormal distribution fitted for the K_{IC} data is shown in Fig. 10. On the basis of the reasonably good fit observed, it is assumed that the statistical variability of the critical stress intensity factor K_{IC} can be represented by the lognormal distribution. The distribution for yield strength σ_y is then obtained through Eq. 34.

Experimental data for the empirical parameter λ is limited. Values of λ estimated from the data involving crack growth-pressure cycle relationship for several 175-mm and 105-mm gun tubes are given in Reference 10. Since more data are readily available for the 105-mm gun tube, they are used to describe the statistical behavior of λ. The probability density function and the cumulative distribution for λ are shown in Figure 11. The mean and the standard deviation are μ_λ = 0.877 and σ_λ = 0.044, respectively. A theoretical normal distribution fitted to this result is shown.

Table III Fatigue Data for 175-mm M113 Gun Tube

Tube	K_{IC}, ksi$\sqrt{in.}$	σ_y, ksi	N_f, Cycles
733	80.0	222.8	373
976	107.0	185.3	844
1185	108.2	183.6	1,001
863*	94.2	203.1	1,011
1382*	98.2	197.5	1,411
972	101.4	193.1	2,194
42	107.3	184.9	2,196
83	106.4	186.1	2,449
971	108.9	182.6	3,025
155	113.6	176.1	3,169
46	117.6	170.5	3,309
7	117.5	170.7	3,325
1255	115.1	174.0	3,438
75	107.7	184.3	3,449
115	125.2	160.0	3,476
113	105.4	187.5	3,606
826	115.8	173.0	3,698
812	107.2	195.0	4,451
739	113.5	176.2	4,671
1099	125.1	160.1	4,679
967	103.3	190.4	4,697
1386*	106.0	196.7	4,697
45	129.8	153.6	4,768
1258	108.7	182.9	5,019
919	109.2	182.2	5,191
1101	115.4	173.6	5,397
158	107.0	185.3	6,193
731	116.9	171.5	7,238
1100	150.0	125.5	7,631
1131	126.0	158.9	9,652

*54.6 ksi cyclic pressure. Otherwise 50 ksi cyclic pressure.

The experimental data for the distribution of initial crack size a_0 in gun tubes are not readily available. For the purpose of this study, the initial crack size a_0 is determined indirectly by substituting the critical crack size a_c from Eq. 33 into Eq. 31 and solving for a_0. In doing so, the mean values for all the system parameters and the fatigue failure data for N_f given in Table III are used in Eq. 31. The following physical data are used in the calculation: $2R_i$ = 7.15 in., $2R_o$ = 15.0 in., P_i = 50 ksi, λ = 0.85, K_{IC} = 111.59 ksi$\sqrt{in.}$, σ_y = 178.89 ksi, m = 3.0, E = 30 x 10^3 ksi, A = 2.26, β = 0.2413. The probability density function and the cumulative distribution for a_0 are also shown in Figure 11. The mean value and the standard deviation of a_0 are μ_{a_0} = 0.17 in. and σ_{a_0} = 0.15. For the analytical representation of the statistical variability of a_0, a lognormal distribution shown in Figure 11 is assumed.

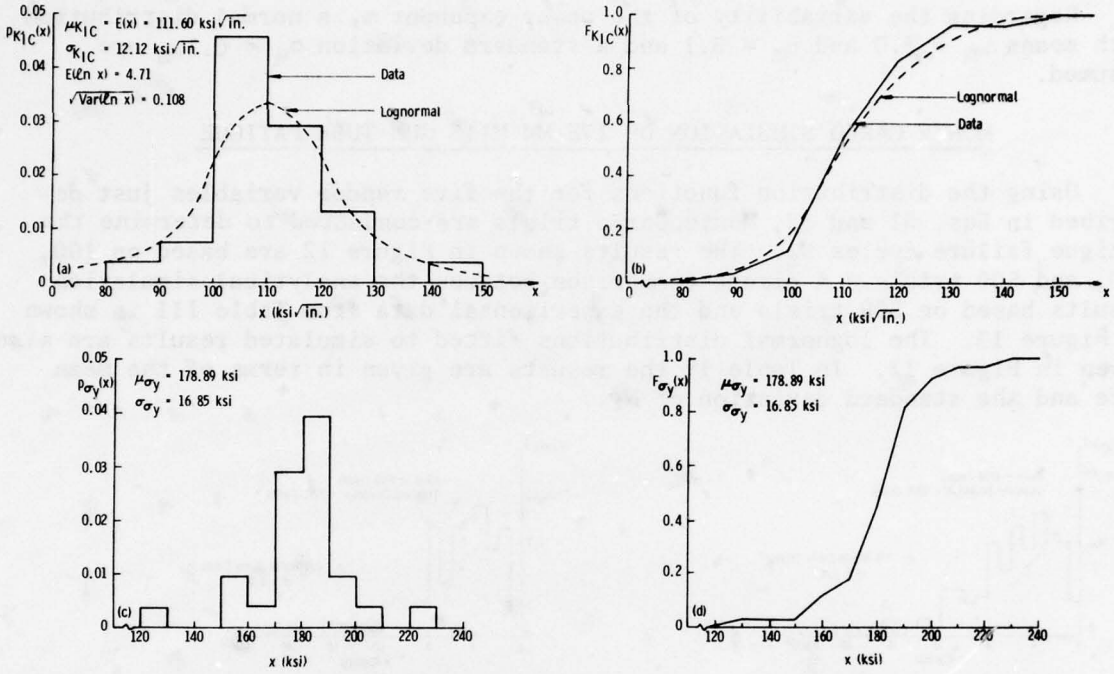


Figure 10 Probability Density and Cumulative Distribution Functions for Critical Stress Intensity Factor K_{IC} and Yield Strength σ_y.

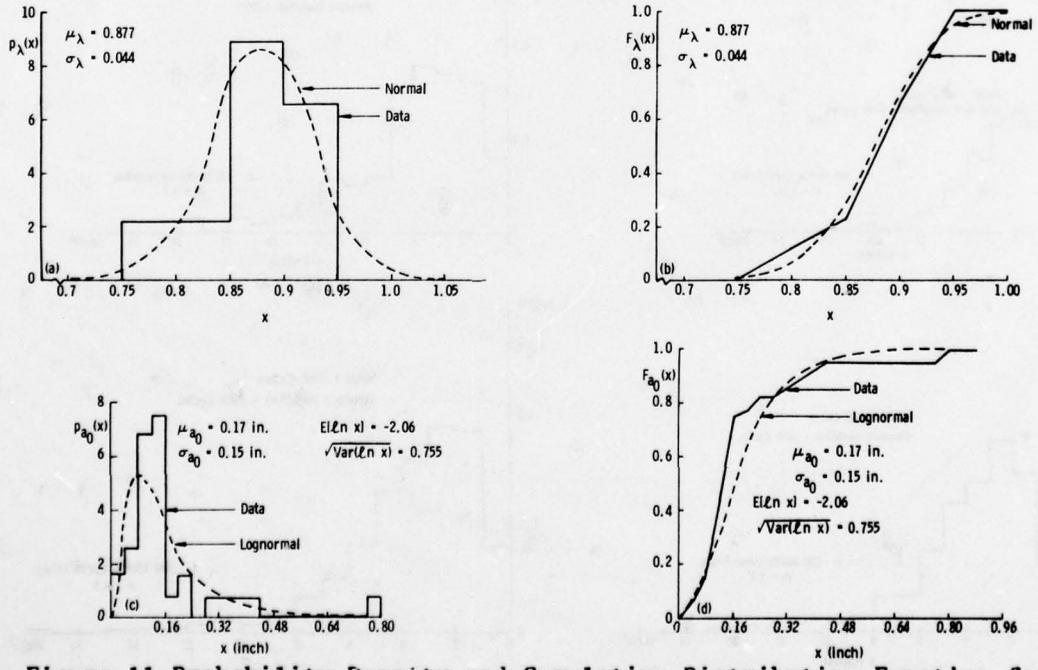


Figure 11 Probability Density and Cumulative Distribution Function for Empirical Parameter λ and Initial Crack Size, a_0.

Regarding the variability of the power exponent m, a normal distribution with means $\mu_m = 3.0$ and $\mu_m = 3.1$ and a standard deviation $\sigma_m = 0.1\mu_m$ are assumed.

MONTE CARLO SIMULATION OF 175-MM M113 GUN TUBE FATIGUE

Using the distribution functions for the five random variables just described in Eqs. 31 and 32, Monte Carlo trials are conducted to determine the fatigue failure cycles N_f. The results shown in Figure 12 are based on 100, 200, and 500 trials. A direct comparison between the analytical simulation results based on 500 trials and the experimental data from Table III is shown in Figure 13. The lognormal distributions fitted to simulated results are also given in Figure 13. In Table IV the results are given in terms of the mean life and the standard deviation of N_f.

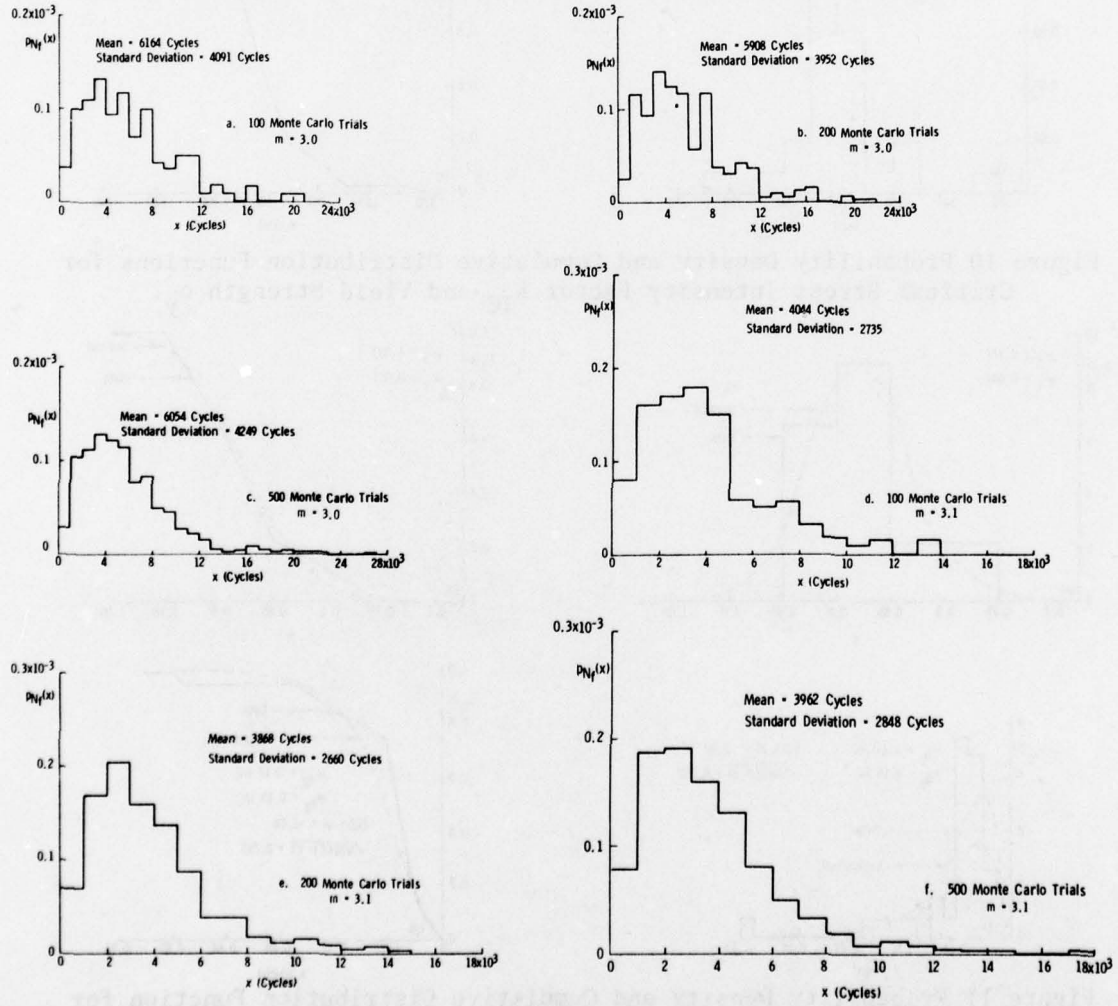


Figure 12 Probability Density Function for Fatigue Failure; 100, 200, and 500 Monte Carlo Trials, m = 3.0 and 3.1.

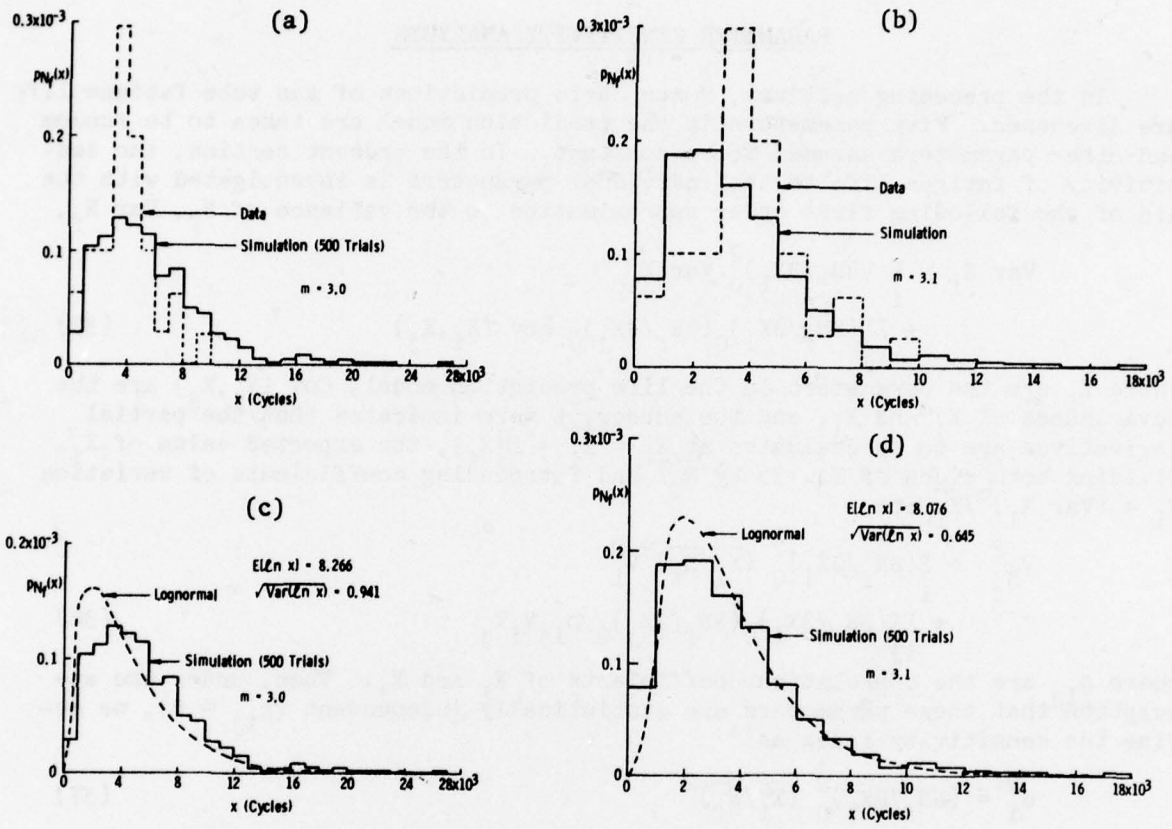


Figure 13 Comparison of Monte Carlo Simulation to Data and Lognormal Probability Density Distributions, m = 3.0, 3.1, 500 Monte Carlo Trials.

Table IV Mean and Standard Deviation of Fatigue Life N_f for 175-mm M113 Gun Tube

Number of Simulation Trials	Mean (Cycles) Simulation			Standard Deviation (Cycles) Simulation		
	m = 3.0	m = 3.1	Experiment	m = 3.0	m = 3.1	Experiment
100	6164	4044		4091	2753	
200	5908	3868	3875	3952	2660	2096
500	6053	3962		4249	2848	

PARAMETER SENSITIVITY ANALYSIS

In the preceding sections, Monte Carlo predictions of gun tube fatigue life are discussed. Five parameters in the prediction model are taken to be random and other parameters assumed to be constant. In the present section, the sensitivity of fatigue life to the individual parameters is investigated with the aid of the following first order approximation to the variance of N_f, Var N_f,

$$\text{Var } N_f \simeq \sum_i (\partial N_f/\partial X_i)_0^2 \text{ Var } X_i + \sum\sum_{ij} (\partial N_f/\partial X_i)_0 (\partial N_f/\partial X_j)_0 \text{ cov } (X_i, X_j) \tag{35}$$

where X_i are the parameters in the life prediction model, Cov (X_i, X_j) are the covariances of X_i and X_j, and the subscript zero indicates that the partial derivatives are to be evaluated at $X_i \simeq \overline{X_i} = E[X_i]$, the expected value of X_i. Dividing both sides of Eq. 35 by $\overline{N_f}^2$ and introducing coefficients of variation $V_i = (\text{Var } X_i)^{\frac{1}{2}}/\overline{X_i}$ etc,

$$V_{N_f}^2 \simeq \sum_i (\partial N_f/\partial X_i)_0^2 (\overline{X_i}/\overline{N_f})^2 V_i^2 + \sum\sum_{ij} (\partial N_f/\partial X_i)_0 (\partial N_f/\partial X_j)_0 \rho_{ij} V_i V_j \tag{36}$$

where ρ_{ij} *are the correlation coefficients of* X_i and X_j. Then, under the assumption that these parameters are statistically independent ($\rho_{ij} = 0$), we define the sensitivity index as[11]

$$\alpha_i^2 = (\partial N_f/\partial X_i)_0^2 (\overline{X_i}/\overline{N_f})^2 \tag{37}$$

This index indicates the contribution of the uncertainty associated with parameter X_i (measured in terms of its coefficient of variation) to the uncertainty of $\overline{N_f} = E[N_f]$.

For the present model seven parameters a_0, K_{IC}, σ_y, λ, m, A, and β are investigated for the sensitivity analysis. In Table V the calculated lives N_f are given in terms of internal pressure cycles. The critical crack size a_c at which N_f is reached is also included in these tables. The results of the sensitivity study in terms of the sensitivity index α_i^2 are given in Table VI. The final results are summarized in Table VII.

CONCLUDING REMARKS

A probabilistic model is constructed to investigate fatigue failure of gun tubes under cyclic pressure. A comparison of the simulated analytical results with given experimental data indicates a fair agreement for the 175-mm M113 gun tube when the mean value of the power exponent m = 3.1. However, for m = 3.0, Monte Carlo simulation predicts much longer fatigue life than for m = 3.1. A theoretical lognormal distribution provided a reasonable fit to the simulated model statistics. To improve the capability of the probabilistic model to predict fatigue life in gun tubes, more information on the statistical distributions of system parameters is desirable.

It is found that the accuracy of analytical prediction of gun tube failure is strongly influenced by the statistical reliability of the parameters selected in the crack growth prediction model. From sensitivity analysis, it is observed that the most sensitive parameter is the power exponent m. A slight change in this parameter results in a significant change of the gun tube fatigue life. The second most sensitive parameter is the empirical constant λ.

These conclusions are, however, based on the condition that all the parameters, particularly β and m, are uncorrelated. The correlation between these parameters, if it exists, can be taken into consideration through the covariance term in Eq. 35 within the framework of the first order approximation. In order to estimate such a correlation, however, we need a sample of n specimens. Upon establishing the values of β and m for each specimen, we obtain a set of n such pairs on the basis of which the covariance value can be estimated. A deterministic relationship $\beta = \exp(10.5 - 4.0\ m)$ is suggested between β and m by Racicot*. The use of this particular relationship does considerably reduce the sensitivity of the number of cycles to failure to power exponent m which agrees with the conclusions given in Ref. 10. However, the experimental results are expected to show scatter around such a deterministic relationship. Indeed, the reality would probably indicate a situation between the case of such total dependence and that of statistical independence. The analytical capability to predict fatigue life of gun tubes will be improved significantly if more statistical information on these and other parameters considered in the study become available.

*Racicot, R.L., "Private Communication," August 1978.

Table V Sensitivity of Various Parameters on Fatigue Life N_f for 175-mm M113 Gun Tube

	Parameter	Parameter Ratio	Critical Crack Size a_c (inch)	Fatigue Life N_f Cycles	Life Ratio $N_f/E[N_f]$
a. Initial Crack Size	a_0 (inch)	$a_0/E[a_0]$			
	0.07	0.412	1.677	6,868	1.819
	0.17*	1.000	1.677	3,775	1.000
	0.25	1.471	1.677	2,804	0.743
b. Critical Stress Intensity Factor	K_{IC} (ksi$\sqrt{in.}$)	$K_{IC}/E[K_{IC}]$			
	90.00	0.807	1.091	3,157	0.836
	111.59*	1.000	1.677	3,775	1.000
	130.00	1.165	2.276	4,018	1.064
c. Yield Strength	σ_y (ksi)	$\sigma_y/E[\sigma_y]$			
	153.30	0.855	2.276	4,018	1.064
	178.89*	1.000	1.677	3,775	1.000
	208.90	1.168	1.091	3,157	0.836
d. Empirical Parameter λ	λ	$\lambda/E[\lambda]$			
	0.770	0.878	2.176	5,896	1.562
	0.877*	1.000	1.677	3,775	1.000
	0.920	1.049	1.524	3,195	0.846
e. Power Exponent m	m	m/E[m]			
	2.5	0.833	1.677	35,275	9.344
	2.9	0.966	1.677	5,890	1.560
	3.0*	1.000	1.677	3,775	1.000
	3.1	1.003	1.677	2,422	0.642
	3.5	1.166	1.677	414	0.110
f. Empirical Constant A	A	A/E[A]			
	2.00	0.885	1.484	3,664	0.971
	2.26*	1.000	1.677	3,775	1.000
	2.52	1.115	1.870	3,869	1.025
g. Empirical Parameter β	β	$\beta/E[\beta]$			
	0.200	0.829	1.677	4,555	1.206
	0.2413*	1.000	1.677	3,775	1.000
	0.2826	1.174	1.677	3,223	0.853

*Corresponds to the mean value of the parameter.

Table VI Results for the Parametric Sensitivity Analysis

Parameter	Value X_i	Life N_f Cycles	Sensitivity Index α_i^2
a_0	0.07 inch	6868	
	0.17*	3775	1.033
	0.25	2804	
K_{IC}	90.00 ksi$\sqrt{in.}$	3157	
	111.59*	3775	0.404
	130.00	4018	
σ_y	153.30 ksi	4018	
	178.89*	3775	0.538
	208.90	3157	
λ	0.770	5896	
	0.877*	3775	17.499
	0.920	3195	
m	2.9	5890	
	3.0*	3775	189.892
	3.1	2422	
A	2.00	3664	
	2.26*	3775	0.056
	2.52	3869	
β	0.2000	4550	
	0.2413*	3775	1.062
	0.2826	3223	

*Corresponds to the mean value of the parameter.

Table VII The Parametric Sensitivity Analysis Results for the 175-mm M113 Gun Tube

Parameter	Description	Mean Value	Sensitivity Index, α_i^2
a_0	Initial crack size before any firing	0.17 inch	1.033
K_{IC}	Critical stress intensity factor	111.59 ksi$\sqrt{in.}$	0.404
σ_y	Yield strength	179.89 ksi	0.538
λ	Empirical parameter which depends on crack shape and residual stress	0.877	17.499
m	Power exponent in the crack propagation model	3.0	189.892
A	Material constant which depends on crack shape	2.26	0.056
β	Material constant which maintains dimensional homogeneity in the crack propagation model	0.2413	1.062

REFERENCES

1. Grover, H.J., and Holden, F.C., "A survey Report on Fatigue in Cannon Bores," Defense Metals Information Center, Battelle Memorial Institute, Columbus, Ohio, Report No. DMIC S-13, May 1967.

2. Proceedings of the Interservice Technical Meeting on Gun Tube Erosion and Control, Ed. by I. Ahmad and J. Picard, Watervliet Arsenal, February 25 and 26, 1970.

3. Creighton, A., "Facts of Barrel Life," American Rifleman, (Jan. 1978), p. 54-59; American Rifleman, (March 1956), p. 22; Kernaghan, Q., and Lewis, B.R., "Barrel Life," American Rifleman, (Feb. 1960), p. 38.

4. Davidson, T.E., Throop, J.F., "Practical Fracture Mechanics Applications to Design of High Pressure Vessels," in Risk and Failure Analysis for Improved Performance and Reliability. New York: Plenum Press, to be published.

5. Unpublished committee report of Army Scientific Advisory Panel Ad Hoc Group on Wear and Erosion Technology, October 20, 1977.

6. Kobayashi, A.S., et al., "Inner and Outer Cracks in Internally Pressurized Cylinders," ASME Paper No. 76-PVP-6, 1976.

7. Gallagher, J.P., "Fatigue Crack Growth Rate Laws Accounting for Stress Ratio Effects," ASTM Task Force E24.04.04, Report No. 1, Wright-Patterson Air Force Base, Ohio.

8. Davidson, T.E., Throop, J.F., "Practical Fracture Mechanics Applications to Design of High Pressure Vessels," in Risk and Failure Analysis for Improved Performance and Reliability. New York: Plenum Press, to be published.

9. Davidson, T.E., Throop, J.F., Reiner, A.N., and Austin, B.A., "Analysis of the Effect of Autofrettage on the Fatigue Life Characteristics of the 175-mm M113 Gun Tube," Watervliet Arsenal, New York, Report No. WVT-6901, January 1969.

10. Racicot, R.L., "A Probabilistic Model of Gun Tube Fatigue," U.S. Army Armament Research and Development Command, Benet Weapons Laboratory, Watervliet Arsenal, New York, Report No. ARLCB-TR-77029, May 1977.

11. Shinozuka, M., "Development of Reliability-Based Aircraft Safety Criteria: An Impact Analysis," Vol. I, AFFDL-TR-76-36, April 1976.

FINITE ELEMENT STRESS ANALYSIS OF U. S. NAVY MARK 83 BASE DETONATING FUZE BODY

O. H. GRIFFIN, JR.
Aerospace Engineer

C. M. BLACKMON
Aerospace Engineer
Naval Surface Weapons Center
Dahlgren, Virginia 22448

ABSTRACT

This paper describes the finite element stress analysis of the body of the U. S. Navy MARK 83 Base Detonating Fuze. Three different finite element computer programs, SAAS, NONSAP, and SAP IV were used for different parts of the analysis. Results are presented, and the programs are contrasted with respect to setup time, accuracy, and computer run times. Yielding of the fuze body during gun launch is predicted. Two possible fixes to reduce the amount of yielding are suggested.

INTRODUCTION

The loads encountered during gun launch are typically the most severe conditions under which an artillery projectile and its components must function. The designer or analyst of such systems must formulate realistic models of the system and/or subsystems, define appropriate "failure" criteria, and proceed to guide their design and production. With the advent of the high speed computer and the proliferation of finite element computer programs, the tools used in ordnance design have undergone a marked increase in complexity. This paper deals with the analysis of an existing projectile component, namely the body of the U.S. Navy MK 83 Base Detonating Fuze (BDF). A variety of analysis tools were used on the problem, and it seems worthwhile to compare the results and relative cost of the different tools, along with some pitfalls which may be encountered.

BACKGROUND

The MK 83 BDF has long been certified for use in U.S. Navy 5"/38 guns. As a part of a product improvement of the 5"/54 MK 121 loaded and fuzed projectile assembly, it was desired to certify the MK 83 BDF for service in 5"/54 gun systems. Although the MK 83 BDF had not been responsible for any malfunctions, it had been present in several 5"/38 malfunctions.(1) However, as part of the investigation the 5"/38 design agent at NSWC requested a thorough stress analysis of the fuze body. Previous analysis* had indicated plastic deformation of the fuze body under 5"/54 firing conditions of 44170 psi (300 MPa) chamber pressure. Plastic deformation, although not always undesirable, is commonly used as as failure criterion in ordnance design.

*Huey, O. J., Personal Communication, Naval Surface Weapons Center.

In the design of a fuze such as the MK 83 (Figure 1), plastic deformation of the body is undesirable since it transfers loads directly to the mechanisms, possibly causing damage or impairing proper function. For this reason, exceeding the elastic limit of the material was defined as failure of the fuze body.

The fuze body (Figure 2) is axisymmetric with the exception of the interior detent hole and the external spanner wrench holes. The material is steel, AISI C-1117, which has a yield strength of 60000 psi (408 MPa), and an ultimate tensile strength of 80000 psi (544 MPa) at 20 percent elongation. For simplicity and since the effects of the spanner wrench and detent holes were previously shown (1), the fuze was modeled as axisymmetric (see Figure 3). The seating face where the body contacts the projectile body was assumed free to slide in the radial direction and fixed with respect to the projectile in the axial direction. The threads were assumed fixed with respect to the projectile body in both the radial and axial directions. Both of these assumptions are valid if the elements laying on either side of the contact line are in compression. Tension indicates the fuze pulling away from the projectile, and the boundary conditions must be modified accordingly. These assumptions proved to be correct for this analysis. The stress-strain curve of the material is relatively flat. For this analysis, it was approximated by the bilinear curve of Figure 4. The 44170 psi (300 MPa) denoted P_B on Figure 5, base pressure results in an acceleration of 11260 g's of the 66 pound (35 kg) projectile assembly. The uniformly distributed reaction pressure on the fuze base resulting from the acceleration of the .46 pound (209 g) internal fuze parts along with the projectile body is 3233 psi (22 MPa), denoted P_I on Figure 5. Due to the small diameters (approximately 1 inch (2.54 cm)) involved, stresses due to angular velocity were neglected. Also neglected were loads due to setback of the explosive load. Previous experience indicated that the two commonly used Navy explosives, composition A-3 and Explosive D, possess considerable structural integrity and at these acceleration levels do not transfer significant load during setback except to the projectile base. In any case, the base of the fuze body was the primary area of concern, and was unaffected by explosive setback. In accord with these assumptions and to reduce computer time for the nonlinear analyses, the finite element mesh was truncated to that shown in Figure 5 where P_B and P_I are as previously described, and P_F is the uniform pressure necessary to accelerate the portion of the fuze body and theclosure cap which were removed. The magnitude of P_F is 6980 psi (47.5 MPa). The mass of the fuze body is subjected to an acceleration of 11,260g's. Thus the finite element grid of Figure 5 was used in all analyses discussed.

FINITE ELEMENT COMPUTER PROGRAMS

Three different finite element computer programs were used to perform the analysis. They were a modification of the SAAS III code, SAP IV, and NONSAP. All the programs are displacement formulations, with different combinations of linear, nonlinear, and geometry capabilities. The capabili-

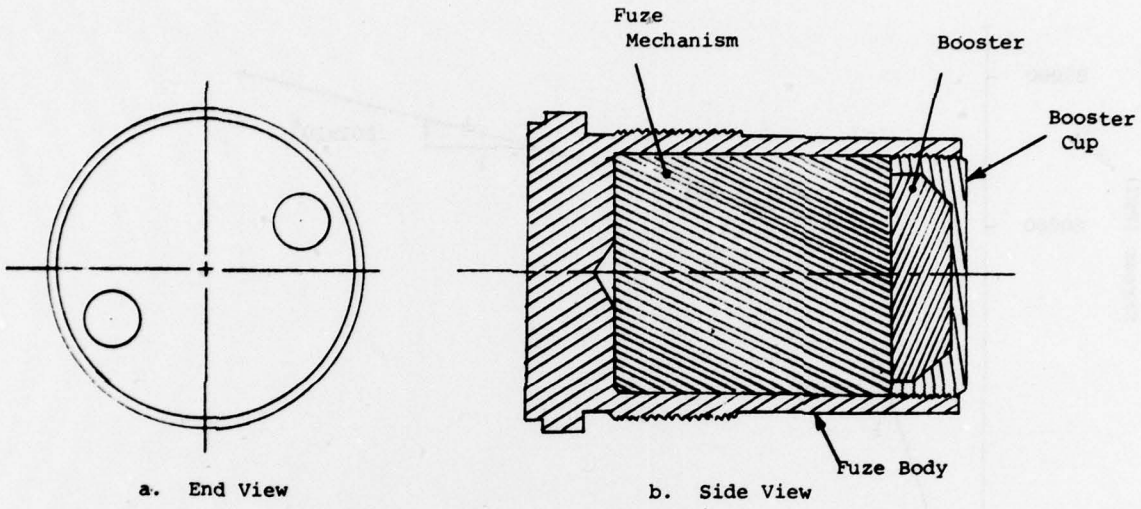


Figure 1. Schematic of U.S. Navy MARK 83 Base Detonating Fuze

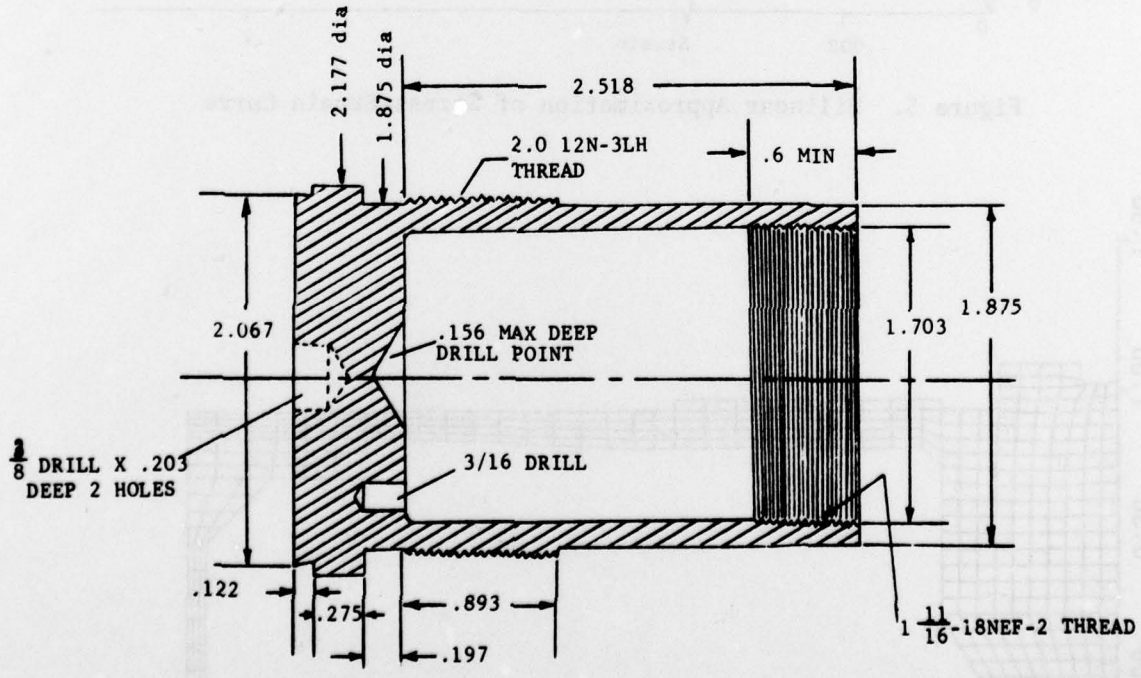


Figure 2. MARK 83 Base Detonating Fuze Body

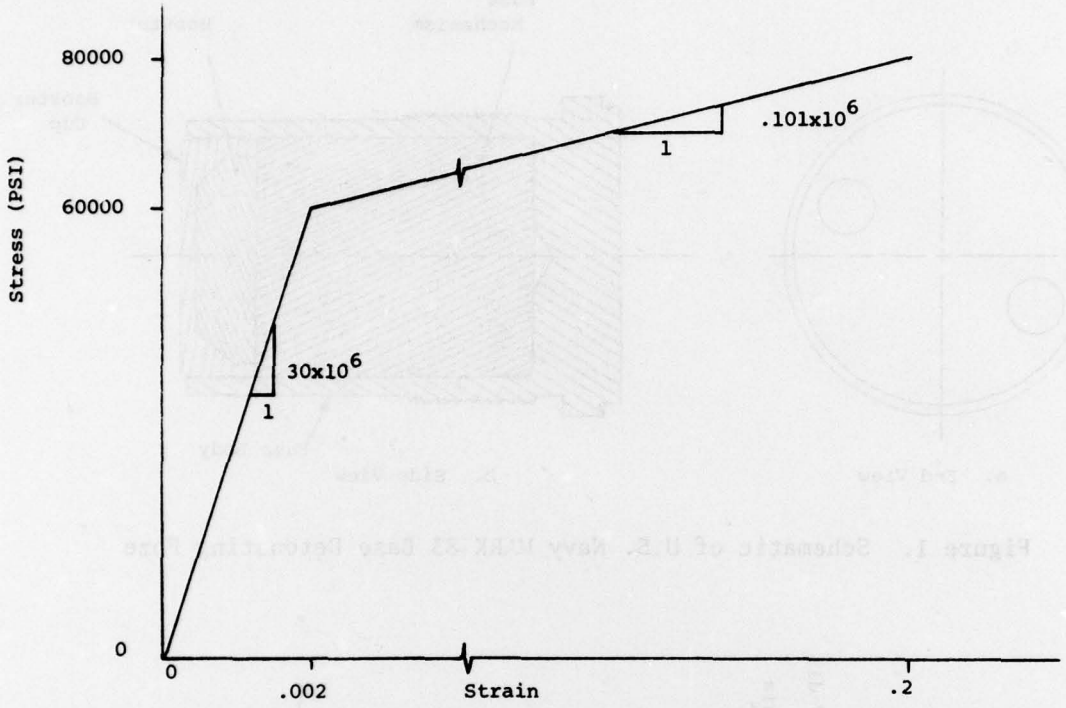


Figure 3. Bilinear Approximation of Stress-Strain Curve

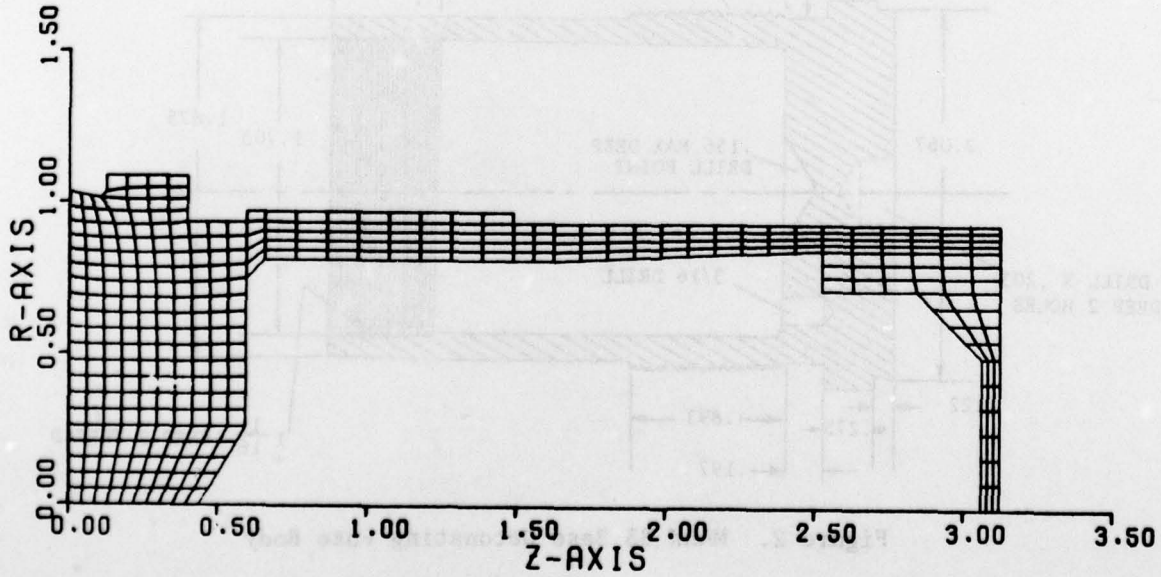


Figure 4. Finite Element Mesh of Complete Fuze Body

ties of each program are briefly described in the following paragraphs. For a detailed discussion of the finite element method, the reader is referred to the text by Zienkiewicz [2].

The SAAS III (Stress Analysis of Axisymmetric Solids, Version 3) program is described in detail in reference 3. It has the capability to perform static stress analysis of axisymmetric or plane solids with linear or bilinear stress-strain relationships. Loads must be axisymmetric and may consist of any combination of pore or surface pressures, point loads, shear loads, acceleration, and angular velocity. Thermal stresses due to arbitrary temperature distributions are treated. An improved mesh generator is incorporated in the NSWC version, as are graphical output of mesh plots and stress and strain contours. The bilinear capability, which may represent either bilinear properties which are equal in tension and compression or linear properties which are unequal in tension and compression, is accomplished by the method of successive elastic approximations. This method is accurate when nonlinear effects are small, but fails to converge as nonlinear effects become a significant portion of the response. Convergence is poor for relatively flat stress-strain curves. The method as implemented is not applicable to elastic-perfectly plastic materials.

The SAP IV (Structural Analysis Program, Version 4) computer program performs one, two, or three dimensional static or dynamic stress analysis of linear elastic bodies [4]. Loads may be surface pressure, point loads, or gravity loads. Static problems are solved via Gauss elimination on the assembled equilibrium equations. Dynamic response problems may be solved either by mode superposition or direct integration. The program has an out-of-core solution capability for large problems.

NONSAP (Nonlinear Structural Analysis Program) performs static or dynamic stress analysis of one, two, or three dimensional solids [5]. Both geometric and material nonlinearities may be modeled. For nonlinear problems, an updated Lagrangian or total Lagrangian formulation is available. A wide variety of nonlinear material models are incorporated into the program Dynamic solutions are done by direct integration using either the Wilson-θ or Newark method.

RESULTS AND DISCUSSION

Elastic static runs made with all three programs indicated yielding of the fuze body. The primary yield areas were near the interior fillet which blends the solid base to the hollow cylindrical forward portion and near the sharp corner where the fuze seats on the projectile body. Elements with equivalent (von Mises) stresses above the 60000 psi (408 MPa) elastic limit are shaded in Figure 6. Results of all programs were comparable. Run times for all programs were comparable (41-78 seconds of CDC 6600 central processor time). Core requirements are very close for all three programs. SAAS took the longest time, and NONSAP the shortest. The reason for this is that SAAS generates the finite element mesh automatically, while NONSAP does not.

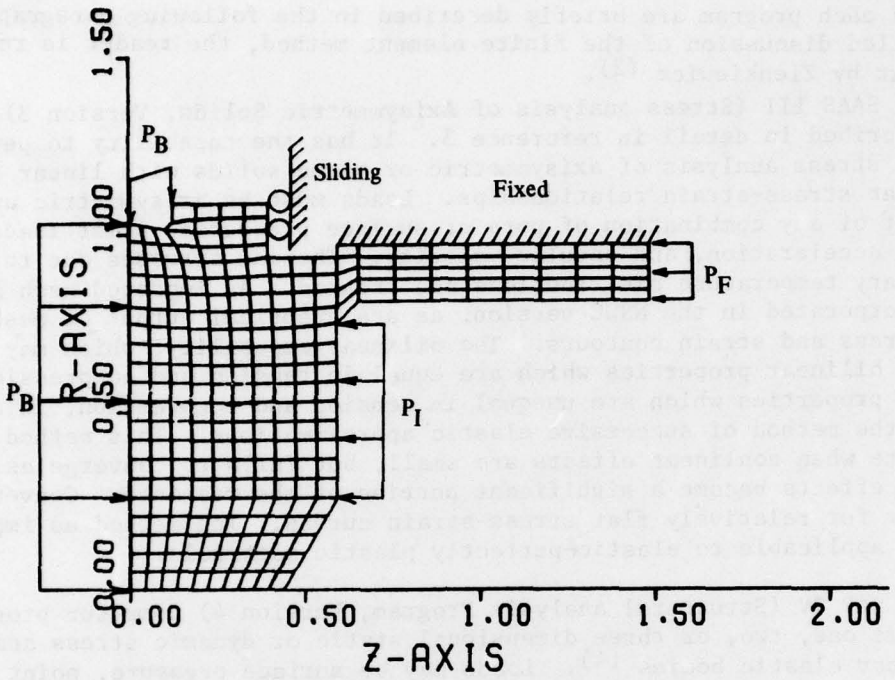


Figure 5. Modified Finite Element Mesh With Loads

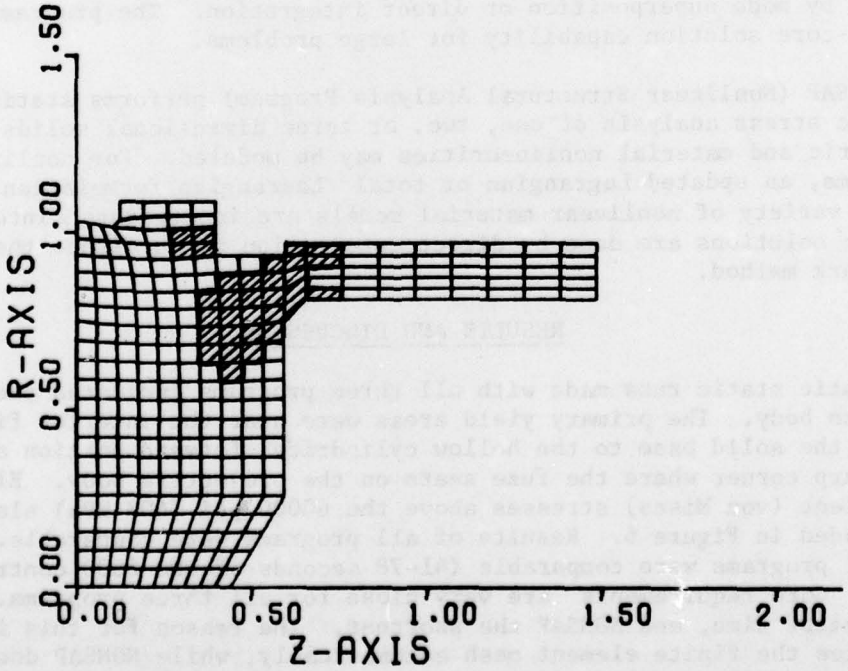


Figure 6. Results of Elastic Analysis Showing Elements with Stress Above Yield

By comparison, the SAAS input deck is 61 cards, while the NONSAP input deck is over 850. The data generation requirements of NONSAP are such that one saves time if he generates a SAAS mesh first and then converts that for NONSAP. Data generation for SAP IV is similar to NONSAP. The NONSAP solution times are believed to be shorter than for SAP IV due to the presence of advanced matrix storage and solution routines, plus the fact that NONSAP is an in-core solver.

Elastic-plastic (bilinear) stress analyses were performed using SAAS and NONSAP. The iterative (successive elastic approximations) solution of SAAS did not converge due to the significant plastic deformation and relatively flat stress-strain curve (Figure 3). The plastic zones for SAAS and NONSAP are shaded in Figures 7 and 8, respectively. Even though the SAAS solution did not converge, the results compare favorably with those from NONSAP. As seen by comparison of Figures 6, 7, and 8, relieving of stresses in the plastic region results in considerable growth of the yield surface. Solution times for SAAS (750 CP seconds) were considerably lower than for NONSAP (1700 CP seconds). It should be pointed out that no attempt was made to minimize the number of load steps used in the NONSAP solution. It should be noted again that setup time for NONSAP data generation is much greater than for SAAS, thus making a NONSAP solution even more costly by comparison than the CP times indicate.

The SAAS program computes an approximate fundamental frequency by taking the static displacement field as an approximate mode shape and forming Rayleigh's quotient for the finite element assemblage. SAP IV was used to determine the lowest natural frequency for comparison. The lowest natural frequency, as obtained by SAP IV is 18598 Hertz. The approximate frequency from SAAS is 37460 Hertz. The Rayleigh quotient method is not accurate, but does indeed give an upper bound on the lowest natural frequency. Comparisons of the SAP IV mode shapes to the SAAS elastic static displacement vector indicate that mode 3 compares, in general, to the SAAS displacements. Mode 3 has a frequency of 32570 Hertz, which compares very well with the 37460 Hertz from SAAS. Rayleigh's quotient, as expected,yields good results when the function chosen is close to the correct mode shape. Furthermore, we see that the choice of a static analysis is justified unless loading conditions with microsecond resolution are available, Such loading conditions were not available for this analysis, as is typically the case.

CONCLUSIONS

The conclusion regarding the structural integrity of the body of the MARK 83 BDF is that yielding of the material does occur during gun launch. If the yield strength of the material were increased to 80000 psi (544 MPa), the yielding would be limited to small areas near stress raisers. Thickening of the hollow portion of the body near the base is advisable if possible without major redesign of the mechanism.

Several conclusions may be drawn concerning the choice of finite element computer programs for particular problems. Simple programs such as SAAS are good choices where they apply. The presence of automatic grid generation

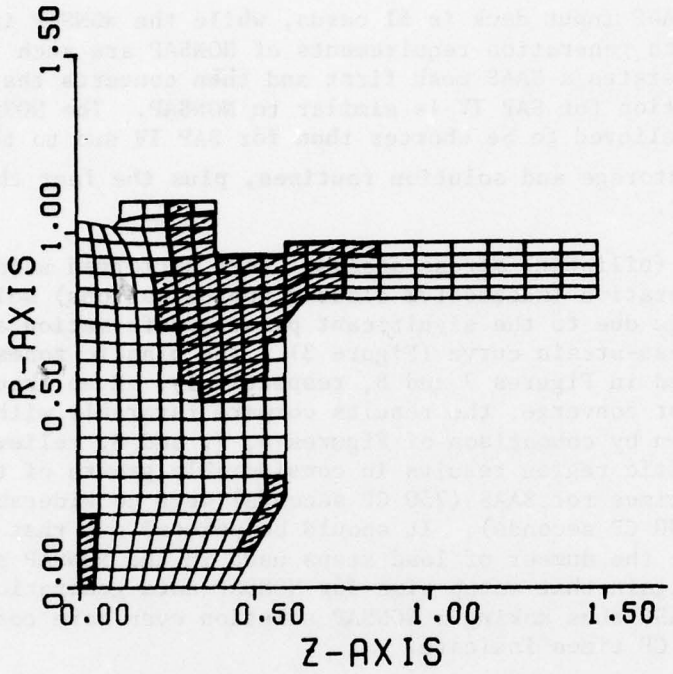


Figure 7. Yielded Areas Obtained from SAAS Without Convergence

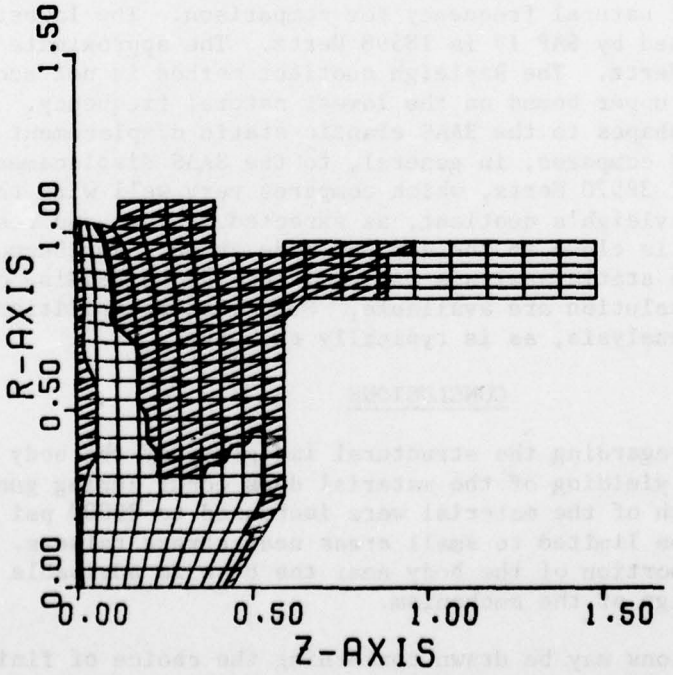


Figure 8. Yielded Areas Obtained from NONSAP

saves considerable man time as well as speeding completion of the analysis. Computer cost for automatic grid generation is usually negligible.
In using SAP IV and NONSAP, which have little grid generation and post-processing capability, one must be careful that the grid is correct and the results are reasonable. Selection of load step size for nonlinear analyses with NONSAP should be checked carefully. Results from runs with varying load steps should not differ significantly.

For the SAAS program in particular, one must be very careful when interpreting the elastic-plastic and fundamental frequency information obtained from SAAS. The elastic-plastic option is only convergent for samll yielding and only guarantee on the fundamental frequency is that it is an upper bound.

In summary, finite element computer programs are readily available, with a wide scope of applications. When used properly, they yield good results. When used improperly or beyond their scope, they produce meaningless information which, if believed, may lead to poor structural design and ultimately to failures.

REFERENCES

1. Culbertson, D. W., Shamblen, M. C., and O'Brasky, J. S., "Investigation of 5" Gun In-Bore Ammunition Malfunctions", NWL Technical Report TR-2624, Dec 1971.

2. Zienkiewicz, O. C.,"The Finite Element Method in Engineering Science," McGraw-Hill, London, 1971.

3. Crose, J. G. and Jones, R. M., "SAAS III: Finite Element Stress Analysis of Axisymmetric and Plane Solids with Different Orthotropic, Temperature-Dependent Material Properties in Tension and Compression", Air Force Report No. SAMSO-TR-71-103, June, 1971.

4. Bathe, K. J., Wilson, E. L., and Peterson, F. E., "SAP IV-A Structural Analysis Program for Static and Dynamic Response of Linear Systems" EERC Report No. 73-11, College of Engineering, University of California, Berkley, June 1973.

5. Bathe, K. J., Wilson, E. L., and Iding, R., "NONSAP-A Structural Analysis Program for Static and Dynamic Response of Nonlinear Systems", UCSESM Report No. 74.3, University of California, Berkeley, February 1974.

PANEL SESSION

Chairman: EDWARD M. LENOE
Chief, Mechanics of Materials Division
Army Materials and Mechanics Research Center

PANEL MEMBERS

ROBERT M. BADER
Chief, Structural Integrity Branch
Air Force Flight Dynamics Laboratory

JOHN R. DAVIDSON
Head, Structural Integrity Branch
NASA-Langley Research Center

RAYMOND FOYE
Aerospace Technologist
Army Research and Technology Laboratory

CAPT JOSEPH MICELI, USN
Deputy Program Manager, Guided Projectiles (Navy)
Army Armament Research and Development Command

DANIEL R. MULVILLE
Research Mechanical Engineer
Naval Research Laboratory

PAUL MUNAFO
Leader, Mechanical Metallurgy Group
NASA-Marshall Space Flight Center

MAURICE WRIGHT
Director of Materials Division
University of Tennessee Space Institute

PRECEDING PAGE BLANK-NOT FILMED

AUTHORS

Adachi, J.	Army Materials & Mechanics Research Center	Watertown, MA	285
Backofen, Jr., J. E.	Battelle-Columbus Laboratories	Columbus, OH	215
Bader, R. M.	Air Force Flight Dynamics Laboratory	Wright-Patterson Air Force Base, OH	11
Benedetti, G. A.	Sandia Livermore Laboratories	Livermore, CA	285
Benicek, M.	Army Materials & Mechanics Research Center	Watertown, MA	285
Bhatia, N. M.	Northrop Corporation	Hawthorne, CA	155
Bilikam, J. E.	FMC Corporation	San Jose, CA	203
Blackmon, C. M.	Naval Surface Weapons Center	Dahlgren, VA	248, 365
Bluhm, J. I.	Army Materials & Mechanics Research Center	Watertown, MA	307
Bordenkircher, B.	FMC Corporation	San Jose, CA	203
Butler, T. W.	U. S. Naval Academy	Annapolis, MD	144
Cloud, G.	Michigan State University	East Lansing, MI	30
Corbly, D.	Air Force Materials Laboratory	Wright-Patterson Air Force Base, OH	30
Dally, J. W.	University of Maryland	College Park, MD	113
Finney, R. H.	Lord Kinematics	Erie, PA	103
Freese, C. E.	Army Materials & Mechanics Research Center	Watertown, MA	307
Grandt, Jr., A. F.	Air Force Materials Laboratory	Wright-Patterson Air Force Base, OH	63
ray, T. D.	Air Force Flight Dynamics Laboratory	Wright-Patterson Air Force Base, OH	63
Griffin, Jr., O. H.	Naval Surface Weapons Center	Dahlgren, VA	365
Gustafson, A. J.	Army Aviation R&D Command	Fort Eustis, VA	132
Hartenberg, R. S.	Northwestern University	Evanston, IL	5
Haskell, D. F.	Army Armament R&D Command	Aberdeen, MD	188
Hendriks, J.	FMC Corporation	San Jose, CA	203
Hopper, A. T.	Battelle-Columbus Laboratories	Columbus, OH	229
Howell, W. E.	NASA-Langley Research Center	Hampton, VA	167
Huffington, Jr.,N.J.	Army Armament R&D Command	Aberdeen, MD	323
Lenoe, E. M.	Army Materials & Mechanics Research Center	Watertown, MA	343
Lorber, S. J.	Army Materiel Development & Readiness Command	Alexandria, VA	9
Marschall, C. W.	Battelle-Columbus Laboratories	Columbus, OH	229
Moll, W. J.	Pennsylvania Electric Company	Johnstown, PA	229
Palmer, C. B.	Naval Surface Weapons Center	Dahlgren, VA	265
Parks, V. J.	The Catholic University of America	Washington, DC	113
Petty, J.	Army Armament R&D Command	Dover, NJ	215
Potter, J. M.	Air Force Flight Dynamics Laboratory	Wright-Patterson Air Force Base, OH	15

PRECEDING PAGE BLANK-NOT FILMED

AUTHOR (continued)

Ratwani, M. M.	Northrop Corporation	Hawthorne, CA	83
Reese, C. D.	University of Kansas	Lawrence, KS	167
Sanford, R. J.	Naval Research Laboratory	Washington, DC	113
Shea, R.	Army Materials and Mechanics Research Center	Watertown, MA	3
Shinozuka, M.	Modern Analysis, Inc.	Ridgeway, NJ	343
Skala, D. P.	Lord Kinematics	Erie, PA	103
Smith, S. H.	Battelle-Columbus Laboratories	Columbus, OH	229
Trott, B. D.	Battelle-Columbus Laboratories	Columbus, OH	215
Tsui, T.	Army Materials and Mechanics Research Center	Watertown, MA	285
Vanderveldt, H.	Naval Sea Systems Command	Washington, DC	10
Vaicaitis, R.	Modern Analysis, Inc.	Ridgeway, NJ	343
White, III, J. J.	Battelle-Columbus Laboratories	Columbus, OH	215